*Author:*
**Davison, Paul M**

*Title:*
**Development, modelling and control of a multi-degree-of-freedom dynamic wind tunnel rig**

# Development, Modelling and Control of a Multi-Degree-of-Freedom Dynamic Wind Tunnel Rig

Paul M. Davison, MEng

A thesis submitted to the University of Bristol in accordance with the requirements of the degree of Doctor of Philosophy in the Faculty of Engineering, Department of Aerospace Engineering.

Submitted: September 2003

Revised: December 2003

# Abstract

Dynamic wind tunnel testing is an important part of the development process of a new aircraft. Whilst computational aerodynamic methods continue to improve, they cannot yet predict the highly complex and non-linear flow phenomena that occur during manoeuvring flight at high angles-of-attack. This is particularly true for unconventional aircraft planforms, such as those of many emerging unmanned combat aerial vehicles. Dynamic wind tunnel testing is therefore needed to develop aircraft models and controllers for flight regimes where the flow becomes uncertain.

In this thesis a novel multi-degree-of-freedom dynamic wind tunnel rig is investigated. The model is unforced, therefore the support structure can be small and low cost. Actuated aerodynamic control surfaces on the model are used to generate arbitrary motions, which also means that their effect on the aircraft aerodynamics will be implicit in any derived aerodynamic models.

The rig described in this thesis, designed and built at the University of Bristol, exhibits interesting non-linear behaviour, even in a single degree-of-freedom. Regions of large-amplitude self-sustaining limit cycle oscillations have been found, with associated Hopf bifurcation points. A novel mathematical modelling approach is developed to allow the observed limit cycles to be accurately modelled.

Of particular concern in this thesis is the use of the rig for control law design. By simultaneously using a single rig for dynamic testing and control law design it is hoped that the cost and time spent in the aircraft development phase can be reduced. Several controllers are tested, using numerical simulations of mathematical models, and on the experimental rig itself. Suitability of the rig for full-scale control law development is discussed.

# Acknowledgements

I would like to thank my supervisors, Mark Lowenberg and Mario di Bernardo for their help, encouragement and support throughout the work carried out. I would also like to thank my family, especially my long-suffering mother, who bore the brunt when things were going badly, and again when they were going well. Thanks also to Tom Richardson for help and advice on control system design, Ian Roberts for continuous input on the theoretical side and Hilton Kyle for making the Hawk model used in the tests and helping with the experimental work. I would also like to thank Clare Fenwick, all the occupants of The Zoo, and British Airways for the spoon that stirred my coffee for 3 years.

This project was funded by the EPSRC, grant no. GR/M97923.

# Declaration

I declare that the work in this dissertation was carried out in accordance with the Regulations of the University of Bristol. The work is original except for the following:

- The BAe Hawk model documented in Chapter 3 and used throughout the thesis was built in conjunction with Hilton Kyle at the University of Bristol. The single degree-of-freedom gimbals were designed entirely by Hilton Kyle.
- Section 5.1 was written by Mark Lowenberg at the University of Bristol.
- Parts of Chapter 5 were written by Mario Di Bernardo at the University of Bristol.
- Chapter 9 documents work carried out in conjunction with Thomas Richardson at the University of Bristol.

No part of the dissertation has been submitted for any other degree. Any views expressed in the dissertation are those of the author and in no way represent those of the University of Bristol.

The dissertation has not been presented to any other University for examination either in the United Kingdom or overseas.

SIGNED.....Paul..... DATE.....10/1/04

# Contents

# List of Figures

# List of Tables

# List of Publications

1. P.M.Davison, M.H.Lowenberg and M.di Bernardo, 'Experimental Analysis and Modeling of Limit Cycles in a Dynamic Wind Tunnel Rig', *Journal of Aircraft*, 40(4):776–785, 2003.

2. P.M.Davison, M.di Bernardo and M.H.Lowenberg, 'Modelling Non-linear Behaviour in a Single Degree-of-Freedom Dynamic Wind Tunnel Rig', In *Proc. AIAA Atmospheric Flight Mechanics Conference*, Austin, Texas, 11th-14th August, 2003, AIAA-2003-5314.

3. P.M.Davison, M.di Bernardo and M.H.Lowenberg, 'Modelling and Control of a Single Degree-of-Freedom Dynamic Wind Tunnel Rig', In *Proc. European Control Conference*, Cambridge, 1st-4th September, 2003, Paper 597.

4. T.S.Richardson, P.M.Davison, M.H.Lowenberg and M.di Bernardo, 'Control of Non-Linear Aircraft Models using State-Feedback Gain Scheduling', In *Proc. AIAA Guidance, Dynamics and Control Conference*, Austin, Texas, 11th-14th August, 2003, AIAA-2003-5503.

# List of Abbreviations

| | | |
|---|---|---|
| AWG | = | American Wire Gauge |
| CG | = | Centre of Gravity |
| COTS | = | Commercial Off-The-Shelf |
| DFM | = | Direct Force Manoeuvre |
| DOF | = | Degree-Of-Freedom |
| EMF | = | Electro-Motive Force |
| HHIRM | = | Hypothetical High-Incidence Research Model |
| LQG | = | Linear Quadratic Gaussian |
| LQR | = | Linear Quadratic Regulator |
| MCS | = | Minimal Control Synthesis |
| NAL | = | National Aerospace Laboratory (Japan) |
| NASA | = | National Aeronautics and Space Administration (USA) |
| NDI | = | Non-linear Dynamic Inversion |
| PD | = | Proportional plus Derivative |
| PID | = | Proportional plus Integral plus Derivative |
| PIO | = | Pilot Induced Oscillation |
| PSI | = | Pounds per Square Inch |
| PSR | = | Pendulum Support Rig |
| PST | = | Post-Stall |
| PWM | = | Pulse Width Modulation |
| RMS | = | Root Mean Square |
| TsAGI | = | Central Aerohydrodynamic Institute (Russia) |
| UAV | = | Unmanned Aerial Vehicle |
| UCAV | = | Unmanned Combat Aerial Vehicle |
| VTOL | = | Vertical Take-Off and Landing |

# Nomenclature

| | | |
|---|---|---|
| $\boldsymbol{A}$ | = | linear state matrix (Jacobian) |
| $\boldsymbol{A_{cl}}$ | = | closed-loop linear state matrix |
| $A$ | = | limit cycle amplitude |
| $A_u$ | = | parameter of the tanh function (Fig. 5.3) |
| $\boldsymbol{B}$ | = | linear input matrix |
| $B$ | = | exponential growth or decay rate |
| $\bar{c}$ | = | aircraft mean aerodynamic chord |
| $\boldsymbol{C}$ | = | linear state-output matrix |
| $C$ | = | constant |
| $C_d$ | = | aircraft drag coefficient |
| $C_l$ | = | aircraft lift coefficient |
| $C_m$ | = | aircraft pitching moment coefficient |
| $\boldsymbol{f}$ | = | smooth non-linear system |
| $\boldsymbol{g}$ | = | smooth non-linear system |
| $I$ | = | aircraft pitch moment of inertia |
| $\boldsymbol{J}$ | = | Jacobian |
| $\boldsymbol{K}$ | = | gain matrix |
| $K$ | = | growth/decay rate of tanh function |
| $K$ | = | static (input-scheduled) gain |
| $N$ | = | number of sub-intervals |
| $q$ | = | $\dot{\theta}$ = aircraft pitch rate |
| $\hat{q}$ | = | $\dot{\hat{\theta}}$ = estimated aircraft pitch rate |
| $r$ | = | reference demand |
| $S$ | = | aircraft wing surface area |

$t$ = time

$T$ = time interval

$\boldsymbol{u}$ = vector of inputs

$V$ = aircraft velocity (tunnel velocity)

$\boldsymbol{V}$ = set of system eigenvectors

$\boldsymbol{x}$ = vector of system states

$x$ = system state

$x_{int}$ = integrator state

$x_0$ = system initial condition

$x_n$ = system state at time-step $n$

$\dot{x}$ = time derivative of $x$

$\mathbf{x}^*$ = equilibrium state value

$\alpha$ = aircraft angle-of-attack

$\alpha$ = MCS adaption weight

$\beta$ = MCS adaption weight

$\gamma$ = longitudinal pendulum strut angle

$\delta_c$ = symmetrical all-moving foreplane deflection

$\delta_e$ = symmetrical horizontal tailplane deflection

$\boldsymbol{\delta}$ = vector of parameters

$\Delta = \frac{1}{2}(A_u - A)$ = parameter of the tanh function (Fig. 5.3)

$\eta$ = elevator deflection

$\theta$ = aircraft pitch angle to horizontal (angle-of-attack)

$\theta_{demand}$ = pitch angle reference signal

$\hat{\theta}$ = estimated pitch angle to horizontal

$\dot{\theta} = q = \frac{\mathrm{d}\theta}{\mathrm{dt}}$ = aircraft pitch rate

$\dot{\hat{\theta}} = \hat{q}$ = estimated model pitch rate

$\ddot{\hat{\theta}}$ = $\dot{\hat{q}}$ = estimated model pitch acceleration

$\lambda$ = system parameter (continuation parameter)

$\Lambda$ = set of system eigenvalues

$\mu$ = vector of system parameters

$\mu^*$ = equilibrium parameter value

$\rho$ = air density

$\sigma(J)$ = eigenstructure of $J$

$\phi$ = phase angle

$\phi$ = dynamic (state-scheduled) gain

$\boldsymbol{\phi}$ = state-scheduled gain matrix

$\bar{\phi}$ = state-scheduled look-up table

$\chi$ = longitudinal pendulum strut angular velocity

$\omega$ = limit cycle frequency

$\dot{}$ = time derivative

# Chapter 1

# Introduction

## 1.1 Motivation

For aircraft to gain a tactical advantage in close-combat aerial scenarios it is desirable to have superior manoeuvrability [1]. Increased manoeuvrability requires high rates of change of motion variables which, when occurring at large angles of attack and sideslip, produce strong coupling between aerodynamics, inertial terms and control surface deflections, and a strong dependence on frequency and amplitudes of motions. This coupling is, as yet, impossible to predict using analytical or computational means in all but the simplest cases, hence some form of sub-scale testing is required.

Dynamic wind tunnel test rigs can take many forms [2, 3]. Most are of the direct forced type which produce constant rotation or sinusoidal oscillations about a single axis. In order to allow large models to be tested the support structures and drive systems are usually large, which increases the cost of performing such tests. Moreover, as the oscillations/rotations are usually about a single axis at a time, it may be necessary to use several different rigs to obtain a full set of dynamic derivatives [4].

Ongoing work at the University of Bristol to develop a multi-axis unforced wind tunnel rig, the Pendulum Support Rig (PSR) [5, 6, 7], hopes to address some of the problems associated with obtaining dynamic derivatives, most notably complexity and cost. The rig is multi-purpose in nature; it can be used for aerodynamic modelling (where periodic and arbitrary motions can be generated), and control system design and evaluation using

active control surfaces. It is envisaged that the rig will allow possible integration of the aerodynamic modelling and control system design cycles, during the aircraft development phase, into a single parallel process.

## 1.2 Objectives

This thesis reports the development and analysis of a PSR at the University of Bristol for control law design and evaluation. The aircraft model is shown to exhibit some interesting non-linear behaviour, even in a single degree-of-freedom. Coupling between the aircraft model and pendulum support structure has also been shown to display some interesting non-linear dynamics.

A novel modelling approach is developed to allow the dynamics of the system to be accurately represented and permit off-line synthesis of control laws. The objective is to demonstrate the feasibility of using wind tunnel models to develop and evaluate control laws for high-performance aircraft, and capture some of their non-linear dynamic behaviour.

## 1.3 Thesis Layout

In Chapter 2 some background to the project is given, and a brief overview of current research literature presented. This includes motivation for high angle-of-attack ($\alpha$) flight, a brief description of high-$\alpha$ phenomena, control system background, an outline of the non-linear dynamics and bifurcation theory used in later chapters and a comprehensive overview of dynamic wind tunnel testing methods used to date. A brief history of the pendulum support rig apparatus is also presented.

Chapter 3 describes the experimental apparatus and testing methods used. An outline of the PSR developed at the University of Bristol is given, including custom gimbal and counterbalance design. The aircraft model (a $1/16^{th}$ scale BAe Hawk), constructed specifically for the PSR at the University of Bristol, is then described in detail. The control surface actuators used in the model are described, and actuation requirements

discussed. Several off-the-shelf servo actuators are then tested for performance characteristics (bandwidth, accuracy, etc.) as a benchmark of the current situation in low-cost actuation. Using the data from these tests an accurate mathematical model of the Hawk model control surface actuators is derived. The dSPACE system used for real-time data acquisition and control is then described. Finally, specifications of the wind tunnel facilities at the University are given.

Chapter 4 presents experimental results taken from the PSR in one and two degrees-of-freedom. The model displays some interesting non-linear behaviour in the form of limit cycle oscillations and associated Hopf and cyclic fold bifurcations. Experimental bifurcation diagrams are constructed to clearly show the global dynamics of the system. Experimental phase-plane plots and time histories are then used to clarify the observed dynamics. Some preliminary open-loop results are also presented for the model in a single degree-of-freedom with all-moving foreplanes.

Having identified the non-linear characteristics of the rig experimentally, in Chapter 5 an approach to modelling the observed dynamics is sought. A brief background of traditional techniques for modelling limit cycle oscillations in the aerospace field is then given, and shortcomings discussed. A new, more accurate method of developing a traditional non-linear aerodynamic model is then presented; this model represents the observed experimental behaviour of the rig. Experimental results such as the bifurcation diagram, limit cycle amplitudes and frequencies are used explicitly in formulating the model. Representative examples are presented to demonstrate the method, before parameter estimation is used to formulate a full-envelope mathematical model of the wind tunnel rig.

In Chapter 6, the mathematical model derived using the technique in Chapter 5 is validated against experimental results and found to give good agreement. The model is then analysed, and three-dimensional pitching moment surface plots at different tailplane deflections presented. Further time simulations of the model (open-loop) are shown. Finally, possible extensions to the model are discussed and conclusions about the modelling method drawn.

Having developed and verified an accurate model of the wind tunnel rig, some preliminary classical feedback control laws are then designed in Chapter 7. Firstly, the control objective is defined in terms of eigenvalue placement and time response, derived from

scaled handling qualities requirements. Pitch rate feedback alone is then used to stabilise the limit cycle oscillations before feed-forward and PID controllers are developed. Good closed-loop agreement is shown between theoretical control system performance in numerical simulations and experimental time histories, validating the use of the mathematical model for control system design.

In Chapter 8, two non-linear control methods are used to design controllers for the rig. Closed-loop response is tested using numerical simulations of the mathematical model, before being demonstrated on the experimental rig. The first controller is formed by scheduling state feedback gains designed using linearisations of the model at a set of operating points along the trim curve. Various forms of this controller are tested using numerical simulations, and in general are shown to work well. An adaptive controller is then tested via simulation, requiring no set-up time, and is shown to perform adequately.

The controllers outlined above are then tested on the experimental rig. Interestingly, the results do not show good agreement with the numerical simulations, and probable causes for the discrepancies are given and discussed. Recommendations are made for future projects to avoid the issues and problems found.

Chapter 9 presents the results of preliminary work on dynamic gain scheduling. The problems associated with classical gain-scheduled control are discussed, and a possible solution presented. Analytical examples are given, before the controller is tested on the mathematical model of the Hawk in a single degree-of-freedom. Ideas for future research are then discussed.

In Chapter 10, a brief summary of the work carried out in this thesis is given, while drawing conclusions from the results. A number of recommendations for researchers undertaking similar work are then given (mainly on the experimental side), based on the lessons learned during the research. Finally, areas of interesting future work are outlined, to provide a starting direction for follow-on projects.

# Chapter 2

# Background

In this chapter, motivation for the work undertaken in this thesis is presented and a brief review of previous work in the area is described. The long-term objective is to develop a method for simplifying, enhancing and increasing the speed of control law development for high-performance aircraft. This has become an area of particular interest recently due to the large expense (in terms of both time and money) traditionally incurred during this phase of the aircraft design process. Background of the non-linear dynamics theory used in this thesis is presented, and a high-level overview of control strategies given. A review of current dynamic wind tunnel testing methods is documented, and a brief history of the experimental rig proposed to overcome some of the traditional problems presented.

## 2.1 Motivation for Reducing Aircraft Procurement Time

There is a large change currently occurring in the type and role of high-performance aircraft. This change is being brought about by the introduction of Unmanned Aerial Vehicles (UAVs). UAVs have been used for many years for high-altitude surveillance, but their use is becoming more widespread, and their role is changing from passive (observing) to active (engaging targets) with the introduction of Unmanned Combat Aerial Vehicles (UCAVs). The development of UCAVs will not only change the way

aerial wars are fought, but will also change the entire aircraft development process. This is due to several factors:

- the major advantage of UAVs and UCAVs is that they are seen to be 'disposable'. This means that they can be used in situations where it is deemed too hazardous to send a manned aircraft (to eliminate anti-aircraft positions, for example). This will inevitably force the purchase price down, as an extremely expensive UAV effectively negates the main advantage of an unmanned aircraft.

- the 'disposable' view of UAVs will decrease the overall life cycle of the aircraft, due to less investment in airframe, support, spares, etc. Demand for new aircraft (utilising the latest technology) will rise, bringing about a major reduction in development time (plus an increased use of Commercial Off-The-Shelf (COTS) components).

- a decrease in development time, and the amount of money that can be spent during this phase, will mean that the development process will have to be streamlined. This will cause processes to be run in parallel, and facilities and testing time minimised.

- a further advantage of UAVs is the increased performance possible due to the lack of pilot constraints ('g' limits). This will bring about a large change in the performance of future air vehicles. Controlled flight at extremely high angles-of-attack and with high rates of change of motion variables will be necessary. With an added trend towards low-observable planforms this will pose a big challenge for aerodynamicists and control engineers.

- flying qualities assessment will no longer be necessary for UAVs, eliminating the need for much control system work (e.g. PIO prevention, handling qualities assessment, etc.). There may, however, still be some performance requirements that must be met by the controllers.

- tentative exploration of the flight envelope during flight tests can be replaced with a more 'bottom up' approach, where it is acceptable if a few inexpensive (sub-scale) prototypes are lost during initial flights. This will drastically cut the time and cost associated with flight testing.

- as well as the use of COTS components, it will be possible to use immature technologies without associated risk to the pilot. For example, new materials, power plants, control effectors, etc., as well as control systems and techniques for control system development that cannot currently be used on manned aircraft.

The decreasing trend in procurement time[1] will no longer permit long periods of cyclic aerodynamic refinement followed by theoretical development of control laws on the detailed aerodynamic model, as performed currently [9]. The processes will have to be performed in parallel, and automated where possible. It is ultimately foreseeable that large parts of the design process can be eliminated completely, for example, generation of a detailed aerodynamic model.

Many of the techniques that will be developed for reducing the design time of highly manoeuvrable aircraft, once mature, will filter into the civil and transport aircraft sectors.

## 2.2 Non-Linear Aircraft Dynamics

Conventional aircraft flying at low angle-of-attack display predominantly linear dynamics. This is not the case, however, at high-$\alpha$, where turbulent and vorticial flow causes time dependencies, hysteresis, limit-cycle oscillations, etc. Non-linearities at high-$\alpha$ are predominantly caused by the aerodynamics (e.g. asymmetric vortex shedding, unpredictable turbulent flow, etc.) but may also be caused by inertial effects (e.g. during velocity-vector rolls). Much of the design phase of an aircraft and control system is spent looking at this relatively small part of the flight envelope.

Flight at high-$\alpha$ is necessary to minimise aircraft turn radius (to get behind an opponent first), allow an aircraft to obtain a firing position whilst still manoeuvring, or evade an incoming threat. The requirement for flight at very high angles-of-attack was formally established by Herbst in the early '80s [1, 10]. Herbst defined 'super-manoeuvrability' and post-stall (PST) capabilities[2], and demonstrated (using manned and unmanned

[1] Current procurement times for new, high-performance aircraft are in the order of 15 years (see, for example, [8]), which means many components (particularly the avionics) may be obsolete before the aircraft even enters service.

[2] PST: the 'ability of the aircraft to perform controlled tactical manoeuvres beyond maximum lift angle-of-attack up to at least 70 degrees'.

simulations) that a suitably designed aircraft with PST capabilities would win 5 out of 6 engagements against a threat of identical conventional performance. Herbst also defined direct force manoeuvre (DFM) capability as 'the ability of the aircraft to yaw and pitch independently of the flight path, or to manoeuvre at constant fuselage attitude', and identified digital fly-by-wire control systems as a key technology for performing PST manoeuvres.

With the development of medium and long-range weapons it is possible to predict a decline in the need for aircraft to enter close-in-combat scenarios [10], however, due to stealth aircraft, threat evasion and the need for visual identification of targets there is still a requirement for superior manoeuvrability [10, 11, 12].

Knowledge of the aerodynamic phenomena that occur at high-$\alpha$ has grown to the point where most of the observed dynamics can be generalised into specific groups, and even attributed to certain aircraft configurations. One common theme with most lateral-directional high-$\alpha$ phenomena is extreme sensitivity to configuration. For example, the two (identically designed) Enhanced Fighter Manoeuvrability (EFM) demonstrators described in [11] showed a large difference in yawing moment at high-$\alpha$ (above 40°). Aircraft Number 1 showed a consistent negative yawing moment as $\alpha$ increased, however, Aircraft Number 2 exhibited a random variation with $\alpha$. The difference in response was attributed to the effect of extremely small variations in geometry on the asymmetric flowfield.

One high-$\alpha$ phenomenon is of particular relevance to this thesis: wing rock. Wing rock is a large amplitude lateral-directional stable limit cycle oscillation occurring at moderate-to-high angles of attack where the vertical tail(s) becomes immersed in the wake of the fuselage/wing. It has been attributed to the Dutch roll mode becoming unstable, and is usually predominant in roll. Slender delta wing aircraft are particularly susceptible to wing rock due to aerodynamic lags associated with vortex lift at high $\alpha$ [13]. Whilst there are longitudinal equivalents to wing rock (called 'bucking' or 'porpoising') which may be of more direct relevance to this thesis, these are less common and as such there has been less work in this area (see Section 5.1). There has, however, been a significant amount of work carried out on wing rock (e.g. [14, 15, 16]); a more detailed review is given in Section 5.1.

## 2.3 Non-Linear Dynamics and Bifurcation Analysis

The mathematical discipline of non-linear dynamics theory has provided a useful tool for the analysis of aircraft dynamics at high angle-of-attack. Non-linear dynamics is a relatively new research area, but has received a vast amount of attention due to its application in just about every field from biology to engineering. There are now many methods and tools for understanding and analysing the complicated dynamics that often arises, even from simple systems. Many references are available on the subject of non-linear dynamics and bifurcation analysis (e.g. [17, 18, 19, 20, 21]).

Application of bifurcation analysis to aircraft dynamics began in the late 1970s [21]. Since then, bifurcation theory has been used in many aircraft applications [17, 18, 22, 23, 24, 25, 26, 27, 28], including the use of bifurcation diagrams as 'road-maps' to aid flight tests in piloted simulations [29]. Many early applications analysed the open-loop dynamics, but the same techniques have since been applied to closed-loop aircraft models (e.g. [17, 30, 31]). A relatively small amount of research has also been carried out into using bifurcation analysis to aid the control law design process [18, 32, 33].

### 2.3.1 Bifurcations

A bifurcation occurs when there is a qualitative change in the system dynamics as a system parameter is varied. In general terms, this means that the stability of a steady state solution, or the number of solutions, has changed. A bifurcation can also be defined as one or more eigenvalues of the Jacobian crossing the imaginary axis (with non-zero speed) as the continuation parameter is varied.

Figure 2.1 shows an example 1-parameter *bifurcation diagram* (using the standard line-type conventions outlined in Table 2.1). A bifurcation diagram shows the steady-state solutions of a dynamical system for a range of quasi-static values of a system parameter (known as the 'continuation parameter'). Bifurcation diagrams are generated using numerical continuation methods, described in Section 2.3.2. 2-parameter bifurcation diagrams, showing a surface of solutions, may also be useful for analysing the system dynamics [17, 21].

Two types of bifurcations are of particular relevance to this thesis: the fold bifurcation and the Hopf bifurcation. These will now be described in more detail. For information on the multitude of other bifurcations see, for example, [17, 18, 19].

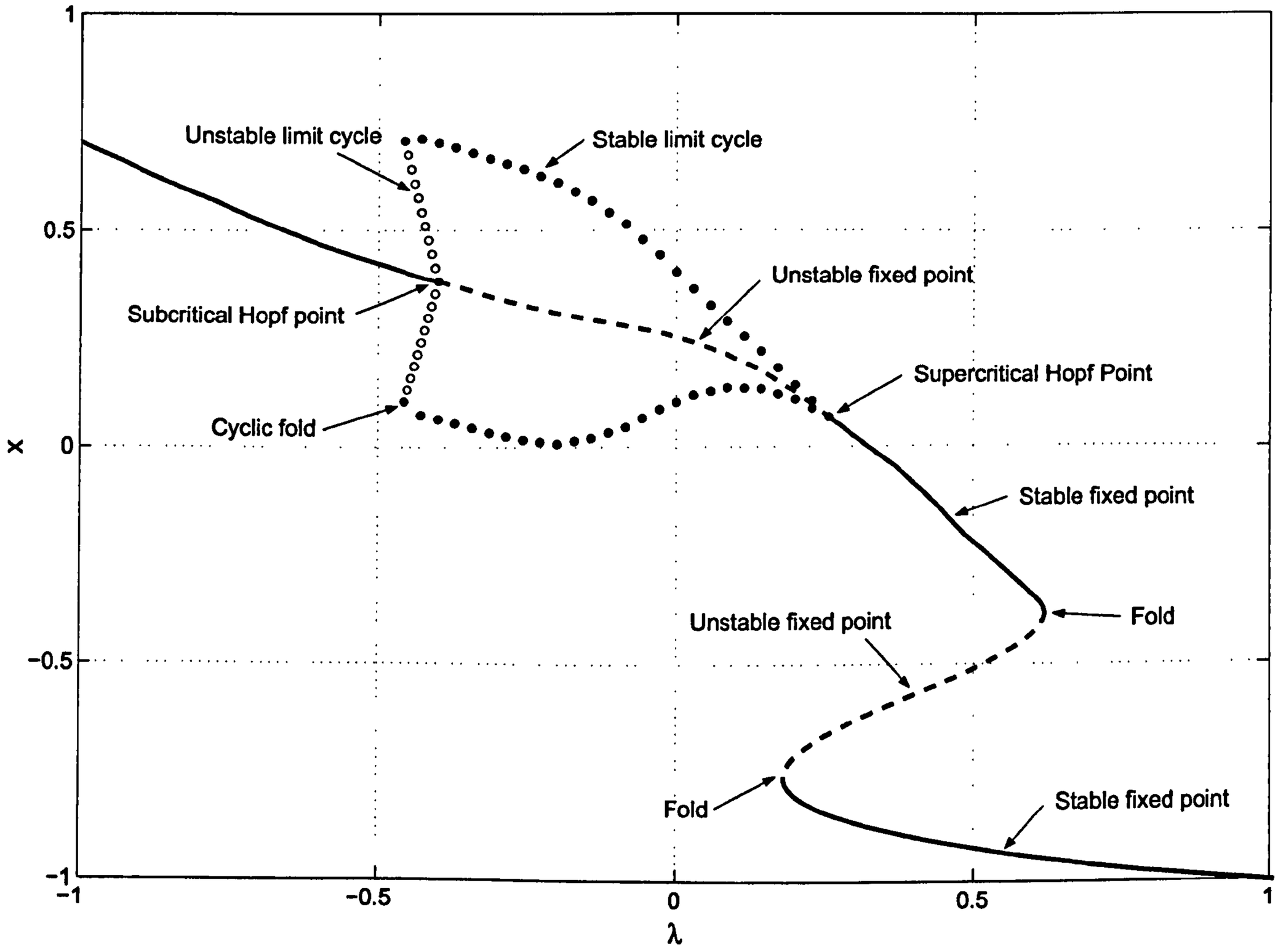


Figure 2.1: Example of a 1-parameter bifurcation diagram.

Table 2.1: Standard line-type conventions for bifurcation diagrams.

| **Steady State** | **Line Type** |
|---|---|
| Stable fixed point | Solid line |
| Unstable fixed point | Dashed line |
| Stable limit-cycle | Filled circles |
| Unstable limit-cycle | Open circles |

### Fold Bifurcation

Fold bifurcations (also known as *saddle-node*, *limit-point* or *turning-point* bifurcations) occur when two steady-state solutions meet and mutually annihilate under smooth parameter variation (see Figure 2.1, $\lambda \approx 0.2$ and $\lambda \approx 0.65$). In this manner, the fold bifurcation is the principle phenomenon by which steady-state solutions of a system are created and destroyed. After a fold bifurcation there is no longer a local attractor, so the system will 'jump' to the nearest steady-state solution. In terms of eigenvalues, a fold bifurcation occurs when a single real eigenvalue crosses the imaginary axis. Fold bifurcations can also occur for periodic orbits - in this case the bifurcation occurs when a Floquet multiplier of the system (an eigenvalue of the linearised Poincaré map [19]) passes through the unit circle at $+1$.

### Hopf Bifurcation

A Hopf bifurcation occurs when a complex pair of eigenvalues cross the imaginary axis and involves the creation or destruction of periodic solutions. There are two main types of Hopf bifurcation: supercritical and subcritical[3]. A supercritical Hopf bifurcation occurs when a stable fixed point changes to an unstable fixed point surrounded by a stable periodic solution: a limit cycle (see Figure 2.1, $\lambda \approx 0.25$). A subcritical Hopf bifurcation occurs when a stable fixed point surrounded by an unstable limit cycle changes to an unstable fixed point - the system will then jump to the nearest attractor (Figure 2.1, $\lambda \approx -0.4$). The subcritical Hopf bifurcation, like the fold bifurcation, is potentially dangerous due to this jump-type behaviour. Another common feature of systems exhibiting subcritical Hopf bifurcations is hysteresis.

## 2.3.2 Numerical Continuation

An extremely useful tool in the area of non-linear dynamics is continuation. This is a mathematical process by which the steady state behaviour of a system can be studied

[3]A third type of Hopf bifurcation exists: the *degenerate Hopf bifurcation*. This occurs when a stationary equilibria changes stability. However, this is not a true Hopf point as the closed orbits around the fixed point are not isolated [19].

as the continuation parameter is varied. There are many references on continuation methods (e.g. [17, 18, 19]) and several continuation programs available (e.g. AUTO97 [34], CONTENT [35], PCS [36], KRIT), however, a brief overview of the process will be given here.

Normally, for analysis purposes, an $n^{th}$ order non-linear system is split into $n$, first-order autonomous differential equations of the form:

$$\dot{\mathbf{x}} = \mathbf{f}(\mathbf{x}, \mu) \qquad \mathbf{x} \in \mathbb{R}^n, \mu \in \mathbb{R}^m \tag{2.1}$$

where $\mathbf{x}$ is the state vector, $\mu$ is a vector of parameters, and $\mathbf{f}$ is a sufficiently smooth[4] function $\mathbf{f} : \mathbb{R}^n \times \mathbb{R}^m \rightarrow \mathbb{R}^n$. Assuming that $\lambda \in \mathbb{R}$ is one element of $\mu$ and becomes the continuation parameter, and that all other parameters in $\mu$ remain fixed, numerical continuation is the process by which the equilibria of (2.1) are traced out as $\lambda$ is varied, i.e. the set of points such that:

$$\mathbf{f}(\mathbf{x}, \lambda) = 0 \tag{2.2}$$

The asymptotic behaviour of the system may be stationary fixed points as in (2.2) above, but could equally be bounded periodic oscillations known as *limit cycle oscillations*, i.e. solutions $\mathbf{x}(t)$ such that:

$$\mathbf{x}(t + T) = \mathbf{x}(t) \tag{2.3}$$

where $T$ is the period of the limit cycle.

Continuation methods make use of the Implicit Function Theorem, which states that if the Jacobian matrix, $\mathbf{J}$, of $\mathbf{f}$ at an equilibrium point, $(\mathbf{x}^*, \mu^*)$, is non-singular (i.e. has no eigenvalue with zero real part) then the equilibrium solution $(\mathbf{x}^*, \mu^*)$ is locally unique; part of a unique continuous curve of solutions. This means that if the continuation parameter is varied smoothly, a smooth curve of equilibria will be traced out, until the Jacobian becomes singular (a bifurcation point). The type of bifurcation can be determined from the location and number of eigenvalues crossing the imaginary axis (relying on the Centre Manifold Theorem, see e.g. [18, 19, 21]). For example, in simple terms, a single real eigenvalue crossing indicates a fold bifurcation; a complex pair crossing indicates a Hopf bifurcation to a limit cycle, etc.

Usually, some sort of predictor-corrector algorithm is used by continuation packages to follow solution branches [17, 18]. Given a starting solution, a successive solution can

[4] In this context, smooth means that $\mathbf{f}$ has at least a continuous first derivative.

be found by incrementing the state in a certain direction (found using $\frac{\partial \mathbf{f}}{\partial \lambda}$). A suitable corrector method (e.g. Newton's method) is then used to reduce the error between the approximation and actual solution. By adding extra columns ($\frac{\partial \mathbf{f}}{\partial \lambda}$) to the Jacobian at a singularity (where the rank of the $n \times n$ Jacobian matrix, $\mathbf{J}$, is less than $n$) it is possible to continue through a bifurcation point and carry on tracing out solutions on the other side. This method is described in more detail in, for example, [17].

Generating starting solutions is one of the difficulties with continuation methods. Often, it is possible to use prior knowledge of the system to get an initial solution (e.g. that at zero elevator deflection and for zero angular rates, the angle-of-attack will be, say, 2°). It may also be possible to use time simulations of the system, if run for long enough to allow transients to decay, to find *stable* starting solutions. If these methods are not possible, a set of initial conditions can be used by trial-and-error to begin the continuation. However, only in very simple non-linear systems is it possible to guarantee that all solution branches have been found.

## 2.4 Control

Since the introduction of basic autopilots by Orville Wright in 1913, and the use of gyroscopic stabilisation by Lawrence Sperry shortly after, aircraft control systems have dramatically grown in complexity. From their first use to provide basic autopilot functions, they were soon being used to enhance the handling qualities of aircraft by significantly changing the dynamics. This eventually lead to aircraft being made open-loop unstable (neglecting the fact that the Wright Brothers' original aircraft were also open-loop unstable) to improve agility and/or performance (e.g. General Dynamics F-16) and, with the use of flight control computers, has greatly expanded the flight envelope of modern high-performance aircraft. As flight control systems have become more complex, the amount of time taken to develop them has also risen. Fortunately for the aircraft industry there is a wealth of control system theory available, and a plethora of different control strategies, that can be applied to aircraft control problems.

There are many possible definitions of a control system, ranging from vague to highly technical. Few control engineering text-books actually offer a concise definition; most

jump straight to fluid level regulation, steam engines and block diagrams. In [37], the authors offer the following:

> "The *control system* is that means by which any quantity of interest in a machine, mechanism or other equipment is maintained or altered in accordance with a desired manner."

No attempt will be made here to describe the history and evolution of modern control theory; there are many texts which include introductory chapters on this topic (e.g. [37, 38, 39]). However, a brief overview of the main control methods will be given.

### 2.4.1 Classical Control

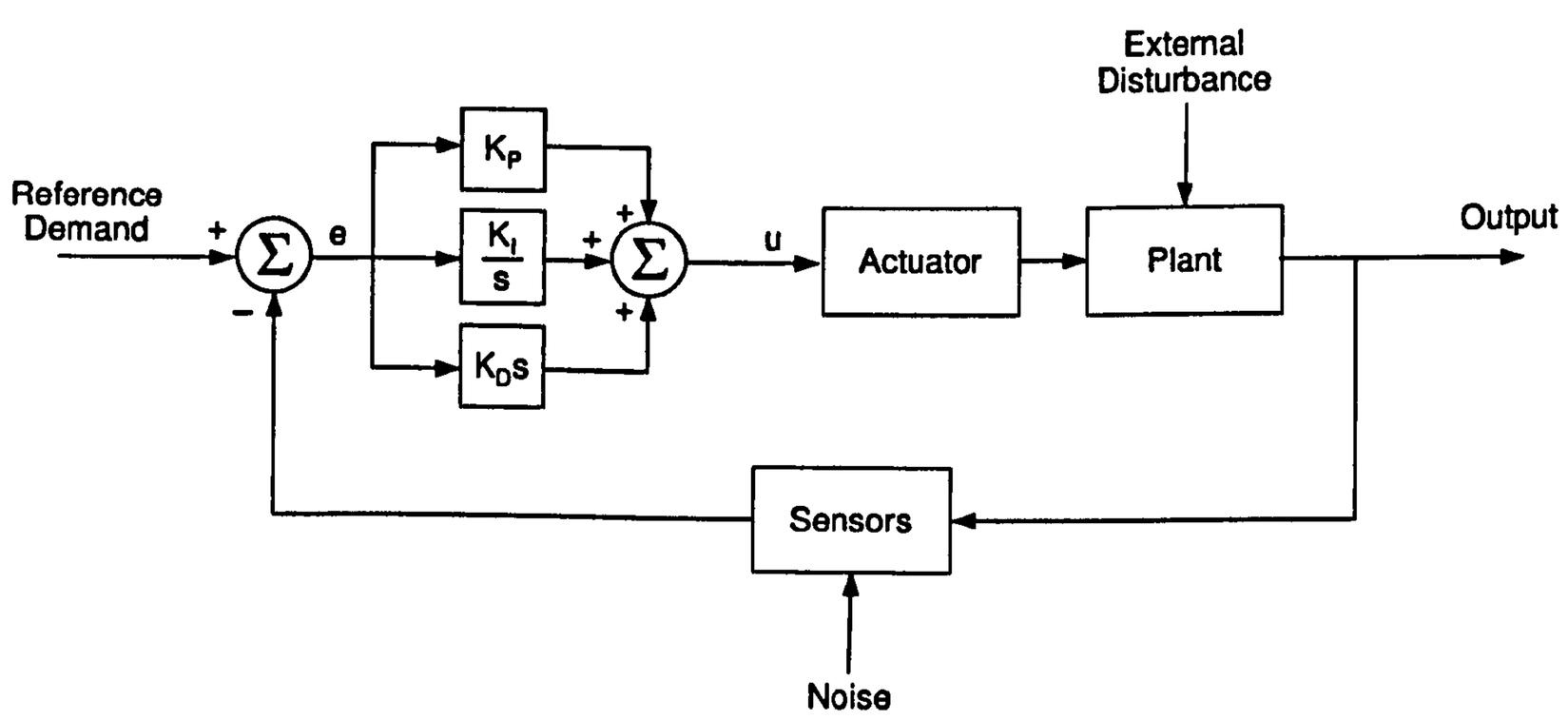


Figure 2.2: Classical PID controller.

Classical control refers to linear control of a plant, or a linearised model of the plant, using standard Proportional, Integral and Derivative (PID) means. The block diagram of a general PID controller is given in Figure 2.2, with corresponding control equation being given as:

$$u = K_P \times e + K_I \times \int e\,dt + K_D \times \frac{de}{dt} \tag{2.4}$$

Suitable filters may be included on the reference demand and/or sensed variables.

In a large proportion of cases a classical approach will yield acceptable performance. Improvements may be made by using other forms of controller (gain scheduled, robust, adaptive, etc.), but often the improvements will be small and involve a substantial increase in development time. For example, in [40], four different controllers (classical, LQR, dynamic inverse and $H_\infty$) are evaluated on a lateral/directional model of the KC-135 military transport aircraft, using a common set of dynamic response criteria. It is found that, in general, the controllers give comparable performance in terms of response and robustness.

One area where classical fixed-gain control may not provide acceptable performance is where the plant to be controlled is highly non-linear. This is often the case for highly-manoeuvrable aircraft, where the dynamics vary significantly with angle-of-attack. It is common practice in these scenarios to take several controllers, designed using classical techniques about different operating conditions, and interpolate between them to form so-called 'gain-scheduled' controllers (see Section 2.4.6). However, there are limitations and non-linearities introduced by the scheduling process, which must be taken into consideration for performance to be maintained.

Classical fixed-gain PID controllers are investigated numerically and experimentally in Chapter 7.

### 2.4.2 Robust Control

Robustness issues, in the context of feedback control, can occur for many different reasons. Errors between a plant and its mathematical model (used for control system design) are a major test of the robustness of a controller, and can be caused by degradation of components, linearisation errors, parameter estimation inaccuracies, simplification assumptions, etc. Robust controllers are designed to continue to meet performance criteria when faced with plant parameter and/or operating condition variations, and in the presence of uncertainties such as noise. This is usually incorporated into the control system design process by considering a 'family' of plant models that will allow for all likely variations. If a controller can be designed which will meet performance criteria under all foreseeable plant variations, the controller has robust stability.

Robust methods are of great interest to aircraft control engineers, predominantly due to

the large parameter and operating condition variations that can occur during flight. Of particular interest is $H_\infty$ multivariable robust control. $H_\infty$ loop-shaping is a linear control design method by which the peak magnitude of a closed-loop Bode plot is minimised. One attraction of this control method is the existence of many computer-based techniques for iteratively solving the control problem. $H_\infty$ loop-shaping has been used in many numerical and practical aeronautical applications (e.g. [41, 42, 43, 44]), including its use in wind tunnel aircraft control experiments [45].

### 2.4.3 Optimal Control

Optimal control strategies attempt to design controllers that take the system from its current position to a desired position in some optimal manner. A key idea in the use of optimal control is the 'performance index' or 'cost function'. This is used as a measure of the controller performance, and defines quantities which are to be minimised by the controller, e.g. time taken, fuel expended, distance travelled, control energy used, etc. Optimal control methods aim to place the system eigenvalues at locations that minimise a given cost function. Therefore, the choice of closed-loop pole location is replaced by the choice of a suitable cost function, and the weightings of individual performance elements. A more rigorous introduction to optimal control may be found in [38].

One popular optimal control design strategy is the Linear Quadratic Regulator (LQR). With this method, the cost function (defined as $Q$ and $R$ matrices: the weighting on the states and control input respectively) is minimised explicitly by the controller. The QR method can be expanded to take into account the presence of Gaussian-distributed noise (LQG control), and often involves the use of state estimators or Kalman filters. In [40], the LQR method is used to design a lateral/directional controller for the KC-135 transport aircraft to meet the desired handling qualities while minimising actuator usage.

### 2.4.4 Dynamic Inverse Control

The control strategies described above are all linear techniques. They rely on linear plant dynamics to deliver theoretical performance and/or robustness in practice. However, all

real dynamical systems are non-linear to some extent, therefore there is a need to cope with these non-linearities when designing controllers.

Dynamic inversion is a non-linear control scheme based on the ability to find the inverse of the plant equations. By calculating this inverse it is possible to find the plant input which will give a desired plant output. In the aircraft case, this involves inverting the three translational equations of motion, and the three rotational equations (all of which are non-linear). This is described in more detail in [46], for example. By inverting the equations, the plant is effectively being exactly linearised, without using traditional linear local approximations [47]. One concern of the dynamic inverse approach is the accuracy of the original plant model, and the robustness of the resulting controller to parameter variations.

Non-linear Dynamic Inversion (NDI) has been applied to many aeronautical control applications. In [46] 'exact' NDI is applied to a high-incidence non-linear combat aircraft model and provides 'ideal' control up to 60° angle-of-attack. In [44] NDI is used in conjunction with robust linear control strategies (differential-game approach and $H_\infty$ loop-shaping) to control a high-fidelity UH-60A helicopter model. A PD controller is also used with the non-linear inverse technique, and found to give good results when tested on the Vertical Motion Simulator at NASA Ames Research Center. In [27], NDI is incorporated into a continuation method to allow complex, coupled equations to be inverted explicitly. This method is demonstrated on a $5^{th}$ order model of the 'Hypothetical High-Incidence Research Model' (HHIRM).

### 2.4.5 Bifurcation Tailoring

Bifurcation tailoring.is a method that uses feed-forward and feedback controllers to alter a system bifurcation diagram to some given desired one. This is achieved using bifurcation analysis to create feed-forward control signals (to alter the shape of the bifurcation diagram) and some form of feedback control (to alter the stability of solution branches). In its original form, bifurcation tailoring involves altering the system bifurcation diagram by appropriately varying other control parameters, in addition to the continuation parameter. This can be done in an open-loop form only – i.e. bifurcation analysis is used to find feed-forward gains that will alter the bifurcation diagram as desired [48].

However, this does not guarantee stability or uniqueness of solutions, therefore feedback control is often added as well (e.g. [49]).

Bifurcation tailoring was originally developed for aircraft applications. In [32, 50] bifurcation tailoring is applied to the $5^{th}$ order HHIRM model, using an adaptive control strategy to stabilise the solution branches. The same structure is used in [51] to control the longitudinal dynamics of the HHIRM, and also in [52], but using a Newton method for finding the feed-forward schedule, rather than a numerical continuation package such as AUTO97. In [53] a continuation design framework is used to tailor the bifurcation diagram of the $5^{th}$ order HHIRM using eigenstructure assignment. In this thesis, bifurcation tailoring is applied both numerically and experimentally (for the first time) in Chapter 8.

### 2.4.6 Gain Scheduled Control

Although there are earlier efforts on record, gain scheduling began in earnest toward the end of the Second World War to overcome difficulties controlling the new, high performance jet aircraft [54]. By the mid 1950s, analogue gain scheduling was being implemented in many different military applications, including missile guidance systems and autopilots for the B-52. The use of gain scheduling in civil applications, both in aerospace and other areas (e.g. automatic process control), did not arise until digital computing reduced the otherwise prohibitive implementation costs. Recently, there has been an increase in research activity on gain scheduling, and there are now many references in the field (e.g. [41, 42, 55]).

The term 'gain scheduling' encompasses a broad range of control strategies. A simple gain pre-compensator can be viewed as a form of gain scheduling, while gain scheduling itself can be classified as a form of open-loop adaptive control [38, 54]. For the purposes of this thesis, gain scheduling is defined as the process of sub-dividing a non-linear control problem into a series of linear ones, design of controllers to suit each linear design condition and then reconstruction of the resultant discrete solutions into a single continuous controller. Numerical and experimental application of gain-scheduled control is presented in Chapter 8.

Although gain scheduled control seems a logical progression from fixed-gain controllers,

there are problems and limitations introduced by the scheduling process. For example, it is usually necessary for the scheduling parameter to be slowly-varying (e.g. altitude or airspeed in the aircraft case). The problems, and possible solutions, associated with gain scheduled control are discussed further in Chapter 9.

**Eigenstructure Assignment**

In order to calculate feedback gains for gain scheduled controllers, some form of linear controller design method is required. Any of the linear design methods outlined above could be employed, however, eigenstructure assignment was used in this thesis for several reasons:

- Ease of automation. Unlike methods where the gains must be 'tuned' manually, eigenstructure assignment involves specifying the desired eigenstructure (in terms of eigenvalues and eigenvectors) of the closed-loop system and explicitly calculating the required feedback gains.
- Compliance with requirements. It is normal for desired aircraft handling qualities to be specified in terms of closed-loop pole locations (see e.g. [56, 57, 58]). Therefore, the desired eigenstructure can be directly copied from the requirements.
- Available knowledge. Eigenstructure assignment routines have been used extensively in the Department for control of non-linear aircraft models [18, 27, 59] and routines were already available for calculating the appropriate state feedback gains.

The eigenstructure assignment methods used in Chapters 8 and 9 are described in more detail in Section 8.1.

### 2.4.7 Adaptive Control

Adaptive controllers aim to provide the benefit of consistent controller performance in the face of changing plant dynamics. This is achieved by 'adapting' the controller parameters to suit the plant operating conditions. Variation in plant dynamics may occur due to many factors, including changes in plant configuration, changing external conditions,

mechanical wear, modelling inaccuracies, etc. It is normally very difficult to prove that adaptive controllers yield a stable response, therefore it may be necessary to limit their authority.

The Minimal Control Synthesis (MCS) model-reference adaptive algorithm was developed at the University of Bristol in the early 1990s [60] and has since been applied to many systems [61, 62, 63, 64]. MCS requires no *a priori* knowledge of plant parameters or values of controller gains (these are often set to zero). Instead, the gains are a function of the integral of the error between a reference system and the plant to be controlled. Adaption weights are used to control the speed of adaption. Although robustness proofs have been found for limited cases of MCS [60, 65], there is no general guarantee that MCS will provide a stable solution. This is particularly true where plant non-linearities and signal noise cause the gains to continually increase. This can be avoided by locking the gains after a suitable adaption period, thereby reverting to a fixed-gain controller strategy. Periodic releasing of the gains may be necessary to adapt to plant variation. The MCS adaptive control strategy is applied in Chapter 8.

## 2.5 Aerodynamic Data Generation

Before numerical analysis and simulation of an aircraft can be undertaken, a representative mathematical model of the system is required. The full 6-DOF equations of motion for a rigid-body aircraft are well known, and will not be repeated here, however, in general terms they contain elements linked to aerodynamics, propulsion and gravity. It is the aerodynamic terms which are of most interest when developing a mathematical model, and the ones which provide the most non-linear behaviour at high angles-of-attack[5]. It is pointed out in [66] that the fidelity of the mathematical model should always match the desired use, to minimise time spent developing unnecessarily large models.

[5]Depending on the fidelity of the propulsion model, this may also contribute significant non-linearities to the model in the form of gyroscopic and transient effects.

### 2.5.1 The Need For Wind Tunnel Testing

It is currently not possible to accurately predict the aerodynamic terms in an aircraft model at high angles-of-attack (where separated, turbulent and/or vorticial flow is dominant) using computational or empirical methods [67]. Matters are further complicated when rates of change of motion variables are high, as is often the case at high $\alpha$ [11]. If constrained to a single degree-of-freedom (DOF) it may be possible to account for the effects of rate and frequency of motions on the aerodynamic forces (i.e. dynamic lift/stall), however, this becomes an almost impossible task when considering a complex 3D shape undergoing full 6 DOF motions, and accurate modelling is unlikely [11]. It would be possible to design an aircraft using computational/empirical methods alone, and tentatively explore the flight envelope using a full-scale demonstrator, however, lessons learned after a full scale aircraft has been produced are costly. Control system design would only be possible for flight at small angles of attack and sideslip, low motion rates and small control surface deflections, due to lack of accurate data at anything other than these flight conditions. For these reasons, some form of sub-scale testing is normally carried out. Preliminary tests are often performed in wind tunnels (where conditions can be pre-determined and closely controlled), but large, free-flying drop models may be used later in the development as an intermediate step from design to full-scale aircraft.

More than one type of wind tunnel test is usually required to generate sufficient aerodynamic data for a representative model. The type and amount of testing will depend heavily on the type and role of the aircraft. For example, a large transport aircraft may only require static and oscillatory wind tunnel tests (plus aeroelastic testing) whereas a highly manoeuvrable aircraft may also require rotary, coning and translational tests. The testing methods described in this section are limited to those required for rigid-body flight mechanics. A large amount of dynamic testing is carried out to investigate aeroelastic modes (including small-amplitude multi-degree-of-freedom tests) but is beyond the scope of this review.

### 2.5.2 Static Testing

Usually, the first set of wind tunnel tests performed on a sub-scale model of a new aircraft will be static tests. This is where the model is mounted rigidly on a balance

(either internal or external to the model) in the tunnel test section. Measurements of the forces and moments on the model at different (static) angles to the flow, and with different deflections of aerodynamic control surfaces are then made. After this set of tests it is possible to create a linear or 'quasi-linear' model of the aircraft, without the effects of aerodynamic damping. By assuming the model obeys the linear property of superposition, the measured data can be combined to give forces and moments as the sum of the individual data components. Linear models (valid in some neighbourhood of an operating point) may be derived by using fixed stability derivatives. 'Quasi-linear' models may be derived for larger operating regions by allowing the stability derivatives to be non-linear functions of motion variables (e.g. $\alpha$ and $\beta$) and parameters (e.g. $\delta_e$), whilst still assuming that the superposition principle is valid.

The mathematical model created from static test data is sufficient for evaluation of aerodynamic characteristics of the aircraft for performance purposes, static stability, Reynolds number dependence of the configuration, maximum/minimum trim angles given the control power available, and initial low-$\alpha$, low motion-rate control law development. Provided the tests are not performed in a highly specialised tunnel (e.g. cryogenic or pressurised) it is relatively cheap (in cost terms, possibly not in time) to test and refine the configuration iteratively at this stage.

### 2.5.3 Dynamic Testing

Following a static test programme, the aerodynamic model will be refined by including data from dynamic wind tunnel tests. Aerodynamic damping terms make up a significant part of the force on a manoeuvring aircraft, even at relatively low motion rates. It is therefore necessary to perform dynamic tests in several different model axes to evaluate stability due to the rate of change of motion variables.

Traditionally, dynamic wind tunnel testing is performed using small-amplitude forced oscillation rigs. The model is rigidly mounted to a sting (usually via a strain gauge balance), which is made to oscillate or rotate about a single axis in the wind tunnel. The forces and moments on the model are then recorded as a function of the motion rate, or oscillation frequency. By subtracting forces recorded during wind-off (tare) conditions, it is possible to work out the forces and moments caused by the motion.

The data generated by forced oscillation tests can be added to the linear model in the form of further stability derivatives, however, forces and moments at high $\alpha$ and with high motion rates are often highly non-linear and strongly coupled, leading to a breakdown in the assumption that superposition is applicable. This implies that either the region in which the linear model is deemed valid should be reduced (leading to many more linear design cases), or the model must be formulated using another method, for example using look-up tables (tabulating each force and moment against several, or all, motion variables and parameters). It is possible, for convenience, to maintain a stability-derivative type model structure when using non-linear aerodynamic terms (so-called 'stability coefficients' [68]), however, the aerodynamic data must be altered to reflect the breakdown in superposition.

Reviews of existing dynamic tunnel testing facilities are given in [69, 70, 71, 72]. Comprehensive reviews of dynamic test techniques are given in [73] (1981), and [3] (1990). In general, dynamic test rigs can be divided into categories depending on the type of data they are designed to collect (Figure 2.3, taken from [73][6]). The main categories will be briefly described here.

### Direct Forced Rigs

Forced oscillation/rotary rigs are the most common method of performing dynamic wind tunnel testing. They are often large (e.g. the Dynamic Plunge-Pitch-Roll rig (DyPPiR) at Virginia Polytechnic Institute, on which the model carriage alone weighs 320kg [74]) to allow high motion rates with large models, and support interference and flexibility can be a problem [75, 76]. They can be broadly categorised as follows:

- **Oscillatory rigs.** Oscillatory rigs, such as those described in e.g. [2, 74, 77, 78, 79] generally use either a continuously rotating motor and linkage arrangement, or direct drive, to achieve oscillatory motion about a single axis. Often the drive systems are large (using hydraulic motors or actuators) to allow a large model to be oscillated at high frequencies and amplitudes. Force and moment data from the model is collected, often from internal strain gauge balances, and used to develop

[6]This figure omits tests that cannot be performed in a wind tunnel (e.g. range and whirling arm tests).

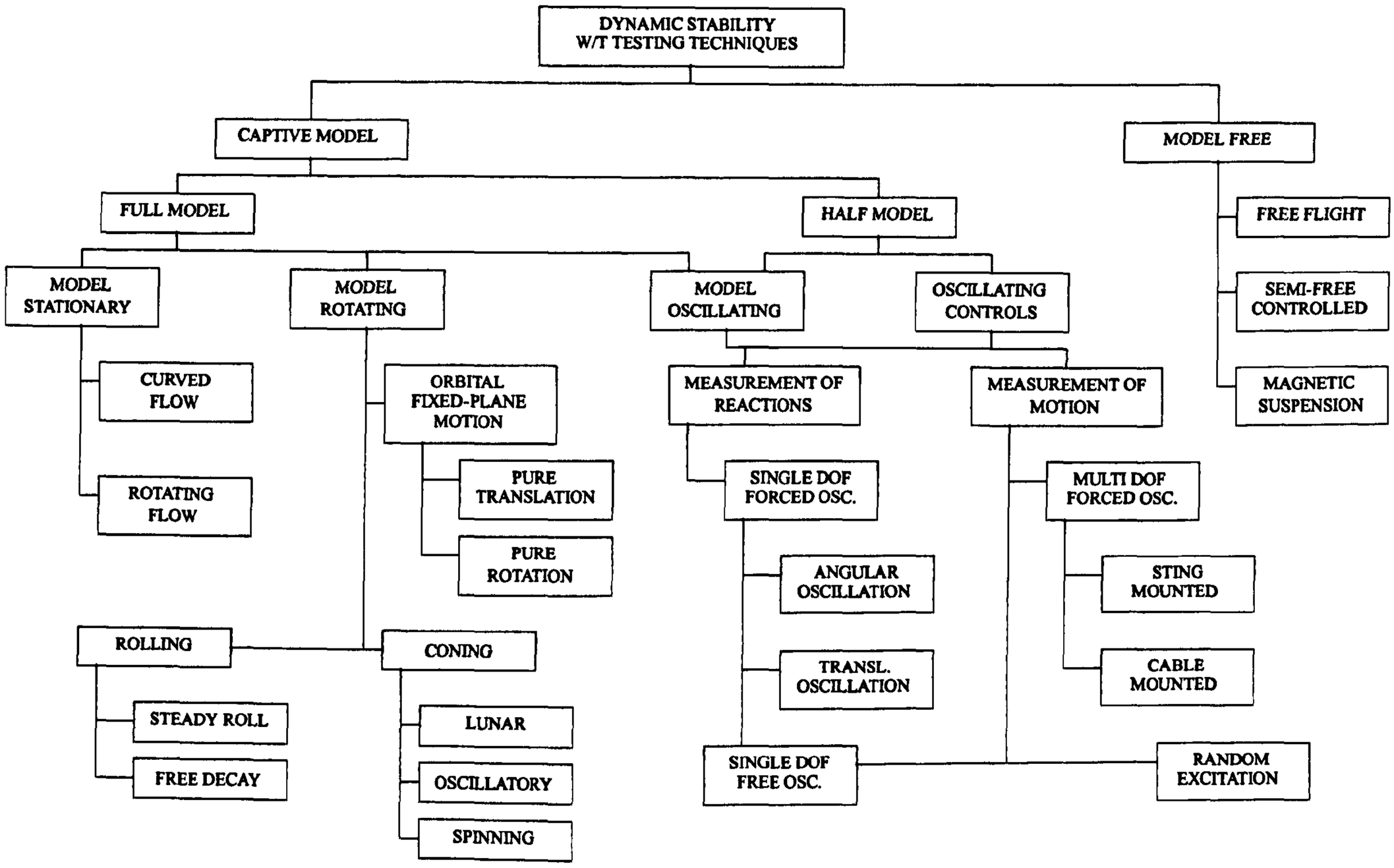


Figure 2.3: Overview of dynamic wind tunnel testing techniques (from [73]).

models that may include motion rate, frequency and amplitude effects. This type of rig can be used to extract both static and dynamic data by examining the in- and out-of-phase components of the response. Derivatives found by this type of rig include $c_{l_p} + c_{l_{\dot{\beta}}} \sin\alpha$, $c_{m_q} + c_{m_{\dot{\alpha}}}$ and $c_{n_r} - c_{n_{\dot{\beta}}} \cos\alpha$ (moments due to angular rates), but they cannot separate the constituent parts of these "combined derivatives".

- **Rotary rigs.** Continuous rotary rigs are used to measure forces and moments caused by continuous roll rate [75]. Again, the support structure and sting are often large to accommodate large models without flexing, while allowing high angular velocities. For example, the rotary rig at the Royal Aircraft Establishment described in [80] uses a 1500 psi hydraulic motor to rotate a 740mm long model at up to 420 rpm at 0.7 Mach. An important use of rotary rigs is to produce coning motion, where the model (at non-zero angle-of-attack) rotates about the wind axis to simulate a frequently performed manoeuvre – the velocity vector roll [81]. Another method for performing this type of test is to use angled vanes to set the flow swirling upstream of a stationary model. As well as finding pure-rotation

derivatives (e.g. $c_{l_p}$), this type of rig can be used for extracting derivatives due to frequency effects (e.g. $c_{n_\Omega}$).

- **Whirling arm rigs.** Whirling arm rigs were one of the first methods to be used for testing the aerodynamic characteristics of model aircraft. The earliest rig, with a radius of 4 feet, was built by Benjamin Robins in England in the early 18th century [82]. Whirling arm rigs are no longer used for general aerodynamic testing, but provide a method of performing specific tests at a constant pitch/yaw rate while maintaining constant angle-of-attack or sideslip (for separating $c_{m_q}$ and $c_{m_{\dot{\alpha}}}$, and $c_{n_p}$ and $c_{n_{\dot{\beta}}}$). Another method for performing these tests is using a tunnel where the flow is given curvature using a curved test section or carefully placed vanes. In [83] a small whirling arm rig (3.5m radius) is used to test the dihedral effect on a simple wing model. A larger rig (approximately 10m diameter) is described in [84], where a 6kg High Incidence Research Model (HIRM) is tested in the longitudinal plane. Both rigs can only test at low Reynolds numbers, and the models must be very strong, due to the large centrifugal forces imposed by the rotation. There are also problems with 'swirl' – movement of air around the test section after the model has passed, affecting results when the model hits the moving air.

Note that the process by which data from more than one of these rigs - usually oscillatory and rotary - is combined into a usable aerodynamic model is usually somewhat ad hoc.

### Forced Arbitrary-Motion Rigs

Several wind tunnel rigs exist, or have been designed, which allow the model to undergo arbitrary motions in one or more degrees of freedom.

In [79] a full 6 DOF rig is designed using the 'simulator' style Stewart platform concept. Using 6 hydraulic actuators (neatly arranged to minimise support interference) it is possible to reproduce arbitrary motions with moderate amplitude and frequency. However, the system would have required a very large hydraulic supply which was deemed too costly. A smaller version using electric actuators was then discussed for use in water tunnels, where motion rates are greatly reduced.

In [85], a rig that was originally designed for aeroelastic testing is used to extract stability derivatives ('with reasonable success') from rigid models of the F-14 and Space Shuttle Orbiter. The model is mounted on two sets of tensioned cables which can be moved to cause vertical and lateral motion.

### Aeroelastic Rigs

Aeroelastic rigs (e.g. [86]) are used for analysing structural modes of an aircraft configuration using scale models with correct mass, mass distribution and stiffness properties. Movable control surfaces are often used to excite the structure, and can be used to test active suppression systems.

### Free-Flight

Free-flight testing allows the aircraft model to undergo full 6 degree-of-freedom motions with little or no external interference. A brief description of some of the techniques used will be given here, however, a more comprehensive review of dynamic free-flight test techniques is presented in [72].

Spin tunnel tests (e.g. [87]) often use free-flying models in a vertical wind tunnel, with posthumous position feedback coming from video image processing. Remotely-operated movable control surfaces may also be employed to test spin recovery methods. The models used are dynamically scaled to give representative results.

Arguably the most advanced wind tunnel free-flight testing rig was developed by NASA in 1949 for the 30' by 60' Langley full-scale tunnel (Figure 2.4) (see e.g. [82, 88]). It has been used for testing many aircraft, including tests on transition from hovering to forward flight in the VSTOL Harrier. The model is fed with compressed air for thrust, control surface signals and power along a slack cable from the roof of the tunnel. Three pilots are required to fly the model (due presumably to high motion rates) – one each for pitch, roll/yaw and thrust control.

Other methods of free-flight testing in wind tunnels include wire-launched and gun-launched models [89]. For the wire launching system, the model is suspended with a thin wire (either piano wire or thin fishing line) in the test section, possibly in a

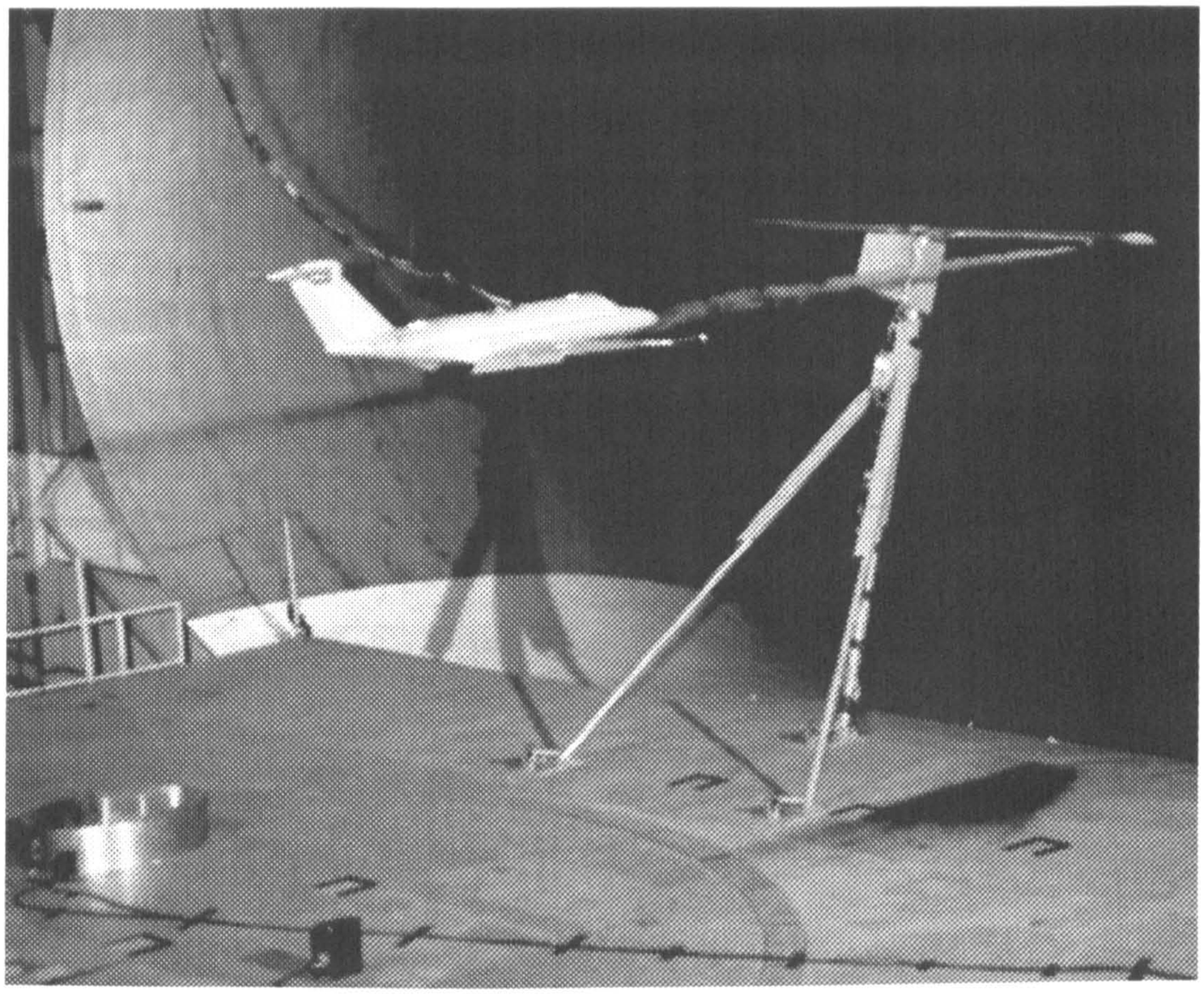

Figure 2.4: NASA free-flight tunnel being used to test effects of trailing-edge vortices on following aircraft (from www.nasa.gov).

vertical tunnel, before the wire is electrically broken inside the model to give free-flight conditions. Gun-launching is similar, except the model is fired from a gun downstream of the test section, which gives two model passes through the test section (upstream and downstream) [89]. Tunnels with tilting test sections have also been used in the early days of free-flight testing, but are no longer used today.

Control-line flight testing methods have been used by the USAF and NASA whereby the model is flown in a circular path on the end of a central boom or control line. NASA built a 130ft control-line facility [90, 91] consisting of a standard crane sitting in the centre of a wooded area that served as a wind break. The crane can rotate about a central axis and the model is flown on the end of the arm using an identical method to the NASA Langley free-flight installation mentioned previously. Four operators are required to control the facility, which was mainly used for Vertical Take-Off and Landing (VTOL) transitioning test flights. Test data was recorded using motion picture cameras.

Drop models have been used for many years to test large, dynamic flight manoeuvres without the constraints of a wind tunnel (e.g. stall, spin entry/recovery, post-stall mo-

tion, etc.). Often, they are remotely-controlled by a pilot on the ground and tracked visually to record the flight. On-board sensors are used to give the pilot feedback, and to posthumously analyse the motion. Drop models of many aircraft have been made (e.g. 22% FA-18 model [92]), and prove especially useful for very new planforms like the NASA X-33 and X-38.

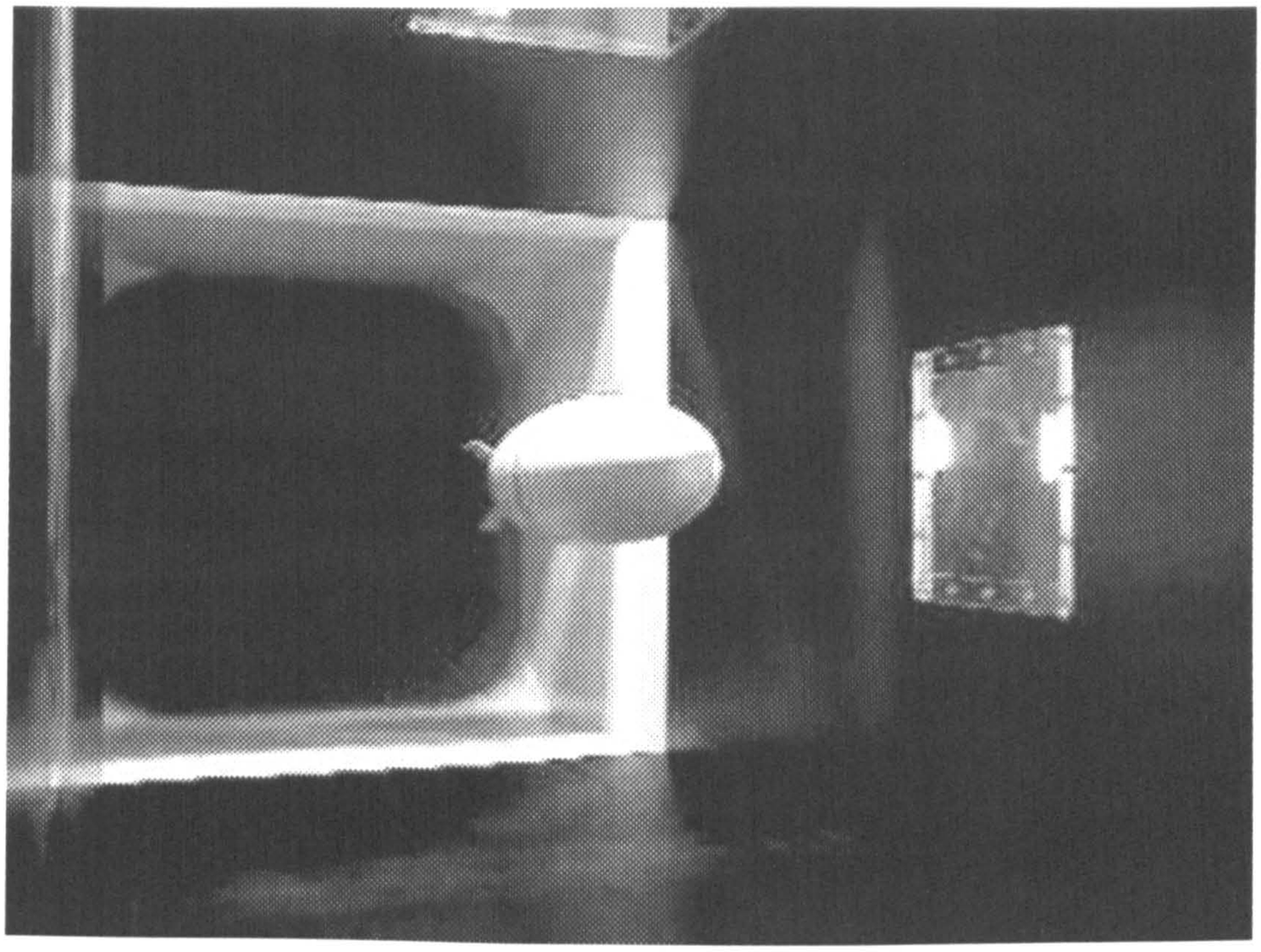

Figure 2.5: NAL magnetic suspension tunnel (from www.nal.go.jp).

Magnetic suspension tunnels have been tested at several institutions, including NASA (USA), TsAGI (Russia) and NAL (Japan). They vary in test section size from 10cm square up to 60cm square at NAL [93] (Figure 2.5). They use several sets of electromagnetic coils to suspend a model with internal magnets in the tunnel test section. Active control is needed to keep the model in the centre of the tunnel, and motion in several degrees of freedom can be imparted on the model by varying the field strength. While still at a developmental stage, they are a very attractive option for performing interference-free tests on small models in the controlled environment of a wind tunnel.

### Constrained Free-Motion Rigs

Between direct forced-oscillation tests and free-flight are single- or multi-degree-of-freedom unforced rigs, possibly with actuated control surfaces. Several free-to-roll rigs have been

made to analyse wing rock on highly swept delta wings. In [94] flat-plate delta wings with 76 and 80 degree leading edge sweep were free-to-roll tested at different angles of attack on a purpose built rig. It was found that only the 80 degree wing would undergo sustained self-induced oscillations (wing rock). An air-bearing system was used in [95] to drastically reduce the amount of friction (90 times) on an 80 degree free-to-roll delta wing. Surface pressure taps and flow visualisation were used in both cases to develop a model of the observed motions.

A two DOF pitch-plane rig (Figure 2.6) was used by Boeing to develop the XB-47 bomber in the mid-1940s, in particular to investigate the stability effects of wing sweep [96]. The model is 'flown' manually by an operator (left of Figure 2.6). The model proved difficult to control however, and often became unstable and disintegrated. Only after thousands of hours of tunnel testing was the design made more viable.

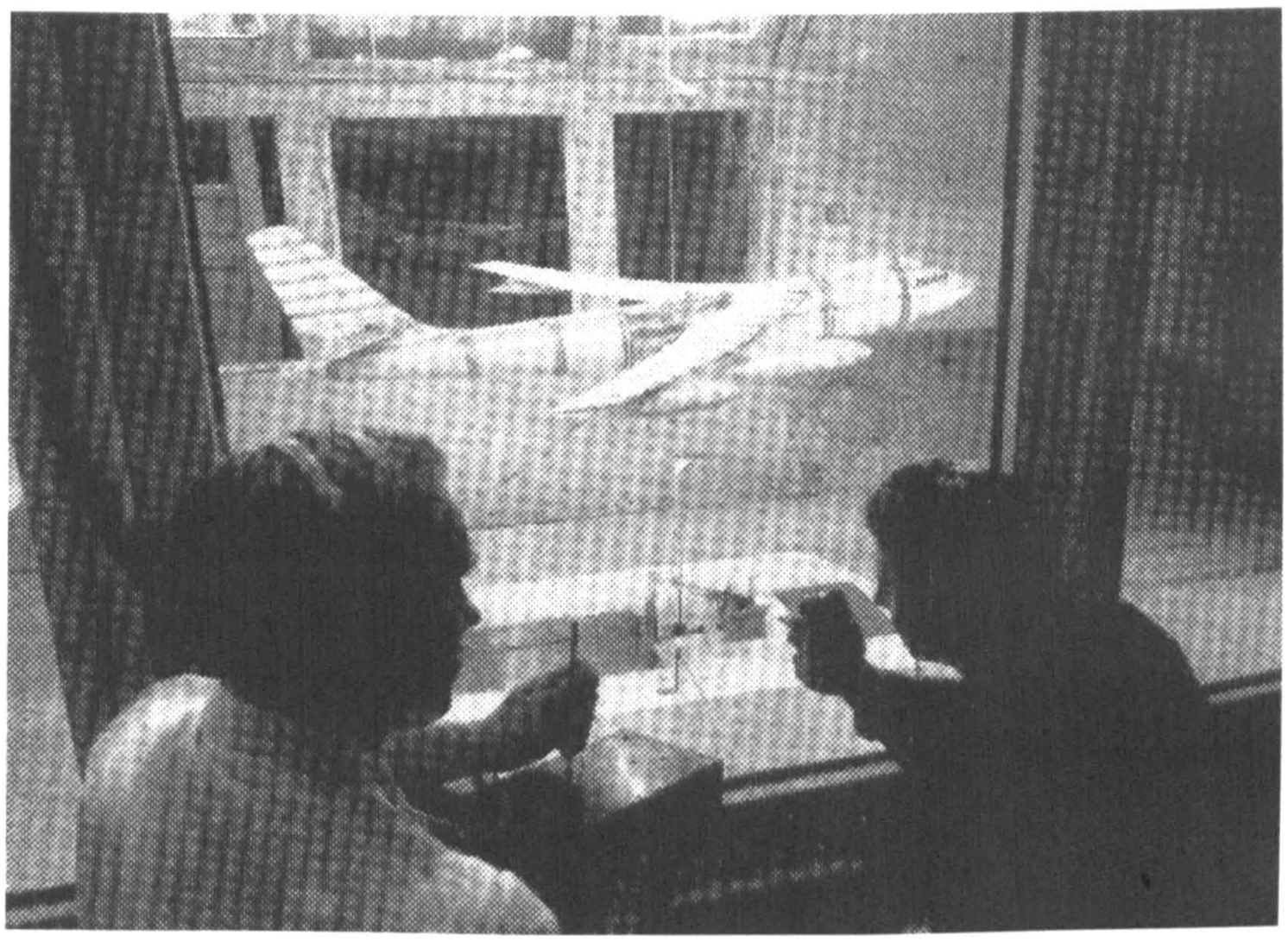

Figure 2.6: Development of the Boeing XB-47 using an externally-piloted wind tunnel model [96].

A single degree-of-freedom pitching rig is described in [97] and is used to generate a longitudinal mathematical model of a generic delta wing aircraft, including unsteady aerodynamic effects. The model has moving elevon surfaces, actuated using radio controlled model servos, which provide pitch angle control input to the model. A load cell, external to the model, is used to measure the lift force generated. Various elevon input

profiles (step, doublet, etc.) are used to achieve large amplitude motions which allow a full unsteady model to be determined.

In [98] a two DOF rig (pitch and plunge) was designed and built, using a generic canard-delta model. The model was free to pitch, and slide up and down a vertical set of guides at the side of the tunnel. The canards were actuated using a high-speed model aircraft servo and are shown to provide sufficient control power for performing arbitrary pitch-plane motions. Use of the rig for design of control laws is not attempted.

In [99] a lateral-directional two degree-of-freedom rig is described which uses servo-actuated aerodynamic control vanes behind the model to pitch and yaw the aircraft about a fixed gimbal. This aerodynamic forcing removes the need for complex drive arrangements, and reduces model complexity by having no moving control surfaces.

### Controller-Design Rigs

Very few dynamic wind tunnel rigs have been used for direct development and testing of control laws for highly manoeuvrable aircraft. In [45, 100] the development of a 2 degree-of-freedom free-rotation wind tunnel rig is described, using a $1/5th$ scale HIRM model. The model is free to rotate in roll and yaw, with pitch angle being set at the beginning of each run. Actuated all-moving tailplanes are fitted to the model, however, these are purely used to trim the model, the main control coming from compressed air blowers external to the model. Nose suction for yaw control at high $\alpha$ was investigated but found to have little effect.

A 3 DOF rig is used in [101] to test adaptive, fault-tolerant controllers. A commercially available delta wing radio-controlled model is adapted to fit a 3 DOF gimbal, allowing the model to pitch, roll and yaw. The model is mounted upright in the tunnel on a fixed sting. Despite relatively high tunnel turbulence, and lack of rate feedback from the model, it is shown that the model-reference control scheme used can adapt to several types of failure.

The 4 DOF rig described in [102] was used for development of gust alleviation on a small turboprop transport aircraft. The model has a 3 DOF gimbal inside, and is free to slide up and down a vertical wire. Dryden gust patterns were generated using hydraulically

actuated vanes upstream of the model, and torque-motors used to actuate elevators, ailerons and trailing edge flaps to improve the gust response.

A similar 4 DOF rig was developed at Cranfield Institute of Technology [72, 103] to extract aerodynamic models, develop control systems and perform wind tunnel simulations of dynamic motions. A $1/12^{th}$ scale BAe Hawk and a $1/15^{th}$ scale forward-swept wing model have been tested on the rig. Both models employed moving aerodynamic surfaces to effect control, with actuation coming from miniature radio controlled model servos. Model weight is in the order of 3kg.

## 2.6 The Pendulum Support Rig (PSR)

The possibility that several expensive and bulky traditional dynamic test rigs could be replaced by a single multi-purpose rig led to the concept of the 'Pendulum Support Rig' (PSR) at TsAGI in Russia [69, 79] (Figure 2.7, from [79]). A dynamically scaled model is mounted on a 'pendulum strut', with a 3 DOF gimbal at the aircraft (giving pitch, roll and yaw) and a 2 DOF gimbal at the mounting point (giving sway (lateral) and heave/surge (longitudinal) motion), thus giving the model constrained 5 DOF motion.

The aircraft model uses active aerodynamic control effectors to obtain the desired attitude and perform manoeuvres in the wind tunnel (no external forcing is used). When performing dynamic motions, for example sinusoidally pitching the model to extract an unsteady mathematical model, aerodynamic effects caused by movement of the control surfaces will be present in the results. This leads to faster model generation than using a conventional forced oscillation rig and changing the control surface deflections manually. A further benefit of an un-forced rig is that when extracting static stability derivatives, the model is *always* at a trim condition (after transient motion has decayed).

Advantages of the PSR concept include:

- reduced costs due to less bulky support system.
- less aerodynamic interference from support system.
- multi-degree-of-freedom.

- multi-purpose – can be used for aerodynamic data generation and control system design.
- arbitrary motion generation using aerodynamic control effectors.

The development process for a new aircraft using the PSR is envisaged as follows. A dynamically-scaled model will be made for testing on a small PSR. Aerodynamic data can be extracted from the model while a controller is being developed. This may require new aerodynamic model formats and generation techniques, such as 'reaction hypersurfaces' [78]. The aerodynamics and control system refinement will take place in parallel, saving a large amount of time. Once the model and control system have been iterated and a viable configuration reached, a large model may be made for testing on a larger PSR. It is entirely feasible that this model may be used initially in tunnel tests, then the same model flown in free-flight (powered or un-powered), with confidence in the control system and aerodynamics from the multi-degree-of-freedom wind tunnel tests. After free-flight testing, the model can be scaled up as necessary. Obviously, this method will work better for small aircraft (e.g. UAVs) where the aerodynamics of the full scale are closer to those of the wind tunnel models. Although the cost of running and maintaining large wind tunnels can be extremely high, by reducing the production time dramatically these costs can be regained.

The PSR can be mounted upright (as shown in Figure 2.7) or inverted in the tunnel. Studies at TsAGI, and De Monfort University, Leicester [79], (later replicated at the University of Bristol) showed using bifurcation analysis and time simulations that with a generic fighter aircraft model there were regions of large-amplitude oscillatory instability (limit cycles) for the upright rig, caused by coupling between the aircraft and strut modes (Figure 2.8). These limit cycles were observed experimentally at TsAGI in Russia, although with a high-wing light aircraft model.

A limitation with mounting the model upright in the tunnel is that the model must be very lightweight. It must be able to lift its own weight, plus the weight of the pendulum strut, in order to get dynamic motion in heave.

A PSR has been developed at the University of Bristol to test the concept further [5, 6, 7] (Figure 2.9). Given the small test section size for the University of Bristol rig (1.1m diameter, see Section 3.5.2), and the instabilities mentioned above, it was decided for

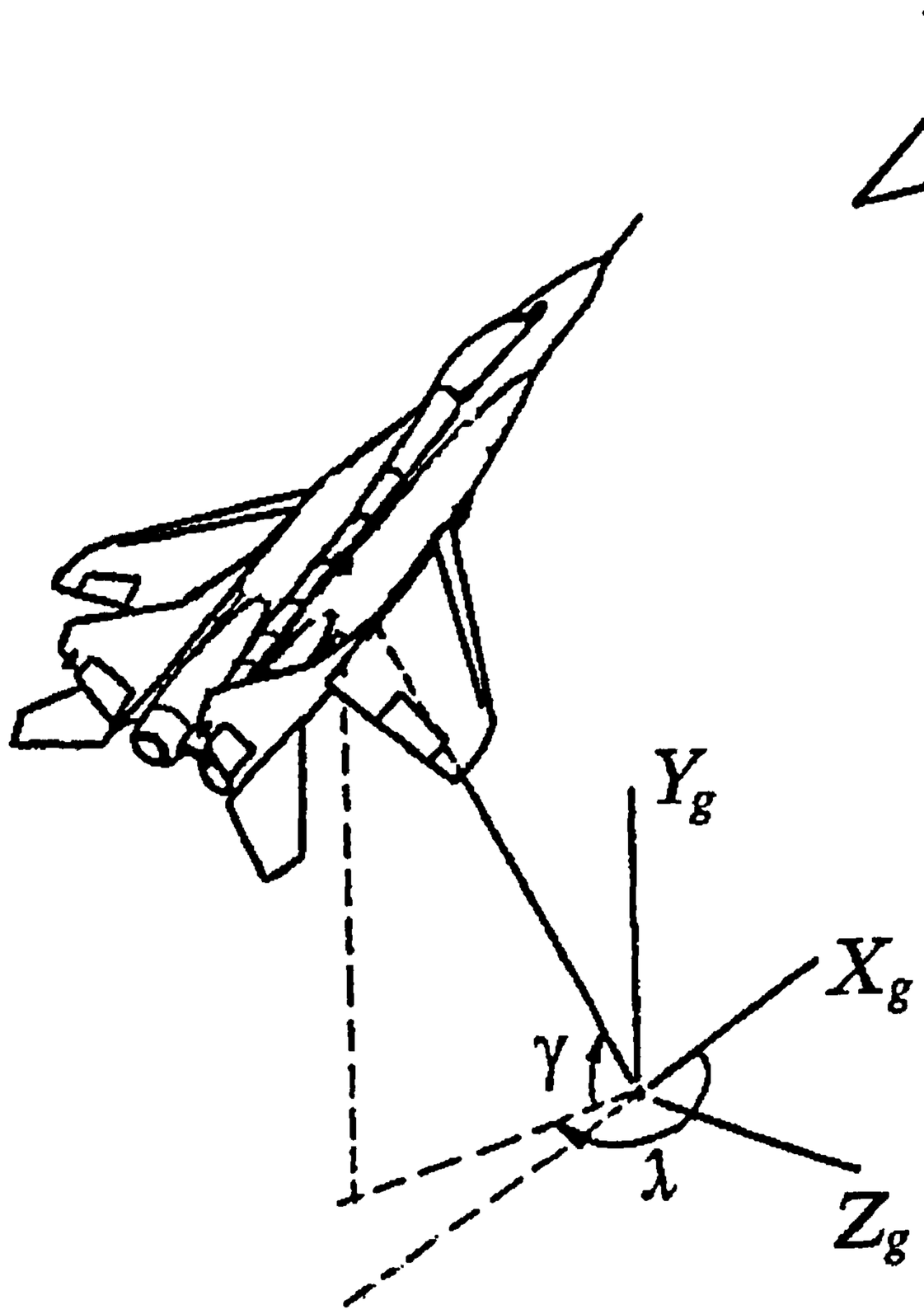


Figure 2.7: Diagram of the Pendulum Support Rig (PSR), from [79].

the pilot rig that the model would be mounted inverted in the tunnel. The rig is therefore inherently stable, however, this method also has restrictions. For example, the mass of the model and the lift vector are both acting in a downwards direction which means the pendulum strut will sit hanging almost vertically down. This limits the movement of the model in heave. A counterbalance system was designed which attaches to the top of the pendulum strut to allow the model to be balanced about the tunnel-fixed rotation point. This allows the nominal angle of the pendulum strut to be reduced, and more heave motion generated (see Section 3.1.2).

Initially, the Bristol University rig was limited to 2 DOF (although most tests in this thesis were performed in a single (pitch) degree-of-freedom only, similar to [97]), however,

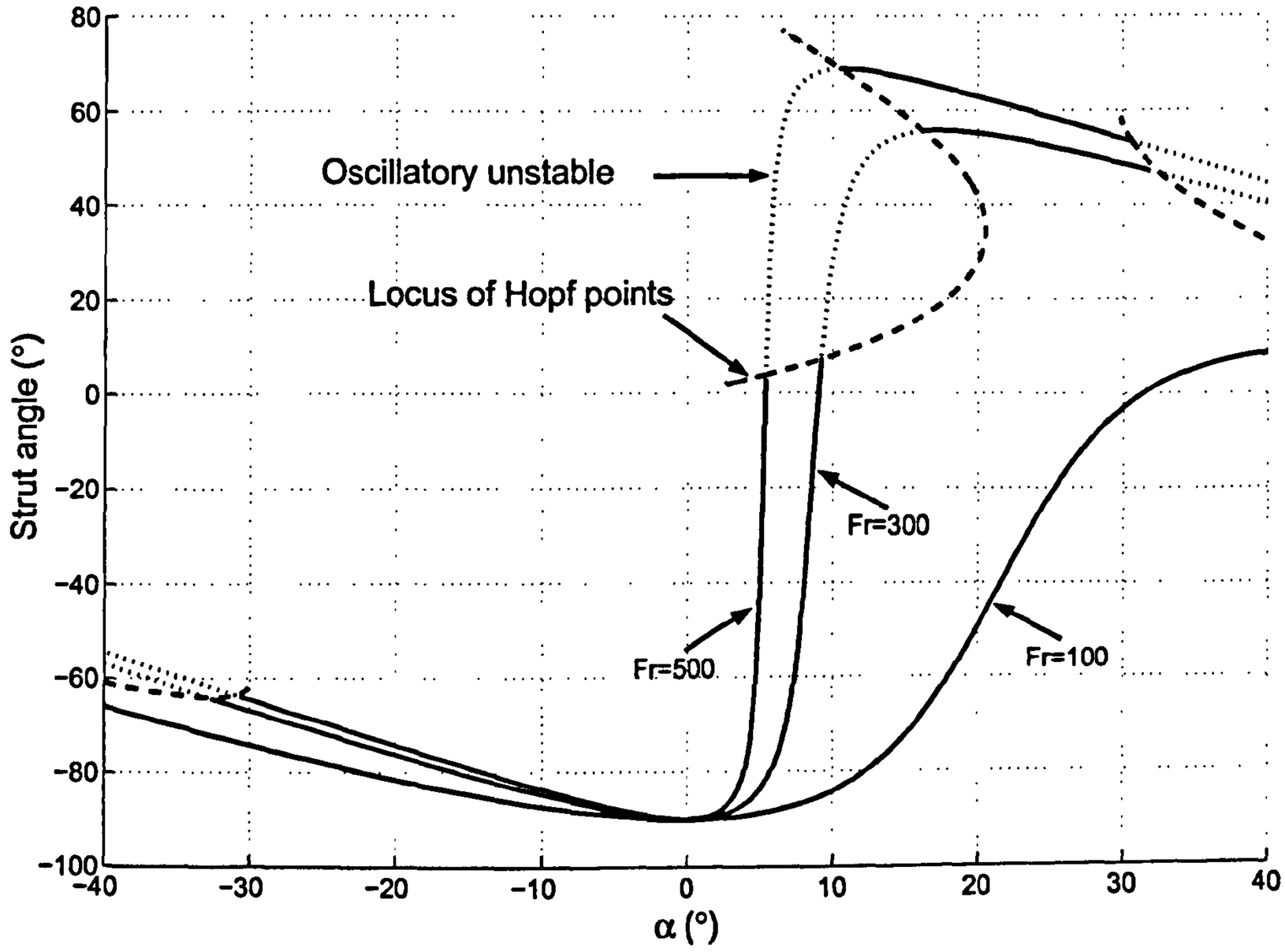


Figure 2.8: Bifurcation diagrams for a generic linear aircraft model (from [79]) on an upright PSR for several Froude numbers.

a full 5 DOF rig was also developed and tested. In Chapter 3 the rig hardware is described in more detail.

The model used for the tests in this thesis (described in Section 3.2) makes use of actuated movable control surfaces. Thus, the model is 'flown' in the tunnel and can be used for aerodynamic model generation (including aerodynamic effects due to dynamic control surface movements) using strain-gauge transducers on the strut and parameter estimation from motion measurements [6]. Also, due to the active control effectors, the rig can be used for testing control laws. This thesis investigates some aspects of the feasibility of using the rig for this purpose.

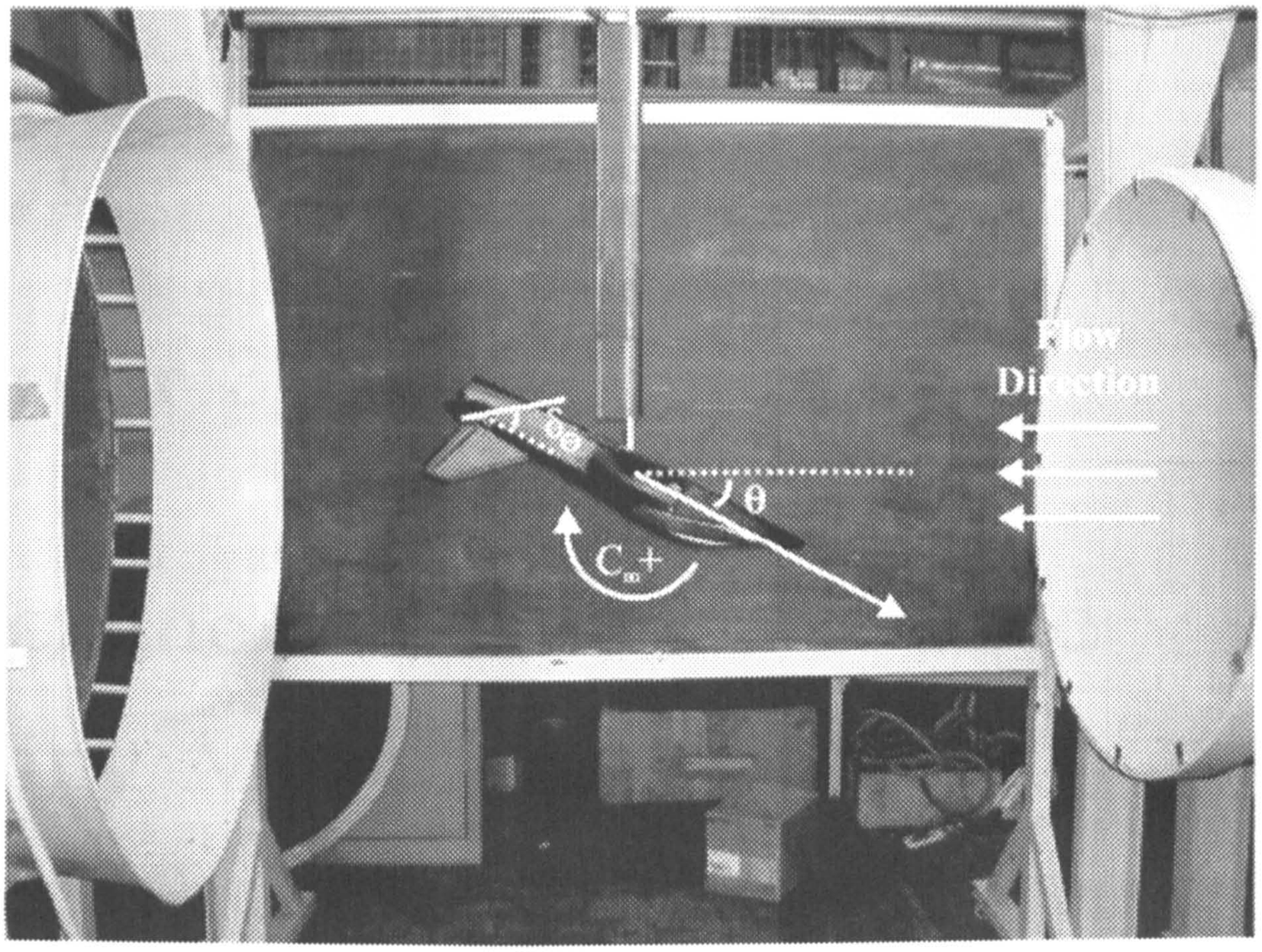


Figure 2.9: Photograph of the University of Bristol PSR (1 DOF configuration) in the Bristol 1.1m open jet tunnel.

## 2.7 Conclusions

In this chapter, motivation for the work carried out in this thesis has been presented. In particular, it was identified that traditional aerodynamic model generation and control system design phases for high-performance aircraft are both lengthy and costly. Almost all design procedures involve the use of one or more expensive and bulky dynamic wind tunnel rigs. A review of the literature revealed that there are many different dynamic wind tunnel test rigs, but that there have been relatively few attempts to design flight control laws using wind tunnel models. An outline of the PSR wind tunnel apparatus was given, and advantages discussed. Brief introductions to non-linear dynamics, non-linear aircraft dynamics and continuation methods were also presented, and a broad overview of both linear and non-linear control design strategies given. In the next chapter, the PSR pilot rig developed at the University of Bristol is described in detail, and testing methods discussed.

# Chapter 3

# Experimental Apparatus and Testing Methods

A pilot pendulum support rig was manufactured at the University of Bristol to help develop the concept and test experimental controllers. A custom aircraft model was also manufactured for the tests. The experimental hardware, facilities and various testing methods used are described in this chapter. Results of servo-actuator tests are presented, and a representative mathematical model of the actuators derived. A brief description of the wind tunnel facilities at the University is also given.

## 3.1 PSR Hardware

A large amount of hardware was manufactured for the Bristol University PSR, some of which is shown in Figure 3.1. All components were built in-house by the Department of Aerospace Engineering Workshop. Besides the gimbals and counterbalance (described below) there are many different shafts and connectors to allow different test configurations. All pendulum rig shafts are made from 5/8" hollow aluminium tube (wall thickness 1/8"). Stationary shafts are manufactured from 1" silver steel. Two custom-made strain transducers were designed by Hilton Kyle [6] at the University of Bristol to measure axial forces in the pendulum strut. To minimise drag on the strut for certain rig configurations, a set of fairings were made from carbon fibre covered foam that can be slipped

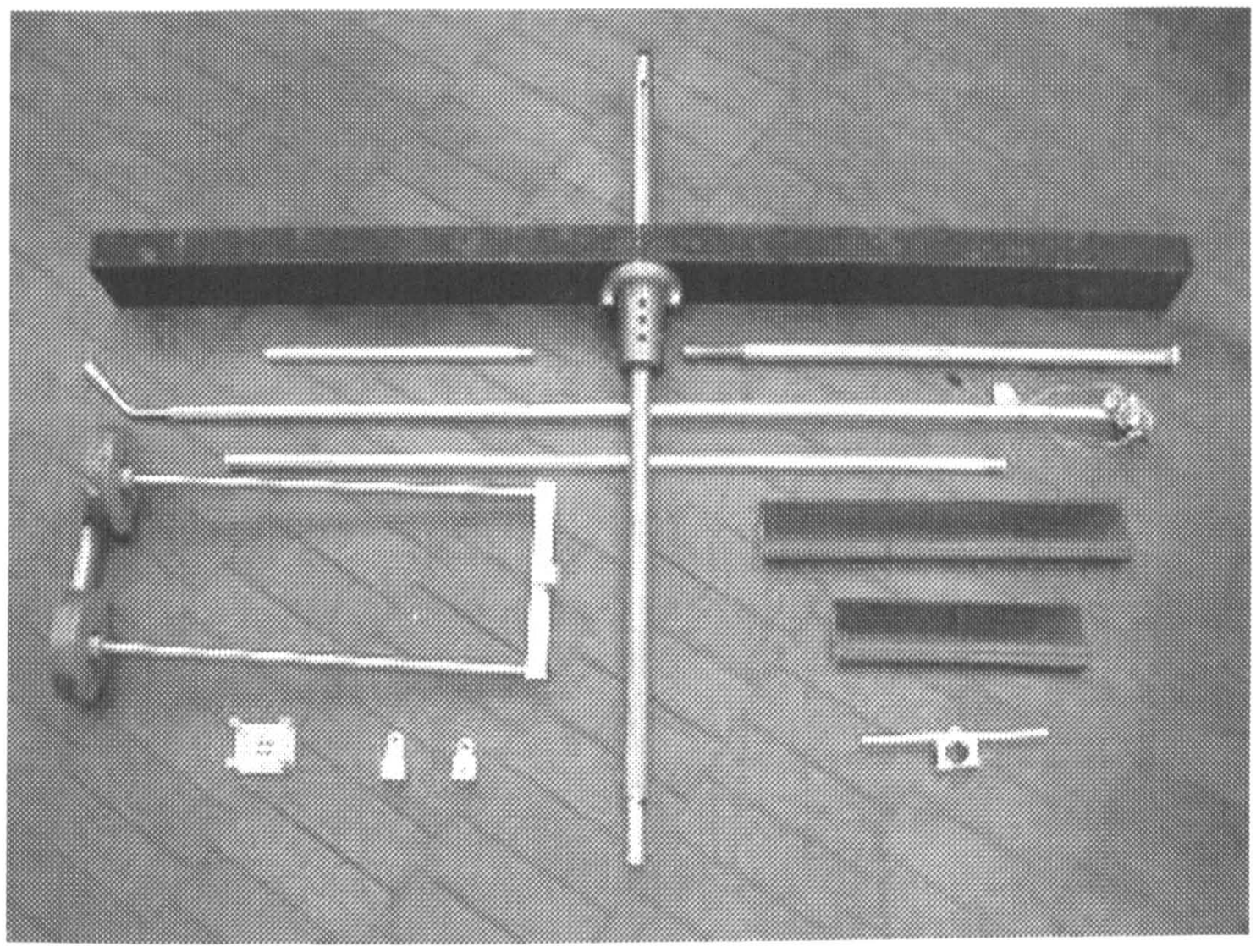

Figure 3.1: Some of the PSR hardware.

over the aluminium shaft. The shaft fairings cannot be used where the model has lateral translational freedom (sway) due to the forces generated by the fairing at non-zero angle-of-attack. The fairing was therefore removed for tests involving sway motion.

### 3.1.1 Gimbals

Four gimbals were designed and manufactured for the rig. Two of them provide single degree-of-freedom movement only (Figure 3.2(a)) to allow 1- and 2-DOF testing. Another has 2 degrees-of-freedom (Figure 3.2(b)) and is used at the tunnel mounting point when lateral translational model motion is required. The fourth gimbal (Figure 3.2(c)) has 3 degrees-of-freedom and is used inside the model. Provision was made for limiting the gimbal rotation angles using machine screws, and in some cases (roll and yaw in the model) they can be locked completely.

All the gimbals are made from HE15 T6 grade aluminium and use ball bearings to minimise friction. In the 2- and 3-DOF gimbals, the internal potentiometer bearings are used to support one side of each shaft, to minimise size. Precision conductive plastic potentiometers from Penny & Giles are used to measure angular position (Table 3.1).

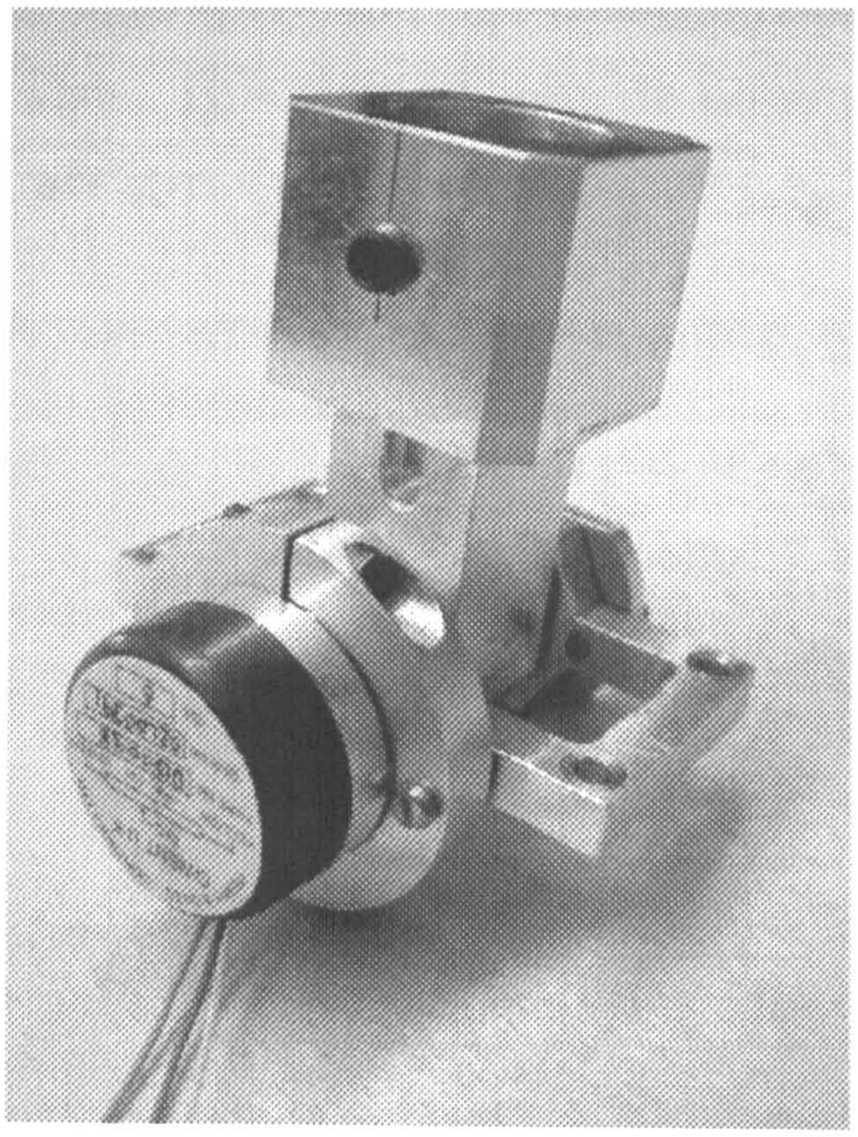

(a) 1 DOF.

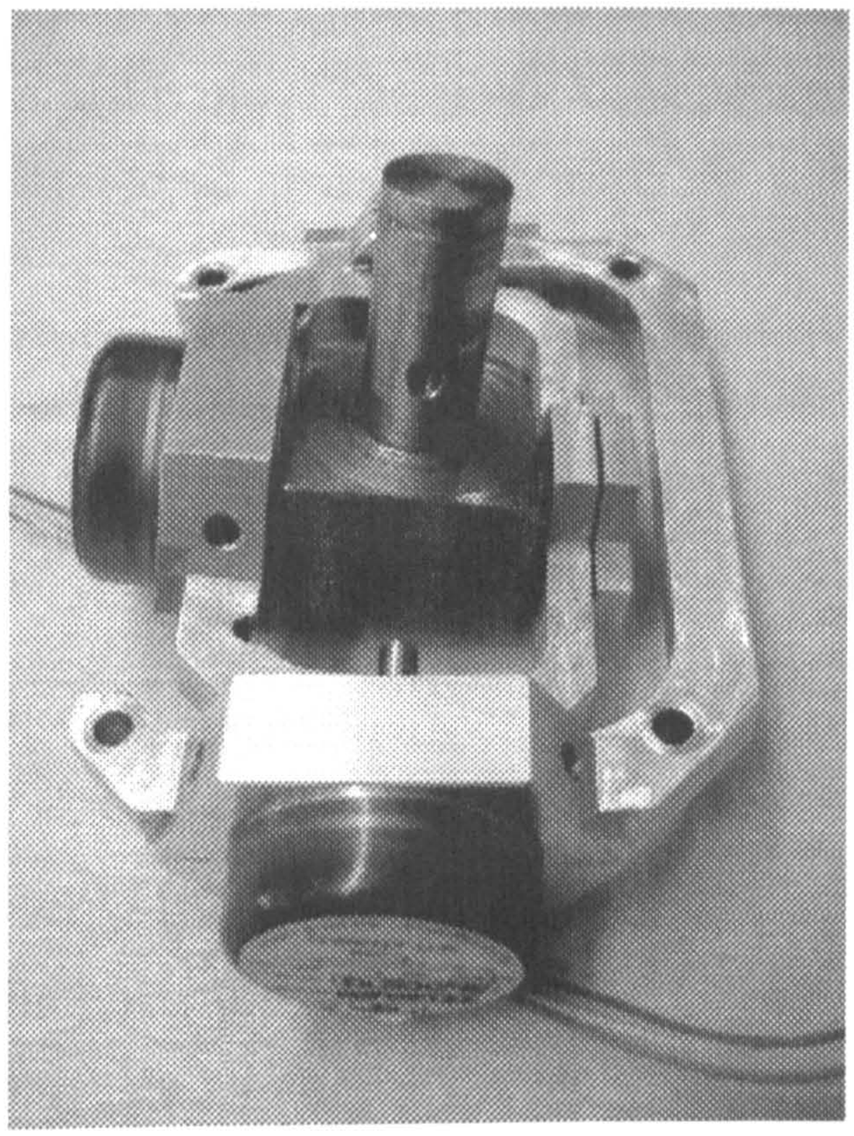

(b) 2 DOF.

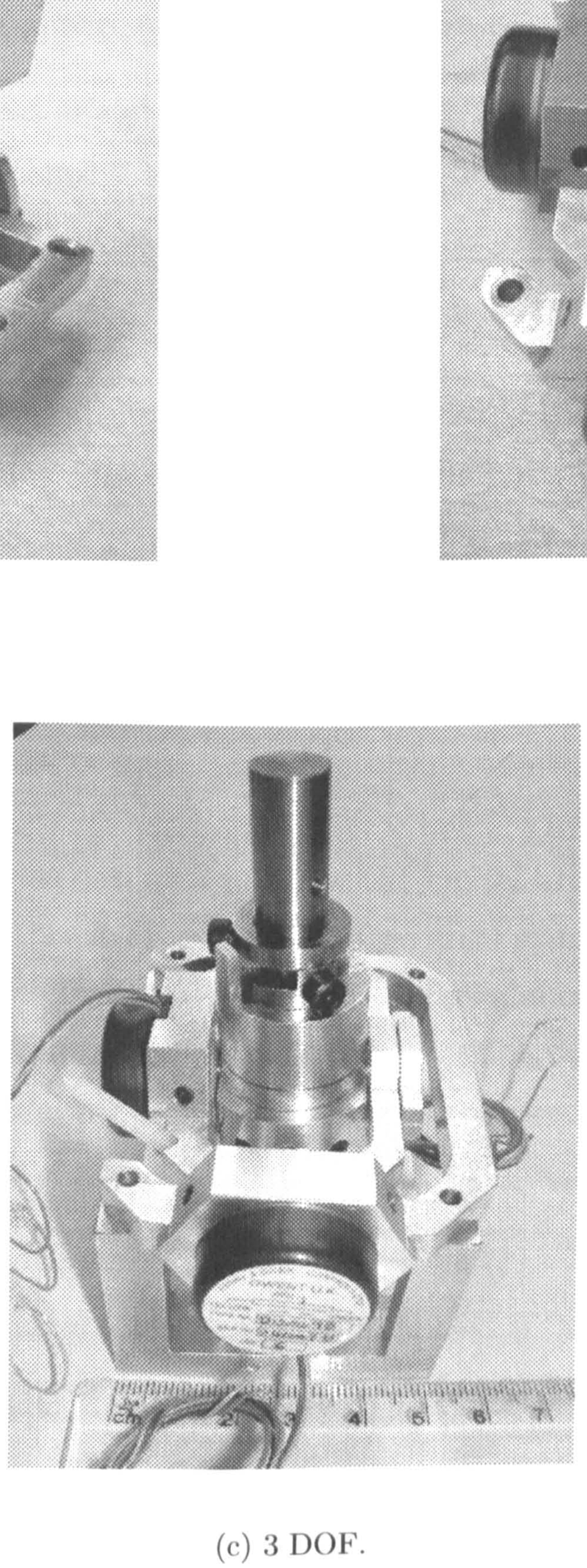

(c) 3 DOF.

Figure 3.2: Gimbals used for various rig configurations.

Due to space and cost constraints it was not possible to use rotary encoders as one would wish. This would eliminate noise problems, and possibly remove the need for separate rate gyros as the clean position signal can be differentiated to give angular rate.

Table 3.1: Penny & Giles RCP09 potentiometer specification.

| | |
|---|---|
| Electrical angle | 342° (±2°) |
| Resistance | 5KΩ (±20%) |
| Independent linearity | ±0.35% |
| Resolution | Virtually infinite |
| Power dissipation @ 20°C | 1.5W maximum |
| Operating temperature range | −25°C to +90°C |
| Operating Life | Greater than 50 million rotations |
| Packaging | 09 synchro mount |

### 3.1.2 Counterbalance

A counterbalance system was designed to allow the model to sit further back in the tunnel, giving more motion in heave (Figure 3.3). Two steel arms are used to carry weights either side and above the mounting point. The counterbalance is attached to the pendulum strut via a removable aluminium mounting arm. When using the counterbalance it is necessary to add a 45° adapter between the end of the pendulum strut and the model (see Figure 3.3) to allow low angles of attack to be attained without the strut hitting the model.

## 3.2 1/16th Scale BAe Hawk Model

The model used for all tests in this thesis is a 1/16th scale BAe Hawk, shown in Figures 3.4 to 3.6, built at the University of Bristol. The model was constructed from scaled-down 1/8th scale radio-controlled model plans, and hence is only an approximation of

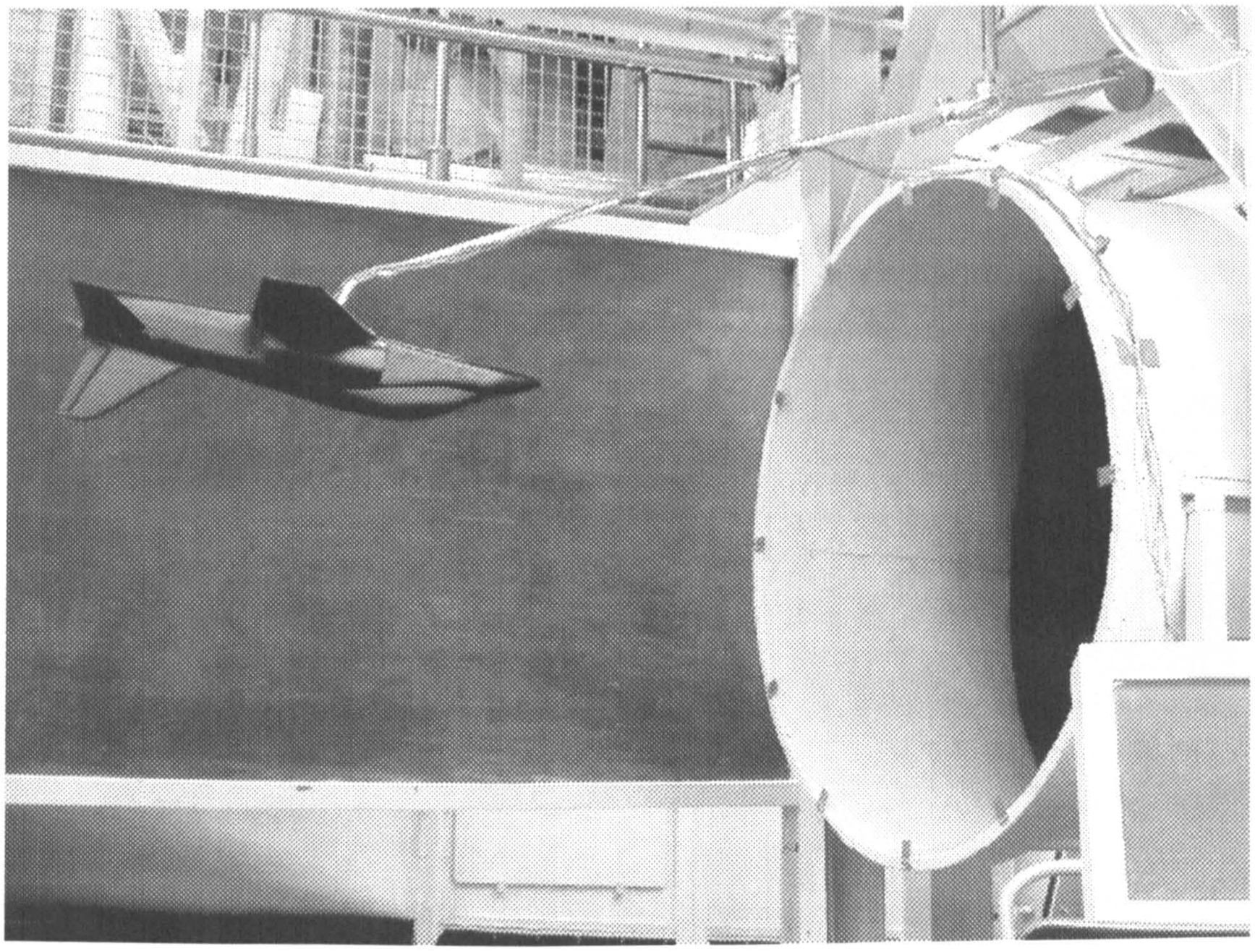

Figure 3.3: Counterbalance arrangement used to give full 5 DOF (constrained) motion.

an actual Hawk[1]. The main structure is plywood, with balsa wood sections and skin. The entire model is covered with a single layer of glass-fibre reinforced plastic, mainly for durability but also to enhance strength. Two-part car body filler was used to achieve a smooth surface finish. Details of the Hawk model are given in Table 3.2.

Table 3.2: Hawk model specification.

| | |
|---|---|
| Length | 0.655m |
| Span | 0.612m |
| Wing surface area | $0.078\text{m}^2$ |
| Mean aerodynamic chord | 0.135m |
| Weight | 1.8kg |
| Moment of inertia ($I_{yy}$) | $0.0343\text{kgm}^2$ |

[1]The main differences are the engine intakes and fuselage cross-section at the rear of the model; both are enlarged for use with a model aircraft ducted fan system.

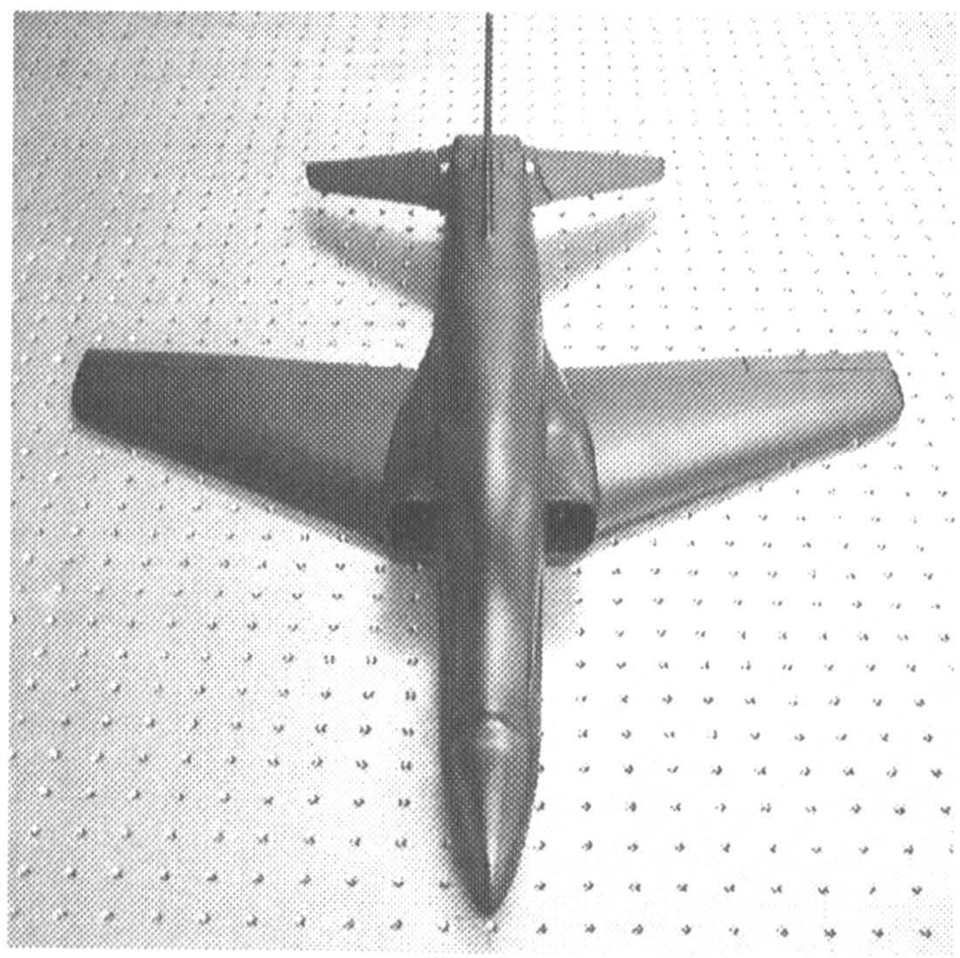

(a) Front view.

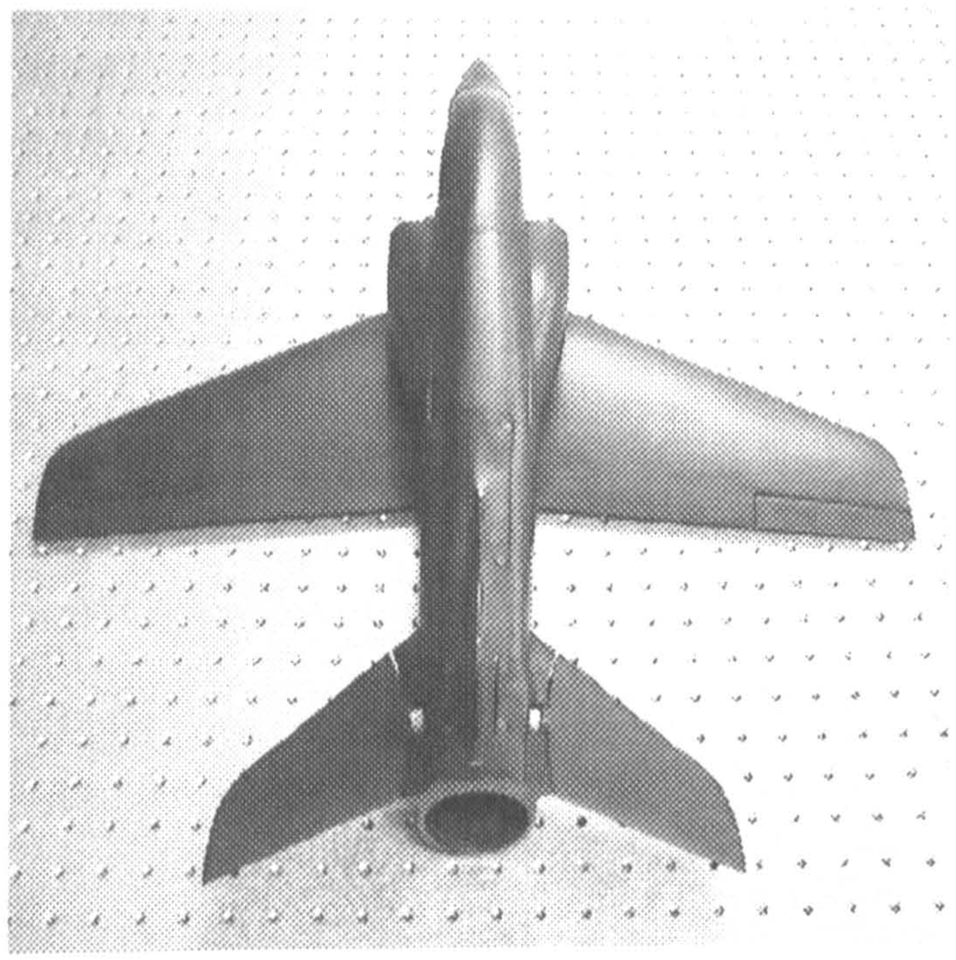

(b) Rear view.

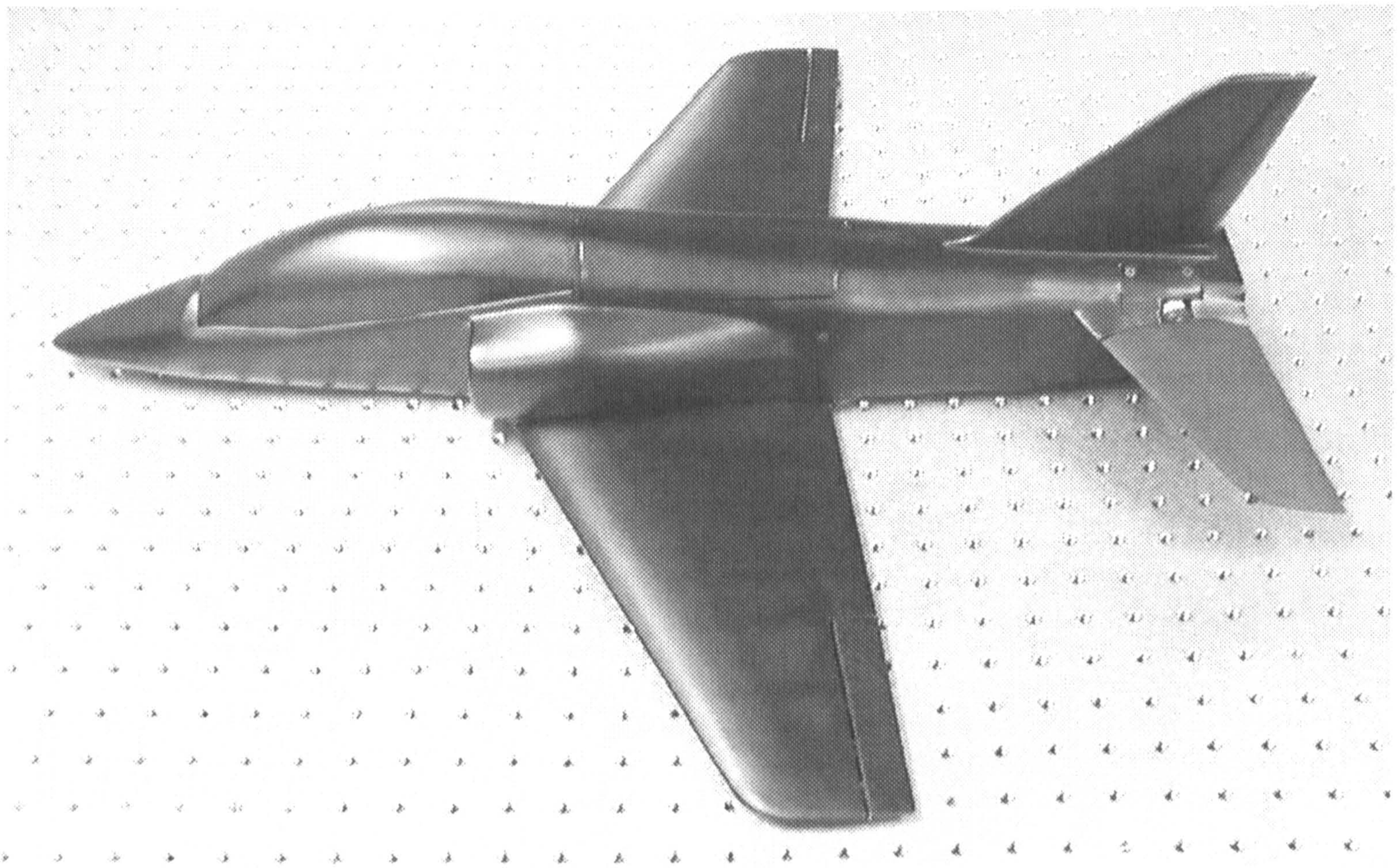

(c) Side view.

Figure 3.4: 1/16th scale BAe Hawk model.

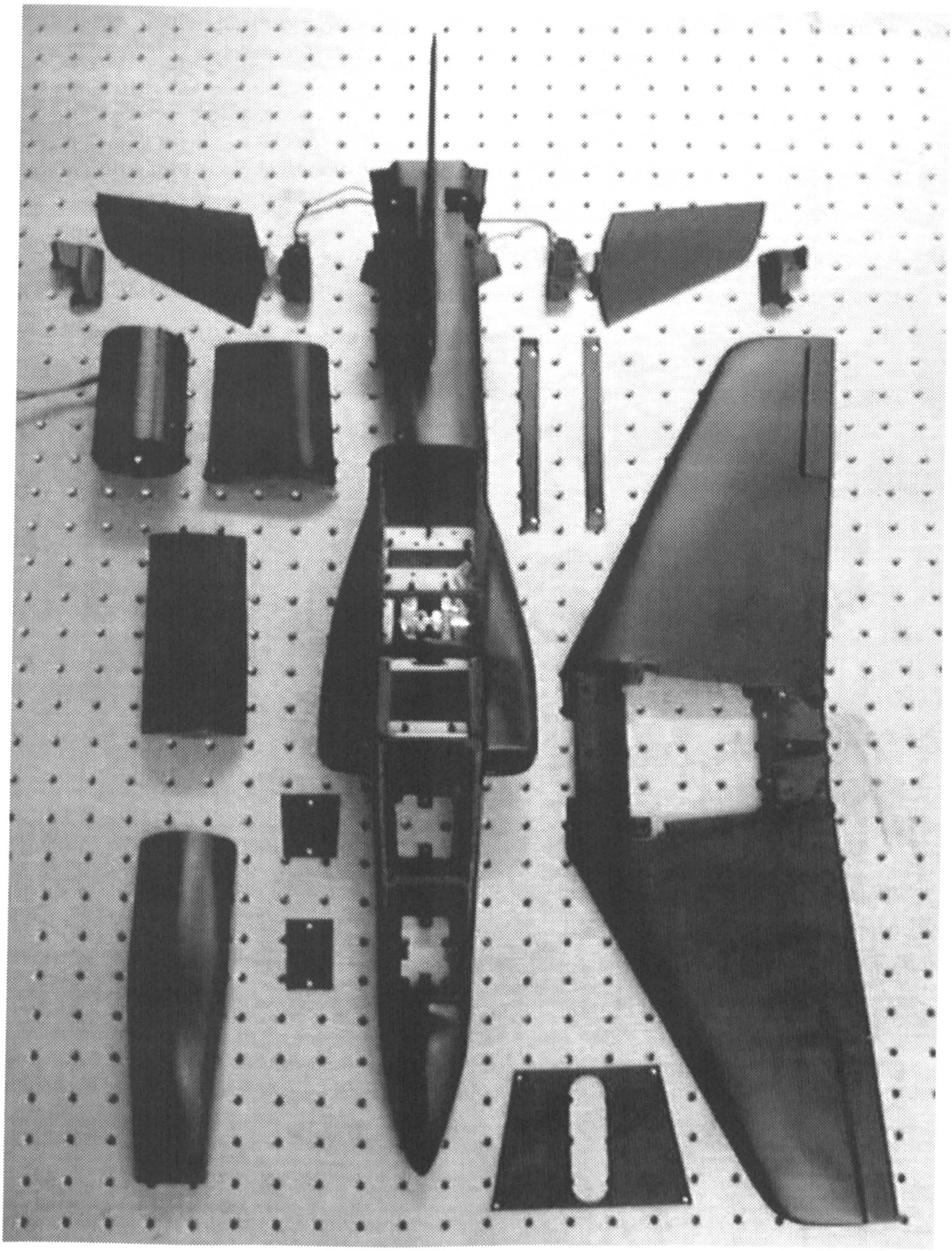

Figure 3.5: Hawk model showing modular design.

No moment-of-inertia data was available for the full-size Hawk aircraft, hence the model is not dynamically scaled (it is likely that the moments-of-inertia of the model are larger than the scaled values).

As shown in Figure 3.5, the model was built in a highly modular fashion to allow different configurations to be tested. The wing is removable to allow access to the central gimbal mount and aileron servos, and all canopies are removable to allow easy access to internal electronics and components. Provision was made for the use of a small electric ducted-fan power plant, which could be inserted into the model through the removable side hatch (Figure 3.6).

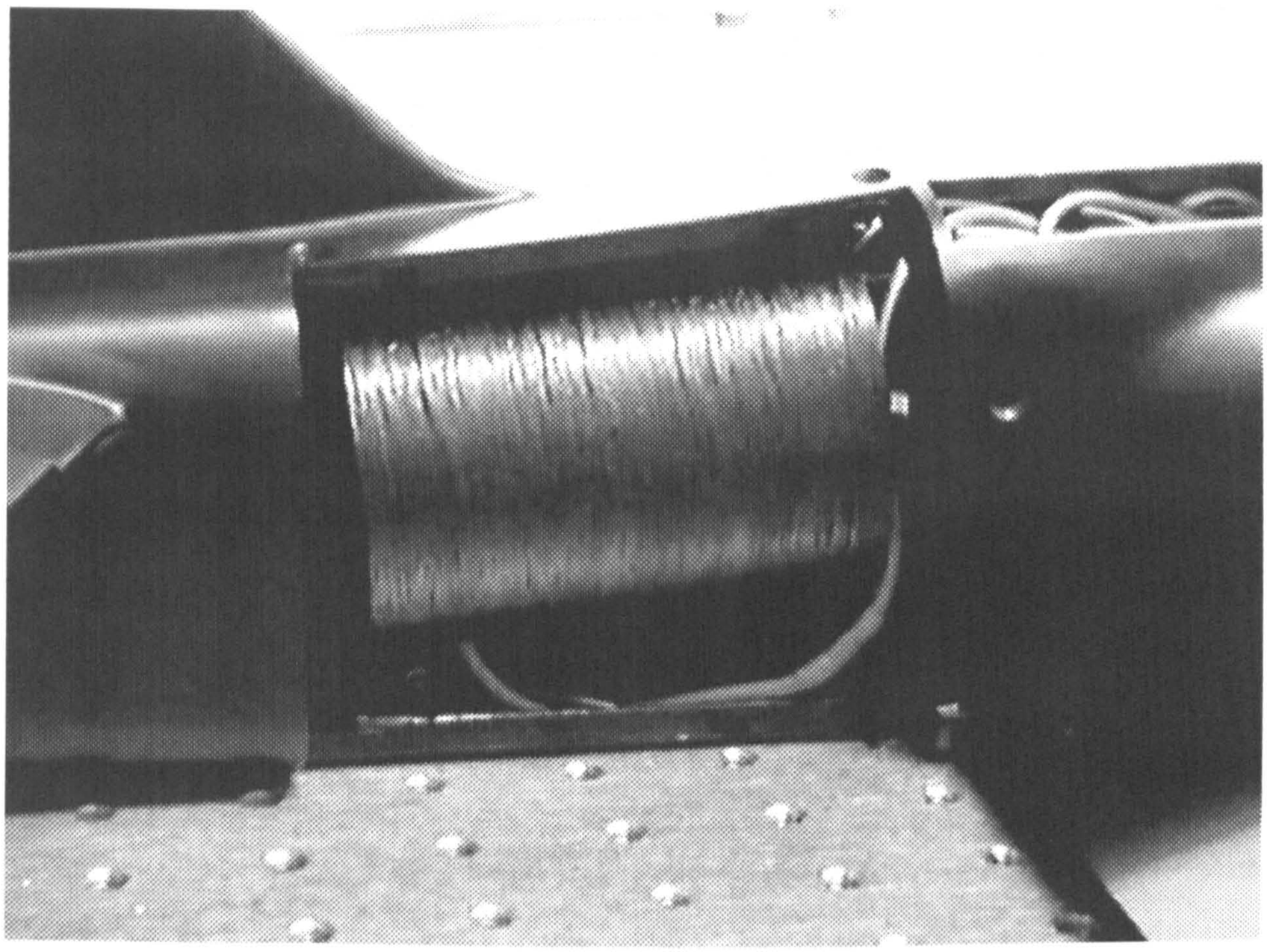

Figure 3.6: Hawk model with side hatch open and electric ducted fan in place.

### 3.2.1 Static Testing

The first tests to be carried out on the Hawk model were longitudinal static tests in the Department $7' \times 5'$ tunnel (see Section 3.5 for a description of the tunnel). The model was mounted in the tunnel on a 1 DOF aluminium gimbal (the same gimbal used for

dynamic 1 DOF tests), allowing it to pitch only. Using the dSPACE system (Section 3.4.1) it was possible to automate the static testing process. A description of the process and static test results for the Hawk model are given in Appendix A.

## 3.3 Control Surface Actuators

### 3.3.1 Actuator scaling

In [66] (Section 5.2) the importance of accurate actuator modelling during the control system design phase is emphasized, within the context of Pilot Induced Oscillation (PIO) prevention. Non-linearities within the actuation system (such as position/rate limiting) expose the pilot to sudden changes in the dynamics of the augmented aircraft. In the case of rate limiting, the pilot sees a slower response and will increase gain accordingly, possibly leading to PIO. The control system is also being subjected to these sudden changes in system dynamics, which, if not taken into account during the control system design phase may cause a significant reduction in performance, or possible instability. The essential parameters needed when specifying an actuation system are given as:

- Rate Capability (RC) : maximum no-load rate
- Nominal Bandwidth (NBW) : no-load bandwidth[2]
- Stall Load (SL) : maximum actuator output force (occurs at zero velocity)
- Control Module Characteristics : direct-drive valve/electro-hydraulic, bandwidth, damping ratio, spool stroke, etc.
- Hysteresis
- Threshold (lowest level of input which will produce a perceptible and measurable output)
- Freeplay

[2]This represents the bandwidth of the actuator for small to medium amplitude inputs

These parameters must be equivalent (when scaled) to the full-scale system if accurate dynamic model tests are to be performed. If the aircraft is open-loop unstable it is even more important that the full-scale and model actuators are equivalent as deficiencies will be amplified by the instability. Actuator positional accuracy and maximum angular velocity are directly related to the aerodynamic effectiveness of the control surface – more powerful control surfaces (such as the tailplanes on the Hawk model) must have high positional accuracy, with less of a requirement for high rotation rates.

Control surface actuator performance requirements are made more demanding by scaling. The positional accuracy requirements remain the same (for example, $\pm 0.05°$ for both full-scale and model), but the angular velocity required scales with the angular rate of the aircraft (for example, if Froude scaling[3] is used angular rates must be multiplied by a factor of $1/N^{\frac{1}{2}}$, where $N$ is the linear scale factor). Angular velocities for primary flight control surfaces on modern aircraft are around 100°/s (see Section 3.3.2), giving a scaled angular velocity requirement of several hundred degrees per second. Add to this the need for the actuators to be extremely small and lightweight, and even bespoke units cannot meet the requirements. Miniature hydraulic actuators are an option in moderately sized models and give good accuracy, high bandwidth and large force output (around 200:1 torque/weight advantage over electromechanical actuators [86]). However, they are expensive to produce, require an external hydraulic pump, and need hydraulic lines to be run into the model, increasing friction and damping. Pneumatic actuation is also possible, but is usually used for on-off control and suffers from the same supply-line problems as the hydraulic actuators.

### 3.3.2 Actuator Requirements

#### Backlash

Backlash is an important property of a control surface and is defined as the range about a set actuator position in which there is zero stiffness at the control surface. Backlash arises from the linkages between control surface and actuator, and possibly from the

[3]Froude number, $\frac{V^2}{lg}$, must be equivalent between full-scale and geometrically-similar model to ensure inertial and gravitational effects are equivalent [104]. Froude number equivalence of free-flying models can be readily satisfied if compressibility (Mach number) effects are negligible.

actuator itself. In the case of a full-scale aircraft (using a hydraulic actuator and control arm) the backlash can be made extremely small, but on small models a different arrangement is generally used (due to rotary-output servo actuators) and backlash is harder to eliminate. Also, a relatively large amount of backlash is found within model servos themselves as they are not specifically designed with low backlash output gearboxes (speed and torque are more important).

Military requirements for control surface freeplay can be found in [105]. This states:

- for a trailing edge control surface which extends outboard of the 75% span station of main surface, the total freeplay shall not exceed 0.13° or 0.0022 rad.
- for an all-movable control surface, the total freeplay shall not exceed 0.034° or 0.0006 rad.

In [106], the all-moving tailplanes on full scale variable-sweep-wing combat aircraft are tested for freeplay and are found to be within the specification set out in MIL-A-8870 in 90% of tests. As absolute angles do not scale with varying model scale factor, a total freeplay requirement for the actual aircraft of 0.034° means that any models must also meet that requirement to remain accurate.

### Positional Accuracy

As far as the author is aware, there are no military specifications for the absolute positional accuracy of flight control surfaces. Little data is published about existing aircraft stating control surface accuracy, but using a hydraulic system a reasonable estimate can be made at 0.1°. Again, positional accuracy has a scale factor of 1, so a scale model of the aircraft must also have a positional accuracy of 0.1°.

### Angular Velocity

In [66] (page 55) it is stated that during initial design of a control system a good estimate of the control surface angular rates is that of 0.2 seconds from neutral to full deflection.

This provides a fast transient response, and allows maximum amplitude oscillatory surface travel at about 5 rad/s at the onset of rate saturation, and up to 8 rad/s while fully rate saturated (neglecting acceleration limiting). Typically this requires maximum rates of about 100°/s. This value was used on the EAP and Eurofighter, which, with severe pitch instability, could not tolerate significant rate limiting. As an example of where very high angular rates were used, the English Electric Lightning had aileron rates of 160°/s (using only ±8° with wheels up).

In [107], specifications for the High Incidence Research Model (HIRM) are given. Although a hypothetical aircraft, it is representative of a modern, highly manoeuvrable fighter aircraft; the specifications give a primary control surface rate saturation value of 80°/s.

Maximum control surface deflections for the BAe Hawk are given in Table 3.3. Using the 0.2s to full deflection rule from [66] gives the maximum angular rates also shown in Table 3.3. Required scaled angular rates for the 1/16th scale BAe Hawk model are shown in the right-hand column (using Froude scaling, $1/N^{\frac{1}{2}}$).

Table 3.3: Control surface deflections and angular rates for full size and 1/16th scale BAe Hawk.

| Control Surface | Maximum Deflection (°) | Minimum Deflection (°) | Maximum Angular Rate (°/s) | 1/16th Scaled Angular Rate (°/s) |
|---|---|---|---|---|
| All-moving tailplanes | 6.6 | -15 | 75 | 300 |
| Ailerons | 12 | -12 | 60 | 240 |
| Rudder | 20 | -20 | 100 | 400 |

### Hysteresis

Hysteresis is caused by backlash and friction in the actuator and drive system, and/or deadband (limited positional accuracy) in the actuator. In [86] an electromechanical

drive system is made for a 1/30 scale B-52 wind tunnel model, and hysteresis of less than ±0.2 degrees is achieved (this is reduced to ±0.06 degrees using hydraulic actuators).

### 3.3.3 Hawk model surface arrangement

In order to minimize freeplay/backlash it was decided that all control surfaces, apart from the foreplanes, would be driven directly by attaching a shaft to the servo output rather than using the conventional radio-controlled model method of pushrods and control horns. In hindsight, this caused several problems:

- backlash in the servo gearbox was excessive (due in part to using micro servos in which compromises have to be made in order to reduce size, see Section 3.3.4) which negated the original reason for using direct drive.

- although the servos have a ball bearing on the output shaft, the shaft is made of nylon which makes it difficult to attach the control surfaces rigidly, and also bends to a certain extent when placed under radial loads. This forced the use of external bearings to support the tailplane shaft (Figure 3.7), increasing weight, width and complexity at the rear of the model.

- direct driving the control surfaces does not allow a change in the resolution, speed and travel. If an indirect method is used (e.g. belt drive or control linkage) these parameters can be changed according to the tests being performed, or if the hardware is changed (e.g. upgraded servo).

- surface position measurement becomes difficult. Using the servo's internal potentiometer proved problematic (Section 3.4.2) and there was insufficient room to use a belt drive to an external potentiometer. Using an indirect drive method would allow a potentiometer to be mounted in-line with the control surface, giving very accurate feedback.

- in the case of the tailplane, the mounting system and cover for the servos were extremely specific to the type of servo being used. This does not give any flexibility for testing other servos or drive methods. It also gave a problem when the dimensions of the servo being used were changed by the manufacturer (the height

was increased by approximately 1mm) leading to problems mounting the servo and cover.

- by having the tailplane and rudder servos mounted at the rear of the model, there was a large mass behind the centre-of-gravity (CG). This meant that a relatively large amount of ballast was required in the front of the model to line the CG up with the gimbal rotation point. This causes a large increase in the moment of inertia of the model.

- again, by having the tailplane and rudder servos mounted in the fuselage at the rear of the model, they caused a large blockage effect behind the mounting point for the ducted-fan power plant. This was a major reason why no tests with the ducted-fan were carried out, as its effectiveness was very limited.

The problems with the tailplane drive mechanism became apparent during initial static testing of the model. Feedback from the internal potentiometers was being used to give position measurement, although the signal was noisy due to the poor quality internal potentiometer and the relatively long wires from the model to the ADC. The accuracy of the tailplanes was estimated at $\pm 1.5°$ during static tests. Static hysteresis of the tailplanes was evident under both wind-on and wind-off conditions.

Having found the control surface drive problem, a conventional radio-controlled push-rod method was briefly tried on one of the tailplanes. Fears about backlash/freeplay caused by the control run were shown to be largely unfounded, and overall it was a large improvement. However, there was not enough space at this stage to permanently convert the model, so the original direct drive method was used for all tests.

### All-Moving Tailplanes

The primary longitudinal control surfaces on the Hawk are all-moving tailplanes. It was decided that they would be driven independently to give maximum flexibility, and to allow development of fault-tolerant control laws in conjunction with another PhD project.

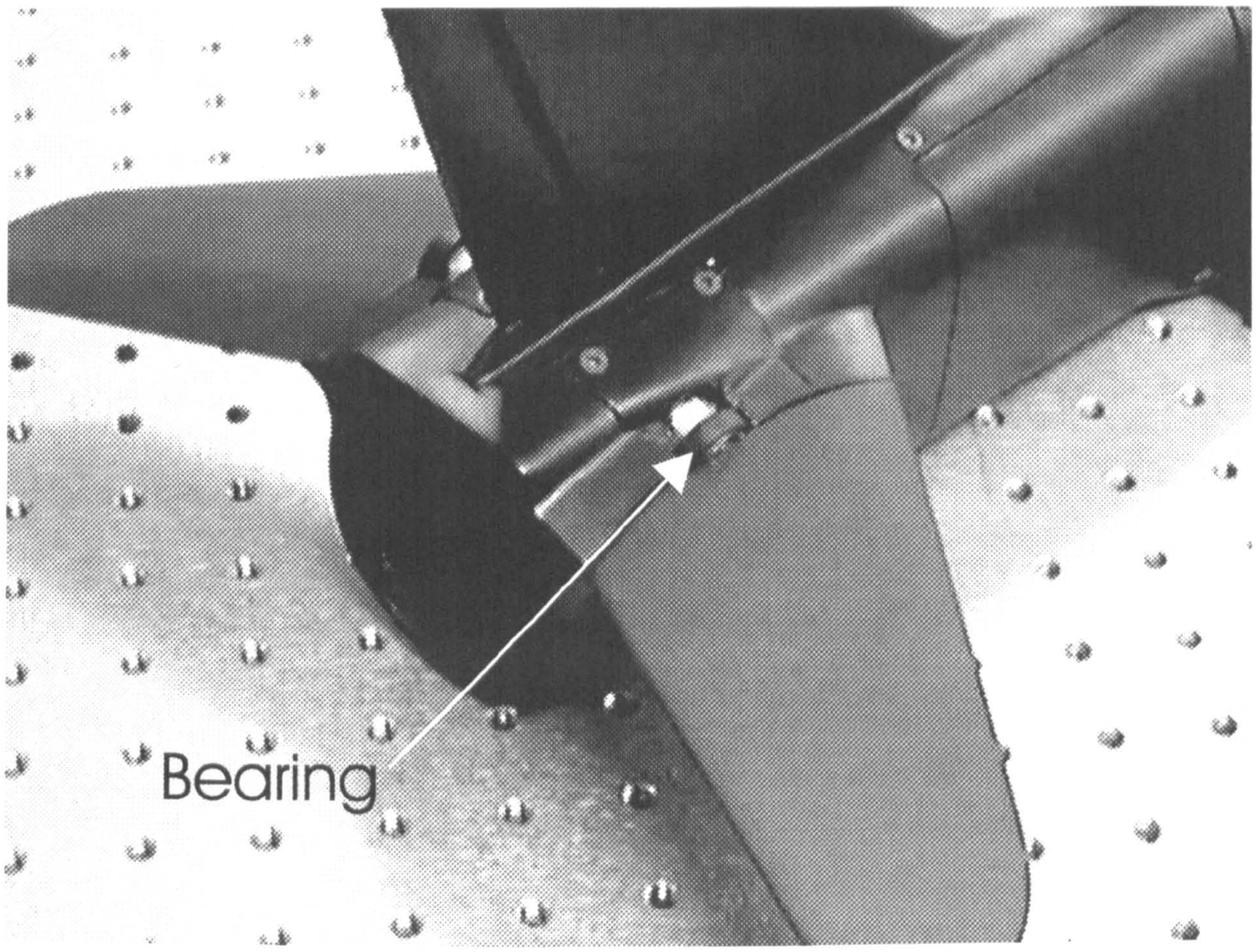


Figure 3.7: All-moving tailplanes. Note the direct drive mechanism and external bearing support.

### Ailerons

The independently actuated ailerons are driven by servos that sit in the centre of the fuselage, in line with their respective surface (Figure 3.8). Drive is transferred from servo to aileron via a 1.45mm diameter (15 AWG) stainless steel welding rod, with a custom made aluminium servo horn. It is not known how much torsional bending there is in this rod, however, there is only a small amount of backlash/freeplay at the control surface. Unfortunately, there is a fairly large amount of friction on the connecting rod, due to it passing through the wing spars, which causes some positional hysteresis and places a large amount of strain on the servo, especially when under continuous feedback control.

### Rudder

The rudder servo is mounted in the rear of the fuselage, in line with the rudder. Again, drive is transferred to the surface using a stainless steel rod, and the same problems are

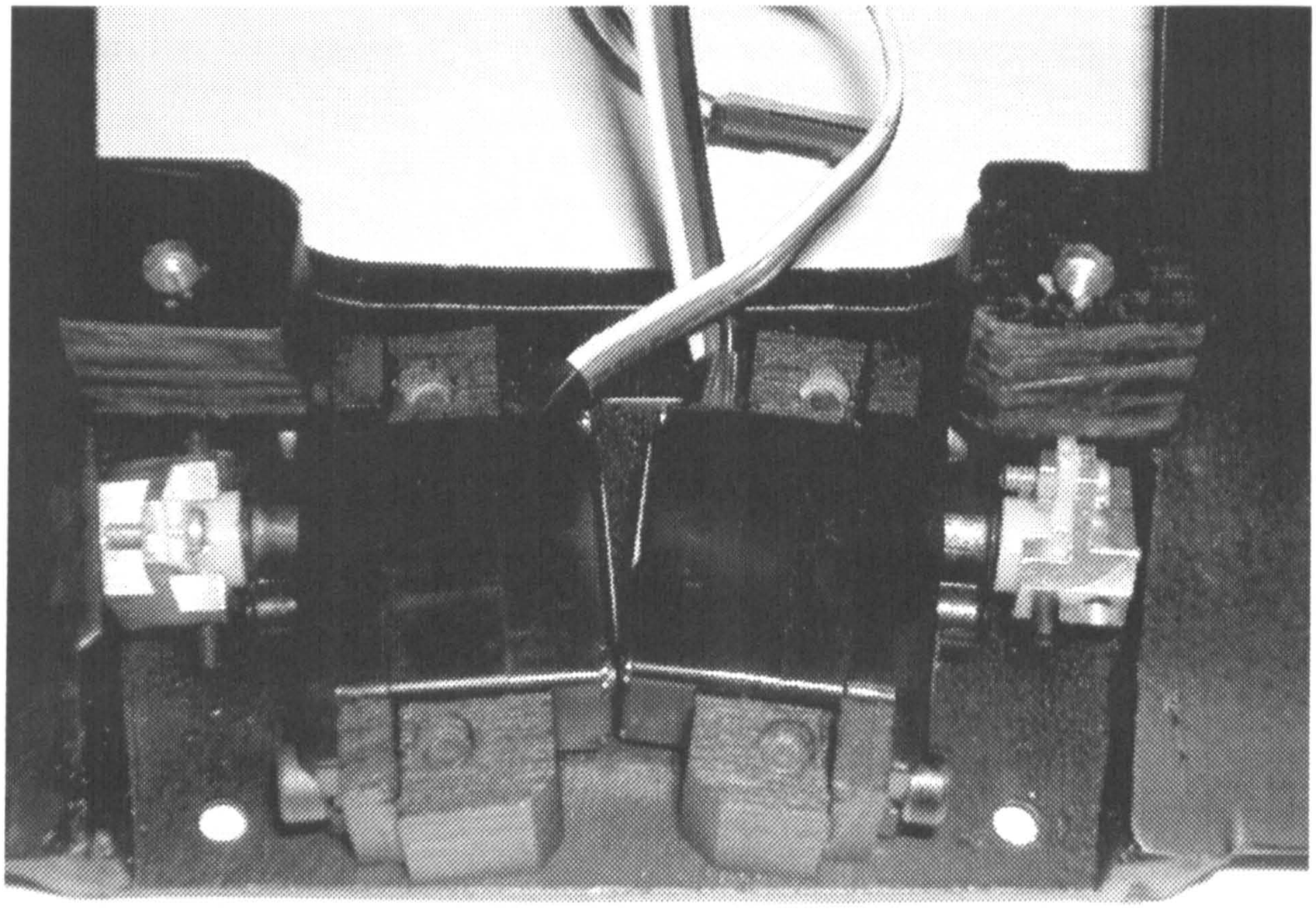

Figure 3.8: View of the central wing box showing aileron servo drive arrangement.

encountered as with the ailerons.

### Foreplanes

The Hawk model was modified with the addition of all-moving foreplanes (Figure 3.9) to test the effectiveness of a digital servo with toothed-belt drive, and to introduce another longitudinal control effector to investigate multiple-input control. Ideally, the shortest belt possible would be used (to minimize stretching) but due to limited space in the front section of the Hawk a slightly longer belt had to be used (Figure 3.9(b)). Also, a full-size servo could not be mounted sideways in the model, so a slightly smaller digital servo was used, a JR DS9411. This has a slightly lower specification than the full-size servo, as evaluated in Section 3.3.4.

The foreplanes themselves (taken from another model) are made from softwood and are not perfectly symmetrical. They rotate on miniature precision bearings glued to the side of the model, which provide low friction with zero radial movement. The foreplanes

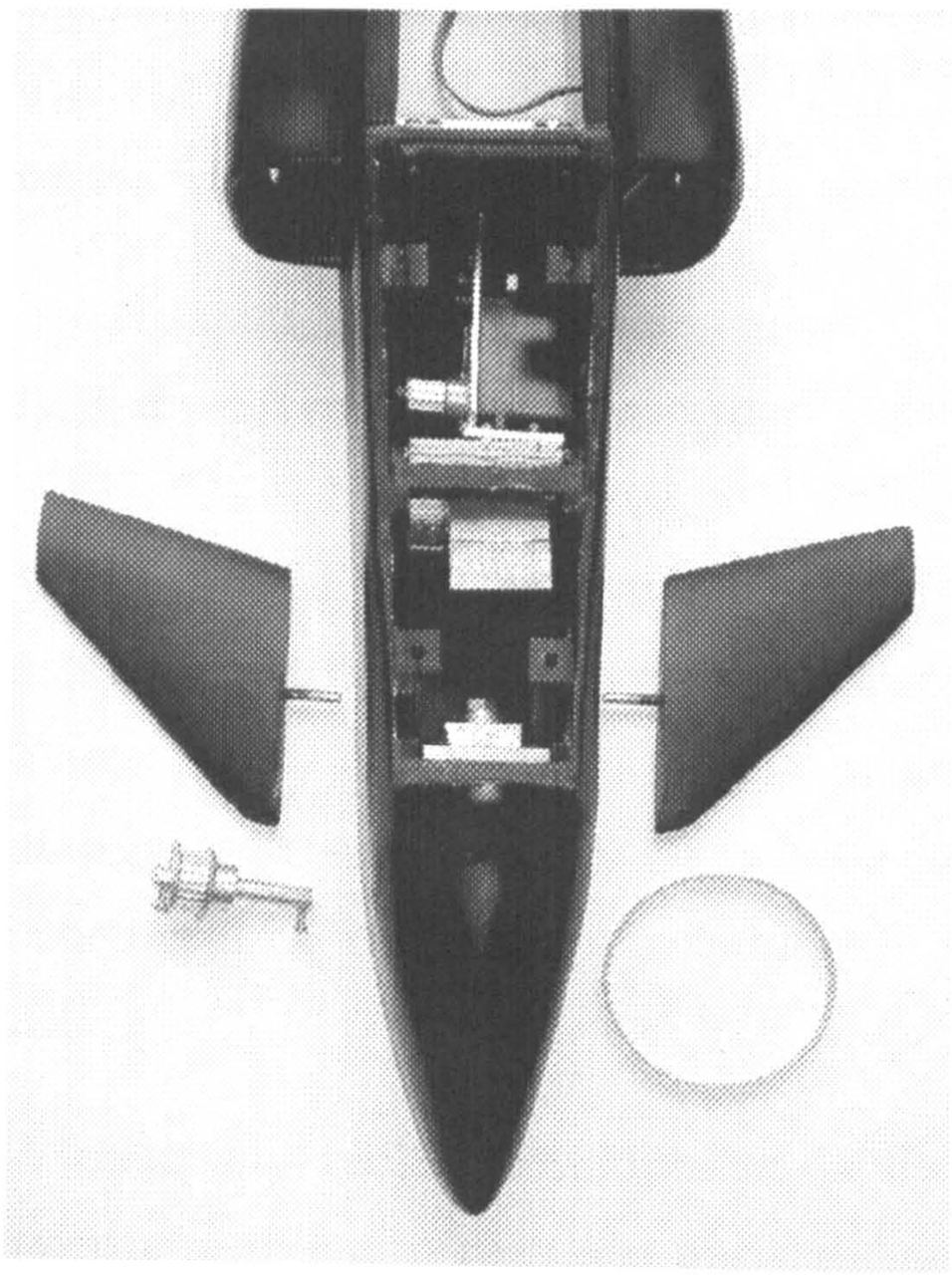

(a) Forward fuselage and detachable foreplanes.

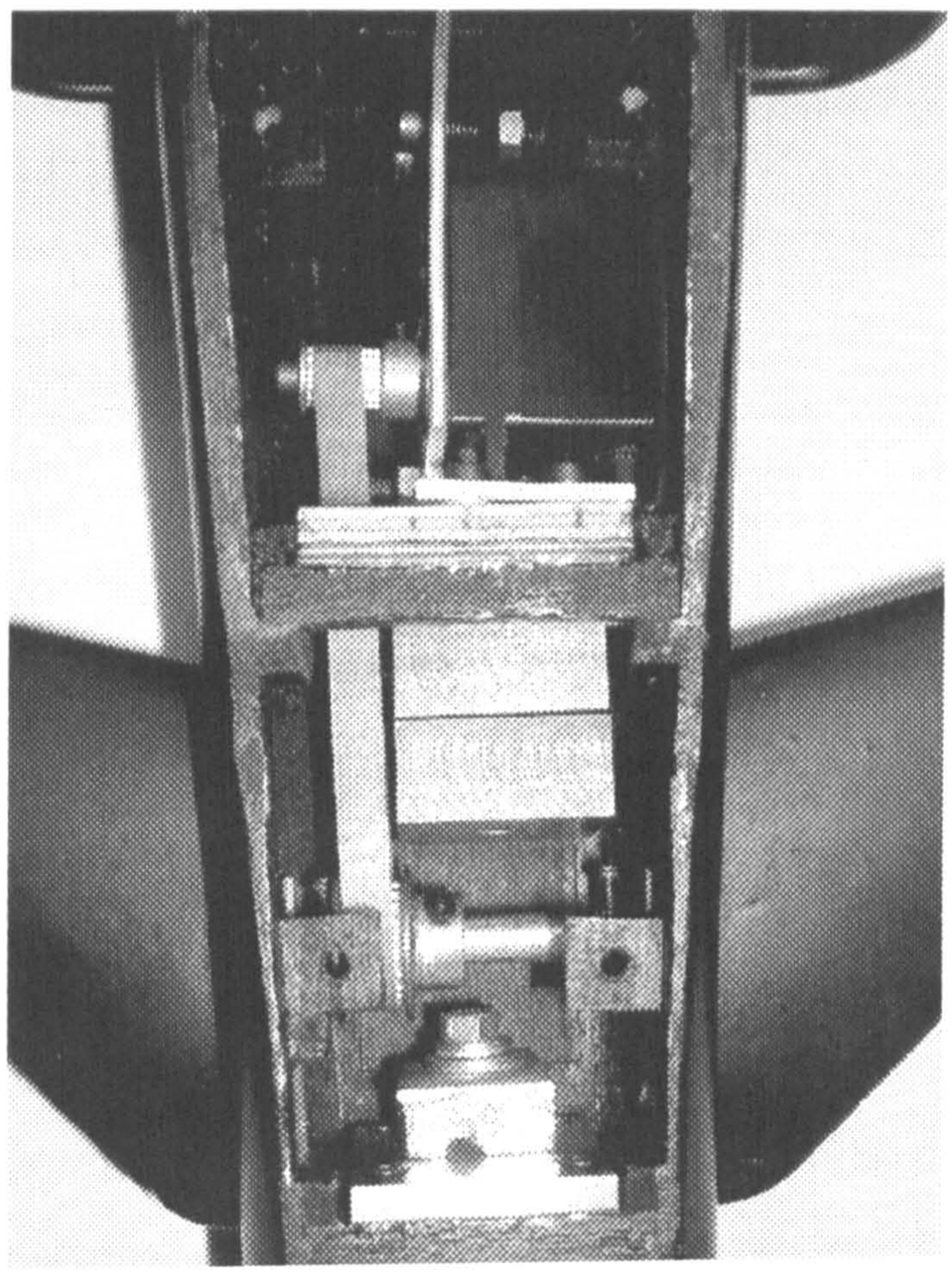

(b) Toothed drive belt arrangement.

Figure 3.9: Top views of the drive arrangement for the all-moving foreplanes.

are joined using a 6mm aluminium shaft, which passes through the toothed pulley. The gearing chosen was 2:1 (servo:canard movement). This was possibly slightly low, as the foreplanes proved to be much less effective than the tailplanes, hence requiring less positional accuracy and higher speed. This emphasizes the need for a flexible mounting system which allows different gearing ratios to be tested. The belt is tensioned by adding washers between the servo mount and the aircraft bulkhead.

The belt drive set-up was a large improvement on the direct drive method. Freeplay was estimated at $\pm 0.25°$, and could have been reduced further with a modified servo mount allowing continuous belt tensioning. Positional accuracy was greatly increased by using the larger digital servo and the gearing provided by the belt and pulleys. Unfortunately there was no room in the front of the model to test position feedback, however, using a very low friction potentiometer (e.g. the Penny & Giles potentiometers used in the gimbals) in line with the control surface should not prove troublesome. This would be

the recommended method for driving control surfaces on future models, and incidentally was the type of drive used in a 2 DOF actively controlled canard-delta rig previously tested at the University [98], but no reasons for using this method were given.

### 3.3.4 Actuator Testing

When dealing with small models (<1m span), even with a large budget the most viable solution is to use electro-mechanical servos from the radio controlled model industry. These rotary-output units fit into a small space, give good output torque, and are relatively high speed. They have been in development for many years and have evolved considerably, and extremely small and lightweight units can now be purchased for around £25.

A relatively recent development is the digital servo. Digital servos use an on-board microcontroller to regulate position, and are controlled using up to 300Hz pulse width modulation (PWM) as opposed to 50Hz for a standard servo (giving improved response time, increased holding torque and improved positional accuracy). This increase in PWM frequency immediately reduces the average delay before the motor starts to move from 10ms (half the PWM period) on standard servos to 1.7ms. This can be seen in the step response time histories in Figures 3.12 and 3.13. Almost all digital servos have metal gears (reducing backlash and wear), coreless motors (lower rotating mass) and 2 ball bearings on the output shaft.

In [108] tests were carried out on a model servo (Futaba S3001 'analogue' servo) for use in a 65° delta wing model. However, tests were only conducted on that servo, and it was thought to be useful if tests on different servos were performed (including the type that is used in the Hawk model to allow a mathematical model to be derived). Tests were carried out on standard, micro and digital servos to establish positional accuracy and bandwidth. The accuracy is not stated by the manufacturer as it is usually of little concern to radio-controlled modellers (they are mainly concerned with speed and torque). Servo manufacturers normally quote a time for 60° movement, giving an indication of bandwidth.

A simple test rig (Figure 3.10) was constructed consisting of a servo connected via a

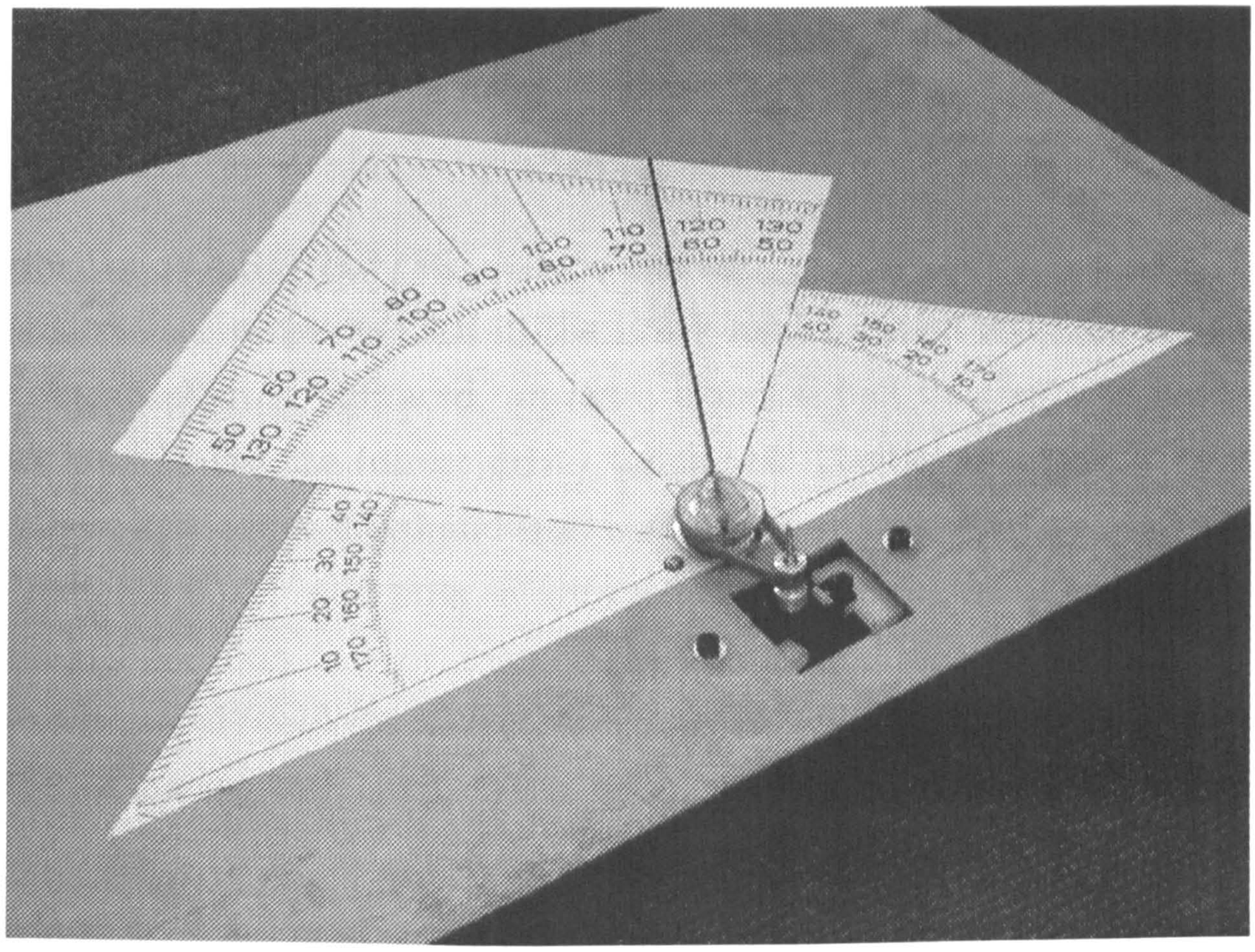

Figure 3.10: The servo test rig.

toothed-belt reduction drive to a Penny + Giles 5KΩ low friction, high-precision carbon-film potentiometer. The potentiometer was connected to a ±15.0V regulated supply, and gave an output RMS noise voltage of approximately 25$\mu$V (approximately 0.0125°). A long carbon rod was connected to the pulley on the potentiometer to allow angular position to be accurately read from a scale. The servo and potentiometer were both connected to the dSPACE system, sampling at 1KHz. Tests were performed on a Futaba FP-S148 standard servo (costing around £10), a SuperTec Naro HP/BB micro servo (£20, used for the tailplanes, ailerons and rudder in the Hawk model), a JR DS9411 compact digital servo (£75, used for the Hawk model foreplanes), and a Futaba S9450 full-size digital servo (£90). Figure 3.11 shows the 4 test servos. Specifications for the servos are given in Table 3.4, and a brief description of each follows.

- **Futaba FP-S148 Analogue Servo**
  This is the cheapest of the servos tested and is very much a 'standard' servo. The lack of ball bearings and use of plastic gears means that there is some movement of the output shaft and noticeable backlash. However, due to its large size the

holding torque is good, the deadband is relatively small and positional accuracy is estimated to be around $\pm 0.5°$. These attributes have been traded for speed however, and the maximum speed of around $115°/s$ is a big limitation.

- **SuperTec NARO HP/BB Micro Servo**
  This is the servo that is used in the Hawk model due to its small size. Although the output shaft is ballraced, an extra external ball bearing was needed on the Hawk to stabilise the (direct drive) tailplanes. Positional accuracy and backlash have been traded for speed and size; backlash of approx. 1.5° is a long way short of the required 0.034° and puts severe limits on the accuracy of controlled motions. Positional accuracy is poor, mainly due to a large deadband and low torque; this gives additional problems with control, especially due to the large control authority of the all-moving tailplanes. These problems will be exaggerated when the servo is under load.

  During frequency-sweep tests it was very difficult to tell the bandwidth of this servo due to its poor positional accuracy. The output position would simply not become a triangular wave and decrease in amplitude like the other servos, but would move around seemingly arbitrarily with spikes sometimes appearing at a greater amplitude than the demand. This demonstrates one limitation of using highly miniaturised components.

- **JR DS9411 Compact Digital Servo**
  This servo is used to drive the foreplanes on the Hawk model and was chosen for its small size while still maintaining performance. The toothed pulley used in the foreplane drive mechanism can be attached directly to the servo's metal output shaft using a locating bolt and grub screw, with no additional backlash. Dual output shaft ball bearings allow high belt tensions to be used without damaging the servo. A microprocessor is used to control position, and can receive the PWM position demand signal at six times the frequency of analogue servos, immediately reducing the average delay from demand to beginning of movement by a factor of six (Figures 3.12 and 3.13).

- **Futaba S9450 Digital Servo**
  This is the most expensive of the servos tested, and represents the current state-of-the-art of model servos. Metal gears and ballraces give very little backlash

(although still an order of magnitude from the desired value) and a metal output shaft aids direct connection of pulleys/control rods without introducing extra inaccuracies. Due to its large size, the holding torque is excellent which helps to maintain a small deadband. A similar motor drive system to that of the compact digital servo is used, allowing high frequency PWM signals to be used. The positional accuracy was estimated to be within $\pm 0.15°$. This servo is also very fast, being only slightly slower than the micro servo (Figures 3.12 and 3.13).

The only disadvantages with the digital servos are their size, weight, power consumption and cost. Size restrictions mean that their use is limited to relatively large models. Due to their large mass it may be necessary to locate them close to the centre of rotation of the model to achieve dynamic similarity, which will cause problems with linkages to the control surface. The increased power consumption is a small disadvantage for models where an external power source is used, requiring a possible increase in cable size (more friction/damping).

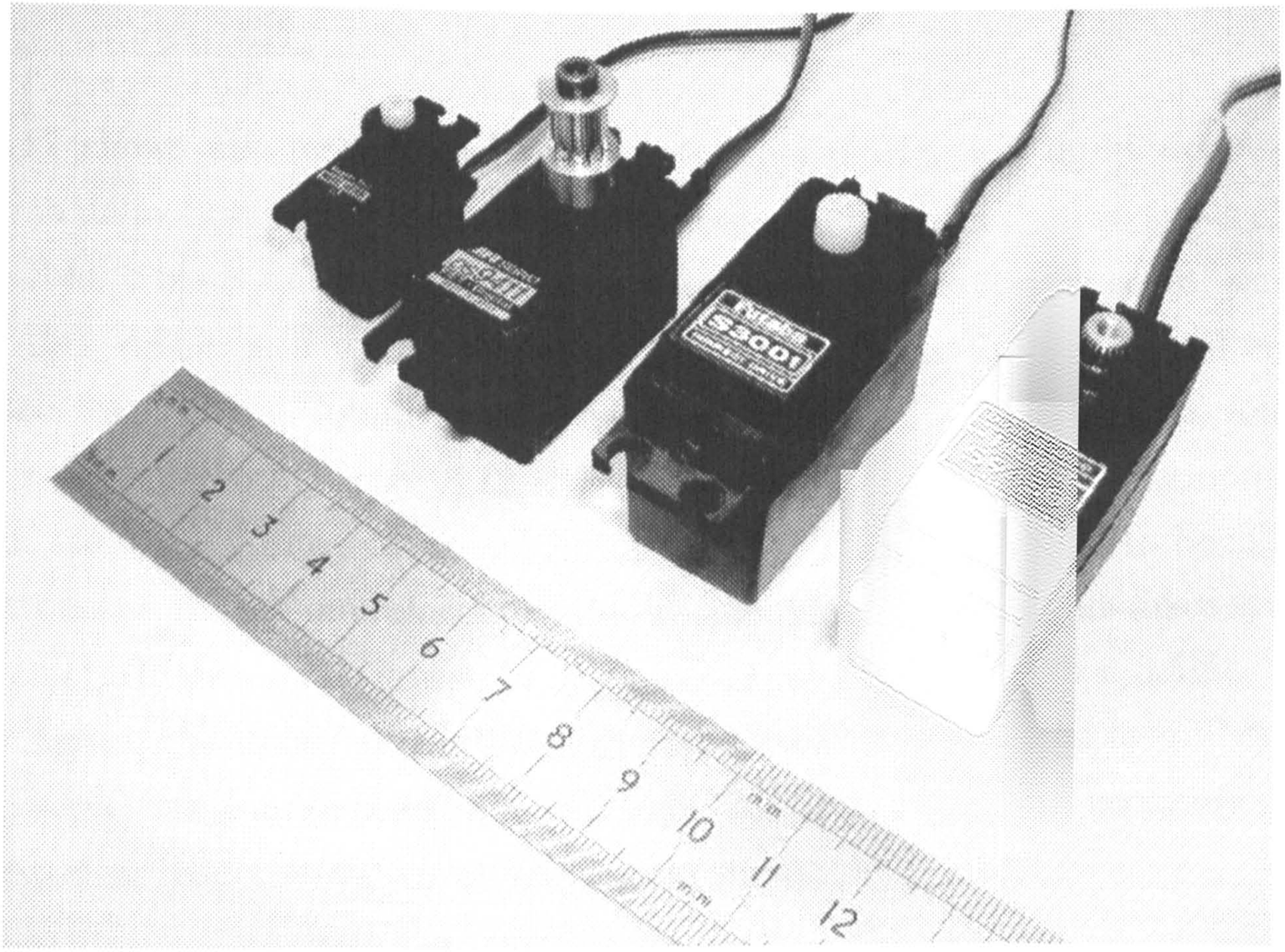


Figure 3.11: The test servos. From left to right: micro, compact digital, standard and full-size digital.

Table 3.4: Comparison of servo actuators.

| | Futaba FP-S148 Analogue | SuperTec NARO HP/BB Micro | JR DS9411 Compact Digital | Futaba S9450 Full-Size Digital |
|---|---|---|---|---|
| Approx. Cost (GBP) | 8 | 20 | 75 | 90 |
| Size (mm) | 19.8x40.4x36.1 | 21.8x19.5x11.0 | 19.2x36.1x26.4 | 20.1x40.4x37.6 |
| Mass (grams) | 42.5 | 9 | 38.5 | 55 |
| Ball bearings | No | Yes | Yes | Yes |
| Metal Gears | No | No | Yes | Yes |
| Quoted Torque (at 4.8V) (Ncm) | 29.5 | 13.7 | 57.9 | 78.4 |
| Voltage (V) | 6.0 | 6.0 | 6.0 | 6.0 |
| PWM frequency (Hz) | 50 | 50 | 300 | 300 |
| Measured deadband (°) | 0.9 | 1.5 | 0.20 | 0.18 |
| Measured backlash (°)[a] | 0.8 | 1.5 | 0.22 | 0.2 |
| Quoted time for 60° | 0.22 | 0.09 | 0.15 | 0.10 |
| Measured maximum angular velocity (°/s) | 345 | 630 | 440 | 570 |

[a]Backlash was measured by applying a force to the output pulley and noting potentiometer movement. Some of the measured backlash will be due to the belt drive, slight movement in the mountings, etc. Actual backlash at the servo output is very difficult to measure.

Figure 3.12 shows the response of the servos to a 0.5Hz, 50° input demand[4]. The difference in delay between demand and servo response between the two types of servos is clearly visible. This is due to the increased frame-rate for the digital servo, as discussed earlier. Also visible is a slight overshoot in one direction for the digital servo. No explanation for this was found, but is typical of the small non-linearities found when testing actuators. From Figure 3.12 it is possible to determine the maximum angular velocity of the servo (values are given in Table 3.4). This is expected to be slightly less than that quoted by the manufacturer, due to the friction in the belt-drive system and potentiometer. Figure 3.13 shows the response of all four servos to a 0.5Hz, 25° input demand. Again, the micro and full-size digital servos are similar in overall speed, but the micro servo has a large overshoot and lower absolute positional accuracy compared to the near-ideal response shown by the digital servo.

Sine wave tests were also conducted on both servos, in order to calculate the (unloaded) bandwidth. As the bandwidth is amplitude dependant (due to rate limiting), frequency

[4]Unfortunately, the JR DS9411 compact digital servo only has a range of 135° so could not perform the full 50° step with the 3:1 reduction gearing, and hence does not appear in Figure 3.12.

sweeps were performed at different amplitudes. The frequencies at which the gain reached –3dB were calculated, and are shown in Table 3.5 and plotted in Figure 3.14.

Table 3.5: Measured bandwidth of test servos.

| Oscillation Amplitude (°) | Futaba FP-S148 Analogue | SuperTec NARO HP/BB Micro | JR DS9411 Digital | Futaba S9450 Digital |
|---|---|---|---|---|
| | Bandwidth (Hz) | | | |
| 25 | 2.1 | 4.5 | 5.4 | 3.6 |
| 20 | 3.0 | 5.1 | 6.6 | 4.8 |
| 15 | 3.6 | 6.9 | 8.4 | 5.7 |
| 10 | 5.1 | 10.5 | 11.4 | 8.7 |
| 5 | 11.7 | 15.3 | 17.4 | 18.0 |
| 2.5 | 17.1 | 18.9 | 24.6 | 28.5 |

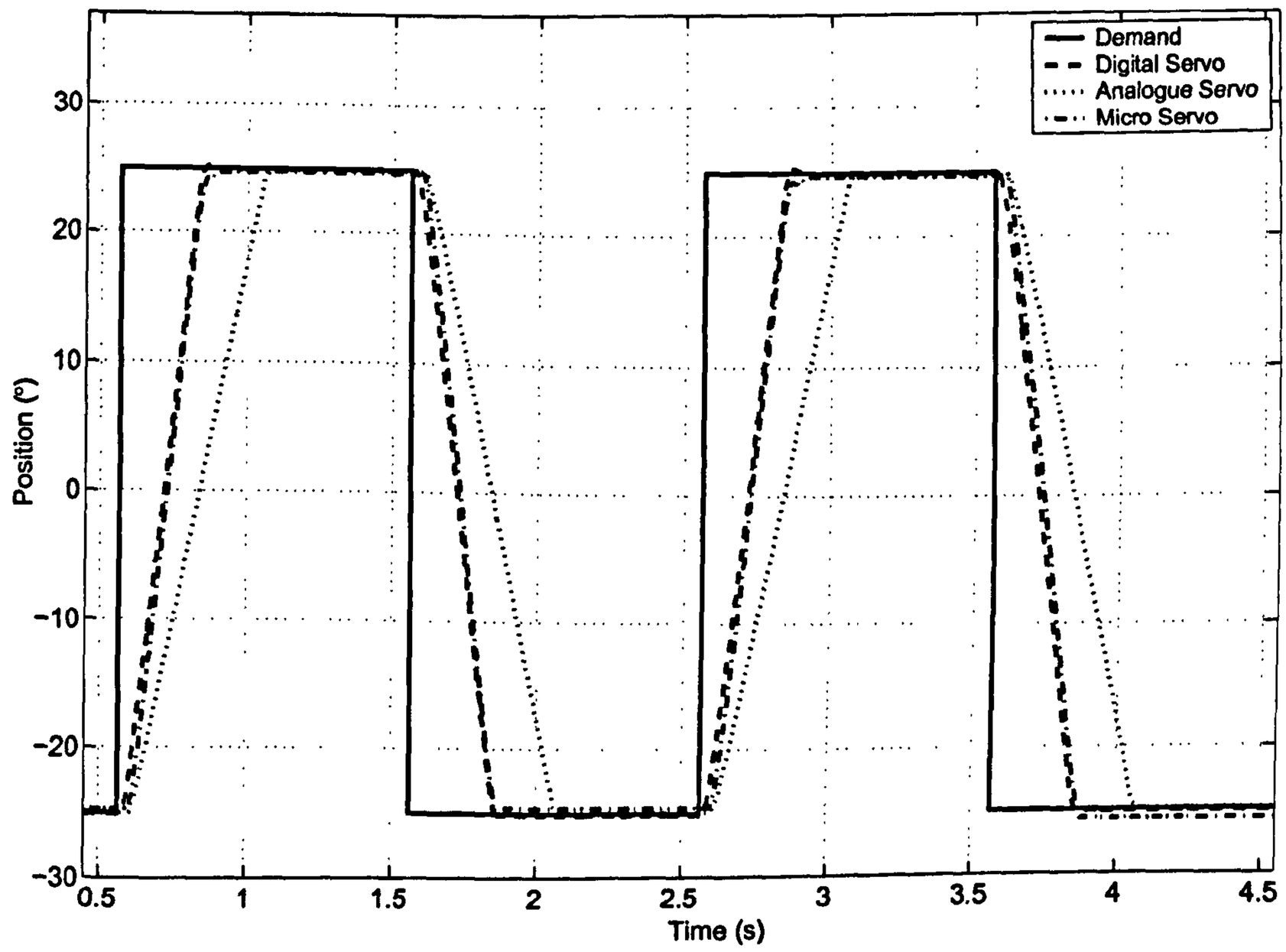


Figure 3.12: Comparison of 50° step responses for analogue, micro and full-size digital servos (using 3:1 belt-drive reduction).

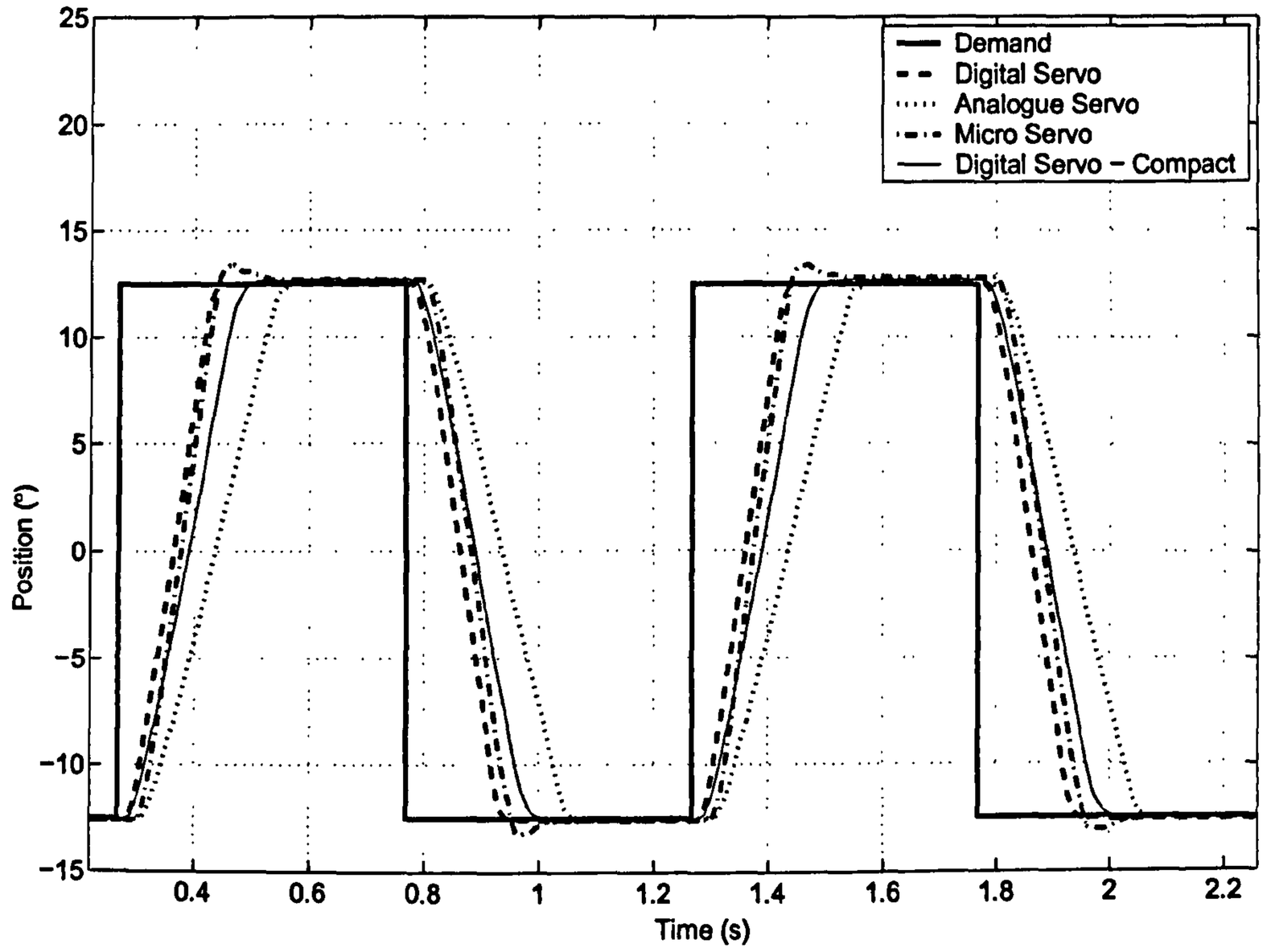


Figure 3.13: Comparison of 25° step responses for analogue, micro, compact digital and full-size digital servos (using 3:1 belt-drive reduction).

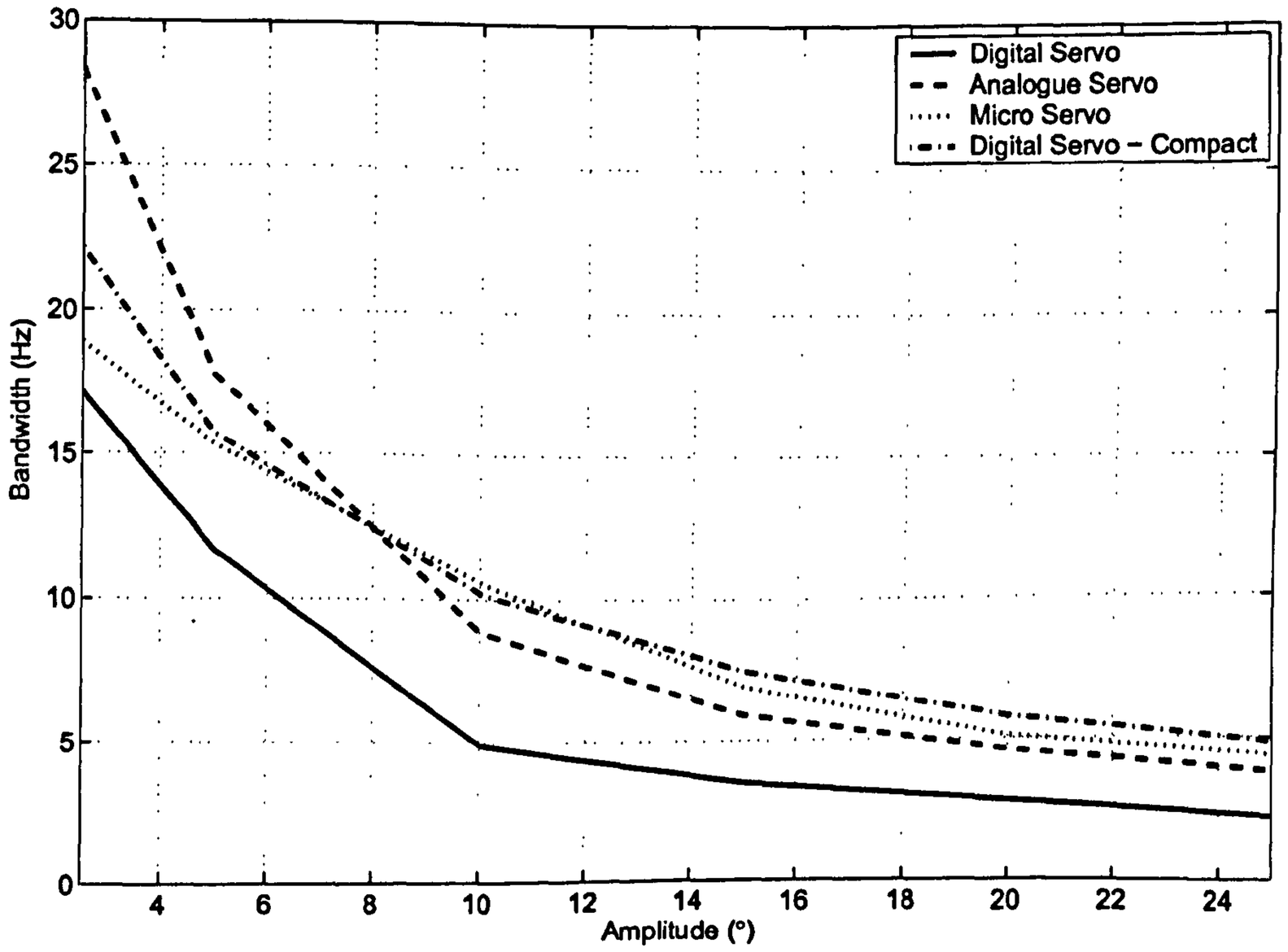


Figure 3.14: Comparison of bandwidth for analogue, micro, digital, and compact digital servos.

### 3.3.5 Actuator Modelling

To allow accurate mathematical modelling of the experimental rig it is important to include the dynamics of the actuator. Actuator dynamics can often be the limiting factor in a control system, therefore predicted performance of the closed loop system by numerical simulations will depend heavily on the accuracy of the actuator model.

For large hydraulic actuators and servo motors it is possible to create models from known parameters such as hydraulic supply pressure, piston mass, spool valve orifice size, rotor moment of inertia, etc. When dealing with small actuators, such as model servos, it is not practical measure moments of inertia or torque constants, and a model must be made based on the input-output relationship. This is not to say that the structure of models for larger actuators is not appropriate on a small scale, but the parameters must be estimated instead of measured. This can be difficult, especially if there are many parameters in the model which can vary, as there are a large number of permutations.

#### Non-linear Model

The Simulink model shown in Figure 3.15 was found to give the closest match to the experimental servo results from Section 3.3.4. The demanded angular position (left) is fed into a delay block (10ms) to simulate the average delay caused by the PWM control method. The actual servo position is then subtracted from this to give the position error. Two non-linear blocks are then used to give the correct response; the deadband block is set to the measured deadband (Table 3.4), and the saturation block is used to limit the motor (plus gearbox) torque to the level quoted by the manufacturer. Provision is made for including the external torque caused by the control surfaces in the model. The current control surface angle is subtracted from the aircraft angle-of-attack to give an equivalent angle-of-attack for the control surface, which is then fed through a gain (e.g. $C_{m_\alpha}$ for the control surface) and added to the torque from the motor. Preliminary investigation of the pitching moment on the tailplanes as $\alpha$ varied was carried out using the XFoil program, and showed negligible pitching moment at any angle-of-attack. The external torque gain was therefore set to zero. A more detailed computational investigation (or wind tunnel tests on the tailplanes alone) could be carried out to get a full non-linear model of the tailplane aerodynamics, however, this was not carried out here.

The resultant torque (motor torque - external torque) is then converted to an acceleration by dividing by an estimate of the motor (and gearbox) moment of inertia. Two integrators are used to convert this acceleration to actual servo position. Velocity feedback represents motor back EMF and damping, and must be adjusted to give the correct maximum angular rate (Table 3.4). Stiction is modelled using the logic blocks and switch (shown in blue) and is important for giving the right qualitative output response. Upper and lower position limits for the tailplanes are set to 5° and −40° respectively.

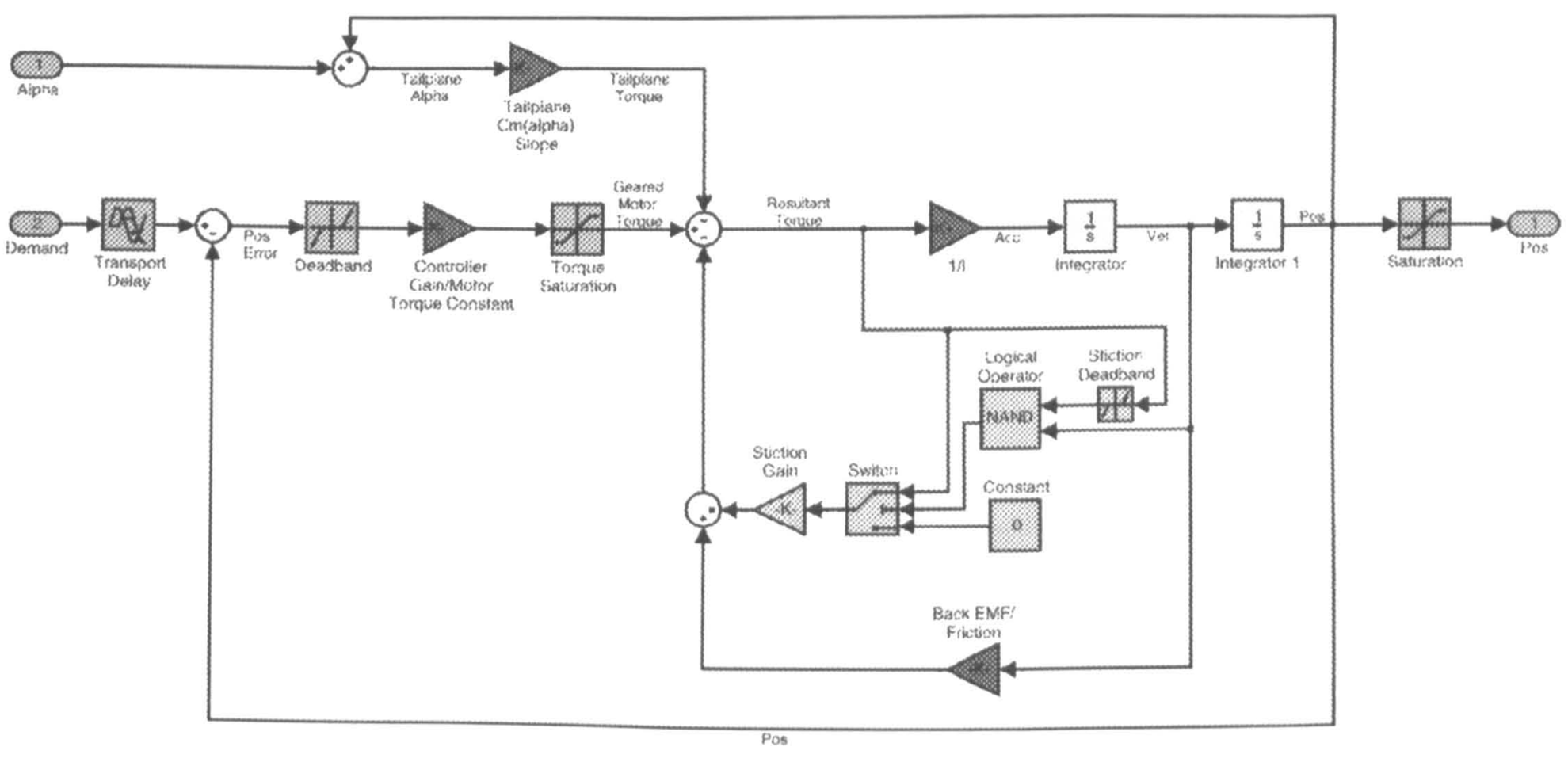


Figure 3.15: Simulink block diagram of servo model.

The parameters in the model were adjusted manually, mainly to get the correct type and rate of step response. A comparison of the actual micro servo and the model are shown in Figure 3.16[5]. It can be seen that the model gives good agreement in some areas, but there seems to be an almost stochastic element to the actual servo response which causes differences from one cycle to the next. This is especially clear when the demand is −25°, where the responses match for the first two cycles, but show a steady state error of over a degree on the third. It is possible to add an element of randomness to the Simulink servo model to give a similar output characteristic, but this would cause problems when repeating simulations so was not included. However, this stochastic element will be present when performing tests using the Hawk model, and will add to the uncertainty and errors in experimental results.

[5]For testing purposes, the position limits in the servo model were increased to allow comparison with experimental results.

### Linear Model

To aid linear control system design, a linear servo model was derived from the Simulink model shown in Figure 3.15. A linear actuator model is useful for comparing controllers, where a representative model is required without the additional complication of freeplay, rate limits, etc. A linear model was derived by comparing step responses with the full non-linear model, to give a second order transfer function (3.1). This does not model the pure delay that occurs in the real system; a Padé approximation to a pure delay could be added, but would increase the order of the model and was not used. A comparison of the linear and non-linear model step responses is shown in Figure 3.17.

$$\frac{\delta_e}{\delta_{e_{dem}}} = \frac{5 \times 10^4}{s^2 + 1250s + 5 \times 10^4} \tag{3.1}$$

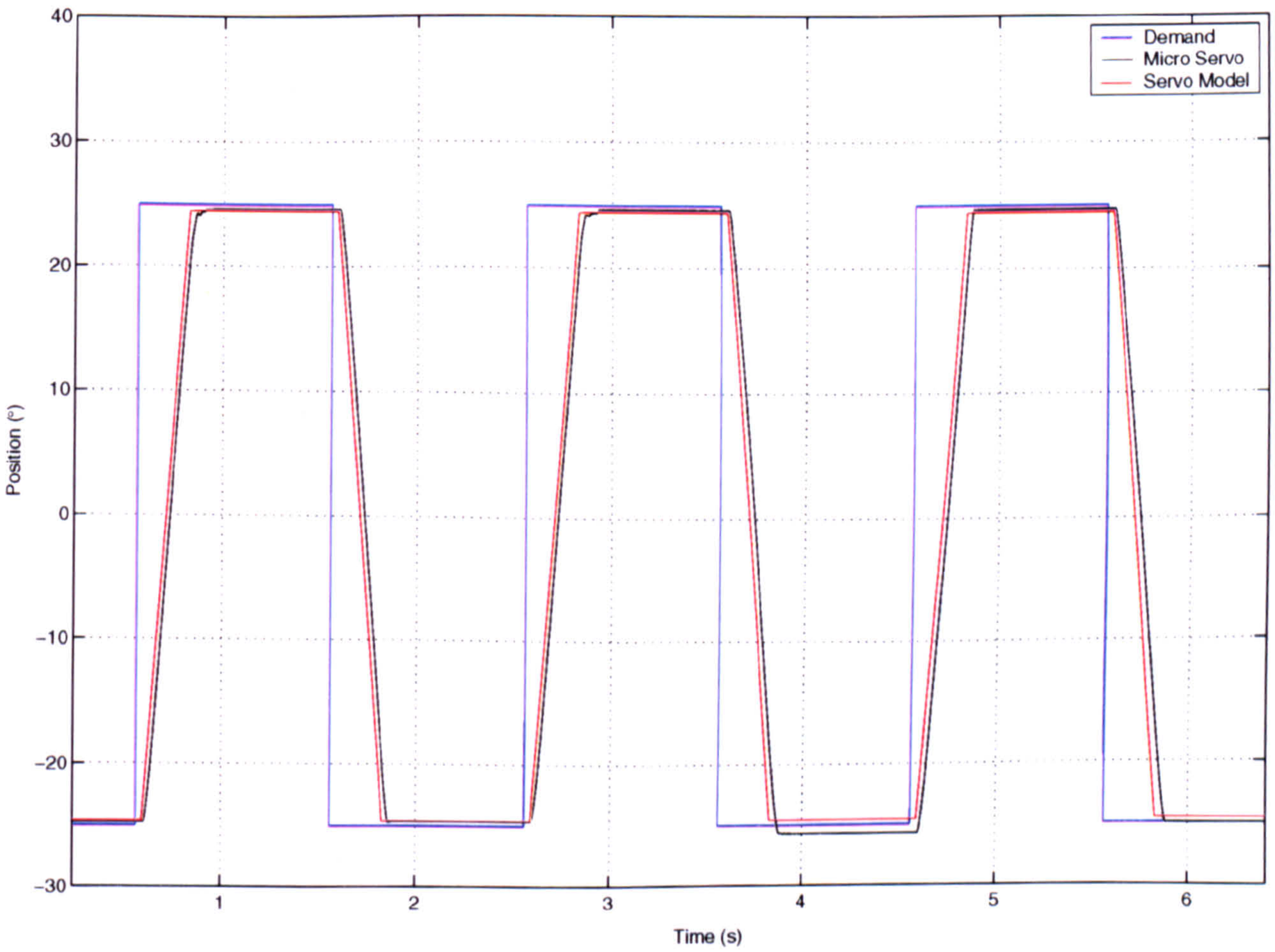


Figure 3.16: Comparison of micro servo and model step responses.

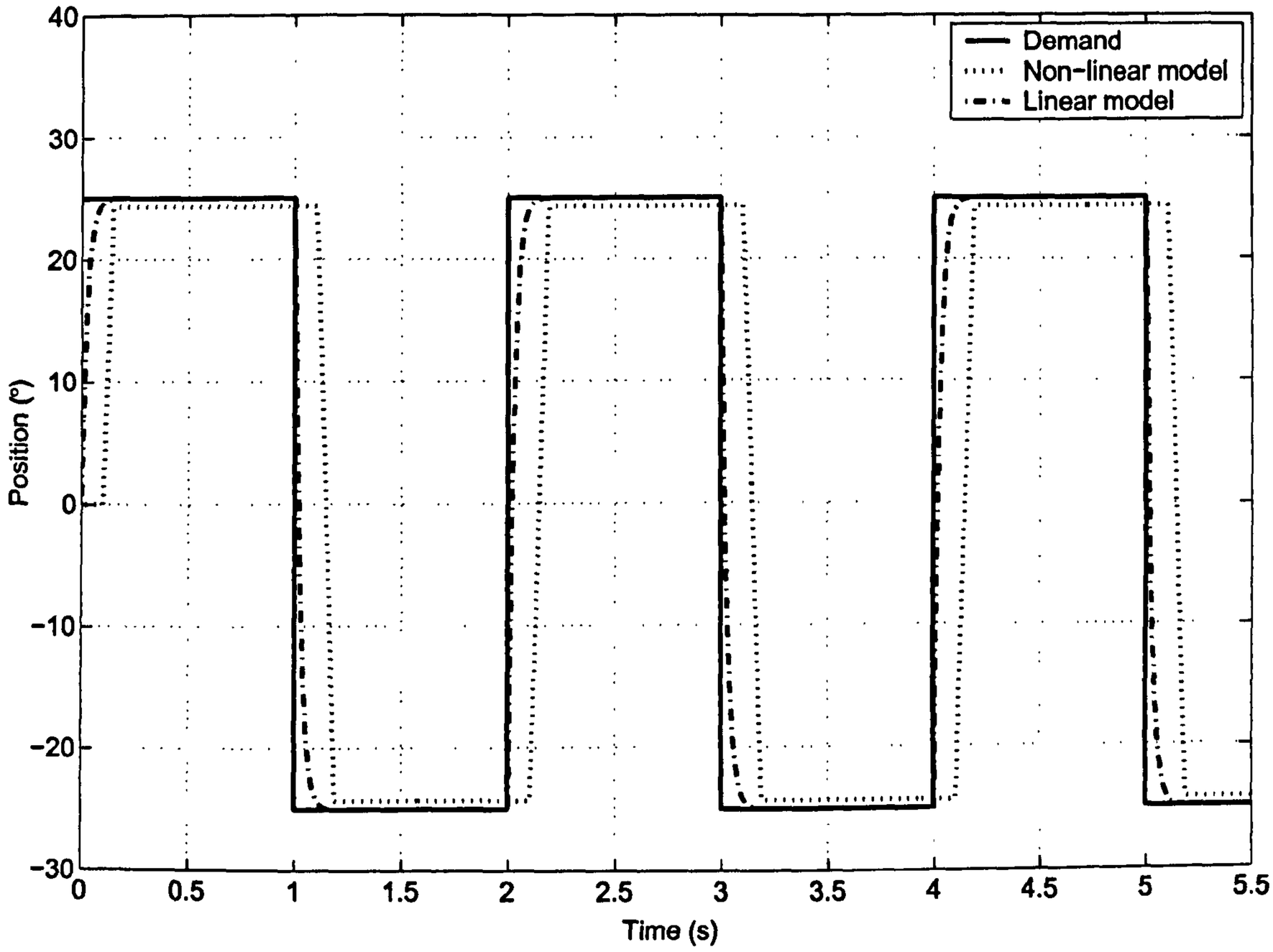


Figure 3.17: Comparison of linear and non-linear servo model step responses.

## 3.4 Data Acquisition and Control

### 3.4.1 dSPACE Real-Time Data Acquisition and Control System

Real-time data acquisition and control capability is an essential part of this project. There are many systems available (e.g. LabView (National Instruments), xPC Target (MathWorks)). A dSPACE DS1103 system, available in the Department, was used for this project. A picture of the system in shown in Figure 3.18, with the specification given in Table 3.6. The ISA computer board uses a 400MHz processor for main processing tasks, has 32MB of local RAM for storing sampled data, and has a slave Digital Signal Processor (DSP) which adds extra IO and pulse-width-modulated output capability. Data sampling can be performed at greater than 2KHz, depending on the application.

The dSPACE system uses its own front-end software, ControlDesk. This allows the user to load and run code on the card, design a graphical user interface to display the real-

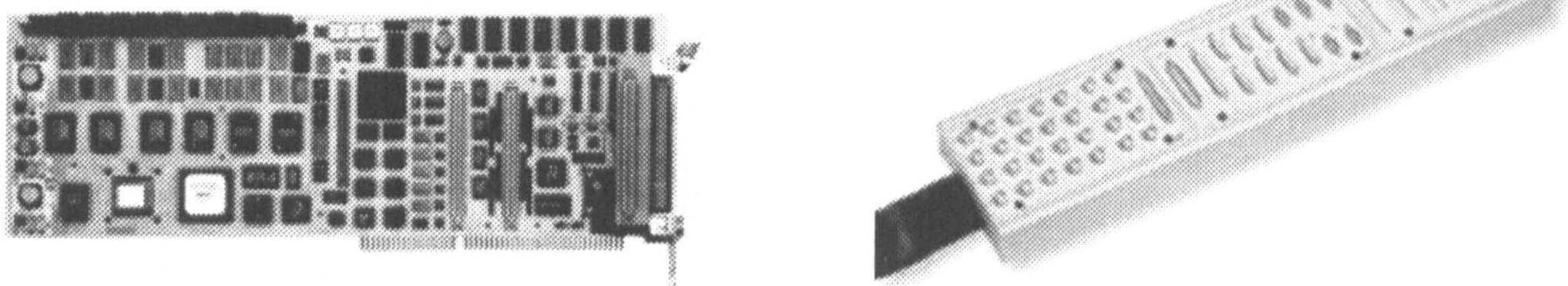

Figure 3.18: dSPACE DS1103 real-time data acquisition and control hardware.

time data and change system parameters, and control the capture of data. Data can be saved in many formats, including directly into a Matlab-structure m-file.

Table 3.6: dSPACE DS1103 system specification.

| | |
|---|---|
| Main processor | PowerPC 604e running at 400 MHz |
| Local SRAM | 2 MB |
| Global DRAM | 32 MB |
| A/D channels, 16 bit | 16 |
| A/D channels, 12 bit | 4 |
| D/A channels, 14 bit | 8 |
| Incremental encoder interfaces | 7 |
| Digital I/O channels | 32 |
| PWM generation | 1- and 3-phase |
| Capture inputs | 4 |
| Slave ADC unit | 2, each with 8 inputs, 10 bit |
| Slave Digital I/O channels | 18 |

The code for the processors is created using Matlab/Simulink block diagrams and then compiled using the auto-coding system, Real-Time Workshop. This method of rapid-prototyping was found to be extremely useful, and no faults in the automatically-generated code were found.

### 3.4.2 On-board electronics

#### Power Distribution and Signal Amplification

A certain amount of electronics was required inside the model. Several prototype boards were tested to perform the following tasks:

- provide a stabilised and repeatable voltage for the gimbal potentiometers using LM7812 (+12V) and LM7912 (−12V) voltage regulators. It was decided, after several prototypes, that this function was best performed inside the model to minimise noise caused by the supply wire.

- measure the angular rate of the model using a muRata ENC-03J solid state rate gyroscope (Table 3.7). The sensor output requires amplification before it is sampled (again, to minimise interference due to noise on the relatively long cable to the ADC), and gives an output voltage proportional to angular velocity (about a mean value of 2.5V). Amplification was performed using a simple differential operational amplifier circuit (using an LM324 quad op-amp). The sensor also has a slowly-varying DC offset, which could be removed using a hardware high-pass filter, however, to keep the electronics in the model to a minimum it was decided that the offset would be removed in software after sampling.

- re-route the +6V power supply to all servos.

Initially, a single ±17V supply to the model was tried, and a voltage regulator (LM7806) used to reduce the +17V to +6V, as required by the servos (one LM7806 per servo). Feeding the servos with a constant voltage is important to get consistent and repeatable results. It was found however that the LM7806 (rated at 1A max.) could not supply enough current to the servo during short periods of high load, and would cause the servo to 'jitter'. A higher current regulator could be used, but when moving to the 5 DOF system with up to 6 servos it is less feasible to have 6 voltage regulators in the model (due to size and heat build-up) and hence it was decided to run an additional high-current +6V supply to the model directly from an external power supply.

Table 3.7: muRata ENC-03J piezoelectric gyroscope specification.

| | |
|---|---|
| Dimensions | 15.4 × 8.0 × 4.3mm |
| Supply voltage | 2.7V to 5.5V DC |
| Current consumption (max.) | 5mA |
| Max. angular velocity | ±300°/s |
| Output (stationary) | 1.35V DC |
| Scale factor | 0.67mV/°/s |
| Linearity | ±5% of full scale |
| Response (max.) | 50Hz |
| Mass | 1.0g |

### Control Surface Position Feedback

Due to the limited space in the tail of the model, and direct servo drive of the tailplanes, it was not possible to use position feedback potentiometers directly on the control surfaces. Instead, each tailplane servo was dismantled and wires connected to the internal potentiometer. The change in voltage across the potentiometer was small (and noisy), and required amplification in the model before being sent back to the PC, adding to the on-board circuitry. To overcome this, the internal potentiometer was disconnected from the servo completely, and the position controlled through dSPACE using a simple PI controller. A larger voltage could then be put across the potentiometer and thus no on-board amplification was necessary. The system worked, but there were several complications:

- the small size of the servos meant that care had to be taken when dismantling them to add the extra wiring. Routing the wires out of the servo was also a problem. As a result, when re-assembled the servos were never as accurate as before the modification.
- having the servo control loop inside the Simulink block diagram added complexity, and tuning the PI controller gains to give optimum control was an on-going task.
- the servos became more susceptible to noise. They were now being controlled by

an analogue signal (as opposed to the digital PWM signal) which had to be routed to the dSPACE system via a relatively long cable.

- each servo required a significant amount of time to set up. After the modifications were made, the no-movement input voltage would have to be found (slightly different for each servo).

It was therefore decided that feeding back position from the servos was adversely affecting their accuracy and could not be used. Feedback from the internal potentiometer is possible on larger servos, but due to the small size of the servos chosen for the Hawk model it proved difficult. On a slightly larger model it would be possible to include external potentiometers directly connected to the control surfaces (as used in [98]), removing the need for servo modifications.

## 3.5 Wind Tunnels

Two of the wind tunnels at the University were used for experiments: a 7'×5' octagonal closed section tunnel, and a 1.1m diameter open-jet tunnel. These will now be described in more detail. Note that turbulence percentages were calculated using the equation:

$$\text{Turbulence (\%)} = \frac{\text{RMS velocity fluctuation}}{\text{mean velocity}} \times 100 \tag{3.2}$$

### 3.5.1 7'×5' Low Speed Tunnel

The Department 7'×5' closed-section tunnel is shown in Figure 3.19. This tunnel was used for initial static testing of the Hawk model (Figure 3.20), and also some preliminary single degree-of-freedom free-oscillation tests [6]. The main features of the tunnel are outlined in Table 3.8; more information on turbulence levels and velocity gradients can be found in [109]. The tunnel has a 3 component mechanical balance mounted above the working section, which was used for static testing.

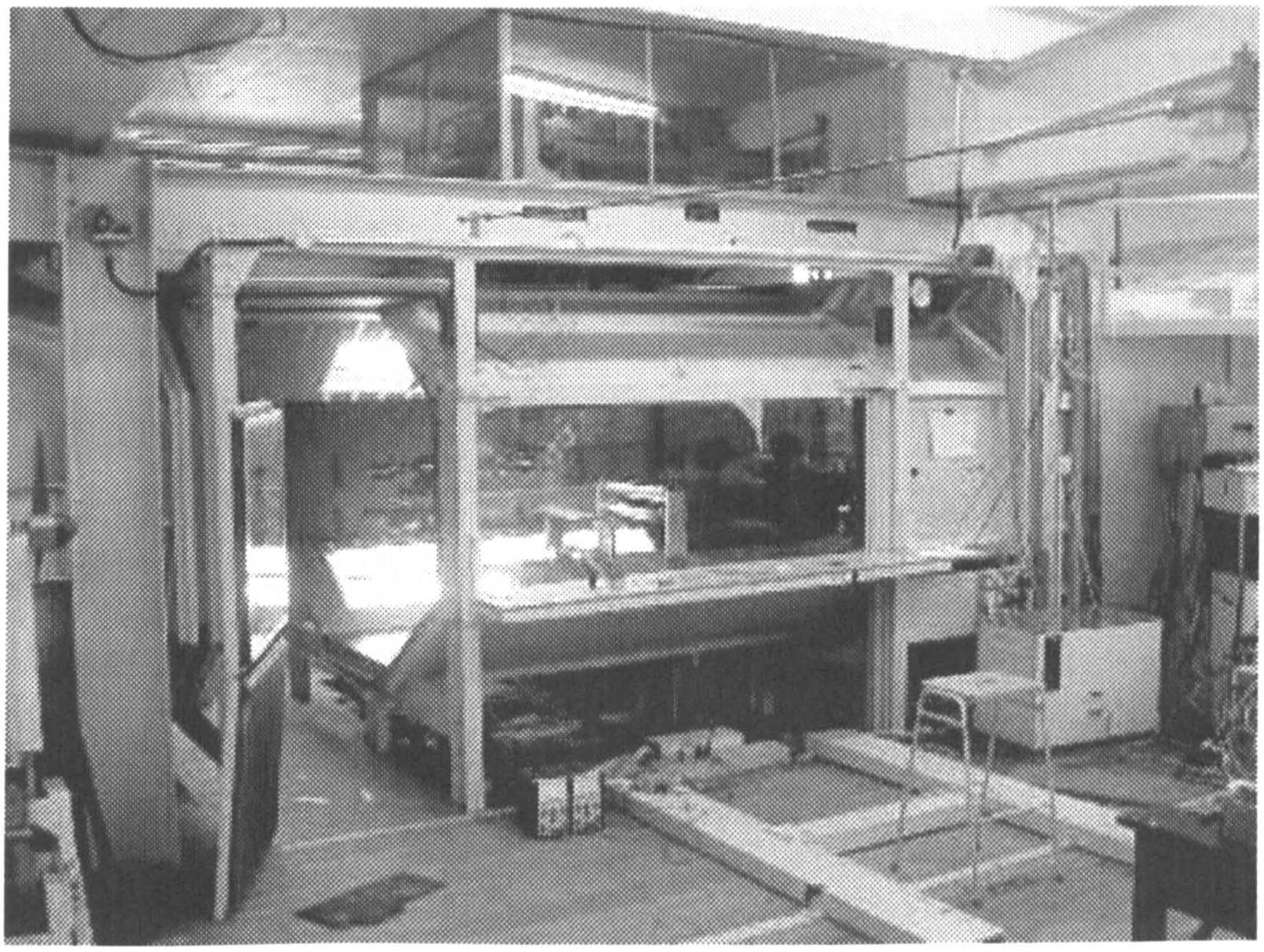

Figure 3.19: Test section of the Department 7'×5' closed-section tunnel.

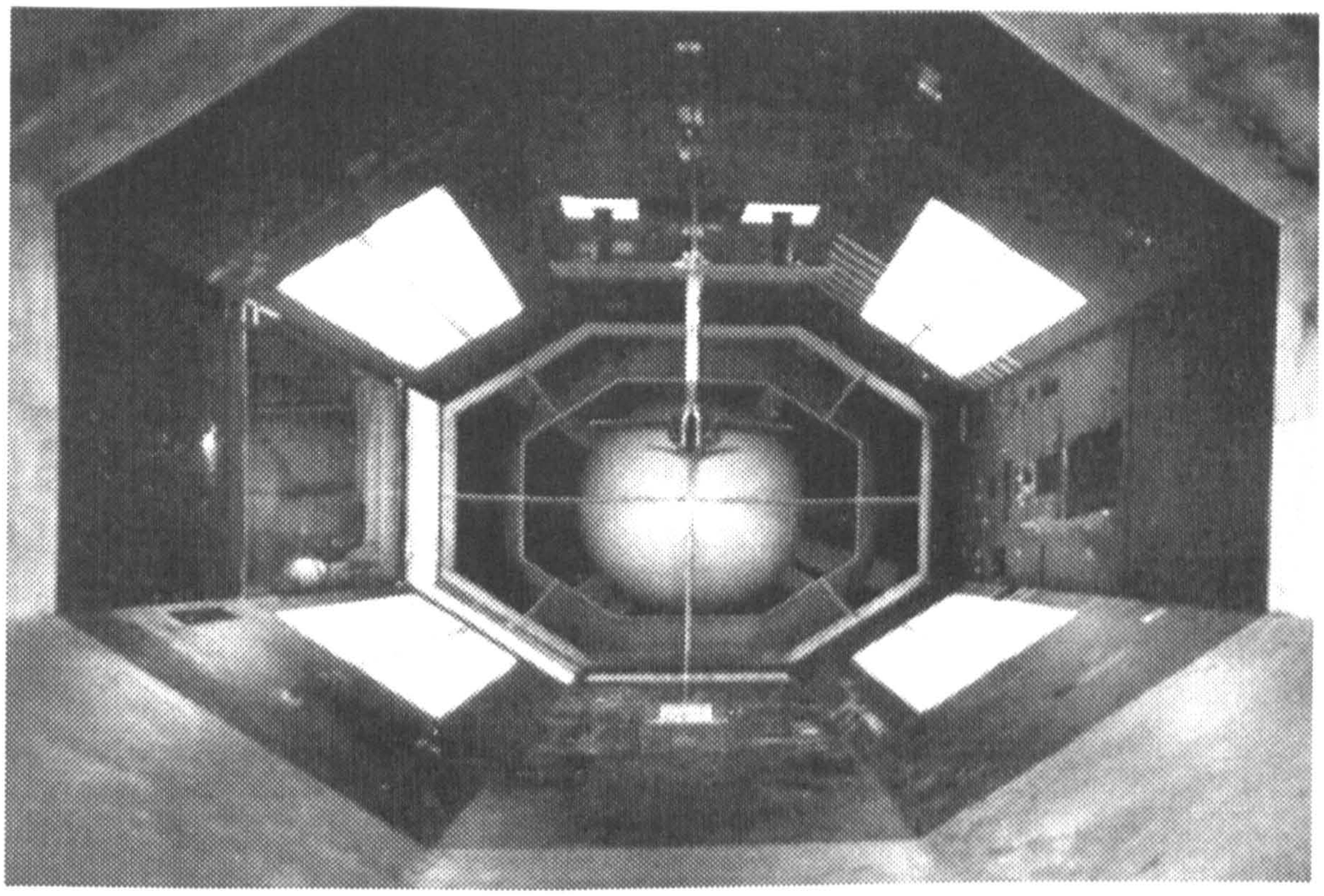

Figure 3.20: Static testing the Hawk model inverted in the Department 7'×5' low speed wind tunnel.

Table 3.8: Specification of the Department 7'×5' closed-section tunnel.

| | |
|---|---|
| Working section | 7'×5' |
| Maximum speed | 60m/s |
| Motor | 200kW DC |
| Fan | 1 × 4, 1 × 3 bladed contra-rotating |
| Contraction Ratio | 5:1 |
| Turbulence level | Approx. 0.75% |

### 3.5.2 1.1m Diameter Open-Jet Tunnel

Most of the experimental results presented in this thesis were obtained in the 1.1m open-jet tunnel (Figure 3.21). It provides easy access to the working section for adjustment of the model configuration, and was the only tunnel with a working section large enough to accommodate testing with the pendulum strut (due to large translational motion). The tunnel was designed mainly for teaching purposes and is therefore not ideally suited for generating accurate and repeatable results, however, this does not obviate the validity of the results obtained. Details of this tunnel are presented in Table 3.9, and quantification of the tunnel turbulence in Appendix B.

Table 3.9: Specification of the Department 1.1m diameter open-jet tunnel.

| | |
|---|---|
| Working section | 1.1m diameter circular (open-jet) |
| Maximum speed | 40m/s[a] |
| Motor | 25kW DC (constant speed with magnetic clutch) |
| Fan | 6 bladed |
| Contraction Ratio | 4.39:1 |
| Turbulence level | Approx. 2%[b] |

[a]Later reduced to approx. 30m/s, see Appendix B.
[b]Later reduced to approx. 1.2%, see Appendix B.

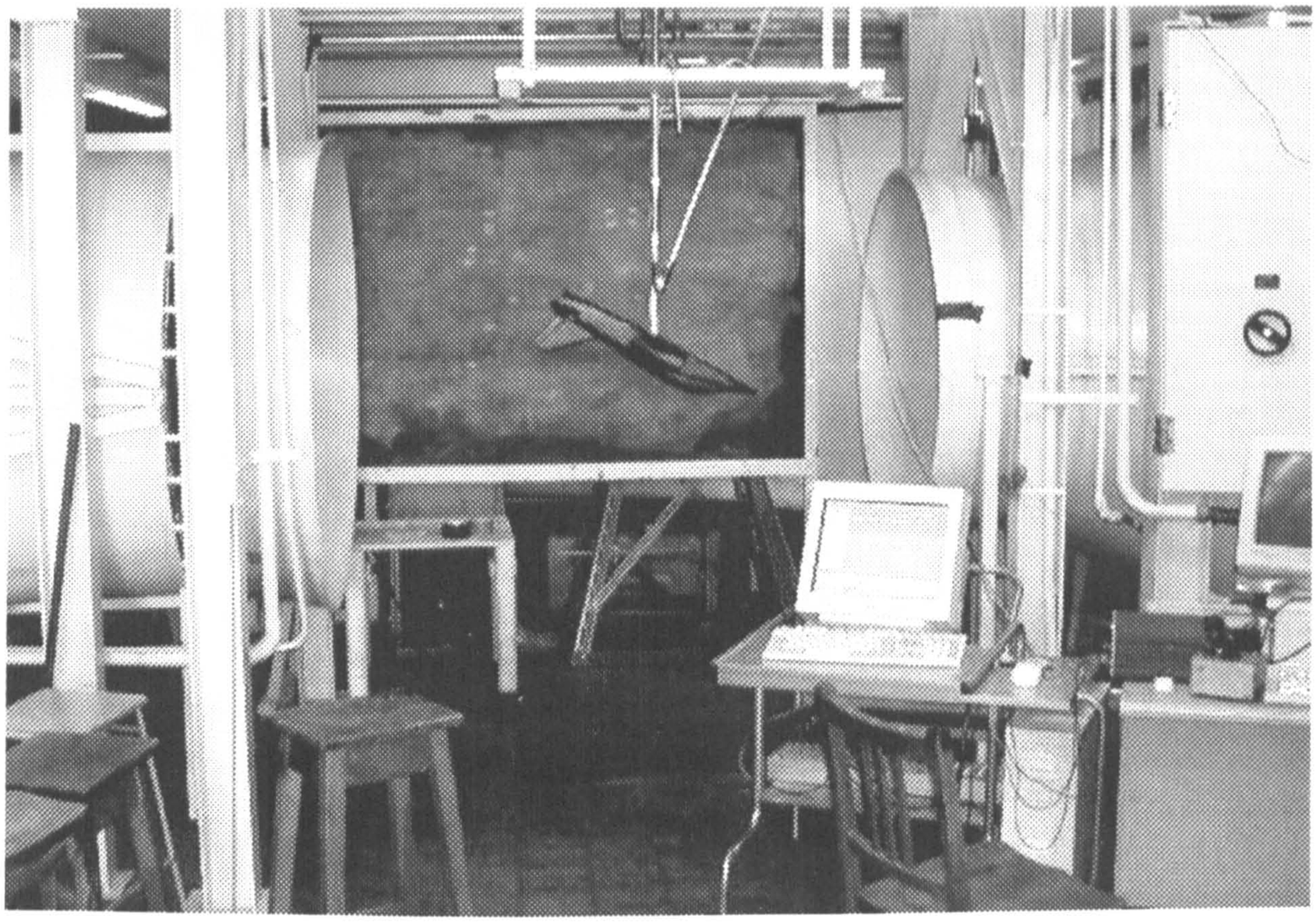

Figure 3.21: The Department open-jet tunnel.

## 3.6 Conclusions

In this chapter, experimental hardware and testing facilities have been described. The custom-made BAe Hawk model used for wind tunnel tests was described in detail, and control surface actuation requirements discussed. A range of off-the-shelf servo actuators were tested for performance criteria and results presented. Linear and non-linear mathematical models of the micro-actuators used in the Hawk model were derived. Finally, the wind tunnel facilities were described and specifications given.

# Chapter 4

# Experimental Results

A large amount of experimental work was carried out for the research presented in this thesis. It is not possible to document every set of results here; most experiments were performed a number of times to test repeatability, leading to a large number of similar-looking results. Also, many experiments were carried out which have no significant impact on the research, but were performed to explore the characteristics of the system and satisfy speculative queries. In this chapter, the most interesting and useful experimental results are presented, and serve to demonstrate the open-loop dynamics of the wind tunnel rig in various configurations. Use is made of tools from non-linear dynamics (bifurcation diagrams and phase-plane plots) that are often used in theoretical work, but not so often on experimental systems. They are found to be extremely useful for examining the behaviour of the system.

## 4.1 1 Degree-of-Freedom Results

Three types of single degree-of-freedom experiments were performed to (1) investigate the system bifurcation behaviour; (2) record time trajectories and (3) deduce the stability of a desired equilibrium solution. More specifically:

1. To construct experimental bifurcation diagrams, it was necessary to perform tests where the horizontal tailplane deflection was varied slowly enough for the system

behaviour not to be affected by transients (experimental bifurcation diagrams were also used in [110] to analyse flutter). Typically, for the rig under investigation this required sweeping the tailplane deflection from one position limit to the other over one hour. These tests establish the stable attractors of the system with respect to a parameter (in this case tailplane deflection, $\delta_e$). They also show any bifurcation phenomena present in the rig (i.e. qualitative changes in the system long-term behaviour as the tailplane angle is varied).

2. To collect data for phase-plane plots and time histories, tests were performed where the horizontal tailplane deflection remained constant while the corresponding time histories of the rig evolution were recorded.

3. To deduce the stability of a given solution at discrete tailplane deflections, tests were performed where, again, the horizontal tailplane remained in a constant position but the model was held at a large positive or negative pitch angle before being released and time histories recorded.

### 4.1.1 Experimental Rig

For single degree-of-freedom tests the model was mounted inverted on fixed silver steel and aluminium struts in the Department 1.1m diameter open-jet tunnel (Figure 4.1). Initially, a second aluminium strut was mounted at an angle between the main strut and the tunnel structure to reduce vibration in the longitudinal and lateral axes. This was later replaced with tensioned steel cable running diagonally to the bottom of the strut, to provide increased rigidity while reducing aerodynamic interference. A single DOF gimbal provided freedom in pitch only. No filtering was applied to the data, and all sampling was performed at 100Hz.

### 4.1.2 Experimental Results

Typically, as tailplane angle, $\delta_e$, is decreased the angle-of-attack, $\alpha$, of the aircraft will increase, leading to a negative overall slope on the $\delta_e$– $\alpha$ bifurcation diagram. In general, aerodynamic non-linearities will cause a reduction in stability at higher $\alpha$ which can lead to loss of control, even with large control surface deflections. This loss of stability

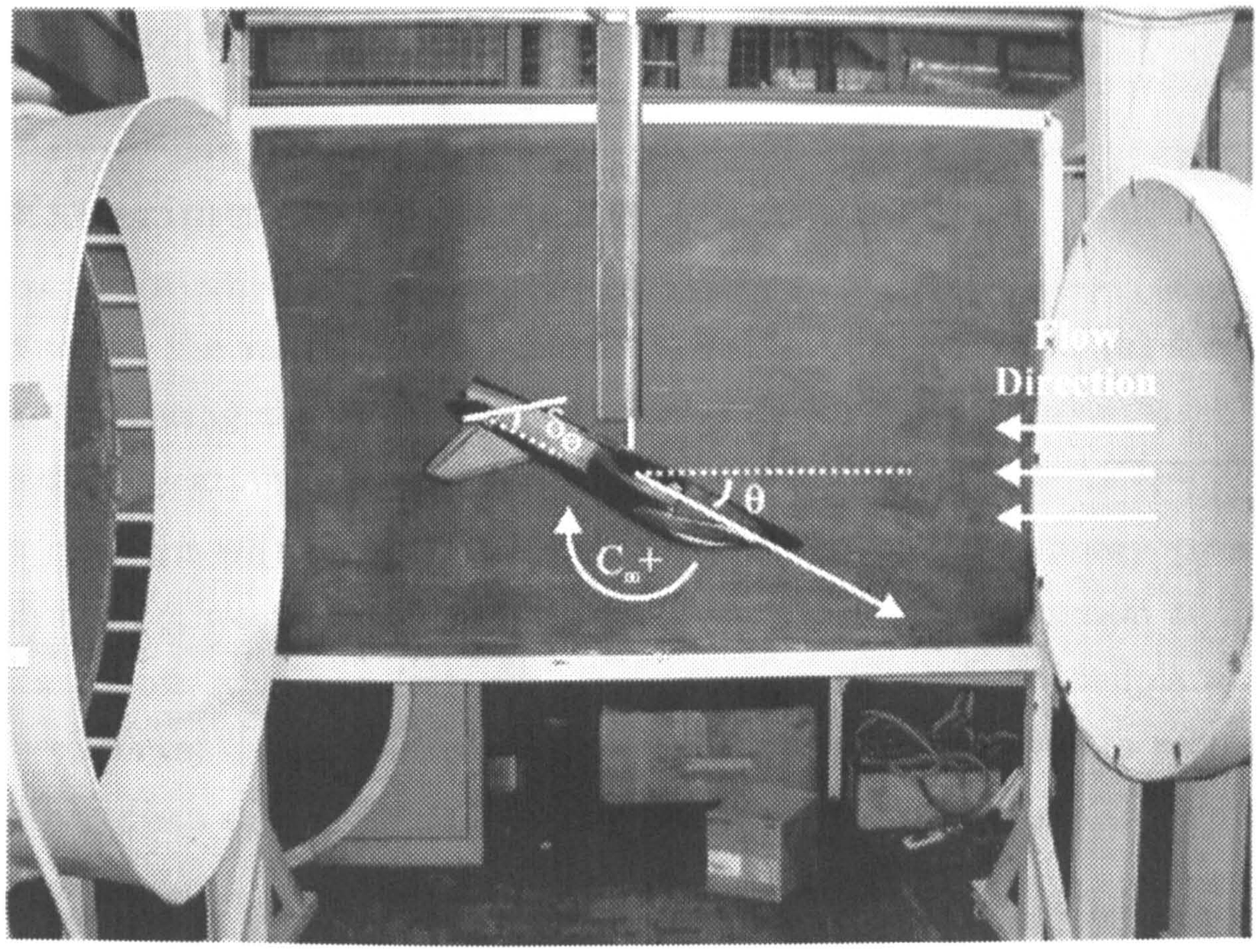


Figure 4.1: Hawk model mounted inverted in the Department open jet tunnel.

can be longitudinal (in the form of deep stall or pitch oscillations) but usually occurs in the lateral/directional sense (see e.g. [111]). It is possible, particularly in delta-wing aircraft and those with long forebodies, for a Hopf bifurcation to a stable limit cycle to occur, mainly in the roll sense, at high $\alpha$ before there is a total loss of stability. This phenomenon is known as 'wing rock' (see Section 5.1).

Another non-linear phenomenon that occurs at high $\alpha$ is the fold bifurcation. This is characterised by a branch of stable equilibria (stationary points) folding back on itself and becoming unstable. This bifurcation is associated with jump-type behaviour where, under parameter variations, stability is lost suddenly, often ending in deep stall or departure into a spin.

With the single degree-of-freedom rig there are no lateral/directional modes present. Static tests have shown the model to be statically stable over the range $-10° < \alpha < 35°$, $-50° < \delta_e < 10°$ (see Appendix A). However, spring-oscillation tests in the Department $7' \times 5'$ closed-section tunnel have shown regions of low pitch damping at approximately $\alpha = 5°$ and $\alpha = 15°$ [6]. The existence of large-amplitude non-linear pitching behaviour

was not known prior to free-motion testing.

### 4.1.3 Experimental Bifurcation Diagrams

Figure 4.2 shows the results of two experimental bifurcation runs; (a) for decreasing and (b) for increasing tailplane deflection. Each run lasted 60 minutes. To plot the experimental bifurcation diagrams (or more precisely, *orbit diagrams* [19] – a form of bifurcation diagram where only attractors are plotted), non-stationary points (points where pitch rate, $q$, was non-zero) were discarded. This gives a diagram of fixed points and maximum limit-cycle amplitudes for the system as a function of tailplane deflection. Due to experimental noise and tunnel turbulence it was not possible to plot only those points at which pitch rate was zero, therefore a tolerance band of $|q| < 2\,°/s$ was applied.

The behaviour seen in Figure 4.2(a) at approximately $\delta_e = -12°$ can be characterised as a supercritical Hopf bifurcation to a limit cycle (see Section 2.3.1 for more information on Hopf bifurcations). This is indicated by the slow growth of the limit cycle from the branch of equilibria as tailplane angle is reduced, i.e. the fixed-point solution branch becomes unstable and the system follows the stable limit cycle branch. Oscillation amplitude increases with decreasing tailplane angle until at approximately $\delta_e = -21°$ the system exhibits a sudden 'jump' back to a stable fixed point (Figure 4.2(a)). This stable branch continues to the maximum elevator deflection.

With increasing tailplane angle (Figure 4.2(b)), the jump from stable fixed point to limit cycle occurs at approximately $\delta_e = -19.5°$. This hysteresis and jump behaviour indicates the presence of a subcritical Hopf point at $\delta_e = -19.5°$. This is where, as tailplane deflection is increased, the stable fixed-point branch becomes unstable and the system jumps to the nearest attractor — the limit cycle.

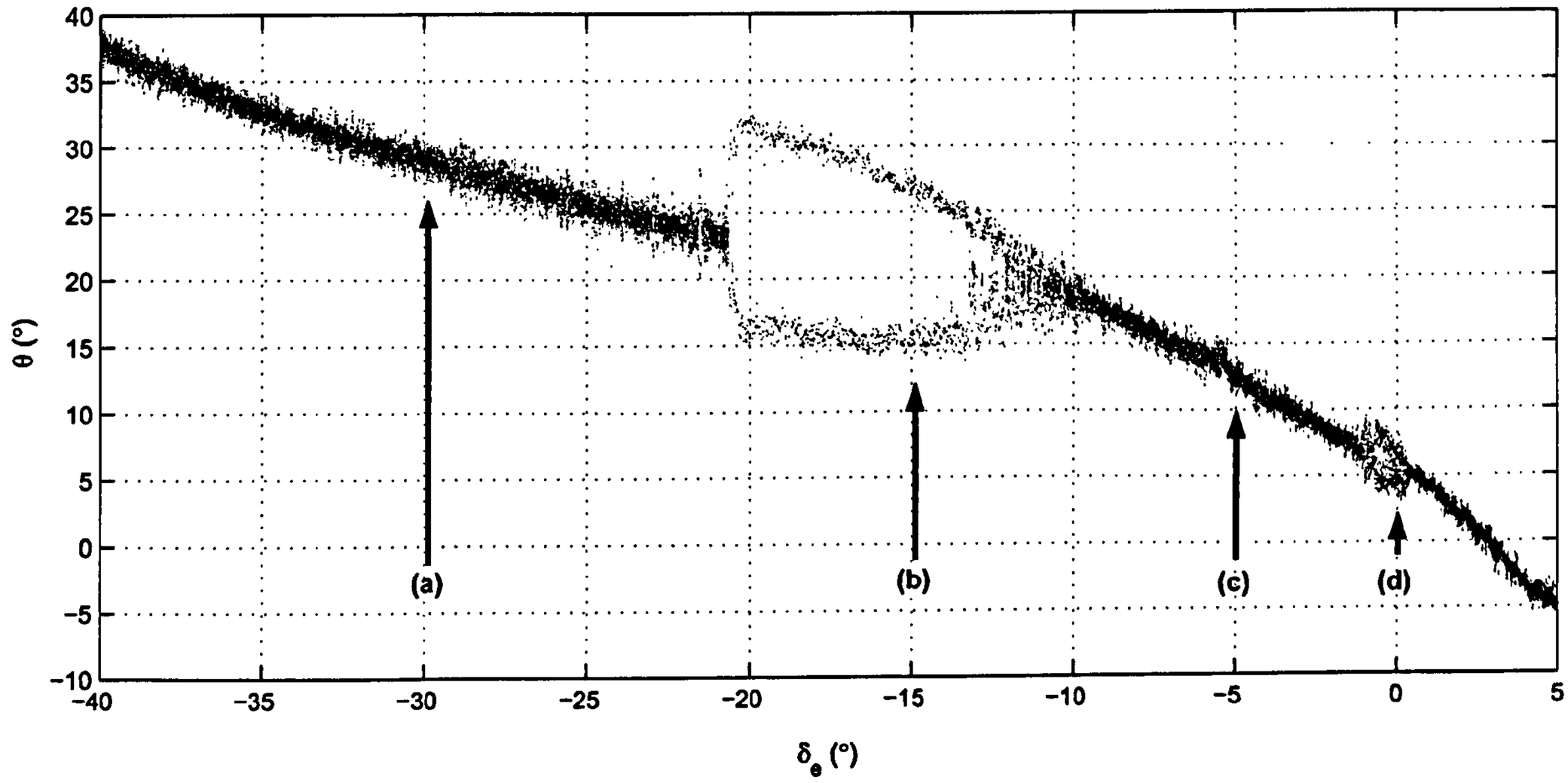


(a) Decreasing tailplane deflection.

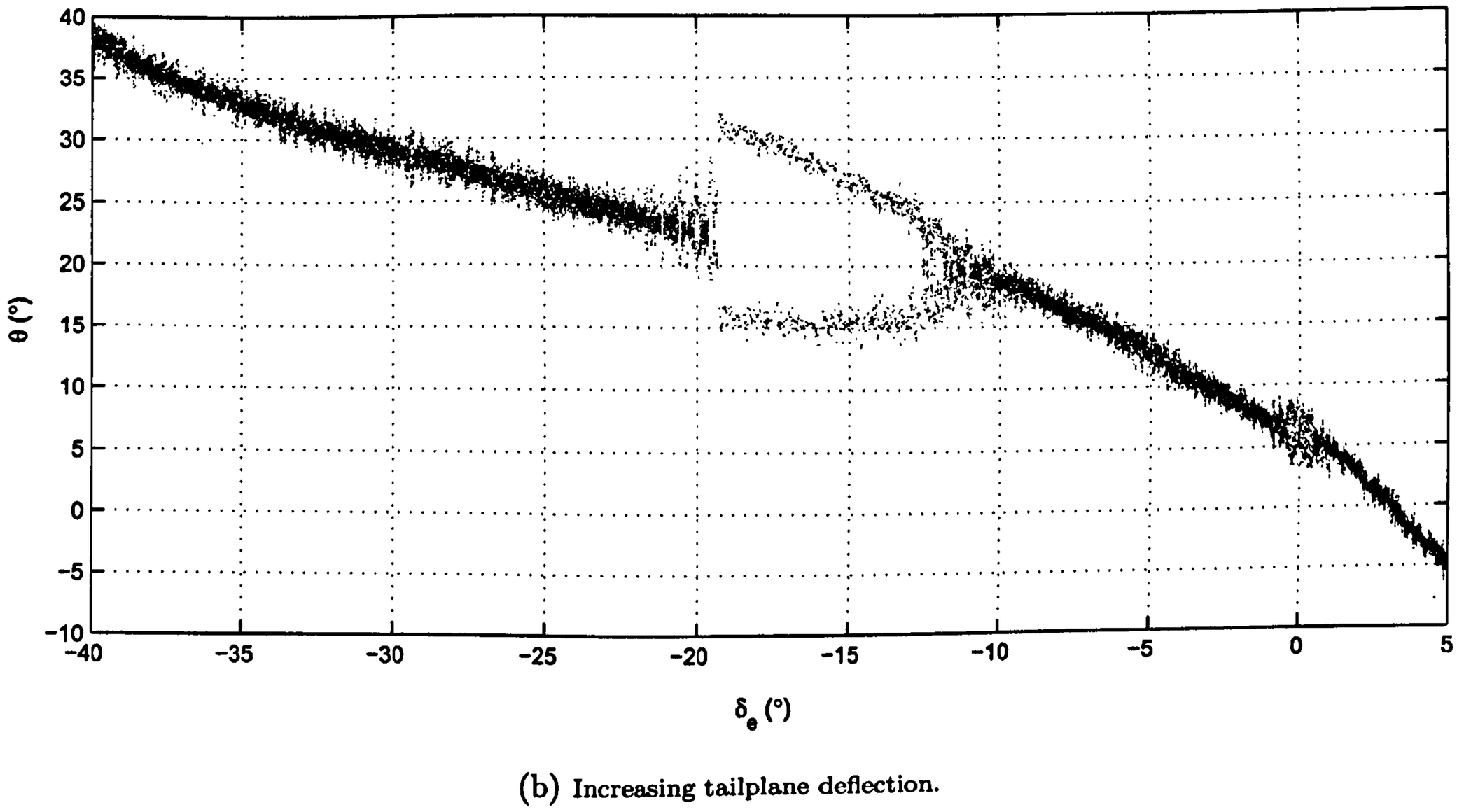


(b) Increasing tailplane deflection.

Figure 4.2: Experimental bifurcation diagrams.

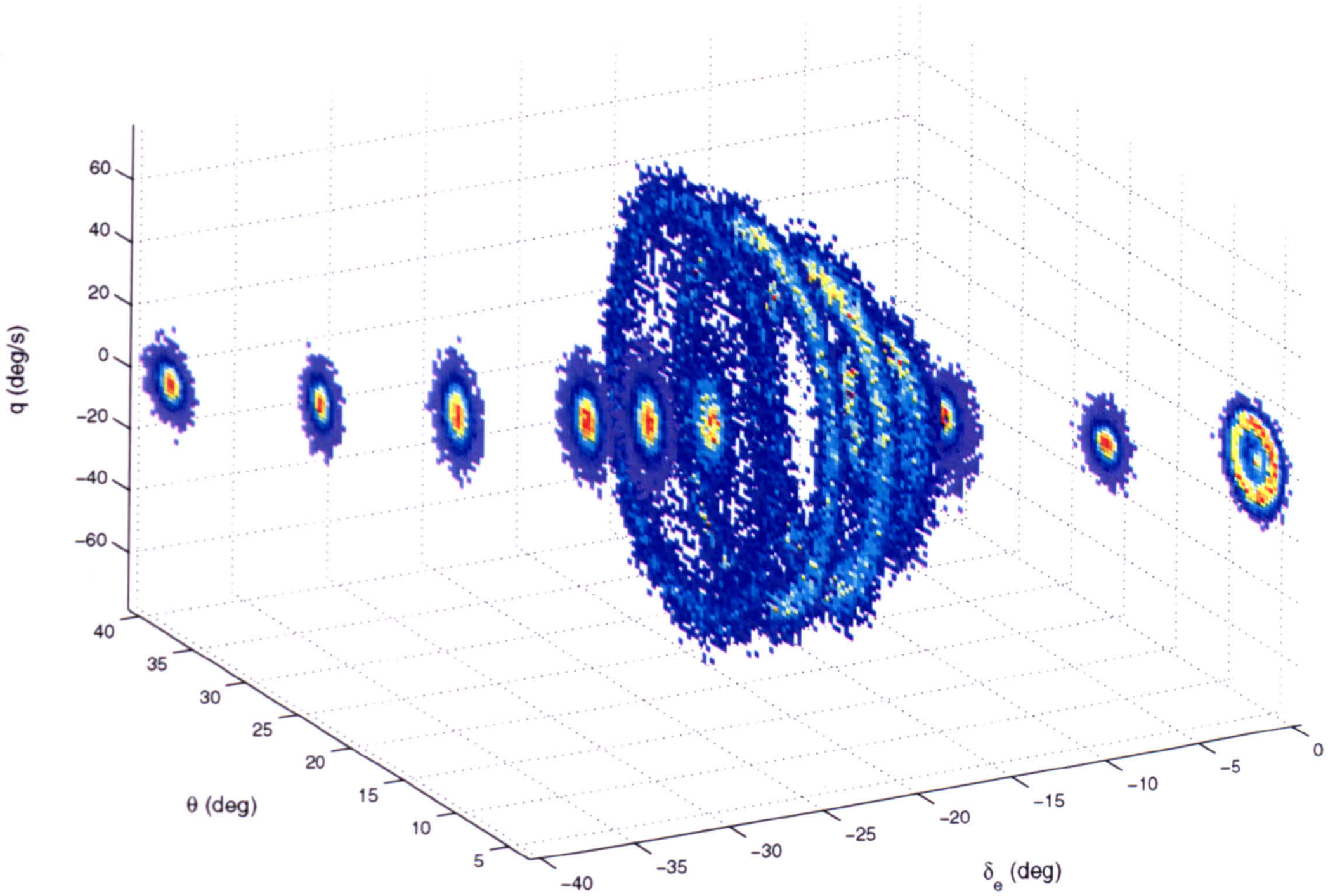


Figure 4.3: Phase-plane plots for fixed tailplane deflections.

### 4.1.4 Experimental Phase-Plane Plots

Further evidence of this phenomenon is given in Figure 4.3, where experimental phase-plane plots are shown for various fixed tailplane deflections. For each tailplane setting, data was recorded for 15 minutes and plotted in Figure 4.3, with "hot" colours showing more time spent in that area. The limit cycle region is clearly visible as a circle of points in the $\theta - \dot{\theta}$ plane.

Figure 4.4 shows phase-plane plots for three of the fixed tailplane deflections in Figure 4.3. It can be seen that at $\delta_e = -17.5°$ there is a well-established stable limit cycle denoted by the circle in the $\theta - \dot{\theta}$ plane. At $\delta_e = -22.5°$ there is a stable fixed point (a 'point' in the $\theta - \dot{\theta}$ plane, enlarged by noise and turbulence) and at $\delta_e = -20°$ a stable limit cycle and stable fixed point coexist and are characterised by different basins of attraction. These attractors correspond to those seen in the experimental bifurcation

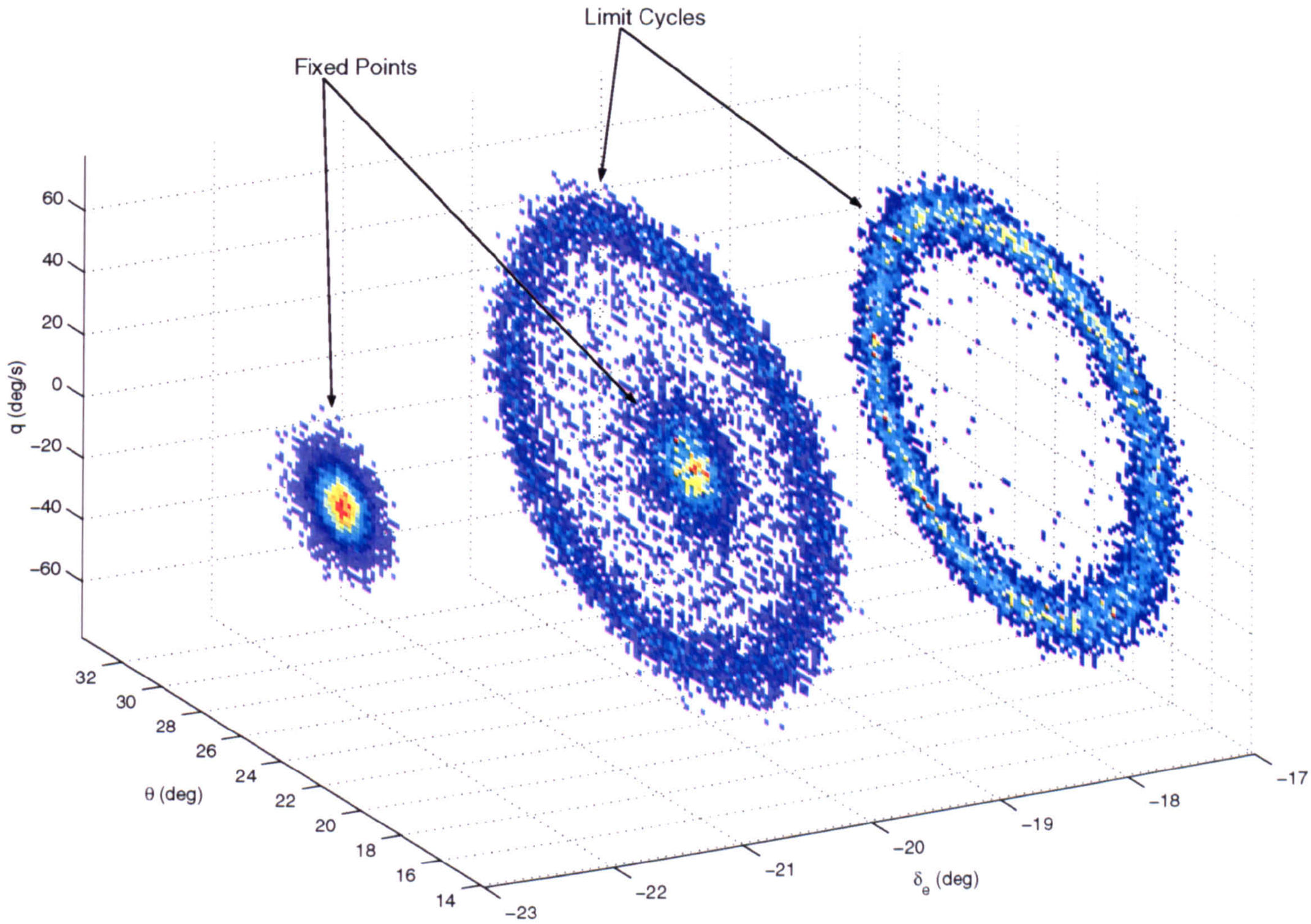


Figure 4.4: Phase-plane plots for three of the tailplane deflections in Figure 4.3.

diagrams (Figure 4.2). Unfortunately, due to relatively large amounts of turbulence in the wind tunnel, it is not possible to release the model from different starting points and find the basins of attraction of the equilibria in the hysteresis region. While recording data for the phase plane plot with $\delta_e = -20°$ in Figure 4.4, occasionally the tunnel turbulence would be great enough to force the model away from its present steady state, past an unstable branch (that cannot be found experimentally) and onto the other coexisting steady state. The resulting transients correspond to the many points which lie between the limit cycle and the fixed point in Figure 4.4.

### 4.1.5 Experimental Time Histories

Figures 4.5(a)-(d) show time histories corresponding to the fixed tailplane deflections labelled in Figure 4.2(a). As expected, points (a) and (c) are fixed equilibria at approx-

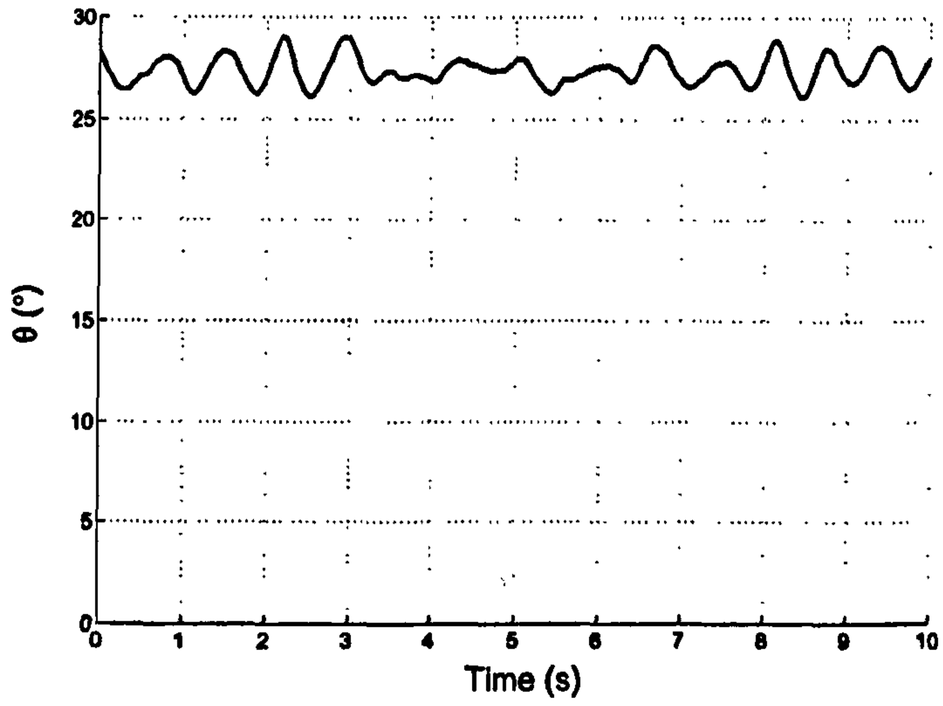


(a) $\delta_e = -30°$

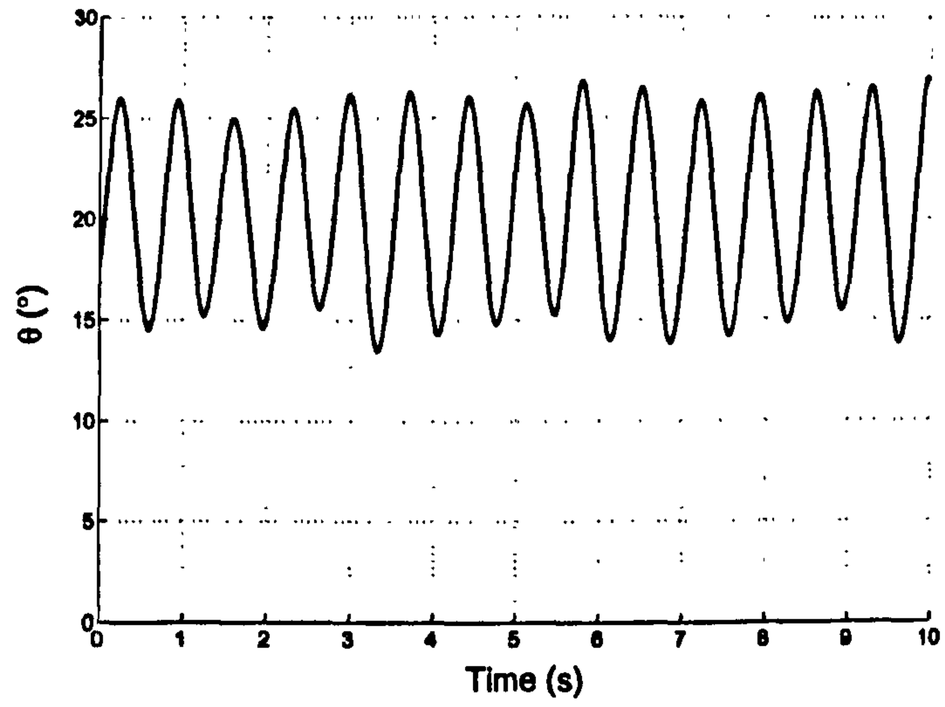


(b) $\delta_e = -15°$

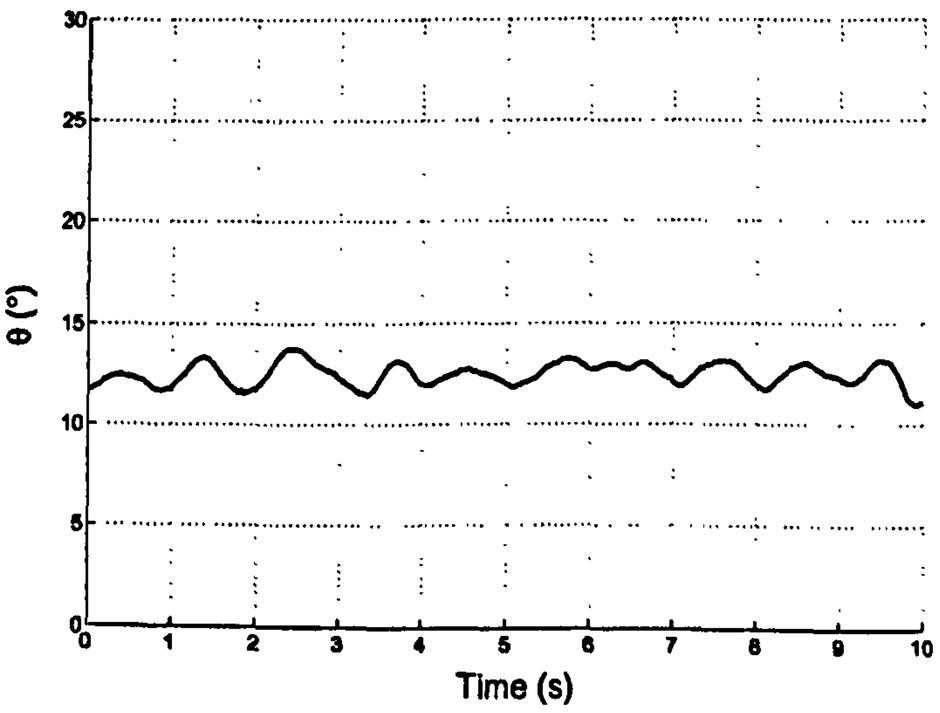


(c) $\delta_e = -5°$

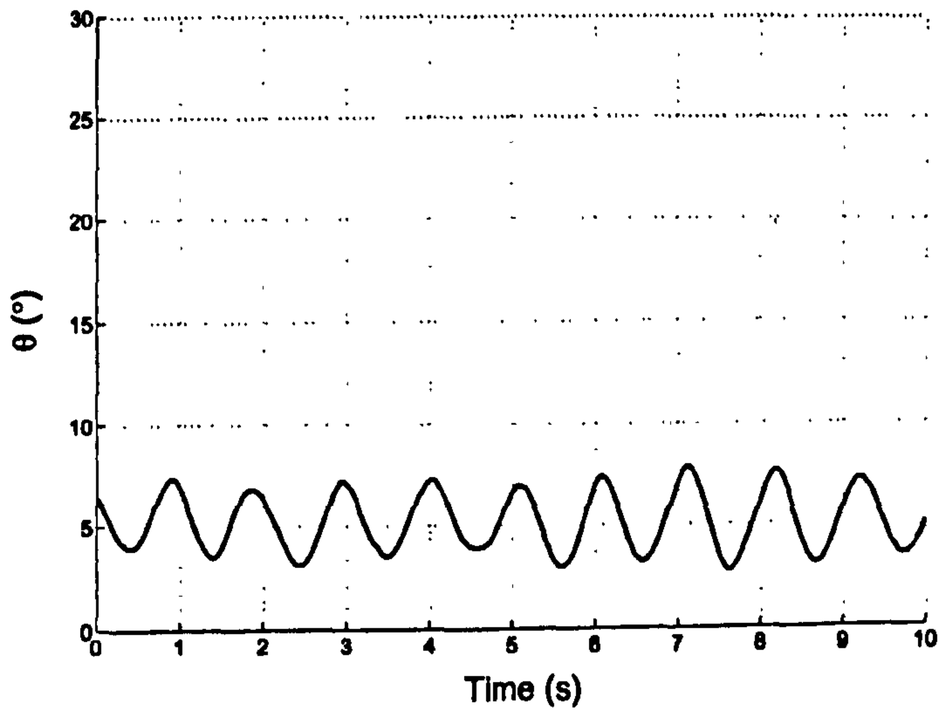


(d) $\delta_e = 0°$

Figure 4.5: Time histories for points marked in Figure 4.2(a).

imately $\theta = 28°$ and $\theta = 12°$ respectively. Point (b) in Figure 4.2 is instead a large amplitude limit cycle oscillation, centred at $\theta = 22°$ with an amplitude of approximately 5°. This is confirmed by the experimental time history depicted in Figure 4.5(b). The experimental bifurcation diagram also reveals a region of small-amplitude limit cycles at point (d), centred at approx. $\theta = 5°$. This corresponds well with a region of low pitch damping identified in small-amplitude spring oscillation tests [6].

Note that tunnel turbulence can become a problem when distinguishing fixed points from small-amplitude limit cycles (for example, smaller than the tolerance band considered). This is particularly relevant for determining the exact location of the Hopf bifurcation points. Close to these points, limit cycles have small amplitudes and therefore other indicators such as periodicity need to be used to locate them with greater accuracy.

Figures 4.6 and 4.7 show time histories for the model at different fixed tailplane deflections when released from the limit-stop in $\theta$. Many runs were recorded and are plotted on the same axes to show repeatability of results. These plots can be used to deduce the stability of the equilibrium solution, and are used for developing a mathematical model of the rig in Chapter 5.

It is thought that the large-amplitude limit cycle exhibited by the model is caused by a reduction in pitch damping[1] occurring due to the tailplanes becoming immersed in the wake of the wing at angles of attack from 18° to 23°. This is a very high $\alpha$ for the full-scale Hawk aircraft, and would almost certainly be preceded by loss of lateral/directional stability. While the oscillations are a specific phenomenon occurring with this model configuration, it is an interesting experimental example of an application of non-linear dynamics theory which has relevance in the analysis of full-scale aircraft dynamics.

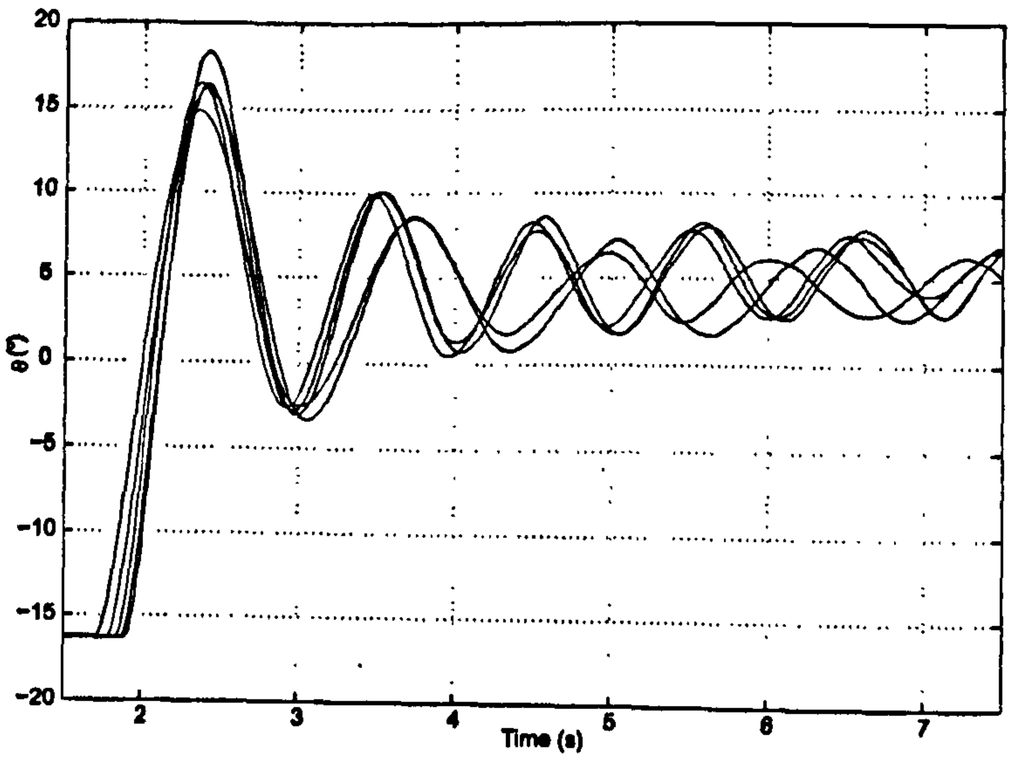


(a) $\delta_e = 0°$

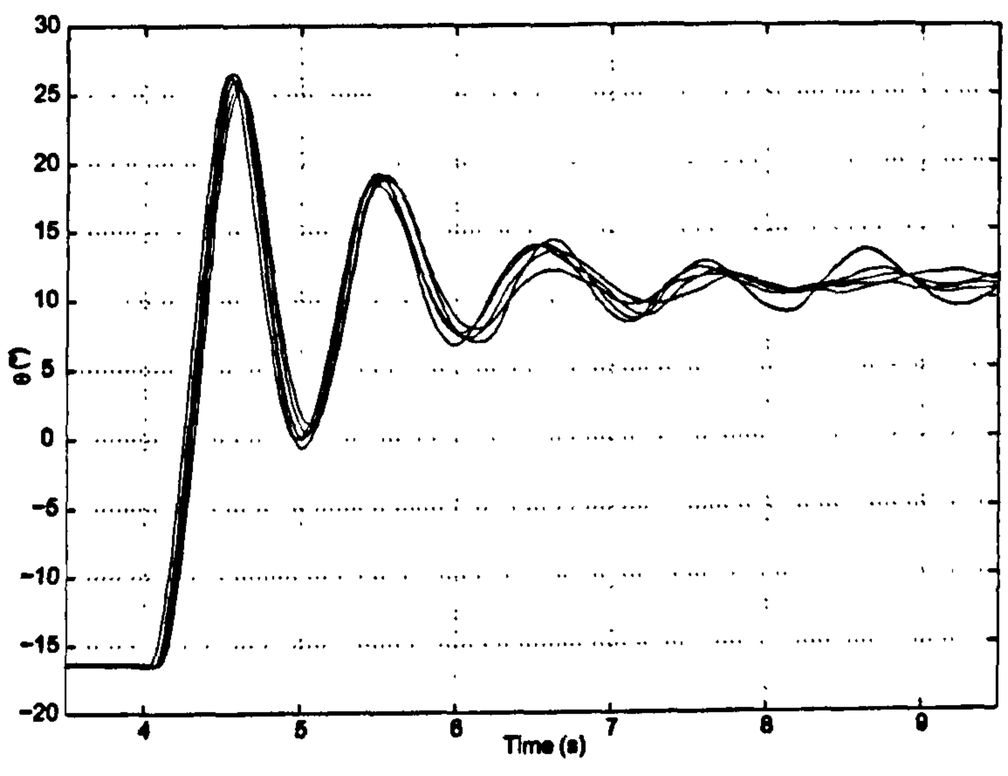


(b) $\delta_e = -5°$

Figure 4.6: Time histories for fixed tailplane deflections.

[1]Note that pitch stiffness, $C_{m_\alpha}$, found from static tests (see Appendix A) remains negative (i.e. stable) at higher angles-of-attack; just the pitch damping changes. This possibly relates to some time-dependent phenomenon in the wing flow.

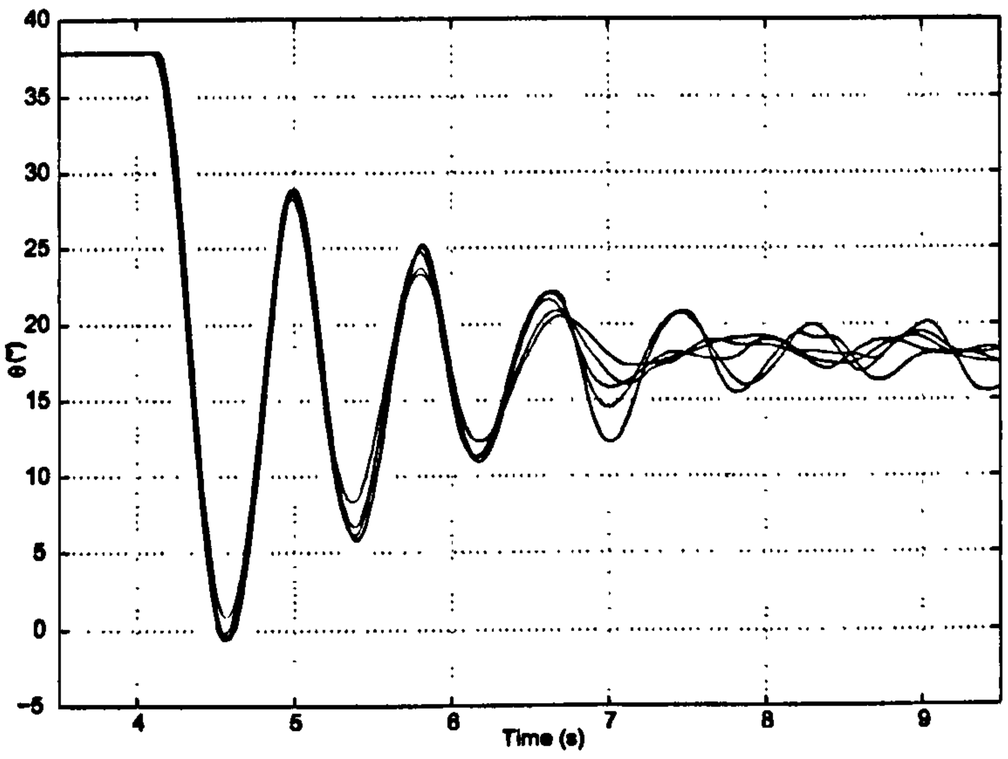


(a) $\delta_e = -10°$

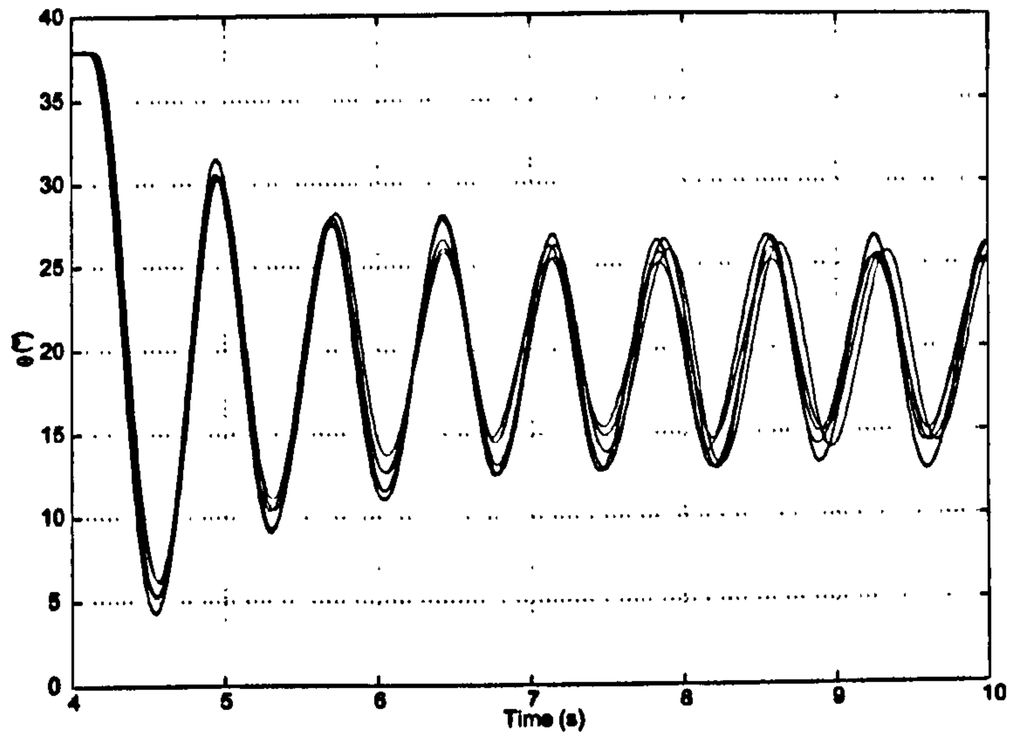


(b) $\delta_e = -15°$

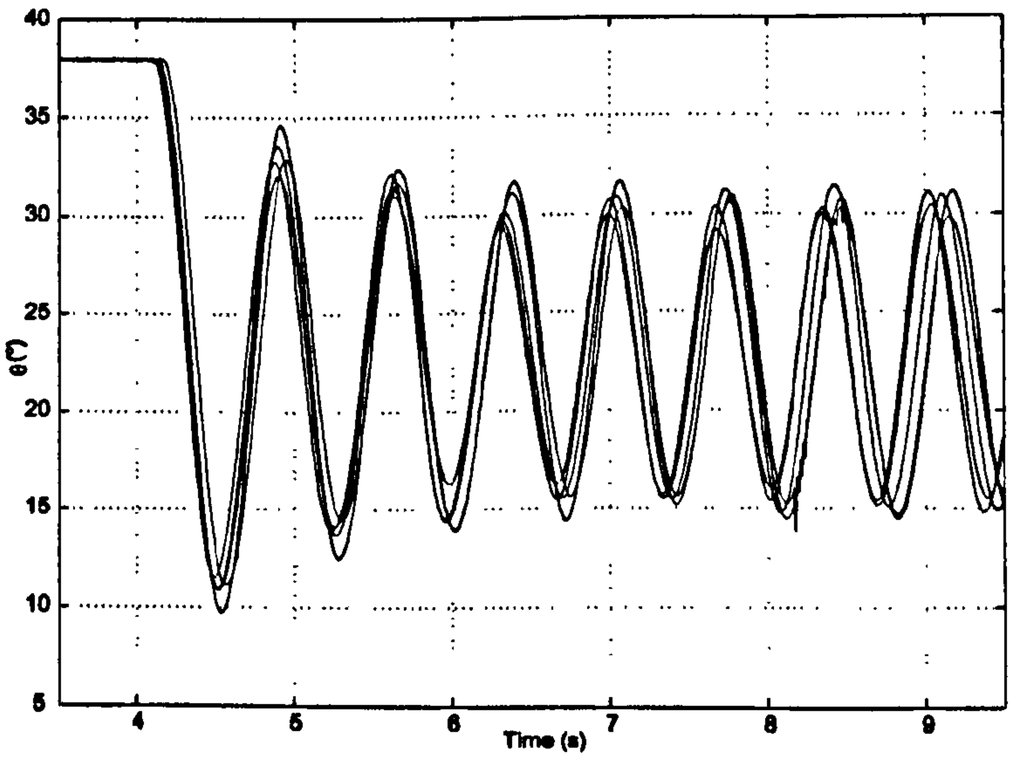


(c) $\delta_e = -20°$

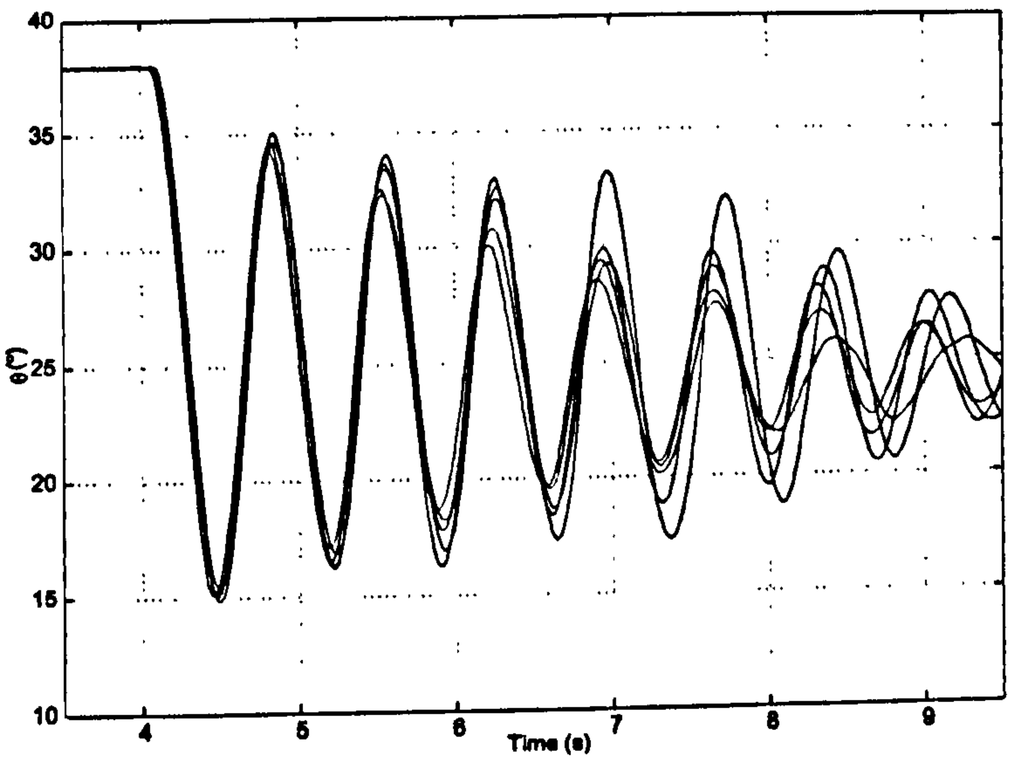


(d) $\delta_e = -25°$

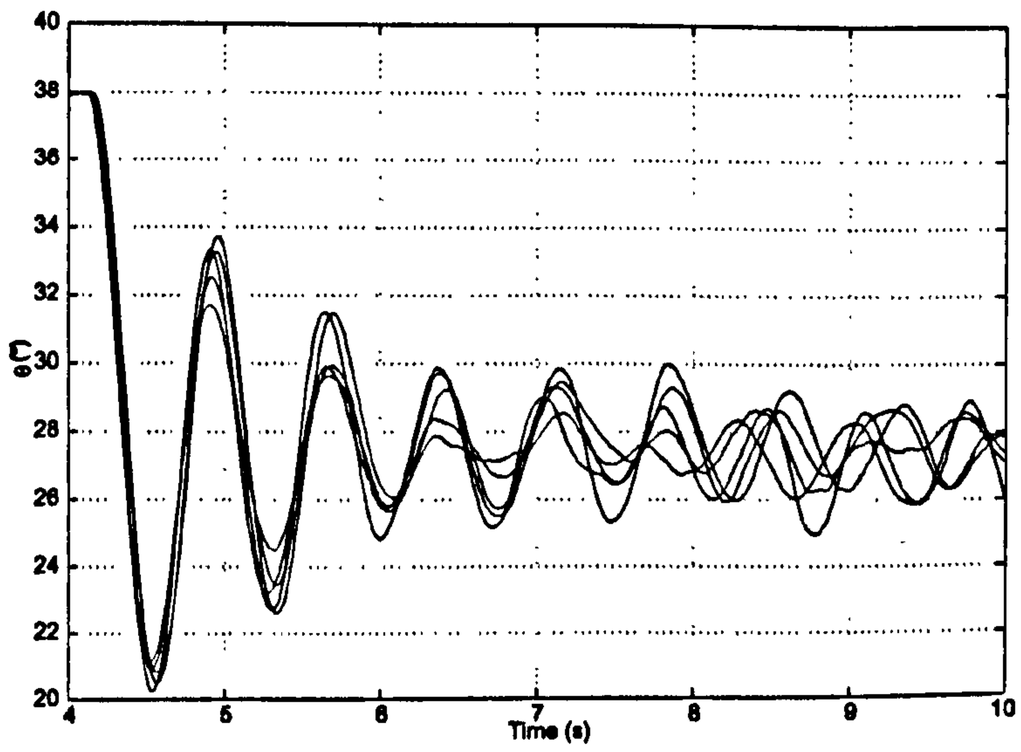


(e) $\delta_e = -30°$

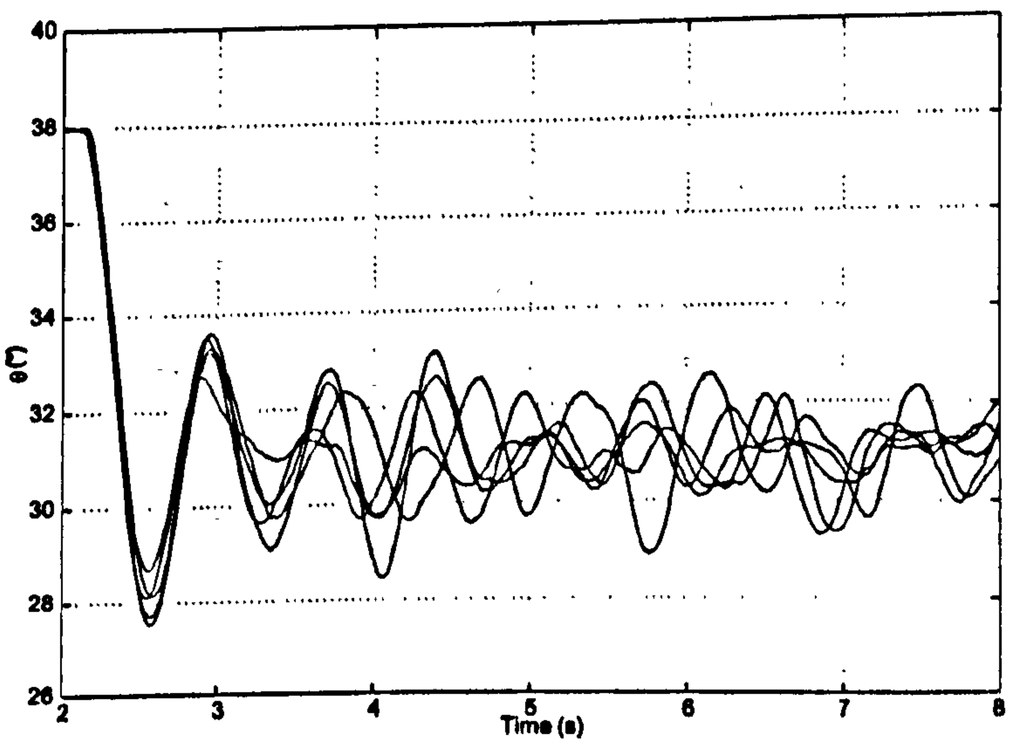


(f) $\delta_e = -35°$

Figure 4.7: Time histories for fixed tailplane deflections.

### 4.1.6 All-Moving Foreplane Results

Although the foreplanes were added primarily to test the feasibility of using digital actuators and belt-drive control, single degree-of-freedom tests were also performed to investigate their impact on the dynamics of the model. Due to their relatively small size and small moment arm from the centre of rotation they have limited authority. However, at certain angles of attack (most notably at moderate $\alpha$, where the tailplanes were immersed in the wake of the wing) they did change the dynamics considerably.

Experimental bifurcation diagrams were again constructed by slowly varying tailplane deflection and plotting the equilibrium conditions of the model. With an added control input however, a series of test runs needed to be performed across a range of foreplane deflections ($\delta_c$).

Figures 4.8 to 4.12 show some of the bifurcation results, with decreasing tailplane angle shown in the upper diagrams, and increasing tailplane in the lower. The fixed-point equilibria became unstable at certain tailplane deflections and angles of attack, leading to fold bifurcations. Figure 4.10 (lower) shows that, at foreplane deflections around 0°, a fold bifurcation occurs and the model jumps straight to the limit cycle. This means that for a single, fixed value of tailplane ($\delta_e \approx 2.5°$) and foreplane ($\delta_c = 0°$) angles there are four separate equilibrium conditions: one stable fixed point, two unstable fixed points, and a stable limit cycle. Note that Figure 4.10 (lower) is qualitatively the same as Figure 2.1.

With two sets of control effectors, test runs to construct bifurcation diagrams can be performed using either (or both) control inputs. Tests were not performed where tailplane deflection was kept constant and canard angle varied slowly. However, it would be expected that at a certain tailplane angle (approximately 6°) the bifurcation diagram would show two supercritical pitchfork bifurcations, with the steady-state branch that the model follows depending on initial conditions and tunnel turbulence.

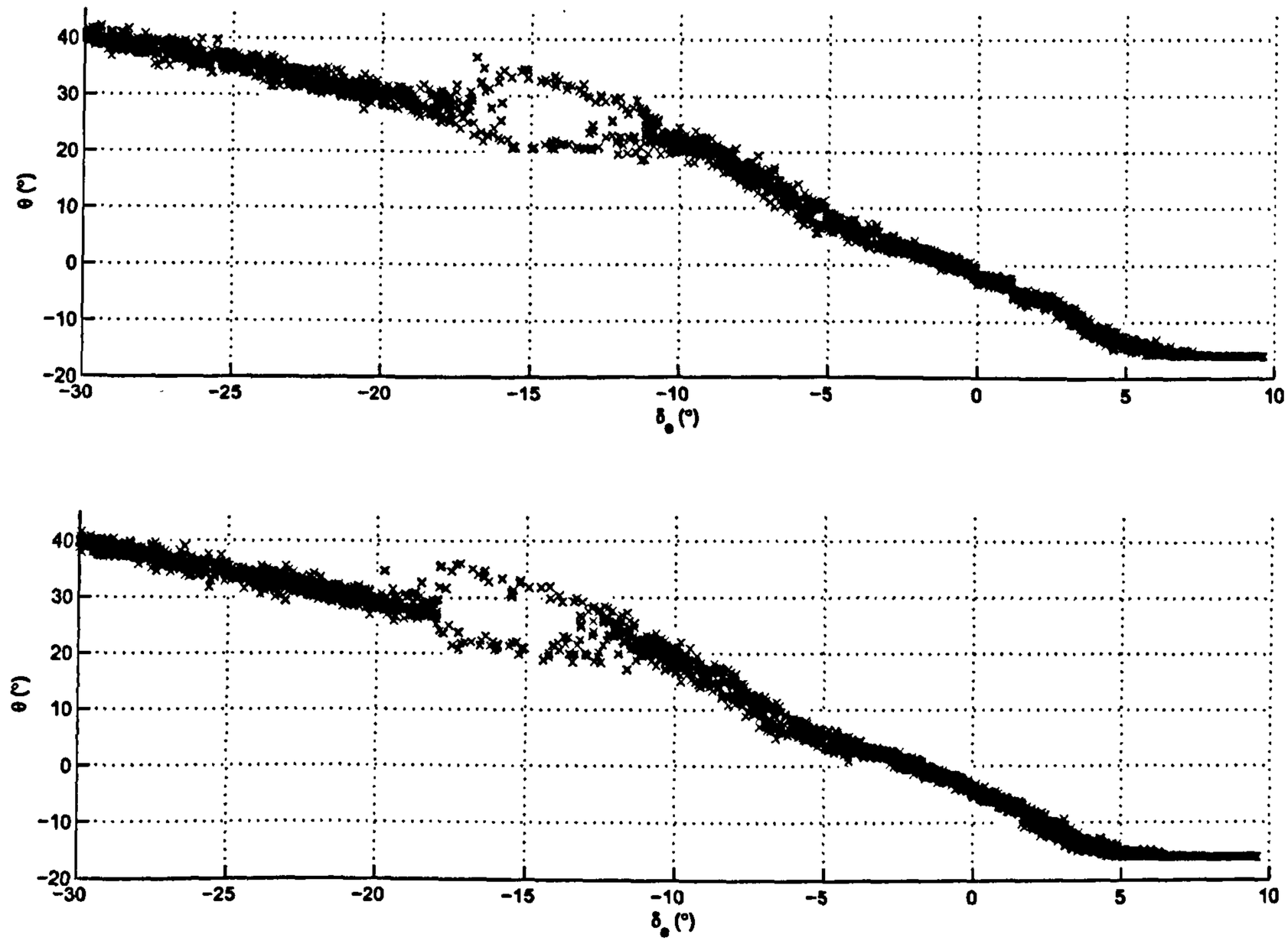


Figure 4.8: Bifurcation diagram for $\delta_c = -30°$.

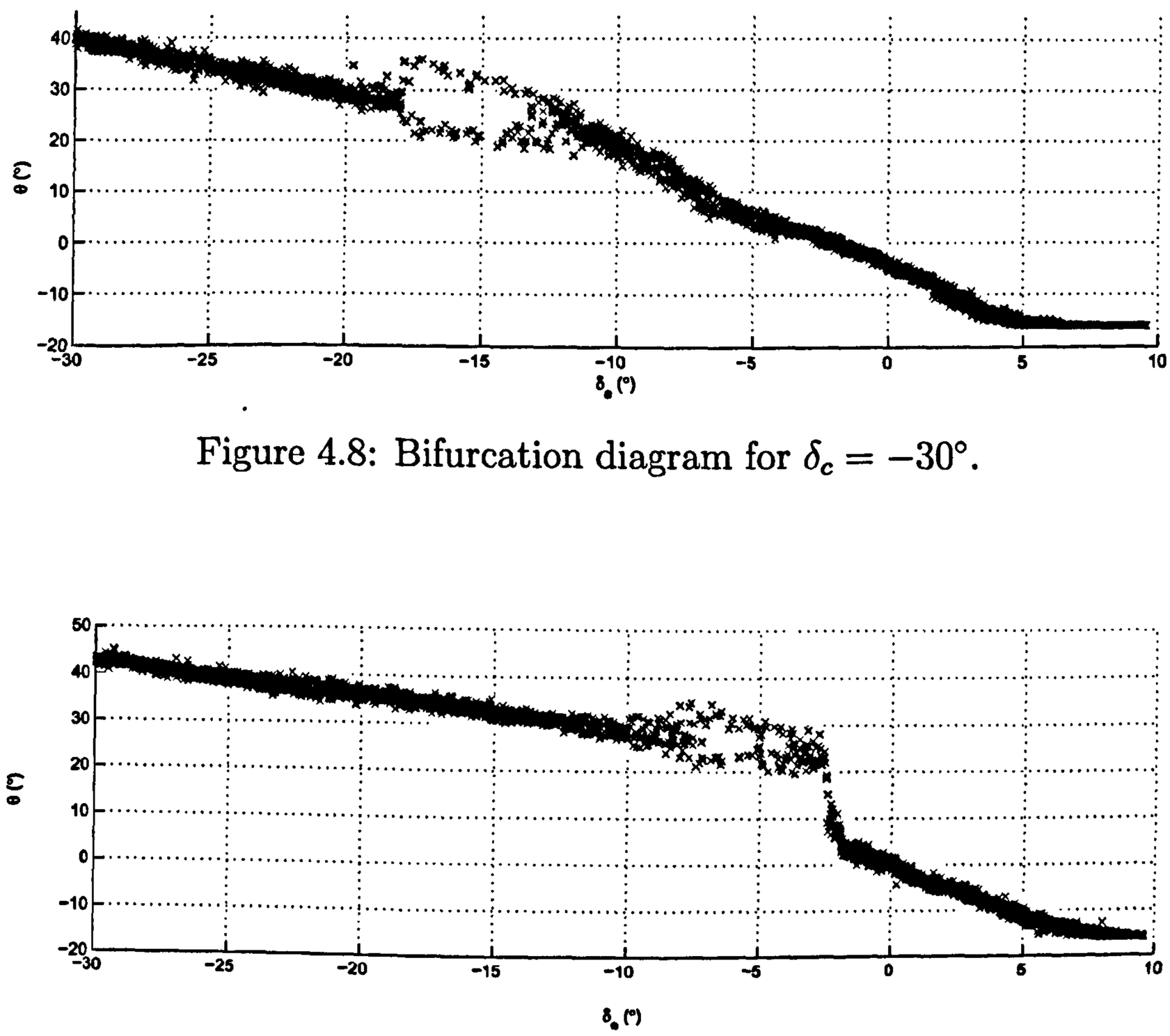


Figure 4.9: Bifurcation diagram for $\delta_c = -15°$.

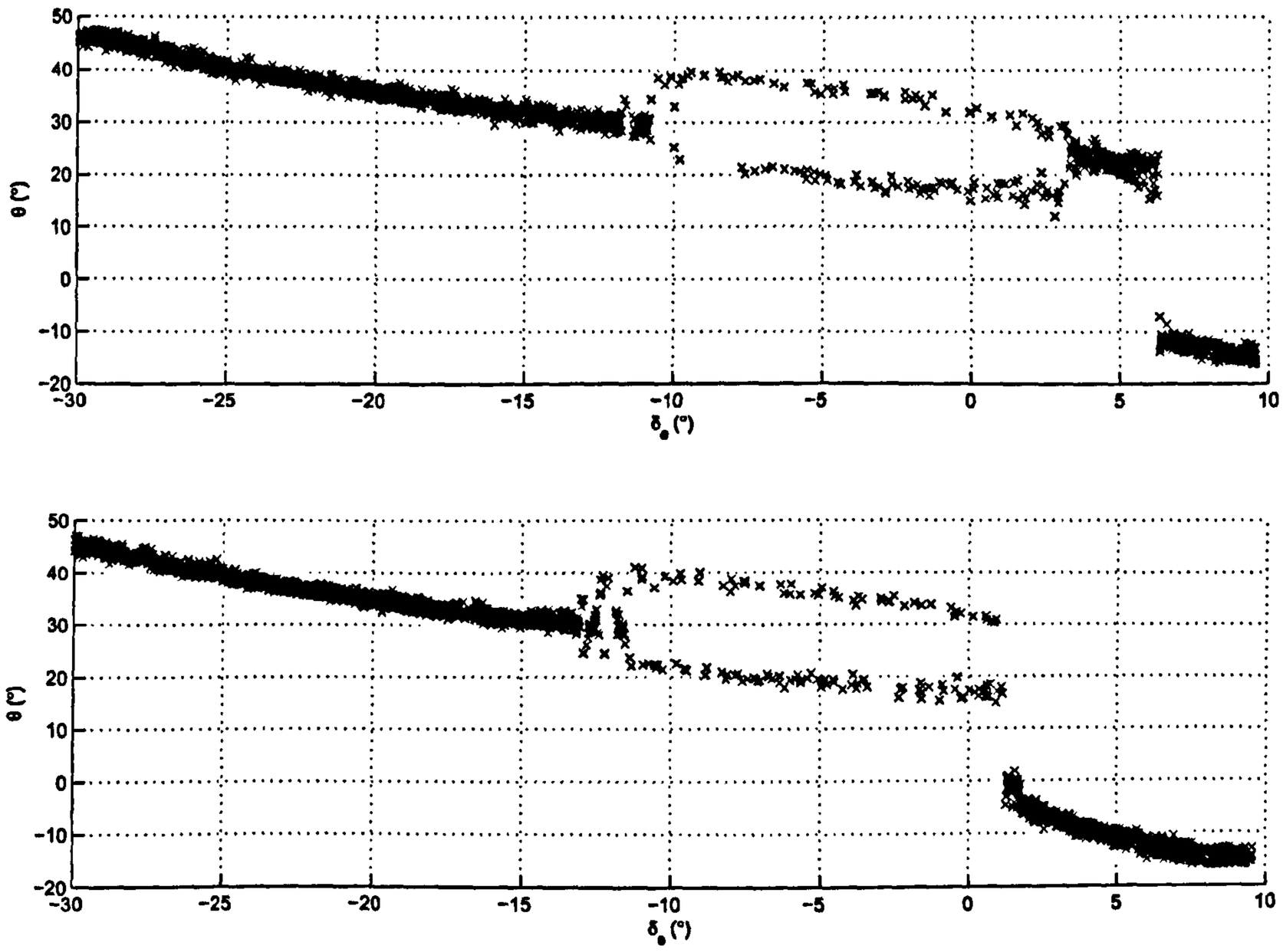


Figure 4.10: Bifurcation diagram for $\delta_c = 0°$.

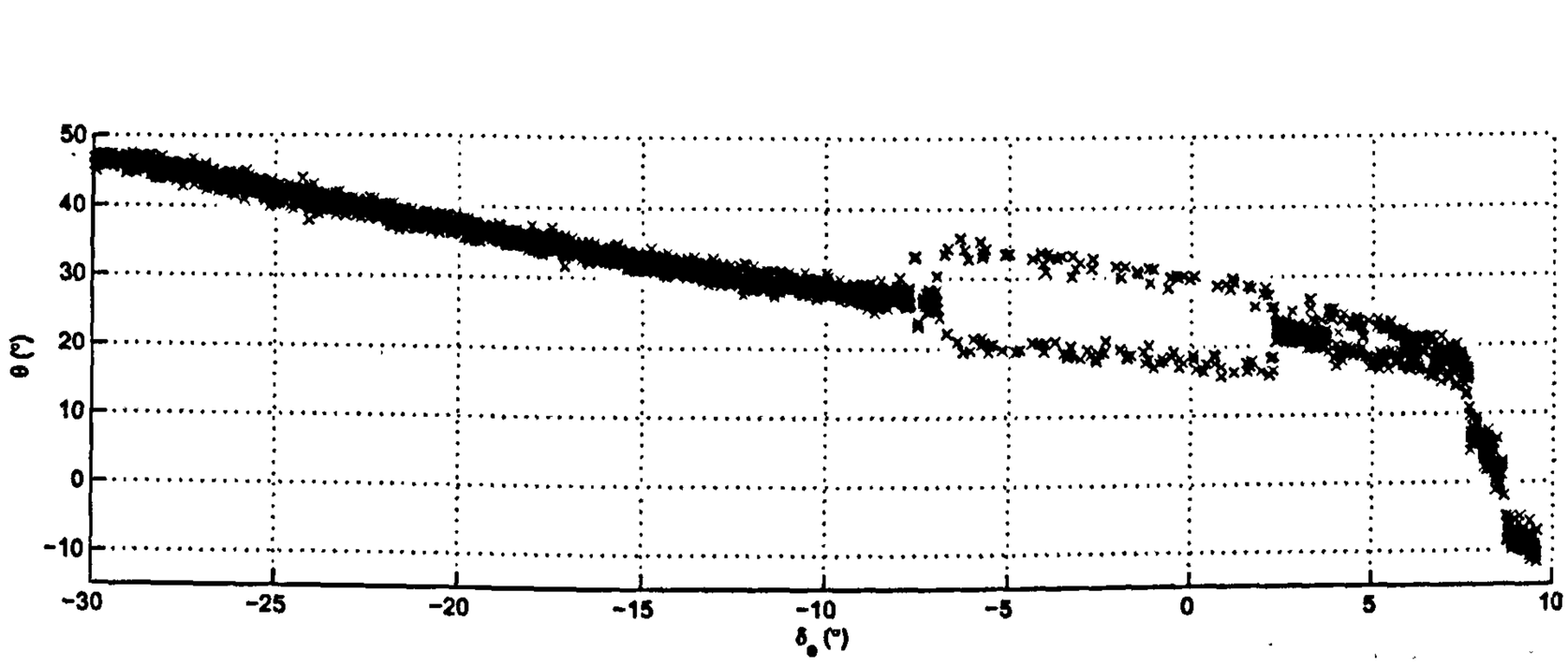


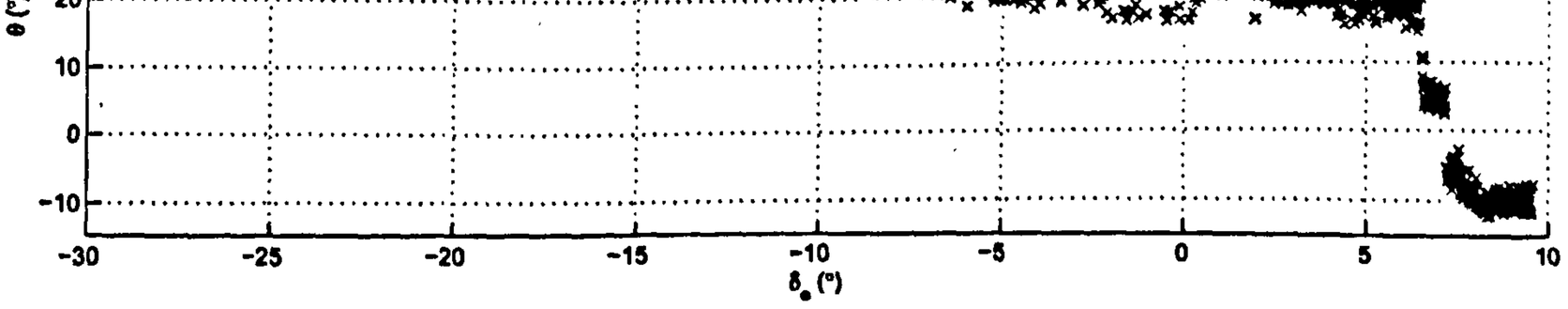


Figure 4.11: Bifurcation diagram for $\delta_c = 15°$.

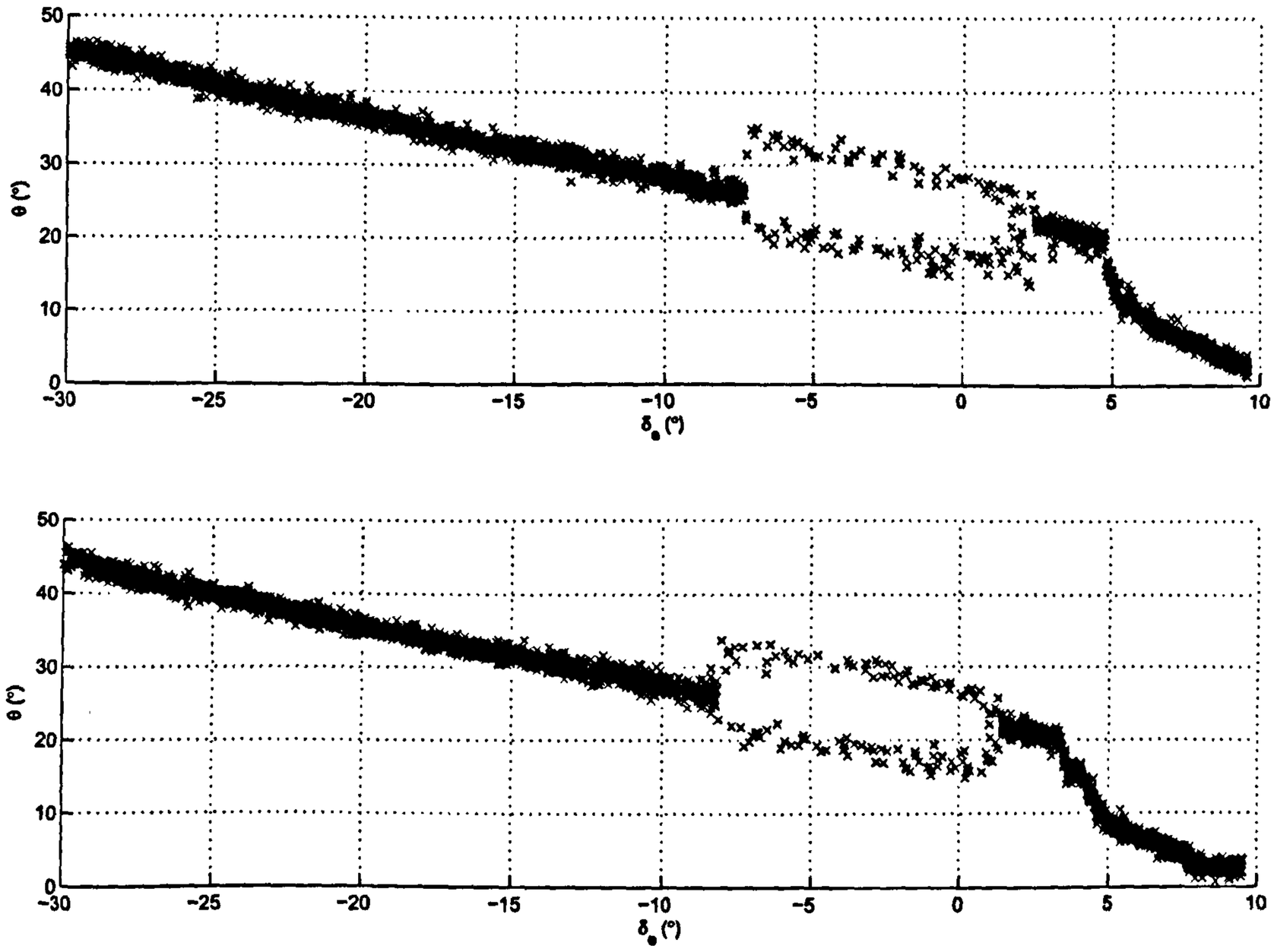


Figure 4.12: Bifurcation diagram for $\delta_c = 30°$.

## 4.2 2 Degree-of-Freedom Results

Longitudinal two DOF tests were performed without the counterbalance, which gave pitch and primarily longitudinal strut motion. The carbon strut fairing was used to reduce the drag on the strut, and was found to help clarify the dynamics by increasing strut limit cycle amplitudes. The same general dynamics can be seen in the 2 DOF arrangement as the pitch-only; a large amplitude limit cycle at moderate $\alpha$ (Figure 4.13). However, there is an additional limit cycle oscillation, mainly in strut angle, $\gamma$, when the model reaches $\alpha \approx 13°$. This can be seen as the narrow band of large amplitude motion at $\delta_e \approx -5.5°$ in Figure 4.14.

Figure 4.15 shows experimental phase-plane plots for the strut at several fixed tailplane deflections. Unfortunately there is no direct feedback of strut angular rate, $\chi$, so the differential of angular position was used, which gives a noisy signal[2]. The results show

[2]Even with a rate gyro fixed to the strut the angular rates are very small and would be susceptible to noise corruption.

the strut-mode limit cycle region at $\delta_e \approx -6°$, however, tunnel turbulence and noise are masking the true amplitude.

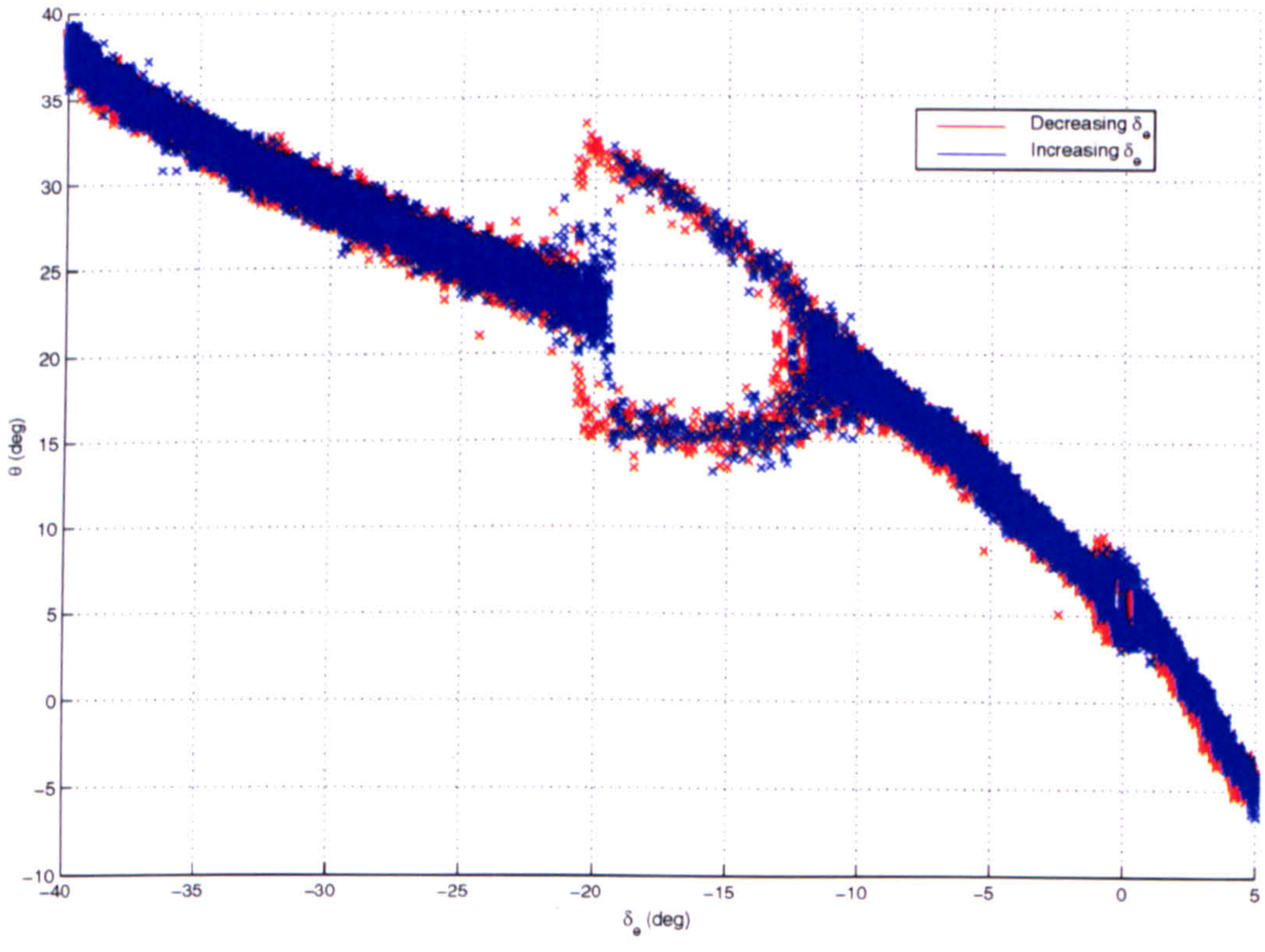


Figure 4.13: Experimental bifurcation diagram for the 2 DOF rig (pitch angle).

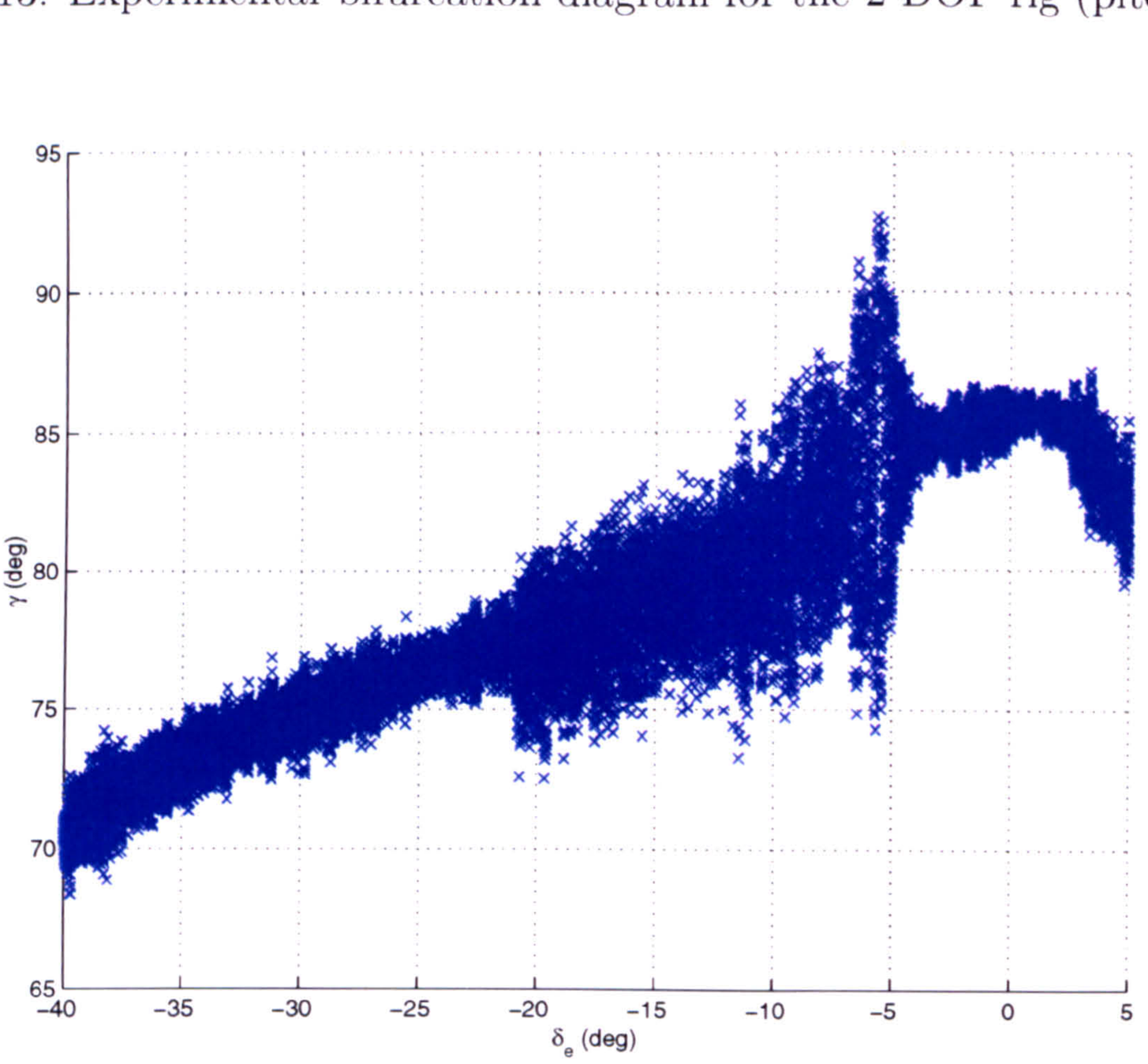


Figure 4.14: Experimental bifurcation diagram for the 2 DOF rig (strut angle).

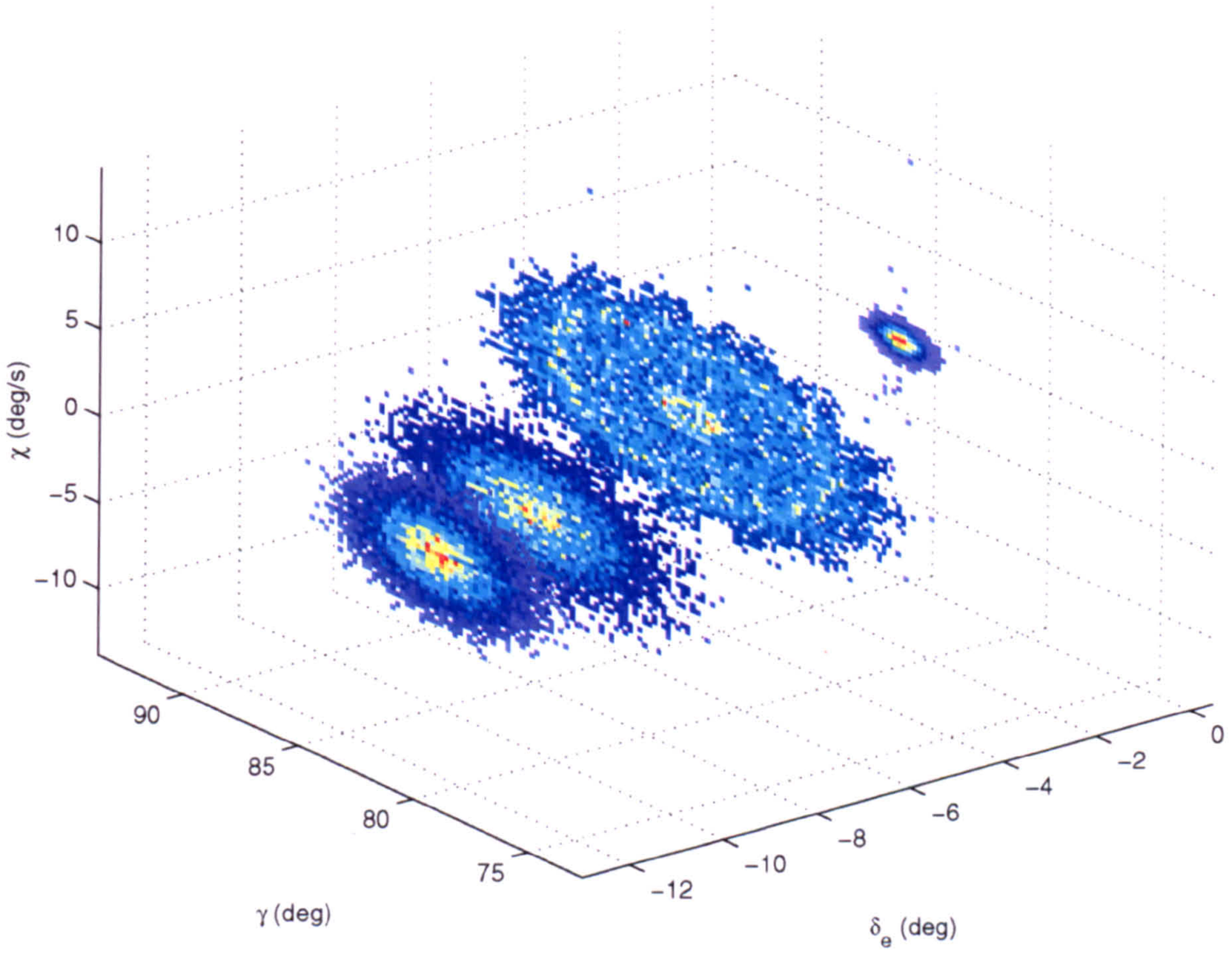


Figure 4.15: Phase plane plots for the strut mode of the 2 DOF rig.

## 4.3 Conclusions

In this chapter experimental results from the Bristol University pendulum support rig in both single and two degree-of-freedom were presented. The results show some interesting non-linear behaviour, including limit cycles, Hopf points and cyclic fold bifurcations. The motivation for the work is to develop and compare feedback control systems; in order to do this a representative model of the rig is needed. In the next chapter, an accurate model of the rig in a single degree-of-freedom (without foreplanes) is developed.

# Chapter 5

# Limit Cycle modelling

To allow off-line development of controllers for the wind tunnel rig it is necessary to derive a mathematical model of the system. In this chapter, a novel modelling approach is presented which accurately captures the non-linear dynamics of the wind tunnel rig observed in the experimental results presented in Chapter 4. Modelling using traditional stability derivative methods will allow limit cycles to be represented, as long as the derivatives are non-linear functions of states and parameters, however the derivatives would have to be extracted and stored in look-up tables. A more efficient solution, particularly where the aerodynamics is highly non-linear and includes bifurcation phenomena, is to develop a model in which observed parameters such as limit cycle amplitude, stability and frequency can be specified explicitly in the model. It is shown how this information can be embedded into an appropriate dynamical estimator of the experimental system by using the results of the experimental bifurcation analysis.

## 5.1 Aerodynamic Modelling Issues

Aerodynamic modelling for the purposes of flight dynamics involves representing the aerodynamic loads in a formulation suitable for use in the equations of motion for arbitrary flight conditions. Typically, the forces and moments are functions of the motion variables and parameters such as control inputs, undercarriage position, etc. The vast majority of such models are quasi-steady and capture only small-amplitude motions.

Where limit cycle motions are known to exist, quasi-steady derivative type models can capture aspects of their dynamics. The usual limit cycle phenomenon is 'wing rock': a lateral-directional oscillation, dominant in roll, that occurs in many fighter aircraft configurations as angle-of-attack is increased [112, 113]. Its onset corresponds to loss in stability of the Dutch roll mode, which can be reflected in the stability derivatives relatively easily. The bounded oscillation is achieved by adopting a non-linear dependence of roll damping coefficient on the state. Whilst the steady state characteristics can be adequately represented in this manner, it is very difficult to model the transient behaviour, stability of the orbits and bifurcationary events following the growth of the cycle.

It has been recognised that unsteady effects can become significant in rapid manoeuvres, or manoeuvres at very low forward speeds. Quasi-steady derivative type models are inadequate in accounting for time-dependent aerodynamic reactions. A substantial body of work has therefore been undertaken on advanced modelling techniques to capture these effects (e.g. [68], [114] – [116]). However, practical implementation of such methods has not as yet been extended to bifurcation and large-amplitude phenomena such as limit cycles.

The majority of limit cycle modelling work has been in connection with wing rock. Relatively few aircraft exhibit longitudinal pitching limit cycle oscillations ('bucking') as in the case of the pendulum rig Hawk model at Bristol. (In fact, if the Hawk model is mounted with lateral-directional degrees of freedom as well as longitudinal, the bucking behaviour is likely to be preceded by a lateral-directional phenomenon, such as wing rock or departure to incipient spin.)

Most of the aerodynamic models derived to represent wing rock from experimental data are single-DOF, although 3-DOF coupled lateral-directional motions have also been explored [15, 113]. In all cases, some form of non-linear roll damping has been incorporated into the formulation and efforts made to correlate amplitude and sometimes frequency with measured data (e.g. [13, 15, 117, 118]); the amplitude of the limit cycle depends on the ratio of linear to non-linear damping terms. Model structures with discontinuities and/or hysteresis in aerodynamic derivatives have also been used to represent wing rock motions ([14] – [16]). Wing rock limit cycles can also be obtained from relatively simple models in which kinematic coupling between longitudinal and lateral-directional modes

occurs [119, 120].

A longitudinal bucking-type limit cycle has been modelled in [120] but this uses a jump in lift coefficient associated with stall, which is not appropriate to the Hawk case.

Both wing rock and aerofoil pitching oscillations have been analysed in the context of bifurcation theory in [121]. Models incorporating non-linear damping were evaluated in terms of bifurcation behaviour leading to limit cycles; the nature of the bifurcations (sub- or supercritical) was assessed, as was the rate of growth of the periodic orbits. However, the identification of model structures suitable for representing *global* bifurcation behaviour over a wide operating envelope – as observed with the Hawk model (Figure 4.2) – has not been addressed elsewhere.

As with all flight dynamics modelling, a balance must be struck between fine detail in localised regions and the need to represent behaviour over a very large operating envelope. Bifurcation analysis can be an invaluable tool in understanding the structure and dynamical features of a flight dynamics model. By providing tools to analyse and characterise different dynamical transitions, it can help to identify the main features to be captured by the model.

Therefore the bifurcation behaviour and limit cycle features are modelled in an approximate manner, with parameters and states as independent variables. The method makes assumptions about the shape of the periodic orbits and about the location and nature of unstable stationary points but is able to capture most of the bifurcation behaviour exhibited in rigid-body flight mechanics to within a degree of accuracy sufficient for flight mechanics analysis. It uses explicitly the results of the bifurcation analysis performed on the experimental rig.

## 5.2 Modelling Method

Unlike systems which show no bifurcation or non-linear behaviour, the main requirement in this case is for the model to capture the predominant features of the bifurcations and oscillatory behaviour exhibited by the experimental rig. The challenge is therefore to find a single model structure that can represent the whole system and estimate correctly the dynamics observed experimentally.

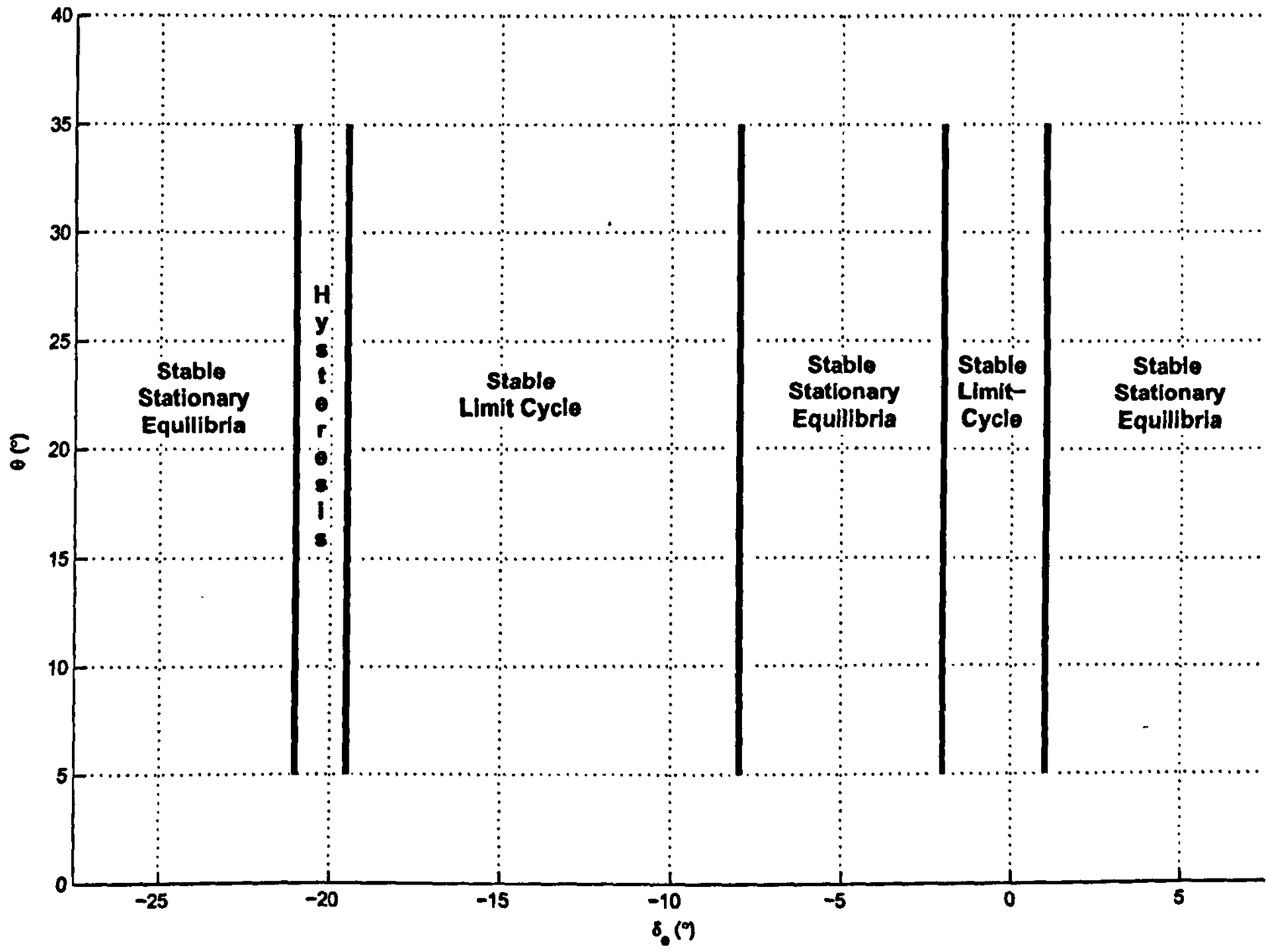


Figure 5.1: Schematic of the main features of the desired model bifurcation diagram, i.e. attractor types and bifurcation points.

In particular, we require that the bifurcation diagram of the model exhibits the main features of the experimental bifurcation diagram depicted in Figure 4.2. These are summarised in Figure 5.1 where the type of asymptotic solution present at each tailplane deflection and the location of the relevant bifurcation points are shown.

As a starting point we examine a typical experimental time history of the rig position, such as the one depicted in Figure 5.2, where the tailplane deflection is fixed at $-15°$ and the rig is released from a phase-space point away from the limit cycle.

As can be noticed from Figure 5.2, the oscillations appear approximately sinusoidal with an exponential-type decay. Also visible are the effects of turbulence on the system (especially at $t \approx 10\,\mathrm{s}$). Assuming the oscillations are symmetrical about the fixed point and neglecting the effects of turbulence, this suggests that the position decays onto the stable period-1 limit cycle according to the equation (as in [122]):

$$\hat{\theta} = A(1 + e^{-Bt}) \sin(\omega t + \phi) \tag{5.1}$$

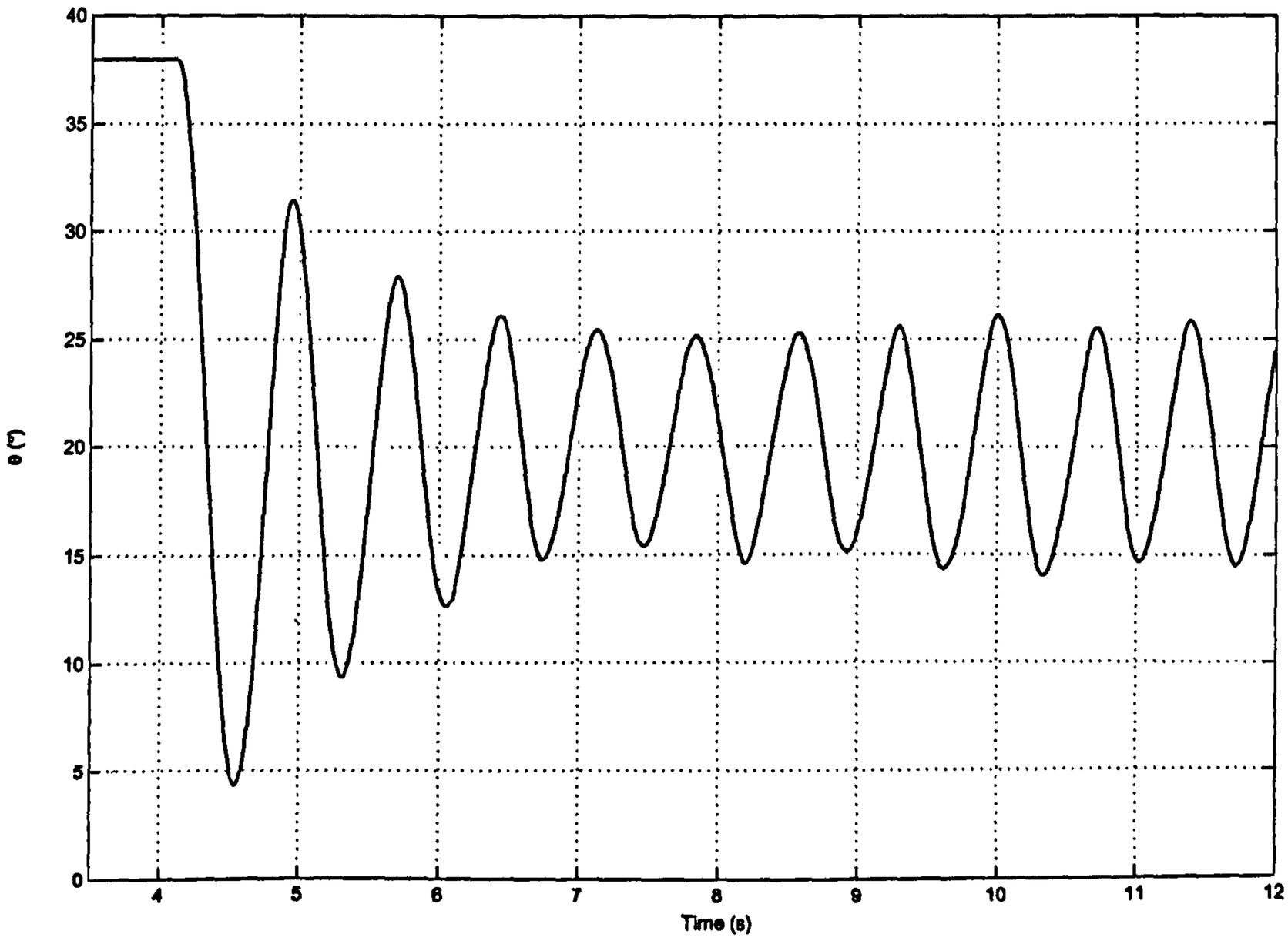


Figure 5.2: Experimental time history showing decay onto the limit cycle ($\delta_e$ fixed at $-15°$).

Using an exponential function to model the decreasing envelope was found to give problems due to the divergence of the exponential for $t \rightarrow -\infty$, see Figure 5.3(a). In fact, this makes it difficult to account for transitions from a stable limit cycle to an equilibrium or a smaller amplitude cycle, such as those actually observed experimentally (for example, in the hysteretic region).

To overcome this problem, a tanh function was selected to model the envelope as this gives the required growth/decay shape (shown in Figure 5.3(b)). Thus, we choose:

$$\hat{\theta} = (A_u - \Delta(1 + \tanh(Kt))) \sin(\omega t + \phi) \tag{5.2}$$

where $A_u$ and $\Delta$ are extra parameters necessary for defining the tanh function characteristics, and $K$ (equivalent to $B$ in (5.1)) defines the growth/decay rate. Note that the parameter[1] $A_u$ in (5.2) can be made arbitrarily large if necessary to model pure exponential growth/decay from/to $\pm\infty$.

[1] $A_u$ has an interesting interpretation, when modelling the evolution of the system from a given limit cycle to another attractor. In this case, $A_u$ corresponds to the amplitude of the limit cycle from which the evolution begins.

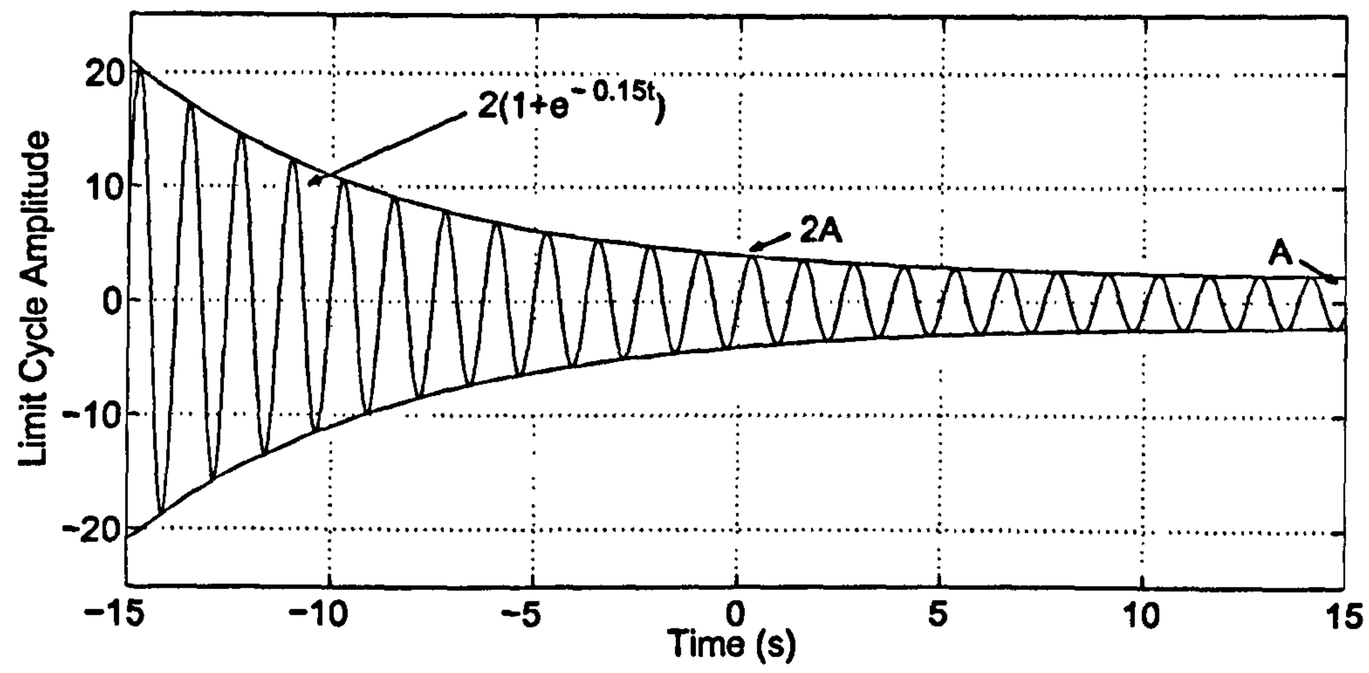


(a) Exponential function.

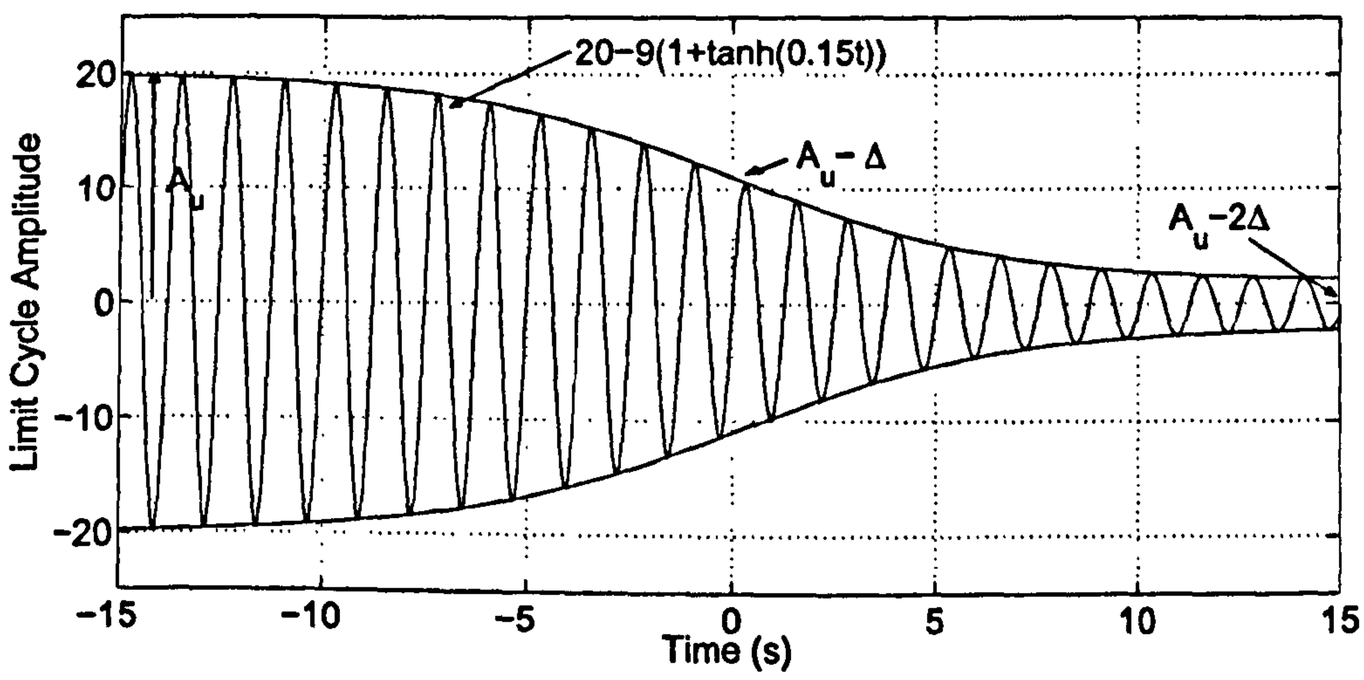


(b) tanh function.

Figure 5.3: Time histories for exponential and tanh function decay to a limit cycle.

Differentiating (5.2) with respect to time we can now get an estimate for the pitch rate, $\dot{\hat{\theta}}$, as:

$$\begin{aligned}\frac{d\hat{\theta}}{dt} &= (A_u - \Delta(1+\tanh(Kt)))\omega\cos(\omega t+\phi) \\ &\quad -K\Delta\mathrm{sech}^2(Kt)\sin(\omega t+\phi) \end{aligned} \tag{5.3}$$

and by further differentiation the acceleration:

$$\begin{aligned}\frac{d^2\hat{\theta}}{dt^2} &= -\omega^2\hat{\theta} - 2K\Delta\omega\cos(\omega t+\phi)\mathrm{sech}^2(Kt) \\ &\quad +2K^2\Delta\sin(\omega t+\phi)\mathrm{sech}^2(Kt)\tanh(Kt). \end{aligned} \tag{5.4}$$

Our aim, now, is to use (5.2)-(5.4) to construct a suitable dynamic estimator of the experimental rig. Namely, given a certain initial position, $\hat{\theta}_0$, and pitch rate, $\dot{\hat{\theta}}_0$, we want

the model to provide an estimate of the system trajectory over a desired time range. In so doing, we need to address two separate problems:

(A) Establishing an appropriate methodology to carry out the estimation;

(B) Evaluating all the necessary parameters involved in the estimation process.

We start by addressing the former problem, leaving to Section 5.2.4 the solution of the latter.

### 5.2.1 Estimation Strategy

The first, more immediate, solution to carry out the estimation could be to integrate (5.4) directly with initial conditions $\hat{\theta}_0$, $\dot{\hat{\theta}}_0$. While providing an acceptable estimate under nominal operating conditions, this methodology would fail to reproduce transient behaviour due to sudden disturbances, parameter variations or noise. This is due to the fact that equation (5.4) is derived on the assumption that the position envelope is monotonically decreasing (or increasing). Thus, the effect of any disturbance occurring when the envelope has already become too small would be artificially attenuated by the model (see example later in this section). To overcome this problem, one would need to reset the integration time whenever an undesired event or parameter variation occurs. This is difficult or even impossible to implement on-line, as it would require some robust event-driven integration algorithm relying on an efficient event-detection routine.

Therefore, we consider an alternative strategy which uses a combination of (5.2)-(5.4) and time discretization. Namely, suppose we want to simulate the system trajectory from $\hat{\theta}_0$, $\dot{\hat{\theta}}_0$ over a given time interval, say $T = (t_{\max} - t_{\min})$. Let $\delta t = (t_{\max} - t_{\min})/N$ be a discretization of $T$ into $N$ sufficiently small sub-intervals.

Then, the key idea is to exploit knowledge of the position and pitch rate, $\hat{\theta}_n, \hat{\theta}_n$, at the generic $n$-th step, to derive an estimate of the corresponding acceleration $\ddot{\hat{\theta}}_n$ and use this to find estimates of the position and pitch rate, $\hat{\theta}_{n+1}, \dot{\hat{\theta}}_{n+1}$ at the next step, $n+1$.

More precisely, from (5.2) and (5.3) we know that:

$$\hat{\theta} = f(t, \phi, \mu) \tag{5.5}$$

$$\dot{\hat{\theta}} = g(t, \phi, \mu) \tag{5.6}$$

where $f, g$ represent the left-hand sides of (5.2)-(5.3) and $\mu$ the vector of parameters. Hence, considering the time $t$ as an independent variable, which for the sake of clarity we relabel as $\tau$, we then have at the $n$-th step that:

$$\hat{\theta}_n - f(\tau_n, \phi_n, \mu) = 0 \tag{5.7}$$

$$\dot{\hat{\theta}}_n - g(\tau_n, \phi_n, \mu) = 0 \tag{5.8}$$

In other words, we know that, for any given value of position, $\hat{\theta}_n$, and pitch rate, $\dot{\hat{\theta}}_n$, if the parameters $\mu$ are fixed, there exist a $\tau_n$ and $\phi_n$ which solve (5.7)-(5.8). Thus, (5.7)-(5.8) define implicitly $\tau_n$ and $\phi_n$ as functions of the position and pitch rate at each step, i.e.:

$$\tau_n = \zeta(\hat{\theta}_n, \dot{\hat{\theta}}_n, \mu) \tag{5.9}$$

$$\phi_n = \eta(\hat{\theta}_n, \dot{\hat{\theta}}_n, \mu) \tag{5.10}$$

Hence, it is theoretically possible to use (5.9) and (5.10) to find values for $\tau_n$ and $\phi_n$ given the current pitch angle, $\hat{\theta}$, and pitch rate, $\dot{\hat{\theta}}$. These values can then be substituted into (5.4) to find an estimate of the pitch acceleration (and pitching moment, if required) at the same step, i.e.:

$$\ddot{\hat{\theta}}_n = \sigma(\tau_n, \phi_n, \mu). \tag{5.11}$$

Finally, the position and pitch rate at the next step can be estimated (if $\delta t$ is sufficiently small) as:

$$\hat{\theta}_{n+1}(t) = \hat{\theta}_n + \ddot{\hat{\theta}}_n(\delta t)^2, \tag{5.12}$$

$$\dot{\hat{\theta}}_{n+1}(t) = \dot{\hat{\theta}}_n + \ddot{\hat{\theta}}_n \delta t. \tag{5.13}$$

The fundamental open problem for this approach to work is to be able to derive $\tau_n$ and $\phi_n$ from equations (5.2)-(5.3), given specific values of the position and pitch rate. In general, these are transcendental equations which cannot be solved explicitly. In what follows we will see that $\tau_n$ and $\phi_n$ can indeed be found at each step by appropriate algebraic manipulations.

### 5.2.2 Finding $\tau_n$ and $\phi_n$

Assume that the position, $\hat{\theta}_n$, and pitch rate, $\dot{\hat{\theta}}_n$, are given. Let:

$$\Psi(\tau_n) = A_u - \Delta(1 + \tanh(K\tau_n)) \tag{5.14}$$

From (5.2), we then get:

$$\phi_n = \arcsin\left(\frac{\hat{\theta}_n}{\Psi(\tau_n)}\right) - \omega\tau_n \tag{5.15}$$

Substituting (5.15) into (5.3) gives:

$$\begin{aligned}\dot{\hat{\theta}}_n &= \Psi(\tau_n)\omega\cos\left[\arcsin\left(\frac{\hat{\theta}_n}{\Psi(\tau_n)}\right)\right] \\ &\quad -K\Delta\mathrm{sech}^2(K\tau_n)\sin\left[\arcsin\left(\frac{\hat{\theta}_n}{\Psi(\tau_n)}\right)\right]\end{aligned} \tag{5.16}$$

Since,

$$\cos(\arcsin(x)) \equiv \sqrt{1-x^2}, \tag{5.17}$$

we then have:

$$\dot{\hat{\theta}}_n = \Psi(\tau_n)\omega\sqrt{1-\left[\frac{\hat{\theta}_n}{\Psi(\tau_n)}\right]^2} - \frac{K\Delta\hat{\theta}_n\mathrm{sech}^2(K\tau_n)}{\Psi(\tau_n)}. \tag{5.18}$$

Rearranging (5.18), we obtain

$$\dot{\hat{\theta}}_n\Psi(\tau_n) + K\Delta\hat{\theta}_n\mathrm{sech}^2(K\tau_n) = \Psi(\tau_n)^2\omega\sqrt{1-\left[\frac{\hat{\theta}_n}{\Psi(\tau_n)}\right]^2}, \tag{5.19}$$

thus:

$$\begin{aligned}\dot{\hat{\theta}}_n^2\Psi(\tau_n)^2 + 2K\Delta\hat{\theta}_n\dot{\hat{\theta}}_n\Psi(\tau_n)\mathrm{sech}^2(K\tau_n) + K^2\Delta^2\hat{\theta}_n^2\mathrm{sech}^4(K\tau_n) \\ = \omega^2\Psi(\tau_n)^4 - \omega^2\hat{\theta}_n^2\Psi(\tau_n)^2.\end{aligned} \tag{5.20}$$

Now, from (5.14),

$$\begin{aligned}\operatorname{sech}^2(K\tau_n) &= 1-\tanh^2(K\tau_n)\\ &= -\frac{\Psi(\tau_n)^2}{\Delta^2}+\frac{2\Psi(\tau_n)A_u}{\Delta^2}-\frac{2\Psi(\tau_n)}{\Delta}-\frac{A_u^2}{\Delta^2}+\frac{2A_u}{\Delta}\end{aligned} \tag{5.21}$$

Substituting (5.21) into (5.20) gives a quartic in $\Psi(t)$:

$$\begin{aligned}&\Psi(\tau_n)^4\left(-\omega^2+\frac{R}{\Delta^4}\right)\\ &+\Psi(\tau_n)^3\left(-\frac{S}{\Delta^2}+R\left(\frac{4}{\Delta^3}-\frac{4A_u}{\Delta^4}\right)\right)\\ &+\Psi(\tau_n)^2\left(\dot{\hat{\theta}}_n^2+\omega^2\hat{\theta}^2+S\left(\frac{2A_u}{\Delta^2}-\frac{2}{\Delta}\right)+R\left(\frac{6A_u^2}{\Delta^4}-\frac{12A_u}{\Delta^3}+\frac{4}{\Delta^2}\right)\right)\\ &+\Psi(\tau_n)\left(S\left(\frac{2A_u}{\Delta}-\frac{A_u^2}{\Delta^2}\right)+R\left(\frac{12A_u^2}{\Delta^3}-\frac{4A_u^3}{\Delta^4}-\frac{8A_u}{\Delta^2}\right)\right)\\ &+R\left(\frac{4A_u^2}{\Delta^2}+\frac{A_u^4}{\Delta^4}-\frac{4A_u^3}{\Delta^3}\right)=0\end{aligned} \tag{5.22}$$

where:

$$R = K^2\Delta^2\hat{\theta}_n^2 \tag{5.23}$$

$$S = 2K\Delta\hat{\theta}_n\dot{\hat{\theta}}_n \tag{5.24}$$

The roots of this quartic, $\Psi(\tau_n)=\tilde{\Psi}$, can then be used to find a value for $\tau_n$. From (5.14), we get:

$$\tau_n = \frac{1}{K}\operatorname{arctanh}\left(\frac{A_u-\tilde{\Psi}}{\Delta}-1\right). \tag{5.25}$$

Note that as (5.22) admits multiple solutions, we need to choose the one that when substituted in (5.25) gives an admissible real-valued $\tau_n$. This is limited by the domain of the arctanh function, which lies between -1 and 1. Hence, we choose a positive real root from (5.22).

Substituting $\tau_n$ into (5.4), we then get an estimate of $\ddot{\hat{\theta}}_n$, i.e. the pitch acceleration at the $n$-th step, that can be used in (5.12)-(5.13) to find an estimate of $\hat{\theta}_{n+1}, \dot{\hat{\theta}}_{n+1}$.

It is worth mentioning here that the pitch DOF equation of motion can then be used to solve for the pitching moment coefficient, $C_m$, given by:

$$C_m = \frac{I\ddot{\hat{\theta}}}{\frac{1}{2}\rho V^2 S\bar{c}}. \tag{5.26}$$

### 5.2.3 Examples

For the sake of clarity, we now use a representative example to illustrate the estimation strategy described above. We assume that all the necessary parameters have been found using the strategy that will be presented in Section 5.2.4. A more extensive validation of the rig model will be presented in Chapter 6.

We consider a model of the experimental system with fixed tailplane deflection, $\delta_e = -20°$. The experimental bifurcation diagram in Figure 4.2 shows that, at this value of the tailplane deflection, there is a stable fixed point at $\hat{\theta} = 23°$ and a stable limit cycle of amplitude 6°.

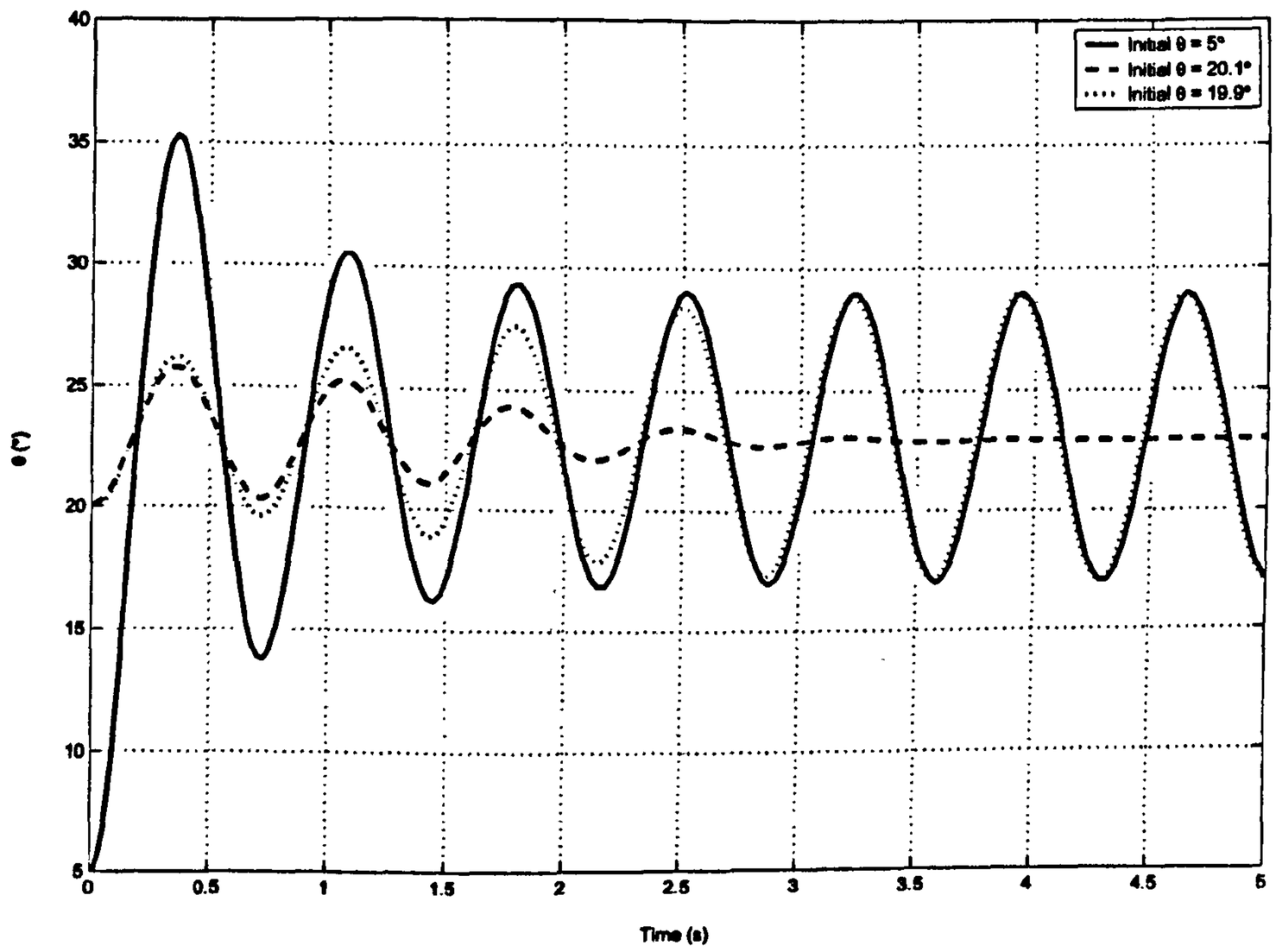


Figure 5.4: Time simulations for three initial conditions.

Time histories produced by the estimation strategy described above for different starting points are shown in Figure 5.4. Figure 5.5(a) shows the pitch *reaction surface* [78]

produced by using (5.26). It is difficult to see the structure of the surface from this plot due to the large gradient in $\hat{\theta}$; subtracting the average gradient gives a clearer picture of the underlying structure (Figure 5.5(b)).

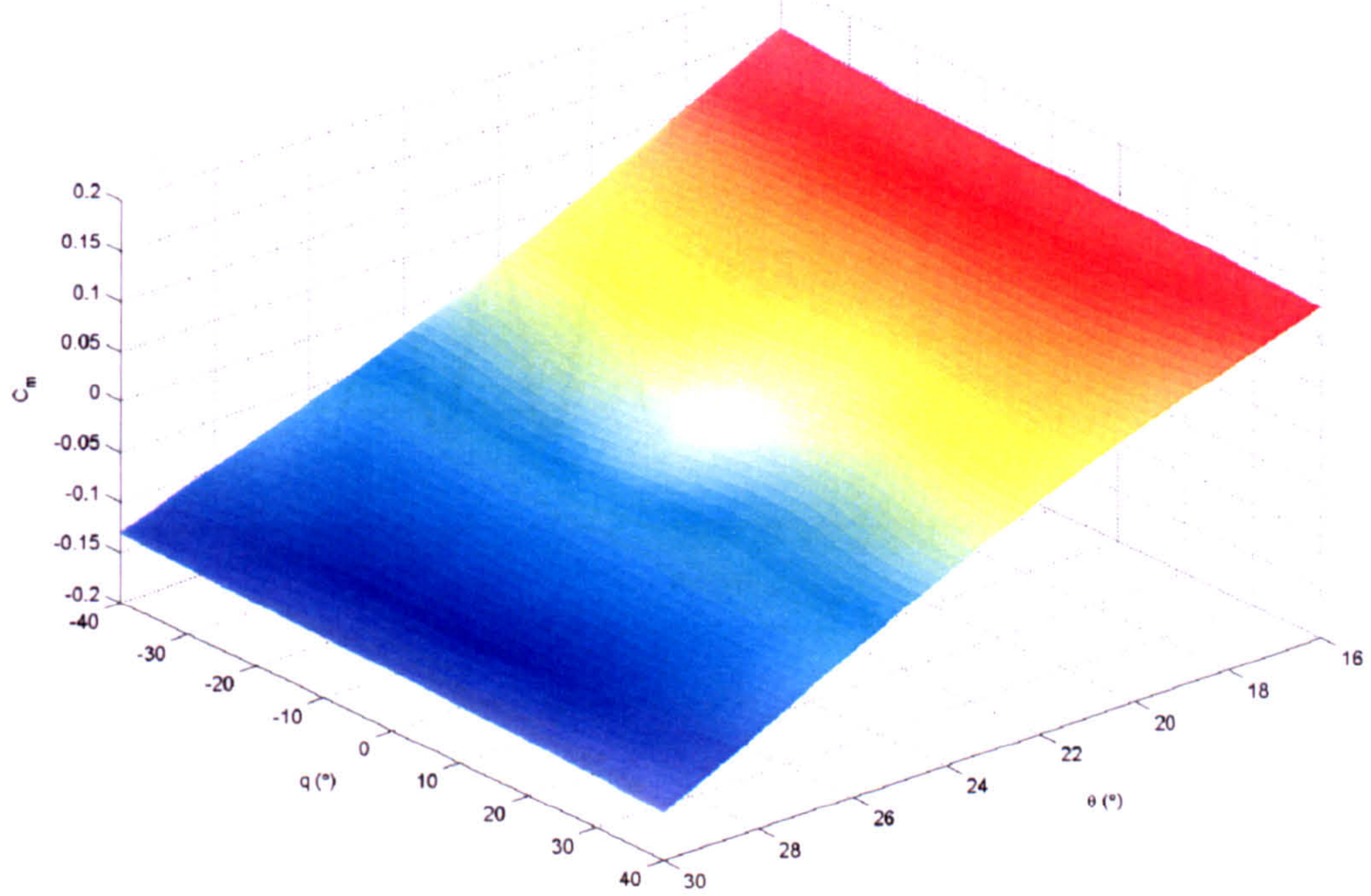


(a) $C_m(\hat{\theta}, \hat{q})$ surface for $\delta_e = -20°$.

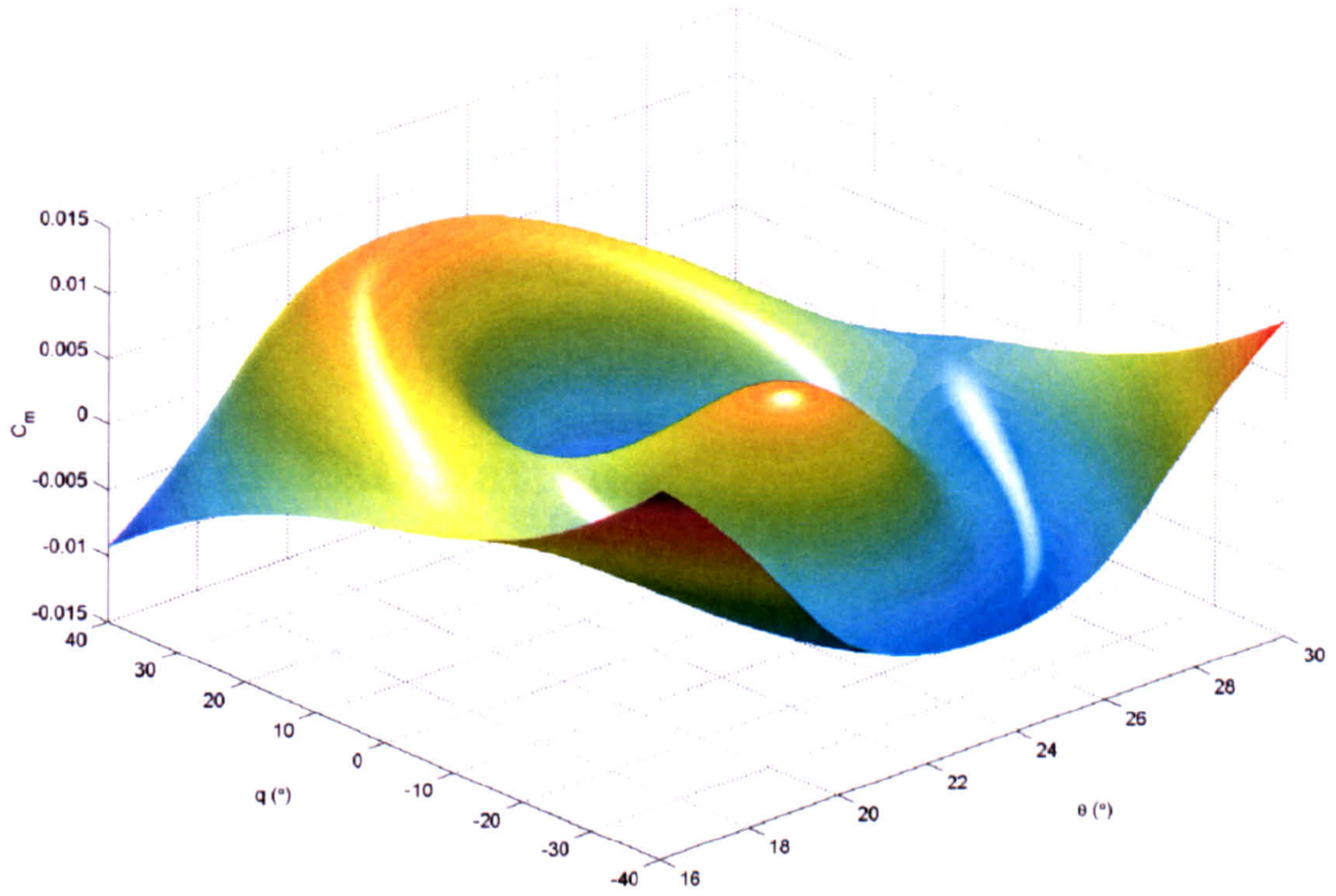


(b) $C_m(\hat{\theta}, \hat{q})$ surface with the average gradient (in $\hat{\theta}$) removed.

Figure 5.5: $C_m(\hat{\theta}, \hat{q})$ surface for $\delta_e = -20°$.

As an example of why direct integration cannot be used, time histories for a second hypothetical system are shown in Figure 5.6, comparing direct integration and the novel method. For both models $A_u = 20$ and $K = 1$. Limit cycle amplitude, $A$, is initially 5 but is changed discontinuously to zero at $t = 5$ s. The direct integration method fails at this point, however, $\tau$ adjusts accordingly and produces the correct decay to a fixed point.

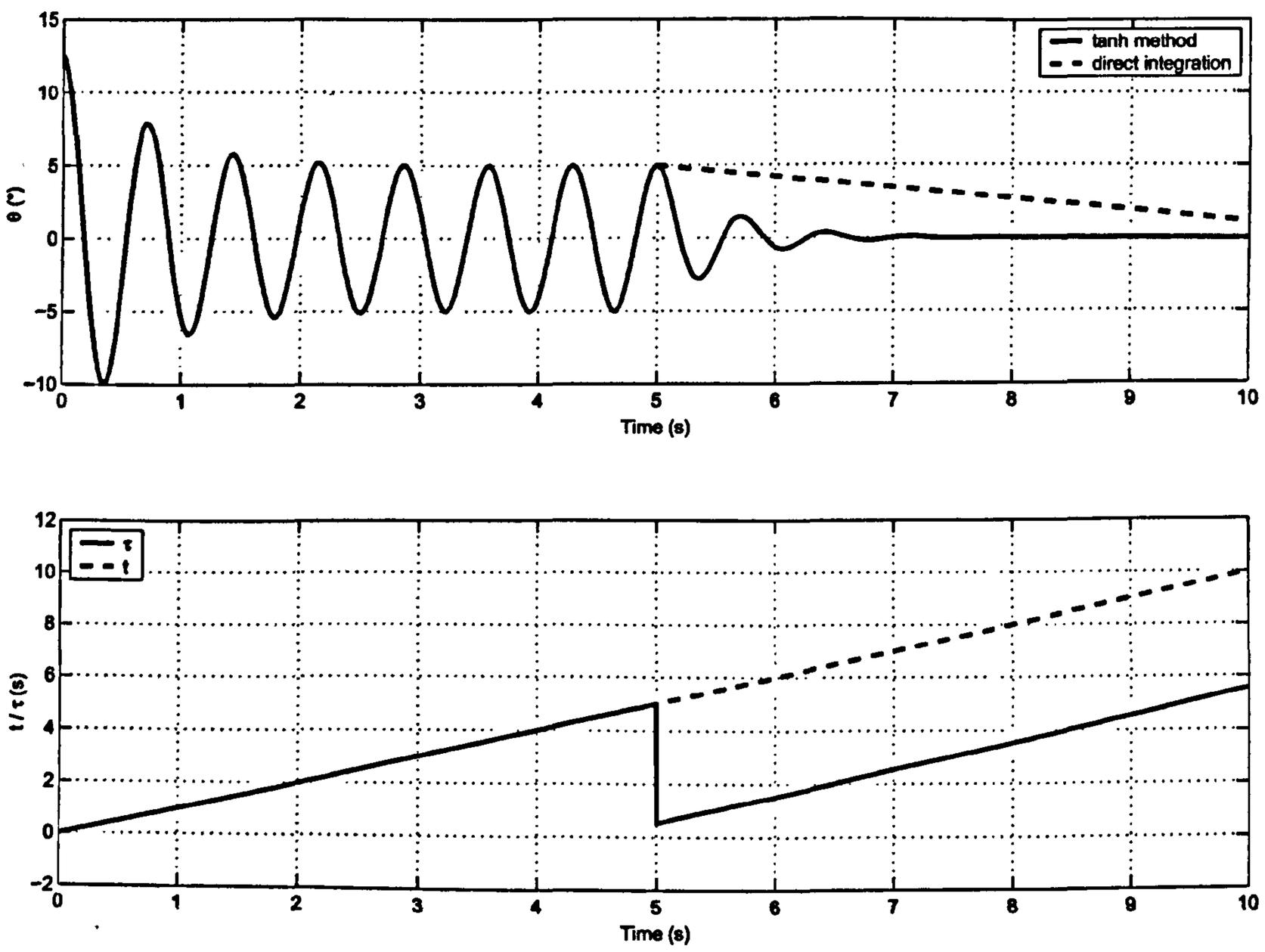


Figure 5.6: Comparison of direct integration and novel strategy.

### 5.2.4 Parameter Estimation

The second stage necessary to complete the derivation of a mathematical model of the experimental system is to find values of all the parameters used in the estimation process.

The parameters we need to find can be broadly grouped into two categories: those that relate to the characteristics of the limit cycle oscillations, $A$ and $\omega$, and those that are related to the shape of the tanh function, $K$ and $A_u$. The estimated parameter values are listed in Table 5.1.

As we are interested in modelling the rig behaviour for different values of the tailplane

deflection, we need to tabulate these parameters as functions of $\delta_e$. For this purpose, we propose to make explicit use of the experimental bifurcation analysis carried out on the rig and presented in Chapter 4.

### Limit Cycle Amplitude ($A$)

From the experimental bifurcation diagram depicted in Figure 4.2, it is possible to extract the bifurcation diagram we want the model to exhibit. This is obtained by finding the trim curve (corresponding to the branch of stable and unstable equilibria in the diagram) and by appropriately fitting the limit cycle amplitudes (found by averaging data readings from Figure 4.2). The result of this process is shown in Figure 5.7.

Non-linear dynamics theory dictates that there must be a branch of unstable equilibria inside the limit cycles as these originate from a Hopf bifurcation point; hence the dashed lines in Figure 5.7. These unstable fixed points cannot be found in the experimental system[2] so, for the sake of simplicity, they were placed in the centre of the limit cycle. In practice, though, the limit cycles are not necessarily symmetrical about the unstable fixed points, as discussed in Chapter 6.

Once the *desired* model bifurcation diagram has been obtained, the amplitudes $A$ of the limit cycles as a function of tailplane deflection can be extracted. Figure 5.8 shows the limit cycle amplitudes as a function of $\delta_e$ (just a different representation of Figure 5.7).

Notice that care must be taken when using this interpolated data to ensure that errors are not introduced at discontinuities. For example, when the stable limit cycle disappears at the cyclic fold ($\delta_e \approx -21°$), its corresponding amplitude must go discontinuously to zero, as the oscillatory behaviour is no longer present. (This causes the jump at $\delta_e \approx -20°$ observed in Fig 5.8.) In the numerical implementation a simple conditional statement is used to overcome this problem.

[2]Theoretically they could be found by trial and error by releasing the model from rest near an unstable equilibrium and observing the response but the level of tunnel turbulence is too high for that to be an option in this case.

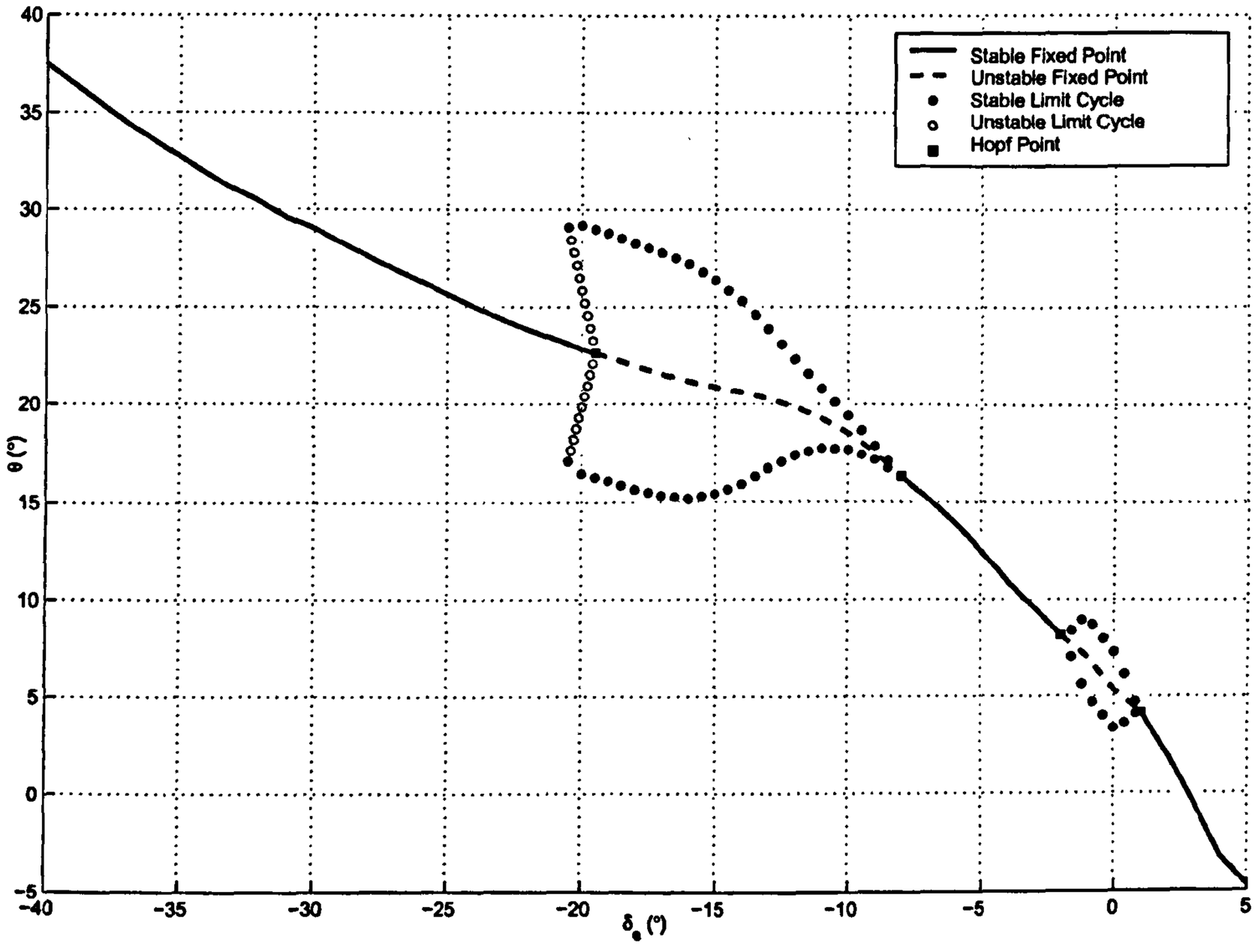


Figure 5.7: Desired bifurcation diagram for the system model.

### Growth/Decay Rate and Frequency ($K$ and $\omega$)

The growth (decay) rates $K$ and the oscillation frequencies as functions of the tailplane deflection were found by recording experimental time histories at different values of $\delta_e$. By comparing experimental results (such as Figure 5.2) with time simulations of the model for different values of $K$ and $\omega$, the best fits for these parameters were found by direct investigation.

By repeating this procedure for several values of the elevator deflections and using linear interpolation the parameters $K$ and $\omega$ were tabulated over the $\delta_e$ range of interest (Table 5.1). It is worth mentioning here that this process could be automated using parameter identification methods but due to the structure of the model this would be complicated and was not seen to be necessary at this stage. Fourier transforming the time series could be used to find the frequency of oscillations, but again was not adopted here.

Table 5.1 shows the tabulated parameters for the model, where $A_i$ represents the amplitude and $S_i$ the stability of the $i^{th}$ limit cycle/fixed point. The number of equilibria varies according to the tailplane deflection, however, there is always a fixed point at

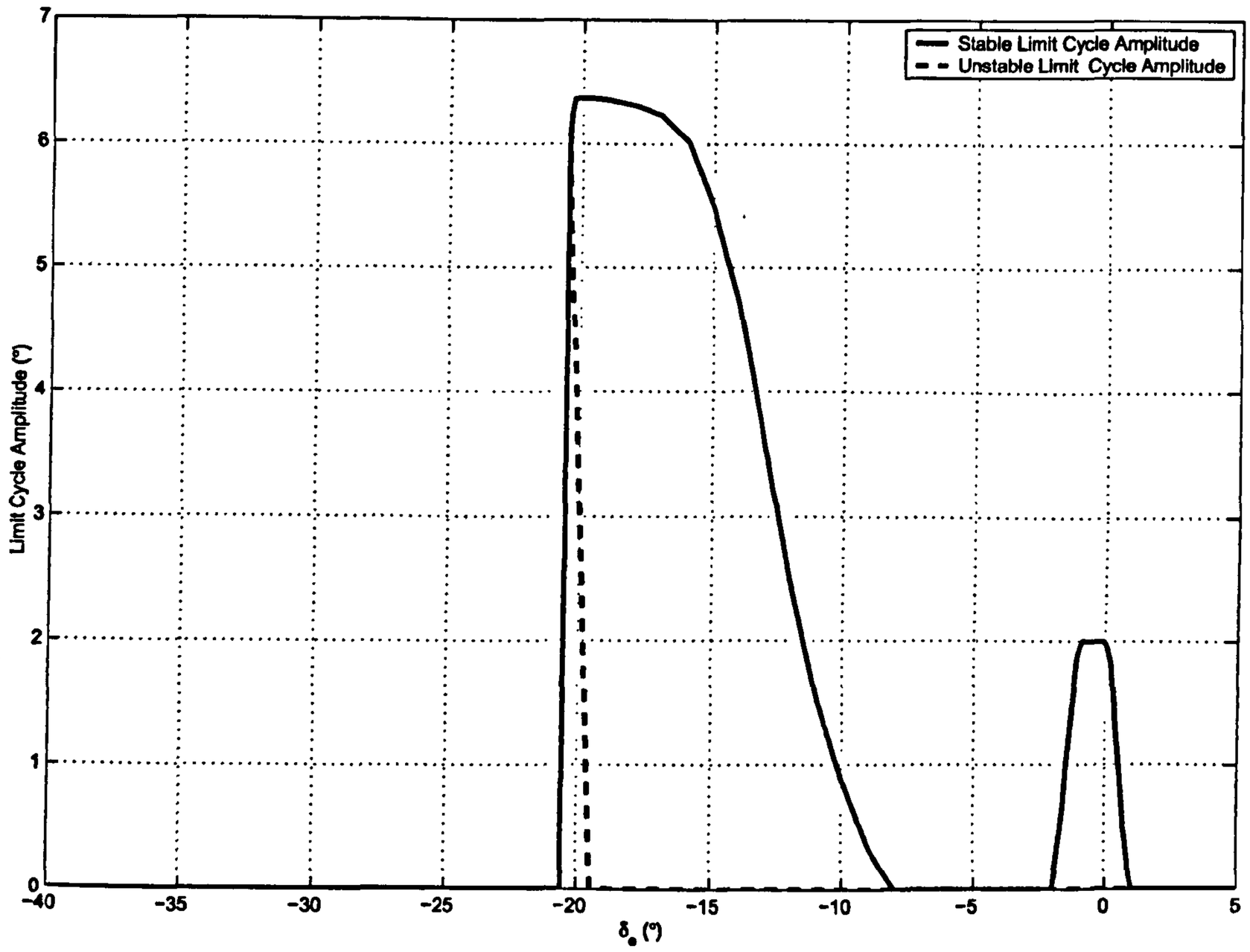


Figure 5.8: Limit cycle amplitudes as functions of tailplane deflection.

the trim angle (amplitude zero, $A_1$ and $S_1$), and an unstable limit cycle with amplitude $A_{max}$ to bound the model. Where there are additional limit cycles their amplitude and stability must also be specified (e.g. $A_2$ and $S_2$). Trim angle and limit cycle amplitudes are tabulated against tailplane deflection every 0.1°, but only 5° intervals are shown in Table 5.1.

### Parameters $A_u$ and $\Delta$

The final step is to find appropriate values for the parameters $A_u$ and $\Delta$ in (5.2). Note that, as shown in Figure 5.3(b), these parameters are related to the amplitude of the limit cycles to which $\hat{\theta}$, as defined by (5.2), tend as $t \to \infty$ and the amplitude of the asymptotic limit cycles (equal to zero in the case of equilibria) exhibited for $t \to \infty$. In particular, $A_u$ is the amplitude of the limit cycle for $t \to -\infty$ and $A_u - 2\Delta$ that of the limit cycle for $t \to \infty$.

Thus, in order for the model to match asymptotically the experimental rig, we need to

Table 5.1: Model parameters (all angles in degrees).

| $\delta_e$ | Trim Angle | $A_1$ | $S_1$ | $A_2$ | $S_2$ | $A_3$ | $S_3$ | $A_4$ | $S_4$ | $\omega$ (rads$^{-1}$) | $K$ |
|---|---|---|---|---|---|---|---|---|---|---|---|
| 0 | 5.3 | 0 | U | 2 | S | $A_{max}$[a] | U | — | — | 5.8 | 0.8 |
| -5 | 12.5 | 0 | S | $A_{max}$ | U | — | — | — | — | 6.2 | 0.5 |
| -10 | 18.5 | 0 | U | 0.9 | S | $A_{max}$ | U | — | — | 7.7 | 0.4 |
| -15 | 20.9 | 0 | U | 5.5 | S | $A_{max}$ | U | — | — | 8.6 | 1.0 |
| -20 | 22.8 | 0 | S | 3.6 | U | 6.4 | S | $A_{max}$ | U | 8.6 | 1.0 |
| -25 | 25.6 | 0 | S | $A_{max}$ | U | — | — | — | — | 8.6 | 1.0 |

[a]This limit cycle is to bound the model. In practice, we choose a value that will encompass all attainable $\theta$.

have:

$$\Delta = \frac{1}{2}(A_u - A). \tag{5.27}$$

where $A$ is the amplitude of the limit cycle for $t \to \infty$. In order to account for whether the envelope is increasing or decreasing, we have to choose $A_u$ at the current time step so that the envelope is increasing if the trajectory, $\hat{\theta}_n$, $\dot{\hat{\theta}}_n$ is inside the target asymptotic limit cycle and decreasing otherwise.

Assuming, for the sake of simplicity, that the limit cycles of interest are approximately circular, it is easy to show that the relative position of a pair of given initial conditions can be checked by using the following criterion:

$$\frac{\hat{\theta}^2}{A^2} + \frac{\dot{\hat{\theta}}^2}{(A\omega)^2} \begin{cases} < 1 & \text{if inside the limit cycle} \\ = 1 & \text{if on the limit cycle} \\ > 1 & \text{if outside the limit cycle} \end{cases}$$

Accordingly, we then set $A_u$ as an arbitrarily large value, $A_u \gg A$, if the current trajectory is outside the limit cycle, while we choose a suitable value $0 \leq A_u < A$ if inside. Note that in the case of a coexisting stable limit cycle and a stable equilibrium (as in the hysteretic region of the bifurcation diagram, see Figure 4.4), $A_u$ should be chosen as close as possible to the amplitude of the unstable limit cycle which, according to a well established result in non-linear dynamics, must exist between the two stable solutions.

Repeating this procedure at each step of the estimation process allows the correct evaluation of all the parameters of interest.

## 5.3 Conclusions

In this chapter, having established that traditional aerodynamic modelling methods do not allow multiple-attractor bifurcationary systems to be modelled easily, a new modelling approach was developed. This method requires assumptions regarding limit cycle orbit shapes and growth/decay functions; in this case that the limit cycle oscillations are sinusoidal, and that the growth and decay from/to equilibria are exponential in nature. Given experimental time histories, although masked by tunnel turbulence, these assumptions seem valid. Having developed a structure for the model, limit cycle amplitudes, frequency and stability are specified as functions of parameters. An analytical solution for the acceleration which gives this motion allows the pitching moment coefficient, $C_m$, to be calculated as a function of $\hat{\theta}$ and $\dot{\hat{\theta}}$.

Using the novel method presented here, the amount of data storage required is greatly reduced from that of a traditional stability derivative model. In the single DOF case with one parameter, a 2D table of derivatives can be replaced by five, 1D tables. The advantage of this method increases as more degrees of freedom or parameters are added.

In the next chapter, we will validate the estimator constructed according to the model structure and parameter evaluation strategy described above for different operating regimes.

# Chapter 6

# Model Validation and Analysis

## 6.1 Model Validation

In Chapter 5, a modelling method suitable for accurately representing the non-linear dynamics exhibited by the wind tunnel rig was derived, and parameters found from a relatively small set of experimental data. In this chapter, the derived model will be analysed and validated against a larger set of wind-tunnel results to assess its accuracy. Experimental and numerical bifurcation diagrams and time histories are compared and the numerical model analysed, before possible extensions and improvements to the modelling method are discussed.

### 6.1.1 Bifurcation Diagram and Time Histories

Having tabulated the system parameters against tailplane deflection it is now possible to use a numerical continuation package to find the bifurcation diagram of the numerical model (AUTO 97 [34] was used in this case).

It was found that, for continuation purposes, it is not essential to have a good fit of the parameter $K$, as the continuation software is only locating equilibria. However, AUTO was extremely sensitive to stepsize (in tailplane deflection, $\delta_e$) along the unstable limit cycle branch (see Figure 6.1): the minimum stepsize had to be made extremely small,

$\approx 1 \times 10^{-9}$ degrees, due to the large gradient of this branch[1].

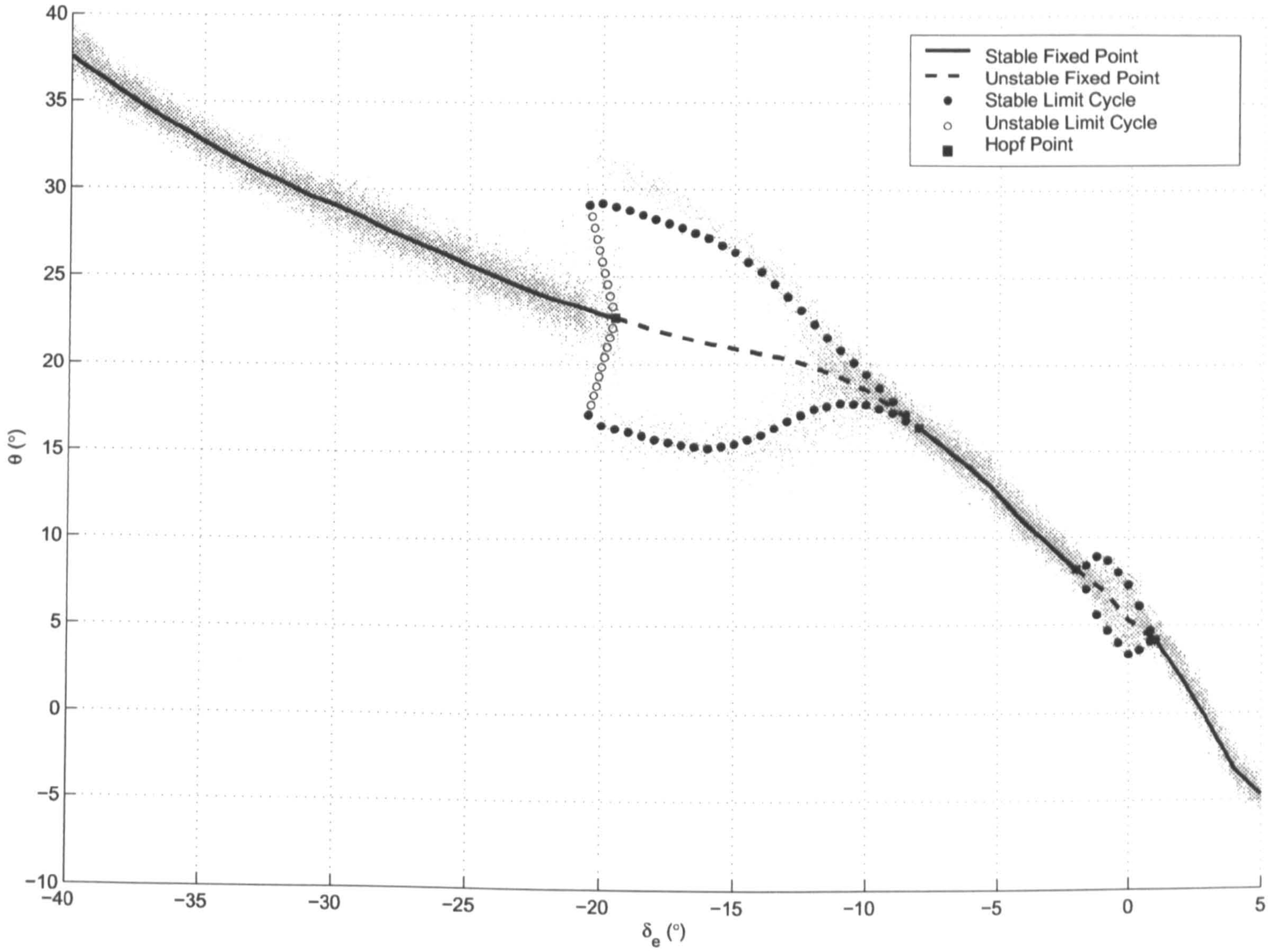


Figure 6.1: Bifurcation diagram produced by AUTO 97 numerical continuation package, with experimental results in grey.

The bifurcation diagram produced by AUTO is shown in Figure 6.1. It can be seen that, as expected, the model and experimental bifurcation diagrams match well; the model bifurcation diagram is actually identical to the specified one shown in Figure 5.7. In particular, the trim curve matches well, the Hopf points are in the correct location, the limit cycle amplitudes are correct and the stability of all the branches are as desired. There is a small discrepancy between the numerical and experimental stable limit cycle amplitudes at $-20° < \delta_e < -15°$; this is possibly due to limit cycle asymmetry and is discussed further in Section 6.2.1. The numerical bifurcation diagram gives a clearer picture of the rig dynamics; unstable equilibria and limit cycles are also shown. The hysteretic behaviour observed in the experimental results can be explained

[1]Typical minimum stepsize for continuation along the other branches was of the order of $1 \times 10^{-3}$.

by the subcritical Hopf at $\delta_e \approx -19.5°$ and the cyclic fold at $\delta_e \approx -20.5°$. The two are joined by a branch of unstable limit cycles which, due to difficulties finding this branch experimentally, was arbitrarily specified to be a straight line connecting the two bifurcation points.

The time histories in Figure 6.2 show good agreement between the experimental results and the numerical model. Note that when the limit cycle amplitudes are small or zero (as in the case of equilibria), for example Figure 6.2 (a),(b) and (c) ($t > 8$s), the effects of low frequency tunnel turbulence causes some discrepancies between the predicted and experimental results. Turbulence is also found to affect the experimental response when large amplitude limit cycle behaviour is present (e.g. Figure 6.2 (d) and (e), $t > 9$s), causing the experimental results to exhibit a slight phase and amplitude mismatch when compared to simulation results. Nevertheless, by tabulating parameters against tailplane deflection the mathematical model adequately represents the experimental system. It is interesting to note that in some of the experimental time histories the oscillation frequency seems to vary with amplitude. This could be modelled by making frequency, $\omega$, a function of both tailplane deflection and limit cycle amplitude. However, there is only a small error caused by this and it has therefore been ignored here.

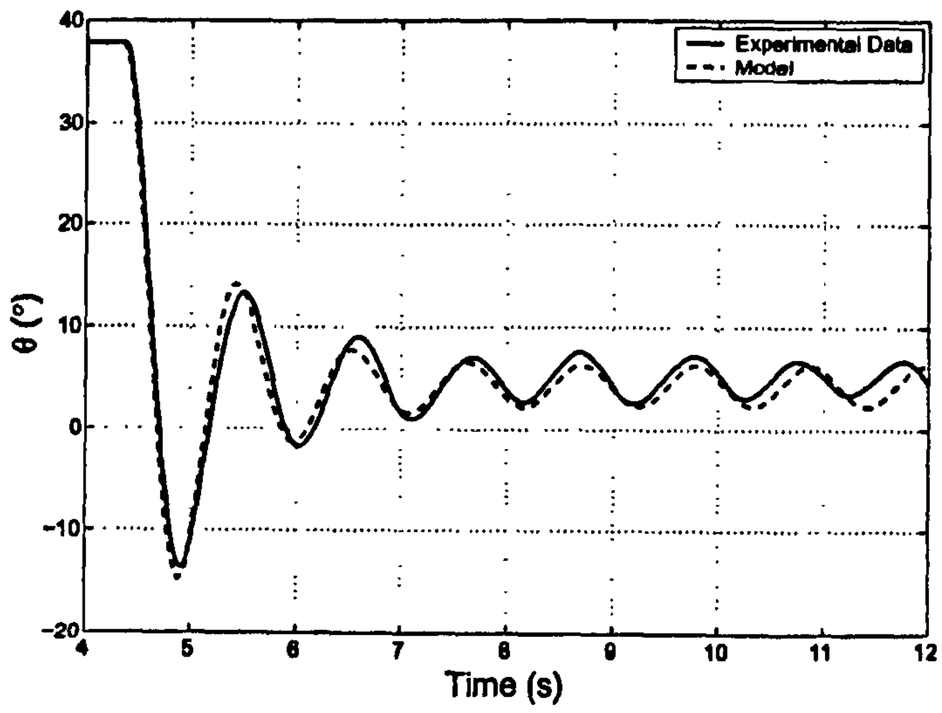


(a) $\delta_e = 0°$, $K = 0.8$, $\omega = 5.8$ rad/s.

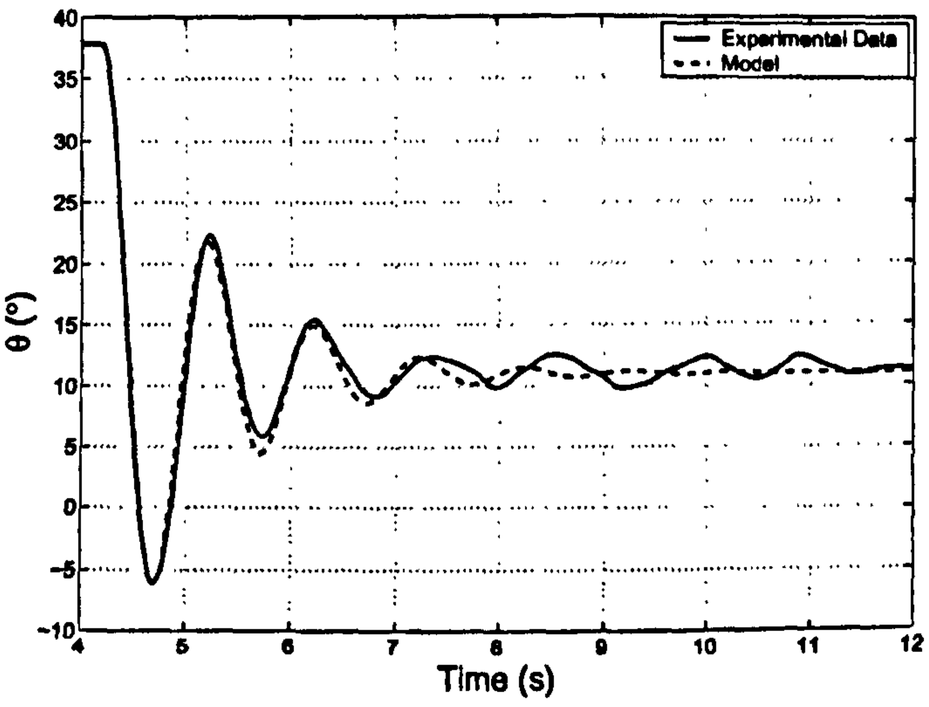


(b) $\delta_e = -5°$, $K = 0.52$, $\omega = 6.2$rad/s.

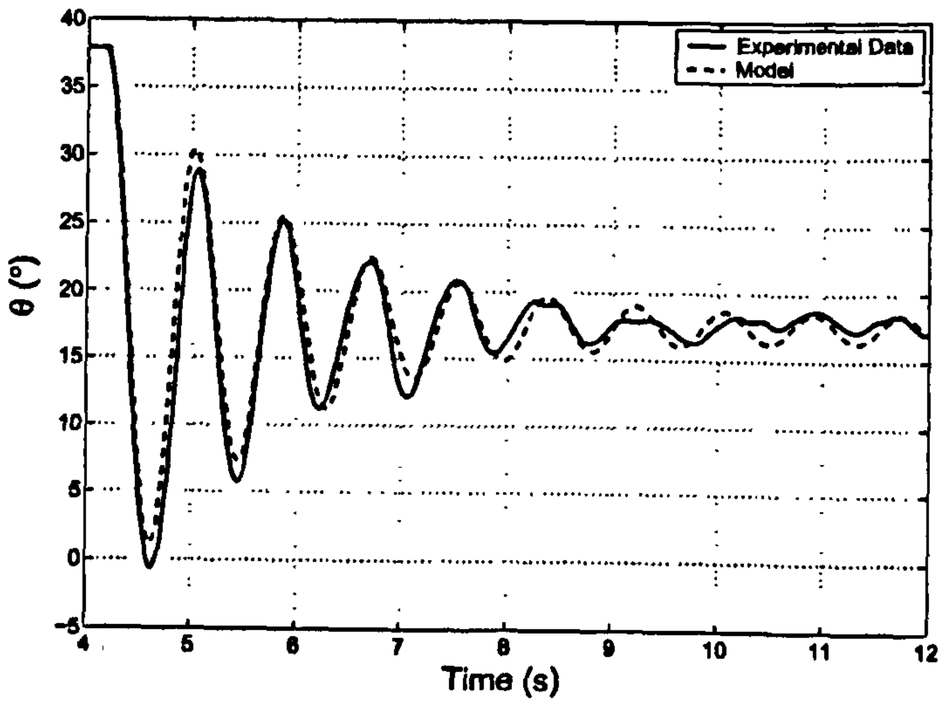


(c) $\delta_e = -10°$, $K = 0.35$, $\omega = 7.7$rad/s.

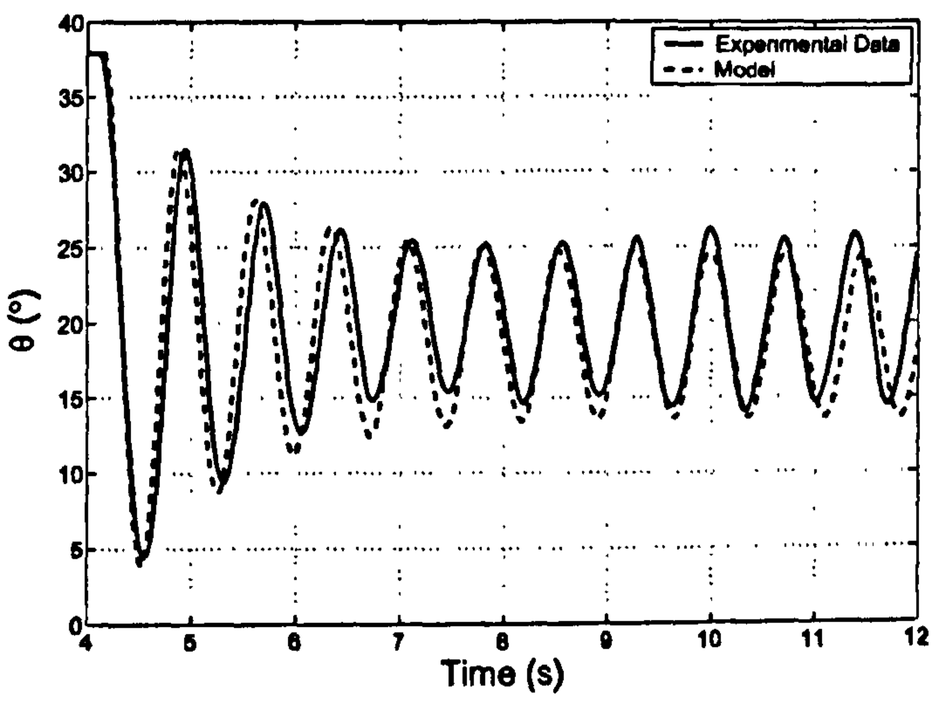


(d) $\delta_e = -15°$, $K = 1$, $\omega = 8.6$rad/s.

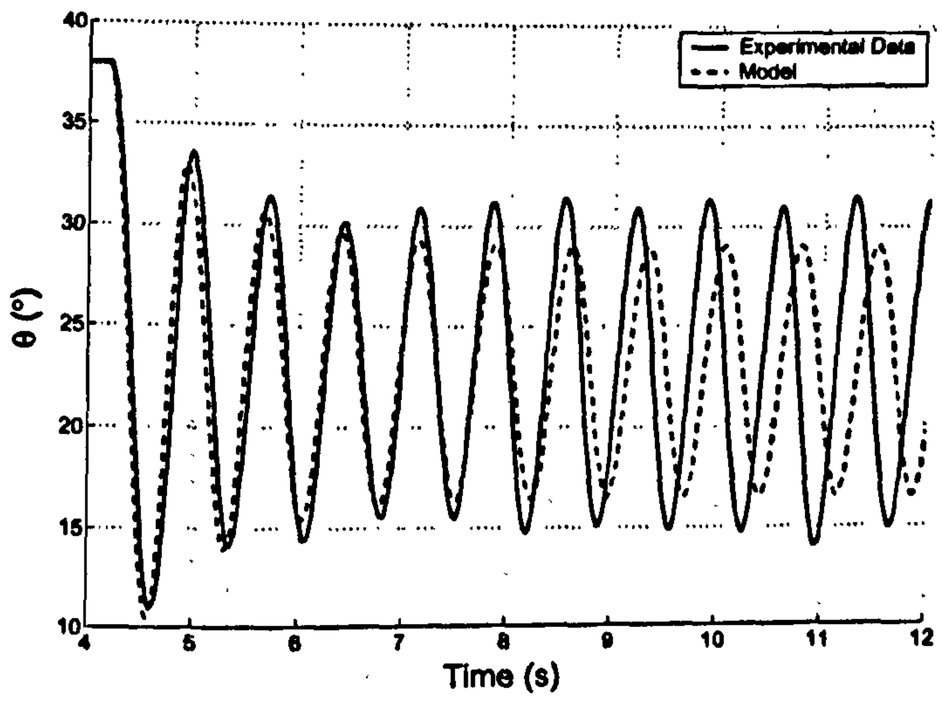


(e) $\delta_e = -20°$, $K = 1$, $\omega = 8.6$rad/s.

Figure 6.2: Comparison of experimental and model time histories at several tailplane deflections. Discrepancies between results are due to large, low frequency tunnel turbulence (see text).

## 6.2 Model Analysis

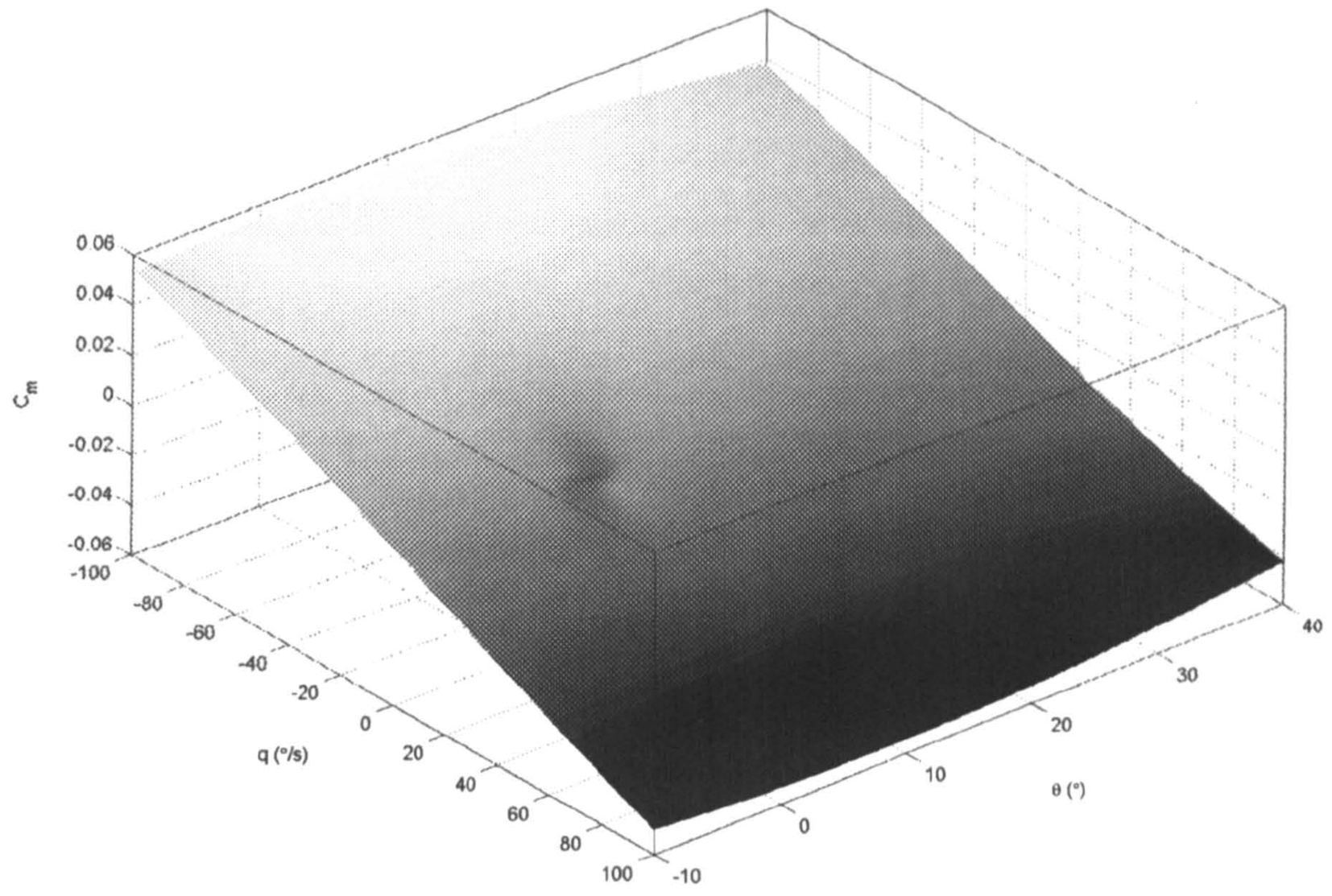


Figure 6.3: $C_m$ surface for $\delta_e = 0°$ with average $\theta$ gradient $(0.6017/°)$ removed.

Although the model can be implemented as a function in the computer code and the pitching acceleration (or moment) calculated analytically, it was found that simulations could be made faster by converting the model to look-up-table format. The model was tabulated over the ranges $\theta = [-20 : 0.2 : 40]$, $q = [-150 : 5 : 150]$ and $\delta_e = [-40 : 0.1 : 5]$ (in degrees and degrees per second). It is useful to look at the structure of the surfaces produced by the model to understand how the limit cycle oscillations develop.

Figures 6.3 to 6.7 show cross-sections through the model at different fixed tailplane deflections from $0°$ to $-30°$, with the average gradients in $\theta$ removed for clarity. Figures 6.4 ($\delta_e = -5°$) and 6.7 ($\delta_e = -30°$) are in regions of the model where no limit cycle oscillations exist, so show a fairly constant variation of $C_m$ with $\theta$ and $q$. Figures 6.3 ($\delta_e = 0°$) and 6.5 ($\delta_e = -15°$) show the pitching moment surfaces when there is a stable limit cycle and unstable fixed point present. There is therefore a single local minimum and corresponding local maximum in the reaction surface around the unstable fixed point (at $\theta \approx 5°$ and $\theta \approx 21°$ respectively), visible more clearly for $\delta_e = -15°$ (Figure 6.5). When both a stable and unstable limit cycle exist simultaneously (Figure 6.6), a second local minimum and maximum is apparent in the surface, corresponding to the addition of another limit cycle.

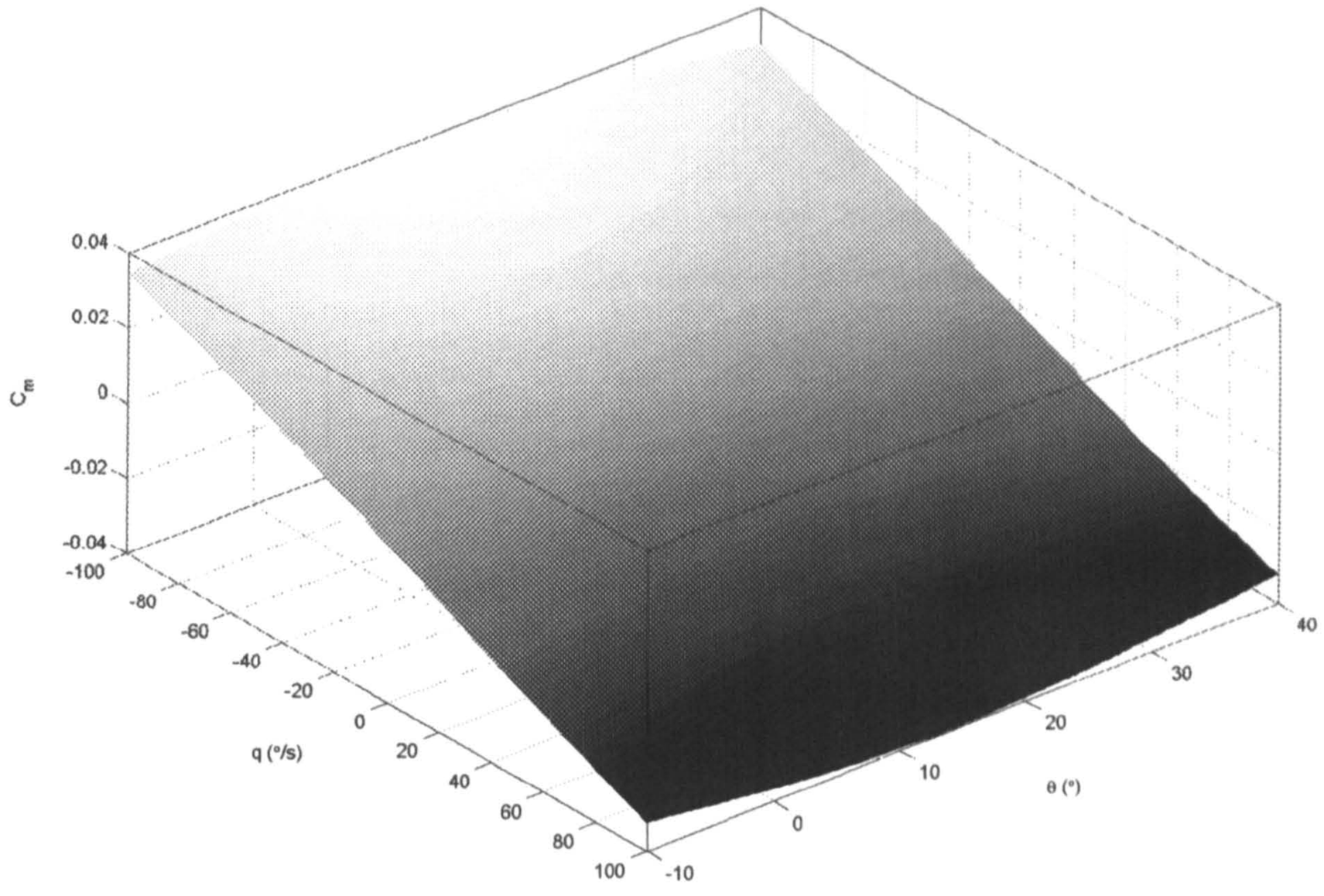


Figure 6.4: $C_m$ surface for $\delta_e = -5°$ with average $\theta$ gradient $(0.6780/°)$ removed.

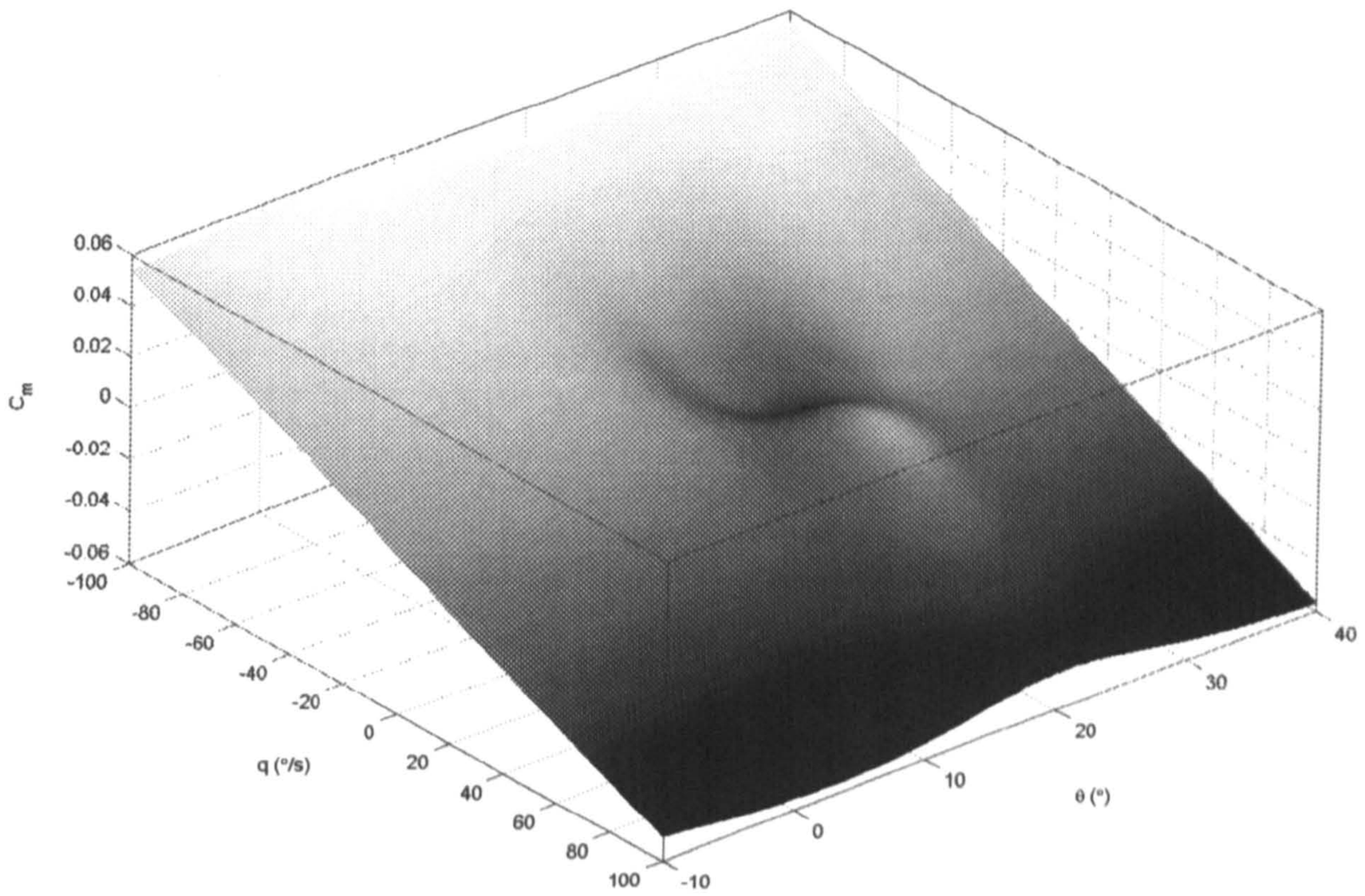


Figure 6.5: $C_m$ surface for $\delta_e = -15°$ with average $\theta$ gradient $(1.3156/°)$ removed.

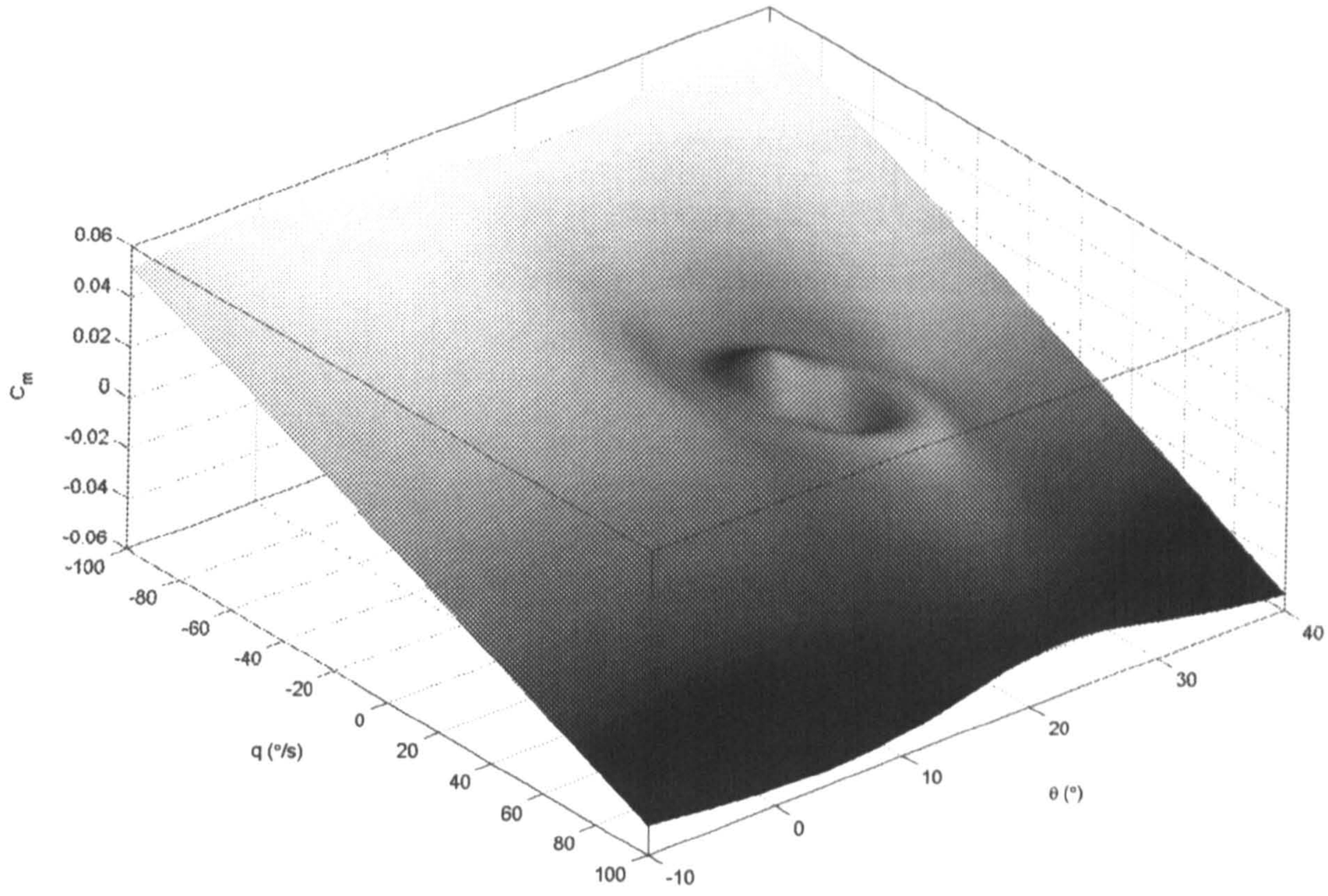


Figure 6.6: $C_m$ surface for $\delta_e = -20°$ with average $\theta$ gradient (1.3142/°) removed.

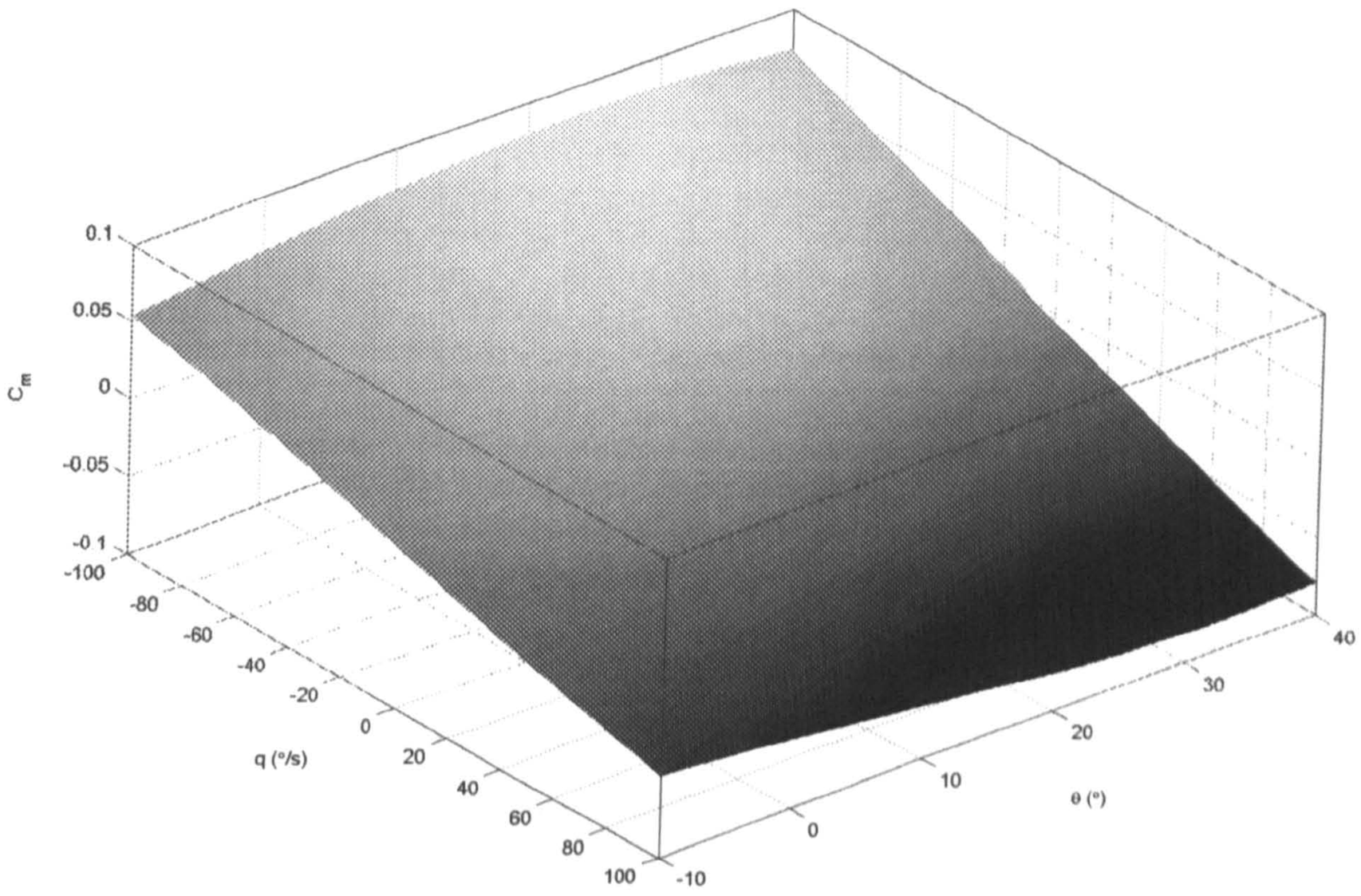


Figure 6.7: $C_m$ surface for $\delta_e = -30°$ with average $\theta$ gradient (1.3183/°) removed.

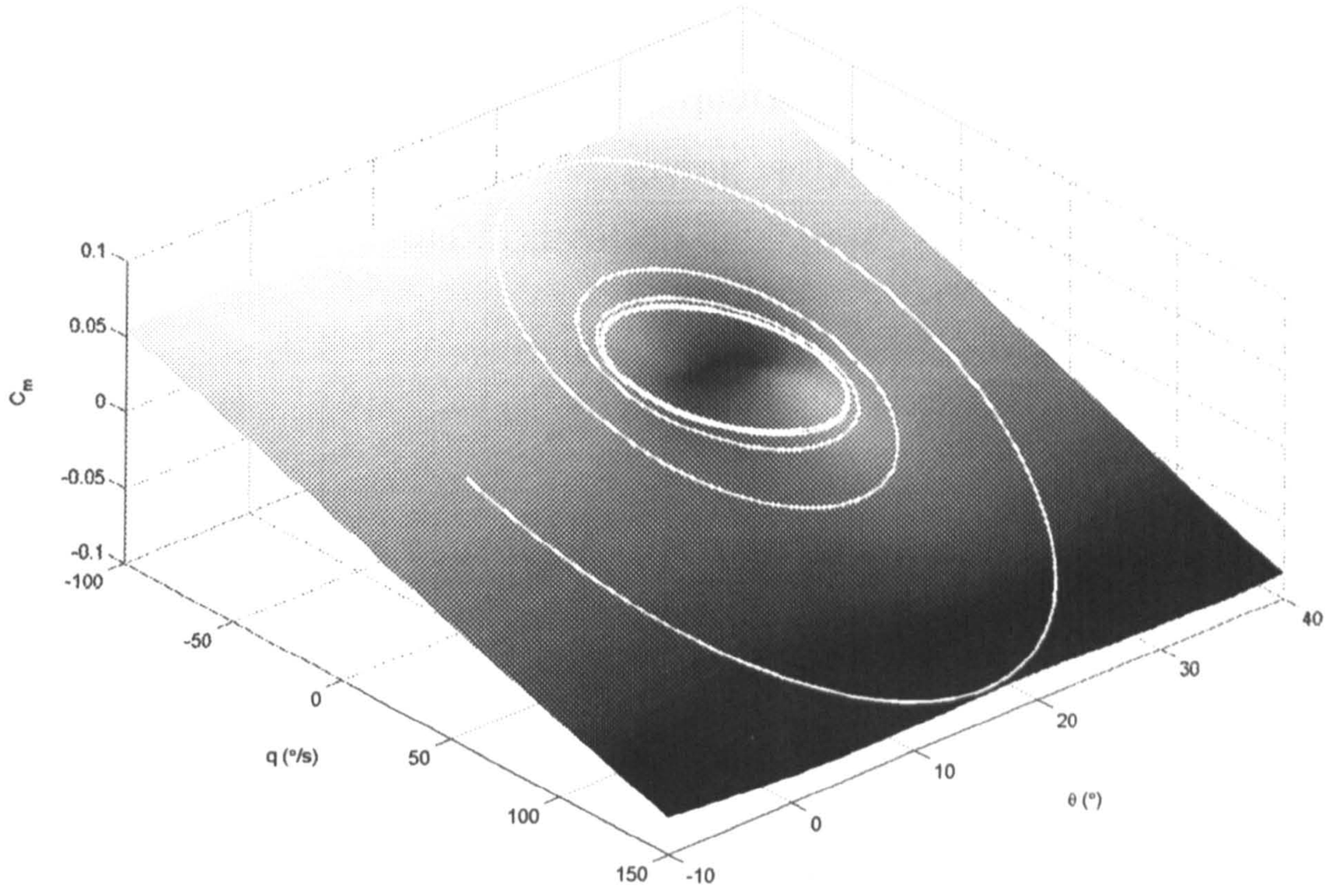


Figure 6.8: $C_m$ surface for $\delta_e = -15°$ with superimposed time history starting from $(\theta, q) = (0, 0)$.

Figure 6.8 shows the reaction surface from Figure 6.5 (where there is a single stable limit cycle present) with a time simulation superimposed in white. The simulation begins at the point $(\theta, q) = (0, 0)$ with the tailplane fixed at $\delta_e = -15°$ and spirals in until it reaches the limit cycle.

### 6.2.1 Discussion

#### Limit Cycle Asymmetry

A relatively large error (approximately 3° at its maximum) can be seen in Figure 6.1 between the maximum $\theta$ of the large limit cycle ($-20° < \delta_e < -15°$) for the experimental system and the model. This is possibly due to the limit cycle being asymmetric but, as mentioned previously, it is not possible to find the unstable fixed points in free-oscillation tests so this cannot be validated. However, the unstable branches could be found from static tests, or by increasing pitch damping via mechanical (e.g. an oil-filled damper at the gimbal) or aerodynamic (e.g. canards with $q$ feedback) means.

It is also possible for the model to accommodate an asymmetric limit cycle by adding an offset multiplied by a tanh function to equation (5.2). The offset value could then be tabulated against tailplane deflection, giving variable asymmetry and a closer match between model and experimental bifurcation diagrams.

### Limit Cycle Shape

Often, limit cycle oscillations cannot be approximated adequately by a pure sine wave. It is therefore useful to be able to model limit cycles of arbitrary shape. By summing the output of several models produced using the technique presented here (with different frequencies and amplitudes) it is possible in theory to produce any shape of limit cycle. An experimental time history of a limit cycle oscillation of arbitrary shape can therefore be Fourier transformed and the dominant sin/cos components used in the model. In this way it is also possible to model limit cycles with periods greater than 1, and to model the associated period-doubling bifurcations.

### Generalisation of the Model

It is also possible to model types of bifurcations other than Hopf points using the method presented here. By using limit cycle amplitudes of zero, systems with fold and pitchfork bifurcations can be created, where decay onto the stable fixed points is exponential in nature. The problem becomes one of tabulating the data for the bifurcation diagram branches and ensuring that the model is correct when discontinuities in the data are necessary (e.g. at a fold point). Other types of decay/growth other than exponential are also possible in theory, however in the majority of cases it is adequate to assume an exponential form.

The type of model presented here, derived from measured motion variables, can in principle be extended to more degrees of freedom. For coupled motions, however, the model would become more difficult to visualise as aerodynamic coefficients would be functions of several state variables.

## 6.3 Conclusions

In this Chapter, comparison of the experimental and model bifurcation diagrams have been presented and show good agreement. Both supercritical and subcritical Hopf points have been created in the correct location, and limit cycle amplitudes correspond well. Numerical simulations have been compared with experimental time histories, and also serve to validate the model. The extension and generalisation of the model are discussed.

Having constructed and validated the model, it is now possible to proceed with development, testing and comparison of control laws which can be used to 'tailor' the bifurcation diagram.

# Chapter 7

# Feedback Control of the Single Degree-of-Freedom Rig

There have been relatively few attempts to design control laws for highly-manoeuvrable aircraft using actively controlled models 'flying' in multiple degrees of freedom in wind tunnels. A single degree-of-freedom (DOF) rig (pitch only) with actuated control surfaces was used at the National Aerospace Laboratories in India to model time-dependent effects on highly swept delta wings [97]. A 2 DOF rig (roll and yaw) using active control surfaces augmented with compressed-air blowing was developed at Cambridge University and successfully used to develop lateral-directional controllers for the HHIRM model using $H_\infty$ methods [45]. A three degree-of-freedom rig is used in [101] to test and evaluate adaptive and fault tolerant controllers on a generic canard-delta model. In [102] a 4 DOF rig was used to develop gust alleviation controllers for a small, high-wing turboprop aircraft. The model was free to roll, pitch and yaw about a central gimbal within the model, and could slide up and down a vertical wire mounted in the tunnel. Torque-motors were used to actuate elevators, ailerons, and trailing edge flaps. A similar 4 DOF rig was developed at Cranfield Institute of Technology [103] to extract aerodynamic models, develop control systems and perform wind tunnel simulations of dynamic motions.

A full 6 DOF free-flight rig was developed by NASA for the 30' by 60' Langley full-scale tunnel (e.g. [88]). The model to be tested was free to fly within the tunnel working section, with electrical power, compressed air (for propulsion) and control and feedback signals being fed from the top of the tunnel via a slack umbilical chord. Controllers were

implemented using computers outside the tunnel, with three 'pilots' providing control inputs and handling quality feedback. The cost of this type of rig is prohibitive in most cases due to the size of the wind tunnel required, complexity of the model and number of operators needed.

In this chapter, classical pitch angle controllers are designed and tested on the single degree-of-freedom wind tunnel rig at the University of Bristol. The controller gains are tuned using a combination of numerical simulations and heuristic methods on the experimental rig. The controllers are tested using numerical simulations of the mathematical model and validated experimentally to examine the suitability of the model for control system design.

## 7.1 Control Objective

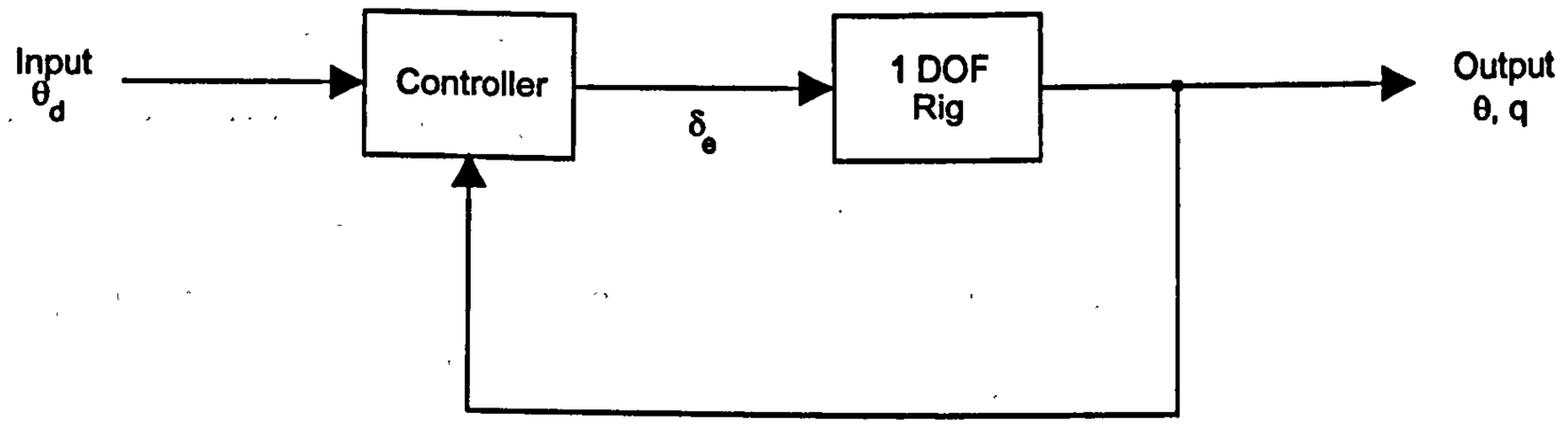


Figure 7.1: High-level block diagram of control system layout.

Before control systems can be designed and evaluated it is necessary to define the control objective. Due to the limited travel of the model in the tunnel ($\approx \pm 50°$ in pitch) it is not feasible to design a pure pitch rate controller (as the model would quickly hit the endstops before the controller could be evaluated). A $\theta$ demand loop must therefore be placed around any controller designed to give a demanded pitch rate. Thus, the input to the overall system becomes pitch angle demand, $\theta_d$, with the outputs pitch angle, $\theta$, and pitch rate, $q$ (Figure 7.1). This will be the basic structure of all controllers designed here.

Suppression of the limit cycles exhibited by the rig (particularly the large amplitude oscillations) is a fundamental design goal of the controllers presented in this thesis. Hence, we would like the branch of equilibria in the experimental bifurcation diagram

(Figure 4.2) to be stable over the entire range of tailplane deflections, and the Hopf bifurcations to be removed. Additionally, the following criteria will be used as design goals and measures by which the controllers can be evaluated:

1. **Steady state error** - for tracking purposes it is desirable that pitch angle, $\theta$, displays zero steady state error with respect to the reference input, $\theta_d$.

2. **Transient response** - in terms of frequency and damping ratio of an equivalent linear system.

To define a desirable transient response it is useful to look at handling qualities requirements for full-scale piloted aircraft. Traditionally, longitudinal requirements are split into Short Period and Phugoid responses. In the case of the Hawk model in single DOF, neither of these is strictly applicable, however the Short Period requirements will be of most use (Short Period motion is related to pitch angle and vertical translation). In [56, 57, 58], the Short Period requirements are given in terms of acceptable damping ratio, $\zeta_{SP}$, and undamped natural frequency, $(\omega_n)_{SP}$, for a response in pitch rate to elevator input. These requirements are also discussed in [18, 66, 123]. No requirements are given for pitch angle response specifically, however, it will be assumed that the pitch rate criteria can be transferred to pitch angle response[1]. Acceptable $\zeta_{SP}$ and $(\omega_n)_{SP}$ for level 1 handling qualities[2] during category A flight phases[3] (the most demanding) for a class IV aircraft[4] are given in Table 7.1.

The requirements are tightened further in [56] by a plot of pilot opinion contours, and the statement that 'for combat aircraft and light aircraft a Short Period damping and frequency of $\zeta_{SP} = 0.6$ and $(\omega_n)_{SP} = 3.0$ rad/s is a good optimum for all general tasks'. These recommended values will be used as a control objective by which to design and evaluate controllers for the Hawk. They must, however, be suitably scaled before being directly applied to the model. Using a standard scale factor for angular rates of $N^{-0.5}$, where $N$ is the model linear scale factor, gives the response requirements outlined in

[1]This assumption is supported in [124], where time histories and Bode diagrams are shown for pitch angle response to elevator input with various damping ratios. Also, when considering linear flight dynamics, the poles of the $\theta/\eta$ and $q/\eta$ transfer functions are identical.

[2]Defined as 'Task achieved without excessive pilot workload'.

[3]'Rapid manoeuvring, precision tracking or precise flight path control'.

[4]'High manoeuvrability aircraft'.

Table 7.1: Acceptable $\zeta_{SP}$ and $(\omega_n)_{SP}$ for level 1 handling qualities during category A flight phases for class IV aircraft.

| | Minimum | Maximum |
|---|---|---|
| $\zeta_{SP}$ | 0.35 | 1.3 |
| $(\omega_n)_{SP}$ (rad/s) | 2.4 | 3.7 |

Table 7.2. The requirements have also been converted to closed-loop pole locations and time response criteria, shown in Table 7.2. Pole location and time simulation for the ideal response are shown in Figures 7.2 and 7.3 respectively. Also shown in Figure 7.2 are regions of level 1 and level 2 handling qualities to allow evaluation of control system which do not achieve the desired pole locations. The output of this second order ideal system will be used in the following chapters to assess controller response, and also as a reference/desired model for the adaptive and eigenstructure-assigned control schemes.

Table 7.2: Response requirements for the closed-loop Hawk model.

| | |
|---|---|
| Scale factor | $\frac{1}{16}^{-0.5} = 4$ |
| $\zeta_{SP}$ | 0.6 |
| $(\omega_n)_{SP}$ | 12 rad/s |
| Pole locations | $-7.2 \pm 9.6i$ |
| Peak overshoot | 9.47% |
| Rise time (to 100%) | 0.23s |
| Settling time (to within 2%) | 0.5s |

Frequency response criteria are also used when designing aircraft, and there are equivalent handling qualities criteria in the frequency domain (mainly for bandwidth investigation and PIO prevention [58]). However, frequency response criteria were not used in this thesis, mainly because the aim is to compare controllers and controller methodologies, rather than design a single specific control law for the rig.

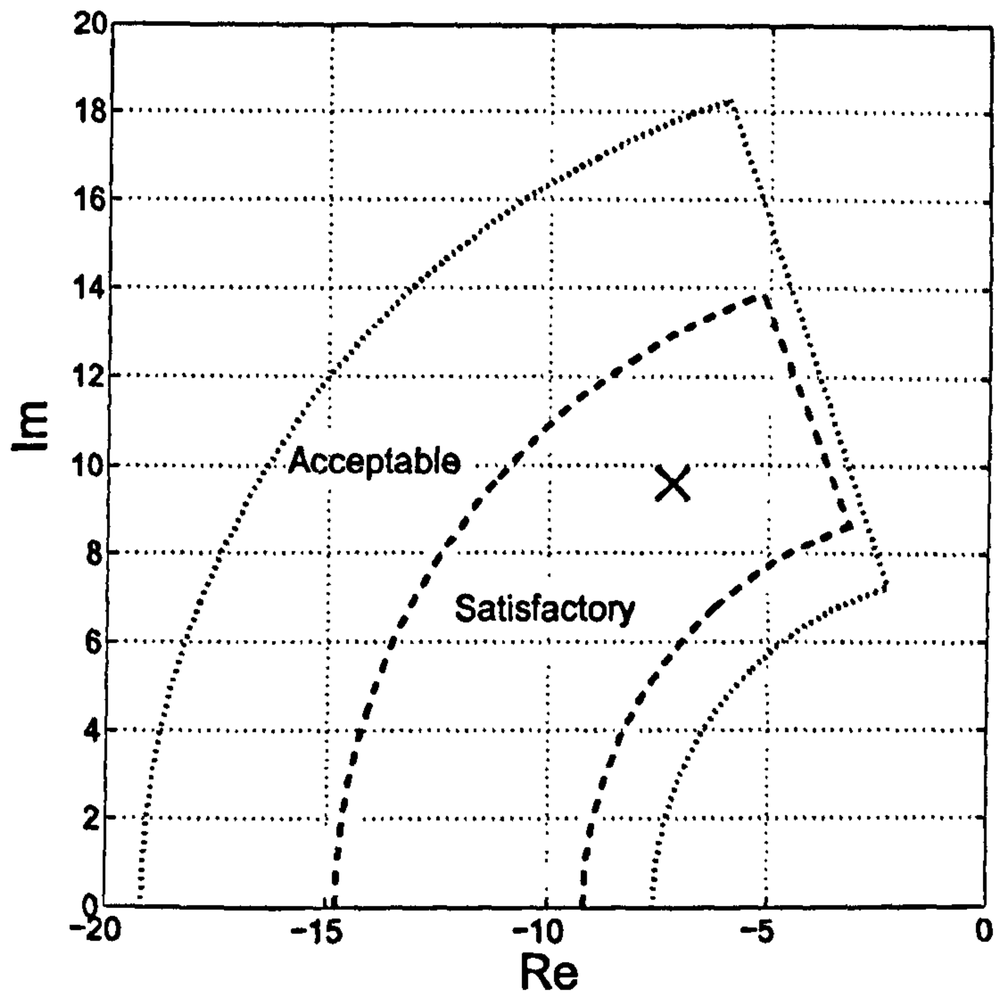


Figure 7.2: Ideal pole location and regions of level 1 (satisfactory) and level 2 (acceptable) handling qualities.

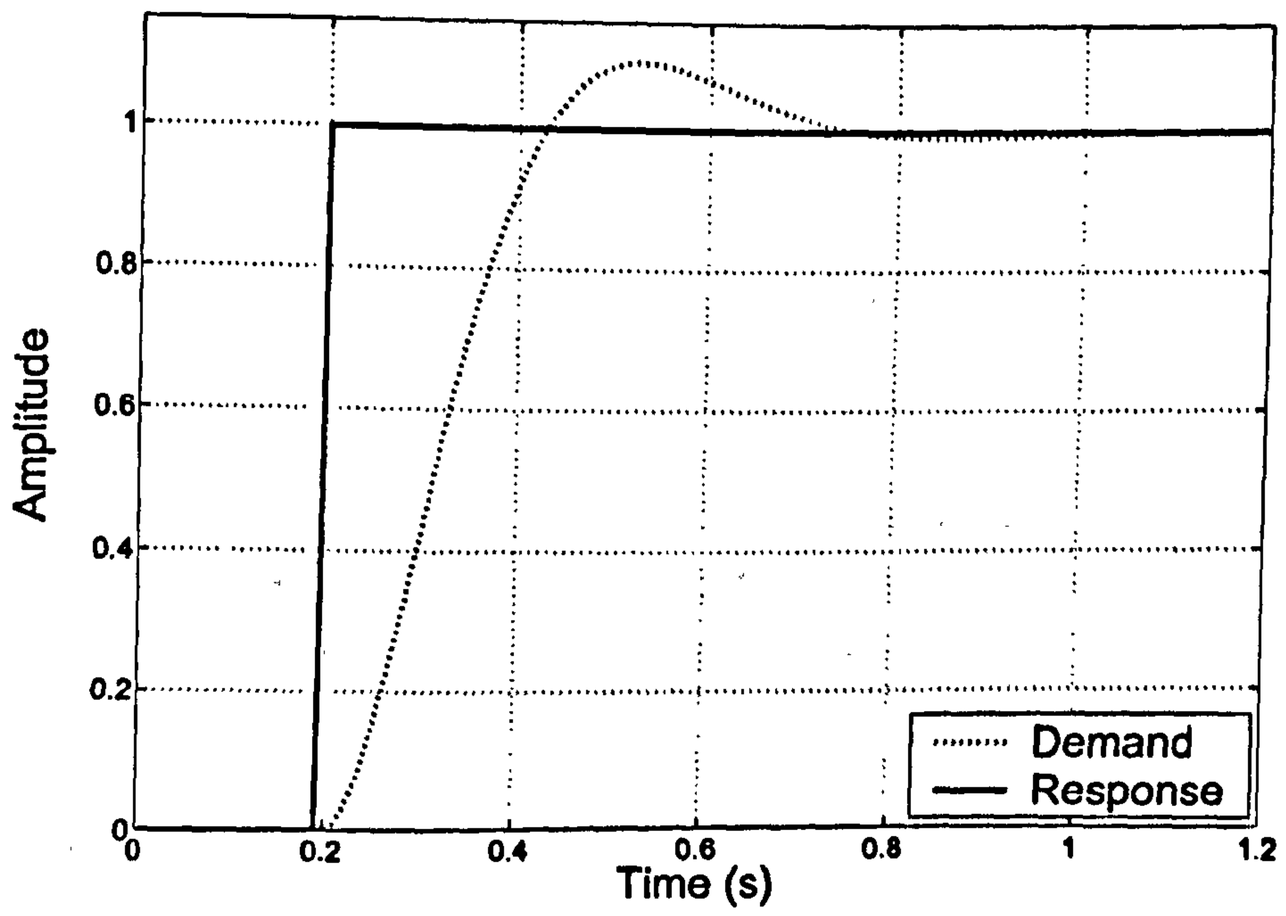


Figure 7.3: Time response for a system with the ideal pole location shown in Figure 7.2.

## 7.2 Control System Design

### 7.2.1 Open-Loop $\theta$ Demand with Pitch Rate Compensator

As a starting point, an open-loop controller was considered consisting of just a proportional feed-forward gain, $K_{ff}$. The reference signal is the demand on the pitch angle, $\theta$, which is simply multiplied by the constant feed-forward gain to produce the control input, $u$, corresponding to the tailplane deflection demand, $\delta_e$. Figure 7.4 shows the simulated and experimental response of the state variables $\theta$ and $q$ under the action of the open-loop controller ($0 < t < 30$, $K_{ff} = -0.75$). Note the good agreement between

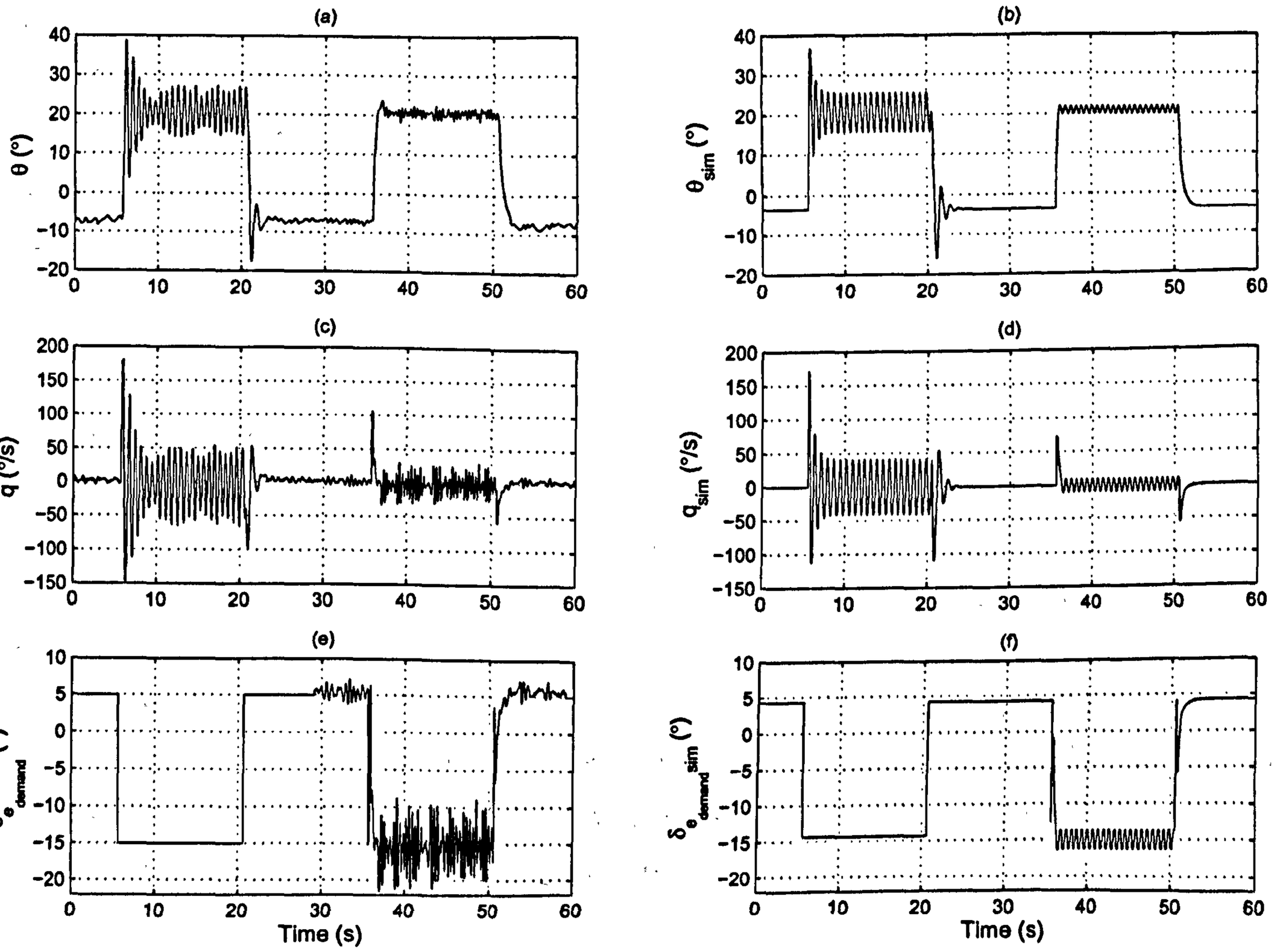


Figure 7.4: Experimental evolution (a),(c),(e) and numerical simulations (b),(d),(f) of the system response to a step reference input with an open-loop feed-forward controller with ($t > 30$s) and without ($t < 30$s) the pitch rate $q$ feedback compensation. Here $K_{ff}$= - 0.75, $K_q = 0.2$.

the control performance predicted by the numerical simulations (Figure 7.4(b)-(d)-(f)) and the actual experimental results (Figure 7.4(a)-(c)-(e)).

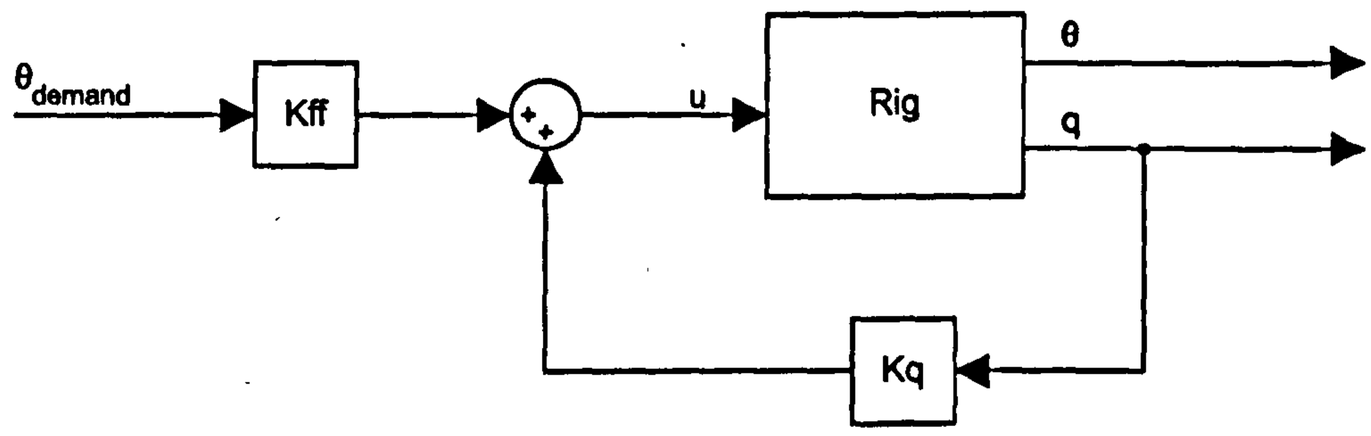


Figure 7.5: Open-loop pitch angle controller with pitch rate compensator.

The fixed feed-forward gain value was chosen to give good correlation between the reference and output for the step responses in Figure 7.4, however, when a reference signal of a different amplitude is used the tracking response is significantly worse given the open-loop nature of the controller and the fact that the rig is a highly non-linear system. Moreover, the open-loop response shown in Figure 7.4 for $t < 30s$ also confirms the presence of highly oscillatory modes at high angles-of-attack. Therefore, pitch damping was increased by adding proportional fixed-gain pitch rate feedback as shown in Figure 7.5.

The resulting performance of the open-loop feed-forward control in the presence of the feedback pitch rate compensator is shown in Figure 7.4 for $t > 30s$. A feedback gain of $K_q = 0.2$ was found to limit RMS amplitude in the limit cycle regions without introducing self-excited oscillations. In fact, a consistent reduction of the oscillatory modes is observed, which reduces the amplitude of the high-$\alpha$ limit cycle from approximately 5° to 1°. As can be seen from Figure 7.4(b)-(d)-(f), again the mathematical model shows good qualitative agreement with the experimental results but for a slight discrepancy in absolute values. A possible reason for this is sensitivity of the rig to centre of gravity location of the model, causing a fixed offset in $\theta$.

### 7.2.2 Non-linear Feed-Forward with Pitch Rate Feedback

To improve the performance of the controller presented in the previous section, the fixed-gain forward path is replaced with a non-linear inverse trim curve derived from the rig model in order to have an improved correlation between the reference input (pitch angle

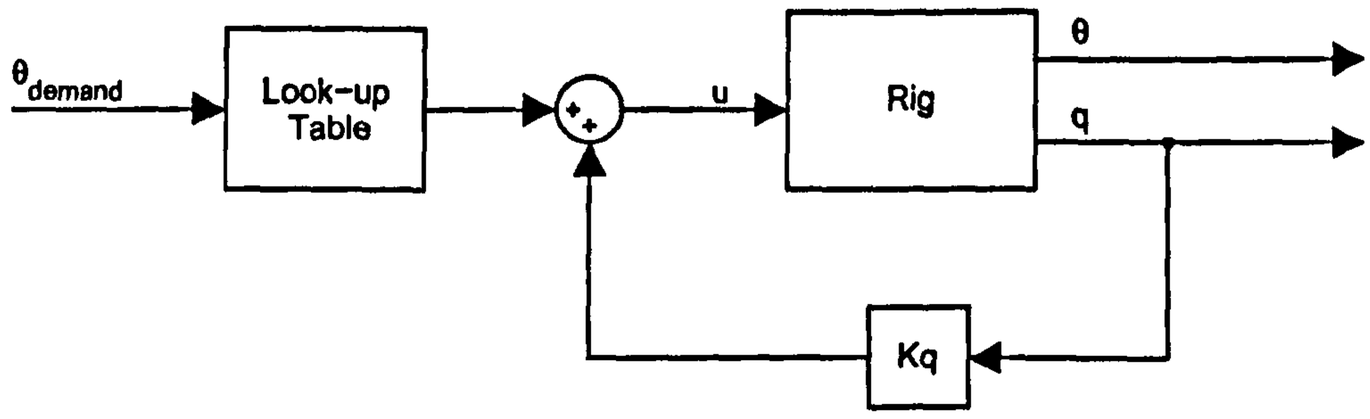


Figure 7.6: Non-linear inverse trim curve feed-forward with pitch rate compensator.

demand) and the state being controlled (pitch angle). The look-up table gives tailplane deflection as a function of pitch angle and was calculated by inverting the trim curve derived from the experimental bifurcation diagram shown in Figure 4.2.

The resulting control scheme is shown in Figure 7.6. Experimental time histories of the controlled rig to sinusoidal and step reference inputs are depicted in Figure 7.7. In both cases, note the presence of a non-zero steady-state error in the system response. This is to be expected because of the mainly open-loop nature of the control on $\theta$. In order to eliminate this unwanted residual error, the synthesis of an appropriate feedback loop on $\theta$ is now investigated.

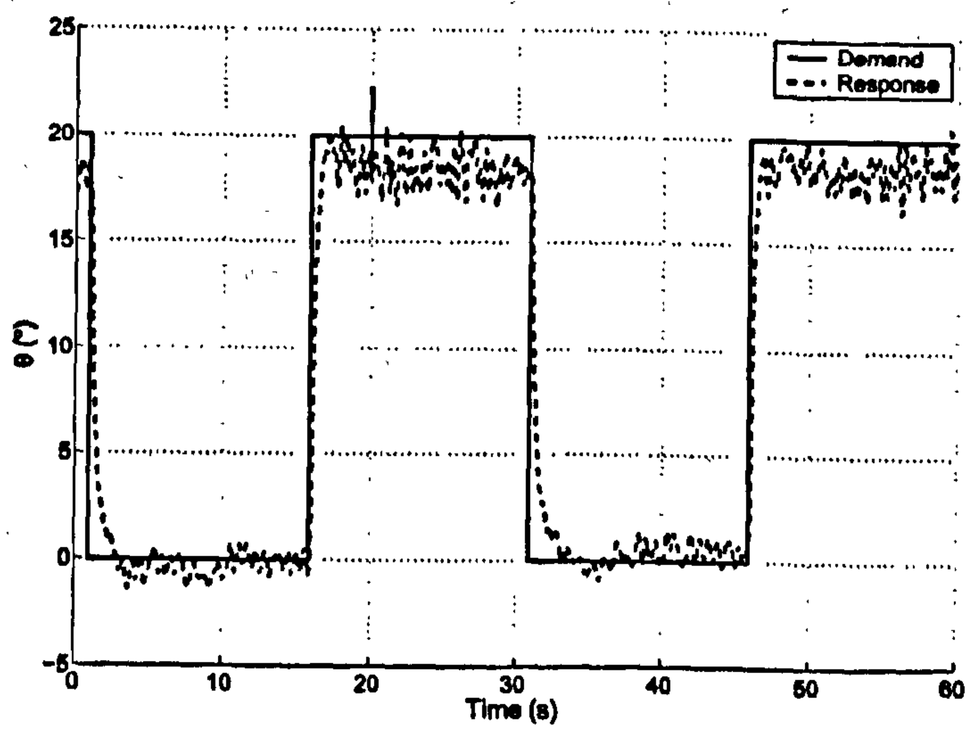


(a)

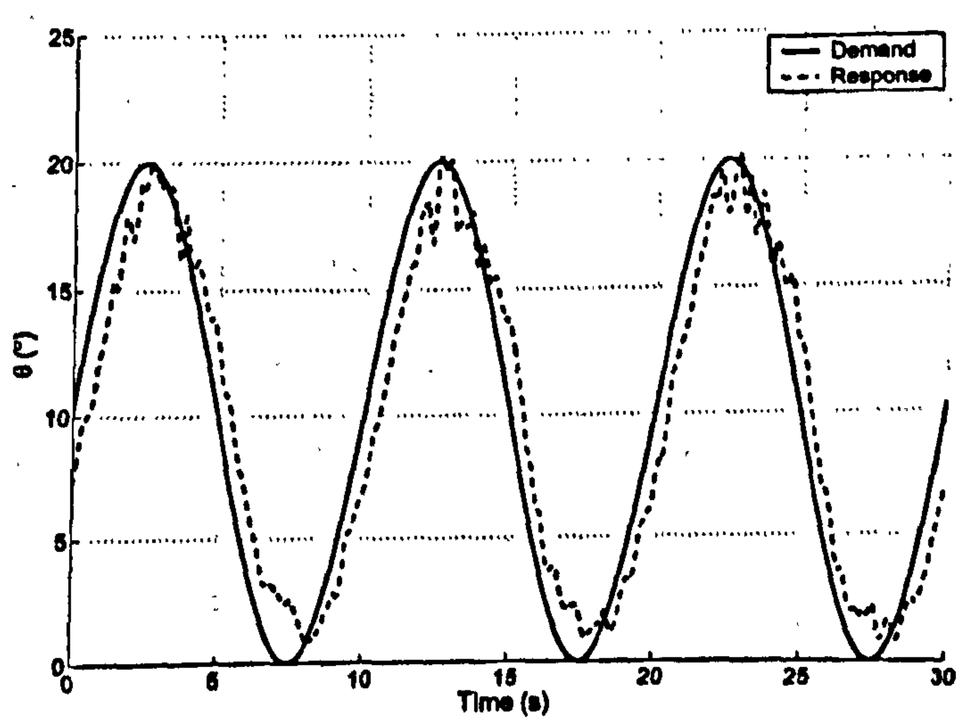


(b)

Figure 7.7: Response of experimental system to step (a) and sine wave (b) reference using non-linear feed-forward control.

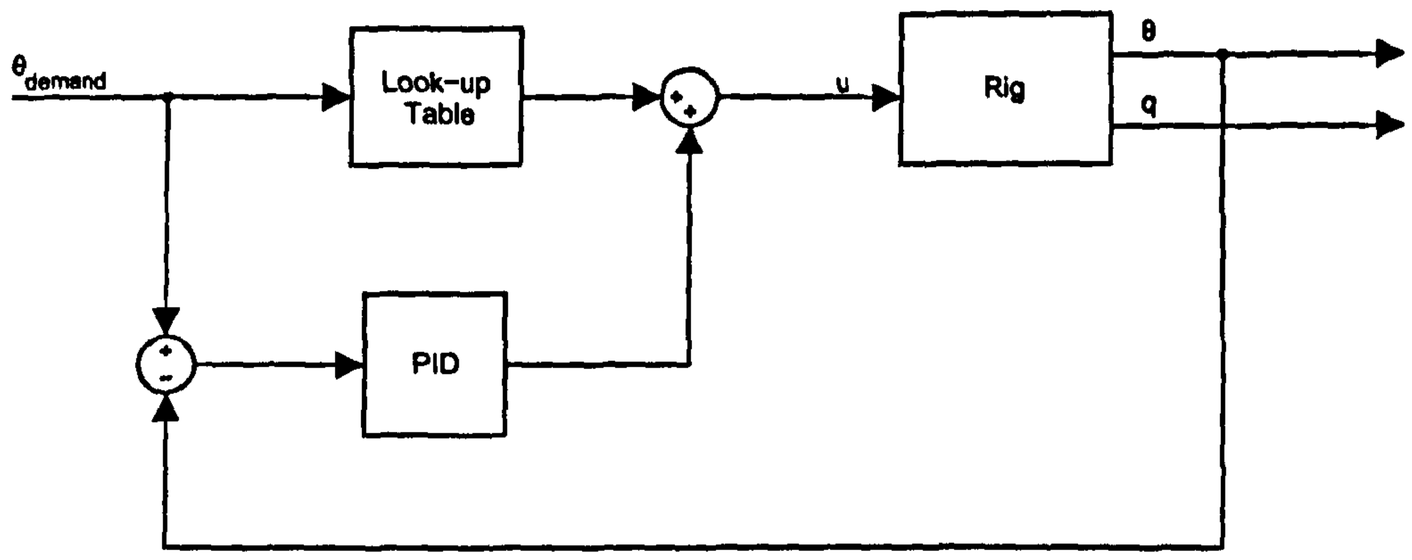


Figure 7.8: Feed-forward and pitch angle feedback control.

### 7.2.3 Non-linear Feed-Forward with PID Pitch Angle Feedback

To compensate for the steady-state error present in the response shown in Figure 7.7, a PID controller on $\theta$ is added, as shown in Figure 7.8. The presence of a derivative action in the PID controller makes the pitch rate compensation redundant, while adding a 'predictive' element by feeding forward the rate-of-change of the reference signal.

The gains of the PID controller were tuned using different methodologies, with the best performance being obtained by trial-and-error. Namely, a small proportional gain was used ($K_p = 0.1$) in order not to cause unwanted oscillatory behaviour. The integral gain, $K_i$ was set to $-1$ to give a good compromise between response and stability, while the derivative gain, $K_d$, was set to 0.2 (i.e. to the same values of the feedback gain $K_q$ used in the pitch rate compensator presented in Section 7.2.1). Responses for this control scheme are presented in Figures 7.9 and 7.10, where the experimental behaviour of the controlled system is compared with the prediction of the numerical simulation of the model.

Again, a good agreement between experiments and numerics can be observed, further confirming the suitability of the model presented in Chapter 5 for control design applications. The control responses show good sine wave tracking performance, with deviations from the demand occurring mainly in the high and low angle-of-attack limit cycle regions. The step response, shown in Figure 7.10, is also good with rapid transients and, when compared with Figure 7.7, showing the absence of any residual steady-state error. A higher overshoot is observed in the downward direction.

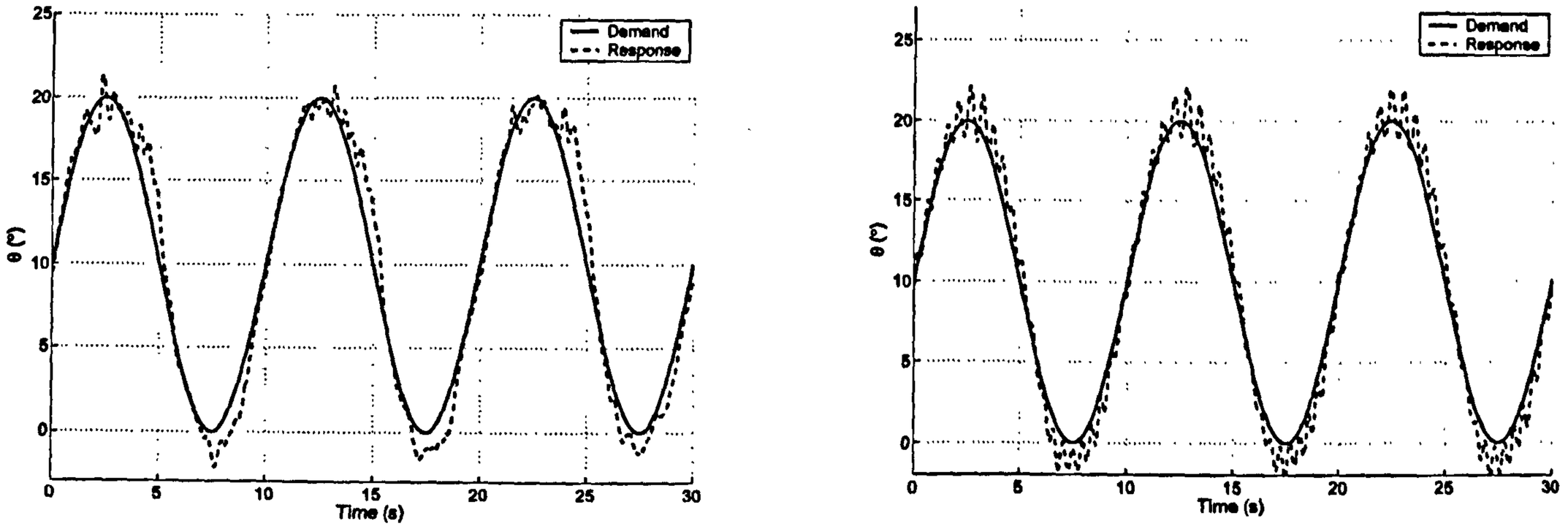


(a) (b)

Figure 7.9: Comparison of experimental (a) and numerical simulation (b) results for large amplitude sine wave reference (non-linear feed-forward plus PID).

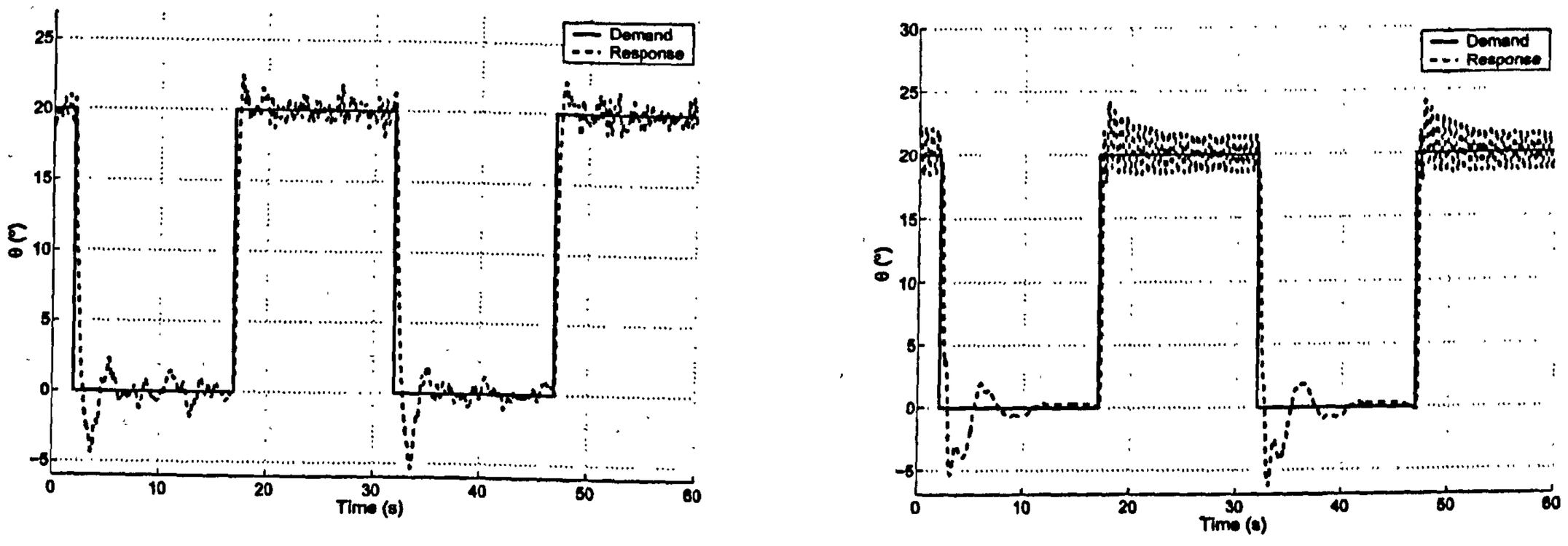


(a) (b)

Figure 7.10: Large-amplitude step response for (a) experimental rig and (b) numerical simulation (non-linear feed-forward plus PID).

Figure 7.11 shows a comparison between the ideal response of the second order reference model (outlined in Section 7.1) and the experimental response of the non-linear feed-forward plus PID feedback controller developed in this section. Despite steady-state tracking of the demand signal, the transient response of the closed-loop system is characterised by a settling time of approximately 1.2s (see Figure 7.11). This is significantly longer than the desired settling time of 0.5s defined in Section 7.1. This is an important

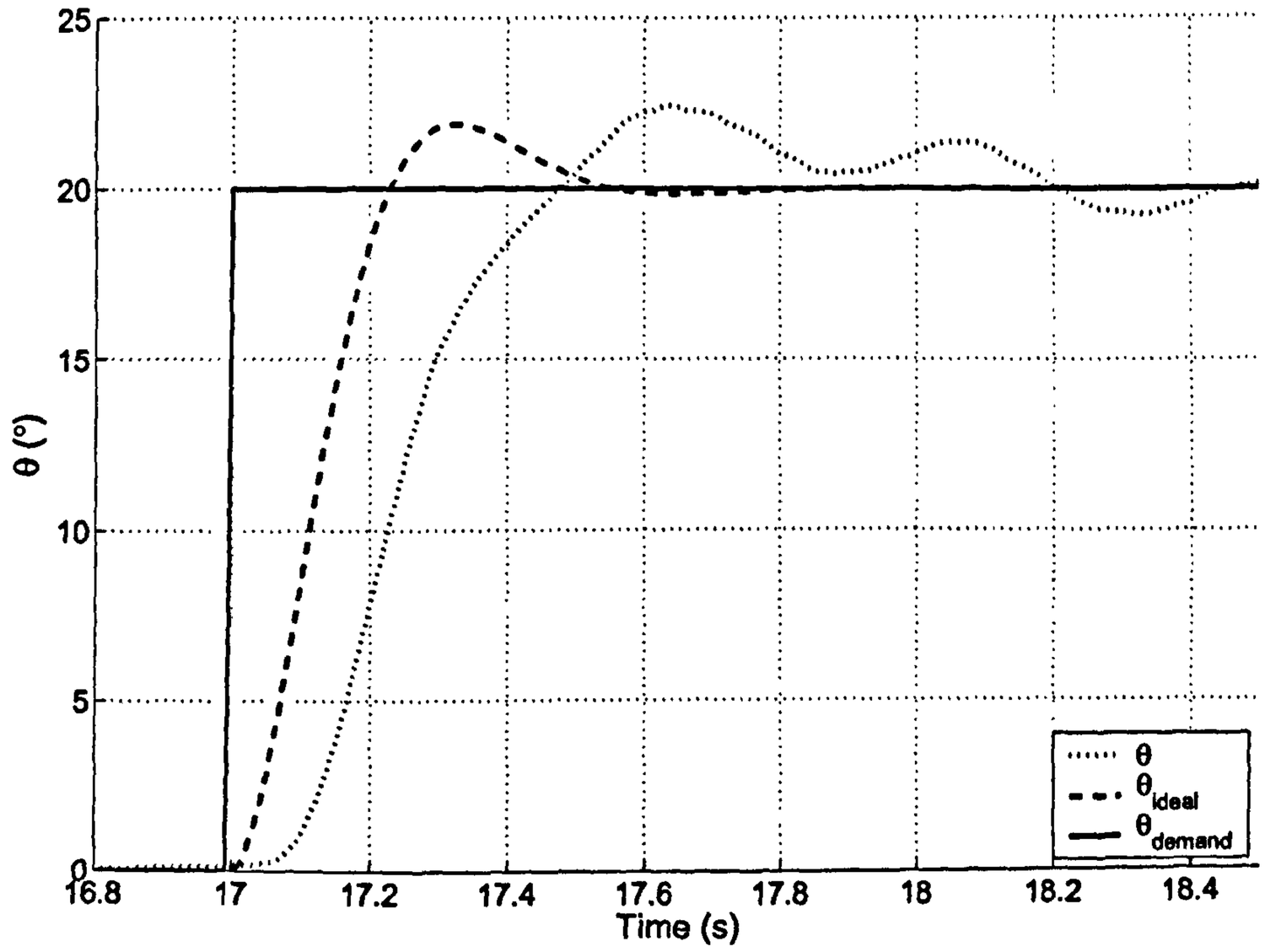


Figure 7.11: Comparison of non-linear feed-forward plus PID controller with ideal response (poles at $-7.2 \pm 9.6i$).

result, as this controller represents the best of the classical controllers that have been developed (in terms of speed of response and tracking performance). The difference in response times for the actual and ideal systems suggests that it is not possible to to achieve true-scale control law design using the rig in this configuration. Reasons for this, and possible solutions, are discussed in Chapter 10.

### 7.2.4 PID Control

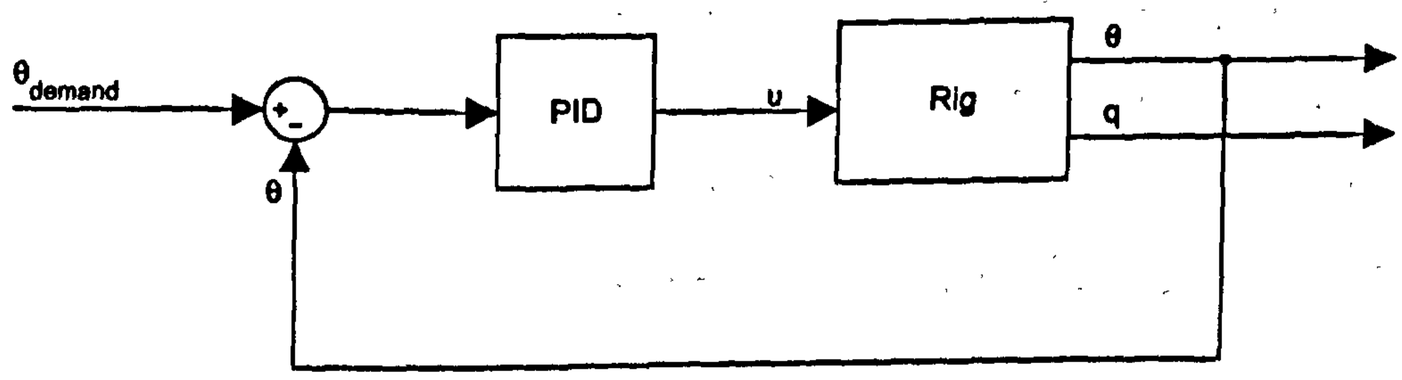


Figure 7.12: PID pitch angle controller.

For the purposes of comparison, the feed-forward non-linear term was removed to assess the performance of a pure PID feedback controller on $\theta$ (Figure 7.12). The controller

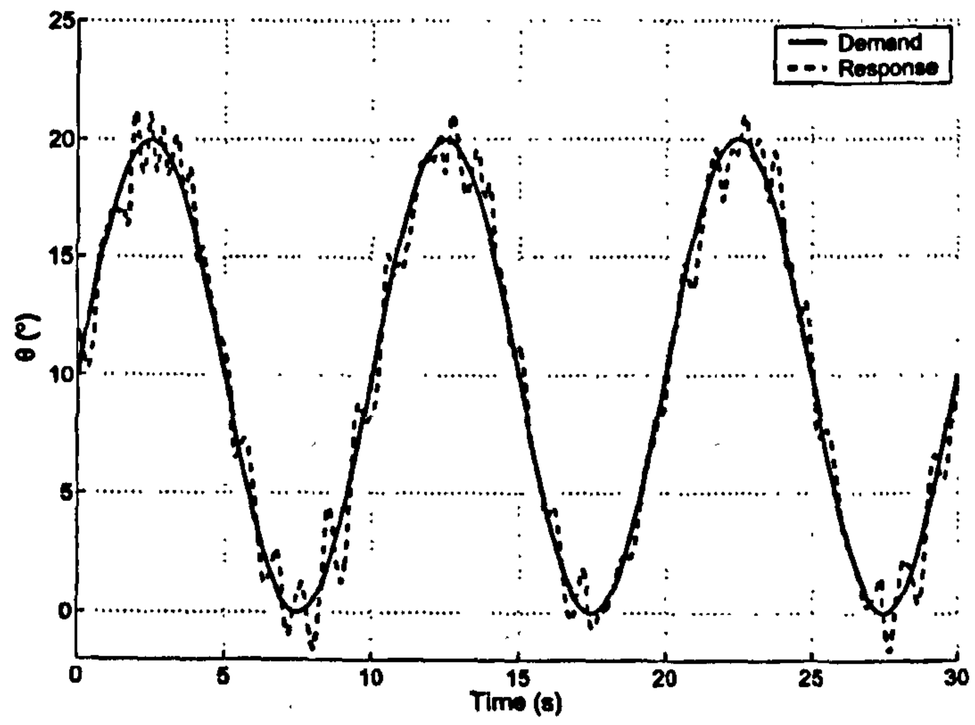


(a)

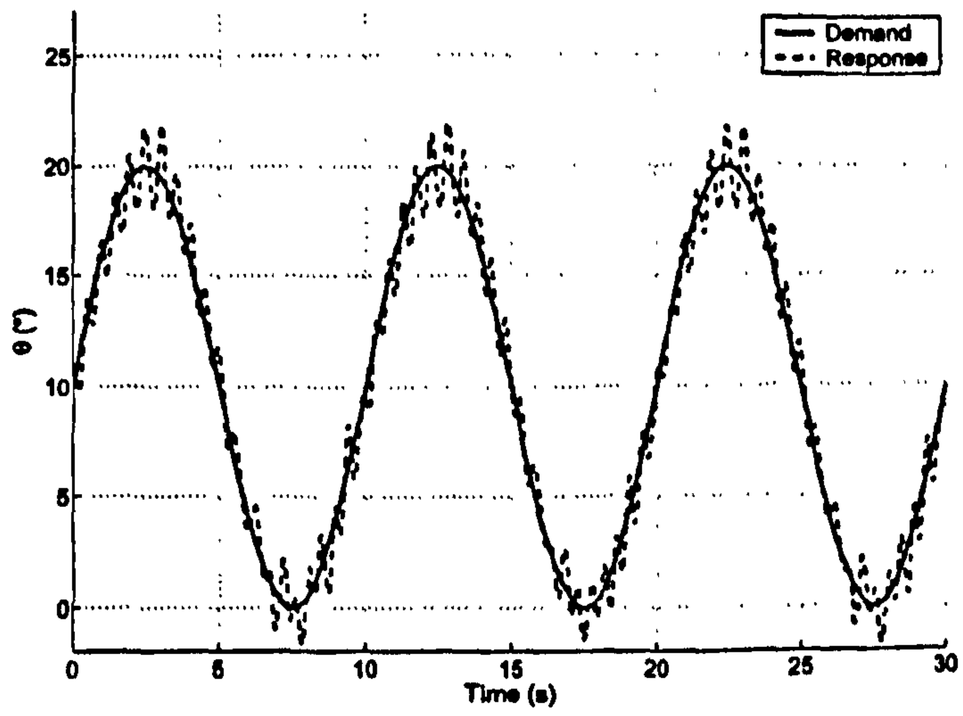


(b)

Figure 7.13: Comparison of experimental (a) and numerical simulation (b) results for large amplitude sine wave reference (PID controller).

gains were tuned via numerical simulations on the model and then tested on the rig. To implement this controller on the experimental rig, the pitch angle reference signal was differentiated and used to give a pitch rate error signal which is then fed through the derivative gain. This is equivalent to differentiating the pitch angle error, but avoids noise problems associated with differentiating the pitch angle signal on the experimental rig.

A non-linear unconstrained optimisation function (Matlab function *fminsearch*) was used to tune the PID controller gains on the model. A series of 30 second simulations were run with a 20° amplitude frequency-swept sine wave pitch angle demand, and a cost function calculated as the integral of pitch angle error over the simulation. The optimisation proved to be local, depending heavily on the values passed to the function, hence the gains were tuned initially by trial-and-error to get a good starting 'guess' for the optimisation routine. The gain values found were $K_p = 0.33$, $K_i = 10.24$ and $K_d = 0.25$. (Note the relatively large integral action needed to compensate for the non-zero steady-state error due to the non-linear perturbations acting on the system.)

An example response of the system using these feedback gains is shown in Figures 7.13 and 7.14. It is observed that, in the absence of the non-linear feed-forward action, the PID controller results in a highly oscillatory response and therefore an overall poorer tracking performance. This increase in oscillation is possibly due to the larger pitch rate

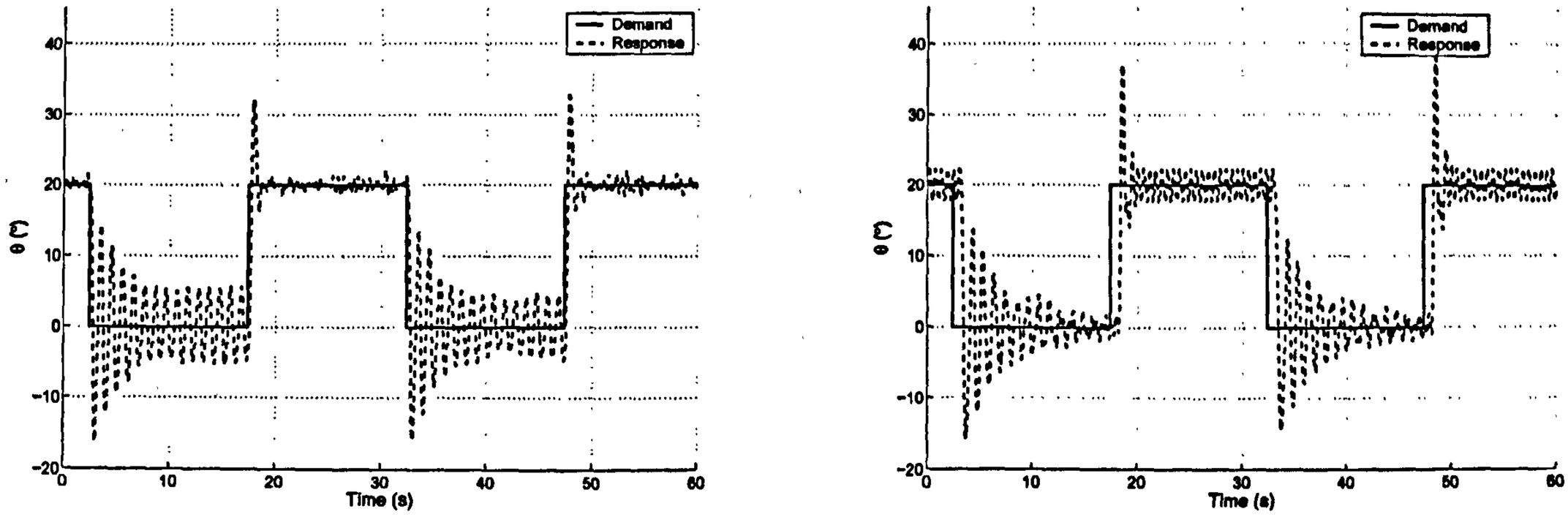


(a) (b)

Figure 7.14: Large-amplitude step response for (a) experimental rig and (b) numerical simulations (PID controller).

feedback gain used by the PID controller ($K_d$) introducing self-excited oscillations, as mentioned in Section 7.2.1. The step response in Figure 7.14 also shows a large amount of oscillation in the low angle-of-attack region. This might be overcome by re-tuning the PID gains which were originally optimised using a sinusoidal reference signal.

To ensure that the oscillatory step response exhibited by the closed-loop PID system (Figure 7.14) was not being excited by the controller feeding-forward the reference input, a 'practical PID' controller was tested using numerical simulations. With this controller (Figure 7.15), only the integral of the pitch angle error is fed forward, with proportional

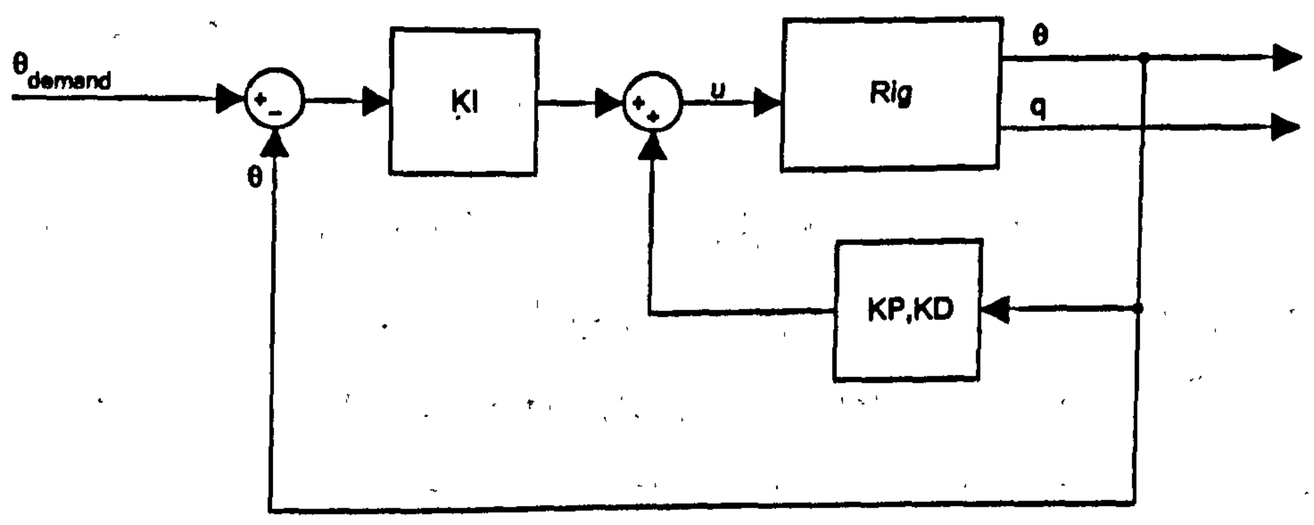


Figure 7.15: Practical PID controller with integral error feedback ($K_p = 0.33$, $K_i = 10.24$ and $K_d = 0.25$).

and derivative gains acting purely on the state. The aim of this controller is to stop high frequency transients being transmitted from the input to the plant by using the integrator as a form of filter. The response of this system to a 20° square wave is shown in Figure 7.16, and is very similar to the response of the standard PID controller tested above. This result leads to the conclusion that the oscillations are being caused by coupling between the non-linearities in the rig and the controller, and not due to high frequency excitation from the input.

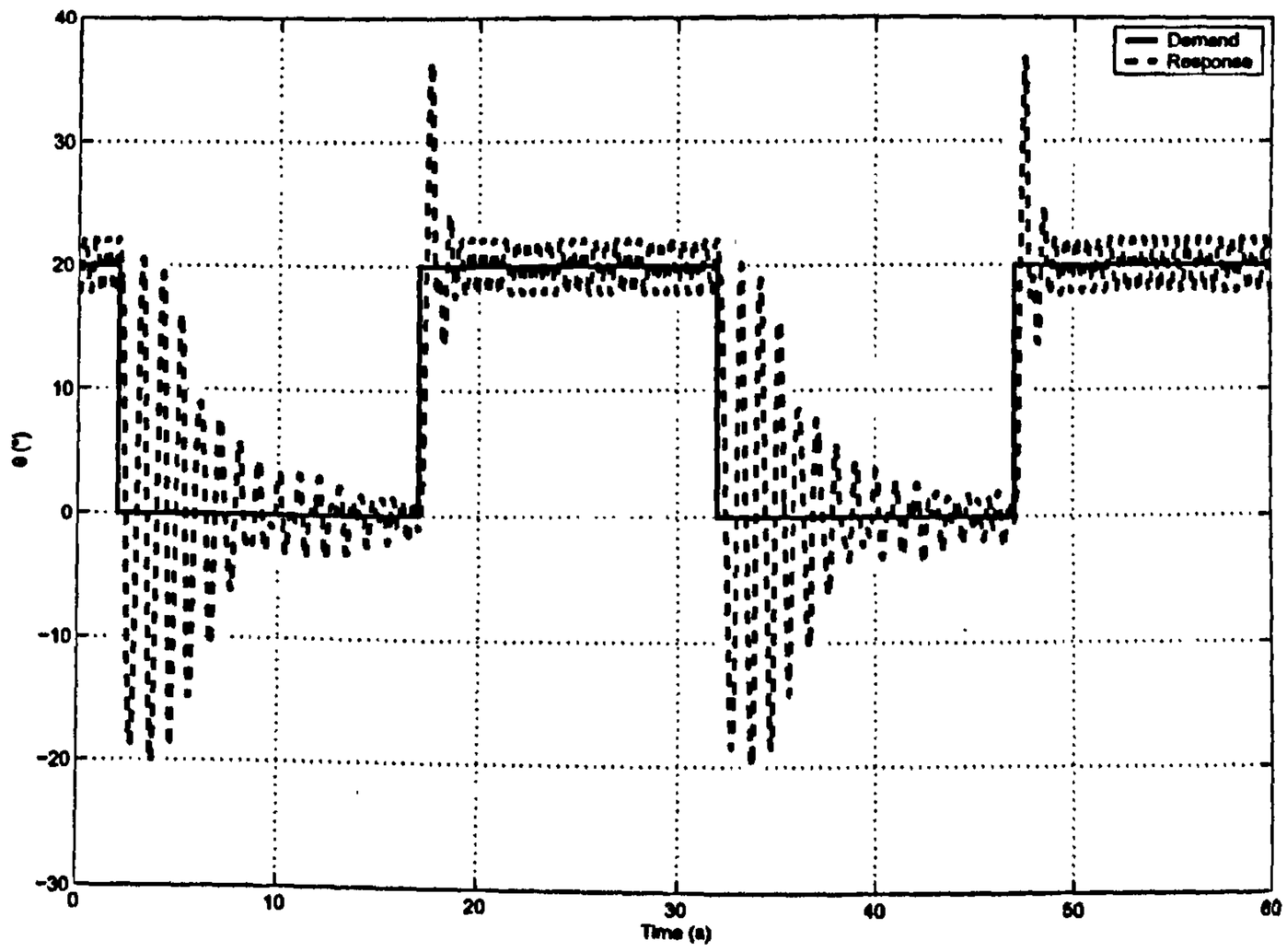


Figure 7.16: Numerical simulation of large-amplitude step response for practical PID controller.

## 7.3 Conclusions

In this chapter, the numerical model of the single degree-of-freedom rig developed in Chapter 5 was used to design classical controllers which have been experimentally implemented and tested. The system response in the presence of different control laws has been presented and evaluated. It was shown that the best performance can be obtained by using a feed-forward non-linear action coupled with a feedback PID controller which guarantees good tracking properties characterised by zero steady-state error and relatively low oscillatory modes. Both the feed-forward inverse look-up table and the tuning of the PID gains were achieved heuristically through the numerical analysis of the model,

confirming its suitability for control system design.

Whilst carrying out the experimental work described in this chapter the use of the rig for control system design has been demonstrated, however, problems and limitations have also been identified. One such limitation is imposed by the actuators used (off-the-shelf miniature radio-controlled model type servos); they have a relatively poor resolution and a large position deadband which limits the accuracy of results (see Chapter 10 for a more complete discussion of the actuator problems encountered). A further limitation is tunnel turbulence, as shown in the time histories presented (e.g. Figure 7.4(a), where tunnel turbulence significantly affects the open-loop limit cycle amplitude).

In the next chapter, design of more sophisticated control laws is investigated, namely gain-scheduled controllers using eigenstructure assignment, and an adaptive strategy.

# Chapter 8

# Bifurcation-Based Control

In Chapter 7, simple fixed-gain classical controllers were designed and tested on the rig. The controller gains were, in general, tuned by trial and error. It was found that a non-linear feed-forward element in the controller helped to remove some of the non-linearities in the system, and performed better than a standard fixed-gain PID controller designed using numerical simulations of the mathematical model.

The objective of using a bifurcation-based methodology for control system design is to make explicit use of the experimental bifurcation analysis on the rig (Figure 4.2) for the synthesis of controllers. In doing so, the controllers account for the bifurcation dynamics of the system, and the designer can get a better understanding of the physical rig. In this chapter, a bifurcation-based control system design strategy is used to develop more advanced controllers using the mathematical model of the Hawk. There are three main aims:

1. to develop an innovative controller design strategy on the mathematical model of the rig and demonstrate its effectiveness via numerical simulations.
2. to test and evaluate the controllers on the experimental rig to demonstrate their effectiveness.
3. to investigate the fidelity of the wind tunnel rig.

In particular, the following control schemes will be presented:

- A simple non-linear feed-forward gain to alter the shape of the bifurcation diagram.
- A controller utilising a non-linear feed-forward term and eigenstructure-assigned state-feedback control to alter the shape and stability of the bifurcation diagram. The feedback gains are designed using linearisations of the model at a set of trim points over the angle-of-attack range. The resulting gains are scheduled against demanded pitch angle to give the appropriate gain variation.
- A non-linear feed-forward controller with gain-scheduled state feedback and tracking-error integrator to add robustness to the controller and ensure a single branch of stable equilibria in the bifurcation diagram.
- A fully eigenstructure-assigned PI controller.
- A model-reference adaptive strategy for the purposes of comparison. The main advantage of the adaptive strategy is that it requires no lengthy design procedure.

Desired eigenvalues for the state feedback controllers and reference models are taken directly from Section 7.1. A brief overview of the eigenstructure assignment process used in this chapter will now be presented.

## 8.1 Eigenstructure Assignment

Consider the following linear system in state-space form:

$$\dot{\boldsymbol{x}} = \boldsymbol{A}\boldsymbol{x} + \boldsymbol{B}u, \qquad \boldsymbol{x} \in \mathbb{R}^n, u \in \mathbb{R} \tag{8.1}$$

$$y = \boldsymbol{C}\boldsymbol{x}. \qquad y \in \mathbb{R} \tag{8.2}$$

The input, $u$, is used to apply output feedback via the gain matrix $\boldsymbol{K}$, i.e. $u = \boldsymbol{K}\boldsymbol{C}\boldsymbol{x}$, yielding the closed-loop system:

$$\dot{\boldsymbol{x}} = \boldsymbol{A}\boldsymbol{x} + \boldsymbol{B}\boldsymbol{K}\boldsymbol{C}\boldsymbol{x}. \tag{8.3}$$

Now, if the system equations are known, and the desired eigenvalues, $\boldsymbol{\Lambda}$, and eigenvectors, $\boldsymbol{V}$, of the closed-loop system are defined, the problem is to calculate the feedback gain matrix, $\boldsymbol{K}$, such that:

$$(\boldsymbol{A} + \boldsymbol{B}\boldsymbol{K}\boldsymbol{C})\boldsymbol{V} = \boldsymbol{V}\boldsymbol{\Lambda}. \tag{8.4}$$

The process is defined in more detail in [18, 125, 126], and can be easily implemented in Matlab.

## 8.2 Gain-Scheduled Controller Design

### 8.2.1 Feed-forward Only Control

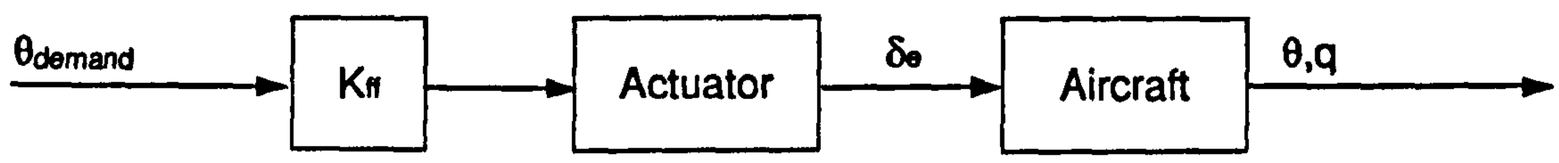


Figure 8.1: Feed-forward only control.

Similarly to Chapter 7, we begin by designing a simple non-linear forward-path gain controller, used to obtain a given relationship between the reference input, $r = \theta_{demand}$, and the equilibrium condition of the model. The objective is to track the input pitch angle demand, which corresponds to obtaining a straight-line relationship between the reference input, $\theta_{demand}$, and the trimmed pitch angle of the model, $\theta$ (i.e. we require that $\theta = \theta_{demand}$). To show this relationship, $\theta_{demand}$ now becomes the continuation parameter. Stability of the solutions will not be affected, hence there is no guarantee that the system will follow the desired equilibrium; there may be other attractors to which the system will evolve over time.

A block diagram of the feed-forward only control system is shown in Figure 8.1, with the controller equation given as:

$$u = f(r) \tag{8.5}$$
$$r = \theta_{demand}$$

The feed-forward gain used in the forward path (Figure 8.2) is again the inverse trim-curve for the model, used in Section 7.2.2, found by inverting the trim curve taken from the experimental bifurcation diagram (Figure 4.2). A simulated bifurcation run for the Hawk model is shown in Figure 8.3(a). The steady-state solution of the model now tracks the reference demand (to give a straight line, as desired) until the stable limit

cycles cause the system to oscillate. The trim branch has indeed been straightened, however, the limit cycles still exist and are clearly visible.

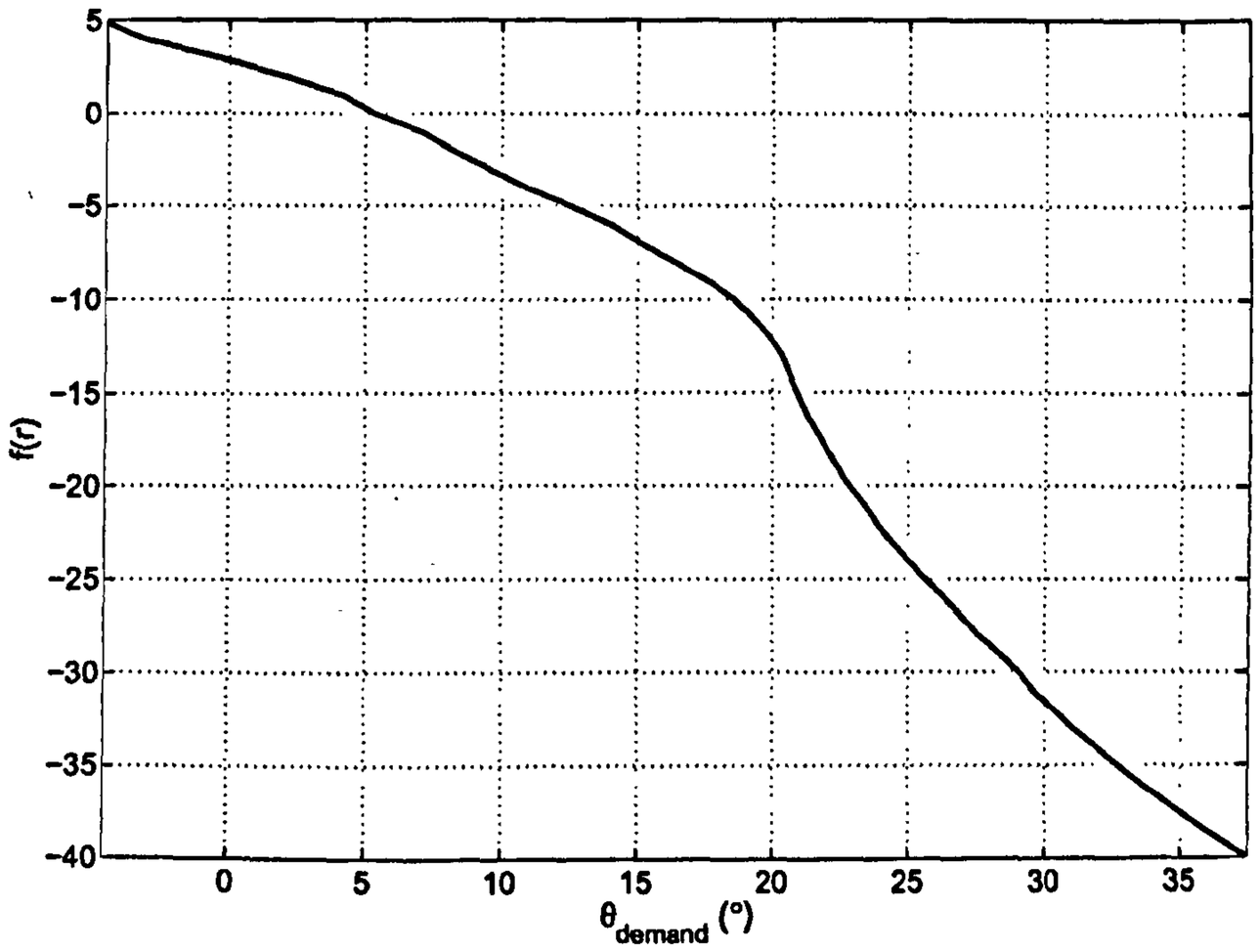


Figure 8.2: Inverse trim curve for the feed-forward controller.

Figure 8.3(b) shows the experimental bifurcation diagram for the non-linear feed-forward only controller, where demanded pitch angle was slowly increased from $-5°$ to $35°$ over 30 minutes. Note the absence of the small-amplitude limit cycle at $\theta \approx 5°$. This may be attributed to changes in the experimental rig/conditions in the period between tests. Possible reasons are discussed further in Section 10.2.1, however, it serves to demonstrate the sensitivity of the experimental rig. The mathematical model of the rig was not altered to reflect this change in the experimental results, mainly to allow comparison of simulations for the different controllers. Removing the small-amplitude limit cycle from the model would simply be a case of changing the stable-limit-cycle-amplitude data points to zero at low angle-of-attack and checking the stability and frequency of the response.

Simulated step responses can be seen in Figure 8.4 and show the undesirable characteristics of this control system. Corresponding tailplane deflection time histories are shown to the right of each step response. The controller is not robust; any errors in the modelled trim curve will cause errors in equilibrium solutions.

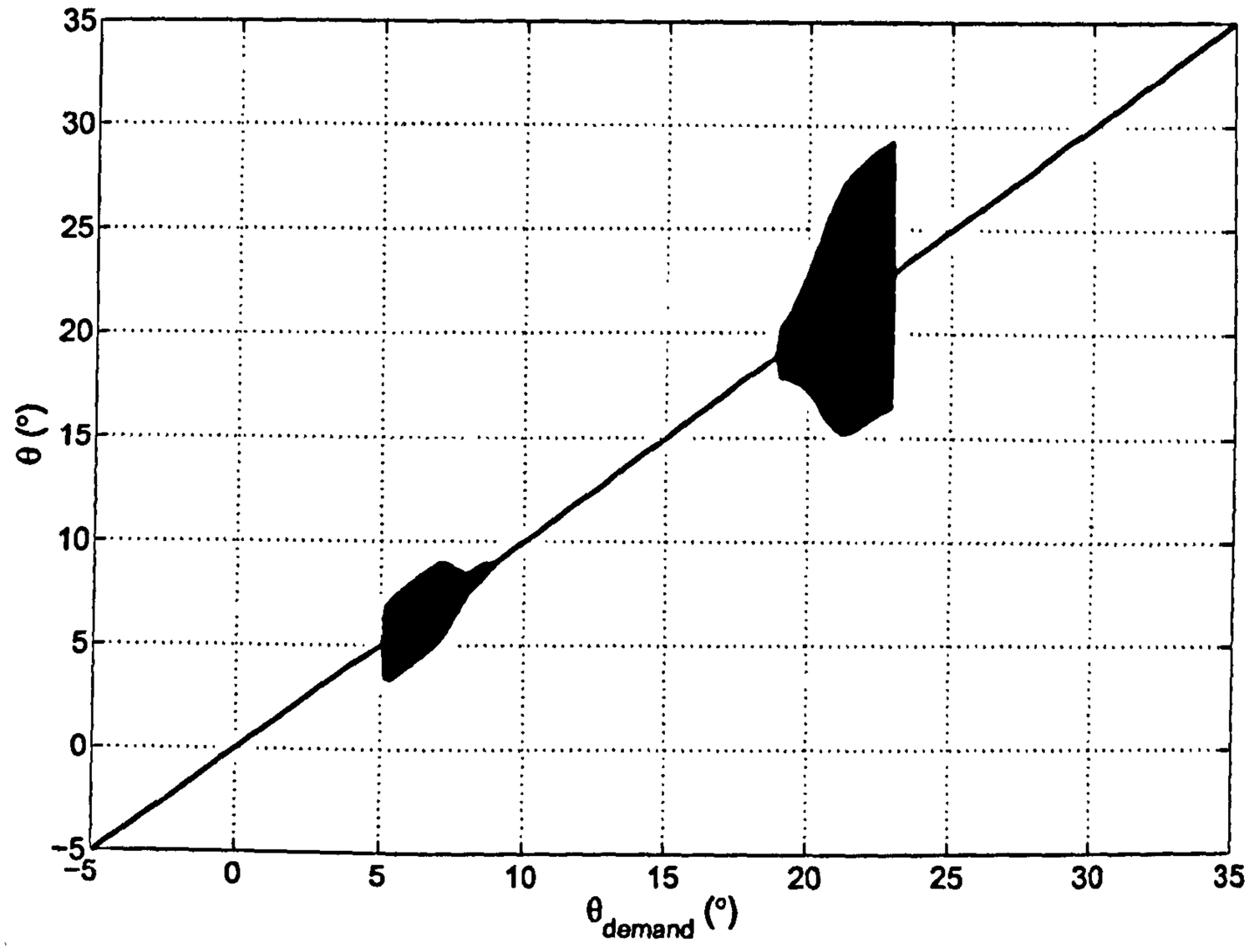


(a) Simulated bifurcation diagram.

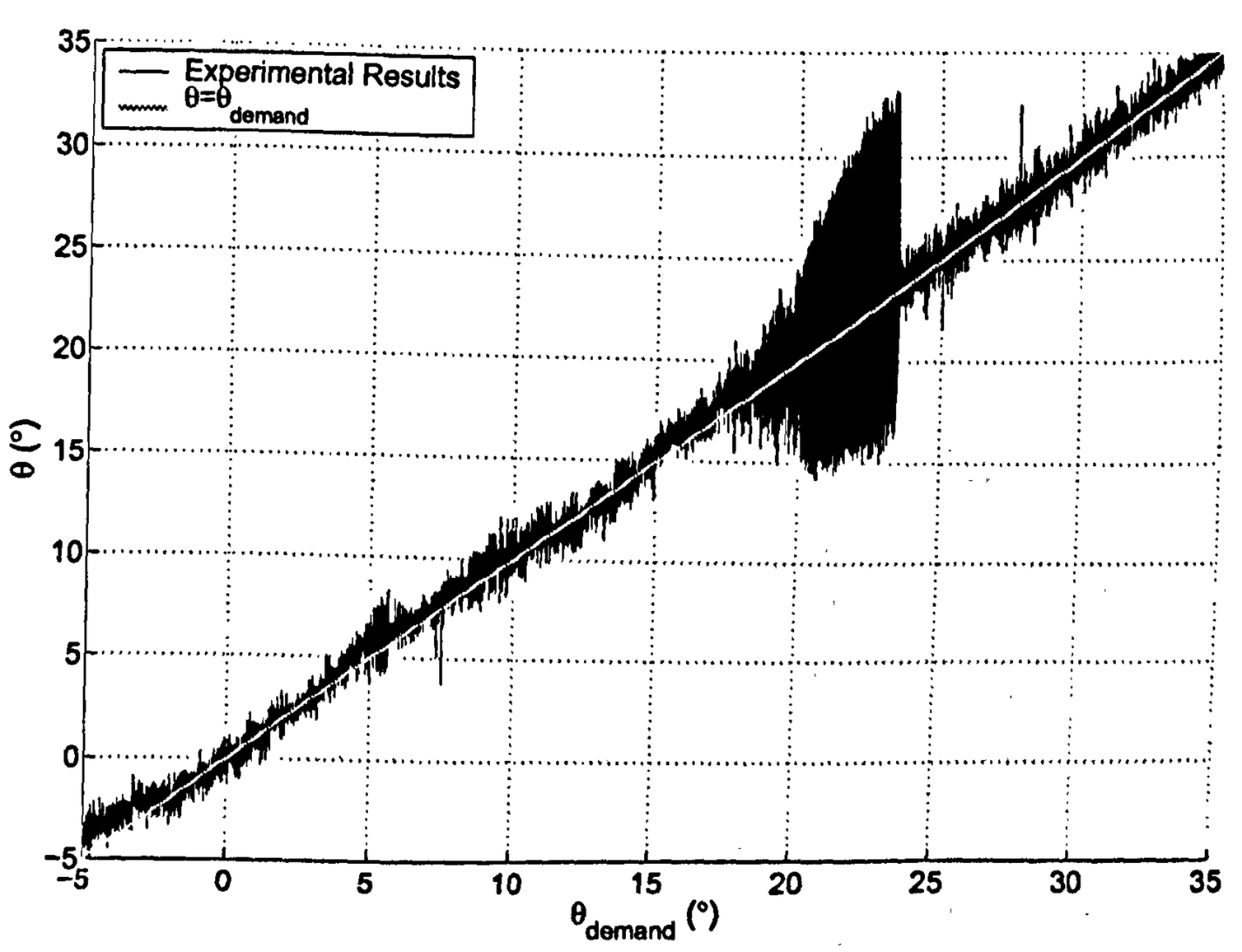


(b) Experimental bifurcation diagram.

Figure 8.3: Simulated (a) and experimental (b) bifurcation diagrams for the feed-forward only controller.

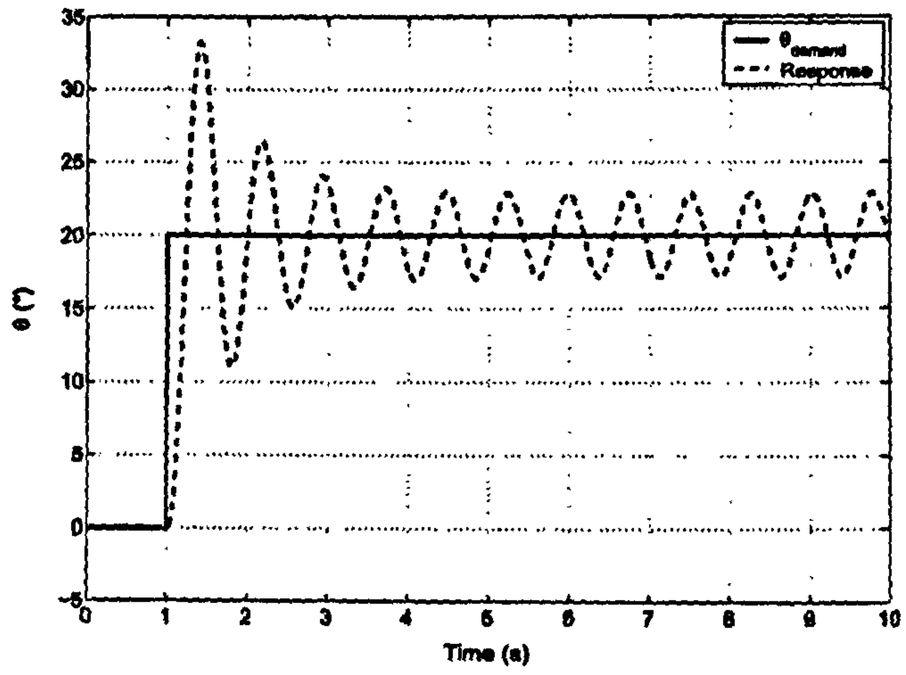


(a)

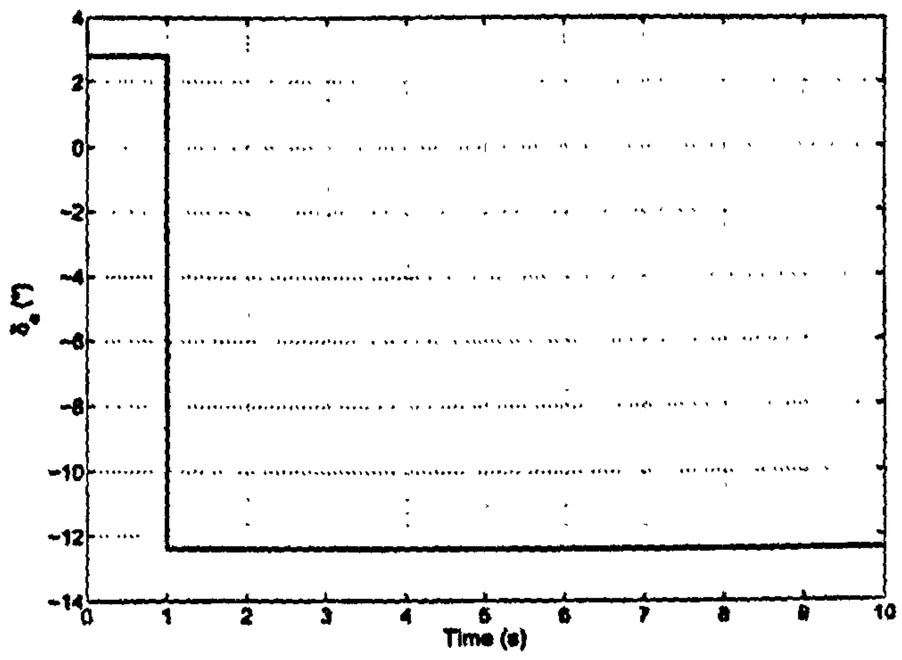


(b)

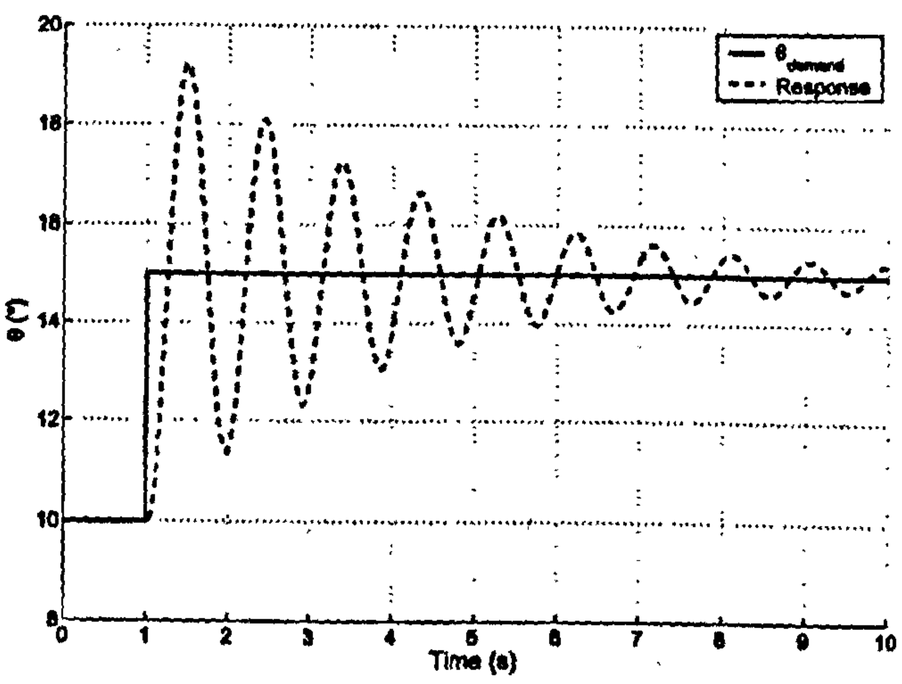


(c)

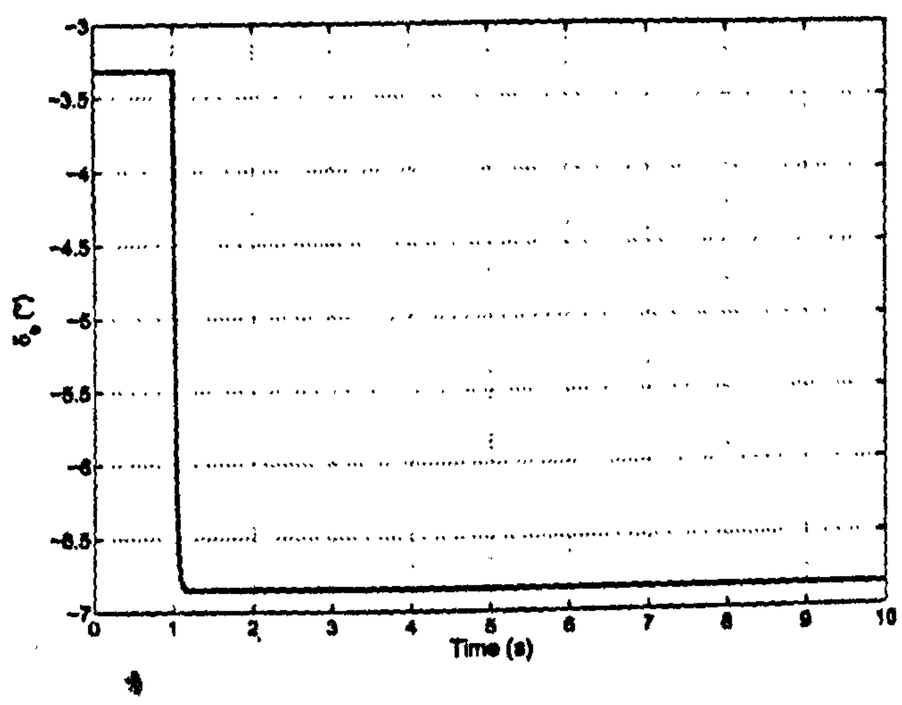


(d)

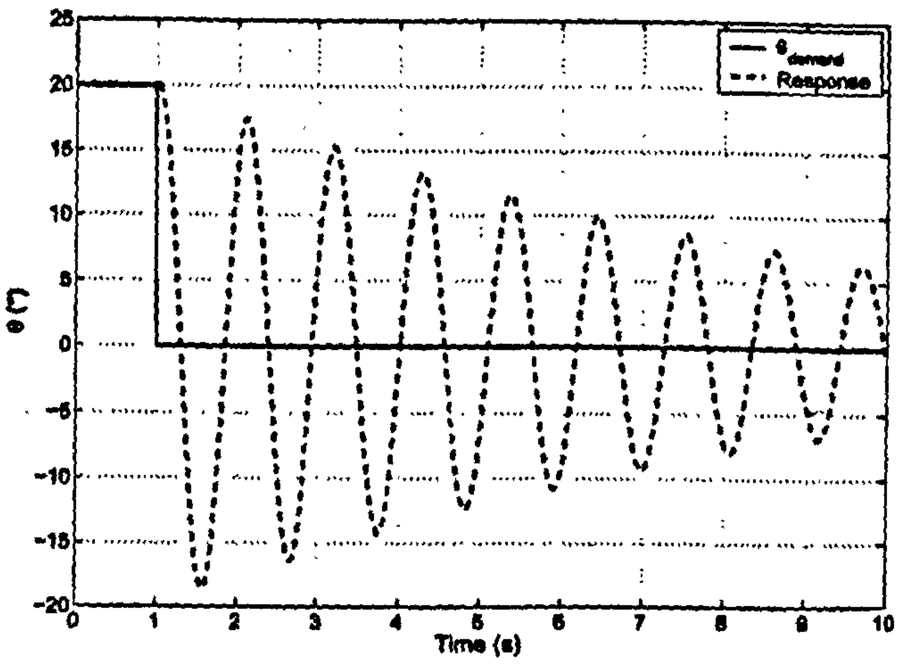


(e)

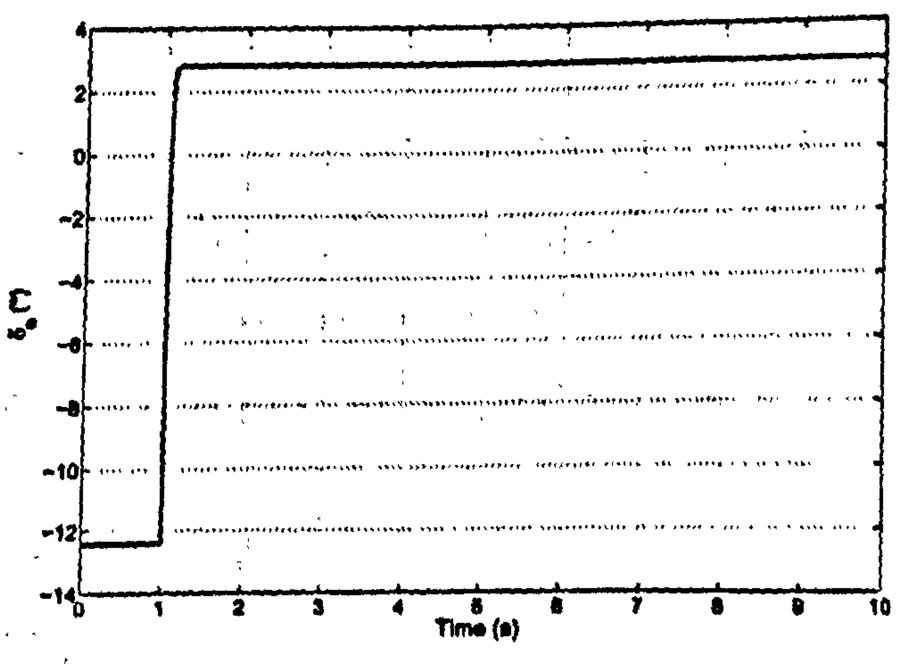


(f)

Figure 8.4: Simulated time histories for the feed-forward only controller.

### 8.2.2 Feed-Forward Plus State Feedback

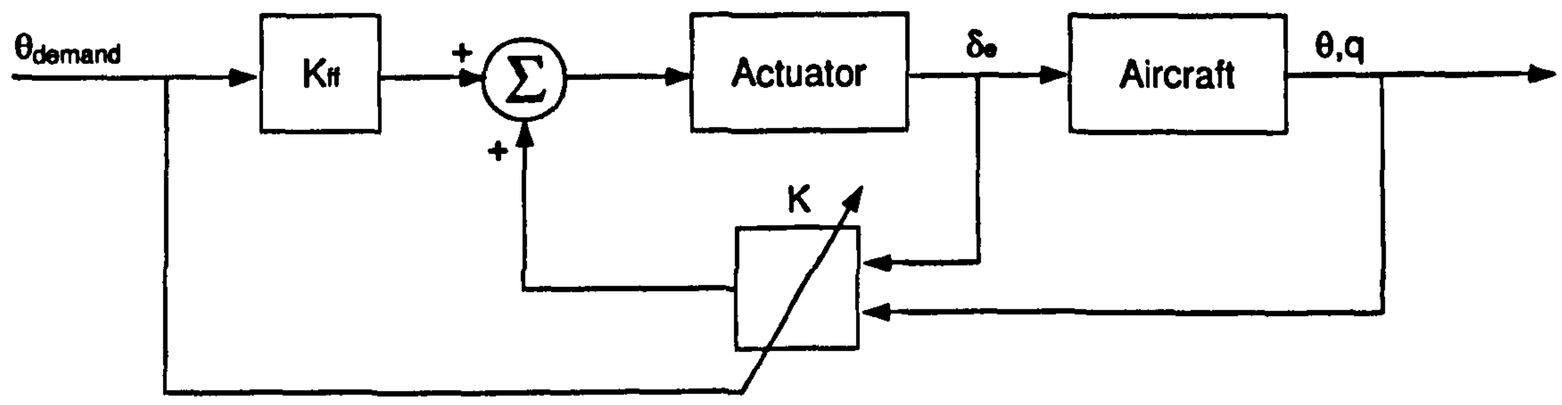


Figure 8.5: Non-linear feed-forward plus demand-scheduled state feedback.

It is desirable to add some form of state feedback to the feed-forward controller described in Section 8.2.1, to stabilise the branch of stationary equilibria. The block diagram for this controller is shown in Figure 8.5, giving the input equation:

$$u = K_{ff}(r) + K_1(\theta)q + K_2(\theta)\theta + K_3(\theta)\delta_e, \tag{8.6}$$

where $K_1$, $K_2$ and $K_3$ correspond to the state-feedback gains on $q$, $\theta$ and $\delta_e$ respectively, and are all look-up tables in $\theta$.

The eigenstruture assignment routine described in Section 8.1 was used to calculate the feedback gain matrix, $\boldsymbol{K}$. The model is linearised at discrete points along the trim curve, a controller designed at each point to satisfy some pre-determined eigenstructure, then the resulting controller gains scheduled against the reference input, $r$. This is equivalent to the quasi-continuous scheduling used in [18], where the eigenstructure assignment routine is integrated within a numerical continuation method. The eigenvalues chosen were those given in Section 7.1, shown in Table 8.1. A second order linear actuator (see Section 3.3.5 for a detailed description) was included in the mathematical model.

Table 8.1: Desired closed-loop eigenvalues.

| | |
|---|---|
| Aircraft | $-7.2 \pm 9.6i$ |
| Actuator | $-41.4, -1208.6$ |

The states of the model are $(q, \theta, \delta_e, \dot{\delta}_e)^T$, where $q$ is the pitch rate of the model, $\theta$ is the pitch angle, $\delta_e$ is the symmetrical tailplane deflection and $\dot{\delta}_e$ is the tailplane angular

velocity. It was decided that only pitch angle, pitch rate and tailplane deflection would be fed back by the controller.

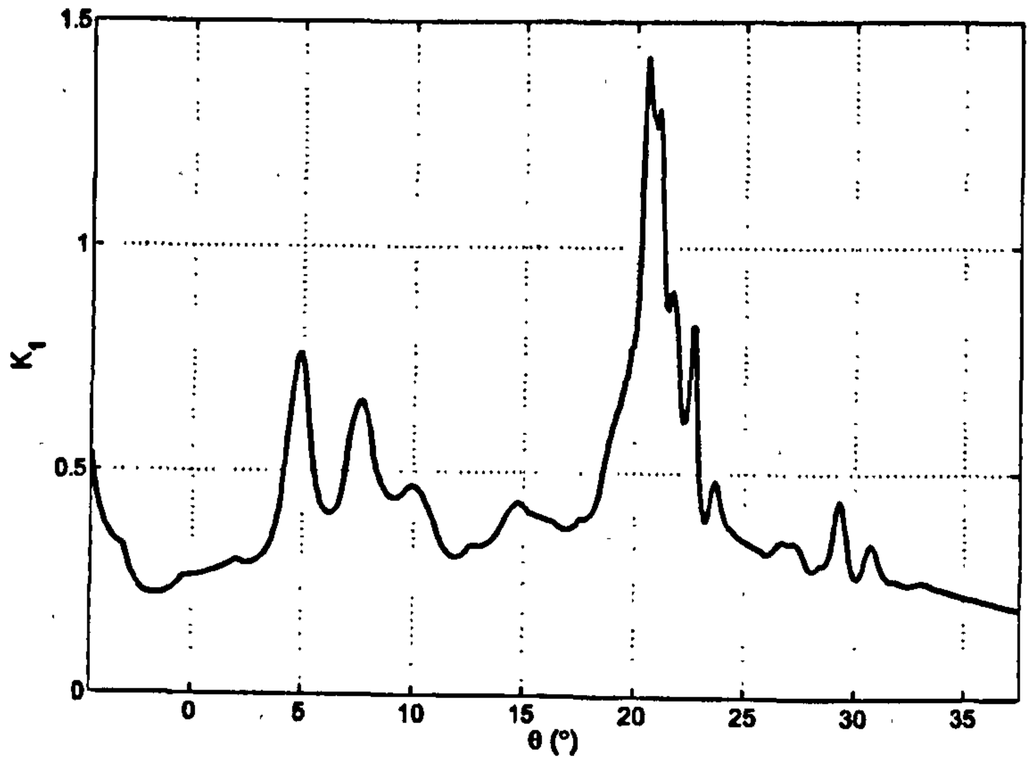


(a) $K_q(\theta)$ – pitch rate feedback gain.

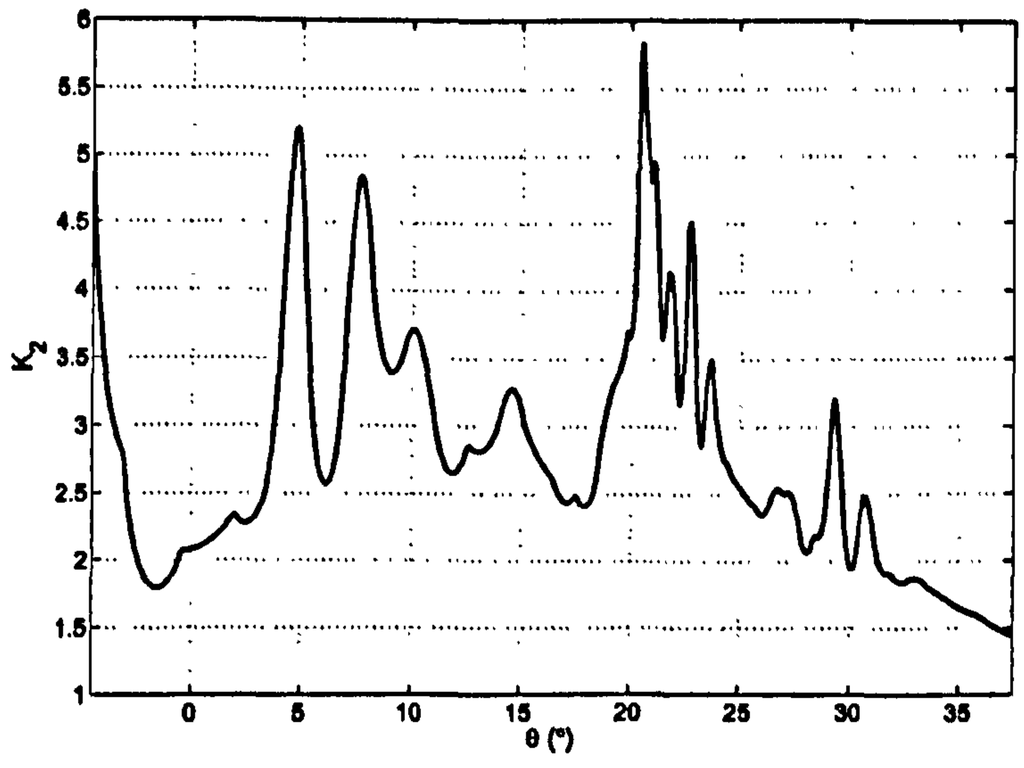


(b) $K_\theta(\theta)$ – pitch angle feedback gain.

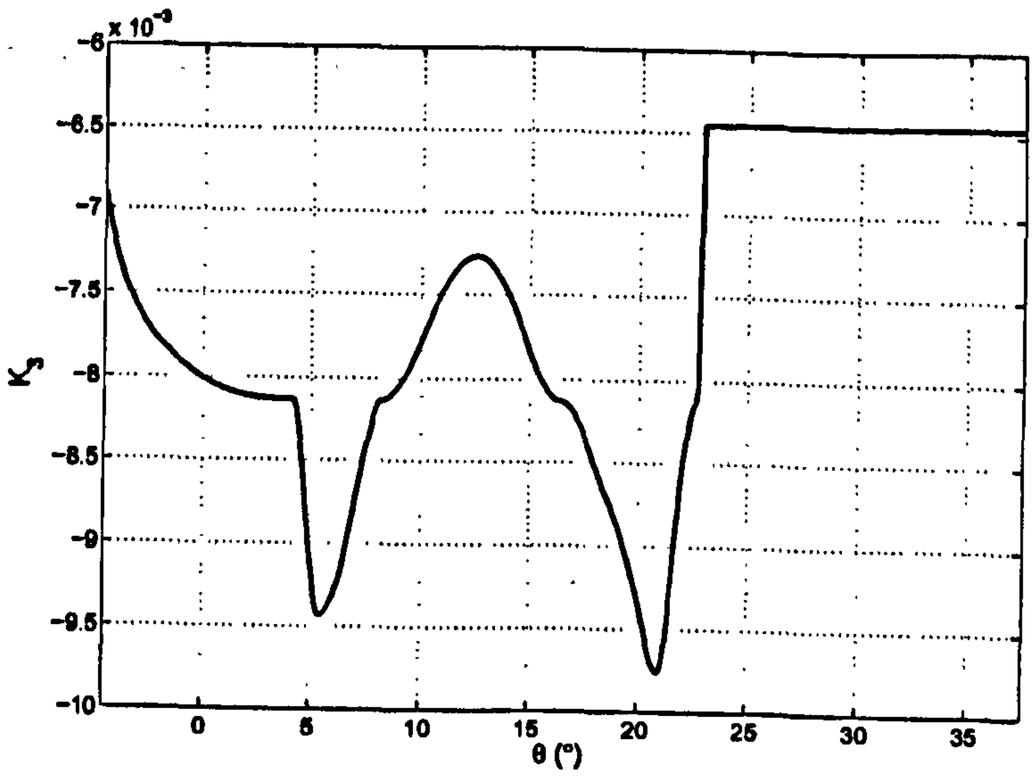


(c) $K_{\delta_e}(\theta)$ – tailplane position feedback gain.

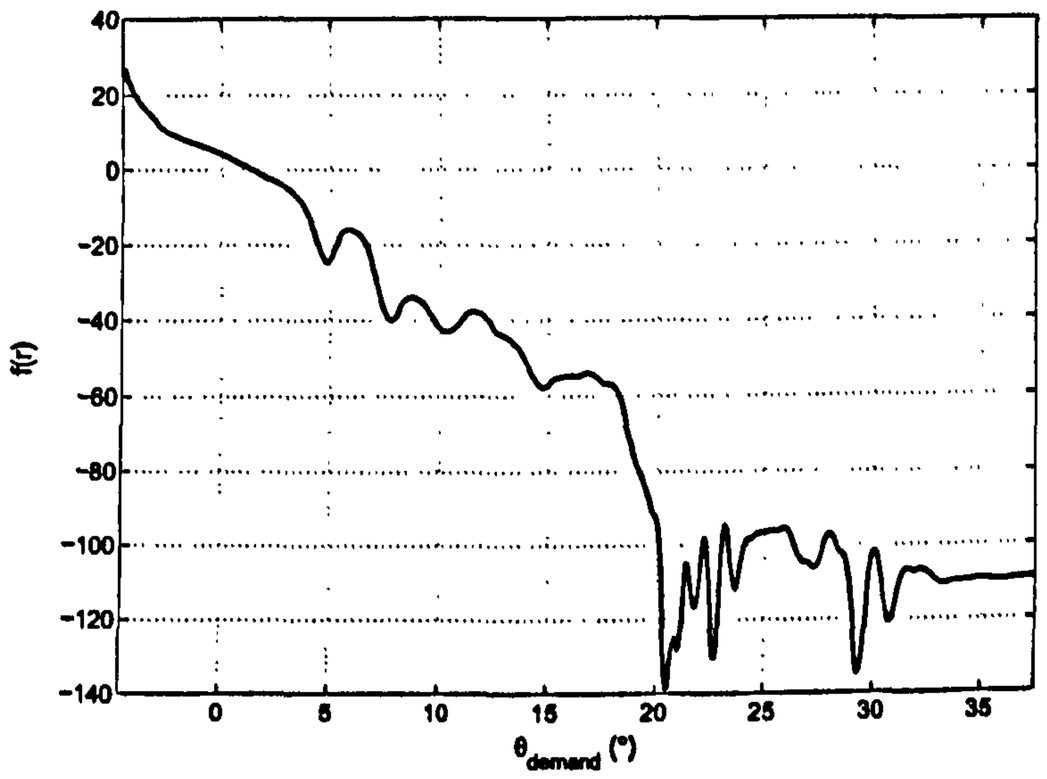


(d) Feed-forward gain.

Figure 8.6: State feedback gains calculated using eigenstructure assignment.

The gains generated by the eigenstructure assignment routine ($K_q$, $K_\theta$ and $K_{\delta_e}$) are shown in Figure 8.6(a), (b) and (c)[1]. It is important to note that the feed-forward gain, $K_{ff}$, used with the state feedback controller (Figure 8.5) is different to that used for the purely feed-forward control in Section 8.2.1. This is due to the proportional feedback on $\theta$ ($x_2$) changing the relationship between the reference input ($\theta_{demand}$) and actual

[1]A custom-written Matlab function, taken from code used in [18], was employed to calculate the feedback gains, however, the Matlab command `place` could equally have been used.

pitch angle. The new feed-forward gain is shown in Figure 8.6(d), calculated by slowly varying the input, $\theta_{demand}$, from $-5°$ to $37.5°$ and inverting the trimmed output pitch angle curve.

As a brief aside, when the eigenstructure assignment routine was first applied to the mathematical model of the Hawk the gains were discontinuous in places. This was traced to the eigenvalues jumping from one side of the s-plane to the other when the stability of the equilibria was specified to change within the model. The solution was to include points in the damping look-up table which were zero at the tailplane deflections corresponding to bifurcation points. By including these points the eigenvalues move towards the imaginary axis as the system approaches a bifurcation, lie on the axis at the bifurcation point, and continue smoothly on the other side after the bifurcation, thus removing the discontinuities.

**Numerical Validation**

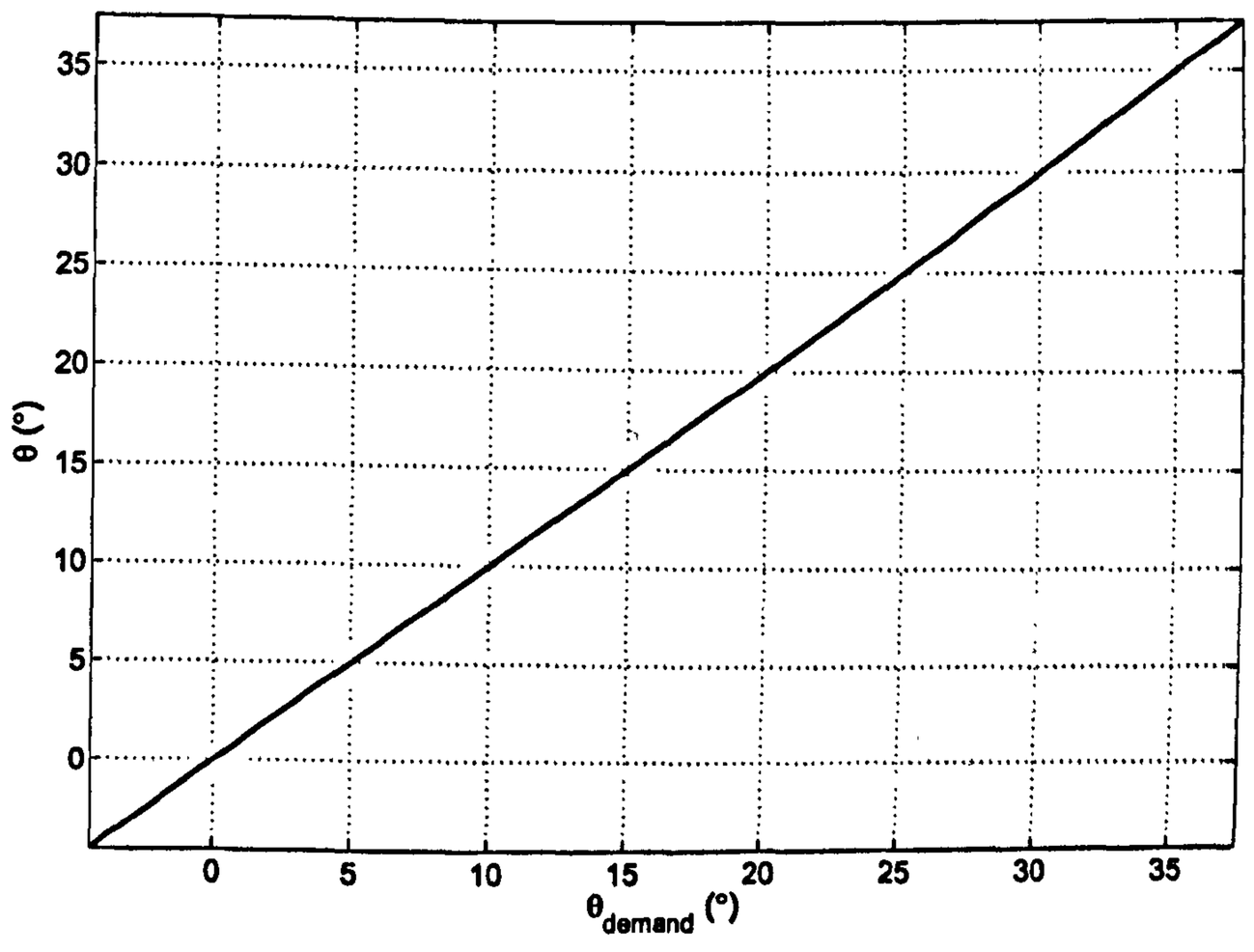


Figure 8.7: Simulated bifurcation diagram for the feed-forward with scheduled state-feedback controller.

The simulated bifurcation diagram for this system (Figure 8.7) shows that the branch of stationary equilibria created using the feed-forward gain has now been stabilised, and no bifurcations are present in the system over the entire flight envelope.

Time simulations were carried out to show the performance of this controller to a step input reference demand (Figure 8.8). In general, the controller performs well; there is no undershoot and the responses are well damped. There is a moderately large error between the ideal response of the second order reference model (defined in Section 7.1)

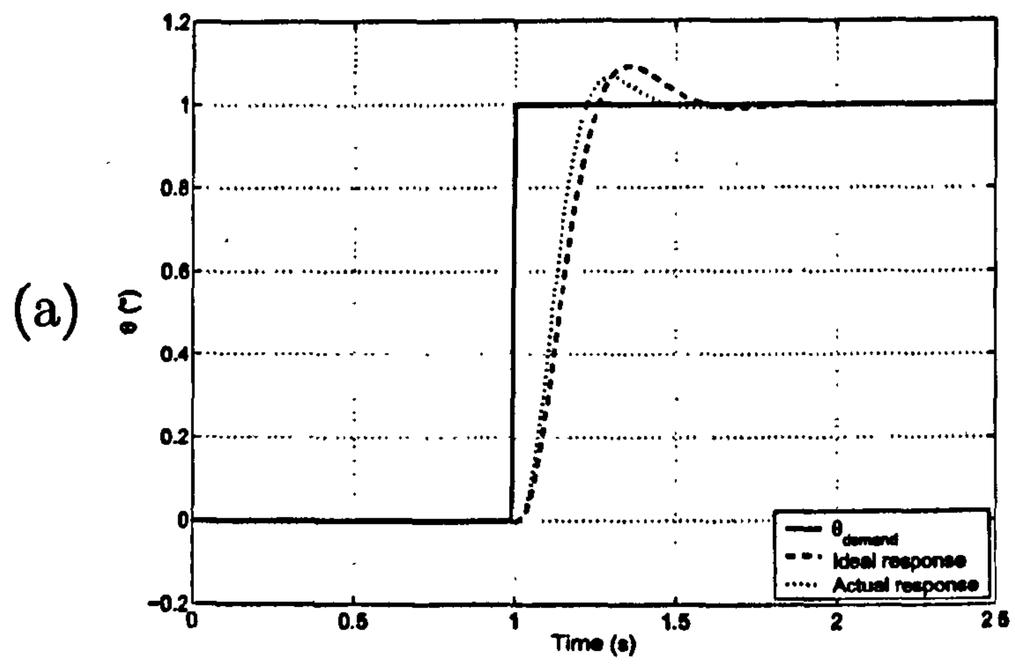


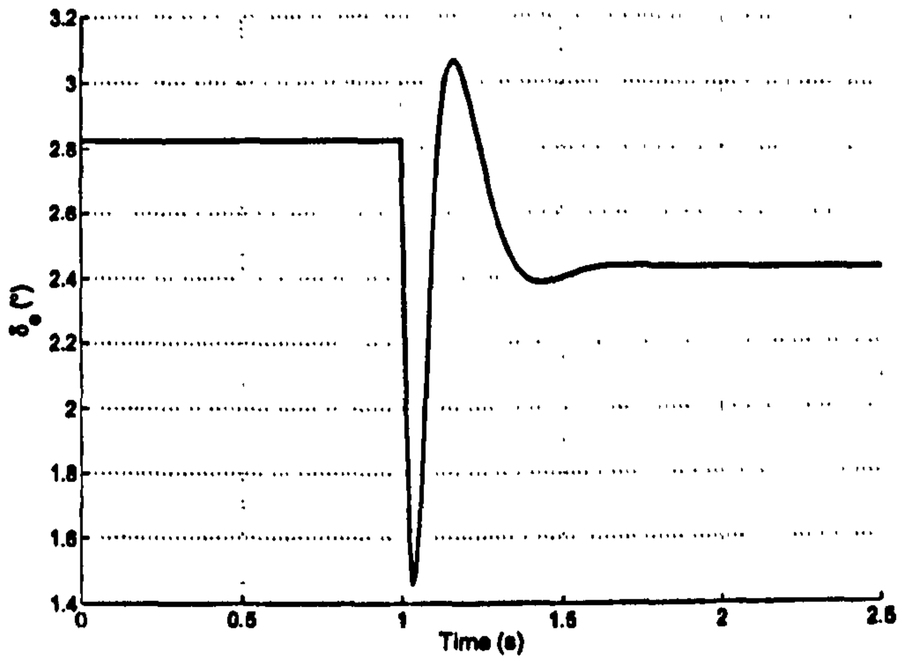


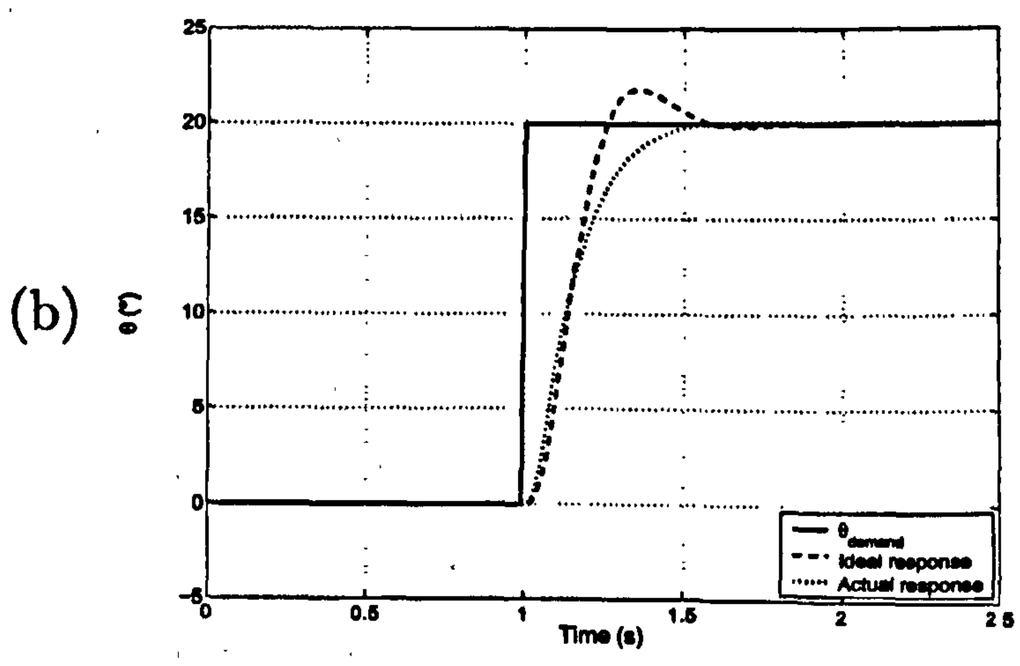


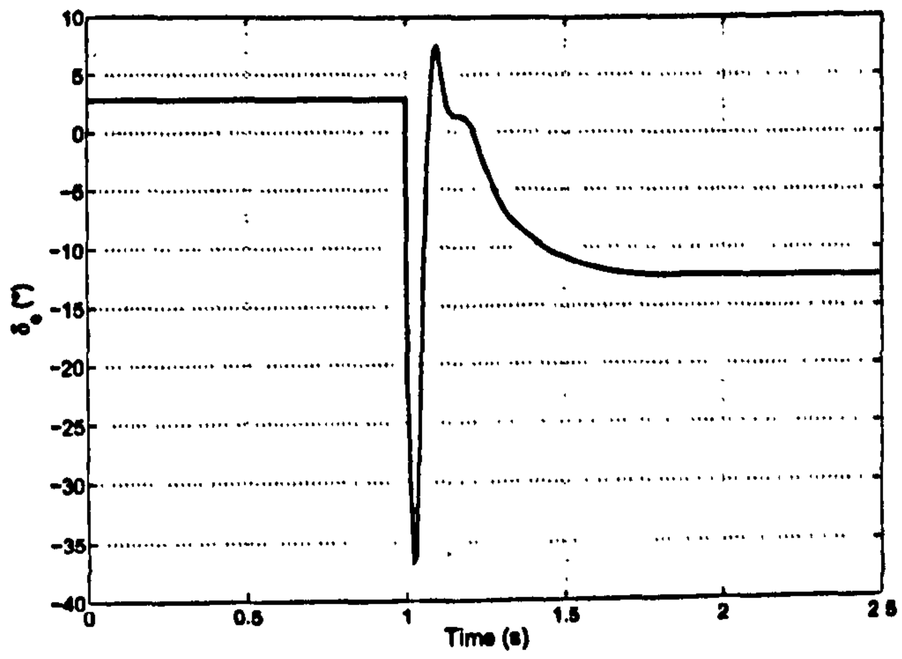


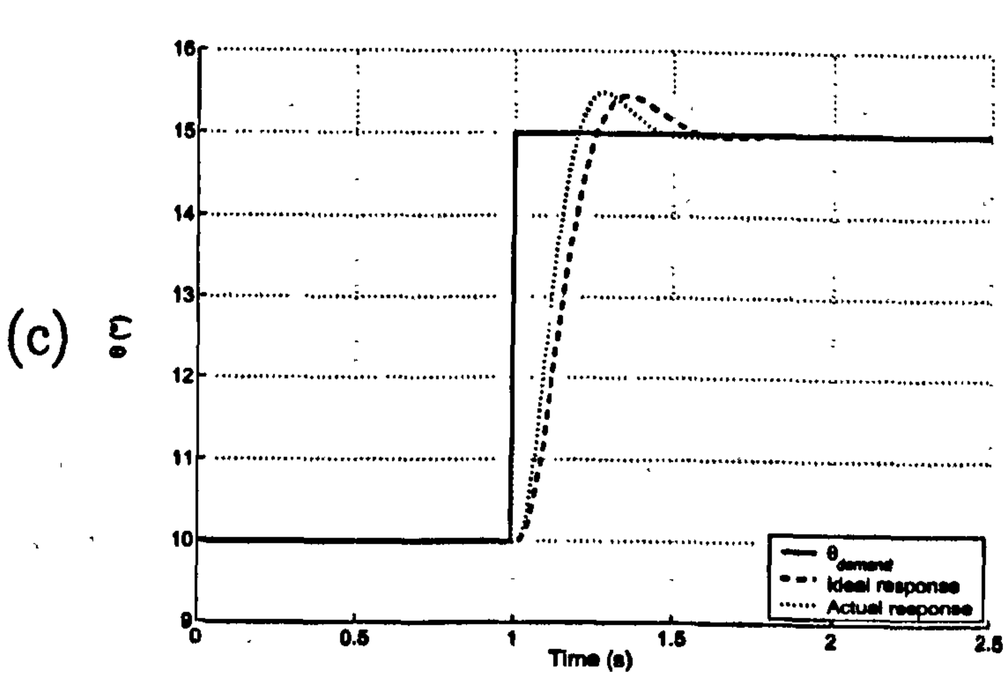


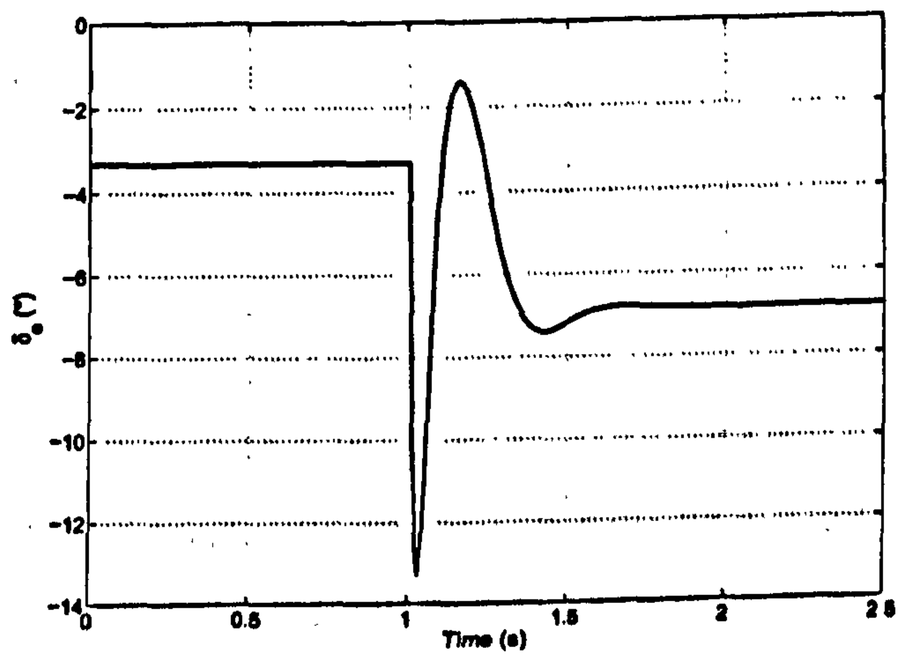


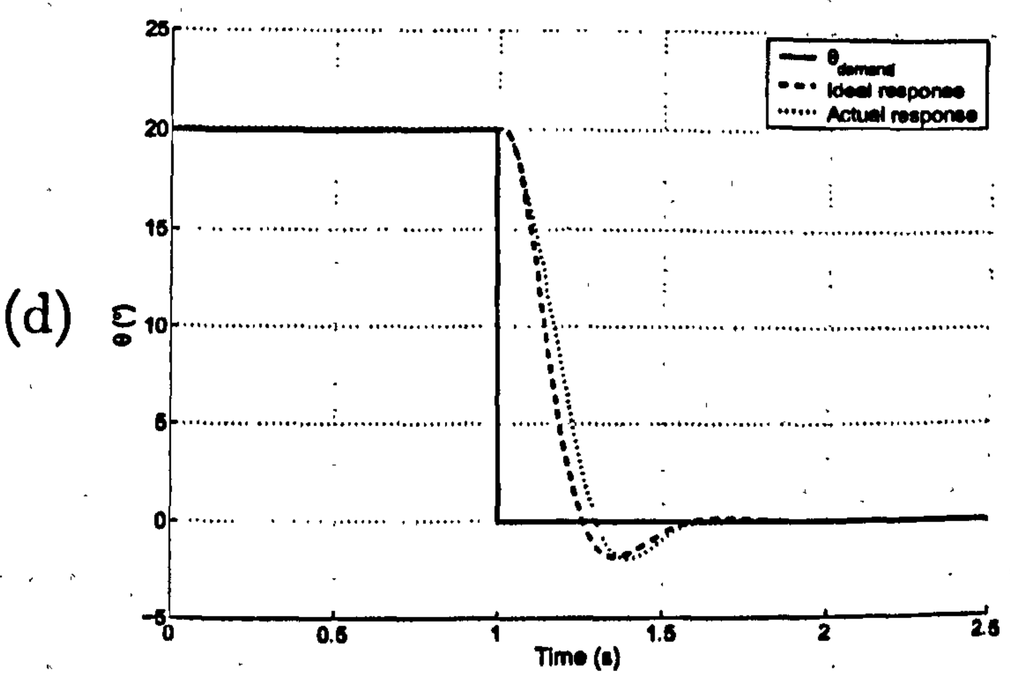


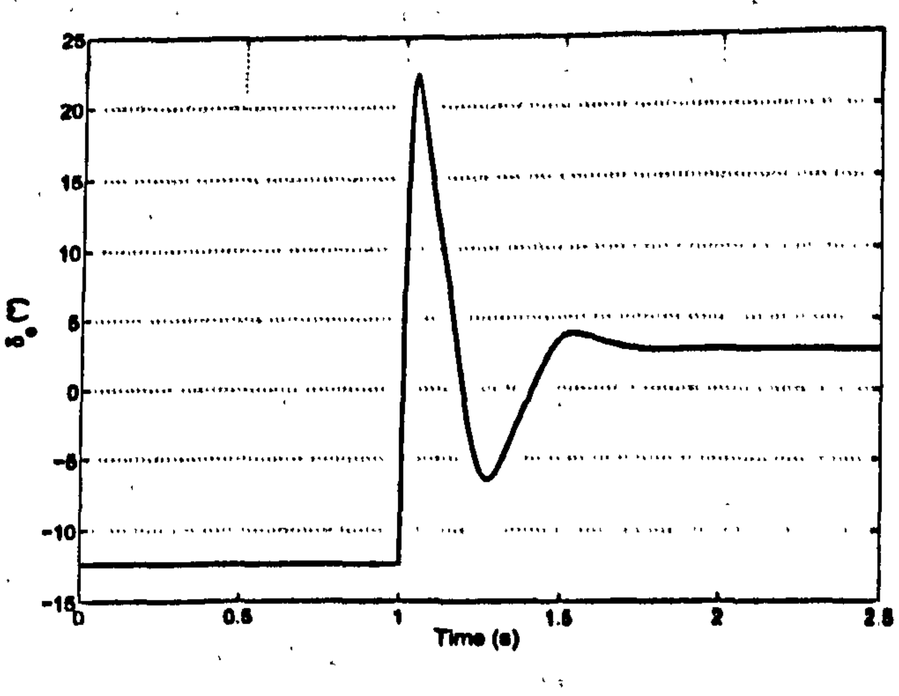


Figure 8.8: Numerical step responses for the non-linear feed-forward controller with eigenstructure-assigned state feedback.

and actual response exhibited for the 0° to 20° step input (Figure 8.8(b)) where the actual response does not overshoot the final value. This may be due to the highly non-linear nature of the model at this angle-of-attack. In general, the discrepancies between ideal and actual responses can be attributed to three factors:

- non-linearity in pitch rate response causing the gains to be incorrect during transient motions. The state feedback gains were found for trimmed conditions ($q = 0$); if the operating point moves from the equilibrium condition (during transient motion, for example) the gains may no longer be correct.

- instantaneous changes in gain caused by scheduling. The state feedback gains will change instantaneously when a step change in reference demand occurs. This should be largely negated by the feed-forward term, but errors in this term and errors in the state-feedback gains may still cause an undesired response. Ideally, to avoid problems such as this one would not schedule the gains against the reference input. However, there are also problems associated with scheduling control system gains against system states. This is discussed further in Chapter 9.

- numerical implementation; errors may be introduced by (amongst other factors) the linearisation process, accuracy of the eigenstructure assignment routine, and interpolation of the resultant gains.

Again, this controller was found to exhibit poor robustness; errors in the model or noise/external disturbances will cause steady state and transient errors in the response. To demonstrate this lack of robustness, simulations were carried out with artificial inaccuracies added to the model. In Figure 8.9, an offset of 0.1 was added to the pitching moment coefficient, $C_m$, in the aircraft model. The response is offset and there is a large steady state error, but stability has been maintained. The transient response has also changed, and exhibits lower-than-ideal overshoot.

Figure 8.10 shows the response of the model to an identical step input, but with a fixed offset of 5 in the feed-forward gain (without the offset in the aircraft model). This simulates inaccuracies in the modelling and control system design phases (as already demonstrated by the differences between responses in Figure 8.8). Again, the response displays a relatively constant offset in pitch angle, with a slight change in transient response.

For the time histories shown in Figure 8.11, the feed-forward curve (Figure 8.6(d)) was replaced with a straight line from 26.9 to −108.5 to simulate errors in the gain calculations. A large offset is observed, with increased damping. Figure 8.12 shows a simulated step response with the full non-linear actuator model in place of the linear actuator used for designing the controller. The response is similar to the linear-actuator response, however, there is continuous actuator movement, even when the system is at a 'steady' state.

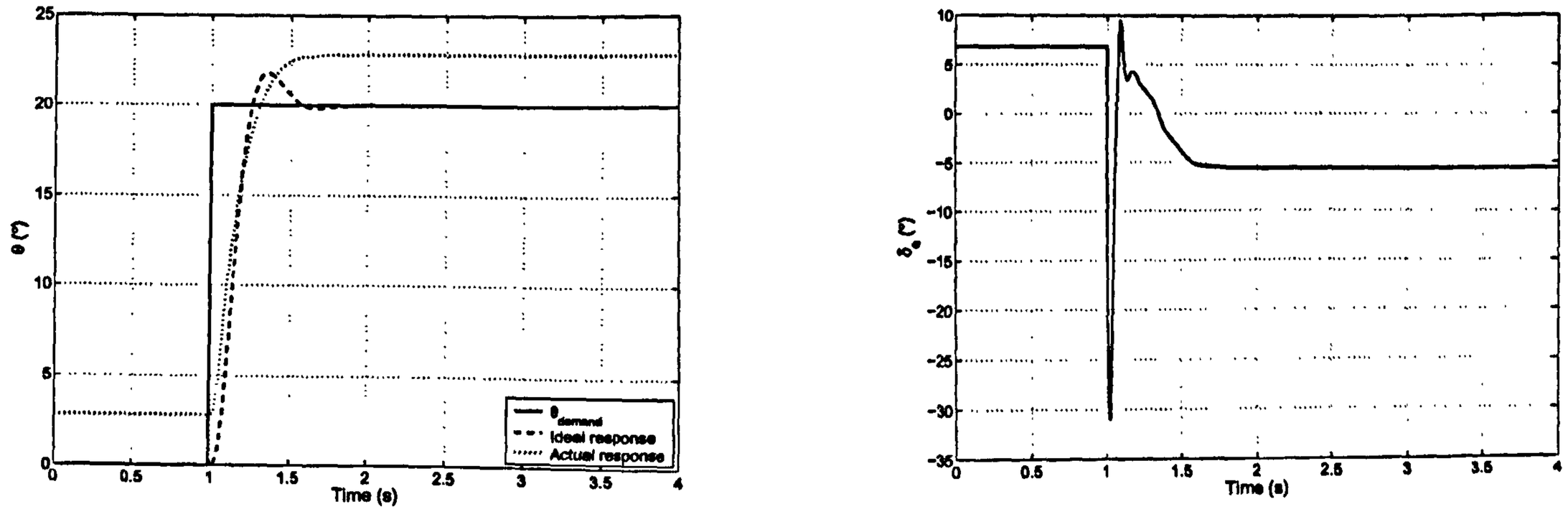


Figure 8.9: With $C_{m_{\text{offset}}} = 0.1$.

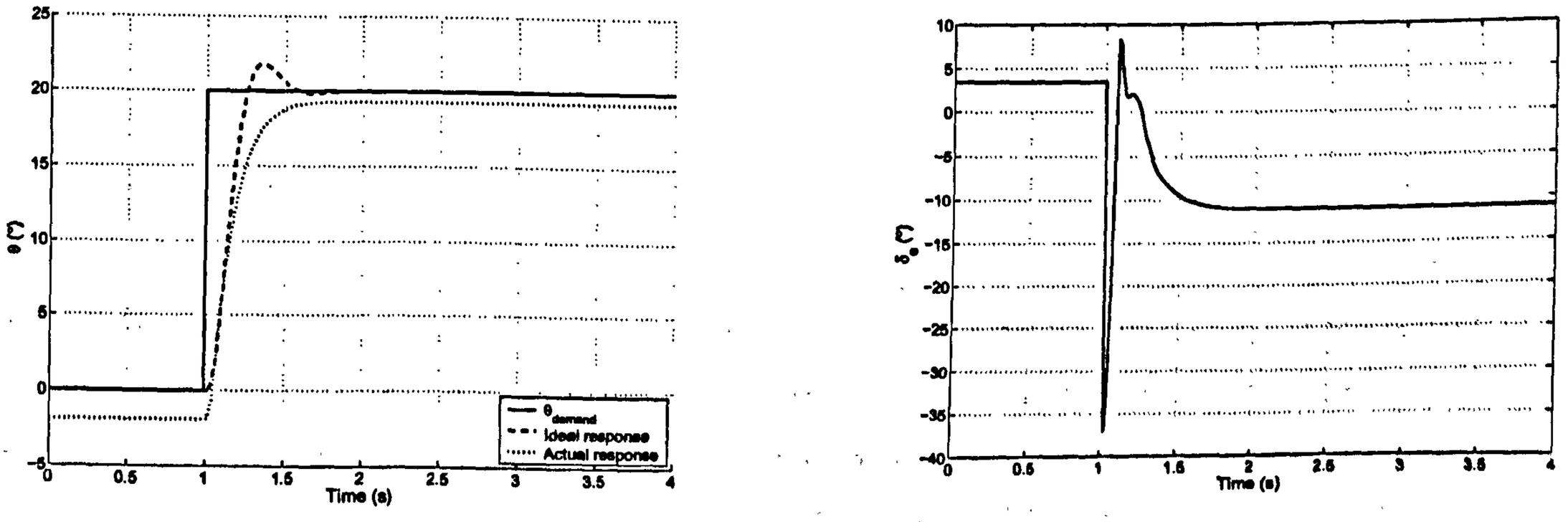


Figure 8.10: With fixed feed-forward offset of 5.

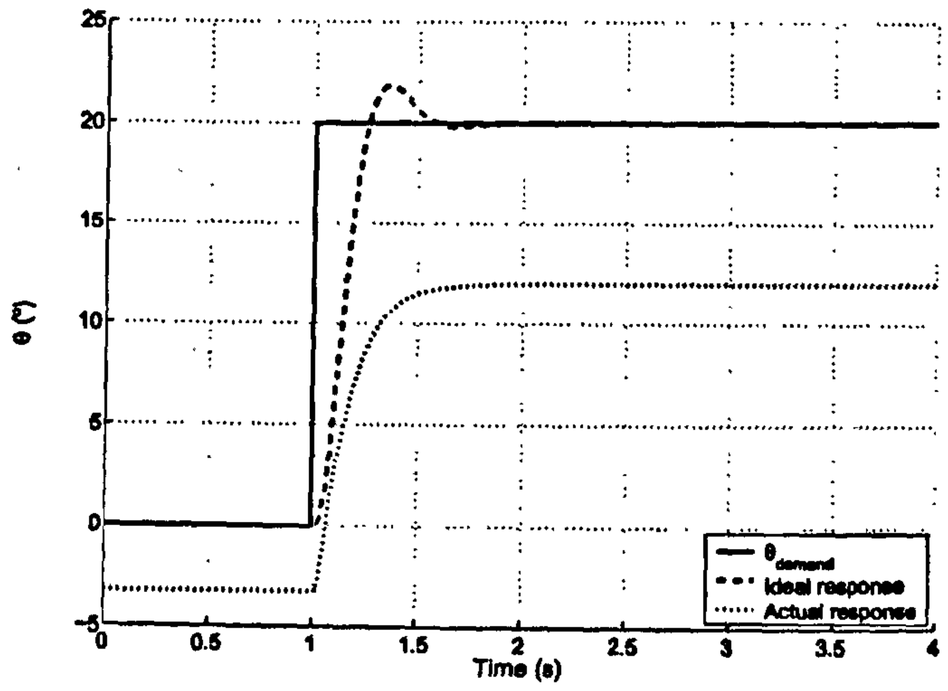


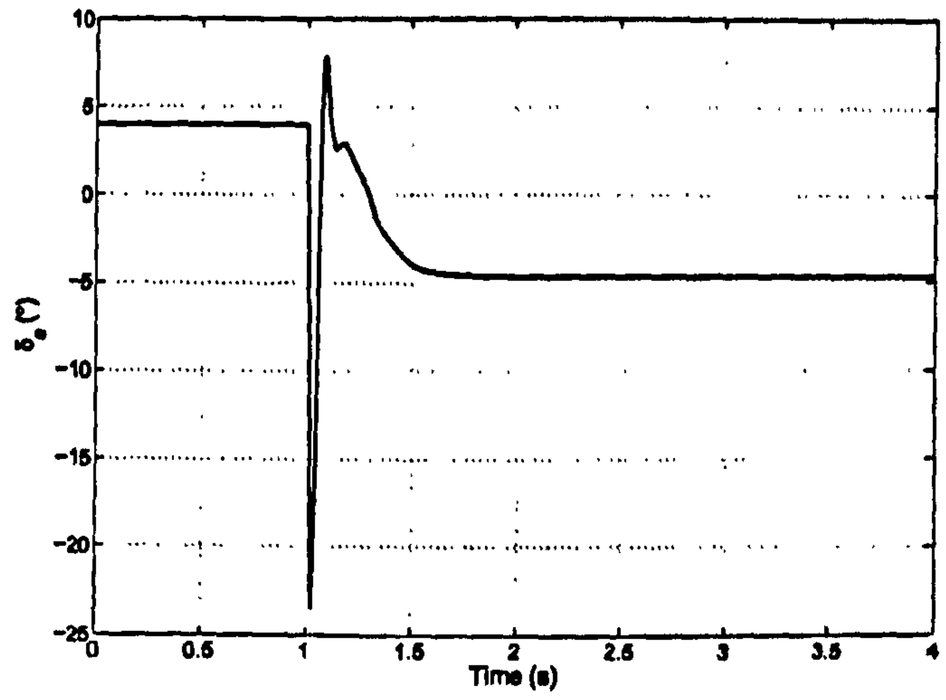


Figure 8.11: With wrong feed-forward gain.

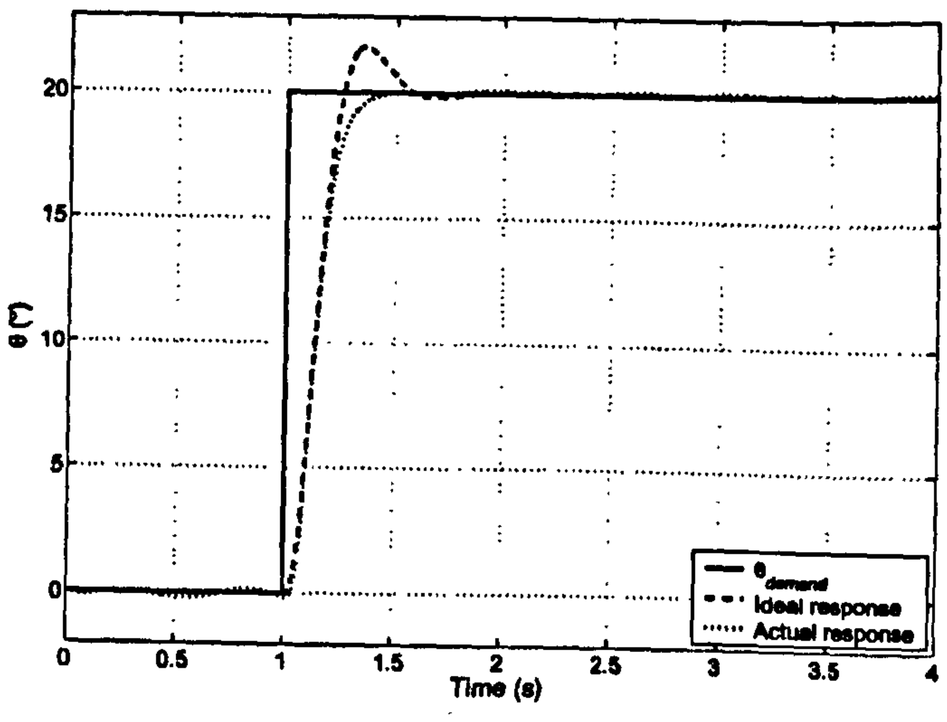


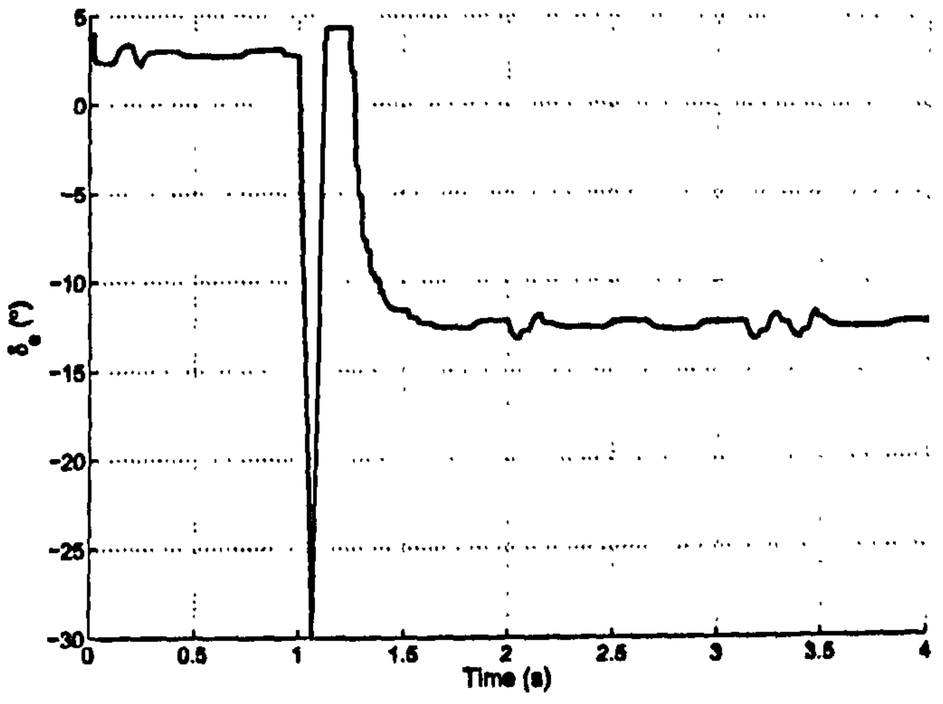


Figure 8.12: With full non-linear actuator model.

### Experimental Validation

When testing this controller on the experimental rig, several regions of large-amplitude self-excited oscillations became apparent, which were only triggered in certain places by rapid input demands. A small window of these oscillations can be seen in the experimental bifurcation diagram in Figure 8.13 at $\theta_{demand} \approx 20°$. However, due to the smooth and slowly-varying nature of the input, the rest of the bifurcation diagram shows a single fixed point attractor[2]. In general, the controller has removed the regions of unwanted oscillation and straightened and stabilised the fixed point branch on the bifurcation di-

[2]It is interesting to note the noise spike visible at $\theta_{demand} \approx 8°$. This is typical of the occasional large interference that would be picked up by the system; it is likely that this was caused by a strip-light being turned on, or another electrical device in the lab, and highlights the need for minimising the length of wiring from/to the model, and the importance of shielding wiring looms.

agram. There is a slight discrepancy (difference in gradient) between the experimental equilibrium branch and the ideal branch ($\theta = \theta_{demand}$, Figure 8.13) due to small inaccuracies in the feed-forward inverse trim curve taken from the open-loop experimental bifurcation diagram (Figure 4.2). However, in general the experimental response remains within a 2° band of the desired steady-state solution.

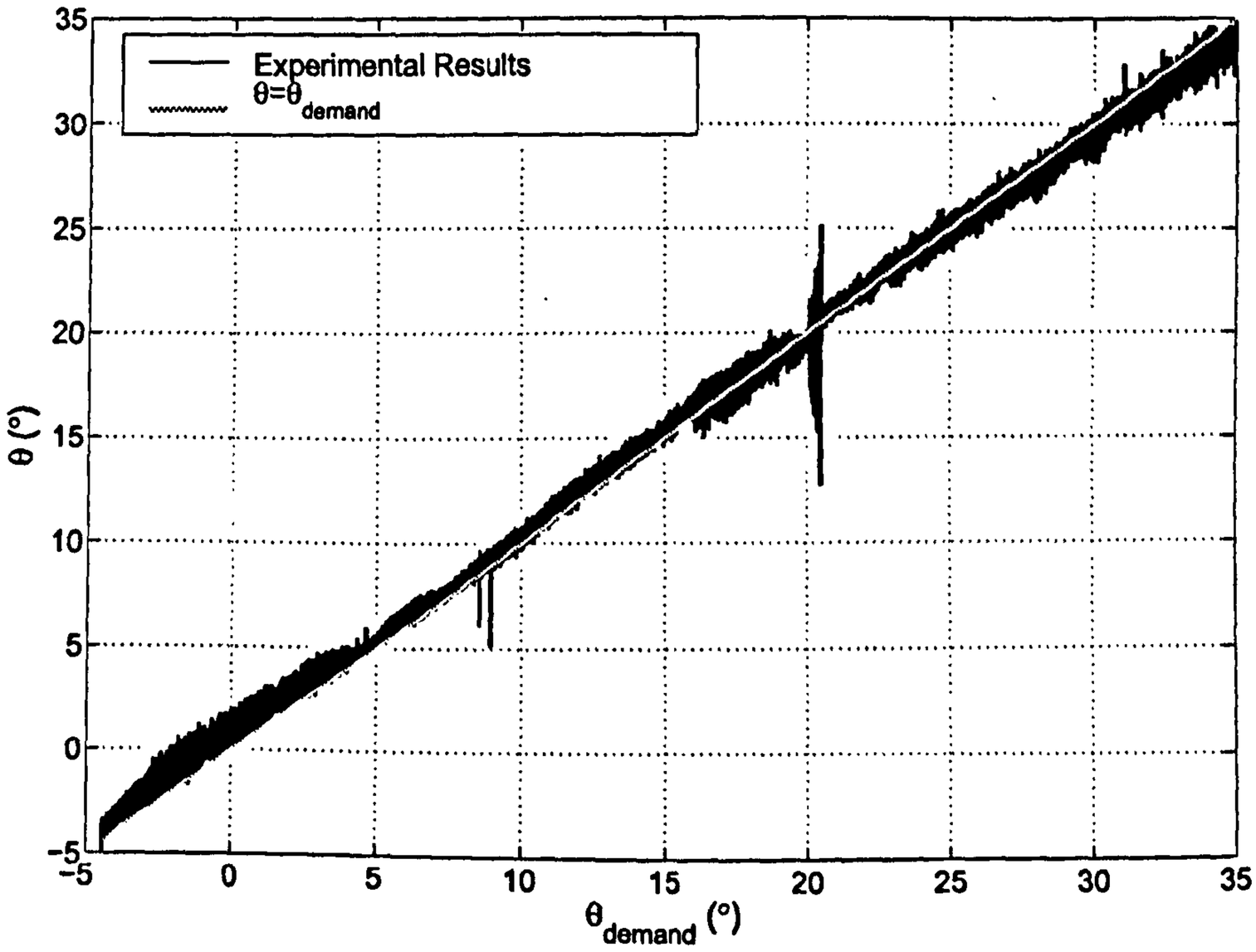


Figure 8.13: Experimental bifurcation diagram for feed-forward and gain-scheduled state feedback controller, showing small window of self-excited oscillations at $\theta_{demand} \approx 20°$.

An experimental step input time history is presented in Figure 8.14, clearly showing the introduction of self-excited oscillations. It was thought that these oscillations were caused by a coupling between large pitch rate feedback gains and lags in the system (aerodynamic and actuator). To investigate the effect of pitch rate feedback, and the apparent multi-attractor nature of the system due to the excitation required to start the oscillations, an experimental bifurcation run was performed where pitch angle demand is kept constant at 5°. According to the gain scheduling law in Figure 8.6(a), this would correspond to a fixed pitch rate feedback gain of 0.75. Therefore, to investigate the effect of varying $K_q$, the gain was varied over the range 0 to 1 (Figure 8.15). Each bifurcation run was recorded over 5 minutes (slightly less than desirable, to avoid possible damage from high actuator usage, hence there may be some small transient effects present). There is a clear region ($0.43 < K_q < 0.78$) where two attractors of the closed loop

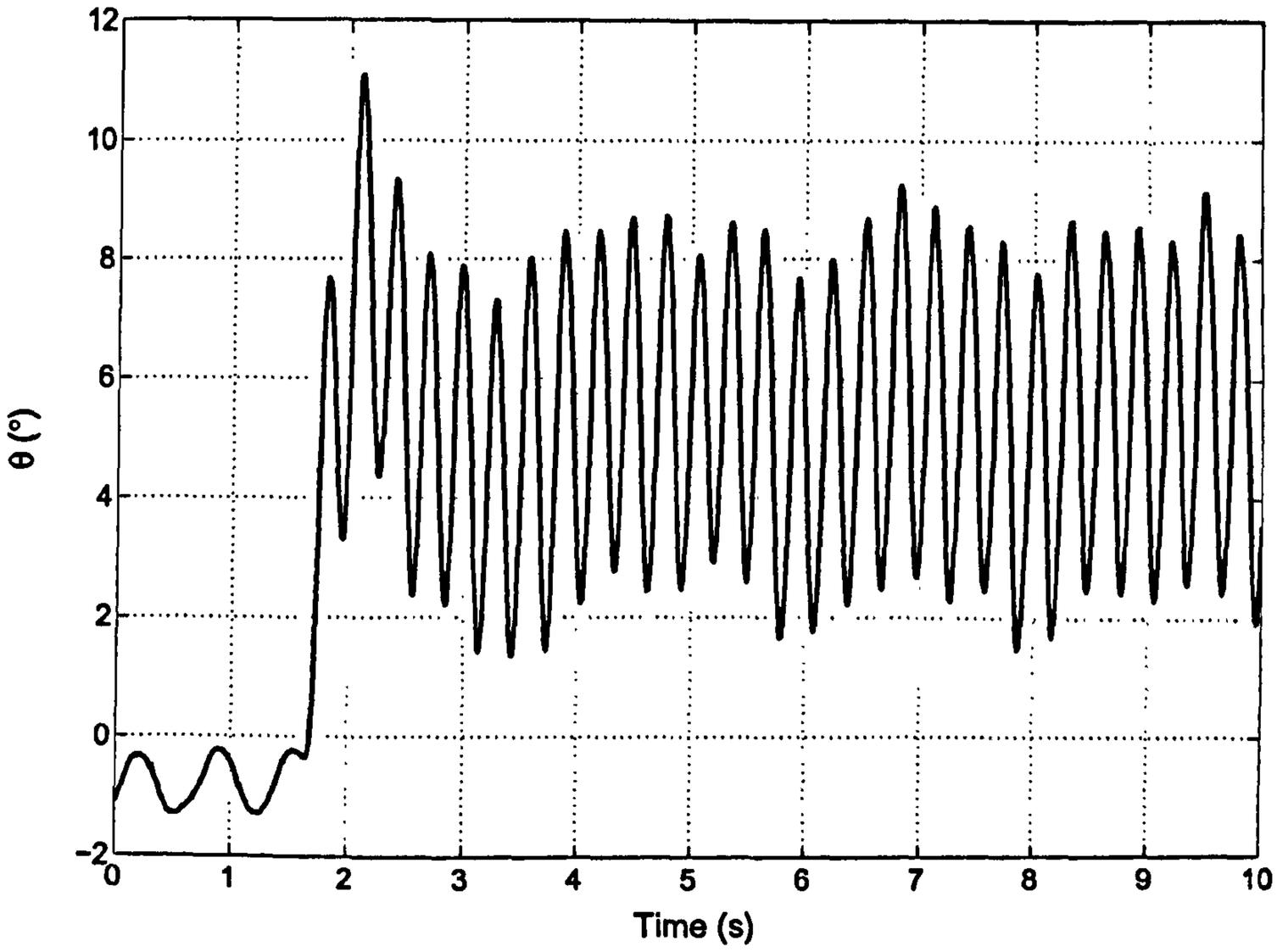


Figure 8.14: Example experimental step response (for feed-forward and gain-scheduled state feedback controller) showing self-excited oscillations.

system exist; a stable limit cycle and a stable fixed point. Note also the hysteresis at very low pitch rate feedback gains: the amplitude of the pitch oscillations is much larger when the pitch rate gain is decreasing.

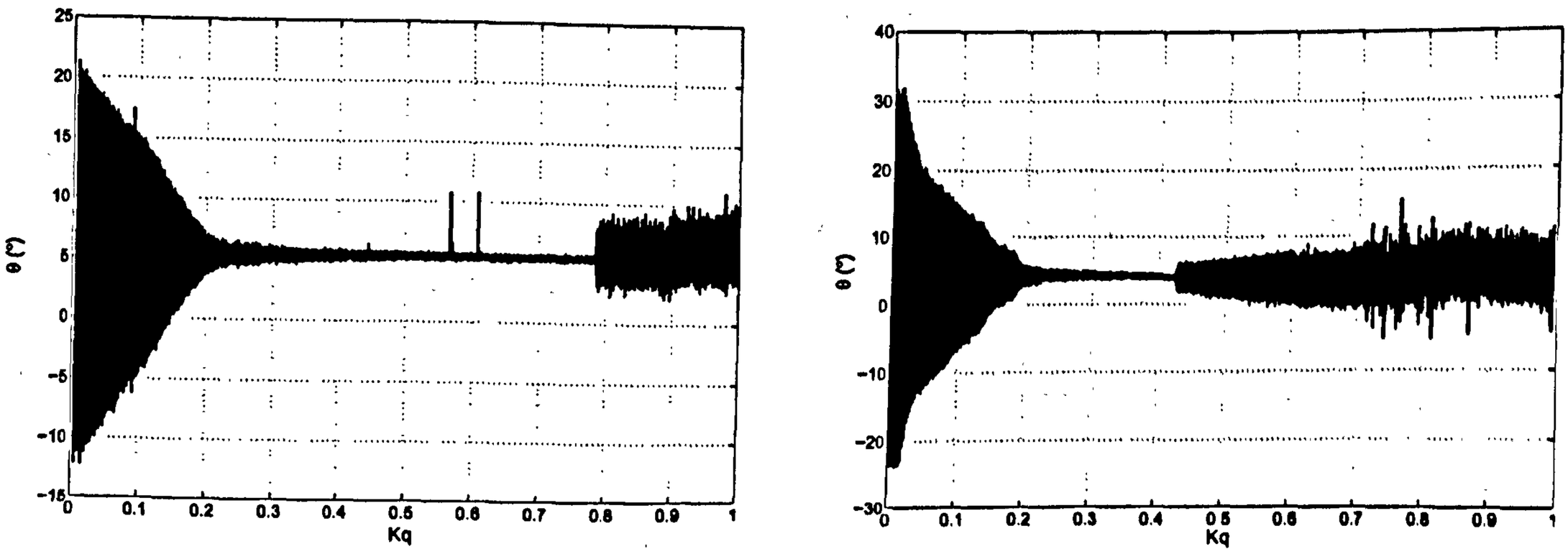


(a) (b)

Figure 8.15: Experimental bifurcation diagrams for $\theta_{demand} = 5°$ with (a) increasing $K_q$ and (b) decreasing $K_q$ showing hysteresis in the range $0.43 < K_q < 0.78$.

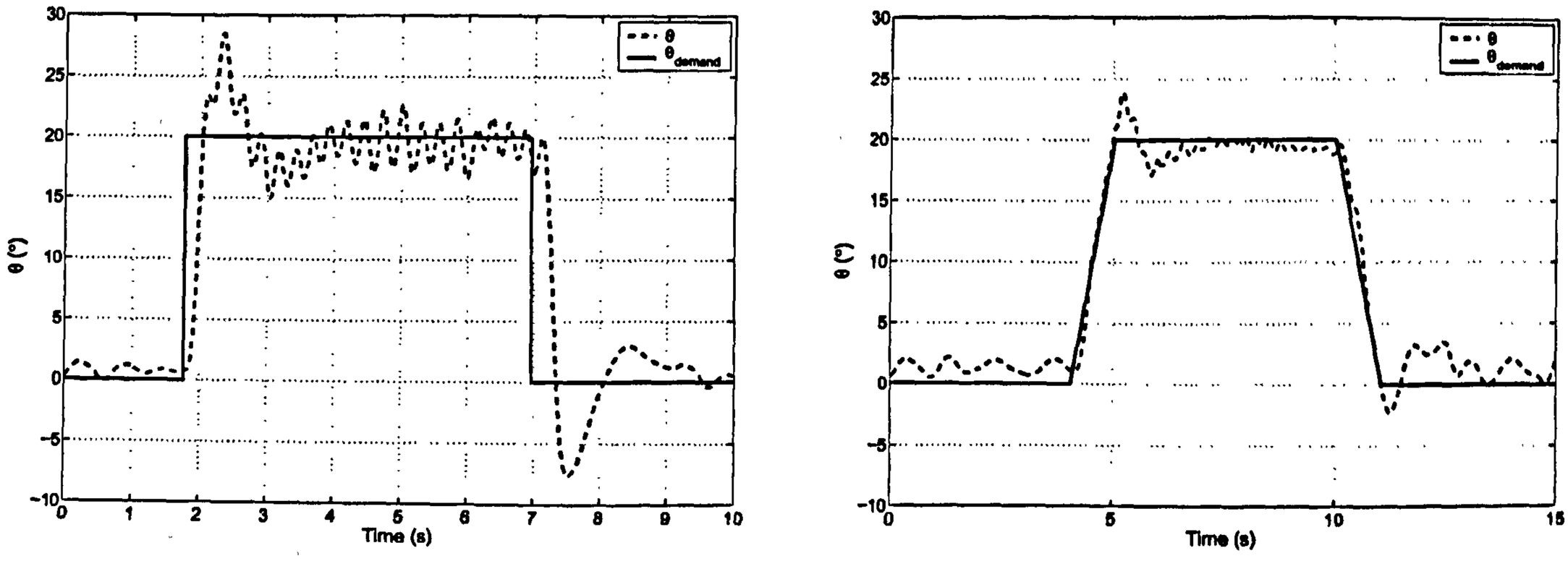


(a) (b)

Figure 8.16: Comparison of 20 degree step and ramp inputs for the feed-forward plus state feedback controller.

Figure 8.15 does indeed show that the oscillations can be eliminated by reducing pitch rate feedback gain; for $\theta_{demand} = 5°$ a value of $K_q < 0.43$ would guarantee that there are no self-excited oscillations.

Figure 8.16 confirms the multi-attractor behaviour of the closed loop system by comparing experimental step (a) and ramp (b) inputs. The step response triggers the oscillatory instability, however, the slower-varying ramp does not and the system settles to the steady-state solution.

The reason for these unexpected oscillations may be that an un-modelled lag was present in the system which, when combined with a pitch rate feedback gain of above approximately 0.5, would give a 180° phase lag and lead to oscillatory instability[3].

The un-modelled lag was most probably in the actuator, for two reasons:

- When designing the control laws, a simple second order linear actuator model was used. The full non-linear actuator model (Section 3.3.5) would not have allowed

[3]It is also possible that there are one or more oscillatory attractors outside the stability region of the model bifurcation diagram shown in Figure 6.1. However, this would almost certainly have been observed during time simulations of the model, or found as a solution branch when performing numerical bifurcation analysis.

the eigenstructure assignment routines to calculate the required feedback gains due to its large deadband (±0.75°). After linearisation of the system with the non-linear actuator model, the $\boldsymbol{B}$ matrix would be zero (unless a very large perturbation is used, which would reduce accuracy of the gains significantly), and the eigenstructure routine would not be able to solve for the state feedback gains. Thus, the second order linear actuator model was used, but this did not represent the dynamics of the real actuators particularly well (see Section 3.3.4). This would certainly cause the gains to be erroneous.

- Both the linear and non-linear servo models were derived with the actuators off the model, under a no-load condition (apart from the potentiometer, see Section 3.3.4). The dynamics of the actuator in the model are almost certainly different, due to aerodynamic forces and moment of inertia of the control surfaces.

Another source of error on the experimental rig is the lack of tailplane angle feedback. The gain-scheduled controllers were designed to use control surface position feedback to enhance the actuator dynamics, however, as this was not available during experiments, the linear actuator model was used to predict the position of the control surface. This predicted position is almost certainly wrong, especially if there is a further un-modelled delay in the actuators.

To support this hypothesis, simulations were performed with an extra delay added to the actuator (Figure 8.17), and did reproduce the type of oscillatory dynamics observed on the rig (although offset from the demanded angle).

As a further test, a gain-scheduled controller was designed using only pitch angle, pitch rate and integrator feedback (no tailplane deflection feedback). Thus, with only three states being fed back, it was only possible to place three eigenvalues; the two aircraft poles and the integrator pole. Without the tailplane deflection feedback, one of the closed-loop actuator poles moved to the region between −7 and −15 (i.e. affecting the transient response considerably given that the aircraft poles were at $-7.2 \pm 9.6i$ and the integrator pole was at −15). It is therefore feasible that, without tailplane position feedback, it is not possible to obtain the desired response. This will be exaggerated by the extra delay/non-linearities in the actuator on the experimental rig. The response of the actuator can be enhanced by feeding back control surface position (to improve the stability at high frequency), but this is not available on the experimental set-up.

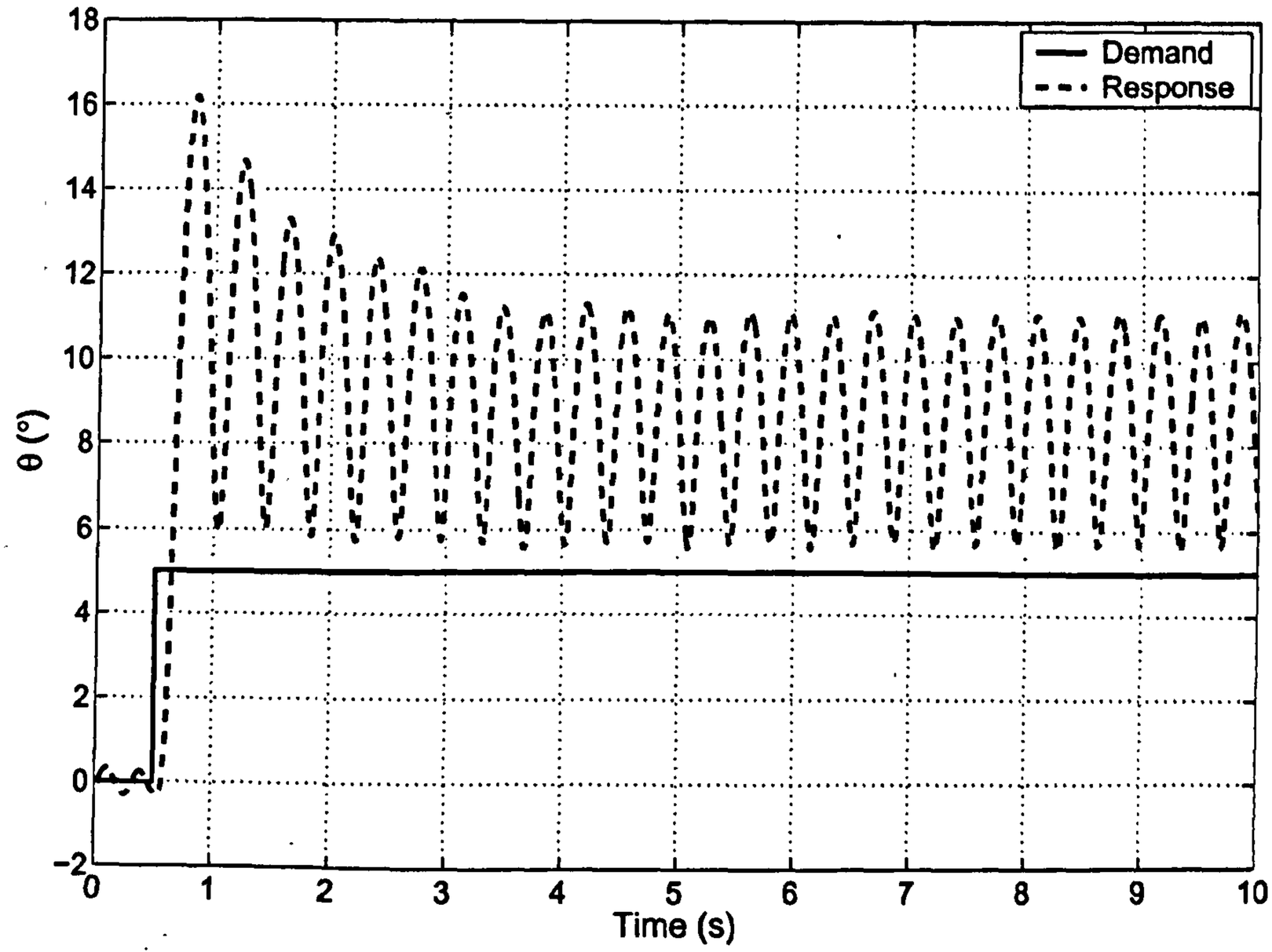


Figure 8.17: Simulated step response with extra delay added to actuator model, showing similar self-excited oscillations to the experimental rig.

### 8.2.3 Feed-Forward Plus Integrator with State Feedback

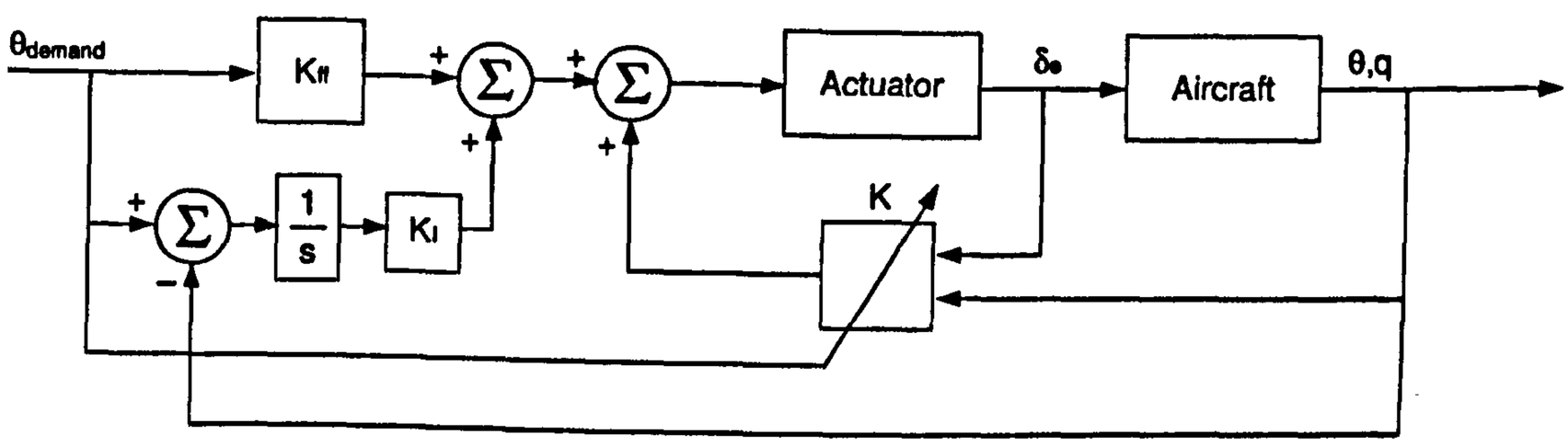


Figure 8.18: Non-linear feed-forward with integrator plus demand-scheduled state feedback.

To improve the robustness of the controllers designed previously, an integrator was added to the control system from Section 8.2.2, acting on pitch angle error. This control system is shown in Figure 8.18 with the corresponding control equation given by:

$$u = K_{ff}(r) + K_1(\theta)q + K_2(\theta)\theta + K_3(\theta)\delta_e + K_I \int (r - \theta)dt. \tag{8.7}$$

An integrator gain of −10 was chosen by trial-and-error to maximise the speed at which steady state error was reduced without introducing oscillatory behaviour.

Simulated step responses for this controller are shown in Figure 8.19. The transient responses have been adversely affected by the addition of the integrator. This is particularly evident in the step response from 20° to 0° (Figure 8.19(d)). However, the robustness has indeed been improved (in terms of steady state error), as shown by Figures 8.20 to 8.22, where the same robustness tests applied to the previous controller are tested. Although the transient responses do not match the ideal response, the responses are stable and the integrator ensures low frequency tracking response.

(a)

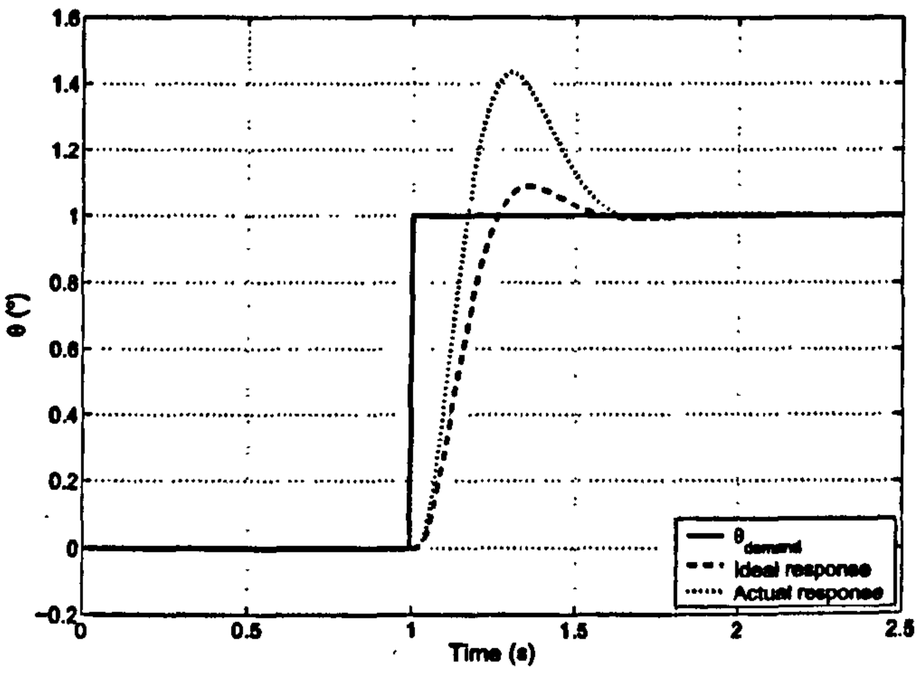


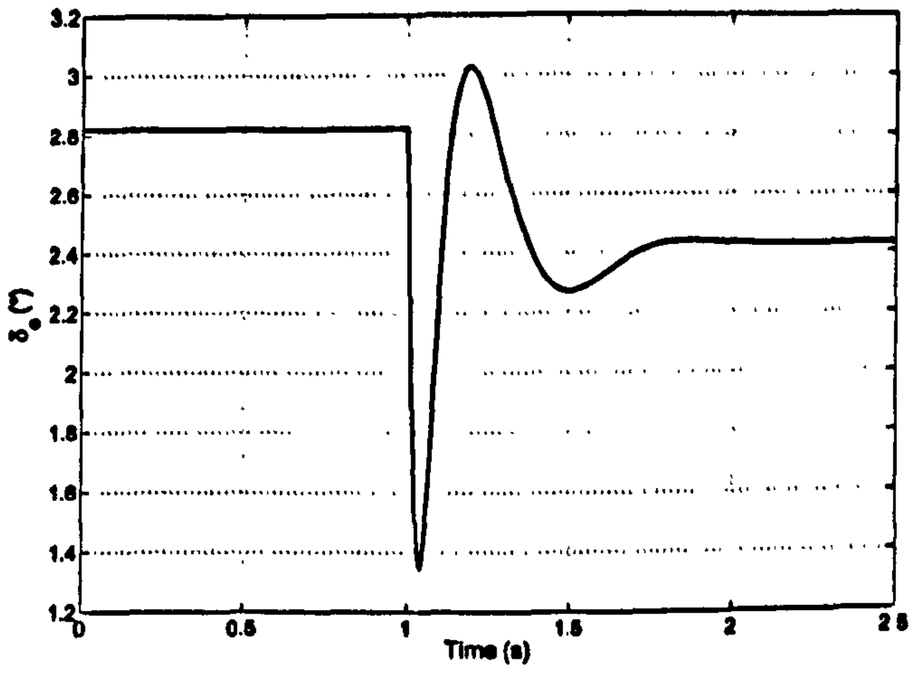


(b)

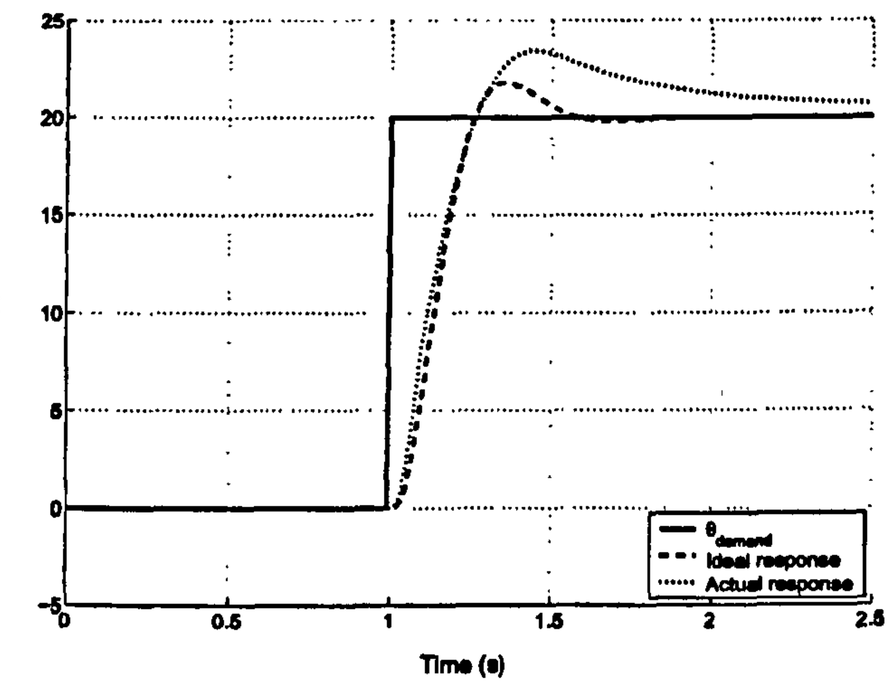


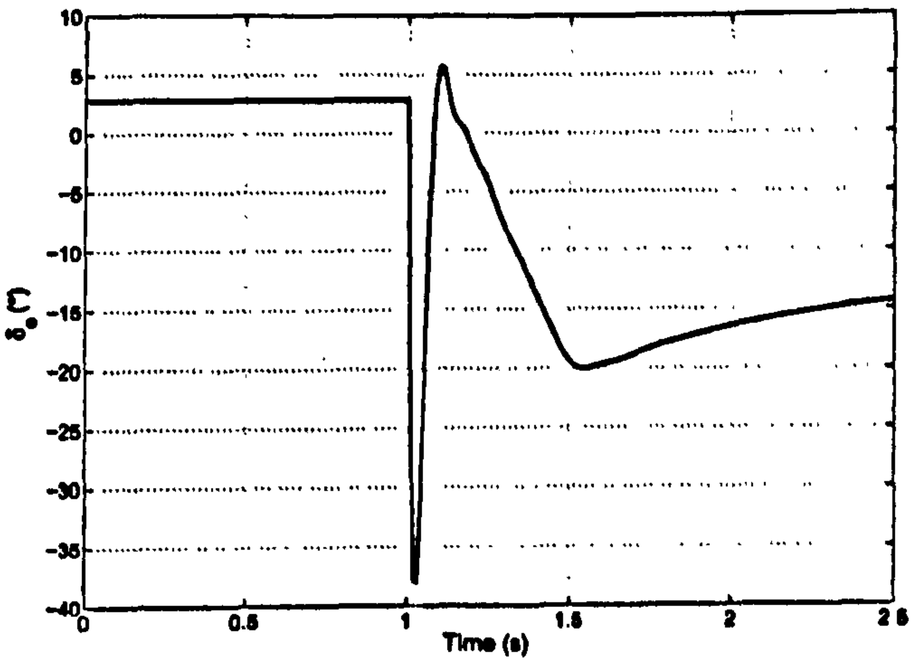


(c)

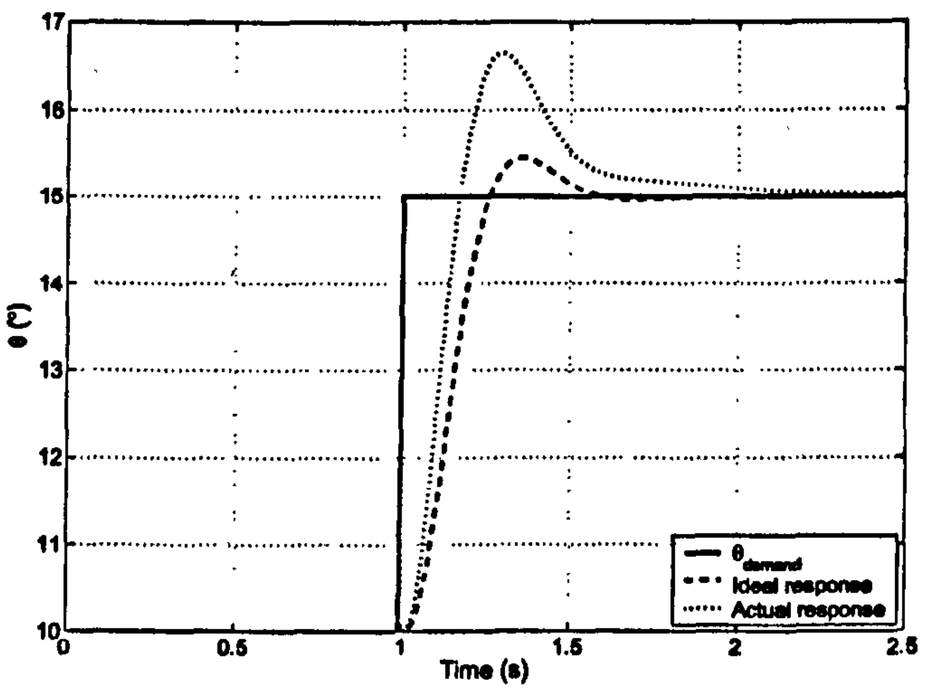


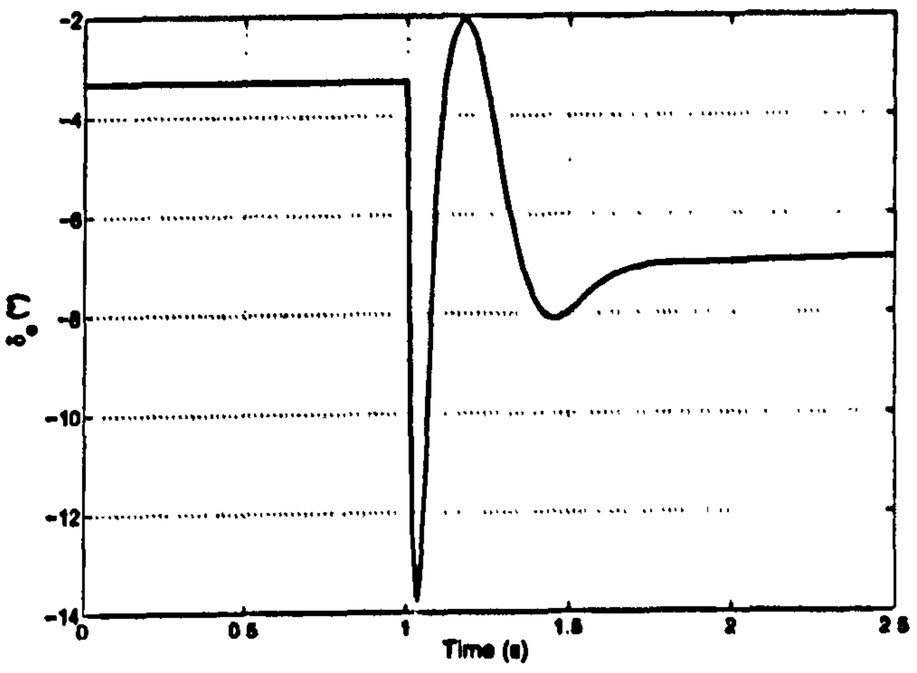


(d)

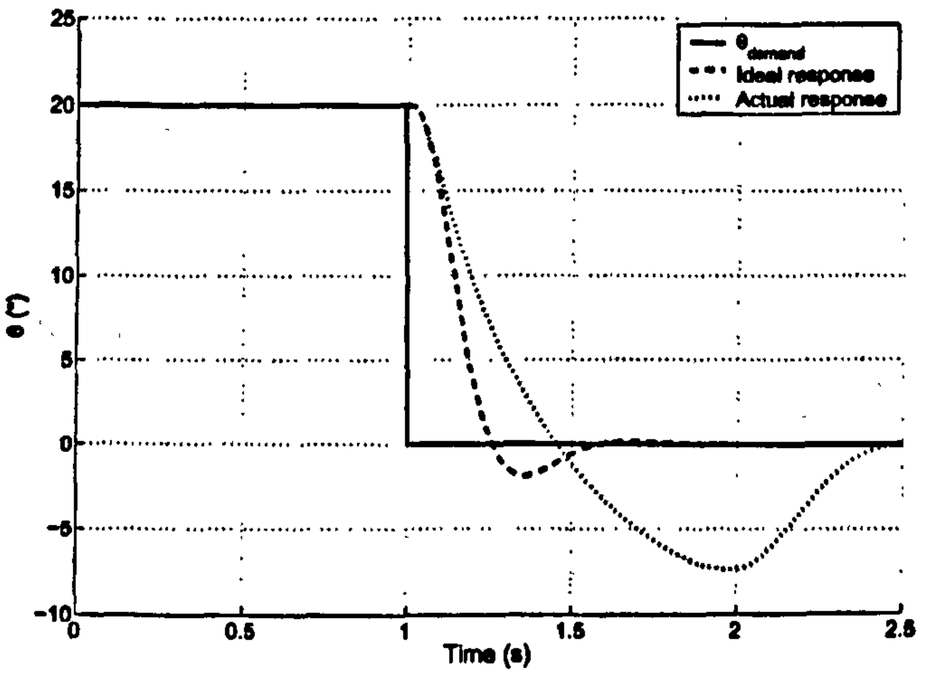


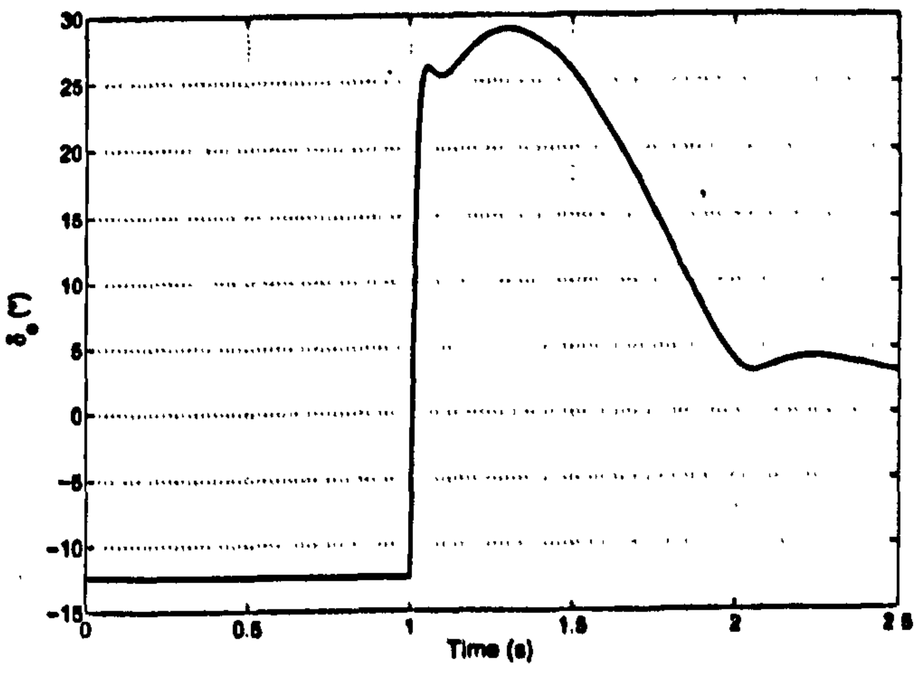


Figure 8.19: Simulated time histories for the feed-forward plus integrator with static feedback controller.

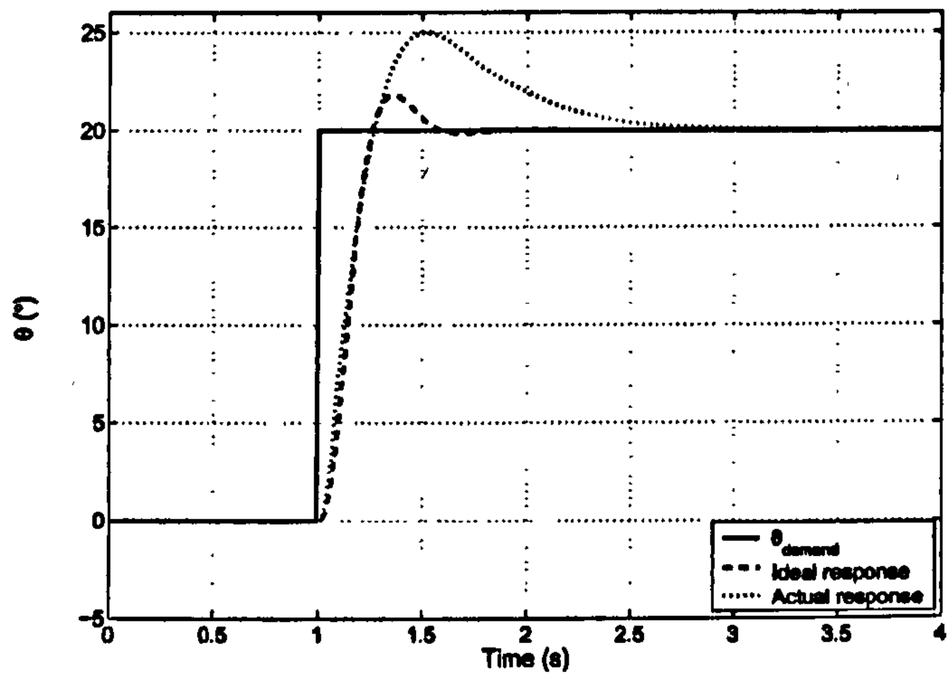


Figure 8.20: With $C_{m_{\text{offset}}} = 0.1$ ($K_{int} = -10$).

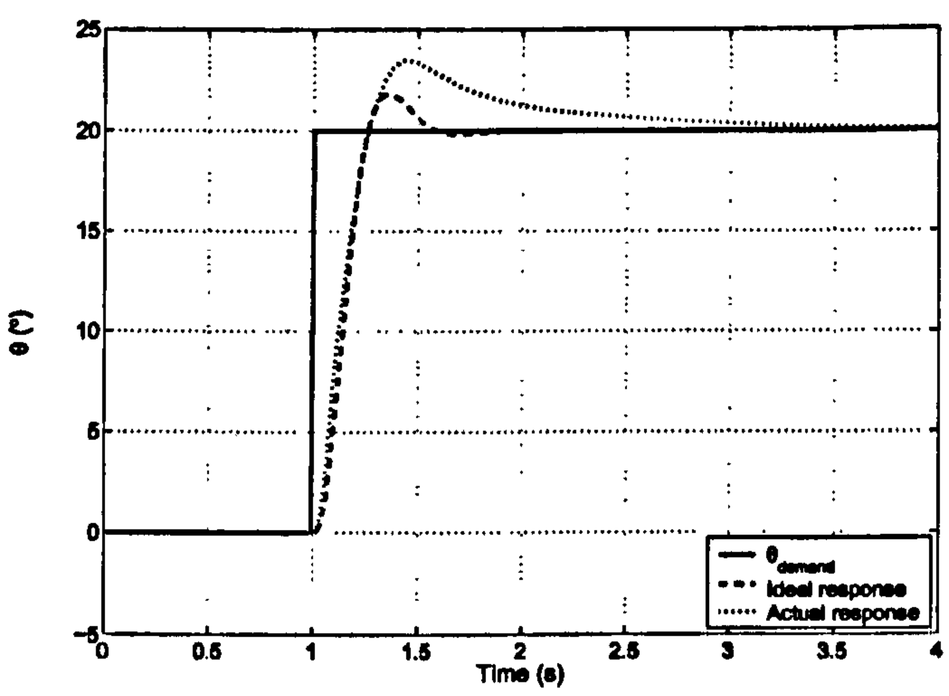


Figure 8.21: Fixed feed-forward offset of 5 ($K_{int} = -10$).

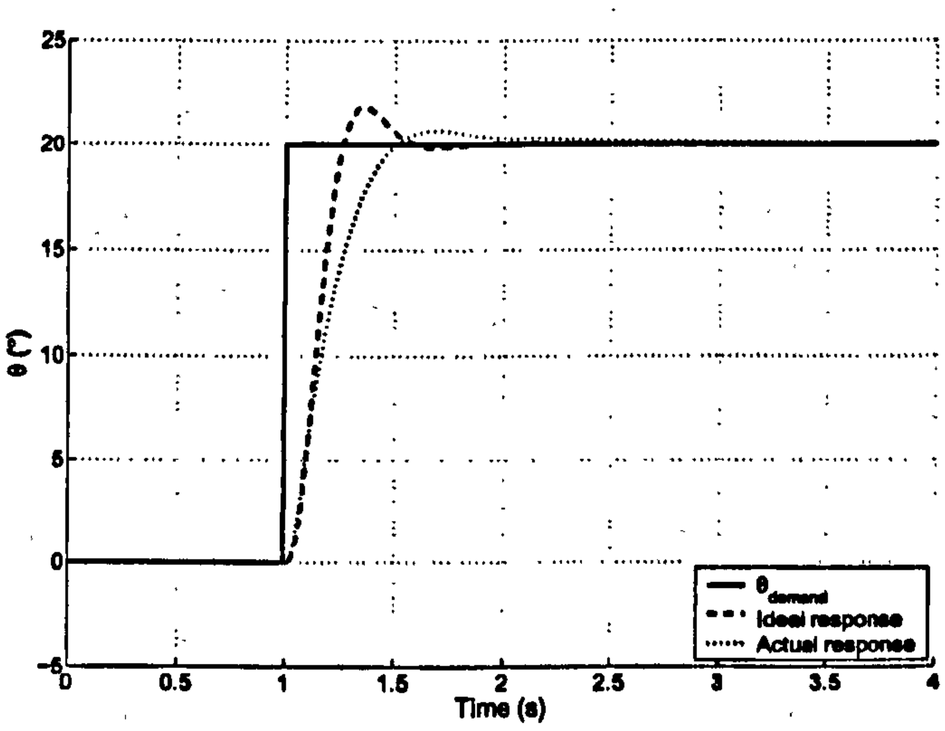


Figure 8.22: Wrong feed-forward gain ($K_{int} = -10$).

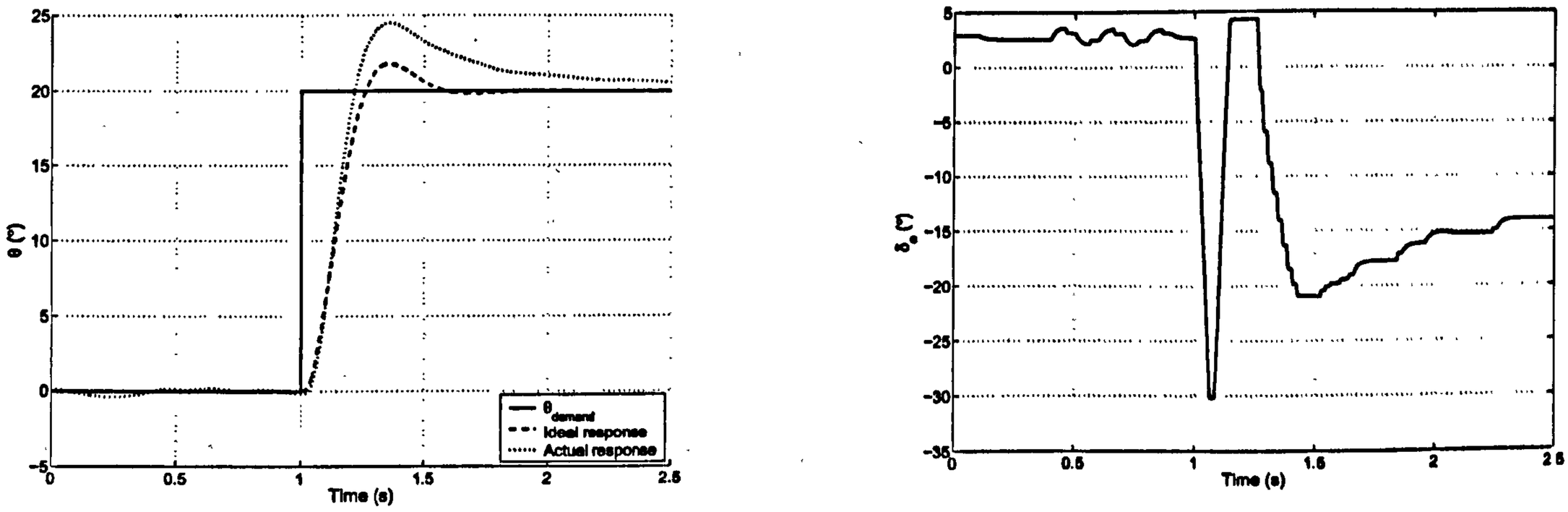


Figure 8.23: With full non-linear actuator ($K_{int} = -10$).

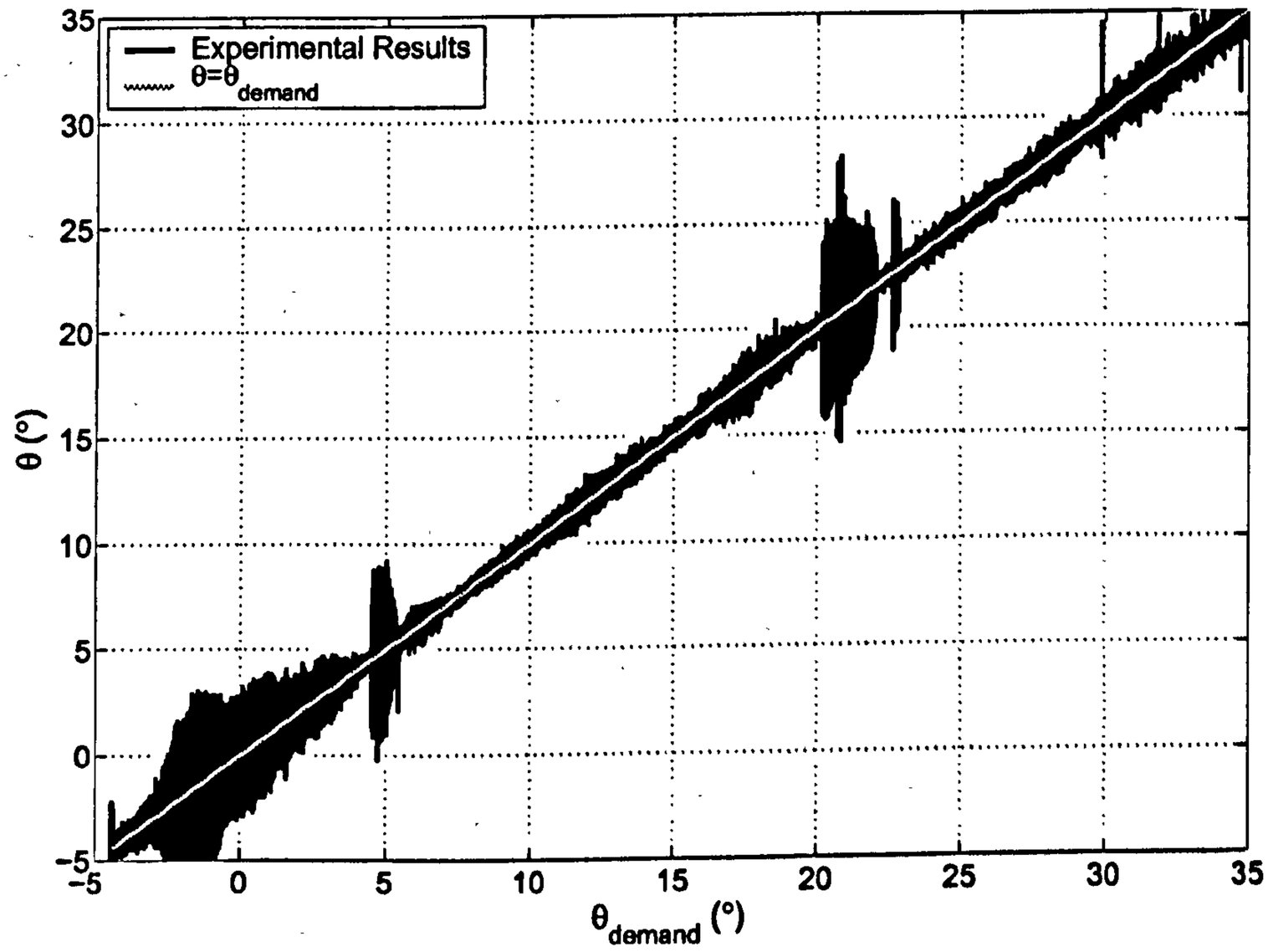


Figure 8.24: Experimental bifurcation diagram for feed-forward and state feedback controller with fixed-gain integrator.

Again, this controller was tested on the experimental rig and showed slow oscillations at all angles, along with faster oscillations at others (e.g. $\theta_{demand} = 5°$). This is illustrated by the experimental bifurcation diagram in Figure 8.24, where the integrator has improved robustness (mean pitch angle matches the desired pitch angle) but has added low frequency oscillations in several regions (e.g. $-4° < \theta_{demand} < 4°$). These oscillations were attributed to two factors:

- Tailplane actuator deadband/backlash/stiction. The tailplanes would sit at a fixed angle while the pitch error was integrated until the demanded input was large enough to cause the actuators to move. This caused them to move beyond the desired position and 'stick' until the integrator had again changed value enough for the actuators to move. This process was self-sustaining, and caused oscillations throughout the envelope, although in some regions (particularly at low $\alpha$) it became more obvious. This phenomenon could be analysed more closely with the availability of tailplane position feedback.

- pitch rate feedback limitations. The pitch rate feedback signal at very low angular rates was not accurate due to noise and drift in the sensor. Therefore, the low pitch rate oscillations caused by the integrator/backlash combination were not being damped by the pitch rate feedback.

The higher frequency pitch-rate-feedback induced oscillations described previously were also evident for this controller, and in some regions both were present (Figure 8.25).

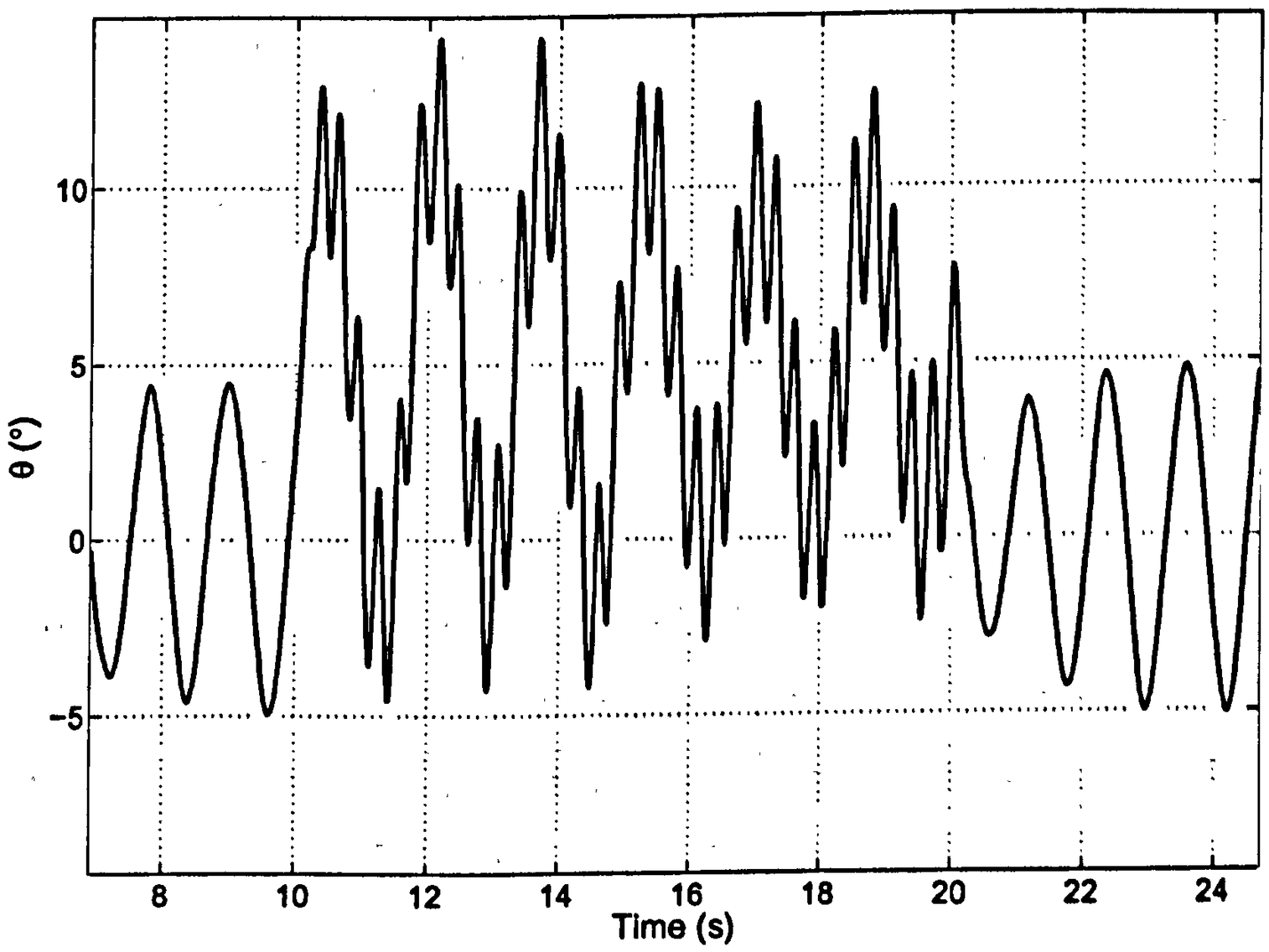


Figure 8.25: Experimental 0 to 5 degree step response (for feed-forward plus integrator and gain-scheduled state feedback controller) showing period-2-type response.

### 8.2.4 Eigenstructure-Assigned PI Controller with State Feedback

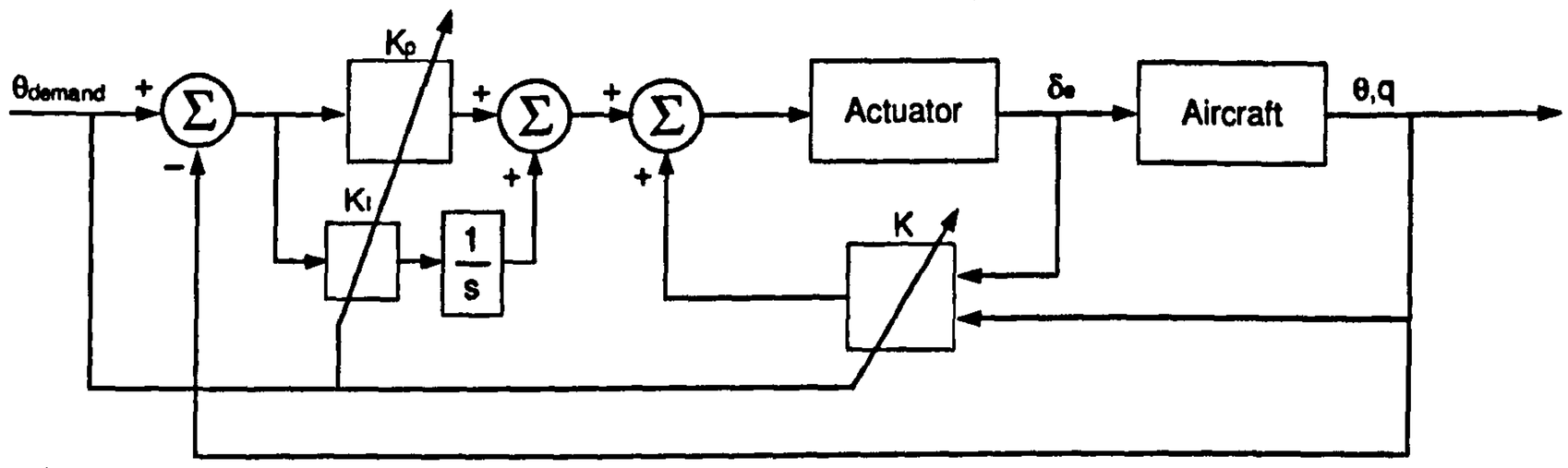


Figure 8.26: Eigenstructure-assigned PI controller with state feedback.

To demonstrate how the gains for the controller presented in Section 8.2.3 can be constructed in a single process, eigenstructure assignment was used to find all 5 gains in a PI-with-state-feedback controller. There is an implementation problem, however, associated with the gain of the proportional term in the forward path, identified in [18]. The eigenstructure assignment routine calculates state feedback gains, however, in Figure 8.18 there is no state on which to calculate a gain. Therefore, the structure was changed slightly to that shown in Figure 8.26 where a proportional gain acts on the pitch angle error. The control equation for this system is therefore:

$$u = K_1(\theta)q + K_2(\theta)\theta + K_3(\theta)\delta_e + K_4(\theta)\int(r-\theta)dt + K_5(\theta)(r-\theta). \qquad (8.8)$$

To allow the eigenstructure routine (which calculates *state* feedback gains) to calculate the forward-path proportional gain it is necessary to add a fast first-order lag directly in front of it, and add this as an extra state to the system equations [18]. In this case a first order lag with its pole at -5000 was used. The new gains are shown in Figure 8.27.

Step response time histories for this control system are shown in Figure 8.28. In general the response is good, closely tracking the ideal response, even with large amplitude inputs. There is a larger discrepancy between the actual and ideal responses for the down-going step; no specific reason for this has been found.

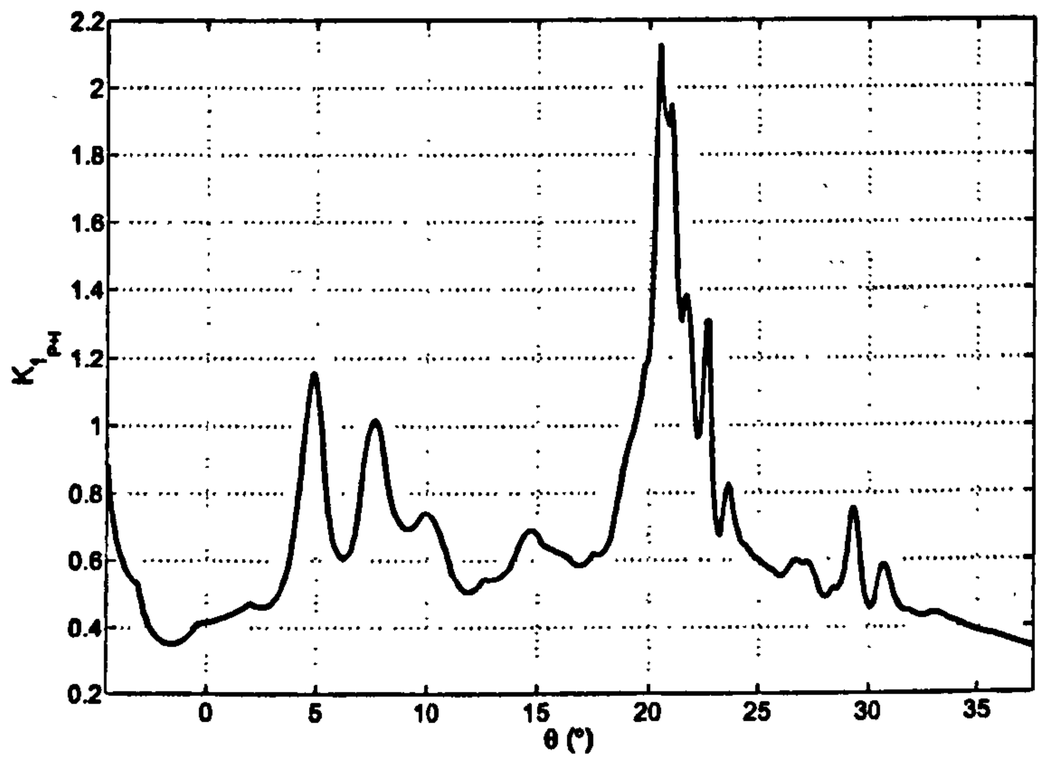


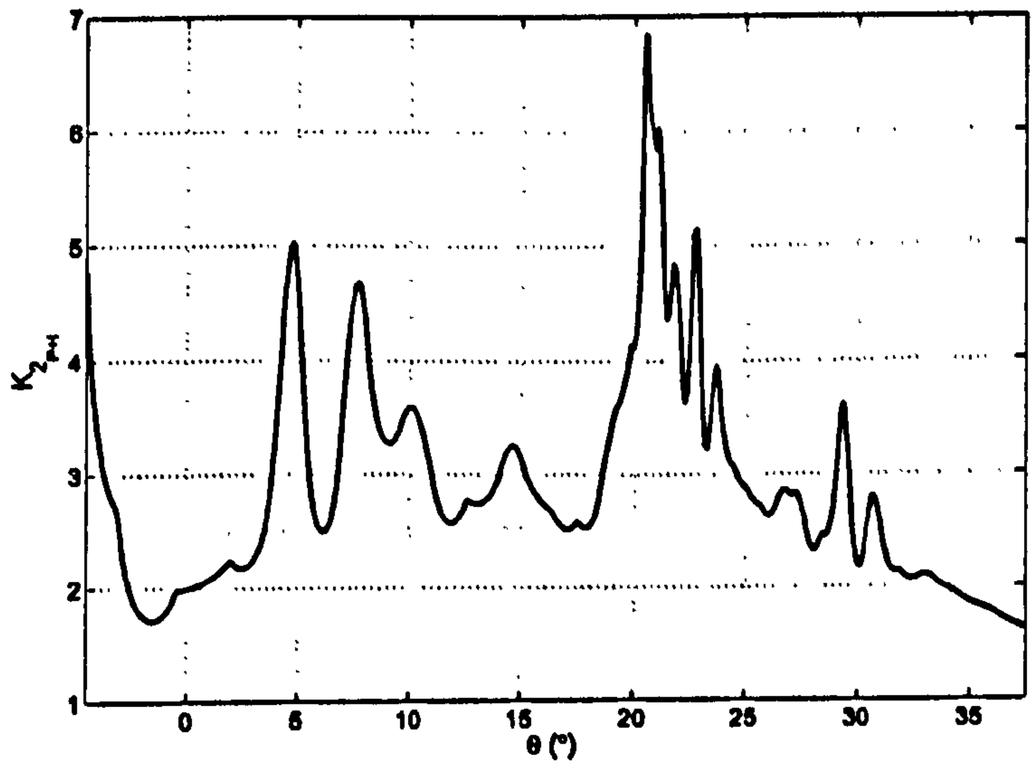


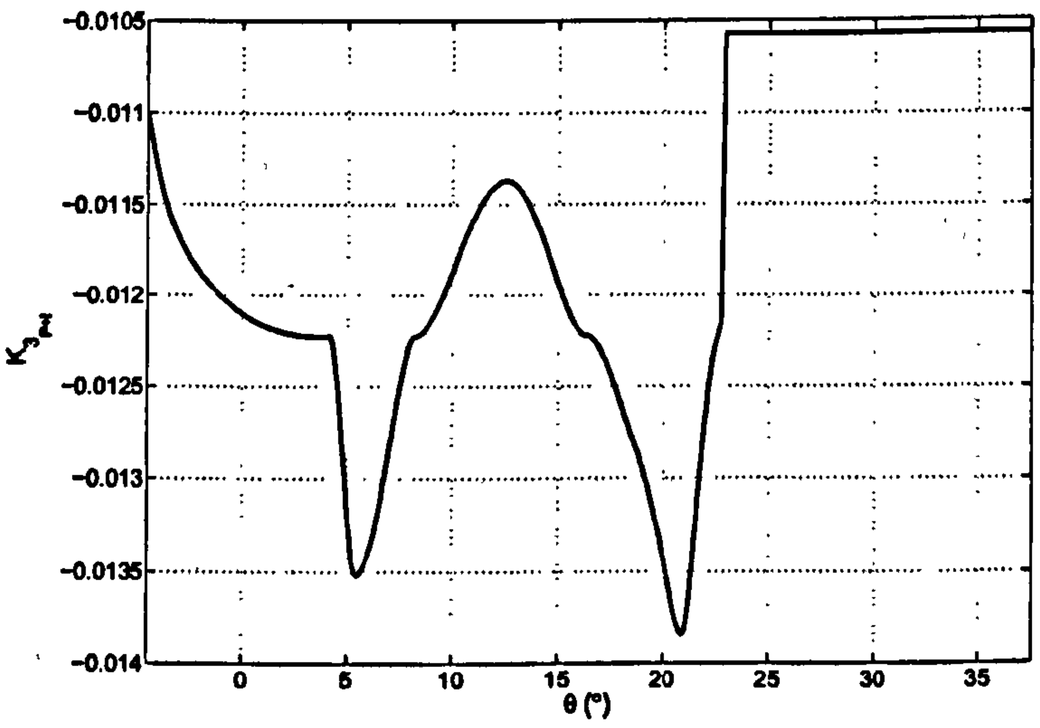


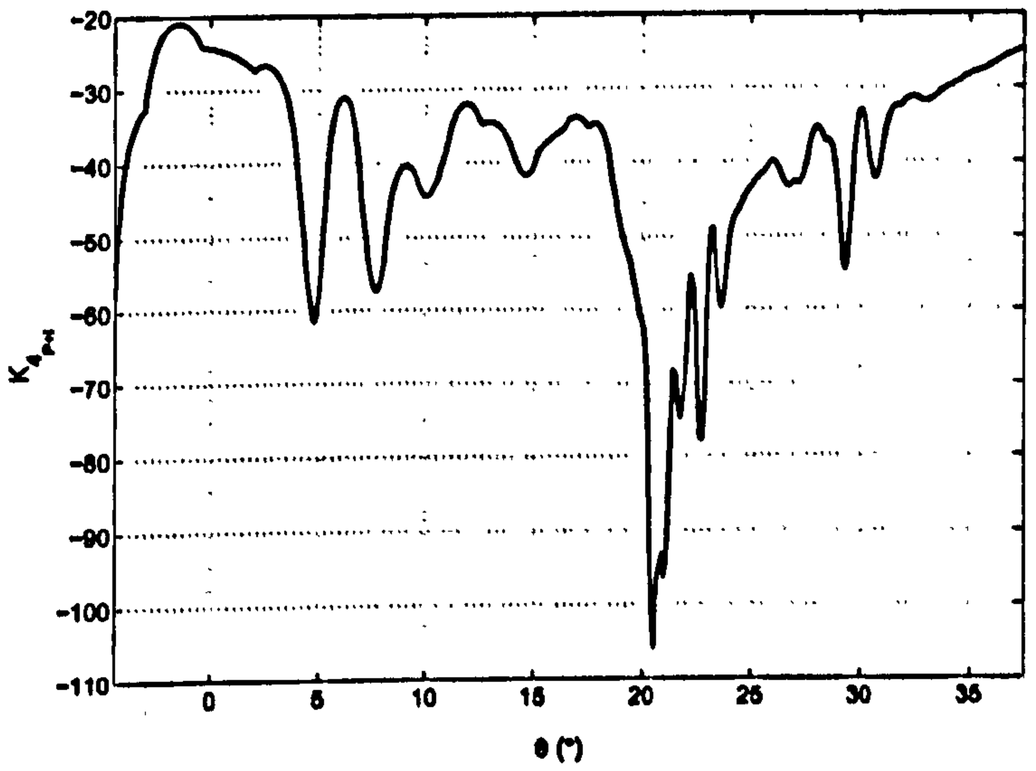


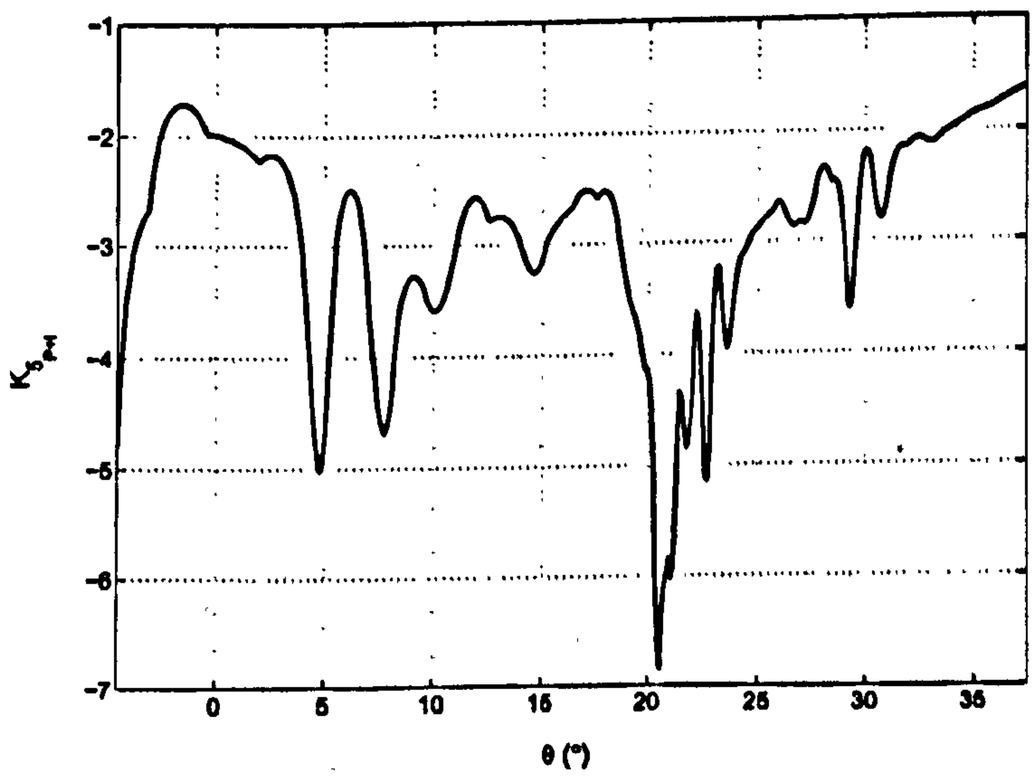


Figure 8.27: Eigenstructure-assigned gains for the PI controller with state feedback.

(a)

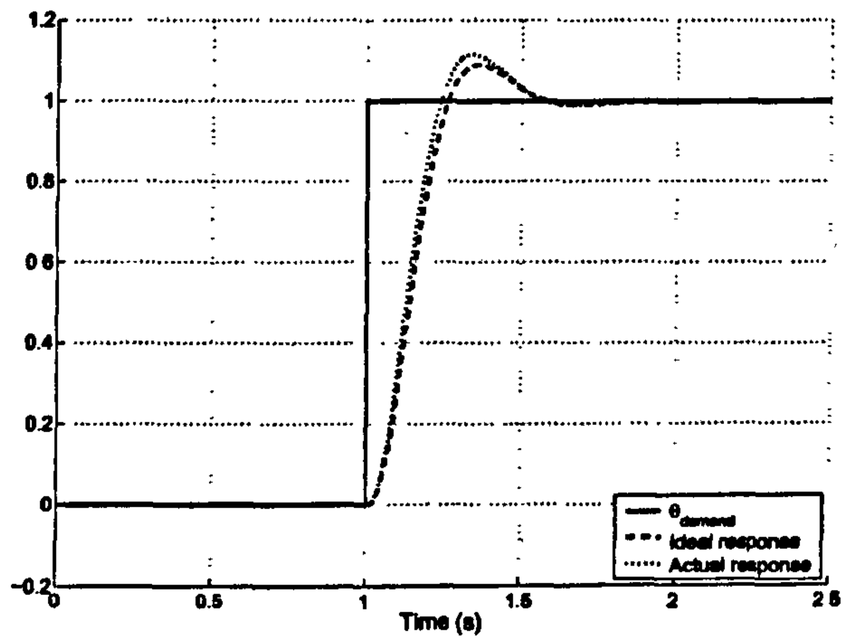


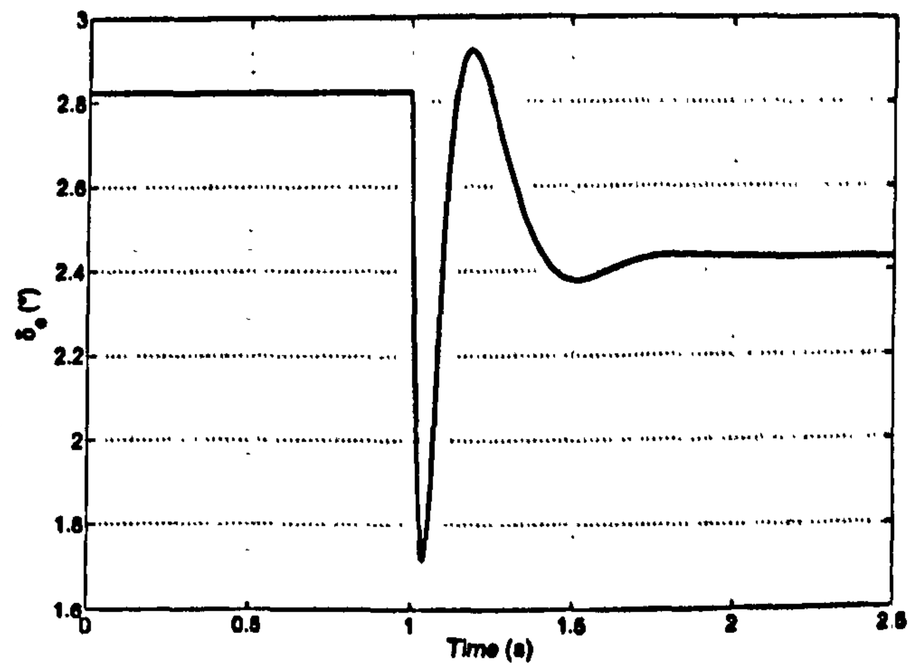


(b)

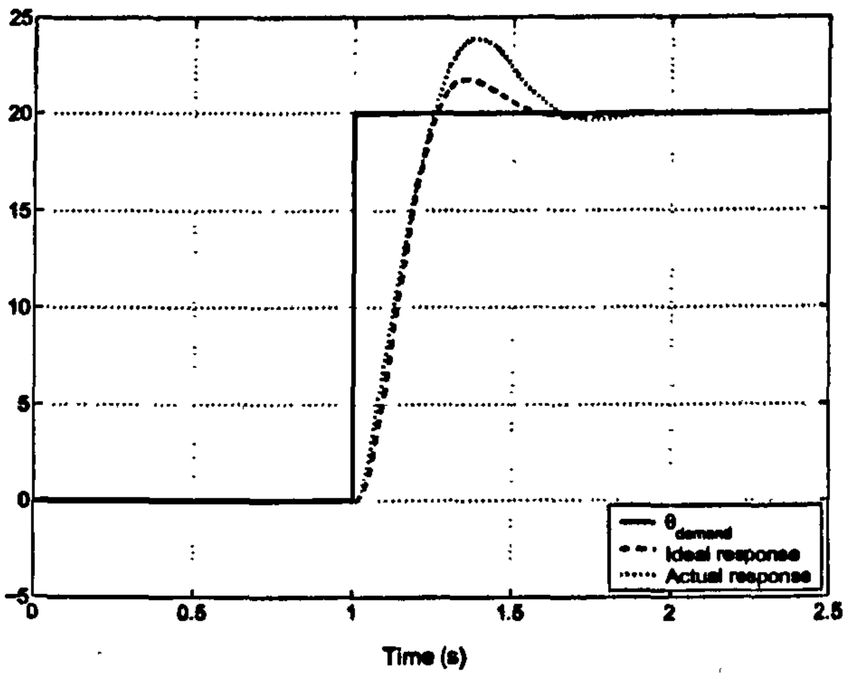


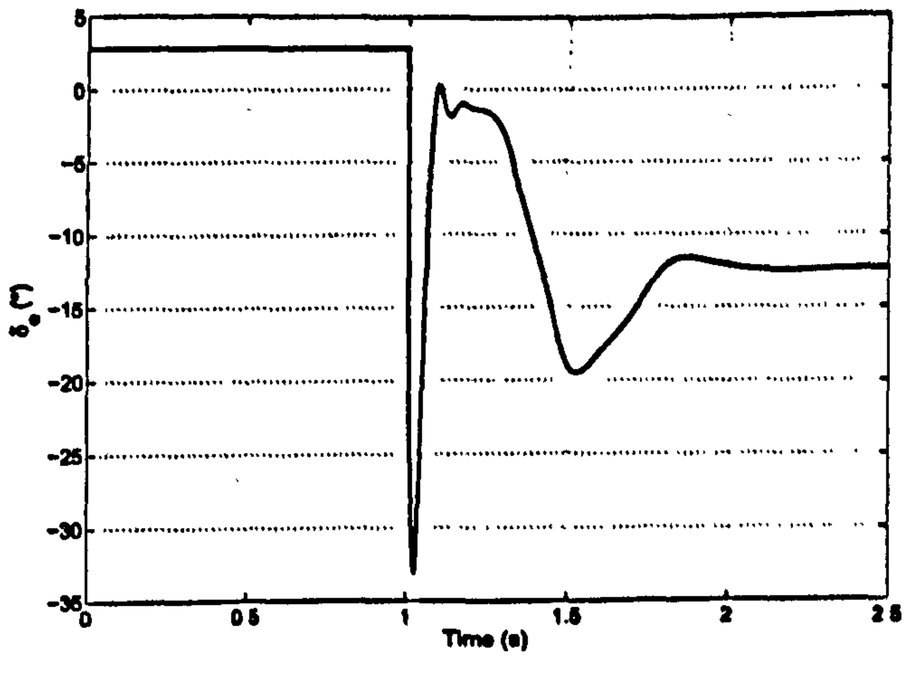


(c)

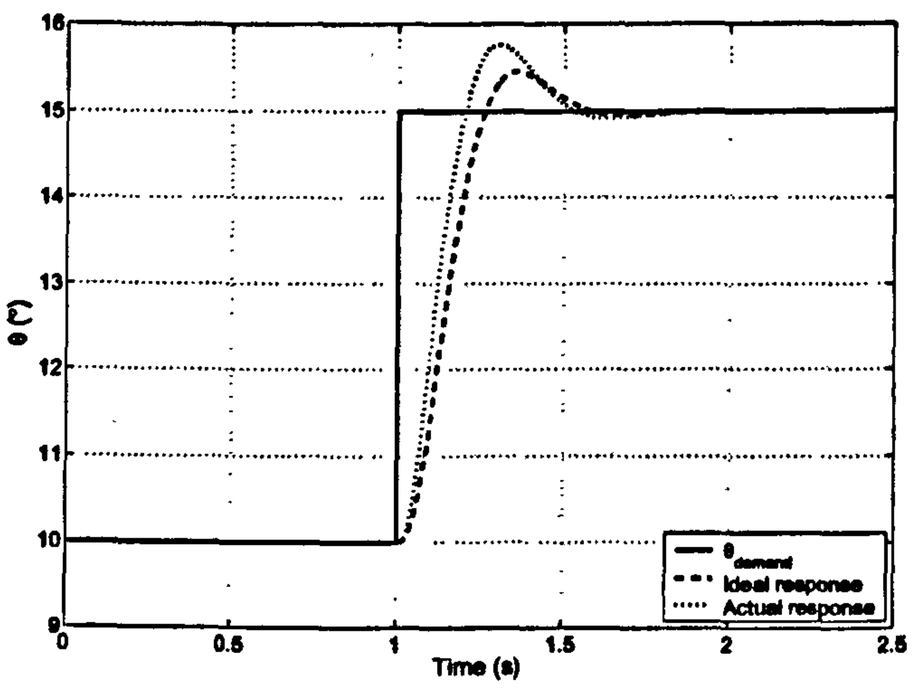


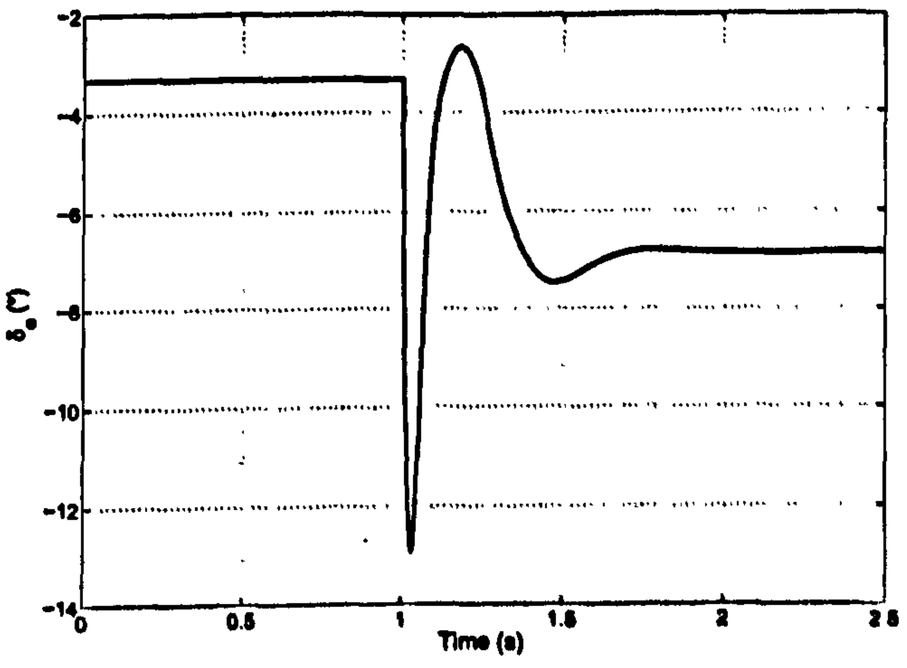


(d)

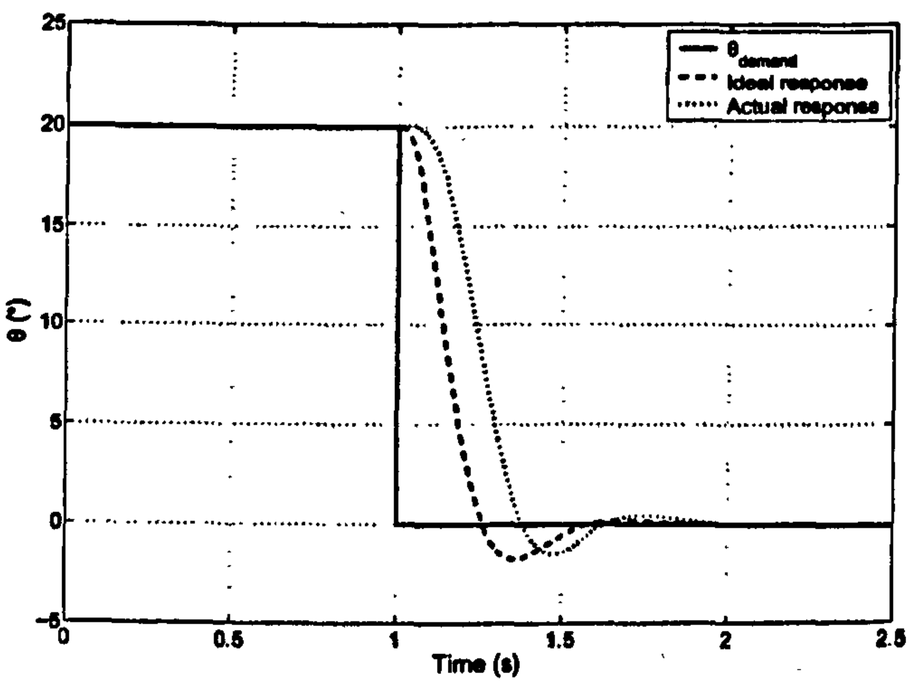


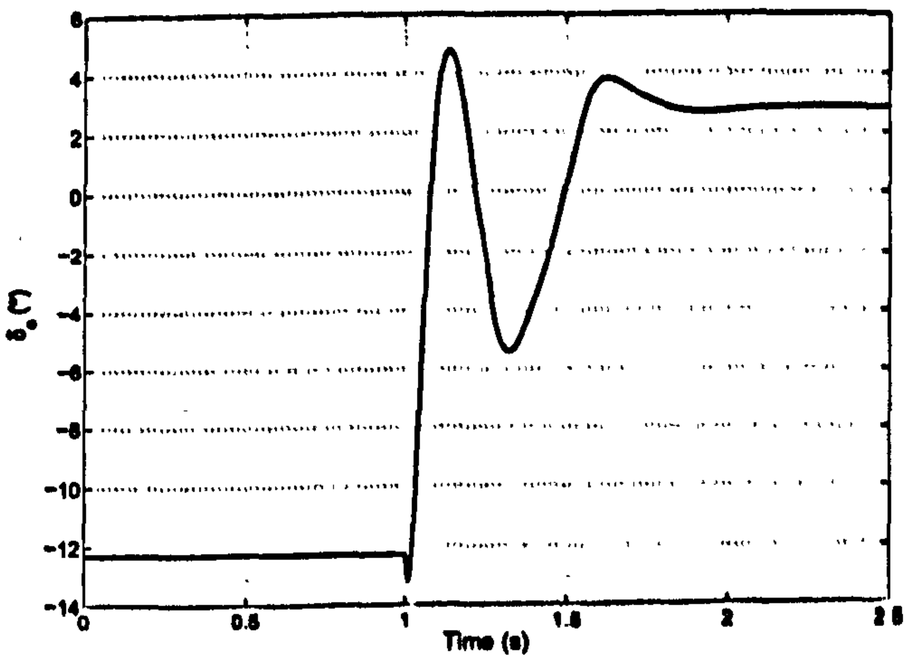


Figure 8.28: Time histories for fully eigenstructure-assigned system.

It is interesting to note that when scheduling the integrator gain against a reference demand, it is important which way around the gain/integrator are placed (see also [127]). Figure 8.29 shows the two possibilities. If a step change in reference demand occurs, having the gain after the integrator will cause a step change in input demand. If the gain is placed before the integrator, there will be a delay while the integrator output builds up (depending on the value of the gain). This is demonstrated in Figure 8.30, where (a) shows the response when the gain is placed before the integrator (as in Figure 8.28), and (b) when the gain is placed after the integrator. This is a problem that only occurs when scheduling the integrator gain against a reference input.

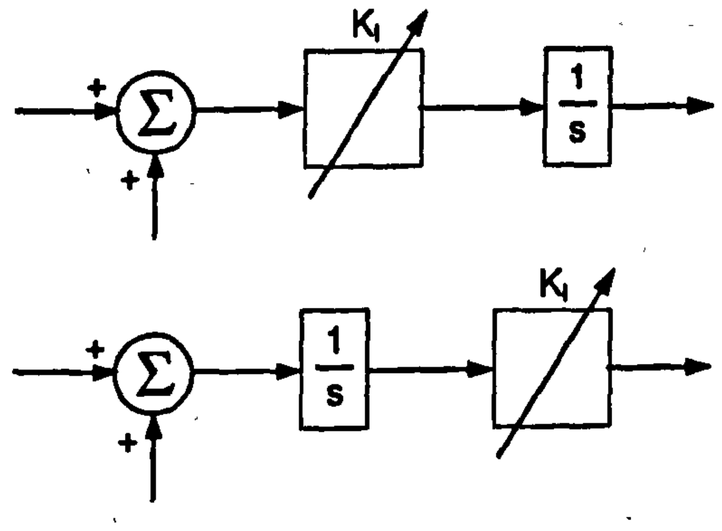


Figure 8.29: When scheduling the integrator gain it is important in which order they are placed.

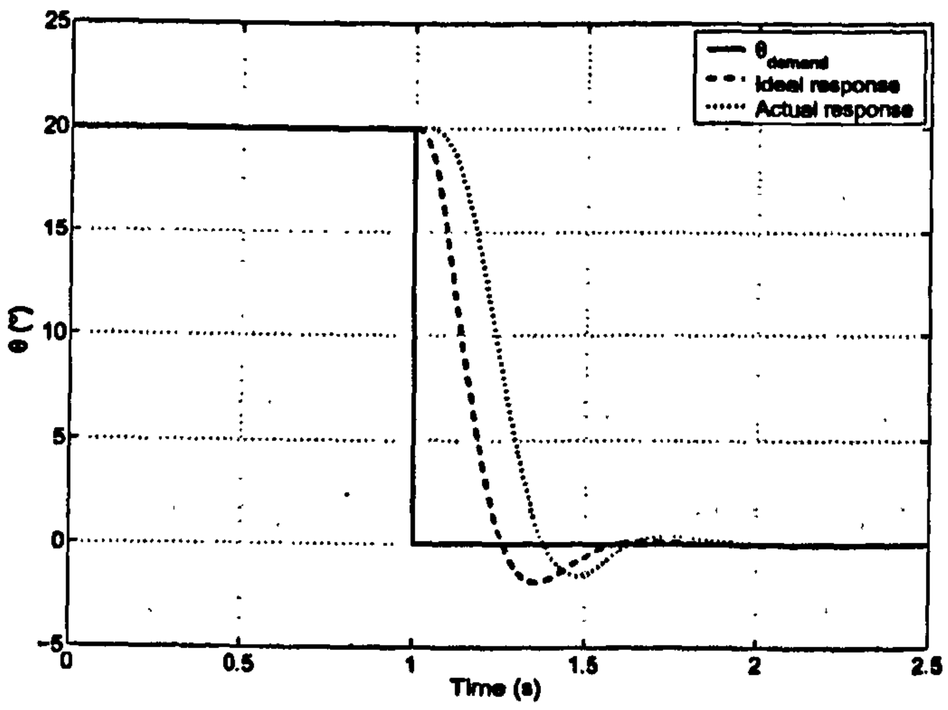


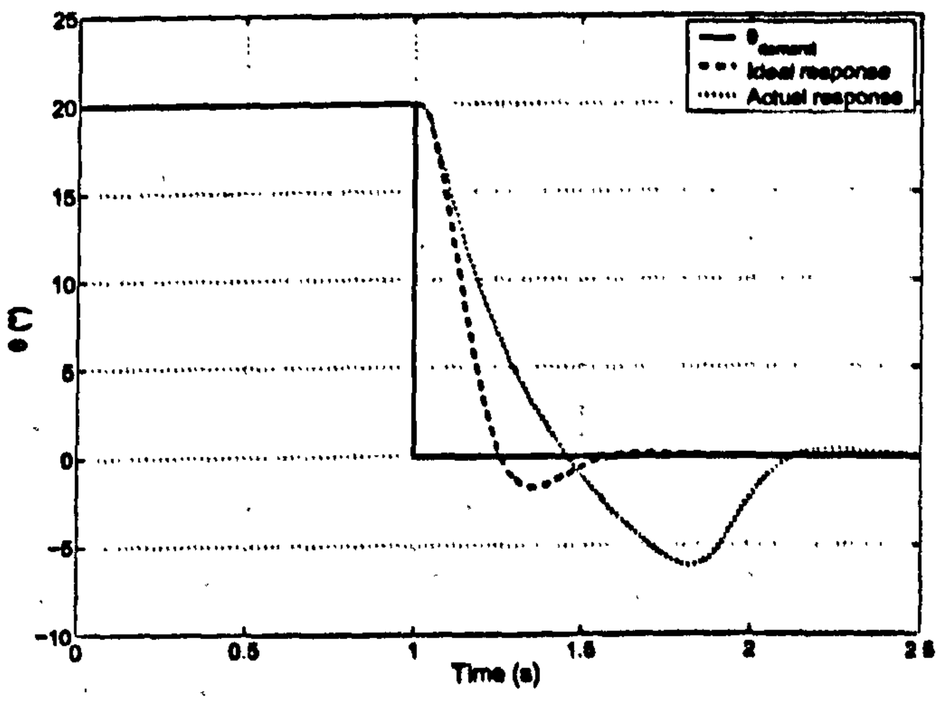


Figure 8.30: Comparison of step responses for (a) system where the gain is placed before the integrator and (b) vice-versa.

Again, robustness tests were performed on this controller, and are shown in Figures 8.31 to 8.33. The controller performs well under model and control system parameter

variations, with slightly more overshoot than desired. This is probably due to the model moving away from the steady-state design case during transient motions.

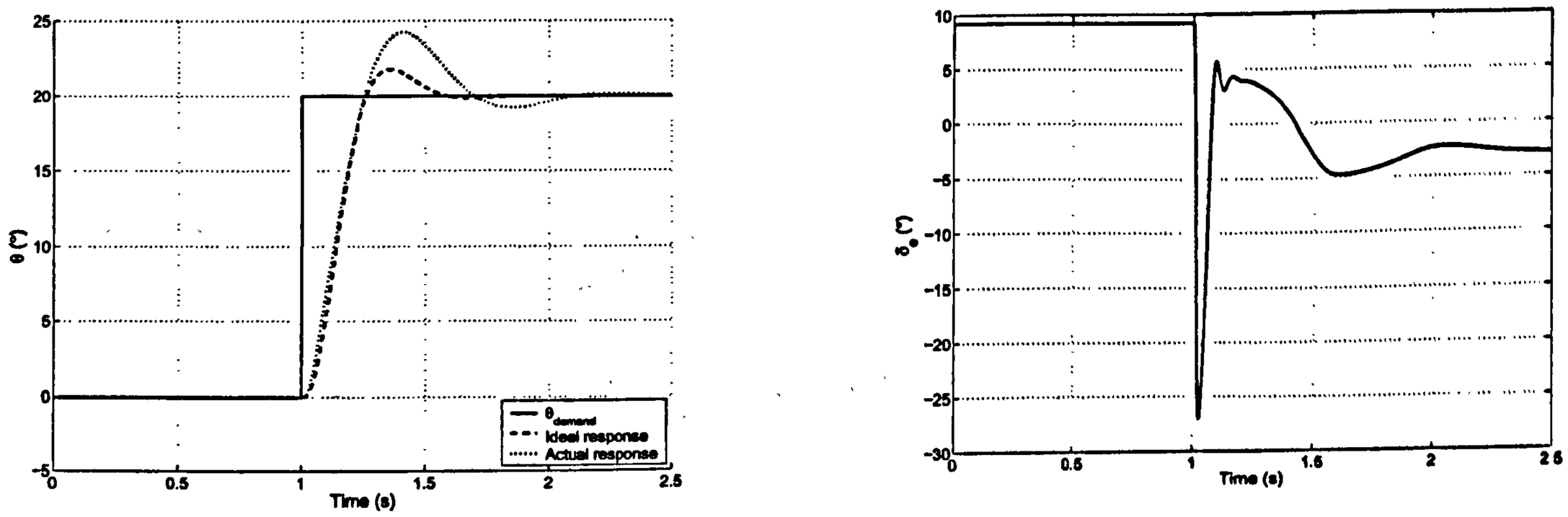


Figure 8.31: With $C_{m_{\text{offset}}} = 0.1$.

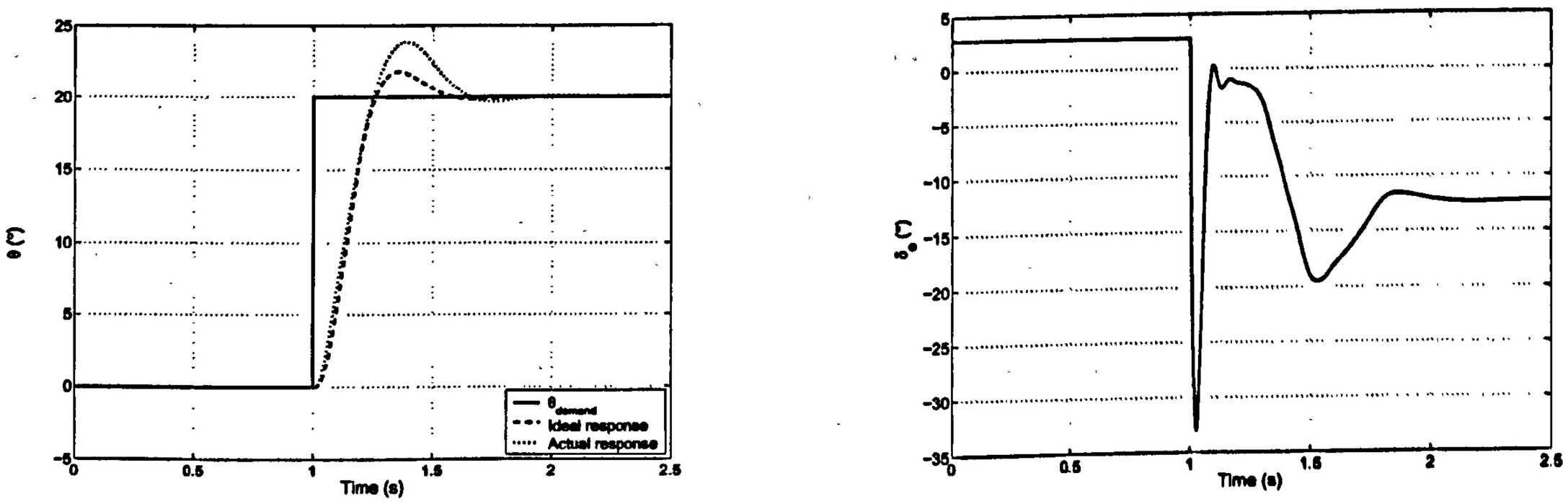


Figure 8.32: Fixed feed-forward offset of 5.

When the fully eigenstructure-assigned controller was tested on the experimental rig, a stable response could only be maintained in certain regions, and with small, low frequency input demands. If large step inputs were used, the model would became unstable and hit the limit stops on the gimbal. It is thought that, again, this is due to an interaction between the tailplanes and pitch rate feedback, however, with the more aggressive gains used in this controller the response is no longer bounded. Another possible reason is that the increasing complexity of the control strategy excites dynamics that are not predicted by the model. This will be further observed in the next section, where an adaptive control scheme is tested.

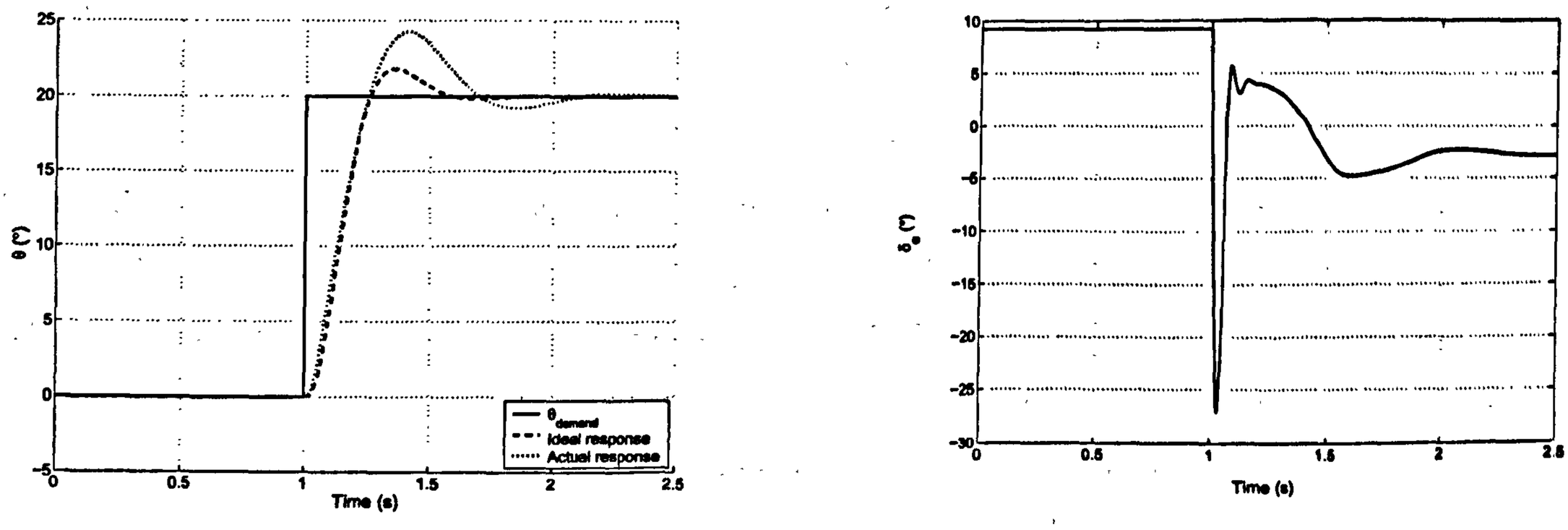


Figure 8.33: With $C_{m_{\text{offset}}} = 0.1$ and feed-forward offset of 5.

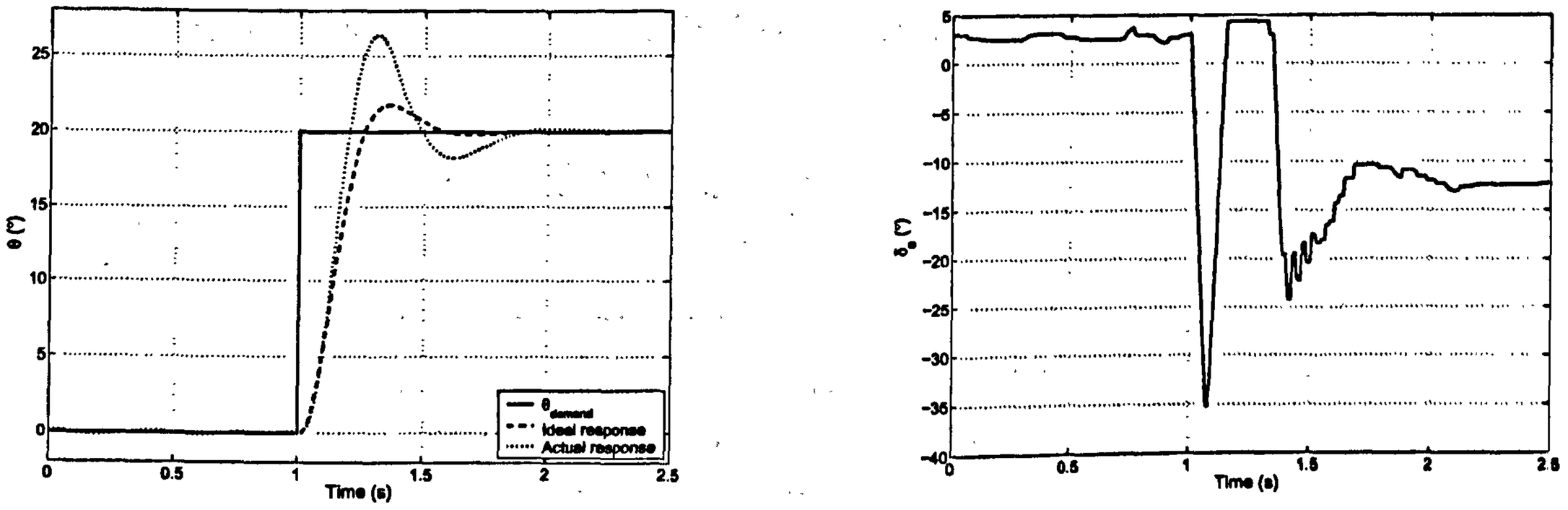


Figure 8.34: With full non-linear actuator.

## 8.3 Minimal Control Synthesis Adaptive Control

As a comparison, an adaptive control strategy was tested on the numerical model and experimental rig. The chosen controller, Minimal Control Synthesis (MCS), is a model-reference adaptive control strategy developed in the Department of Mechanical Engineering at the University of Bristol [60]. Derivation, features and application of the algorithm can be found elsewhere [61, 62, 63, 64], however, the main benefit is that no plant parameter estimates are required, removing the need for system identification.

### 8.3.1 Error-Driven Minimal Control Synthesis with Integral Action

Several extensions to MCS have been developed, including error-driven MCS (er-MCS), MCS with integral action (MCSIA) [128], extended MCS (EMCS) [129], MCS with plant identification (MCSID) [130] and decentralised MCS (DMCS). MCSIA is the most applicable form for the control of systems with non-zero mean bias terms, e.g. an aircraft pitch angle demand system where a non-zero elevator deflection may be needed to maintain a given pitch angle. Using the error-driven MCSIA (where the reference demand is not used by the controller) was found to yield similar results to standard MCS, but with fewer gains, therefore this strategy was adopted. A high level block diagram of the error-driven MCS controller is shown in Figure 8.35.

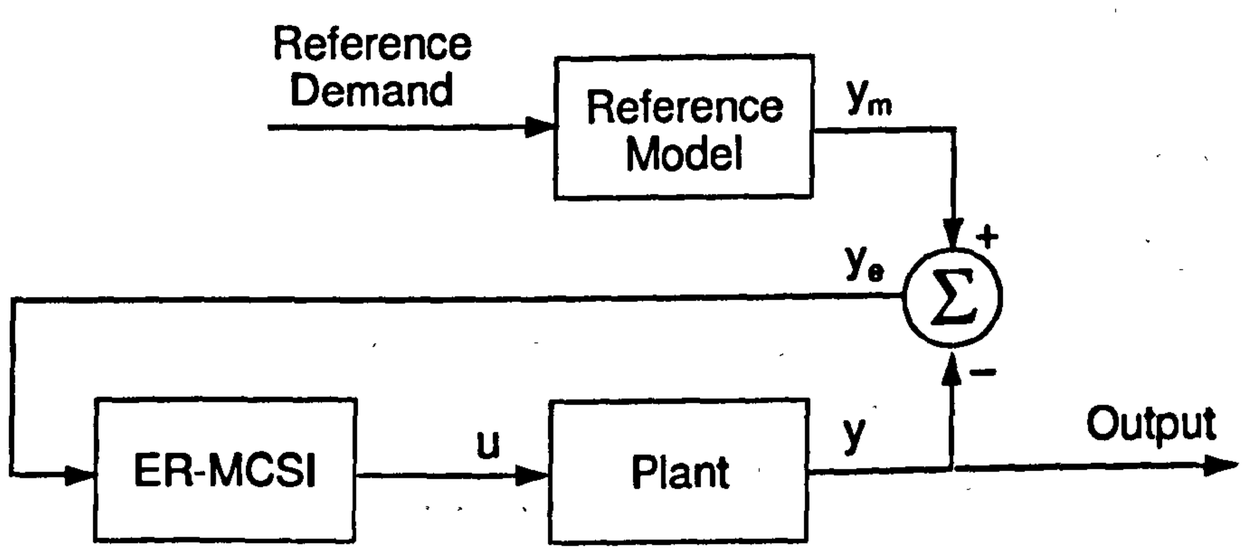


Figure 8.35: Error-driven MCS adaptive controller with integral action.

The er-MCSIA control signal for an $n^{\text{th}}$ order, single input system is given as (from [128]):

$$u(t) = \boldsymbol{K}(t)\boldsymbol{x}(t) + \boldsymbol{K_I}(t)\boldsymbol{x_I}(t) \qquad \boldsymbol{K}, \boldsymbol{K_I} \in \mathbb{R}^n \tag{8.9}$$

where $\boldsymbol{x}(t)$ and $\boldsymbol{x_I}(t)$ correspond to the state vector and its time integral respectively. The corresponding time-varying gains are then calculated according to:

$$K(t)_i = \alpha \int_0^t y_e(\tau)_i x(\tau)_i d\tau + \beta y_e(t)_i x(t)_i \qquad i = 1..n \tag{8.10}$$

$$K_I(t)_i = \alpha \int_0^t y_e(\tau)_i x_I(\tau)_i d\tau + \beta y_e(t)_i x_I(t)_i \tag{8.11}$$

where $\alpha > 0$ and $\beta \geq 0$ are the scalar adaption weights and $y_e(t)$ is the output error (between the plant and reference model).

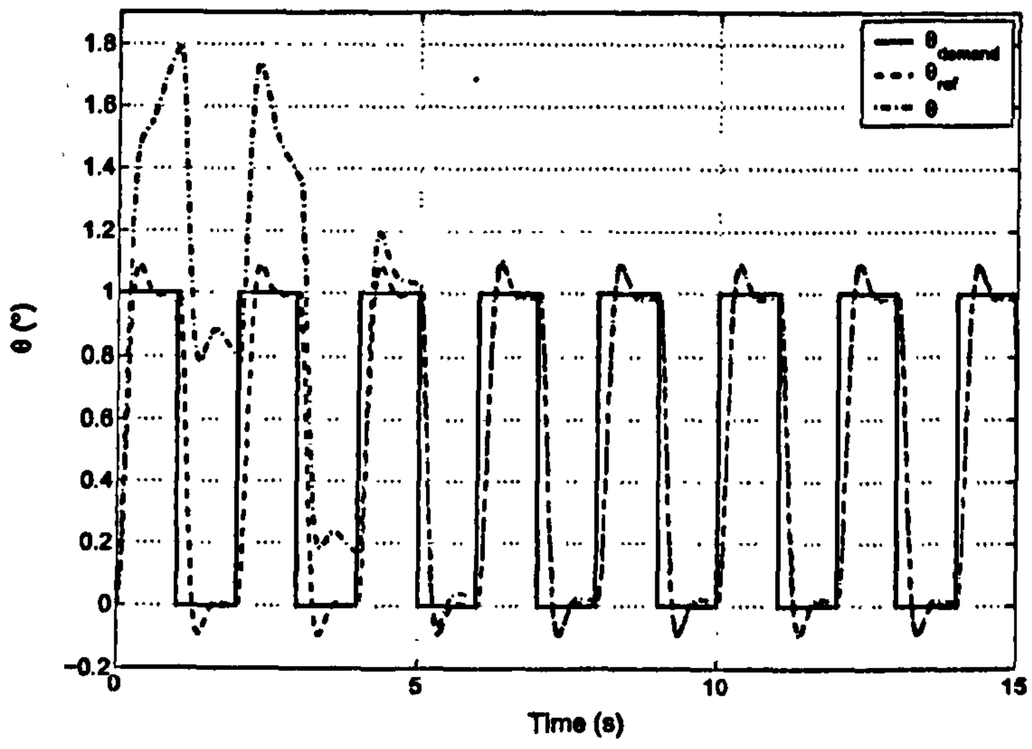


(a)

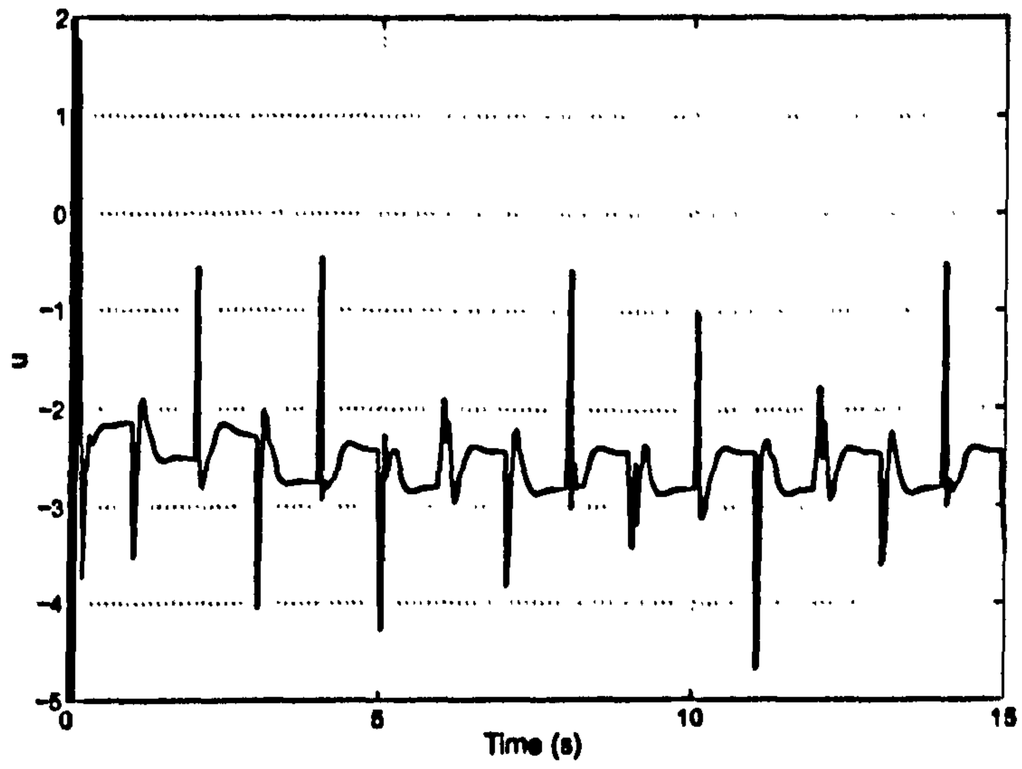


(b)

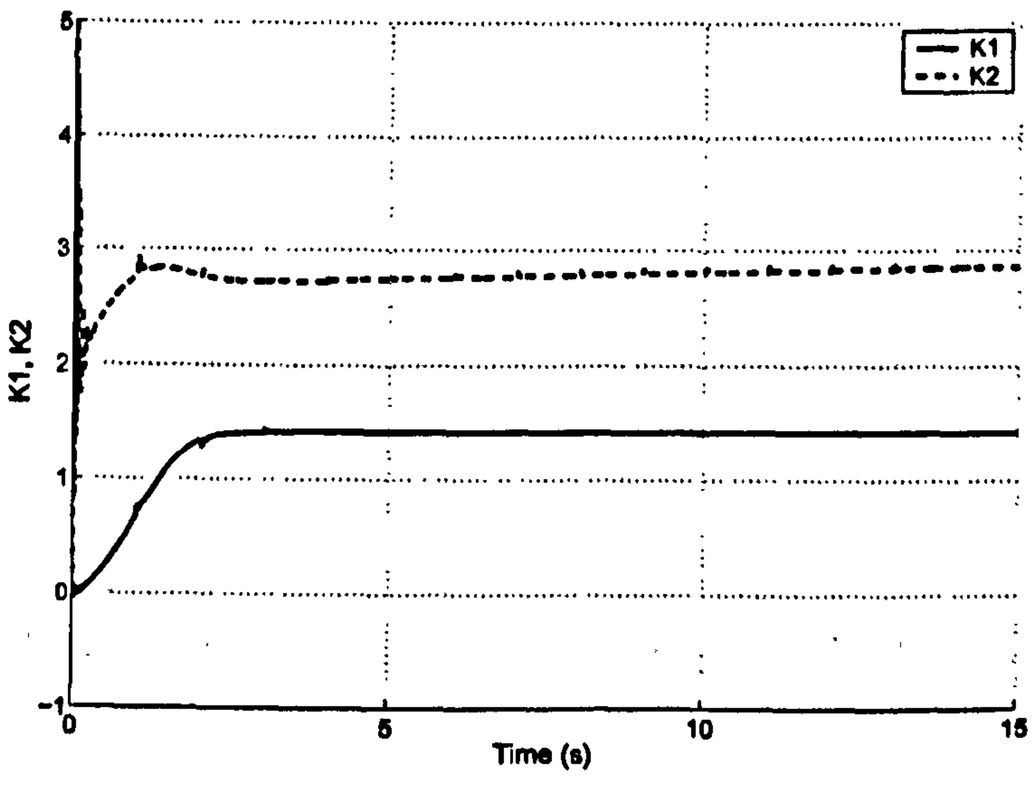


(c)

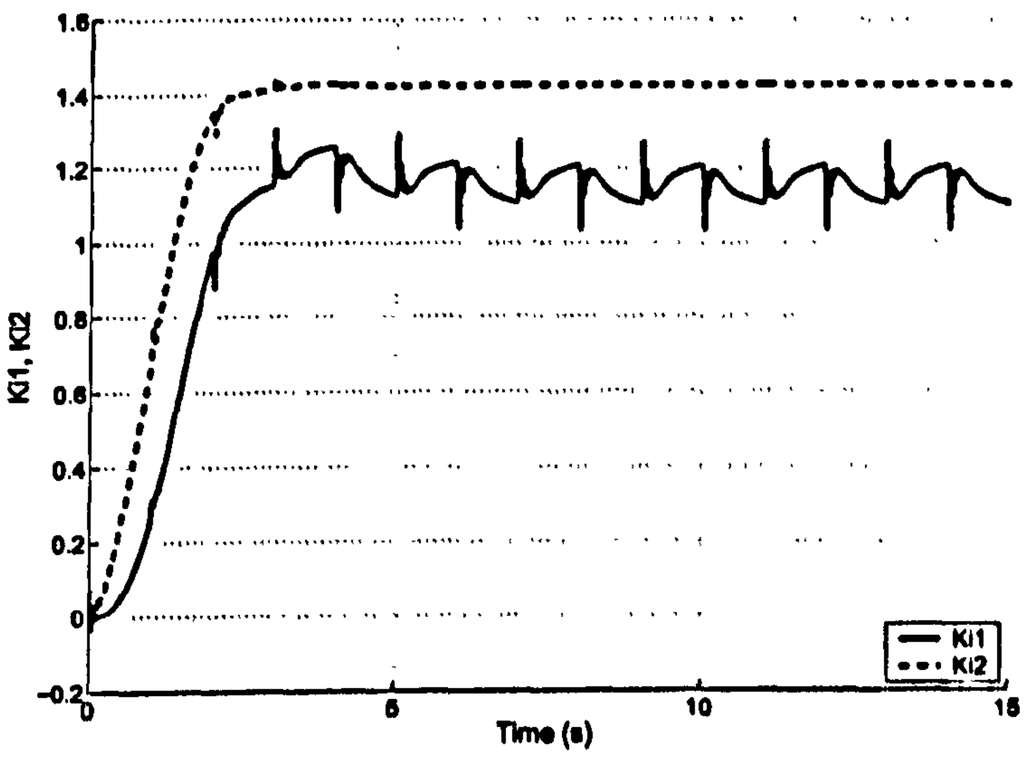


(d)

Figure 8.36: Time simulations of MCS controller with small amplitude step input ($\alpha = 1.0$, $\beta = 0.1$).

Figures 8.36 and 8.37 show simulations of step responses for the MCS adaptive controller, using the linear actuator model developed in Section 3.3.5. Good response to a small-amplitude step input can be seen in Figure 8.36(a), with the gains asymptotically reaching a fixed value (Figure 8.36(c)-(d)). A larger error can be seen in Figure 8.37(a), where the response to a 10° step input is demonstrated. The adaptation parameters $\alpha$ and $\beta$ had to be reduced significantly (from $\alpha = 1.0, \beta = 0.1$ used in Figure 8.36 to $\alpha = 0.01, \beta = 0.001$) to avoid the system becoming rapidly unstable. However, reducing

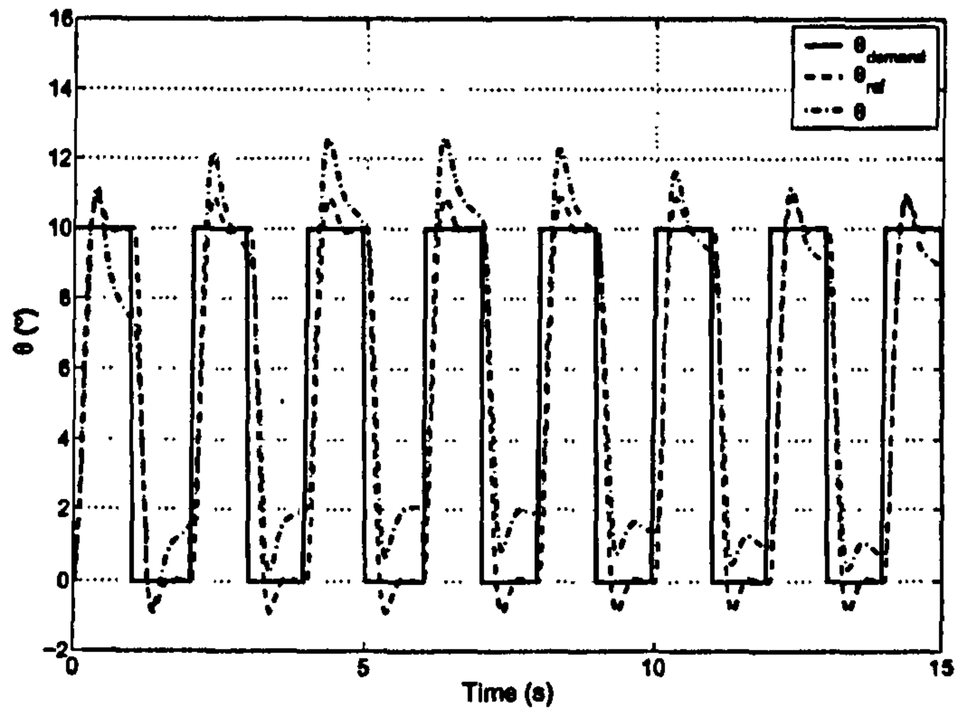


(a)

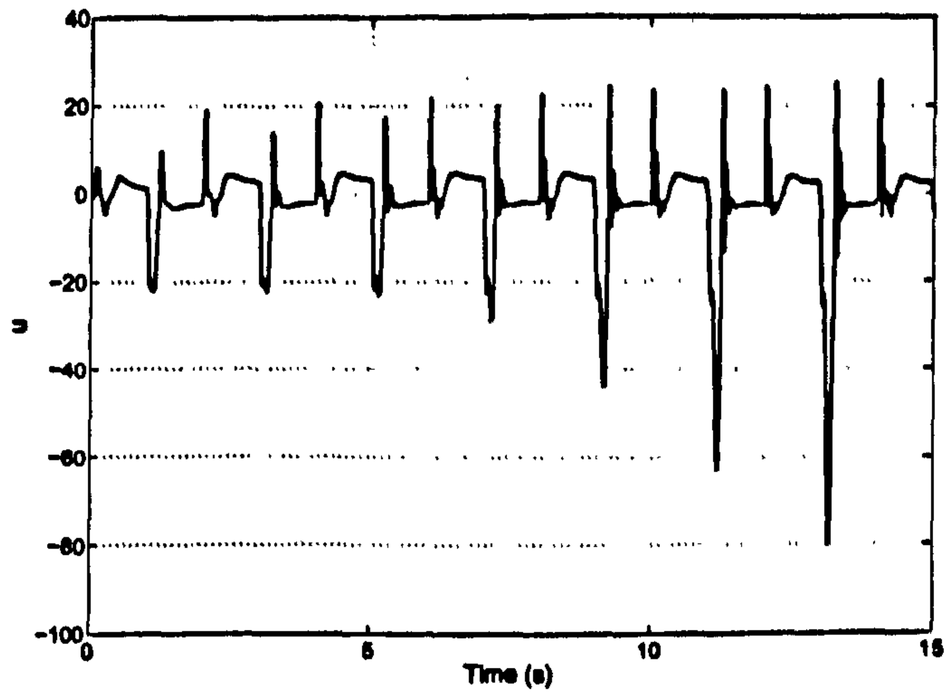


(b)

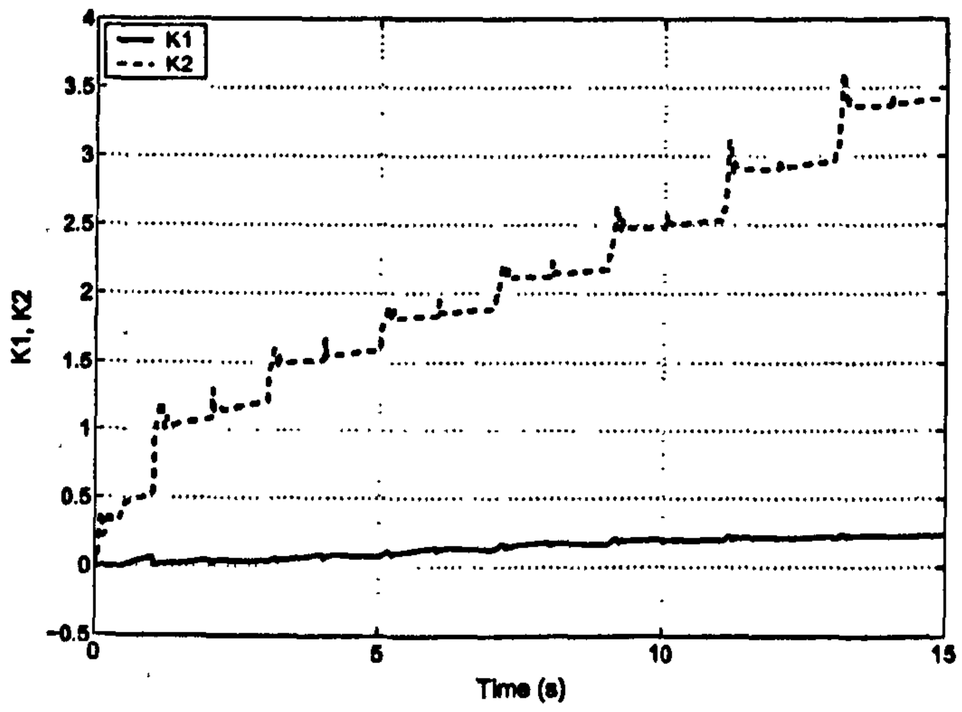


(c)

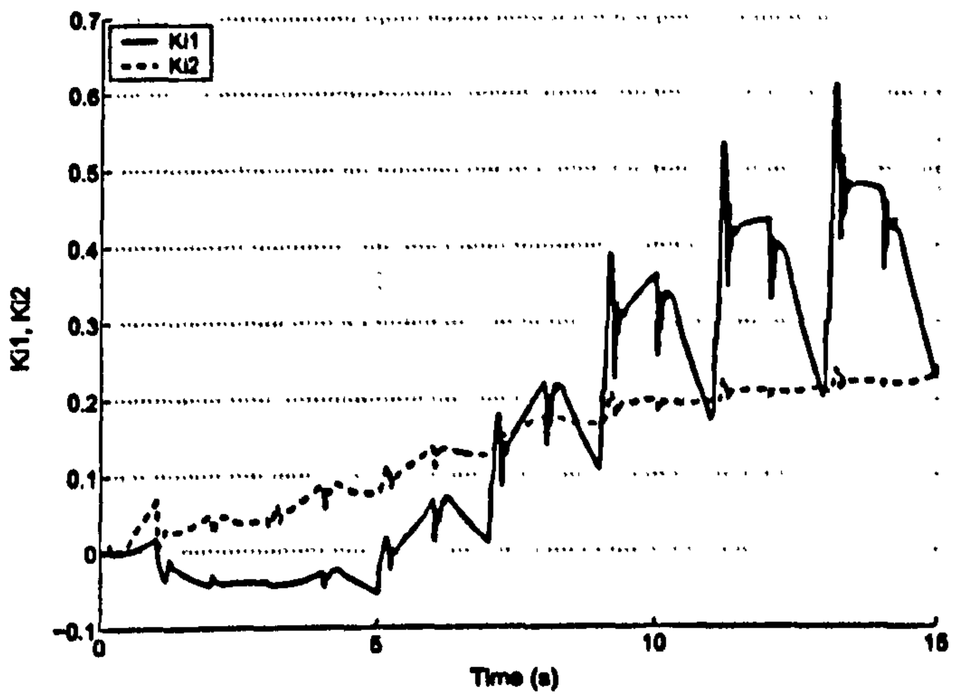


(d)

Figure 8.37: Time simulations of MCS controller with 10° amplitude step input ($\alpha = 0.01$, $\beta = 0.001$).

the adaptation weights only postpones the instability, as shown by the gains consistently ramping up in Figure 8.37(c)-(d).

Figures 8.38 and 8.39 show simulated sine wave response for the adaptive controller. In general, tracking performance is good and the gains are correspondingly small. However, the gains show a general increasing trend (particularly the integral gains shown in Figure 8.38(d)), eventually leading to instability.

Figure 8.40 shows a simulated response of the Hawk model to a 5° amplitude sine wave input with the full non-linear actuator model (developed in Section 3.3.5) included in the model. As seen in Figure 8.40(c) and (d), the gains become large very quickly (even with

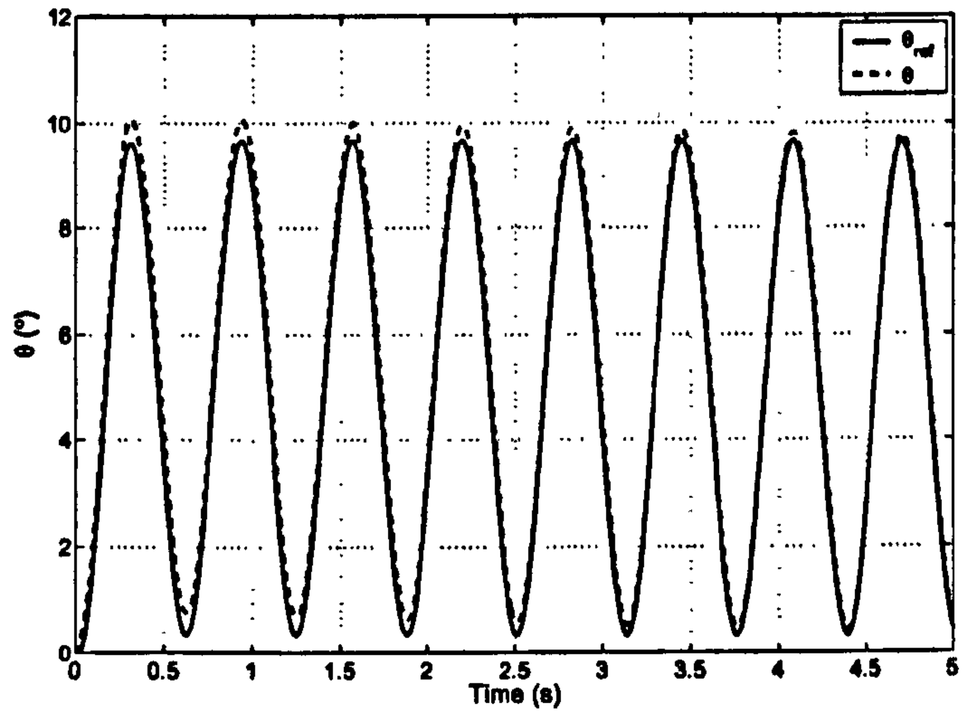


(a)

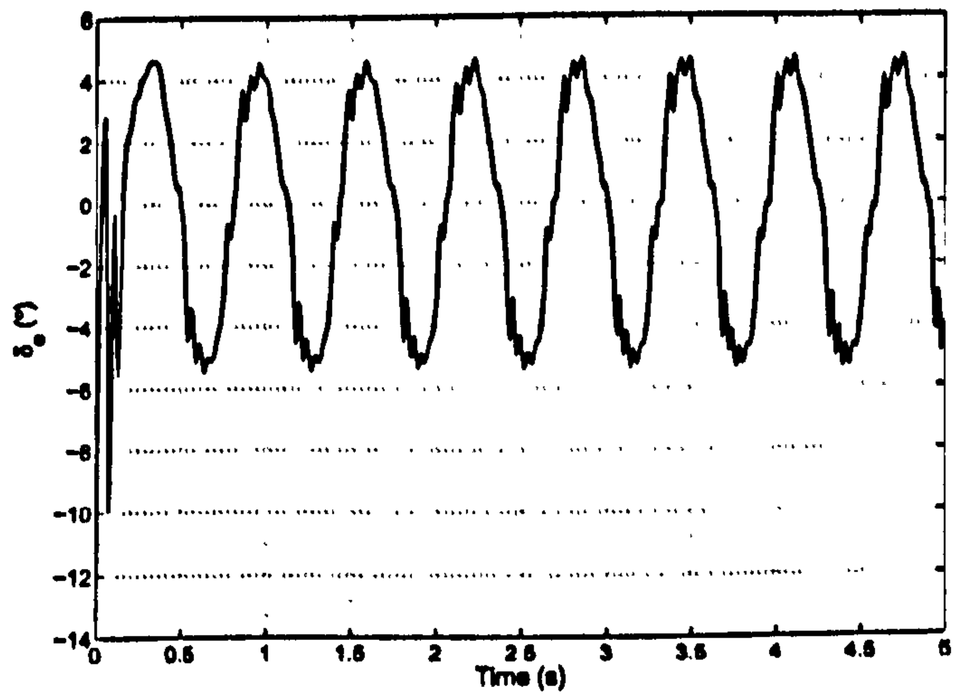


(b)

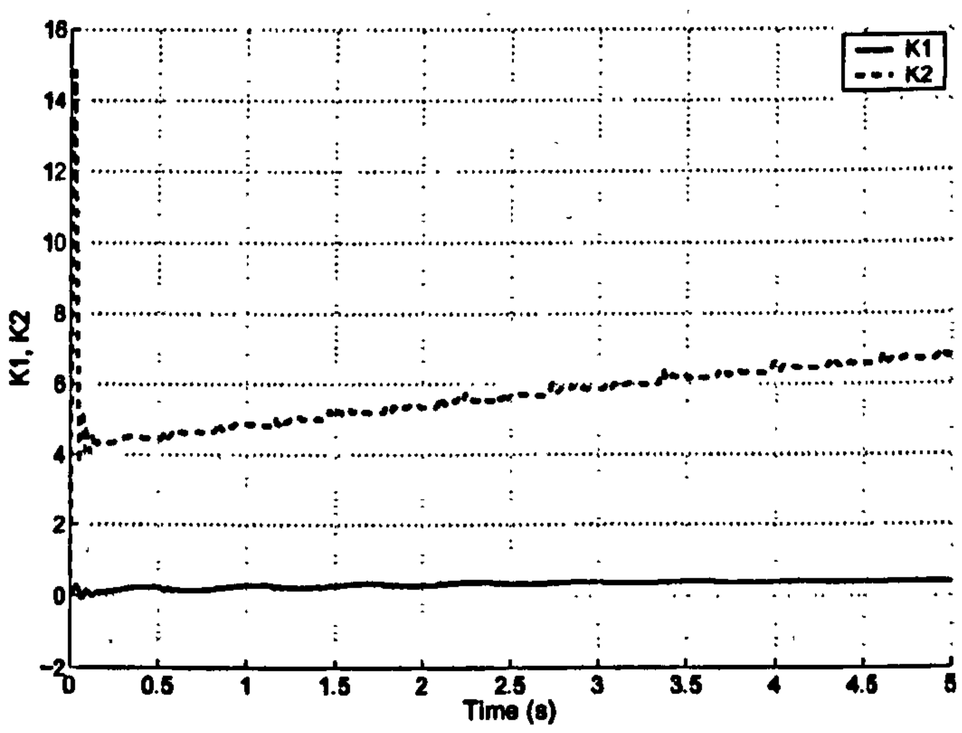


(c)

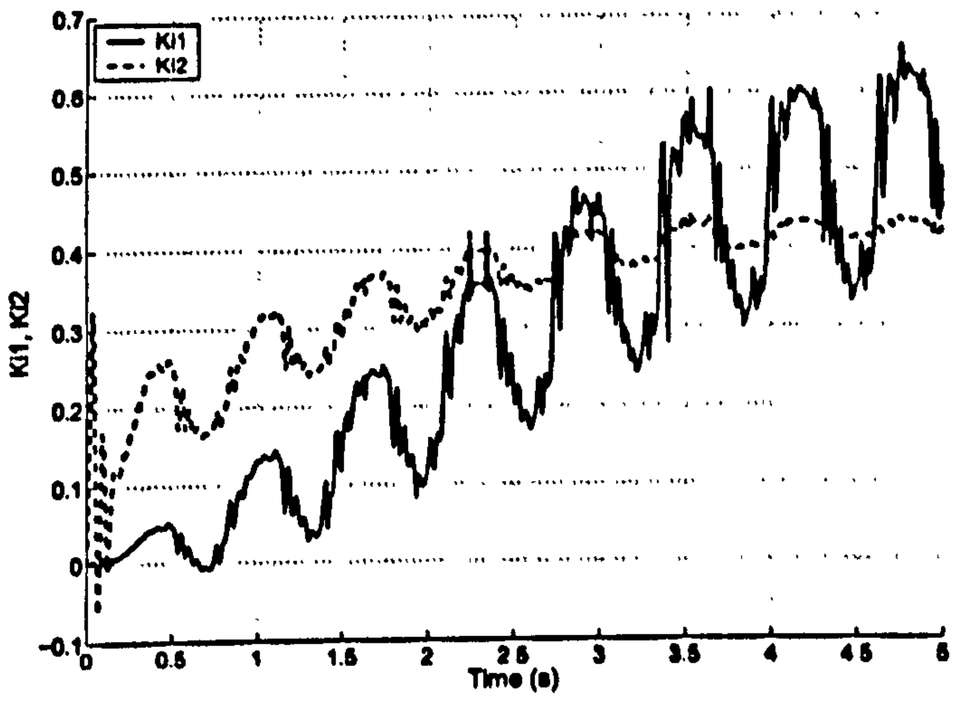


(d)

Figure 8.38: MCS controller with 5° amplitude sine wave input ($\alpha = 0.01$, $\beta = 0.001$).

small $\alpha$ and $\beta$) which would eventually lead to instability. The tracking performance is poor (Figure 8.40(a)), and demonstrates the practical limitations of this adaptive control scheme due to highly non-linear system dynamics.

When testing MCS on the experimental rig, noise and non-linearities caused the gains to wind up and make the system unstable, even with much smaller values of the adaption weights, $\alpha$ and $\beta$. A method for stopping the gains winding up was developed in [101], where an extra 'gain leakage' term is added to the controller to reduce the gains when the tracking error is small. However, it was also found experimentally in [101] that when using a gain leakage term with an MCS controller that includes integral action, such large values of gain leakage term were required that the integral action had negligible

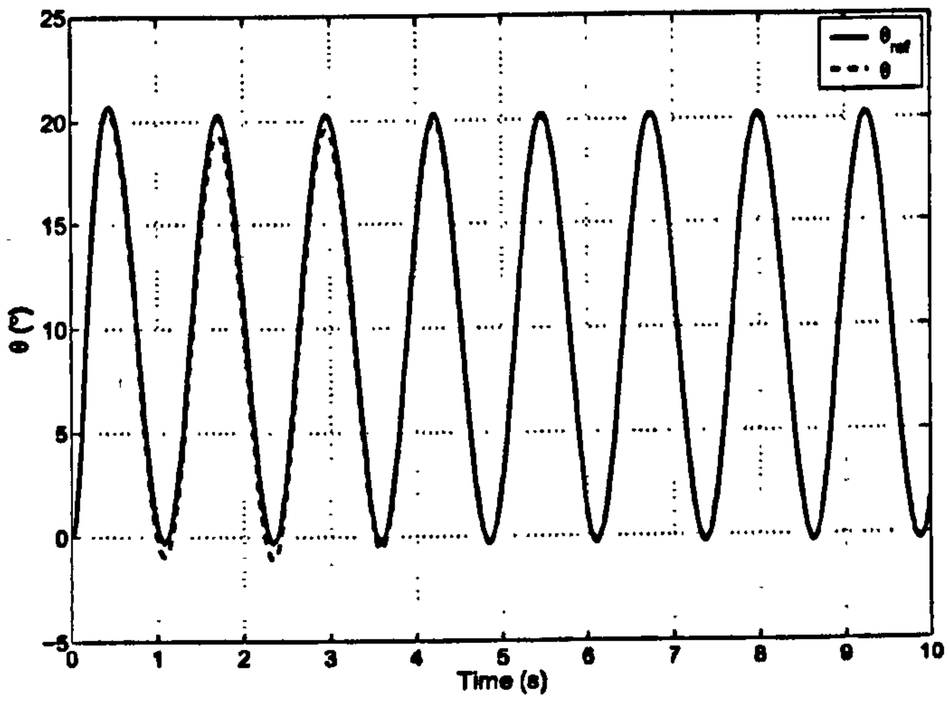


(a)

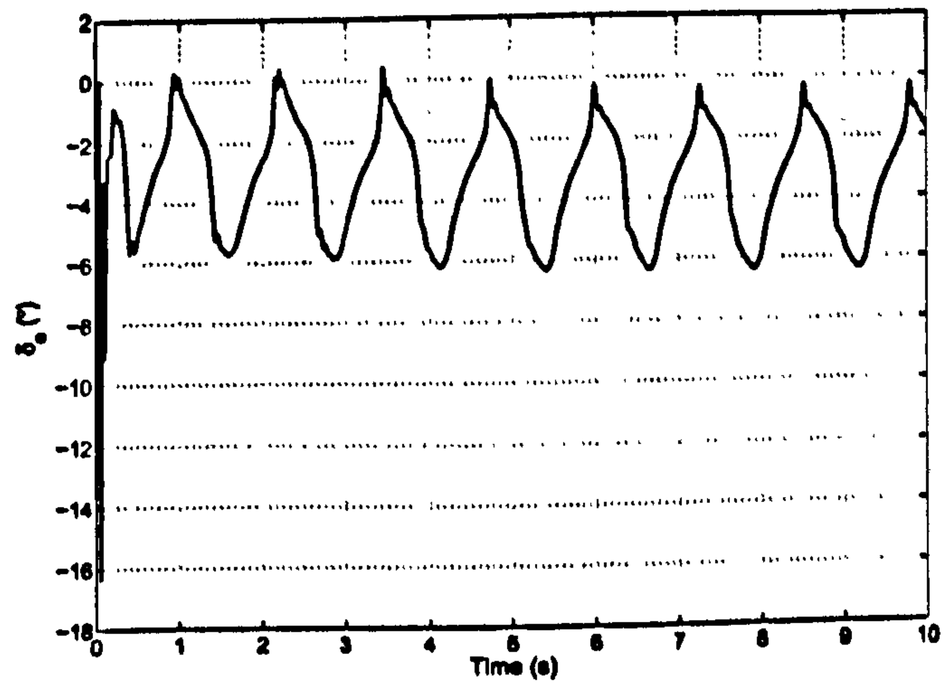


(b)

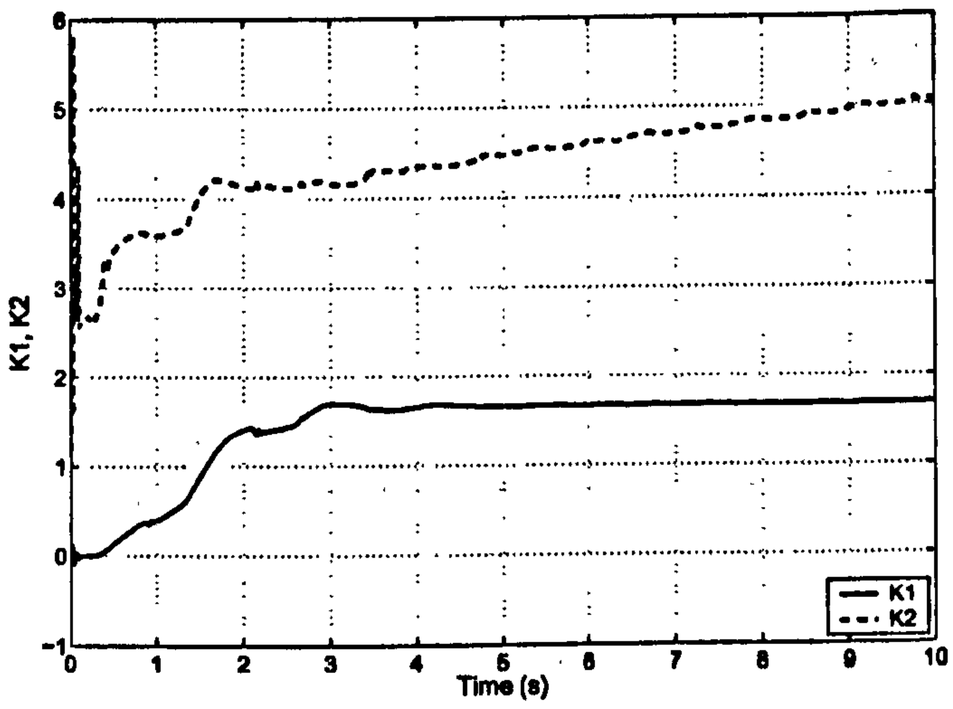


(c)

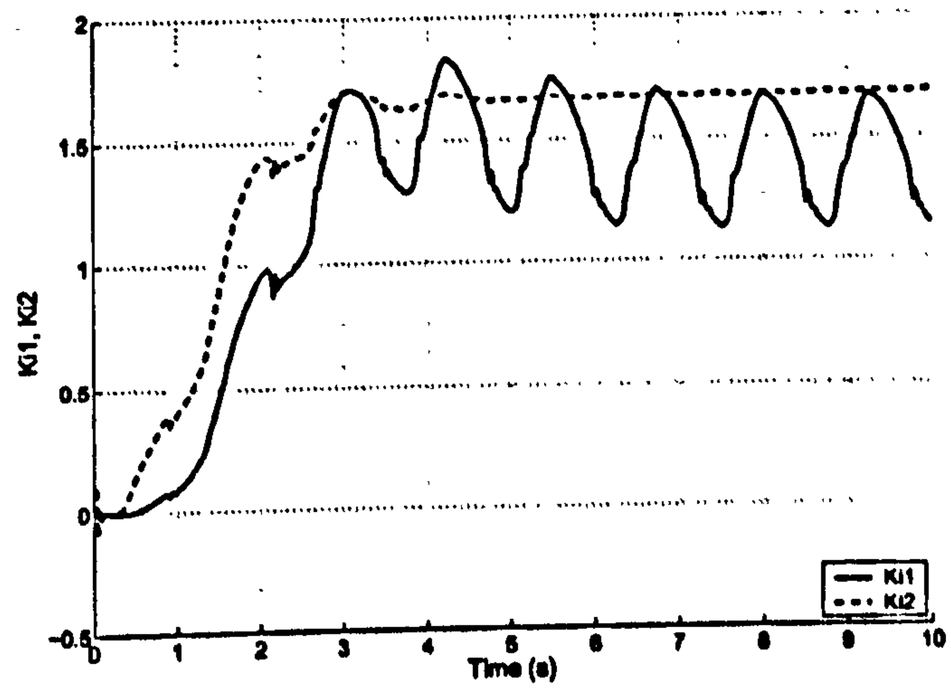


(d)

Figure 8.39: MCS controller with 10° amplitude sine wave input ($\alpha = 0.01$, $\beta = 0.001$).

effect. This would effectively revert the controller to standard MCS without integral action, which would not allow non-zero demanded pitch angles to be attained, and was therefore not tested.

## 8.4 Conclusions

In this chapter state-feedback controllers were designed using both gain scheduling and adaptive methods. Numerical simulations of the mathematical model were carried out to assess the performance of each controller.

The gain-scheduled controllers were designed using linearisations of the non-linear air-

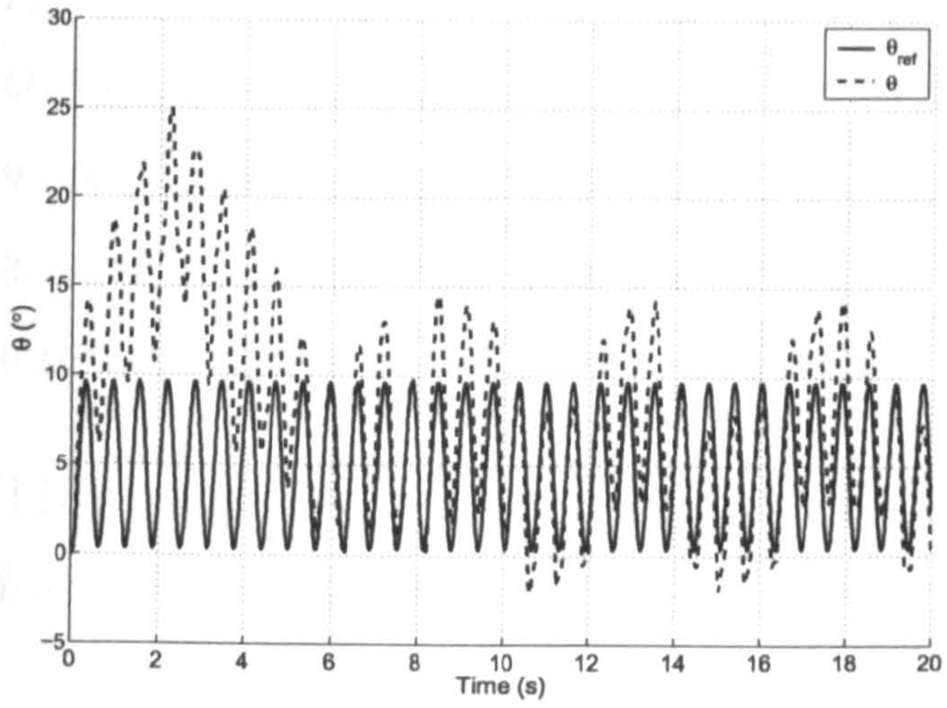


(a)

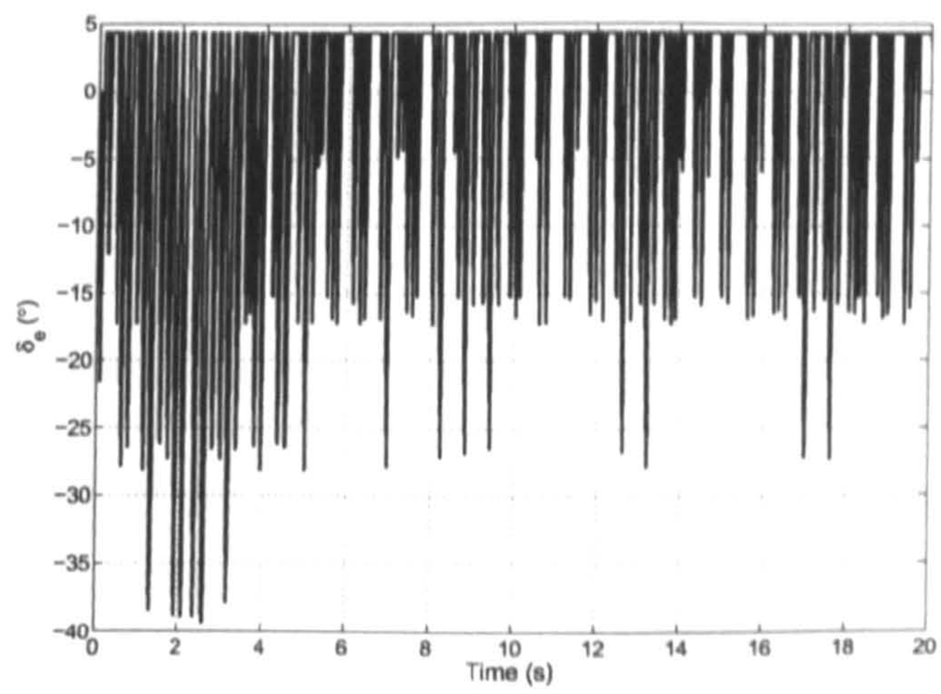


(b)

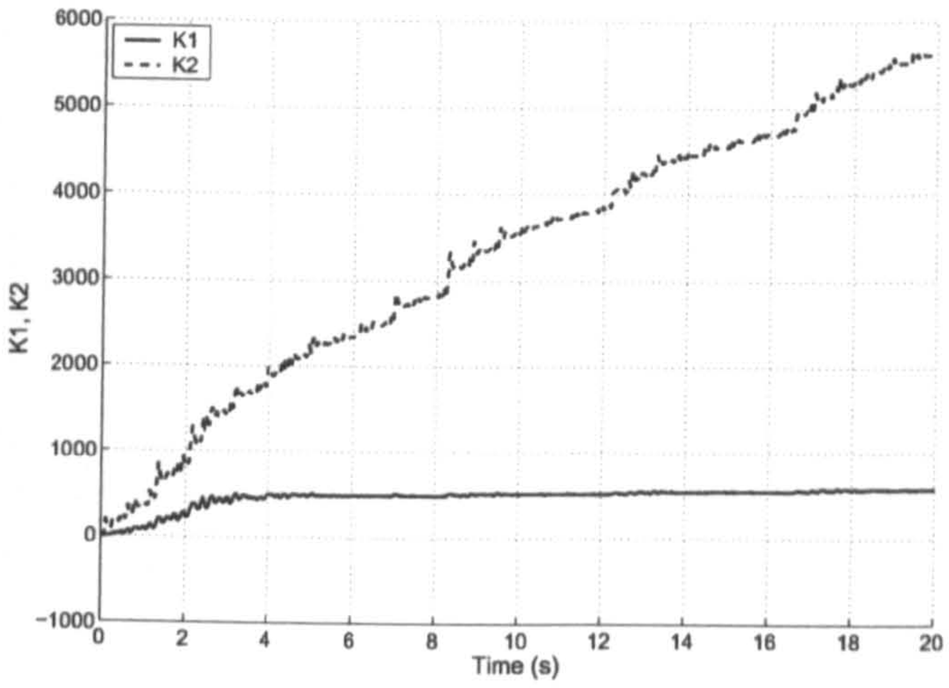


(c)

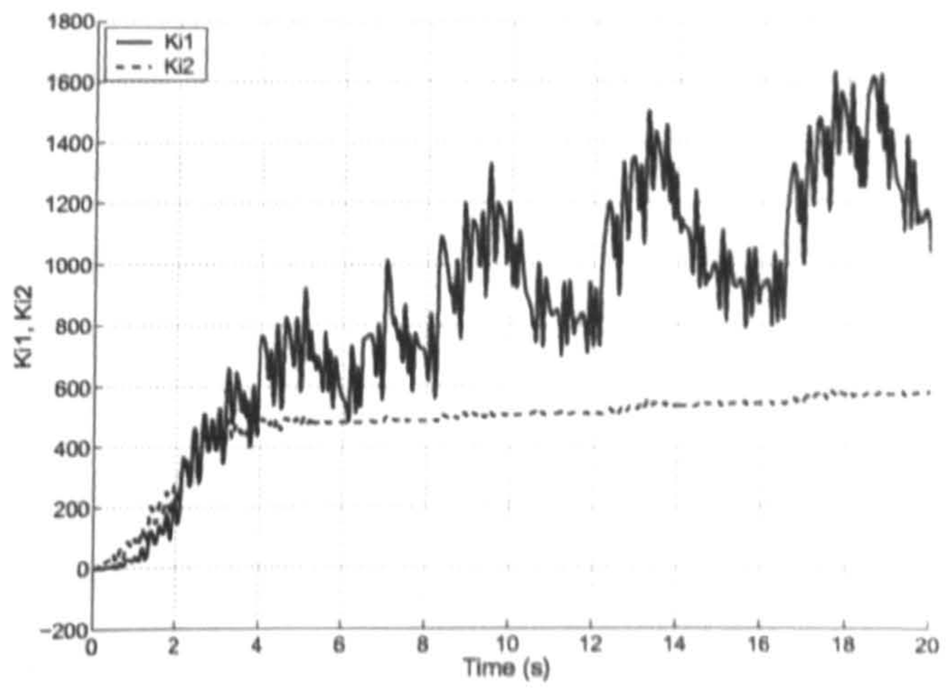


(d)

Figure 8.40: MCS controller with 5° amplitude sine wave input, with non-linear actuator model ($\alpha = 0.01$, $\beta = 0.001$).

craft model (with linear actuator) about a set of trim conditions over the angle-of-attack range. The resulting gains were then scheduled against demanded pitch angle, $\theta_{demand}$. A model reference adaptive controller was then tested on the model, which required no *a priori* design apart from selection of two adaption weights.

All controllers were tested on the experimental rig, with limited success. In particular, the experimental bifurcation diagram could indeed be straightened and the limit cycle oscillations suppressed, however, in general there would be other transient and self-excited dynamics associated with the response. The unwanted dynamics were observed to become more problematic as controller complexity increased, shown by decreasing performance of controllers on the experimental rig.

A major limitation when evaluating the controllers was actuator performance. All of the gain-scheduled methods suffered from high-frequency self-excited oscillations which were thought to be caused by un-modelled delays and non-linearities in the tailplane actuators. This was demonstrated by adding an extra delay to the numerical model and running a time simulation, showing a similar oscillatory response.

There are several points to note, and lessons learned, from the experimental tests performed in this chapter:

1. The importance of accurate actuator modelling. If the actuators exhibit significant non-linearities it may be necessary to have an actuator model of much higher order than the aircraft model to capture the dynamics. However, some non-linearities are extremely difficult to model accurately in a linear approximation (e.g. backlash/freeplay), therefore a linear control design method may not be suitable for developing controllers.

2. The importance of accurate control surface position feedback (particularly if the actuators exhibit non-linearities). This would allow accurate assessment of where the deficiencies in control performance lie, and would also allow a more accurate actuator model to be developed.

3. The problems caused by non-linearities within the actuators. It is highly desirable to have actuators that exhibit a consistent, linear response. This would aid the comparison of controllers significantly.

4. Placement of the closed-loop poles at the correct scale location. Although the maximum (no-load) rate of the actuators appears to be satisfactory (see Section 3.3.4), the results from the this chapter and Chapter 7 indicate that there is insufficient control response speed to place the aircraft eigenvalues at the correct scale location. This could be due to performance degradation of the actuators while on the model (aerodynamic forces, control surface moment-of-inertia, PWM control delay, etc.), but the larger-than-scale moment of inertia of the model will also cause a slower response. Currently, the servo actuators used in the Hawk model are some of the fastest available (0.09s to 60°), so unless significantly faster actuators become available, the only option to achieve correct scaled closed-loop eigenvalue locations is to increase the scale of the model.

5. Wind tunnel turbulence problems. Although the actuators proved to be the main problem when attempting to compare controllers, wind tunnel turbulence made it difficult to see differences in results. It was also impossible to compare responses to very small control inputs, as the results would be swamped by turbulence effects. If the problems with the actuators were eliminated, tunnel turbulence would quickly become the major factor in limiting achievable results.

6. Repeatability of results. Problems with repeatability of results were demonstrated by the disappearance of the small-amplitude limit cycle when the rig was set up to test the controllers developed in this chapter. As well as illustrating the need for more meticulous documentation of the test conditions, it also shows the importance of having facilities which allow certain test conditions to be recreated. For example, provision for accurate, measurable weight positioning within the model would greatly help in producing repeatable mass and mass distribution within the model, and a wireless data acquisition system would eliminate variations caused by slight position changes of the wiring loom running up the sting.

# Chapter 9

# Gain-Scheduled Control

In the previous chapter a series of controllers was tested on the numerical model of the Hawk, and on the experimental rig. Some of the controllers involved scheduling a set of gains calculated using linearisations of the model at a series of operating points along the trim curve. When implementing the gain-scheduled controllers it was not certain which scheduling parameter to use. There are three main possibilities as concerns the choice of scheduling parameter:

- **Schedule against reference demand** – this method works when the input is slowly-varying and the system is not perturbed far from the trimmed equilibrium condition about which the gains were designed. This is the method used for all the gain-scheduled controllers in the previous chapter. As an example of a limitation of this method, if a large input is rapidly applied to a non-linear system, it is possible that the gains (which will be instantaneously changed when the input is applied) will be set for a completely different operating condition to the current location of the system.

- **Schedule against a slowly-varying system state** – this method is used in many practical controllers (for example, scheduling aircraft controller gains with altitude or velocity) but again suffers from the limitations imposed by scheduling against reference demand, namely slow variation conditions and restriction to near-equilibrium solutions.

- **Schedule against any (rapidly-varying) system state, accounting for hidden coupling terms** – this ensures that the controller gains, and hence plant response, are correct even when large, rapid inputs are applied. If controllers are designed at all phase-space locations (using off-equilibrium linearisations) it is possible, in theory, for the system to exhibit an ideal response at any location in phase space with any input (within the limitations of the physical system).

The possibility of improving the gain-scheduled controllers presented in Chapter 8 by scheduling the controller gains directly against system states led to the preliminary work presented in this chapter. In particular, it was possible that some of the unwanted transient responses shown in the time histories in Chapter 8 could be eliminated by using this form of 'dynamic scheduling'. A literature survey revealed that work had been carried out in this area, but no explicit method had been presented. In particular, in [131] it is proposed that the recent upsurge in work on gain-scheduled controllers is with the aim of relaxing two restrictions associated with classical gain scheduling methods:

1. the slow variation conditions associated with ensuring that the overall system does not evolve between operating regions in too rapid a manner;

2. the restriction to near equilibrium operation that arises from the use of only equilibrium information (namely, the equilibrium linearisations of the plant) for control design purposes.

The preliminary work presented in this chapter aims to formalise a method of gain scheduling which addresses both these issues. Firstly, a controller is designed that relaxes condition (1) above by allowing the scheduling variable to be one of the rapidly-varying system states. This ensures that the controller gains are set for the current state space location and therefore provide a response that is close to optimal. It is achieved by finding non-linear functions of single states which satisfy stability and response requirements on desired equilibrium branches. Although trimmed equilibrium points are not required (simply a smooth variation in the state considered), gain scheduling for trimmed steady states results in a controller that gives the desired response about trimmed operating conditions. The method is demonstrated on a second order analytical example before

being applied to the mathematical model of the Hawk. Due to the preliminary nature of the work, it was not tested experimentally.

Secondly, it is shown that condition (2) can be relaxed for certain non-linear systems by using off-equilibrium linearisation. This ensures an ideal dynamic response anywhere in the system phase space, not just about an equilibrium condition. A second order analytical example is used to demonstrate the design method.

## 9.1 State Scheduling

Consider the non-linear system:

$$\dot{\boldsymbol{x}} = \boldsymbol{f}(\boldsymbol{x}, \boldsymbol{\delta}) \tag{9.1}$$

| where: | | |
|---|---|---|
| | $\boldsymbol{x} \in \mathbb{R}^n$ | is a vector of system states |
| | $\boldsymbol{\delta} \in \mathbb{R}^p$ | is a vector of parameters |
| | $\boldsymbol{f} : \mathbb{R}^{n+p} \rightarrow \mathbb{R}^n$ | is a smooth non-linear system |

Adding a non-linear controller to the system and fixing all parameters except one, $\mu$, we have the affine system:

$$\dot{\boldsymbol{x}} = \boldsymbol{f}(\boldsymbol{x}, \mu) + \boldsymbol{g}(\boldsymbol{x}, \mu)\boldsymbol{u} \tag{9.2}$$

| where: | | |
|---|---|---|
| | $\boldsymbol{x} \in \mathbb{R}^n$ | is a vector of system states |
| | $\boldsymbol{u} \in \mathbb{R}^m$ | is a vector of inputs |
| | $\boldsymbol{f} : \mathbb{R}^{n+1} \rightarrow \mathbb{R}^n$ | is a smooth non-linear system |
| | $\boldsymbol{g} : \mathbb{R}^{n+1} \rightarrow \mathbb{R}^n$ | is a smooth non-linear system |

Linearising with $\mu$ fixed and where $\hat{\boldsymbol{x}}$ and $\hat{\boldsymbol{u}}$ are perturbations from the linearisation point gives the equation:

$$\dot{\hat{\boldsymbol{x}}} = \boldsymbol{A}\hat{\boldsymbol{x}} + \boldsymbol{B}\hat{\boldsymbol{u}} \tag{9.3}$$

If a state feedback scheme is considered then the input $\hat{\boldsymbol{u}}$ is expressed in terms of the states $\hat{\boldsymbol{x}}$ and an appropriate feedback gain matrix $\boldsymbol{K}$. This results in the closed loop system:

$$\dot{\hat{\boldsymbol{x}}} = \boldsymbol{A}\hat{\boldsymbol{x}} + \boldsymbol{B}\boldsymbol{K}\hat{\boldsymbol{x}} = \boldsymbol{A}_{\boldsymbol{cl}}\hat{\boldsymbol{x}} \tag{9.4}$$

Using this linearisation the gain matrix can be calculated using a linear method such as eigenstructure assignment [125, 126]. In general, with a highly non-linear plant, this linearisation is carried out at multiple points in state space. Thus a series of gain matrices is calculated. Note that the required gains may vary considerably over the state space region of interest and so scheduling of the gain matrices may be necessary to maintain an acceptable control performance.

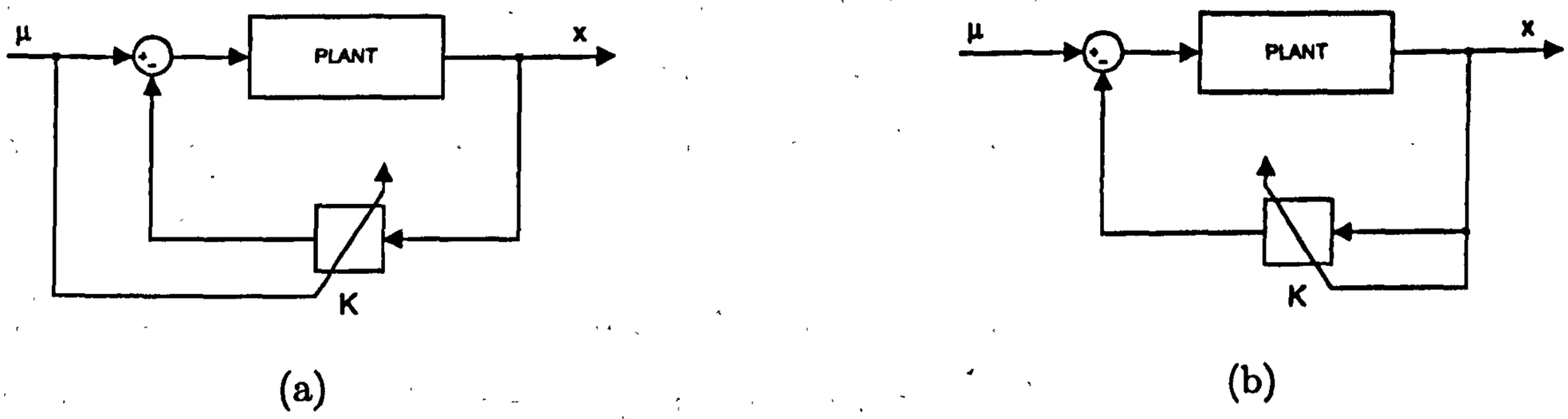


Figure 9.1: $\mu$ scheduling (a) and state scheduling (b) methods.

It is possible to schedule these gains against either $\mu$ (Figure 9.1(a)) or $\boldsymbol{x}$ (Figure 9.1(b)). Scheduling against $\boldsymbol{x}$ leads to a problem. The gain matrix $\boldsymbol{K}$ is calculated assuming constant gains at each linearisation and therefore requires sufficiently slow state variations when implemented. However, in the presence of rapid state variations, gain scheduling against system states introduces unwanted additional dynamics to leading order in the form of $\frac{\partial \boldsymbol{K}}{\partial \boldsymbol{x}}$.

The aim of this chapter is to lay out a methodology by which the gain matrices may be scheduled against system states ('dynamic' gains) whilst compensating for, or exploiting, the non-linear variation in gain arising from the scheduling process. Returning to the non-linear system and taking $\boldsymbol{x}^*$ as a trim point about which to take a linearisation, the Jacobian for the open loop system can be defined as:

$$\boldsymbol{J} = \left.\frac{\partial \boldsymbol{f}}{\partial \boldsymbol{x}}\right|_{\boldsymbol{x}^*} \tag{9.5}$$

Defining $\boldsymbol{\sigma}(\boldsymbol{J})$ as a specified eigenstructure with desired eigenvalues for the closed loop system, the problem associated with gain scheduling against system states can be stated as follows:

*Find a non-linear gain matrix, $\phi(x)$, such that the non-linear feedback control law $u = \phi(x)x$ guarantees that the closed-loop system has a desired eigenstructure under state variations.*

Note that the eigenstructure can either be fixed for all $x$ or be scheduled against $x$. The key step in synthesising such a controller is to find an appropriate functional form for $\phi(x)$. For instance, for simple systems, $\phi(x)$ can be found simply by cancelling the non-linear terms within the system equations. For more complex systems and for systems where only small changes to the non-linear behaviour are required then a numerical method for calculating $\phi(x)$ would be desirable. Hence gain scheduling against strongly coupled system states is considered.

We propose that the non-linear gains, $\phi(x)$, can be found by considering constant gains, $K$, obtained by standard eigenstructure assignment applied to the linearised model at a set of discrete phase space points. Note that for the trimmed case it is possible to find $K$ using a continuation algorithm. The control design algorithm can be incorporated within a continuation method and $K$ solved for explicitly as solution branches are traced out. By doing this, gains are determined pseudo-continuously rather than at discrete operating points. Traditionally, when $K$ is implemented in the controller, it is scheduled against the continuation parameter, $\mu$, or a decoupled or slowly varying state. If the scheduling parameter varies rapidly then the stability will not be as desired.

## 9.2 State Scheduling Methodology

### 9.2.1 Finding $K$

Consider the first order system:

$$\dot{x} = f(x, \mu) + u \tag{9.6}$$

where $x \in \mathbb{R}$, $u \in \mathbb{R}$. Assume we wish to design a state feedback controller, $u = Kx$, whose feedback gains are obtained by eigenstructure assignment of the linearised model about a set of trimmed points. Then, about each of these points, $K$ will be chosen such

that the Jacobian of the closed loop system:

$$J_1 = \left[\frac{\partial f}{\partial x} + K\right] \tag{9.7}$$

has a desired eigenvalue, $\lambda_d$, i.e.

$$\left|\frac{\partial f}{\partial x} + K - \lambda_d\right| = 0. \tag{9.8}$$

Thus, at the end of the process we will have a set of feedback gains scheduled against a set of state points over the range of interest.

### 9.2.2 Finding $\phi(x)$

Suppose now we want to solve the same problem by considering the non-linear controller $u(x) = \phi(x)x$. The closed loop system will then be described by:

$$\dot{x} = f(x, \mu) + \phi(x)x \tag{9.9}$$

The Jacobian $J_2$ of equation (9.9) can be defined as:

$$J_2 = \left[\frac{\partial f}{\partial x} + \frac{\partial \phi}{\partial x}x + \phi(x)\right] \tag{9.10}$$

With a desired $\phi(x)$ such that the closed loop system has the identical eigenstructure to (9.8), the following must hold for all $x$:

$$\left|\frac{\partial f}{\partial x} + \frac{\partial \phi}{\partial x}x + \phi(x) - \lambda_d\right| = 0 \tag{9.11}$$

### 9.2.3 Equating the systems $K$ and $\phi(x)$

By comparing (9.8) and (9.11) we then get:

$$\left|\frac{\partial f}{\partial x} + K - \lambda_d\right| = \left|\frac{\partial f}{\partial x} + \frac{\partial \phi}{\partial x}x + \phi(x) - \lambda_d\right| = 0$$

Hence, for the first order system:

$$\frac{\partial f}{\partial x} + K - \lambda_d = \frac{\partial f}{\partial x} + \frac{\partial \phi}{\partial x}x + \phi(x) - \lambda_d \tag{9.12}$$

Cancellation results in:

$$K = \frac{\partial \phi}{\partial x} x + \phi(x) \tag{9.13}$$

A point to note from equation (9.13) is that the two gains are equivalent at points where the partial differential $\frac{\partial \phi}{\partial x} = 0$. Therefore where both $K$ and $\phi(x)$ are plotted against $x$ they will intersect at all points where the slope of $\phi(x)$ is zero.

As stated before, it is possible to find $K$ via a controller design process such as eigenstructure assignment (given sufficient control power). To implement a state-scheduled controller however, $\phi(x)$ is required. This dynamic gain can be found by integrating equation (9.13), to get:

$$\int K dx + c = \phi(x) x \tag{9.14}$$

i.e.

$$\phi(x) = \frac{\int K dx + c}{x} \tag{9.15}$$

Therefore, for any first order system, the closed loop eigenvalues can be placed as desired using a dynamic gain derived via the numerical approach. Furthermore, as demonstrated in the next section, this can be extended to allow single-state scheduling in any $n^{th}$ order system.

### 9.2.4 Single-state scheduling for any $n^{th}$ order system

The transformation from static gain, $\boldsymbol{K}$, to dynamic gain, $\boldsymbol{\phi(x)}$, can be applied to any general $n^{th}$ order non-linear system provided that each gain is only scheduled against the state on which it is acting. If there is feedback on any state in any of the $n$ equations then the transformation that was found for the general first order system may be used to find the dynamic gain, $\boldsymbol{\phi(x)}$, from the pseudo-continuous static gain, $\boldsymbol{K}$. For example, if:

$$\dot{x}_1 = \boldsymbol{f(x)} + K_1(x_1)x_1 + K_2(x_2)x_2 + \cdots + K_n(x_n)x_n \tag{9.16}$$

then, using an identical proof as in the previous section, it is possible to find:

$$\dot{x}_1 = \boldsymbol{f(x)} + \phi_1(x_1)x_1 + \phi_2(x_2)x_2 + \cdots + \phi_n(x_n)x_n \tag{9.17}$$

### 9.2.5 Implementation in Practice

In practice, $K$ will be determined between a lower $x_l$ and upper $x_u$ limit. For any general point, $x_i$, such that $x_l < x_i < x_u$, we calculate the definite integral between $x_l$ and $x_i$:

$$\int_{x_l}^{x_i} K dx = K(x_i)x_i - K(x_l)x_l \tag{9.18}$$

Rearranging the equation for $K(x_i)x_i$ results in:

$$K(x_i)x_i = \int_{x_l}^{x_i} K dx + K(x_l)x_l \tag{9.19}$$

The term $K(x_l)x_l$ is a constant and is zero when the integration is started from zero. So if $K$ has been found numerically then a numerical integration can be used to find $\phi(x)$.

## 9.3 Two-dimensional gain scheduling

Although the single-state scheduling method presented in Section 9.2.4 can be performed on *any* $n^{th}$ order system, it may only give the desired response when close to the operating point about which the gains were designed (usually the trim curve in the aircraft case). To achieve a more optimal response it is desirable to have dynamic state-feedback gains that are functions of all the state variables[1]. This implies that the state-feedback gains must be calculated at all state-space locations, not just the equilibrium conditions, using so-called off-equilibrium linearisation. At present, it has only been possible to implement this method on second-order affine systems; ongoing research is addressing higher order and non-affine systems.

As an example of two dimensional gain scheduling, consider a second order non-linear system of the form:

$$\dot{x}_1 = \boldsymbol{f}(\boldsymbol{x}) + \boldsymbol{K}(\boldsymbol{x}) + \mu \tag{9.20}$$

$$\dot{x}_2 = x_1 \tag{9.21}$$

[1]This is equivalent to having a multi-dimensional look-up table with the system states as inputs, and a single feedback term as the output.

where $\boldsymbol{K}(\boldsymbol{x})$ is the control input, using state feedback, and $\mu$ is the continuation parameter. We now show how the dynamic gain schedule can be derived from the static schedule in a similar way to the derivation in Section 9.2. Note, however, that the proof below only holds for systems where the input acts on *one* of the system states.

Assume that $\boldsymbol{K}(\boldsymbol{x})$ is a combination of linear state feedback of each state; expressing each static gain as a schedule against $x_1$ and $x_2$, i.e. $\boldsymbol{K}(\boldsymbol{x}) = K_1(\boldsymbol{x})x_1 + K_2(\boldsymbol{x})x_2$, we have:

$$\dot{x}_1 = \boldsymbol{f}(\boldsymbol{x}) + K_1(\boldsymbol{x})x_1 + K_2(\boldsymbol{x})x_2 + \mu \tag{9.22}$$

$$\dot{x}_2 = x_1 \tag{9.23}$$

And the equivalent equations for the dynamic state-scheduled gain are:

$$\dot{x}_1 = \boldsymbol{f}(\boldsymbol{x}) + \bar{\phi}(\boldsymbol{x}) + \mu \tag{9.24}$$

$$\dot{x}_2 = x_1 \tag{9.25}$$

where, to simplify the derivation, $\bar{\phi}(\boldsymbol{x})$ (a look-up table in $\boldsymbol{x}$) replaces $\phi(\boldsymbol{x})\boldsymbol{x}$ (scheduled state feedback gains) from now on. As before, we can now equate the two Jacobians to find an equivalent dynamic state-scheduled gain from the continuation parameter scheduled gain. However, now we have two requirements for $\bar{\phi}(\boldsymbol{x})$:

$$\bar{\phi}(\boldsymbol{x}) = \int K_1 dx_1 + C_1(x_2) \tag{9.26}$$

$$\bar{\phi}(\boldsymbol{x}) = \int K_2 dx_2 + C_2(x_1) \tag{9.27}$$

Where $C_1(x_2)$ and $C_2(x_1)$ are 'constants' of integration which will, in practice, be dependent on the state values $x_1$ and $x_2$. Evaluating (9.26) at fixed values of $(x_1, x_2) = (x_1^*, x_2^*)$ gives[2]:

[2]Integrating from zero is convenient, but the result can be derived for any starting point (the integration constant will simply be shifted by a fixed amount).

$$\bar{\phi}(x_1^*, x_2^*) = \int_0^{x_1^*} K_1(x)dx_1 + C_1(x_2^*) \tag{9.28}$$

Now, at $x_1^* = 0$:

$$\int_0^{x_1^*} K_1(x)dx_1 = 0 \tag{9.29}$$

$$\Rightarrow \bar{\phi}(0, x_2^*) = C_1(x_2^*) \tag{9.30}$$

From (9.27), with $(x_1, x_2) = (0, x_2^*)$:

$$\bar{\phi}(0, x_2^*) = \int_0^{x_2^*} K_2(0, x_2)dx_2 + C_2(x_1^*) \tag{9.31}$$

with the added constraint (as with all state-variable feedback systems, where feedback will be zero at zero state values) that:

$$\bar{\phi}(0, 0) = 0 \tag{9.32}$$

$$\Rightarrow C_2(0) = 0 \tag{9.33}$$

Now combining (9.30), (9.31) and (9.33) gives:

$$\bar{\phi}(0, x_2^*) = C_1(x_2^*) = \int_0^{x_2^*} K_2(0, x_2)dx_2 \tag{9.34}$$

Thus, from (9.28):

$$\bar{\phi}(x_1^*, x_2^*) = \int_0^{x_1^*} K_1(x_1, x_2)dx_1 + \int_0^{x_2^*} K_2(0, x_2)dx_2 \tag{9.35}$$

Due to the coupling between the gains (given by Equations (9.26) and (9.27)), this is equivalent to:

$$\bar{\phi}(x_1^*, x_2^*) = \int_0^{x_2^*} K_2(x_1, x_2)dx_2 + \int_0^{x_1^*} K_1(x_1, 0)dx_1 \tag{9.36}$$

This transformation can be easily implemented numerically, using an extension of the implementation given in Section 9.2.5.

## 9.4 $2^{nd}$ Order Analytical Example

As an example of two-dimensional gain scheduling, consider the $2^{nd}$ order system of the form given in equations 9.20 and 9.21:

$$\dot{x}_1 = x_1^2 x_2^2 + 24x_1x_2 + 4x_1 + 3x_2 + K_1x_1 + K_2x_2 + \mu \tag{9.37}$$

$$\dot{x}_2 = x_1 \tag{9.38}$$

Where, for clarity, the dependence of the feedback gains, $K_1$ and $K_2$, on the state vector has been omitted. The Jacobian matrix is:

$$J = \begin{bmatrix} 2\,x_1\,{x_2}^2 + 24x_2 + 4 + K_1 & 2\,{x_1}^2\,x_2 + 24x_1 + 3 + K_2 \\ 1 & 0 \end{bmatrix} \tag{9.39}$$

Using $|J - \lambda I| = 0$ gives:

$$\left| \begin{bmatrix} 2\,x_1\,{x_2}^2 + 24x_2 + 4 + K_1 - \lambda & 2\,{x_1}^2\,x_2 + 24x_1 + 3 + K_2 \\ 1 & -\lambda \end{bmatrix} \right| = 0 \tag{9.40}$$

$$\rightarrow \lambda^2 + (-2x_1x_2^2 - 24x_2 - 4 - K_1)\lambda - 2x_1^2x_2 - 24x_1 - 3 - K_2 = 0 \tag{9.41}$$

Solving for the eigenvalues, $\lambda$, and assuming arbitrarily that we want the poles of the closed-loop system to be at $-2 \pm 2i$ we get:

$$K_1 = -2x_1x_2^2 - 24x_2 - 8 \tag{9.42}$$

$$K_2 = -2x_1^2x_2 - 24x_1 - 11 \tag{9.43}$$

These are the static gains required to place the eigenvalues of the steady-state system at the specified location; they do not take into account the gradient of the gain schedule. Using equation (9.35) or (9.36) to convert them into a single dynamic state-scheduled gain[3], $\bar{\phi}$ (again, for simplicity notation indicating state dependence is omitted), gives:

$$\bar{\phi} = -x_1^2x_2^2 - 8x_1 - 11x_2 \tag{9.44}$$

Although the static and dynamic gain schedules give identical steady-state pole locations, when transient responses are considered the dynamic state-scheduled gain keeps the eigenvalues in the correct location at *all* times. Performance of the $\mu$ scheduled (static) gain system reduces as the response moves away from the steady-state condition. In addition, if rapid input demands are made, the $\mu$ scheduled gains change rapidly which will give additional unwanted transient dynamics. Figure 9.2 shows time histories for the $2^{nd}$ order example presented above for both $\mu$- and state-scheduled gains. In this example, the step change in gain for the $\mu$ scheduled system causes the system to move in the right direction (i.e. toward the desired final position). However, it is equally possible that this step change in gain could initially move the system in the opposite direction to the commanded input (see e.g. [59]). Note the decreasing performance of the static gain system as the step input increases in magnitude.

## 9.5 Hawk Example

As a further illustrative example of the state scheduling method presented in this section, a controller will now be designed for the single DOF mathematical model of the Hawk. The results from a standard input-scheduled controller (Figure 9.3) will be compared with those of the state-scheduled system (Figure 9.4). It is important to note that

[3]where, in this case, $\dot{x}_1 = x_1^2x_2^2 + 24x_1x_2 + 4x_1 + 3x_2 + \bar{\phi} + \mu, \dot{x}_2 = x_1$.

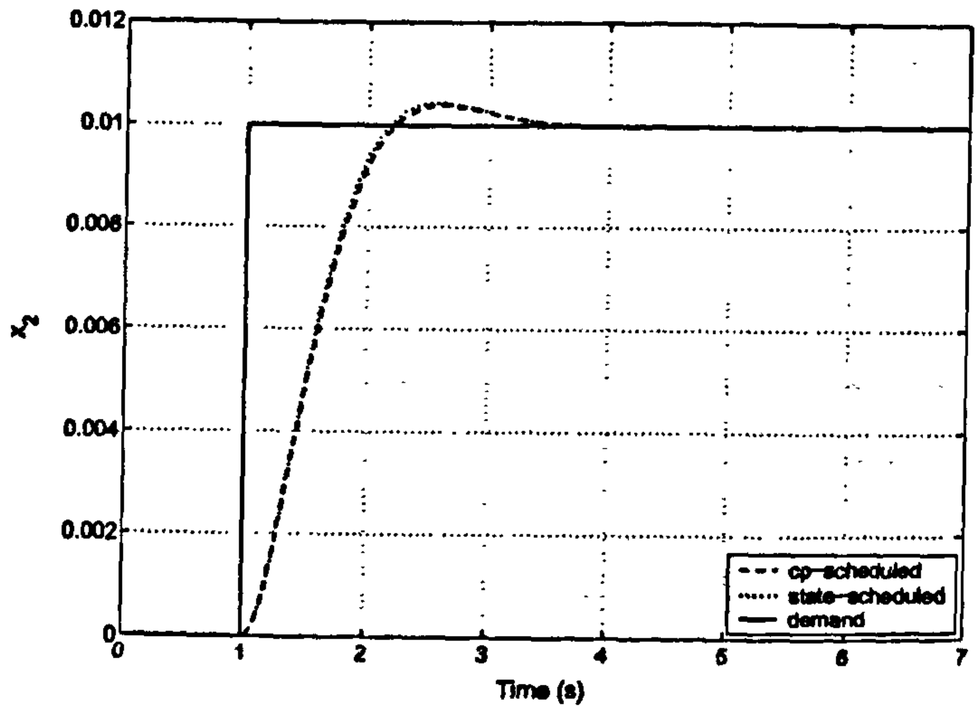


(a)

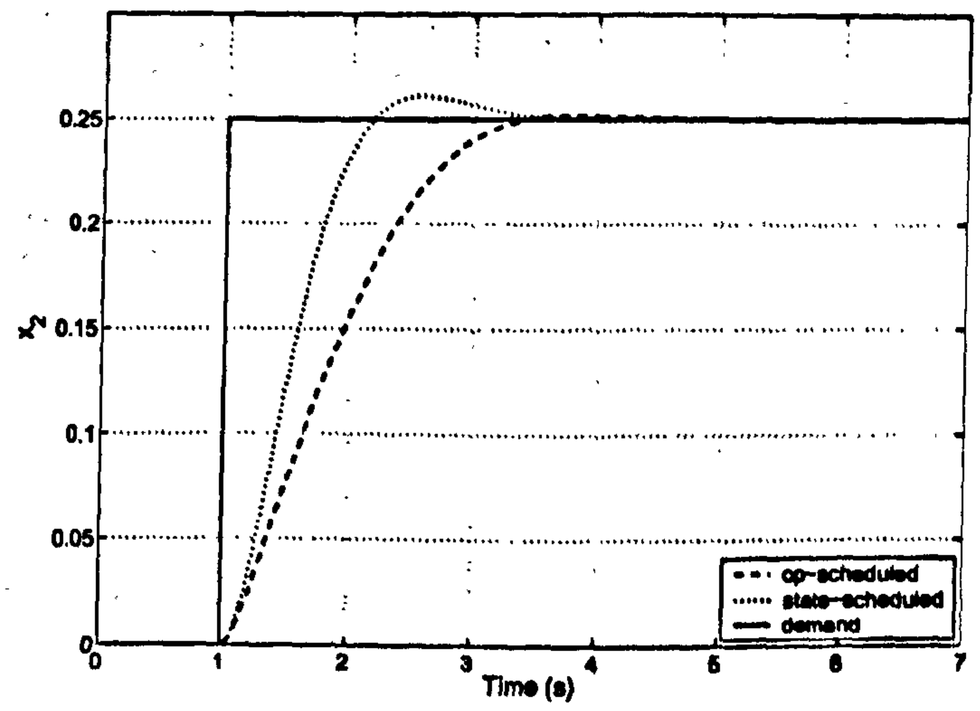


(b)

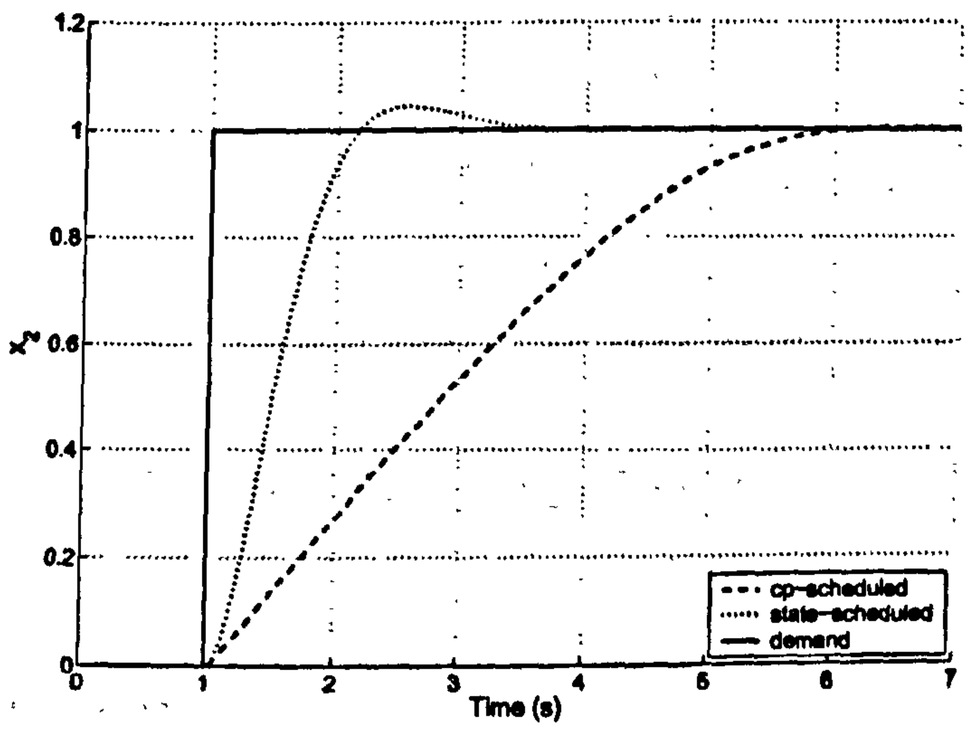


(c)

Figure 9.2: Step responses of $2^{nd}$ order example using $\mu$- and state-scheduled controllers.

the state scheduling will only be carried out in $\theta$, i.e. the controller gains will all be scheduled against pitch angle, $\theta$, as opposed to pitch angle demand, $\theta_{demand}$, in the input-scheduling case. It is not possible to carry out single-state scheduling on both $\theta$ and $q$, outlined in Section 9.2.4, as the pitch rate along the trim curve (about which the controller is designed) is always zero. The ideal solution to this problem would be to use multi-dimensional scheduling; the standard controller would be designed at a grid of phase-space points (using off-equilibrium linearisations), before the grid is converted to state-scheduled gains. Unfortunately, as yet, the method for finding this multi-dimensional state-scheduled grid will only work for a limited set of systems (as described in Section 9.3). The solution of this problem for higher order systems is the subject of ongoing research.

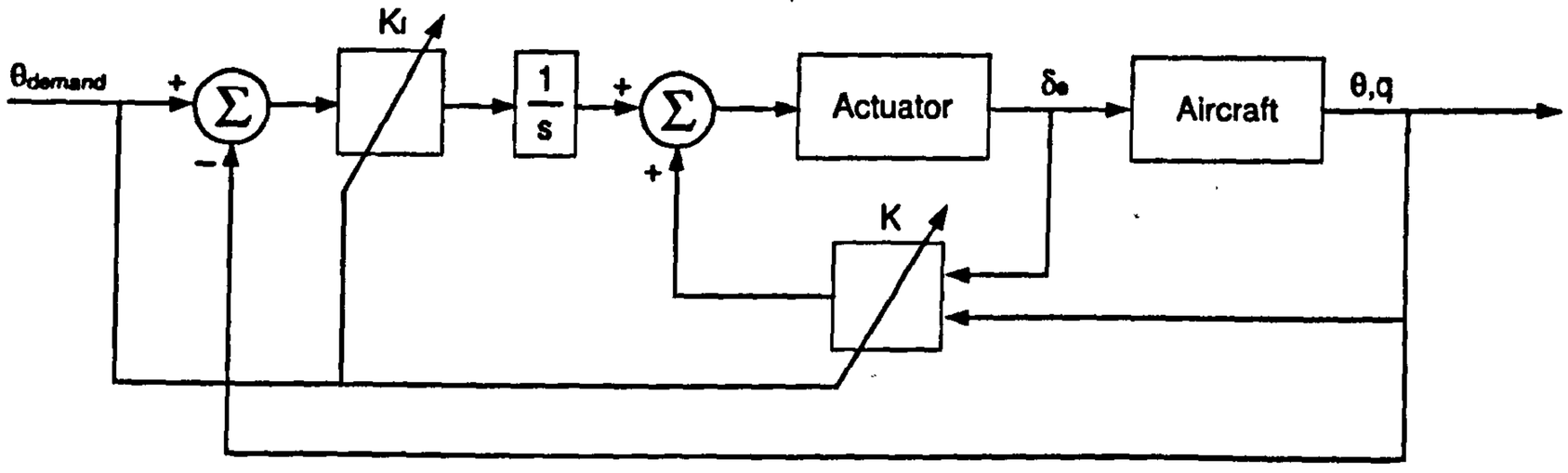


Figure 9.3: Input-scheduled control layout.

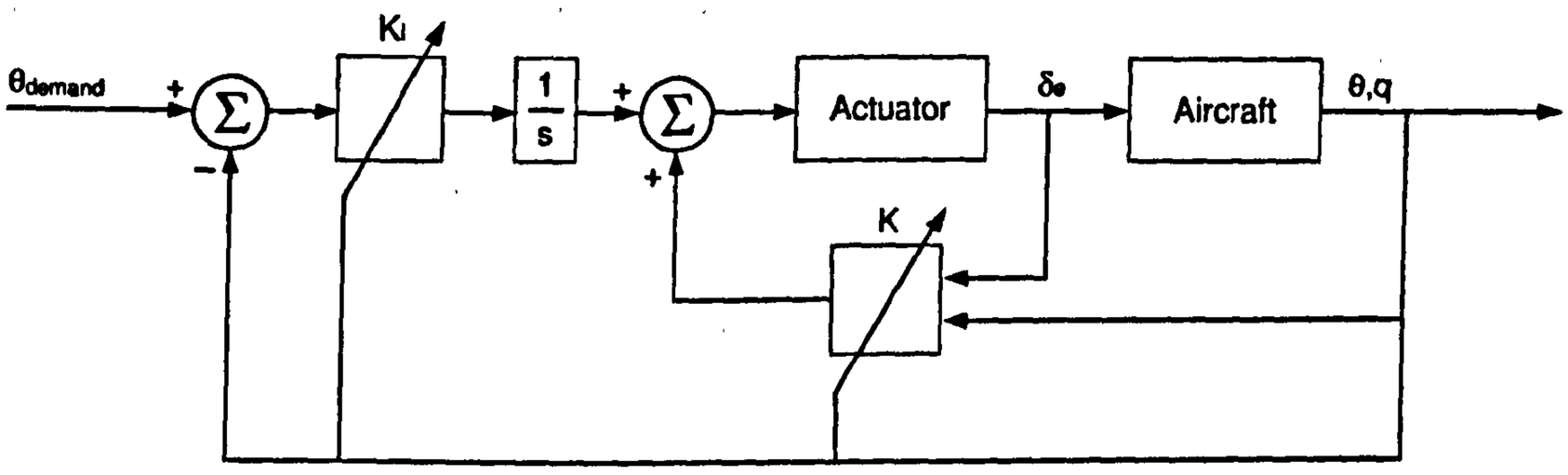


Figure 9.4: State-scheduled control layout.

### 9.5.1 Implementation

The eigenstructure assignment routine described in Section 8.1 was used to find the state-feedback gains for the fifth order system shown in Figure 9.3. The states of the model are $[q, \theta, \delta_e, \dot{\delta}_e, x_{int}]^T$ (where $x_{int}$ is the integrator state) and, again, tailplane rate feedback is not used. The control equation for the input-scheduled controller is:

$$u = K\mu_1 \times q + K\mu_2 \times \theta + K\mu_3 \times \delta_e + K\mu_4 \times x_{int}. \tag{9.45}$$

The state-scheduled control equation is identical to this, but with the input-scheduled gains, $K\mu$, replace with the corresponding state-scheduled gains, $Ks$. The aircraft poles were placed at the scale locations given in Section 7.1, the integrator was placed at −15, and the actuator poles remained in their open-loop location. The open-loop system poles are shown in Figure 9.5 and the state-feedback gains given in Figure 9.6. The closed-loop poles remained at the desired location throughout the pitch angle range of interest.

The method described in Section 9.2 was then used to convert the input-scheduled gains into state-scheduled gains, by integrating and dividing with respect to $\theta$ only, for im-

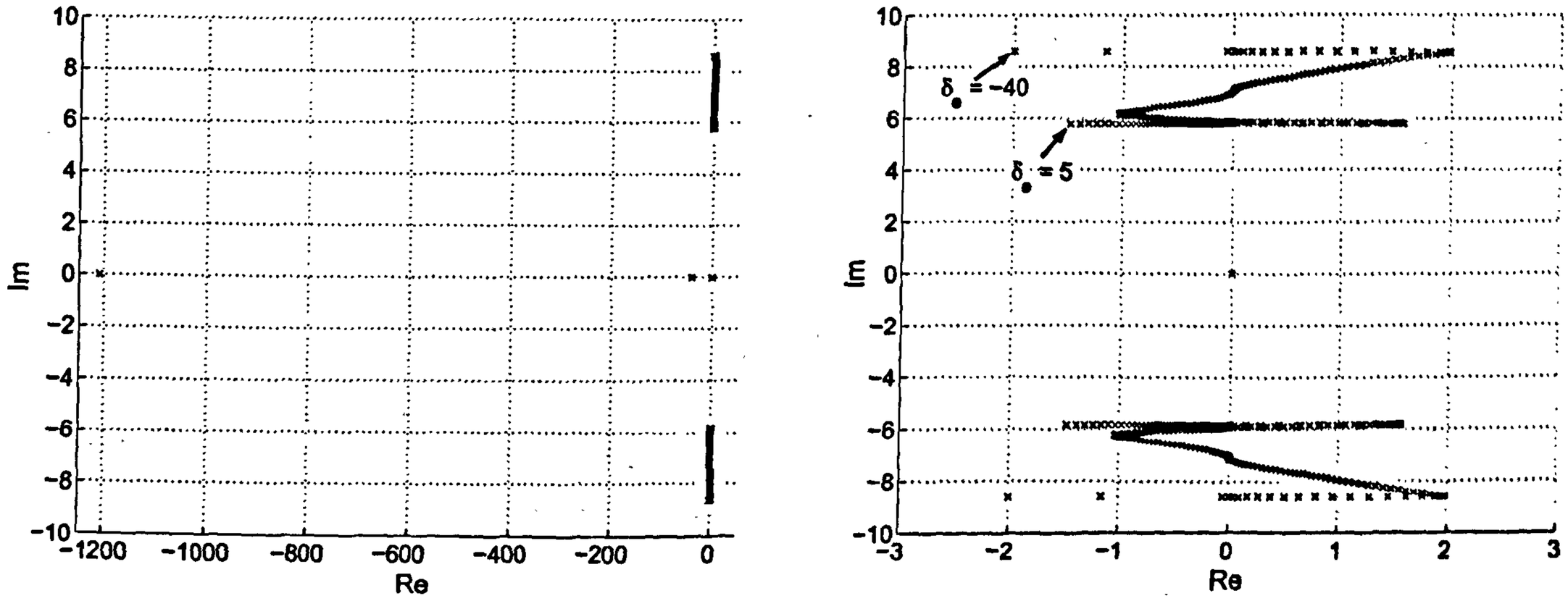


(a) Open-loop poles for the Hawk.

(b) Zoom-in of the open-loop poles.

Figure 9.5: Open-loop poles along the trim curve.

plementation in the system shown in Figure 9.4. These gains are also shown in Figure 9.6. Note that, as mentioned before, the static and dynamic gains are equal when the gradient of the dynamic schedule (with respect to $\theta$) is zero (i.e. $\frac{\partial Ks}{\partial \theta} = 0$).

### 9.5.2 Simulation Results

Figures 9.7 to 9.11 show simulated step responses of the input- and state-scheduled systems. The low-amplitude responses are similar for the two controllers, however, the large amplitude step response (Figure 9.9) shows that the state-scheduled controller actually performs worse (less-than ideal damping) than the input-scheduled controller. It is almost certain that this is due to the problem mentioned above, where the gains are scheduled against pitch angle only, therefore they will be incorrect when the system is at phase-space points off the trim curve. The advantage of the state-scheduling method is demonstrated in Figure 9.11, where the input-scheduled system exhibits initial motion in the opposite direction to the demanded step input. The state-scheduled system avoids this problem, and displays a close-to-ideal response.

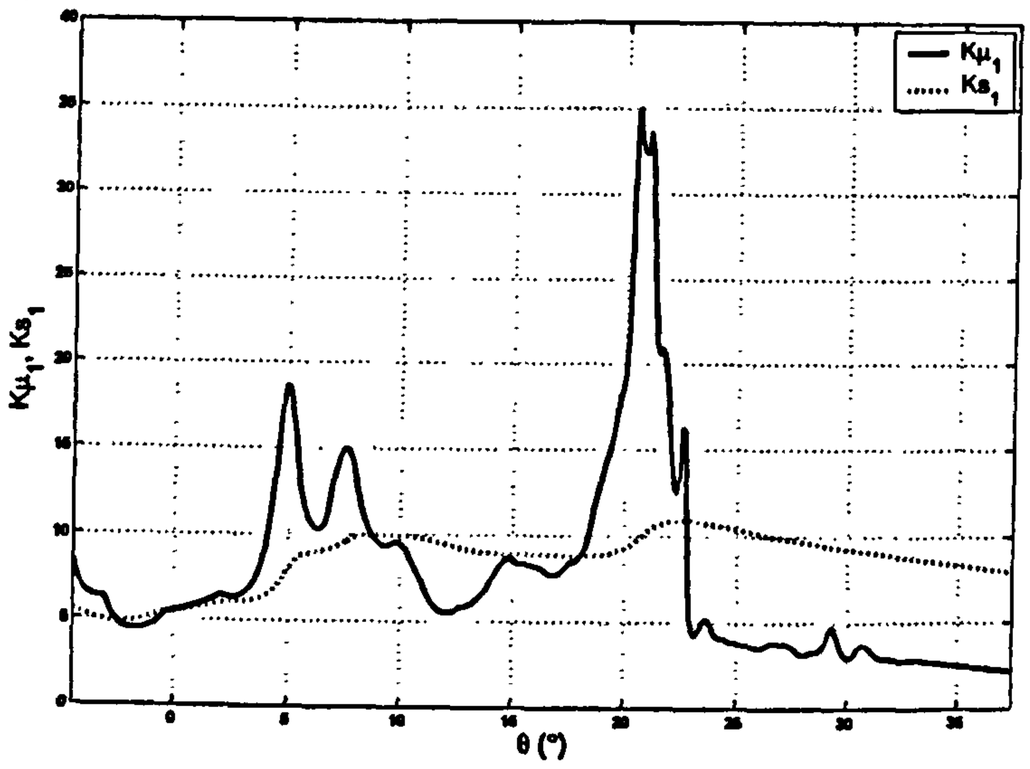


(a) $K\mu_1$, $Ks_1$.

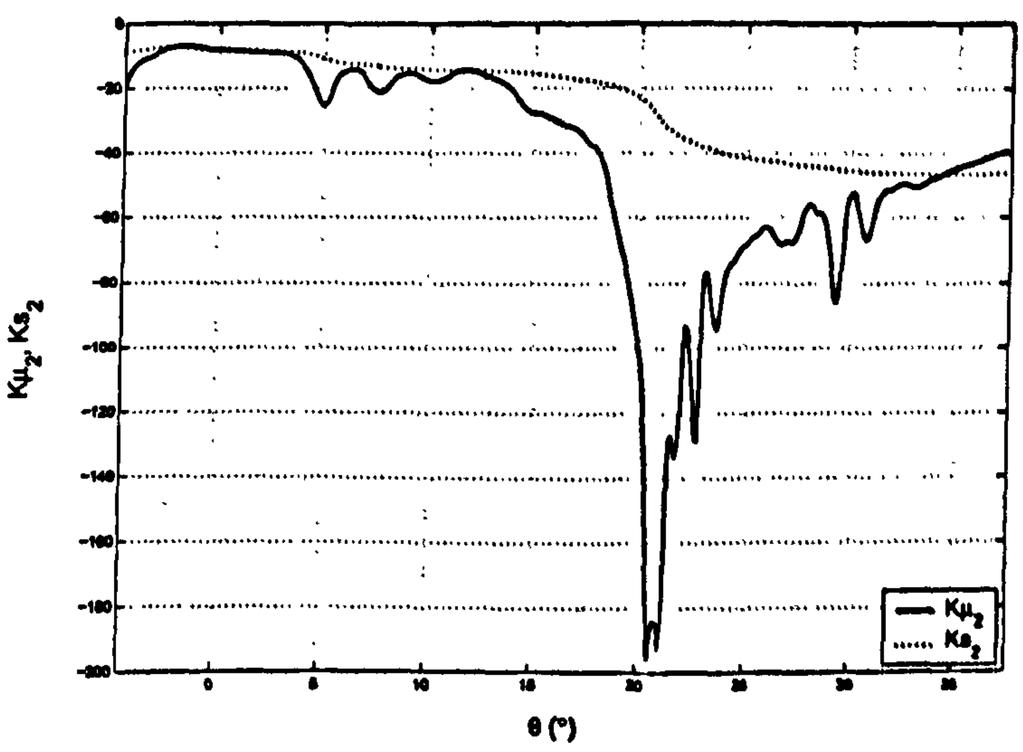


(b) $K\mu_2$, $Ks_2$.

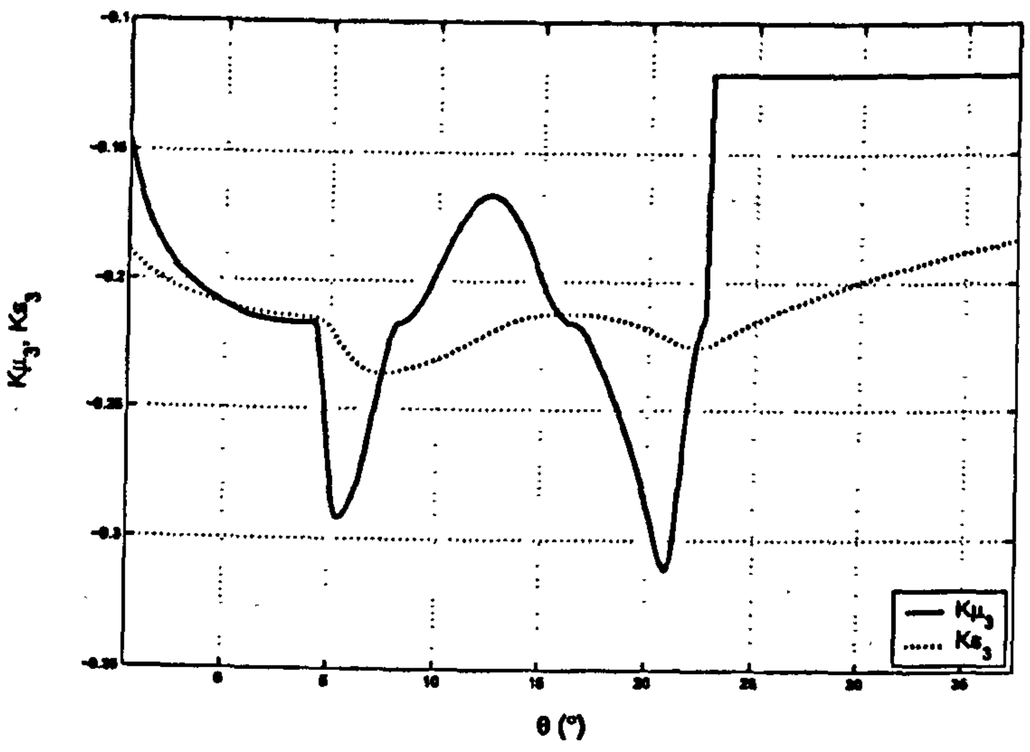


(c) $K\mu_3$, $Ks_3$.

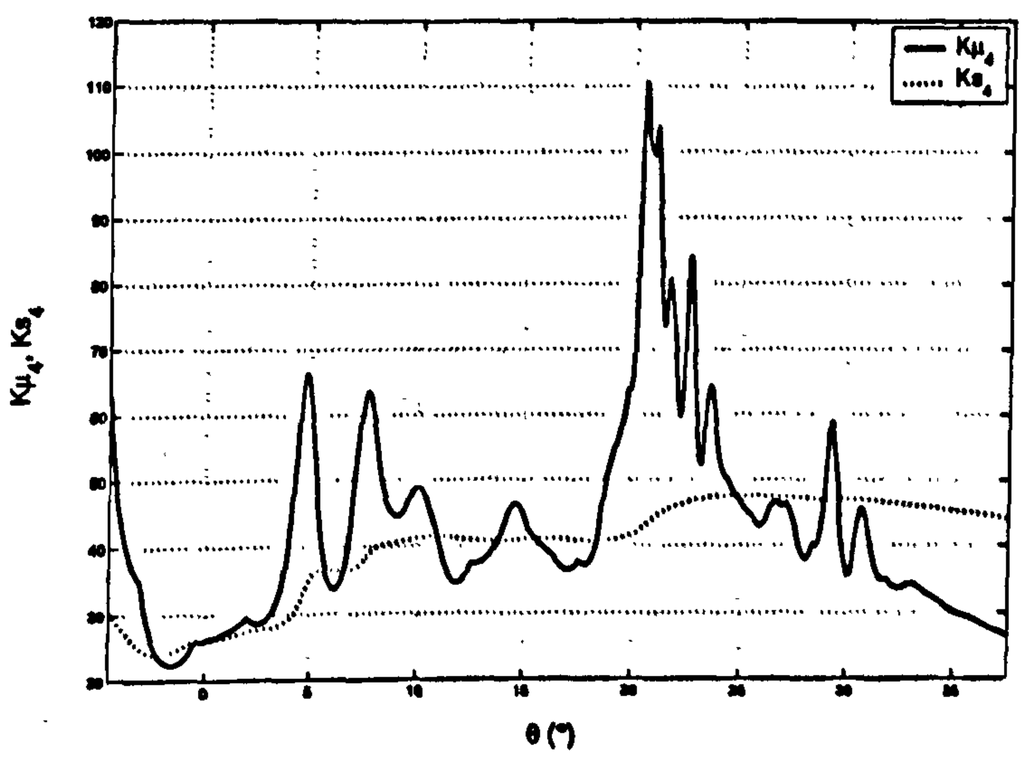


(d) $K\mu_4$, $Ks_4$.

Figure 9.6: Input- and state-scheduled gains.

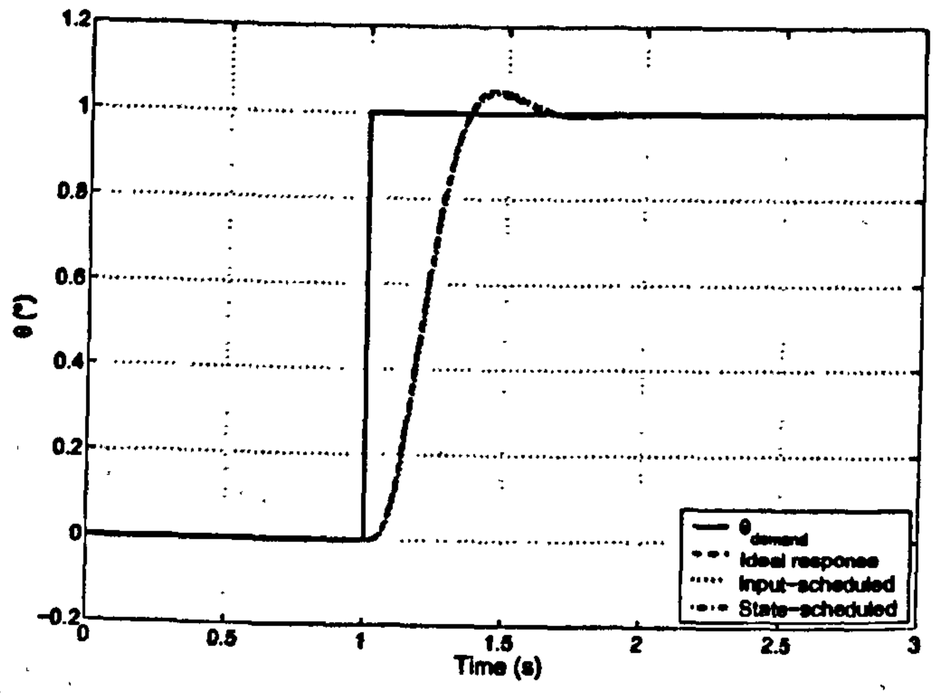


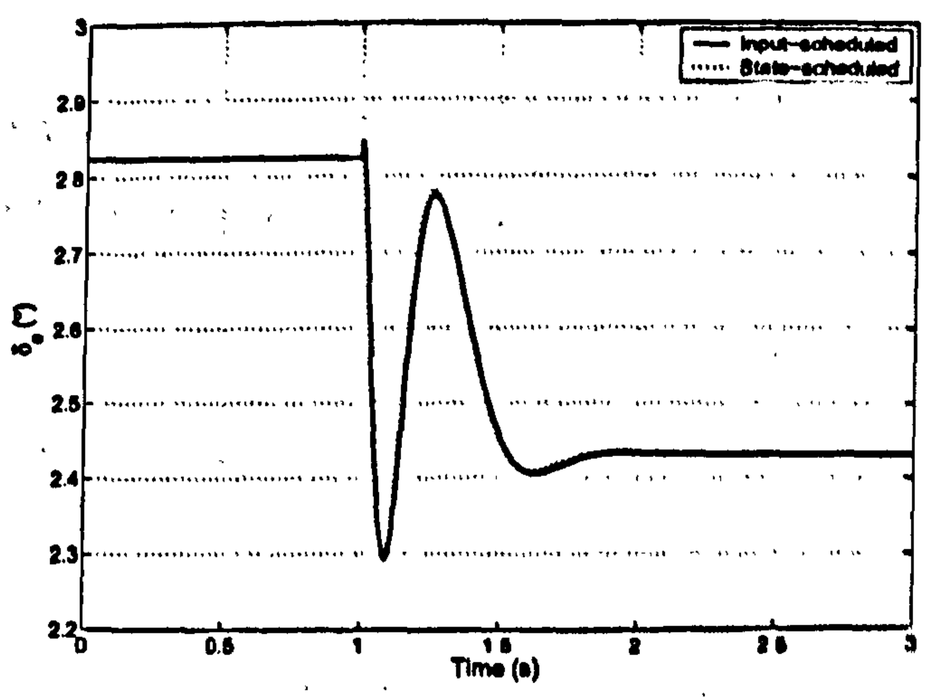


Figure 9.7: 1° step response for input- and state-scheduled controllers.

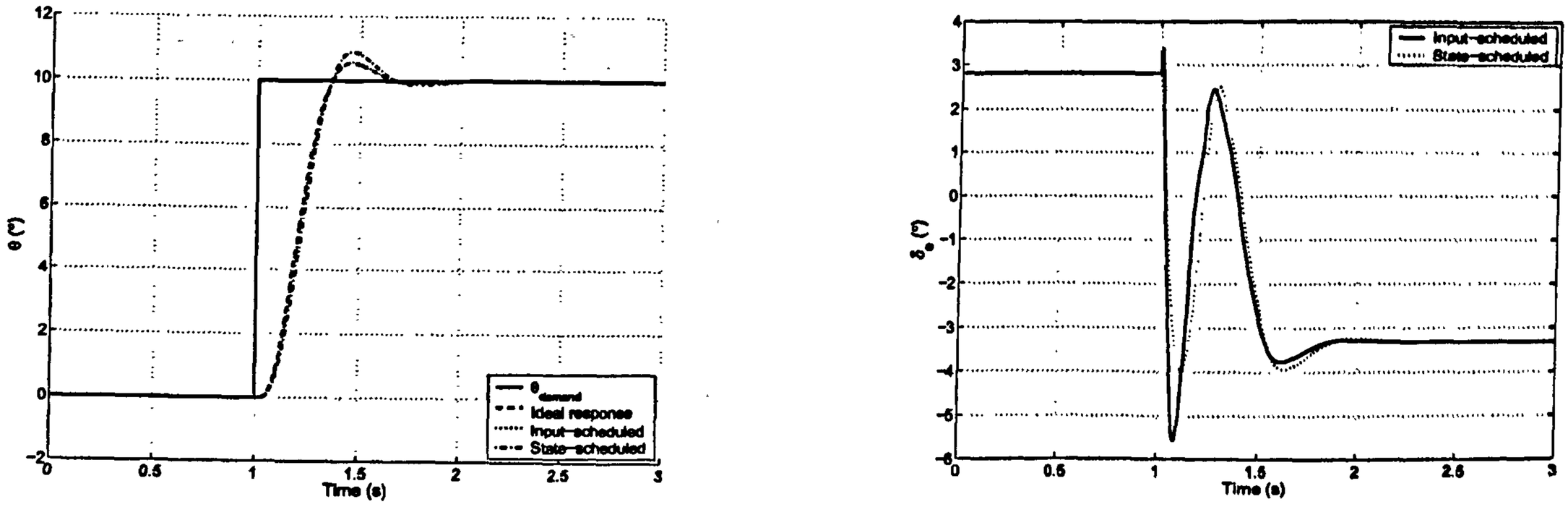


Figure 9.8: 10° step response for input- and state-scheduled controllers.

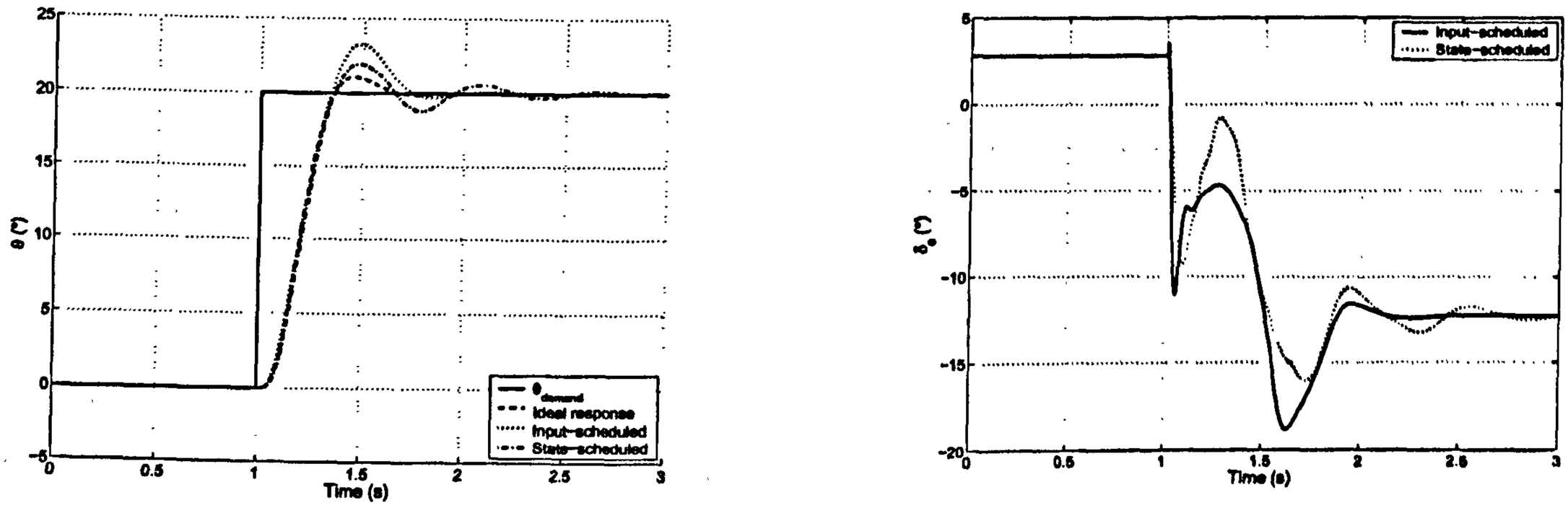


Figure 9.9: 20° step response for input- and state-scheduled controllers.

Unfortunately it was not possible to demonstrate the use of state-scheduled controllers on the experimental rig, due to the problems encountered in Chapter 8. The controller gains designed using the mathematical model were too demanding for the experimental rig, causing oscillations and instability across the flight envelope.

## 9.6 Conclusions

In this chapter, some problems associated with gain-scheduled control methods have been identified, and discussed. A possible solution is presented in the form of state-scheduled control, where the state feedback gains become a function of the states on which they are

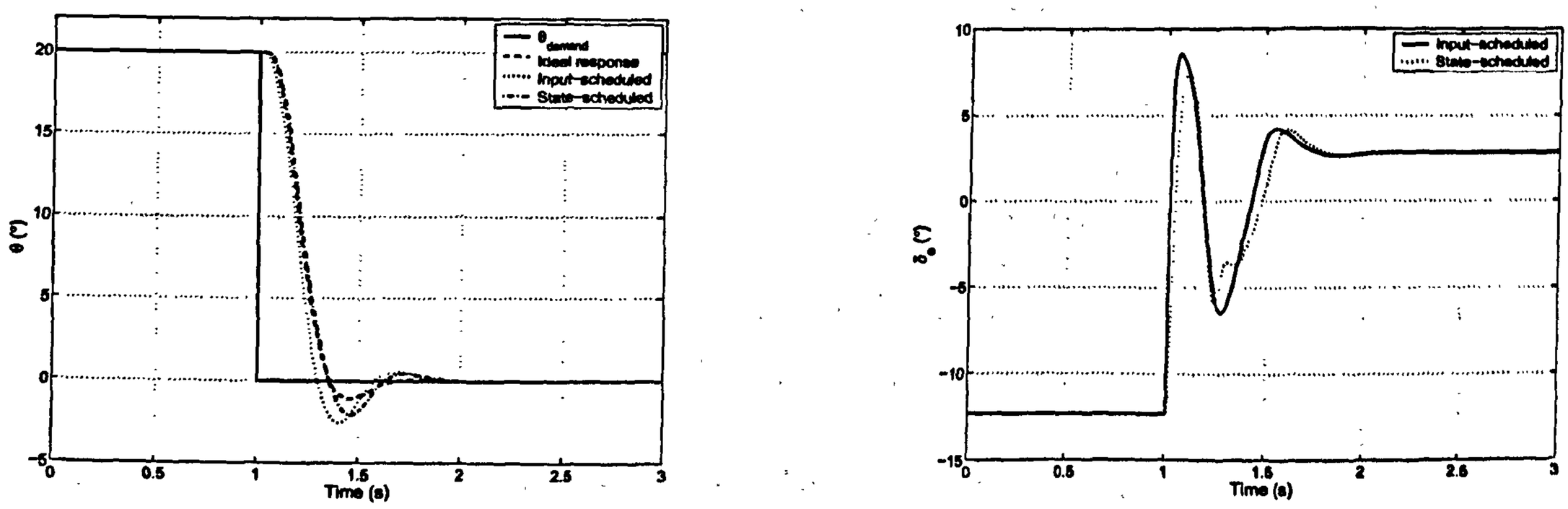


Figure 9.10: Large-amplitude step response for input- and state-scheduled controllers.

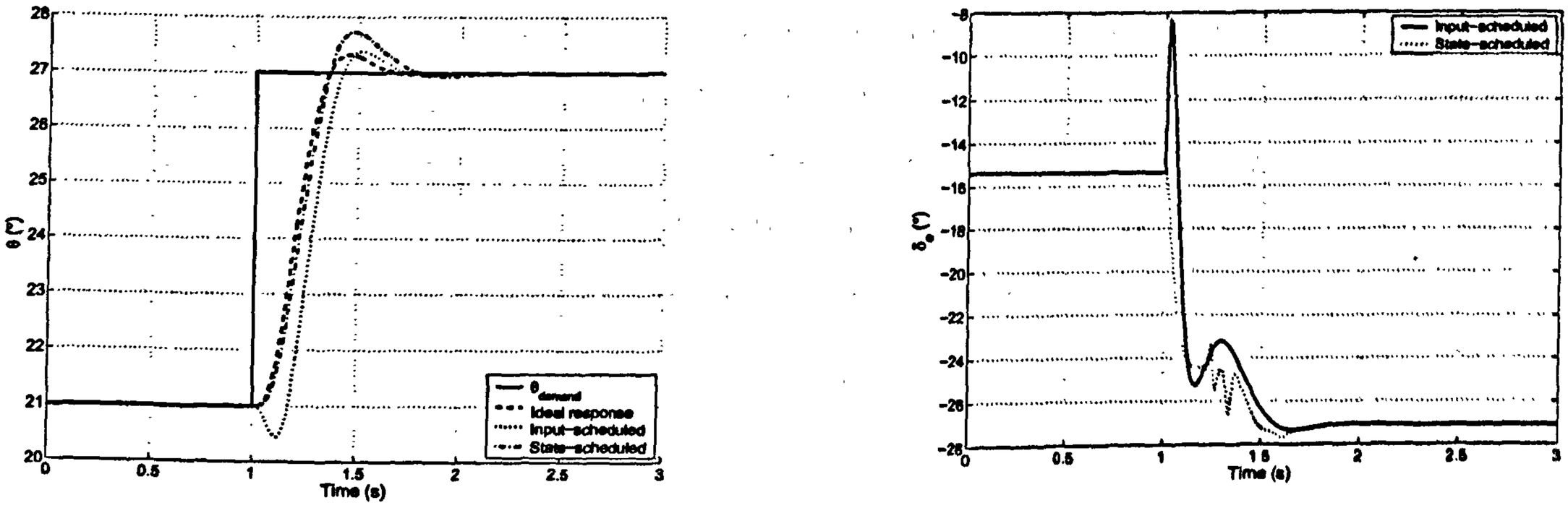


Figure 9.11: Step response for input- and state-scheduled controllers, showing non-minimum phase-type behaviour.

acting. It is only possible to implement the controller in this way if the so-called 'hidden coupling' terms (change in gain due to the schedule) are taken into account. It was found that, for certain systems, it is possible to convert a conventional gain-scheduled controller, where the gains are a function of a slowly-varying decoupled parameter, into a state-scheduled controller using a post-processing approach. This method was demonstrated in 1 and 2 degrees-of-freedom and shown to alleviate some of the problems found with standard scheduled controllers. The method was also applied to the mathematical model of the Hawk, and, although the performance was limited, it showed again that state-scheduling had removed some common gain scheduling implementation problems.

There is a large amount of research still to do in the area of state scheduling. Some of the open problems are:

- How to implement the gain conversion on more general systems.
- Whether it is possible to derive fully state-scheduled controllers (where each gain is a function of all system states) for third order systems and higher.
- To establish the link between the method presented here, and non-linear dynamic inversion.

It is thought that this approach will give an identical end result to NDI, but provide a different methodology for designing the controller. The two main advantages of the method presented in this chapter over NDI are its ability to specify the desired response during the design phase (without the need to introduce additional dynamics), and the fact that gain-scheduled control is already used extensively in industry, which would allow a simple transition to the dynamic scheduling case.

# Chapter 10

# Conclusions, Future Work and Recommendations

As aircraft design techniques develop there will always be a demand for lower procurement time and costs. This is particularly true of the new generation of unmanned aircraft and unmanned combat aircraft, where low cost 'disposable' solutions are necessary.

A considerable amount of development time is spent designing and evaluating flight control laws. Increasing performance demands and the use of more unorthodox aircraft planforms (due, for example, to stealth requirements) mean that the challenge of designing flight control laws for aircraft in a shorter timeframe is not becoming easier.

There are several options available to help cut the development time for future high-performance aircraft. One of these is to introduce a design method where aircraft aerodynamics and control systems are developed in parallel, rather than the costly cyclic development which currently occurs. This has the potential to drastically cut procurement times by reducing the impact of aerodynamic or control system changes on other areas of the design.

An important part of the development process is wind tunnel testing. A large amount of time and money can be spent performing static and dynamic wind tunnel tests during the initial design phase. These tests may need to be repeated several times if the aerodynamic or control characteristics are not satisfactory. If changes to the configuration have to be made due to control system considerations, it is very likely that a considerable amount

of time and money have already been spent developing a detailed mathematical model of the aircraft.

In this thesis, aspects of a potential method of reducing aircraft development time and costs has been investigated. The so-called 'Pendulum Support Rig' (PSR) is a method of dynamically wind tunnel testing aircraft models in multiple degrees-of-freedom. The rig is designed to be multi-purpose in nature. Using remotely-actuated moving control surfaces it is in theory possible to produce arbitrary motions (within the kinematic constraints of the rig) for aerodynamic model generation which include the effect of dynamic surface movement, and to develop and evaluate flight control laws.

A $1/16^{th}$ scale BAe Hawk model was purpose designed and built to test on a small PSR at the University of Bristol. Descriptions of the model, its actuators, and static wind tunnel characteristics were presented in Chapter 3. A large amount of hardware was designed and constructed to allow various PSR configurations to be tested, ranging from single degree-of-freedom to full 5 DOF with counterbalance. A description of initial development of belt-driven all-moving foreplanes was also given in Chapter 3.

It was found that the Hawk model displays some interesting dynamic characteristics, even in single degree-of-freedom configuration. Results from single and 2 DOF tests, and preliminary tests using all-moving foreplanes, were presented in Chapter 4. Experimental bifurcation diagrams were constructed to clearly show the steady-state behaviour of the model, and revealed two regions of self-sustaining periodic oscillations. These limit cycle oscillations are thought to be caused by aerodynamic phenomena when the all-moving tailplanes become immersed in the wake of the wing. In particular, the system exhibits subcritical and supercritical Hopf bifurcations, and a cyclic fold bifurcation, giving a region of hysteresis where multiple attractors co-exist. Experimental phase-plane plots and time histories are used to confirm the non-linear behaviour of the system. The study of rigid-body non-linear wind tunnel model behaviour via a detailed bifurcation approach is new.

A novel modelling method was developed in Chapter 5 where the experimental bifurcation diagrams are used explicitly in the model to reproduce the observed dynamics. In contrast to previous traditional modelling methods, parameters such as limit cycle amplitude, frequency and stability can be specified exactly in the model. By making assumptions about the response of the system (namely that the limit cycle oscillations are

sinusoidal with exponential-type decay) a new modelling method was formulated which accurately captured the global dynamics of the system. Examples were used to illustrate the process before parameters for the Hawk model were estimated from experimental data. In Chapter 6 the mathematical model was compared with experimental results and found to give a close match. In particular, it was shown that the Hopf and fold bifurcations were in the correct location, limit cycle amplitudes were correct, and stability of all equilibria branches was as desired. Pitching moment surfaces were generated for several tailplane deflections, and revealed the structure of the non-linearities in the model.

Having found a representative mathematical model, investigation into the feasibility of using the rig for control system design and validation was presented. In Chapter 7, having defined the control objective, simple single-state feedback pitch-angle-demand controllers were designed and tested on the experimental rig. A combination of numerical simulations and experimental testing was used to tune the controller gains. Good closed-loop agreement was shown between numerical simulations and experimental results, validating the use of both the numerical model and experimental rig for control system design. Results showed that the limit cycle regions can be stabilised using pitch rate feedback to the tailplanes, and that accurate pitch angle tracking performance is possible. It was shown that a combination of non-linear feed-forward and PID feedback gave the best performance in terms of transient response and steady-state error. Actuator resolution and wind tunnel turbulence were found to be the limiting factors on tracking performance.

In Chapter 8 some more advanced controllers were tested on the numerical model and experimental rig, namely gain-scheduled eigenstructure assignment and adaptive strategies. In general, both gain-scheduled and adaptive controllers showed good results when tested using numerical simulations. The experimental investigation of novel continuation-based gain-scheduled controllers was reported here for the first time. Using the gain-scheduling method allowed a consistent closed-loop response to be achieved at any point in the flight envelope. Some limitations were found when testing the controllers on the experimental rig; these were highlighted and discussed. In particular, the gain-scheduled controllers were designed using a fourth order mathematical model of the rig (with linear actuator model), and the non-linearities and un-modelled delays in the physical rig caused instabilities due to high feedback gains. The adaptive scheme tested in Chapter 8 did not

require any design stage, and worked well in simulations, but noise and non-linearities on the experimental rig caused the gains to ramp up until the system went unstable. This is a common problem with adaptive strategies being used in noisy environments with large external disturbances.

Chapter 9 presented preliminary work to relax some of the constraints currently placed on gain-scheduled controllers: slow variation conditions, and restriction to near-equilibrium solutions. A form of state-scheduling was demonstrated where, instead of the controller gains being scheduled against slowly-varying states or parameters, the state-feedback gains are scheduled against themselves. This leads to so-called 'hidden coupling' terms due to the rate-of-change of the gain with the state. It was shown that for certain systems these hidden-coupling terms can be accounted for in the design stage, and, using a suitable transformation, traditional parameter-scheduled gains converted to state-scheduled gains. The method is demonstrated on analytical examples before being applied to the mathematical model of the Hawk. The state-scheduling method was shown to alleviate some of the restrictions on traditional gain-scheduled controllers, thereby improving closed-loop system response.

## 10.1 Future Work

Many areas for future research were found while carrying out the work presented in this thesis. These will be broken down into the practical side (wind tunnel experiments), modelling work, and control system design.

### 10.1.1 Future Experimental Work

1. Further testing of control laws for the Hawk model in 3, 4 and 5 degrees of freedom. Although a simple roll-angle demand controller was used on the 5 DOF rig to stabilise the model, no significant investigation was performed. It was observed that in 5 DOF mode the model would lose lateral/directional stability as angle-of-attack increased, due presumably to the vertical stabiliser becoming immersed in the fuselage/wing wake. This would be a very interesting phenomenon to investigate, and design controllers to prevent, and is extremely relevant to full size aircraft.

2. Investigation into the relationship between the flow physics and observed motions of the Hawk model using flow visualisation techniques. A limited amount of work was carried out with an oil-based smoke generator, but a more comprehensive investigation would provide a useful insight into the cause of the observed non-linearities.

3. Further testing of the Hawk model with canard foreplanes to investigate multivariable and fault-tolerant control. It is also possible that symmetric aileron deflection would give some limited longitudinal control, giving three control inputs in pitch.

4. Manufacture of a slightly larger model with better quality control surface actuation (including accurate surface position feedback), for use in the return section of the Department $7' \times 5'$ wind tunnel. This would allow the use of digital rotary encoders for position (and rate) sensing, thus eliminating electrical noise problems and simplifying on-board electronics. Ideally, it would be possible to remove the model from the tunnel and perform drop tests with it once control laws have been designed, thus verifying the design process.

5. Testing the Hawk model in an upright configuration. This would require manufacturing a support structure that could be attached to the floor of the working section of the tunnel, allowing enough clearance for the counterbalance system. A comparison could then be performed between upright and inverted testing, and the stability issues which arise.

### 10.1.2 Future Modelling Work

1. Improving the mathematical model of the rig to include lateral/directional dynamics, other control surface actuators, etc. for off-line development of more advanced controllers.

2. Investigate extensions to the modelling method presented in Chapter 5. A small amount of work was carried out trying to reproduce period two limit cycles and the associated period doubling bifurcation, but no conclusive method was found. Modelling fold bifurcations was also attempted, but problems were encountered where several fixed point solutions coexist. Another extension to the model would

be the addition of interaction between longitudinal and lateral/directional dynamics. If limit cycles exist in more than one degree of freedom, their interaction is extremely important.

### 10.1.3 Future Control System Work

1. Design and evaluation (on- and off-line) of multivariable longitudinal controllers using an improved mathematical model of the Hawk which includes the effects of canards and symmetric aileron deflection.

2. Perform numerical simulations of the state-scheduled control scheme presented in Chapter 9 on the full 5-DOF rig.

3. Solution of the control problem posed in Chapter 9, namely, for any general non-affine $n^{th}$ order system, find a method of creating state scheduled gains using off-equilibrium linearisations to give ideal dynamics at any phase space location (within control power constraints, etc.). It is thought that this problem can be solved using methods similar to those outlined in Chapter 9. The resulting controller would be identical to one designed using Non-linear Dynamic Inversion (NDI), but may provide a more intuitive method of arriving at the gains, especially for industry where gain scheduling is a well established control method.

## 10.2 Recommendations

There were many lessons learned while carrying out the work documented in this thesis, particularly on the practical side. These are:

1. Whilst radio controlled model-type servo actuators continue to improve both in bandwidth and positional accuracy, it is extremely important to minimise backlash/freeplay in the control surfaces and control linkage arrangement. This was also emphasized in [72], where it was found that the accuracy of the trim condition depended entirely on the positional accuracy of the control surface. When attempting to develop and, in particular, compare control laws, again it is very important to minimise non-linearities due to backlash in the surfaces.

Servo actuator lifespan was affected by using closed-loop feedback control. Several servos failed (particularly the aileron and rudder servos, where friction in the control surface was higher) when testing control laws, possibly due to the high demands and continuous fine movement being imposed on them. Reducing control surface friction and using a heavy duty servo should overcome this problem.

Problems with the miniature servos and direct drive arrangement used in the Hawk model hampered comparison of the control laws developed in Chapters 7 to 9. Fine adjustments to the pitch attitude were not possible, leading to each controller showing a similar small-amplitude response.

The following practice is recommended for control surface actuation and layout on future models:

- Use of digital servos with ballraced output shaft and metal gears. Digital servos provide higher torque, increased bandwidth (in general) and reduced backlash and deadzone. Metal gears provide improved consistency of results over time, as gear-wear is not an issue. Ball bearings on the output shaft allow pulleys for tensioned belts to be attached directly to the output shaft without reducing performance.
- Use of a tensioned toothed-belt drive arrangement. This was tested on the canards of the Hawk model (see Chapter 3) and found to provide greatly improved accuracy over direct drive arrangements. Control pushrods were also tested, and while providing increased accuracy over direct drive methods (due to possible gearing due to control arm lengths), there were disadvantages such as backlash at the control arm/pushrod join, and non-linearity of movement.
- Friction and stiction of the control surfaces must be minimised to allow accurate positional control. The ailerons and rudder on the Hawk model used stainless steel rod held in plywood holes, which caused too much friction. This affected positional accuracy, rate saturation and servo degradation. It is therefore recommended that either brass bushes, bearings or suitable low-friction hinges be used to support the control surfaces.
- Accurate feedback of control surface position. Due to limited space in the model and not planning this feature when at the design stage, no provision was made in the Hawk model for control surface position feedback, apart from

the internal servo potentiometers. This method, although possible, was not found to be satisfactory. A better solution would be to have high-accuracy potentiometers (or better encoders) directly coupled to the control surface in some way.

A good control surface drive and feedback arrangement using the methods recommended here was used in [98]. Obviously, the larger the model the easier it is to accomplish an accurate drive arrangement. On small dynamically scaled models where space, mass and in particular moment of inertia are critical, control surface drive may have to be compromised to meet other more important criteria.

2. It is recommended that some form of accurate centre-of-gravity (CG) adjustment device is installed in future dynamic models. Provision was made for a sliding-mass type adjuster in the Hawk model, but did not prove adequate (in terms of mass-carrying capability) or accurate enough. Dynamic test results were very sensitive to CG location; often the best way to produce repeatable results was to balance the model with the tailplanes fixed and the tunnel running. This was not a very accurate method of ensuring repeatability. Ideally, a remotely-controlled CG varying device would be included in the model to allow accurate movement and adjustment of the model balance. This method was used in the HIRM model described in [45, 100], where a high torque DC motor is used to regulate the CG position by moving a lead weight.

3. A method of accurately adjusting the position of the gimbal rotation point within the model would be useful. The stability of the model and accuracy of estimated aerodynamic parameters depends greatly on the position of the gimbal rotation point with respect to the model CG. It may be necessary to move the rotation point to coincide with the CG (for example, if dynamic scaling constraints need to be met), or it may be desirable to intentionally offset the rotation point (to stabilise an aircraft mode during initial tests, or remove the need for the gimbal to be mounted inside the model). Use of the equations for the double-pendulum (created by having a non-coincident gimbal rotation point and model CG) will require accurate CG offset measurements.

4. Minimising the number of wires running between the model and computer should be a priority when designing future data acquisition and control equipment. Whilst

no specific study was undertaken as to the effect of the wires on the model stiffness and damping, they were seen to have an effect on the results. Positioning the wires in the same location with the same amount of slack for each set of experiments was not feasible, so the effect of the cables varies from run to run.

It is entirely feasible to construct a data acquisition board for use inside the model, using a small microcontroller, which would send the data to a host PC via a serial link. This would have the added advantage of reducing the amount of noise picked up by the sampled signals in long cables coming from the model. It would also be possible to use a radio link and batteries inside the model to give an entirely wireless system. If the model is made large enough, a suitable off-the-shelf telemetry unit could be purchased instead.

### 10.2.1 Repeatability of Results

Repeatability of results proved to be an issue throughout the experimental work, and especially when the gain-scheduled and adaptive controllers were tested on the rig. The main issues were:

- Mass and mass-distribution of the model. Due to the relatively large number of configurations in which the model could be tested (with/without ailerons/rudder/canards, 1-5 DOF, etc.) it was difficult to obtain the same mass distribution within the model between tests. This was also partly due to lack of accurate/repeatable balancing provision inside the model. While it is relatively easy to reproduce the model mass by weighing before tests (although this was not done in a lot of cases, due to differences in mass distribution causing the need for fine balancing when in the tunnel), reproducing moments of inertia would take a long time as the trifilar rig would have to be used at the beginning of each test. This was not done, mainly to save time. The impact of having non-equivalent mass and moment of inertia on the repeatability of results is debatable given the variations in other parameters. However, the natural frequency of the model will definitely change, giving a change in quantitative results, if not qualitative.
- Aerodynamic changes. Slight changes in the aerodynamics between tests may also cause the rig to behave differently. For example, slight differential variation in

the tailplane deflections, or slight movement in the other (possibly fixed) control surfaces may cause or remove highly sensitive phenomena from the system. Slight changes in the sting arrangement may also cause changes in observed dynamics.

- Friction/damping changes. Changes in the physical friction and damping on the model may be brought about by degradation of the gimbal bearings or different position/number of electrical wires going into the model. This is particularly true for tests performed toward the end of the work, where the wiring loom going into the model was increased to accommodate the 5 DOF rig[1].

- Control surface actuator degradation. Although difficult to measure, degradation of the actuators on the model almost certainly caused inconsistencies between test sessions. The micro servos used in the model have many parts which become worn over time, i.e. plastic gears, output shaft, bearings, and the motor itself. All of these increase non-linearities within the actuator, and change the measured characteristics.

- Centre of gravity/centre of rotation changes. The relationship between the positions of the centre of gravity and centre of rotation of the model are critical to the dynamic response. For the tests presented in this thesis, attempts were made before each set of experiments to obtain a coincident CG and centre of rotation. The dynamics of a system where the two are separated becomes very difficult to model in any configuration above 2 DOF. It was not possible to tell reliably where the centre of mass of the model was, particularly in the vertical (Z) direction. Therefore, results may have been affected by having a 'pendulum', even in a single degree-of-freedom.

  It was also possible to move the centre of rotation up and down within the model. Performing tests with the centre of rotation at different vertical positions, even with coincident CG, would definitely have an impact on results.

- Wind tunnel changes. The improvements to the Department open-jet tunnel (documented in Appendix B) were carried out in phases during the research, and therefore affected results at different times. The addition of the flow smoothing tabs

[1] A single wiring loom was used for all rig configurations, even though many wires were unused when in 1 or 2 DOF mode. This is where a serial or wireless system would be extremely valuable and save a considerable amount of set-up time.

around the circumference of the tunnel (the first improvement) had a dramatic effect by not only reducing the overall turbulence level, but also almost eliminating a very evident low frequency oscillation in the flow. It is possible that this flow oscillation was interacting with the model to give a dynamic response which may not have been observed in smooth flow conditions.

Lack of closed-loop wind speed control on the open-jet tunnel made it necessary to use a hand-held anemometer to set the velocity at the start of each set of tests. The anemometer was sensitive to exact angle in the tunnel, which, when coupled with the imprecise analogue controls on the motor drive, made it difficult to set the tunnel speed accurately ($\approx \pm 1$m/s, i.e. 5% at 20m/s). This definitely had an impact on repeatablility of results.

As an example of repeatability problems, the small-amplitude limit cycle which was observed and modelled during initial tests of the 1- and 2-DOF rigs was not found to exist when testing the gain scheduled and adaptive controllers at the end of the research programme. Although much time was spent investigating why this had occurred, no single reason could be found. Therefore, the change in observed dynamics was attributed to one or more of the items given above, and serves as a good illustration of the sensitivity of dynamics on relatively small changes in configuration. It also indicates the need for more attention to detail and documentation of test set-ups in order to produce repeatable results, or to be able to attribute changes to individual factors.

# References


[1] W.B. Herbst. Future fighter technologies. *Journal of Aircraft*, 17(8):561–566, August 1980.

[2] E.S. Hanff. Direct forced-oscillation techniques for the determination of stability derivatives in wind tunnels. In *AGARD LS-114*, March 1981.

[3] K.J. Orlick-Ruckemann (ed.). Report of the fluid dynamics panel working group 11 - rotary-balance testing for aircraft dynamics. Technical Report AGARD-AR-265, AGARD, December 1990.

[4] M.E. Beyers. A new concept for aircraft dynamic stability testing. *Journal of Aircraft*, 20(1):5–14, January 1983.

[5] M.H. Lowenberg and H.L. Kyle. Dynamic multi-axis wind tunnel rig development. In *Proc. RAeS Conference*, April 2001.

[6] M.H. Lowenberg and H.L. Kyle. Development of a pendulum support rig dynamic wind tunnel apparatus. In *Proc. AIAA Atmospheric Flight Mechanics Conference and Exhibition*, number AIAA-02-4879, August 2002.

[7] M.H. Lowenberg and H.L. Kyle. Derivation of unsteady aerodynamic models from wind tunnel multi-axis test rigs. In *Proc. International Council of the Aeronautical Sciences*, number 2002-3.11.2, September 2002.

[8] B.R. Rich and L. Janos. *Skunk Works.* Warner Books, ISBN: 0-7515-1503-5, 1995.

[9] M.G. Goman. Research and development cycle for high incidence flight. In *Nonlinear Flight Mechanics: Modelling, Analysis and Simulation IGDS Bristol Consortium Short Course.* IGDS Bristol Consortium, March 2002.

[10] W.B. Herbst. Dynamics of combat aircraft. *Journal of Aircraft*, 20(7):594–598, July 1983.

[11] C.W. Alcorn, M.A. Croom, M.S. Francis, and H. Ross. The X-31 aircraft: Advances in aircraft agility and performance. *Prog. Aerospace Sci.*, 32:377–413, 1996.

[12] A.J. Ostroff, K.D. Hoffler, and M.S. Proffitt. High-alpha research vehicle (harv) longitudinal controller: Design, analyses, and simulation results. Technical Paper NASA TP 3446, NASA, July 1994.

[13] L.T. Nguyen, L. Yip, and J.R. Chambers. Self-induced wing rock of slender delta wings. In *Proc. AIAA Atmospheric Flight Mechanics Conference*, number AIAA-81-1883, August 1981.

[14] L.V. Schmidt. Wing rock due to aerodynamic hysteresis. *Journal of Aircraft*, 16(3):129–133, 1979.

[15] A.J. Ross and L.T. Nguyen. Some observations regarding wing rock oscillations at high angles of attack. Technical Report RAE TM Aero. 2143, Royal Aerospace Establishment, September 1988.

[16] L.E. Ericsson, M.R. Mendenhall, and S.C. Perkins. Review of forebody-induced wing rock. *Journal of Aircraft*, 33(2):253–259, March–April 1996.

[17] M.H. Lowenberg. *Application of Bifurcation Analysis to Multiple Attractor Flight Dynamics.* PhD thesis, University of Bristol, February 1998.

[18] T.S. Richardson. *Continuation Methods Applied to Nonlinear Flight Dynamics and Control.* PhD thesis, University of Bristol, September 2002.

[19] S.H. Strogatz. *Nonlinear Dynamics and Chaos with Applications to Physics, Biology, Chemistry and Engineering.* Addison-Wesley, ISBN: 0-201-54344-3, 1994.

[20] L.N. Virgin. *Introduction to Experimental Nonlinear Dynamics - A Case Study in Mechanical Vibration.* Cambridge University Press, ISBN: 0-521-77931-6, 2000.

[21] R.K. Mehra, W.C. Kessel, and J.V. Carroll. Global stability and control analysis of aircraft at high angles-of attack. Technical Report ONR-CR215-248-1, Office of Naval Research, June 1977.

[22] D.C. Liaw and C.C. Song. Analysis of longitudinal flight dynamics: A bifurcation theoretic approach. *Journal of Guidance, Control and Dynamics*, 34(1):109–116, January–February 2001.

[23] J.V. Carroll and R.K. Mehra. Bifurcation analysis of nonlinear aircraft dynamics. *Journal of Guidance*, 5(5):529–536, 1982.

[24] C.C. Jahnke and F.E.C. Culick. Application of bifurcation theory to the high-angle-of-attack dynamics of the F-14. *Journal of Aircraft*, 31(1):26–34, 1994.

[25] M.H. Lowenberg. Bifurcation analysis of multiple-attractor flight dynamics. *Phil. Trans. R. Soc. Lond. A*, (356):2297–2319, 1998.

[26] M.H. Lowenberg and A.R. Champneys. Shil'nikov homoclinic dynamics and the escape from roll autorotation in an F-4 model. *Phil. Trans. R. Soc. Lond. A*, (356):2241–2256, 1998.

[27] M.H. Lowenberg and T.S. Richardson. Derivation of non-linear control strategies via numerical continuation. In *Proc. AIAA Atmospheric Flight Mechanics Conference*, number AIAA-99-4111, August 1999.

[28] M.G. Goman, G.I. Zagainov, and V. Khramtsovsky. Application of bifurcation methods to nonlinear flight dynamics problems. *Prog. Aerospace Sci.*, 33(PII:S0376-0421(97)00001-8):539–586, 1997.

[29] M.H. Lowenberg and Y. Patel. Use of bifurcation diagrams in piloted test procedures. *The Aeronautical Journal*, (2339):225–235, May 2000.

[30] D.M. Littleboy and Y. Patel. High angle of attack control law design & analysis using non-linear bifurcation methods. In *Proc. AIAA Guidance, Navigation and Control Conference*, number AIAA-98-4205, August 1998.

[31] X.F. Wang, M. di Bernardo, D.P. Stoten, M.H. Lowenberg, and G.A. Charles. Bifurcation tailoring via newton flow aided adaptive control. *International Journal of Bifurcation and Chaos*, 13(3):677–684, 2003.

[32] G.A. Charles, M. di Bernardo, M.H. Lowenberg, D.P. Stoten, and X.F. Wang. Bifurcation tailoring of equilibria: a feedback control approach. *Latin American Applied Research Journal (LAAR)*, 31(3):199–210, July 2001.

[33] G.A. Charles. *Bifurcation Tailoring Applied to Nonlinear Flight Dynamics.* PhD thesis, University of Bristol, May 2003.

[34] E.J. Doedel, A.R. Champneys, T.F. Fairgrieve, Y.A. Kuznetsov, B. Sandstede, and X. Wang. Auto 97: Continuation and bifurcation software for ordinary differential equations (with homcont). Technical report, Concordia University, Montreal, Canada, march 1998.

[35] Y.A. Kuznetsov and V.V. Levitin. Content: A multiplatform environment for continuation and bifurcation analysis of dynamical systems. Technical report, Centrum voor Wiskunde en Informatica, Kruislaan 413, 1098 SJ Amsterdam, The Netherlands, 1997.

[36] M.H. Lowenberg. Application of the bifurcation analysis technique to non-linear aircraft dynamics. Master's thesis, University of Witwatersrand, South Africa, 1991.

[37] I.J. Nagrath and M. Gopal. *Control Systems Engineering.* Wiley Eastern Limited, ISBN: 0-85226-602-2, 1975.

[38] K. Dutton, S. Thompson, and B. Barraclough. *The Art of Control Engineering.* Addison Wesley Longman, ISBN: 0-201-17545-2, 1997.

[39] G.F. Franklin, J.D. Powell, and A. Emami-Naeini. *Feedback Control of Dynamic Systems (Fourth Edition).* Prentice-Hall, Inc., ISBN: 0-13-032393-4, 2002.

[40] M.B. Tischler, J.A. Lee, and J.D. Colbourne. Optimization and comparison of alternative flight control system design methods using a common set of handling-qualities criteria. In *Proc. AIAA Guidance, Navigation and Control Conference,* number AIAA 2001-4266, August 2001.

[41] R.T. Reichert. Dynamic scheduling of modern-robust-control autopilot designs for missiles. *IEEE Control Systems Magazine,* 12(5):35–42, 1992.

[42] R.A. Nichols, R.T. Reichert, and W.J. Rugh. Gain scheduling for h-infinity controllers: A flight control example. Technical Report JHU/ECE - 92/03.1, John Hopkins University, Baltimore, MD, 1992.

[43] G. Papageorgiou and K. Glover. H-infinity loop shaping:why is it a sensible procedure for designing robust flight controllers? In *Proc. AIAA Guidance, Navigation and Control Conference*, number AIAA-99-4272/3, August 1999.

[44] V.H.L. Cheng, C.E. Njaka, and P.K. Menon. Practical design methodologies for robust nonlinear flight control. In *Proc. AIAA Guidance, Navigation and Control Conference*, number AIAA-96-3785, July 1996.

[45] G. Papageorgiou and K. Glover. Design, development and control of the HIRM wind tunnel model. In *Proc. IEEE Conference on Decision and Control*, December 1999.

[46] P.R. Smith. Derivation of non-linear control strategies via numerical continuation. In *Proc. AIAA Atmospheric Flight Mechanics Conference*, number 94-3516-CP, August 1994.

[47] R.R. da Costa, Q.P. Chu, and J.A. Mulder. Re-entry flight controller design using nonlinear dynamic inversion. In *Proc. AIAA Guidance, Navigation and Control Conference*, number AIAA-2001-4219, August 2001.

[48] M.H. Lowenberg. Development of control schedules to modify spin behaviour. In *Proc. AIAA Atmospheric Flight Mechanics Conference*, number AIAA-98-4267, 1998.

[49] X.F. Wang, M. di Bernardo, M.H. Lowenberg, D.P. Stoten, and G.A. Charles. Bifurcation tailoring of nonlinear systems. In *Proc. International Federation of Automatic Control*, number T-We-A21, 2002.

[50] G.A. Charles, M.H. Lowenberg, D.P. Stoten, X.F. Wang, and M. di Bernardo. Aircraft flight dynamics analysis and controller design using bifurcation tailoring. In *Proc. AIAA Guidance, Navigation and Control Conference*, number AIAA-2002-4751, 2002.

[51] G.A. Charles, M.H. Lowenberg, X.F. Wang, D.P. Stoten, and M. di Bernardo. Feedback stabilised bifurcation tailoring applied to aircraft models. In *Proc. International Congress of Aerospace Sciences*, number ICAS-2002-5.3.1, 2002.

[52] G.A. Charles, M. di Bernardo, M.H. Lowenberg, D.P. Stoten, and X.F. Wang. On-line bifurcation tailoring: An application to a nonlinear aircraft model. In *Proc. International Federation of Automatic Control*, number T-Mo-M6, 2002.

[53] M.H. Lowenberg and T.S Richardson. The continuation design framework for nonlinear aircraft control. In *Proc. AIAA Guidance, Navigation and Control Conference*, number AIAA-2001-4100, August 2001.

[54] W.J. Rugh and J.S. Shamma. Research on gain scheduling. *Automatica*, 36(10):1401–1425, 2000.

[55] S.M. Shahruz and S. Behtash. Design of controllers for linear parameter-varying systems by the gain scheduling technique. *Journal of Mathematical Analysis and Applications*, 168(1):195–217, 1992.

[56] ESDU. A background to the handling qualities of aircraft. Technical Report 92006, ESDU, 1992.

[57] USAF. Military specification: Flying qualities of piloted airplanes. Technical Report MIL-F-8785C, USAF, 1980.

[58] US DOD. Flying qualities of piloted airplanes. Technical Report MIL-HDBK-1797, DOD, December 1997.

[59] T.S. Richardson, P.M. Davison, M.H. Lowenberg, and M. di Bernardo. Control of non-linear aircraft models using state-feedback gain scheduling. In *Proc. AIAA Guidance, Navigation and Control Conference*, number AIAA-2003-5503, August 2003.

[60] D.P. Stoten. An overview of the minimal control synthesis algorithm. In *Proc. I. Mech. E. Conference on Aerospace Hydraulics and Systems*, number C474-033, 1993.

[61] D.P. Stoten and S.P. Hodgson. The application of the minimal control synthesis algorithm to the hybrid control of a class 1 manipulator. *Int. J. Control*, 56(3):499-513, 1992.

[62] D.P. Stoten. Implementation of minimal control synthesis on a servo-hydraulic testing machine. *Proc. I Mech E - Part I, Journal of Systems and Control Engineering*, 206(I3):189–194, 1992.

[63] D.P. Stoten and M. Webb. The implementation of the minimal control synthesis algorithm on a web control problem. *Proc. I Mech E - Part I, Journal of Systems and Control Engineering*, 208(I1):53–60, 1993.

[64] D.P. Stoten and M. di Bernardo. Application of the minimal control synthesis algorithm to the control and synchronisation of chaotic systems. *Int. J. Control*, 65(6):925–938, 1996.

[65] D.P. Stoten and H. Benchoubane. Robustness of a minimal controller synthesis algorithm. *Int. J. Control*, 51(4):851–861, 1990.

[66] NATO Research and Technology Organization. Flight control design - best practices. Technical Report RTO-TR-029, North Atlantic Treaty Organization, December 2000.

[67] B. Hunt. The role of computational fluid dynamics in high angle-of-attack aerodynamics. *AGARD-LS-121*, March 1982.

[68] M. Tobak and L.B. Schiff. Aerodynamic mathematical modelling basic concepts. In *AGARD Lecture Series on Dynamic Stability Parameters*, number 1 in AGARD-LS-114. NATO, April 1981.

[69] M.G. Goman and D.I. Greenwell. Wind tunnel simulation of combat aircraft manoeuvres. Research Monograph 14, School of Computing Sciences, De Monfort University, Leicester, August 1998.

[70] B.A. Gerryts. Literature survey into dynamic stability derivatives and testing techniques. Technical report, Aerotek Division, Council for Scientific and Industrial Research, South Africa, 1992.

[71] E.S. Hanff and C.O. O'Leary. Oscillatory test techniques. In *Special Course on Aircraft Dynamics at High Angles-of-Attack: Experiments and Modelling*, number AGARD-R-776, April 1991.

[72] I.A. Malik. *The Design Development and Evaluation of an Active Control Aircraft Model Wind Tunnel Facility.* PhD thesis, Cranfield Institute of Technology Aerodynamics Department, September 1982.

[73] K.J. Orlik-Ruckemann (Ed.). Review of techniques for determination of dynamic stability parameters in wind tunnels. Lecture Series LS-114, AGARD, 1981.

[74] R.L. Simpson. Unsteady aero/hydrodynamics for maneuvring aircraft, submarines, and automobiles. Technical Report VPI-AOE-253, Department of Aerospace and Ocean Engineering, Virginia Polytechnic Institute and State University, November 1997.

[75] L.E. Ericsson. Reflections regarding recent rotary rig results. *Journal of Aircraft*, 24(1):25–30, January 1987.

[76] G.E. Burt and J.C. Uselton. Effect of sting oscillations on the measurement of dynamic stability derivatives. *Journal of Aircraft*, 13(3):210–216, March 1976.

[77] E.S. Hanff and S.B. Jenkins. Large-amplitude high-rate roll experiments on a delta and double delta wing. *AIAA Journal*, 1990.

[78] E.S. Hanff. Large amplitude oscillations. In *Special Course on Aircraft Dynamics at High Angles-of-Attack: Experiments and Modelling*, number AGARD-R-776, April 1991.

[79] M.G. Goman. Mathematical modelling of high angle of attack aerodynamics for solving flight dynamics problems. Technical report, De Monfort University, Leicester, June 1998. Research Monograph 13.

[80] C.O. O'Leary and E.N. Rowthorn. New rotary rig at rae and experiments on hirm. *The Aeronautical Journal*, December 1986.

[81] L.E. Ericsson and M.E. Beyers. Wind-tunnel aerodynamics in rotary tests of combat aircraft models. *Journal of Aircraft*, 35(4):521–528, July-August 1998.

[82] D.D. Baals and W.R. Corliss. *Wind Tunnels of NASA*. U.S. Government Printing Office, Washington, D.C. 20402, 1981.

[83] P.A. Gili and M. Battipede. Experimental validation of the wing dihedral effect using a whirling arm equipment. *Journal of Aircraft*, 38(6):1069–1075, November-December 2001.

[84] M.J. Mulkens and A.O. Ormerod. Measurements of aerodynamic rotary stability derivatives using a whirling arm facility. *Journal of Aircraft*, 30(2):178–183, March-April 1993.

[85] R.M. Bennett, M.G. Farmer, R.L. Mohr, and W.E. Hall Jr. Wind-tunnel technique for determining stability derivatives from cable-mounted models. *Journal of Aircraft*, 15(5):304–310, May 1978.

[86] G.E. Bergmann and F.D. Sevart. Design and evaluation of miniature control surface actuation systems for aeroelastic models. *Journal of Aircraft*, 12(3):29–134, March 1975.

[87] C.M. Fremaux. Spin-tunnel investigation of a 1/28-scale model of the nasa f-18 high alpha research vehicle (harv) with and without vertical tails. Contractor Paper CR 201687, NASA, April 1997.

[88] S.B. Grafton, J.R. Chambers, and P.L. Coe Jr. Wind-tunnel free-flight investigation of a model of a spin-resistant fighter configuration. Technical Note TN D-7716, NASA, 1974.

[89] B. Dayman Jr. Free-flight testing in high-speed wind tunnels. AGARDograph 113, AGARD, May 1966.

[90] R.O. Schade. Flight test investigation on the langley control-line facility of a propeller-driven tail-sitter-type vertical-take-off airplane with delta wing during rapid transitions. Technical Report NACA TN 4070, NACA, 1957.

[91] J.P. Campbell. Techniques for testing models of vtol and stol airplanes. Technical Report AGARD REPORT 61, AGARD, August 1956.

[92] M. Croom, H. Kenney, D. Murri, and K. Lawson. Research on the F/A-18E/F using a 22%-dynamically-scaled drop model. In *Proc. AIAA Atmospheric Flight Mechanics Conference and Exhibition*, number AIAA-2000-3913, August 2000.

[93] H. Sawada, H. Suenaga, T. Suzuki, and N. Ikeda. Status of MSBS study at NAL. In *Proc. Second International Symposium on Magnetic Suspension Technology*, number CP 3247. NASA, May 1994.

[94] D. Levin and J. Katz. Dynamic load measurements with delta wings undergoing self-induced roll oscillations. *Journal of Guidance*, 21(1):30–36, January 1984.

[95] A.S. Arena Jr. and R.C. Nelson. Experimental investigations on limit cycle wing rock of slender wings. *Journal of Aircraft*, 31(5):1148–1155, September-October 1994.

[96] C. Irving. *Wide-Body.* Hodder and Stoughton, ISBN: 0-340-53487-7, 1993.

[97] M.S. Rajamurthy. Generation of comprehensive longitudinal aerodynamic data using dynamic wind-tunnel simulation. *Journal of Aircraft*, 34(1):29–33, January-February 1997.

[98] S. Mytilineous and G. Papageorgiou. Actively controlled two degree-of-freedom wind tunnel model. Master's thesis, University of Bristol, 1994.

[99] J.C. Magill, L.A. Darden, and N.M. Komerath. Flow visualisation during multiple-axis motions using a wind-driven manipulator. *Journal of Aircraft*, 33(1):163–170, January-February 1996.

[100] G. Papageorgiou. *Robust Control System Design: H-infinity Loop Shaping and Aerospace Applications.* PhD thesis, University of Cambridge, July 1998.

[101] R. Campbell. *Reconfigurable Flight Control Using a Model Reference Approach.* PhD thesis, University of Bristol, September 2002.

[102] B. Krag. Gust-vehicle parameter identification by dynamic simulation in wind tunnels. *AGARD-CP-235*, November 1978.

[103] M.V. Cook. On the use of small scale aircraft models for dynamic wind tunnel investigation of stability and control. *Trans. Inst. M. C.*, 9(4):190–197, Oct–Dec 1987.

[104] C.H. Wolowicz, J.S. Bowman, and W.P. Gilbert. Similitude requirements and scaling relationships as applied to model testing. Technical Report TP 1435, NASA, August 1979.

[105] US DOD. Airplane strength and rigidity, vibration, flutter and divergence. Technical Report MIL-A-8870, DOD.

[106] W.G. Luber. Flutter prediction on a combat aircraft involving backlash on control surfaces. In *Proc. 16th International Modal Analysis Conference*, volume 1, pages 291–299, February 1998.

[107] E.A.M. Muir, J.C. Terlouw, and J.T.M Van Doorn. Robust flight control design challenge problem formulation and manual: the high incidence research model (HIRM). Technical Report TP-088-4, GARTEUR, 1997.

[108] A. Khrabrov, K. Kolinko, O. Miatov, and A. Zhuk. Development of mathematical model of control surface actuators. Technical report, TsAGI, Russia, 2001. Report on the supplement to the contract CU004-0000001608.

[109] T. Stagg and A. Colquhoun. Flow quality analysis of the department's wind tunnels. Master's thesis, University of Bristol, May 2001.

[110] S.T. Trickey, L.N. Virgin, and E.H. Dowell. The stability of limit cycle oscillations in a nonlinear aeroelastic system. *Mathematical, Physical and Engineering Sciences (The Royal Society)*, 458(2025):2203–2226, September 2002.

[111] K.J. Orlik-Ruckemann. Aerodynamic aspects of aircraft dynamics at high angles of attack. *Journal of Aircraft*, 20(9):737–752, September 1983.

[112] B.S. Liebst. The dynamics, prediction, and control of wing rock in high-performance aircraft. *Philosophical Transactions: Mathematical, Physical and Engineering Sciences*, 356(1745):2257, October 1998.

[113] C-H. Hsu and C.E. Lan. Theory of wing rock. *Journal of Aircraft*, 22(10):920–924, 1985.

[114] M.G. Goman and A. Khrabrov. State-space representation of aerodynamic characteristics of an aircraft at high angles of attack. *Journal of Aircraft*, 31(5):1109–1115, 1994.

[115] V. Klein and K.D. Noderer. Modelling of aircraft unsteady aerodynamic characteristics. part 1 - postulated models. Technical Report TM 109120, NASA, May 1994.

[116] H.J. Myatt. A nonlinear indicial response model for the rolling 65-degree delta wing. In *Proc. AIAA Atmospheric Flight Mechanics Conference*, number AIAA-96-3406, August 1996.

[117] G. Guglieri and F. Quagliotti. Experimental observation and discussion of the wing rock phenomenon. *Aerospace Science and Technology*, 1(2):111–123, 1997.

[118] S.D. Vaidya and N. Ananthkrishnan. Adaptive control of slender delta wing rock in stability wind tunnel. *J. Aero. Soc. Of India*, 49(4):183–187, 1997.

[119] A.J. Ross, G.F. Edwards, V. Klein, and J.G. Batterson. Validation of aerodynamic parameters for high-incidence research models. *Journal of Aircraft*, 26(7):621–628, July 1989.

[120] L.V. Schmidt. Introduction to flight dynamics. Technical report, AIAA Education Series, 1998.

[121] W.H. Hui and M. Tobak. Bifurcation theory applied to aircraft motions. Technical Report NASA-TM-86704, NASA, March 1985.

[122] F.B. Hsiao and J.S. Yang. The study of wing-rock characteristics on slender delta wings at high angle-of-attack. In *Proc. International Congress of Aerospace Sciences*, number ICAS-96-3.1.1, September 1996.

[123] Tischler,M.B. (Ed.). *Advances in Aircraft Flight Control.* Taylor & Francis Ltd., ISBN: 07484-0479-1, 1996.

[124] Pratt,R.W. (Ed.). *Flight Control Systems: Practical Issues in Design and Implementation.* Copublished by IEE and AIAA, ISBN: 0-85296-766-7, 2000.

[125] A.N. Andry, E.Y. Shapiro, and J.C. Chung. Eigenstructure assignment for linear systems. In *IEEE Transactions on Aerospace and Electronic Systems*, volume 19, pages 711–729, 1983.

[126] K.M. Sobel, E.Y. Shapiro, and A.N. Andry. Eigenstructure assignment. *Int. J. Control*, 59(1):13–37, 1994.

[127] D.J. Leith and W.E. Leithead. Comments on 'gain scheduling dynamic linear controllers for a nonlinear plant'. *Automatica*, 34(8):1041–1043, 1998.

[128] D.P. Stoten. The adaptive minimal control synthesis algorithm with integral action. In *Proc. 21st IEEE Conf. Ind. Elec., Control and Inst., Orlando, FLA*, pages 1616–1651, 1995.

[129] D.P. Stoten and H. Benchoubane. The extended minimal controller synthesis algorithm. *Int. J. Control*, 56(5):1139–1165, 1992.

[130] D.P. Stoten and H. Benchoubane. The minimal control synthesis identification algorithm. *Int. J. Control*, 58(3):685–696, 1993.

[131] D.J. Leith and W.E. Leithead. Survey of gain-scheduling analysis & design. *Int. Journal of Control*, 73(11):1001–1025, 2000.

# Appendix A

# Hawk Model Static Testing

Static testing of the Hawk model was performed in the Department 7'×5' closed-section tunnel. Calibration of the lift, drag and pitching moment balances (mechanical, stepper-motor driven) was performed before and after the tests, and a fixed conversion factor of 0.10631 found necessary to convert pitching moment reading into actual moment. Linearity in all three balances was found to be adequate.

The static testing process was automated using the dSPACE data acquisition hardware. A Matlab m-file was written to control the procedure, which consisted of the following tasks:

1. attain the starting angle-of-attack (−5°) by commanding a pitch wire movement (via a relay box that emulated a person manually pressing the pitch wire control buttons) and monitoring pitch angle feedback from the gimbal potentiometer. The tailplanes were also commanded to their initial position (+10°).

2. take 1000 readings (each) of lift, drag and pitching moment using the digital output from the stepper motor controller in the balance, over a time period of approximately 45 seconds.

3. take an average of the readings and store the results.

4. decrease tailplane angle by 5°.

5. repeat steps 2–4 until maximum tailplane deflection (−45°) is reached.

6. set the next angle-of-attack by again demanding a pitch wire movement and monitoring model pitch angle feedback from the gimbal potentiometer. Reset tailplanes.

7. repeat steps 2 to 6 until the model had reached 40° angle-of-attack.

Total time for a test run was in the order of 5 hours. Results for the static tests are shown in Figures A.1 to A.7. Tests were run at 10, 15, 20 and 25 m/s, however, 10m/s was too low to get accurate readings (due to low loading/balance sensitivity) and the plots have therefore been omitted. As seen from Figures A.4 to A.6, the most consistent results were recorded at 20m/s. Vibration of the model due to the airflow was acceptable at this speed, but caused some concern for the structural integrity of the model at higher speeds, particularly at high $\alpha$. For these reasons, a tunnel speed of 20m/s (Re= $0.2\times10^6$, full-scale speed=80m/s) was used for the majority of tests presented in this thesis.

While static testing the model it was found that the readings from the mechanical balance varied noticeably with time. This was eventually attributed to the temperature of the analogue electronics system driving the balance. Wind-off readings were taken before and after each run and correction factors used, however, the problem was solved by leaving the electronics switched on overnight to reach an equilibrium temperature.

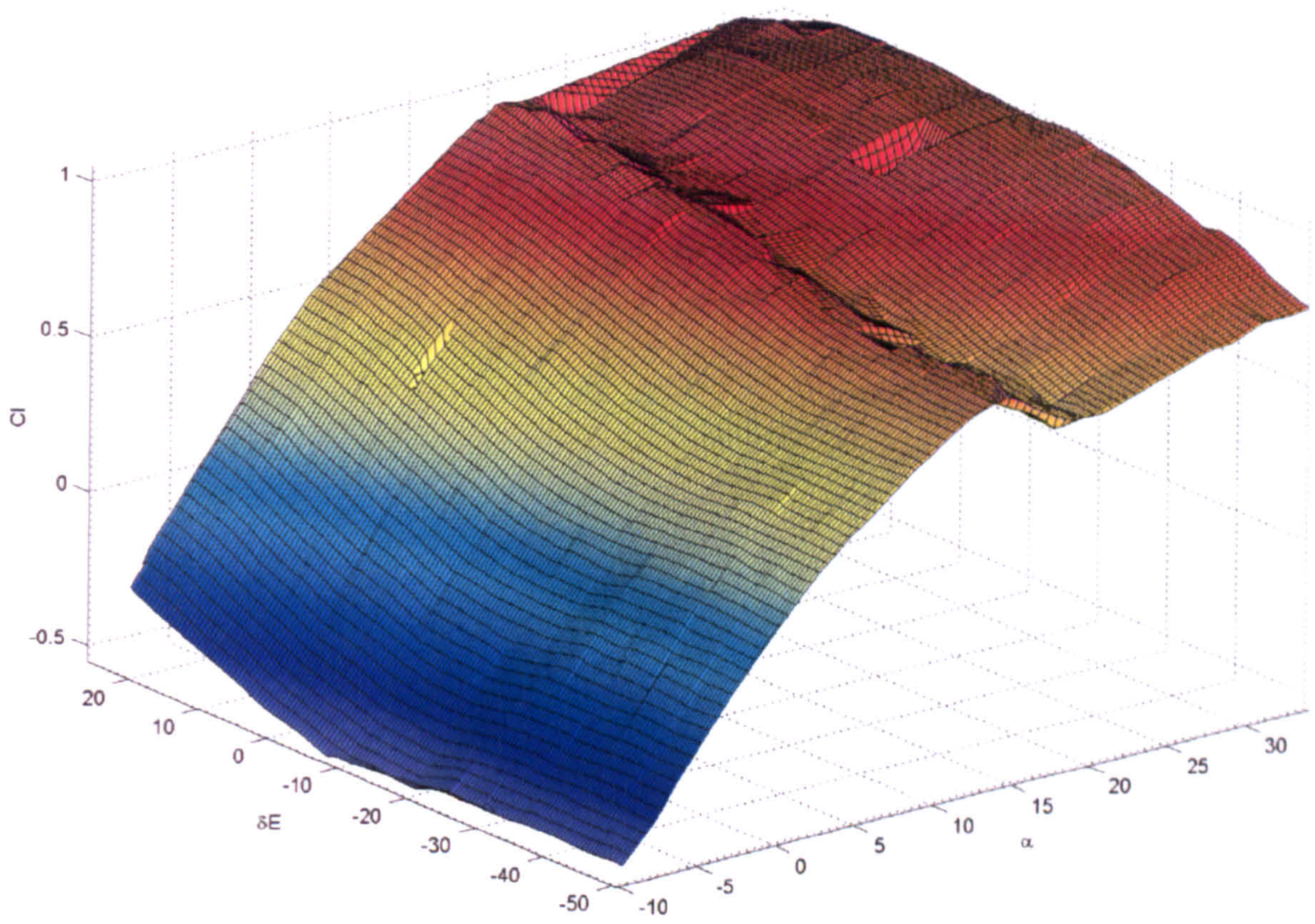


Figure A.1: $C_l(\alpha, \delta_e)$ - 15m/s.

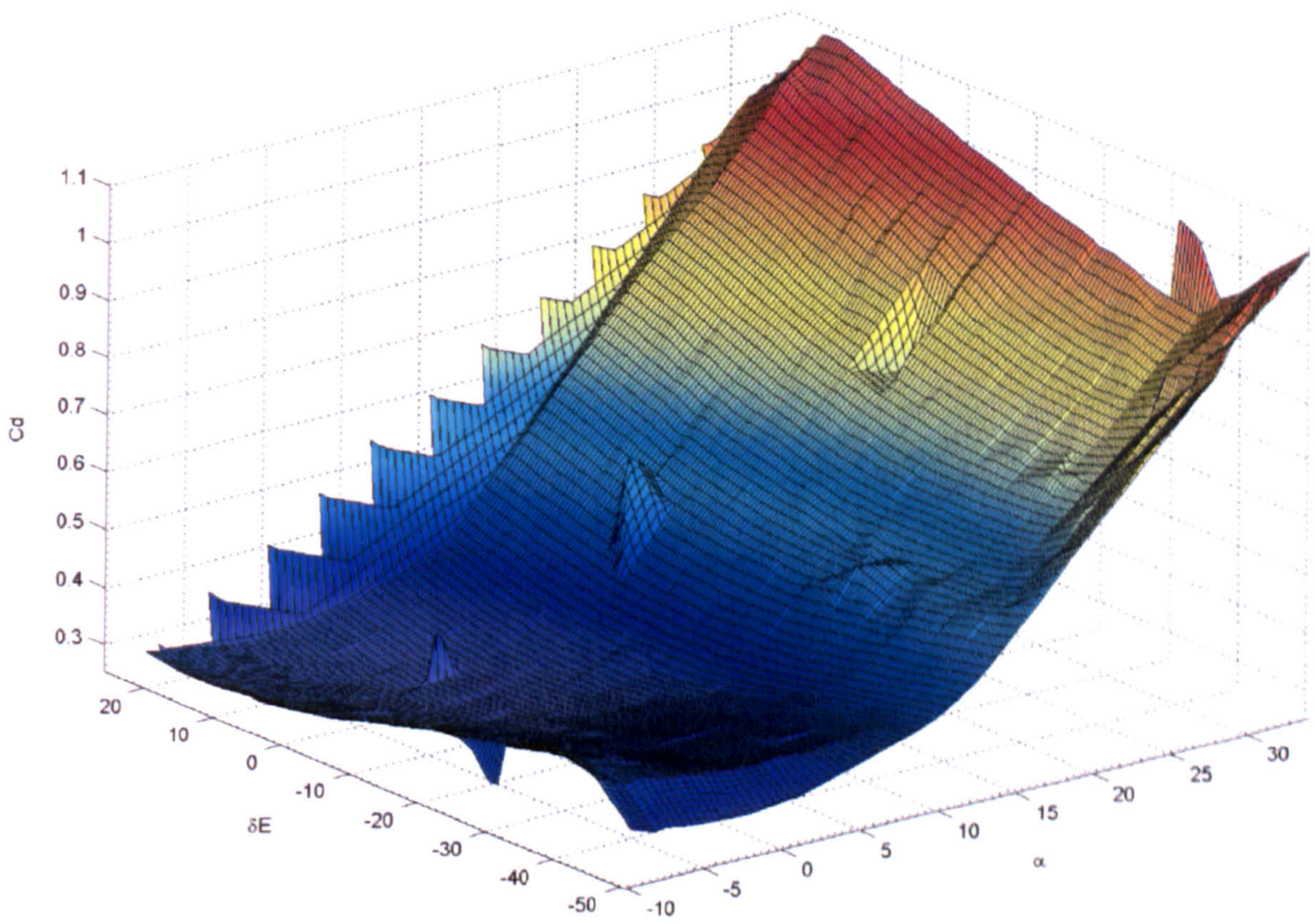


Figure A.2: $C_d(\alpha, \delta_e)$ - 15m/s.

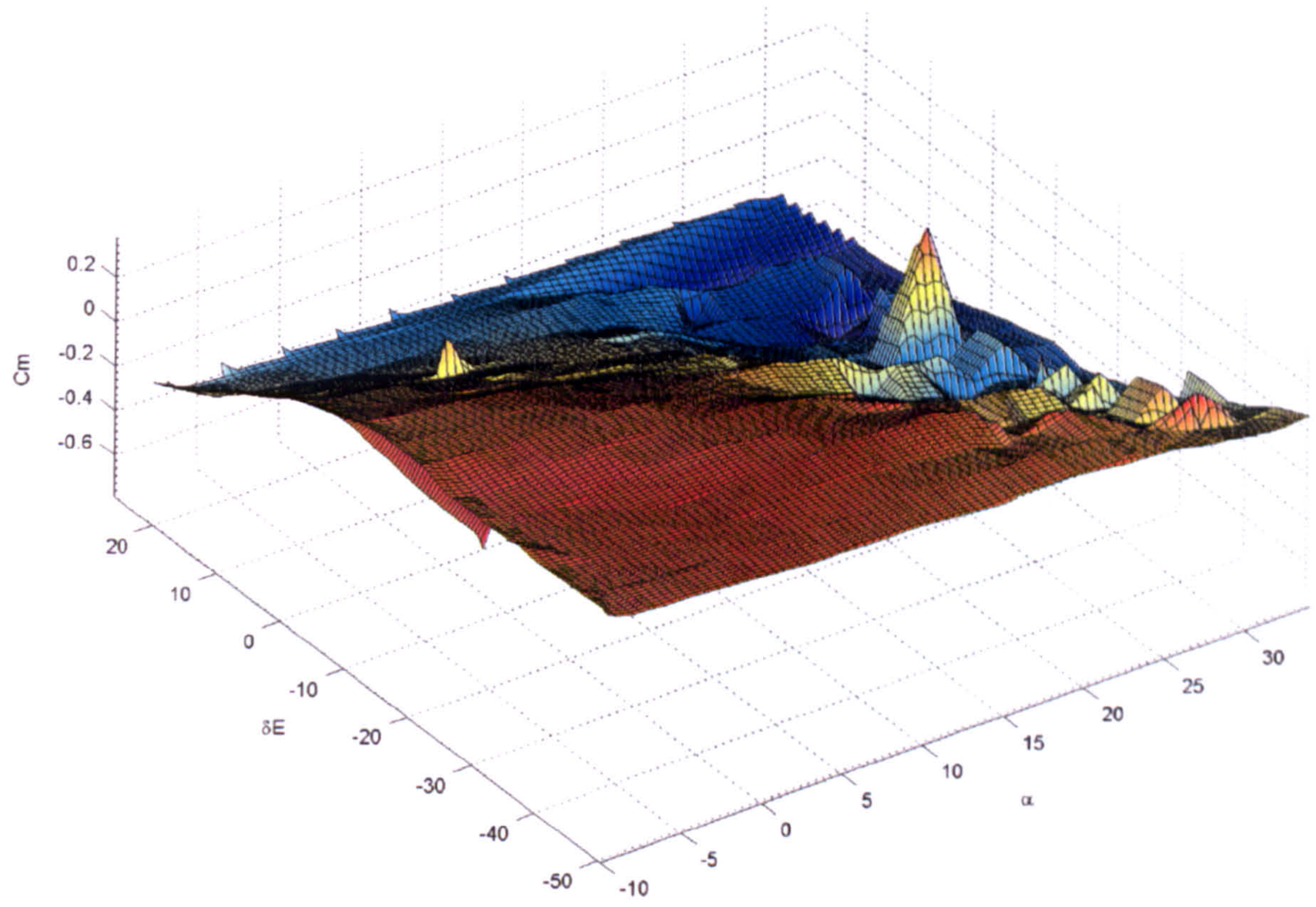


Figure A.3: $C_m(\alpha, \delta_e)$ - 15m/s.

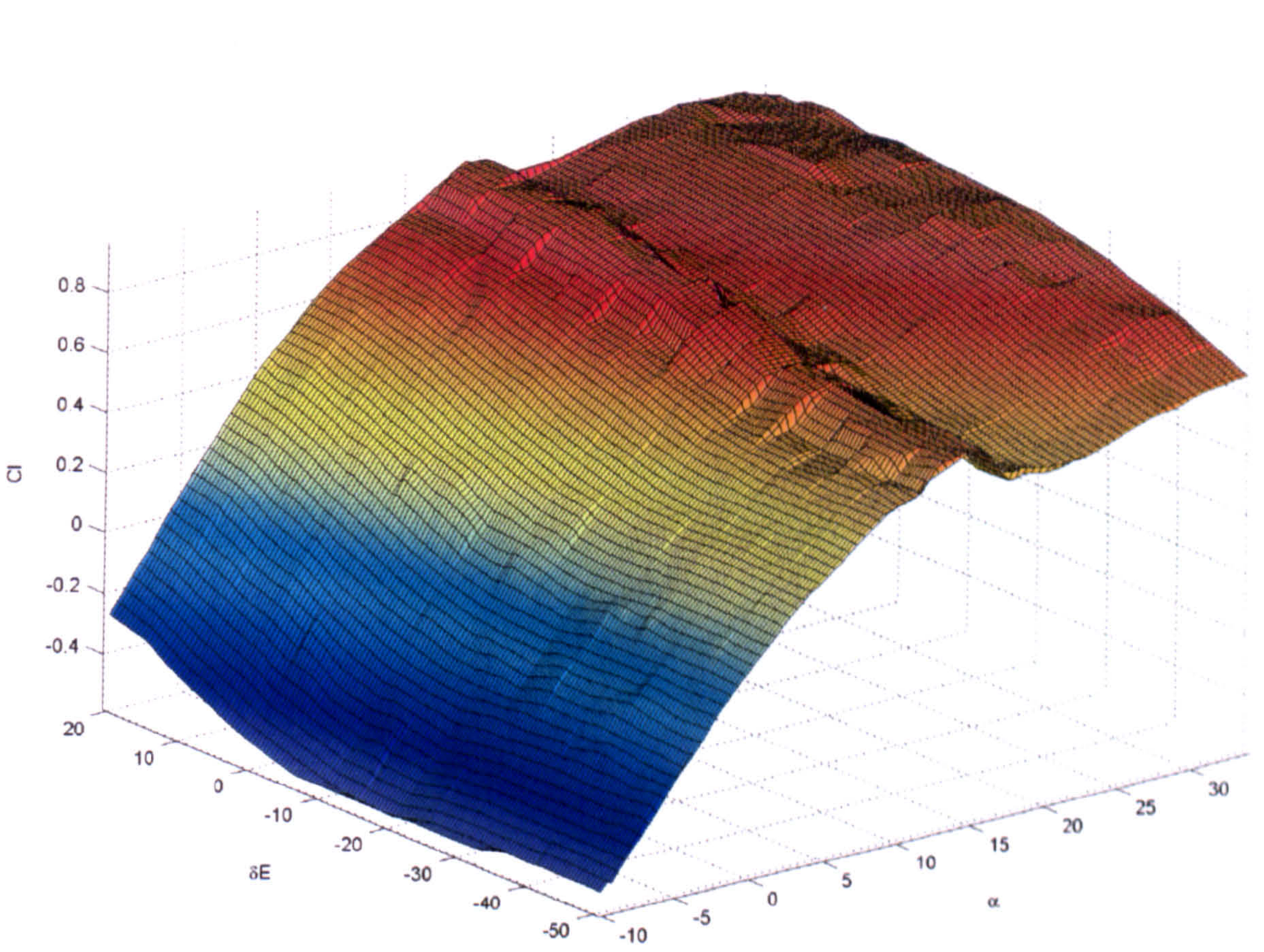


Figure A.4: $C_l(\alpha, \delta_e)$ - 20m/s.

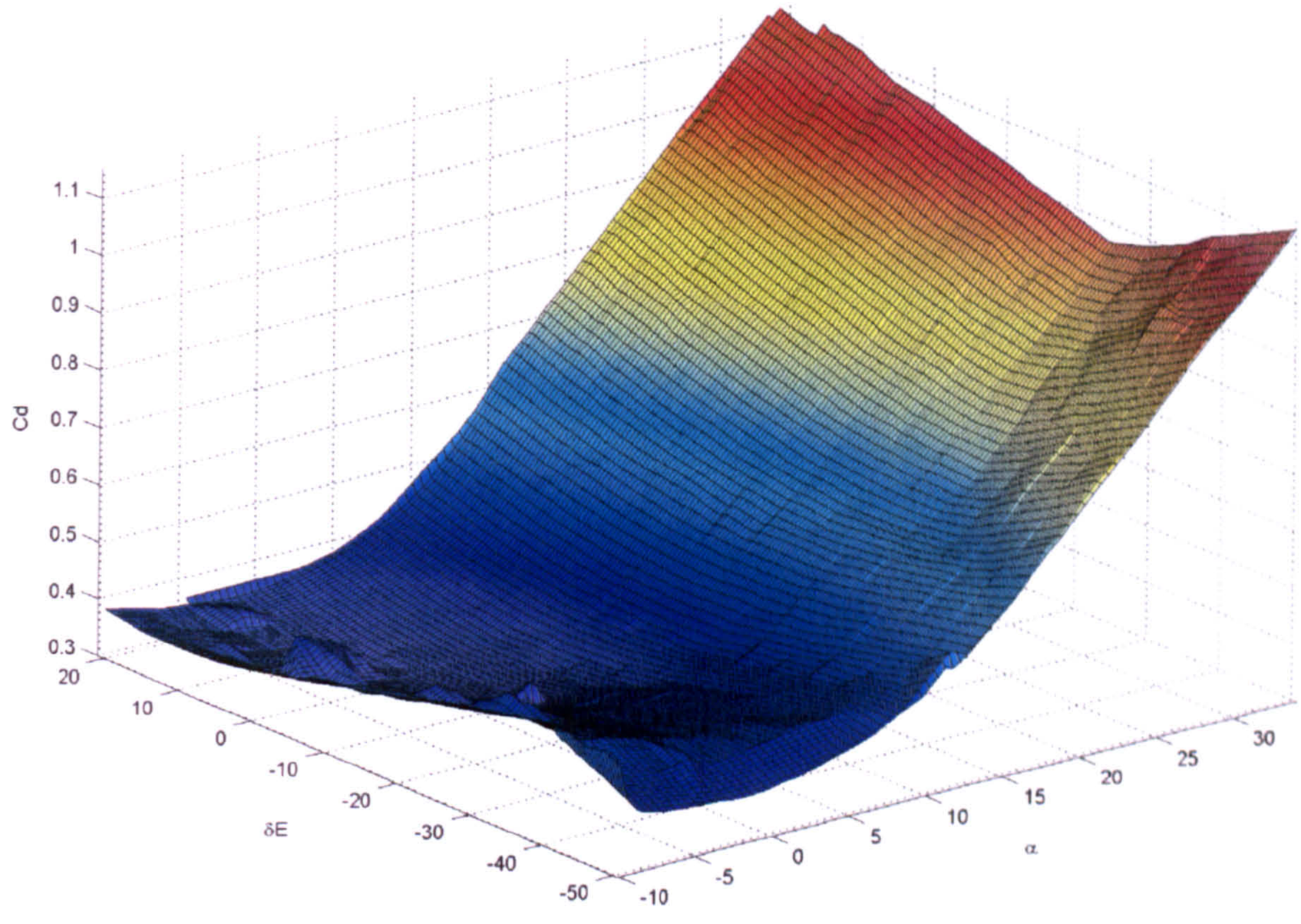


Figure A.5: $C_d(\alpha, \delta_e)$ - 20m/s.

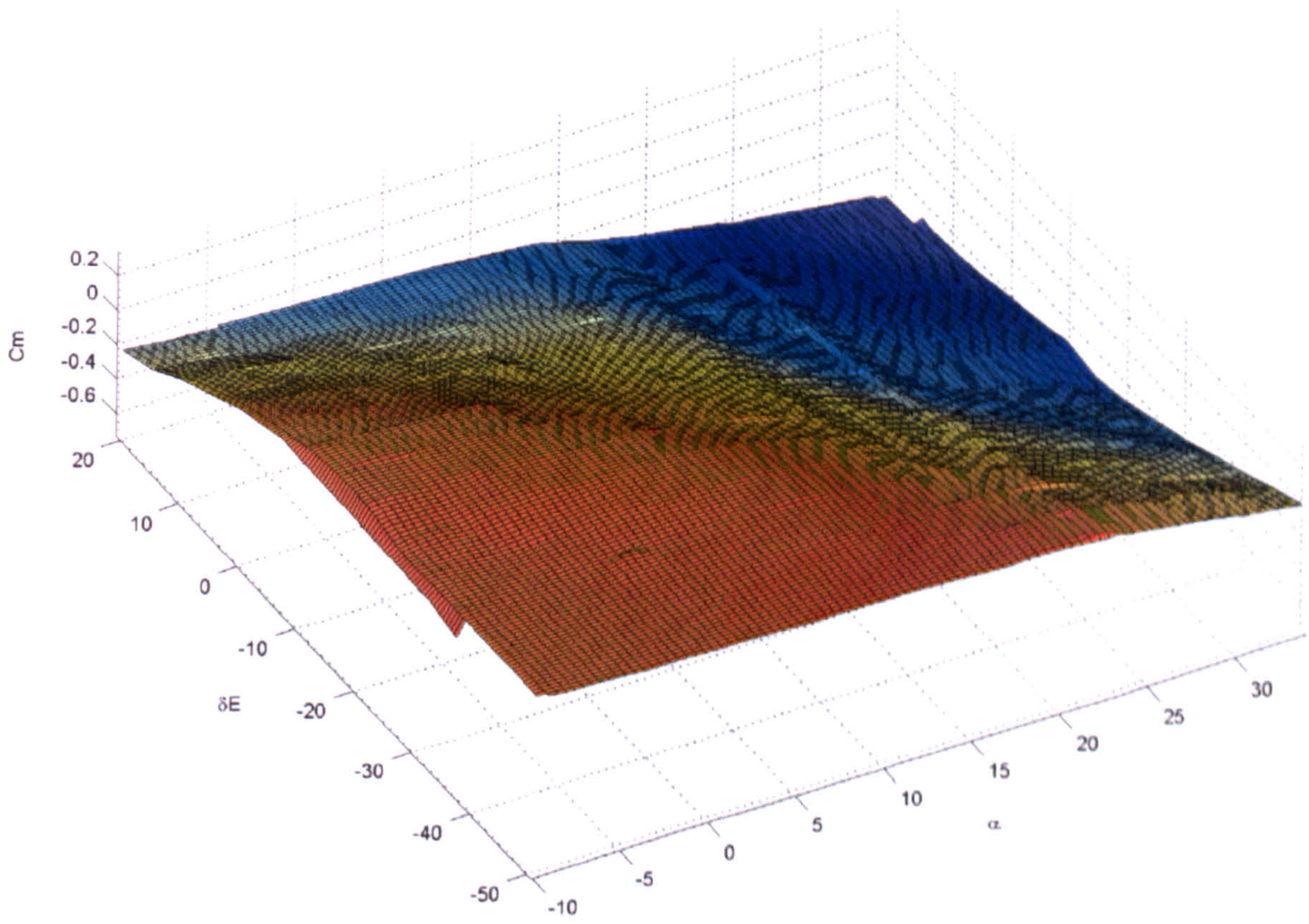


Figure A.6: $C_m(\alpha, \delta_e)$ - 20m/s.

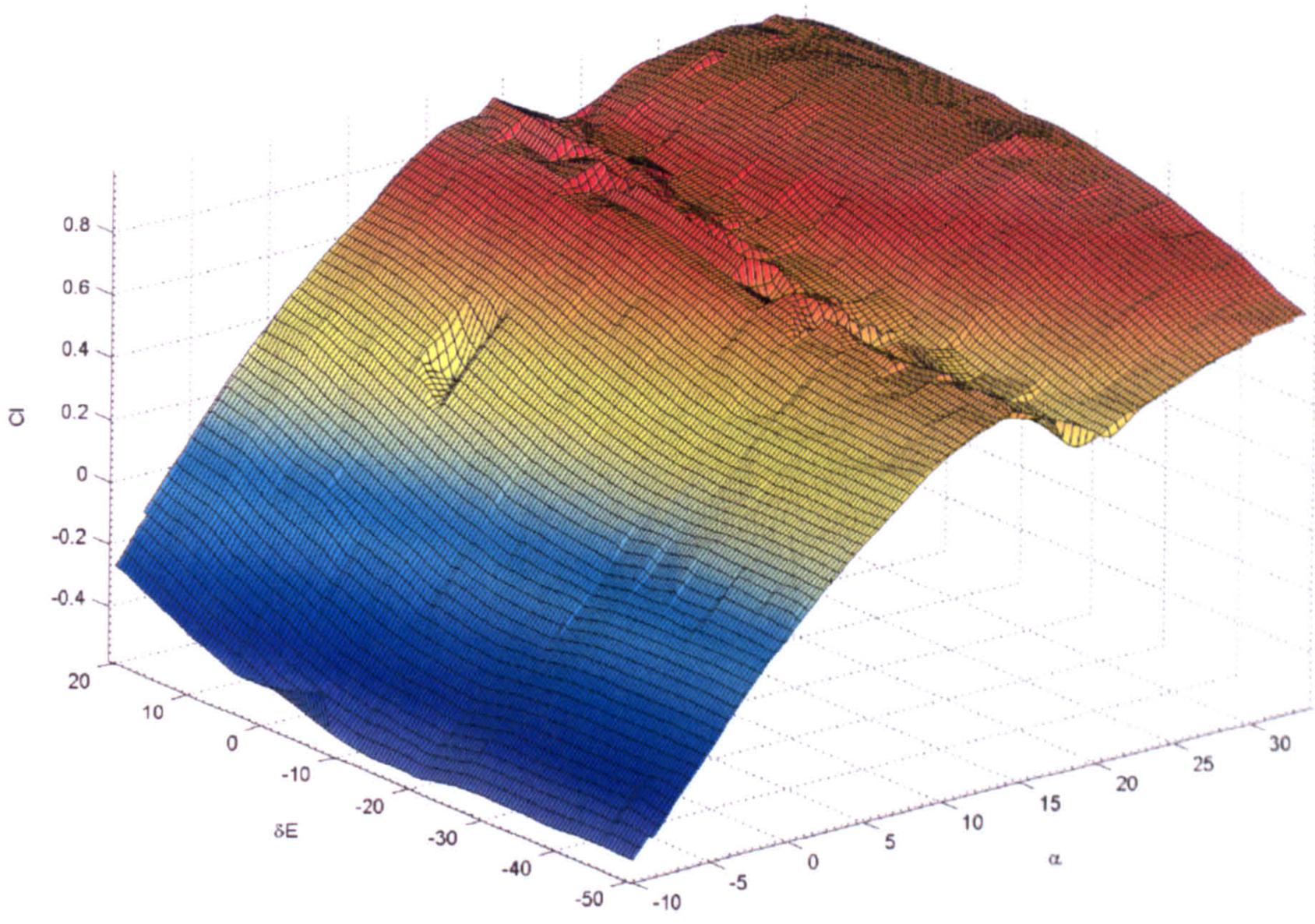


Figure A.7: $C_l(\alpha, \delta_e)$ - 25m/s.

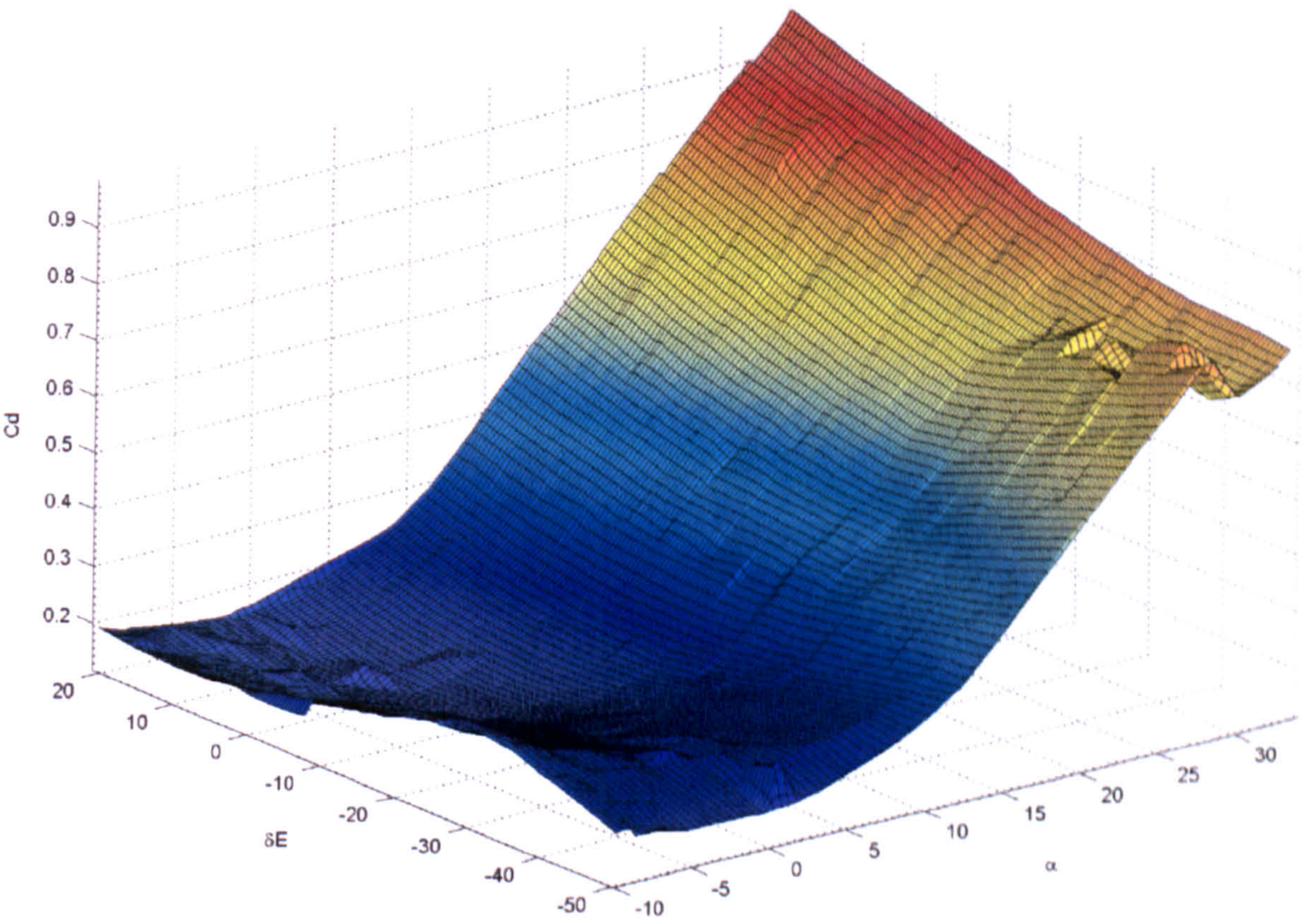


Figure A.8: $C_d(\alpha, \delta_e)$ - 25m/s.

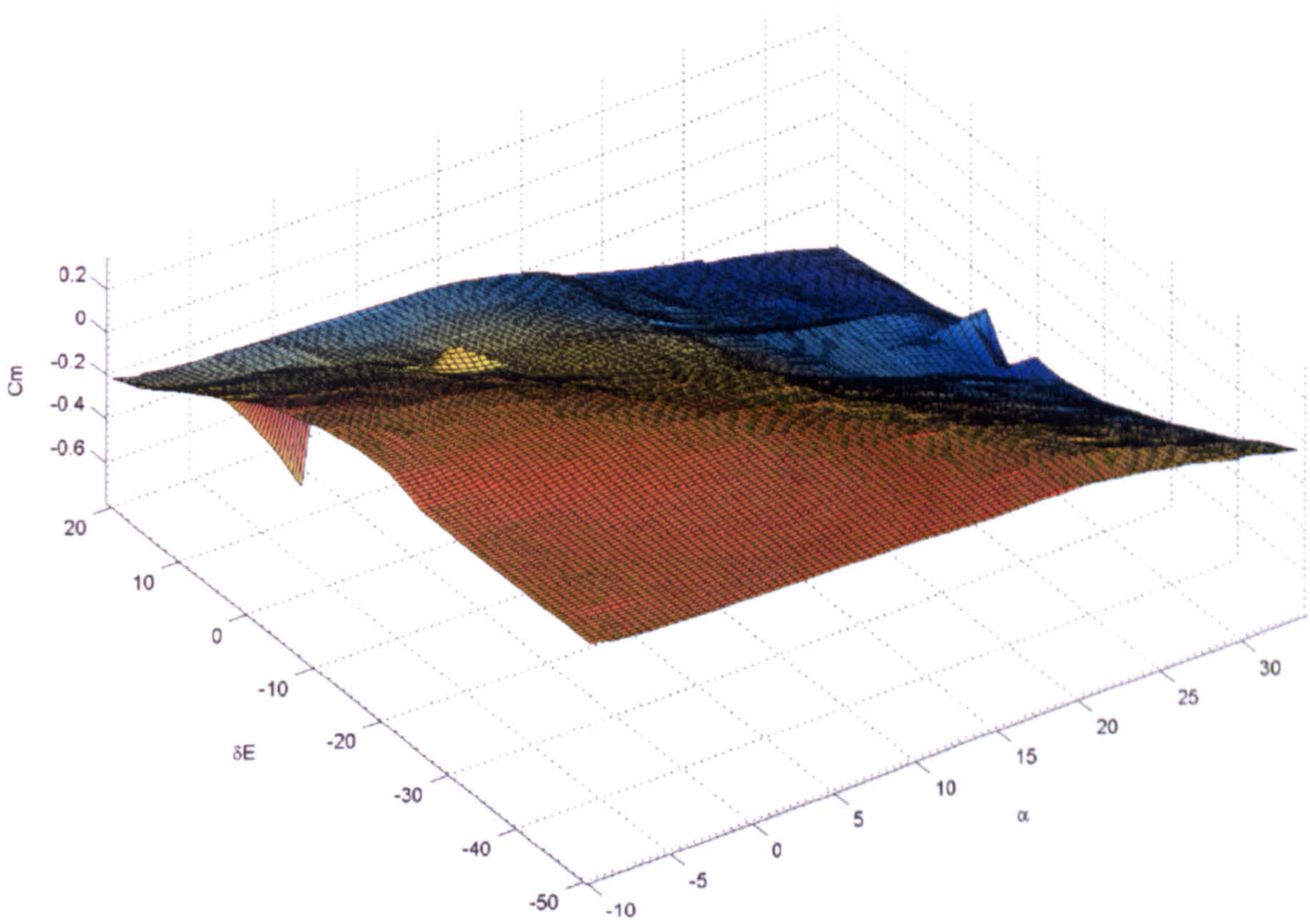


Figure A.9: $C_m(\alpha, \delta_e)$ - 25m/s.

# Appendix B

# Open-Jet Tunnel Turbulence

## Open-Jet Tunnel Turbulence

To quantify the level of turbulence in the open-jet tunnel, tests were conducted using a single component hot-wire anemometer. Turbulence levels were measured at 27 locations in the flow before and after the addition of flow-straightening tabs around the jet opening and a wire mesh in the settling chamber. The results are shown in Figures B.1 to B.3, where flow-wise turbulence levels are plotted against tunnel position for a tunnel speed of 20m/s. Turbulence levels were calculated according to (3.2).

The addition of flow-smoothing tabs reduces the turbulence level in the centre of the tunnel by approximately 0.4% overall, however, the turbulence levels towards the back and at the sides of the tunnel (away from the outlet) are greatly increased (Figure B.2). This effectively reduces the working section of the tunnel. While this is not a problem for non-translating tests, there is a significant change in turbulence level away from the centre of the jet outlet. This may cause problems when testing with the pendulum strut in fore/aft and, most significantly, lateral degrees-of-freedom. Note also the apparent swirl in the flow, visible from the asymmetric nature of the flow at the top and bottom of the tunnel in Figure B.2.

The turbulence-reducing wire mesh can be seen to reduce turbulence levels in the centre of the tunnel by a further 0.5% to approximately 1.2% (Figure B.3). This seems to have increased the level of turbulence in some positions around the outside of the working

section. The maximum speed of the tunnel has now been reduced to approximately 30m/s by the inclusion of the screen, due to the relatively high velocity of the flow in the settling chamber (the contraction ratio is little over 4:1). This did not affect subsequent tests, as all tests were performed at 20m/s.

Figure B.4 shows a comparison of the turbulence levels in the centre of the working section before and after the addition of the flow smoothing devices.

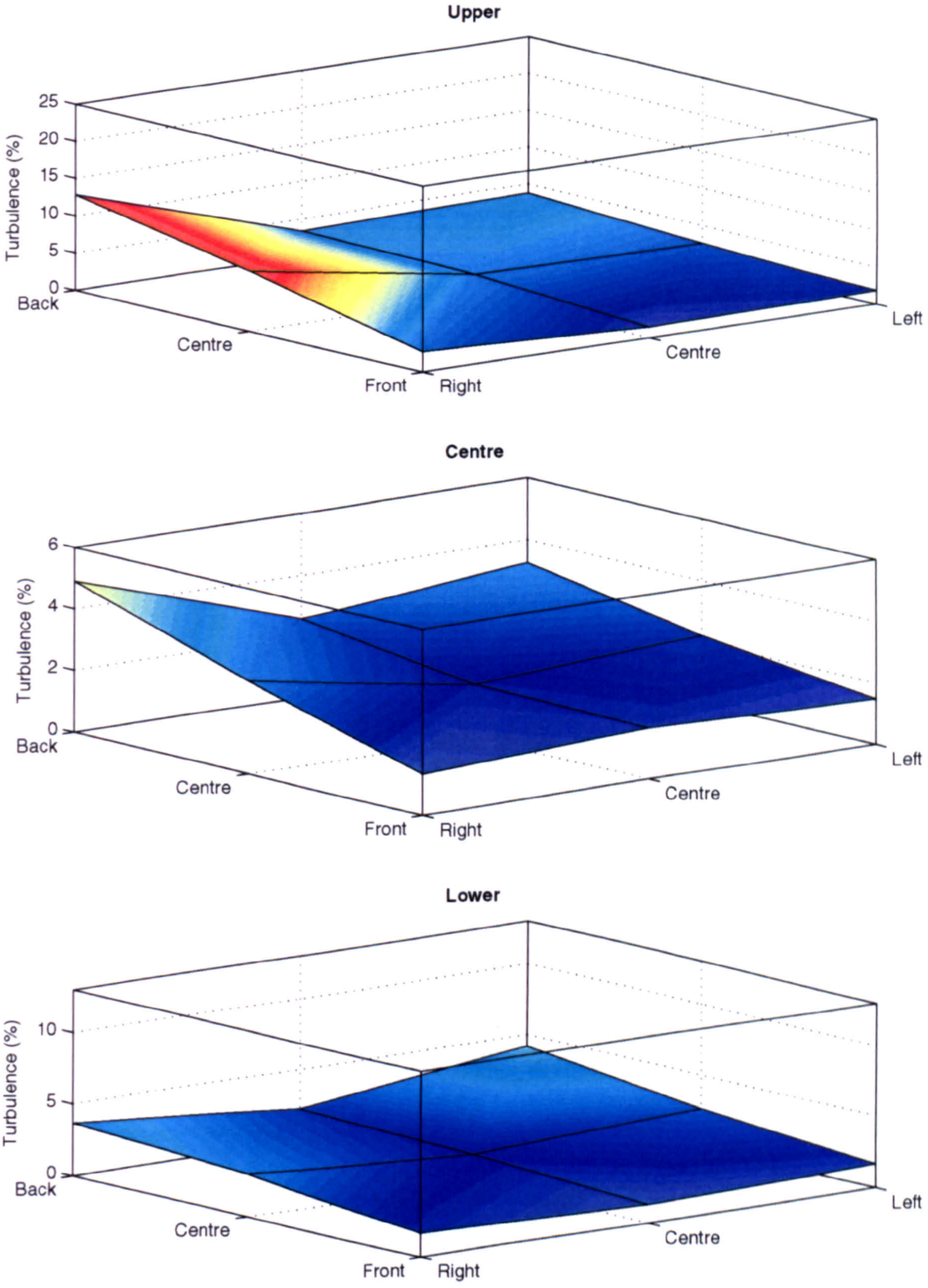


Figure B.1: Open-jet tunnel turbulence levels before flow-smoothing improvements (20m/s).

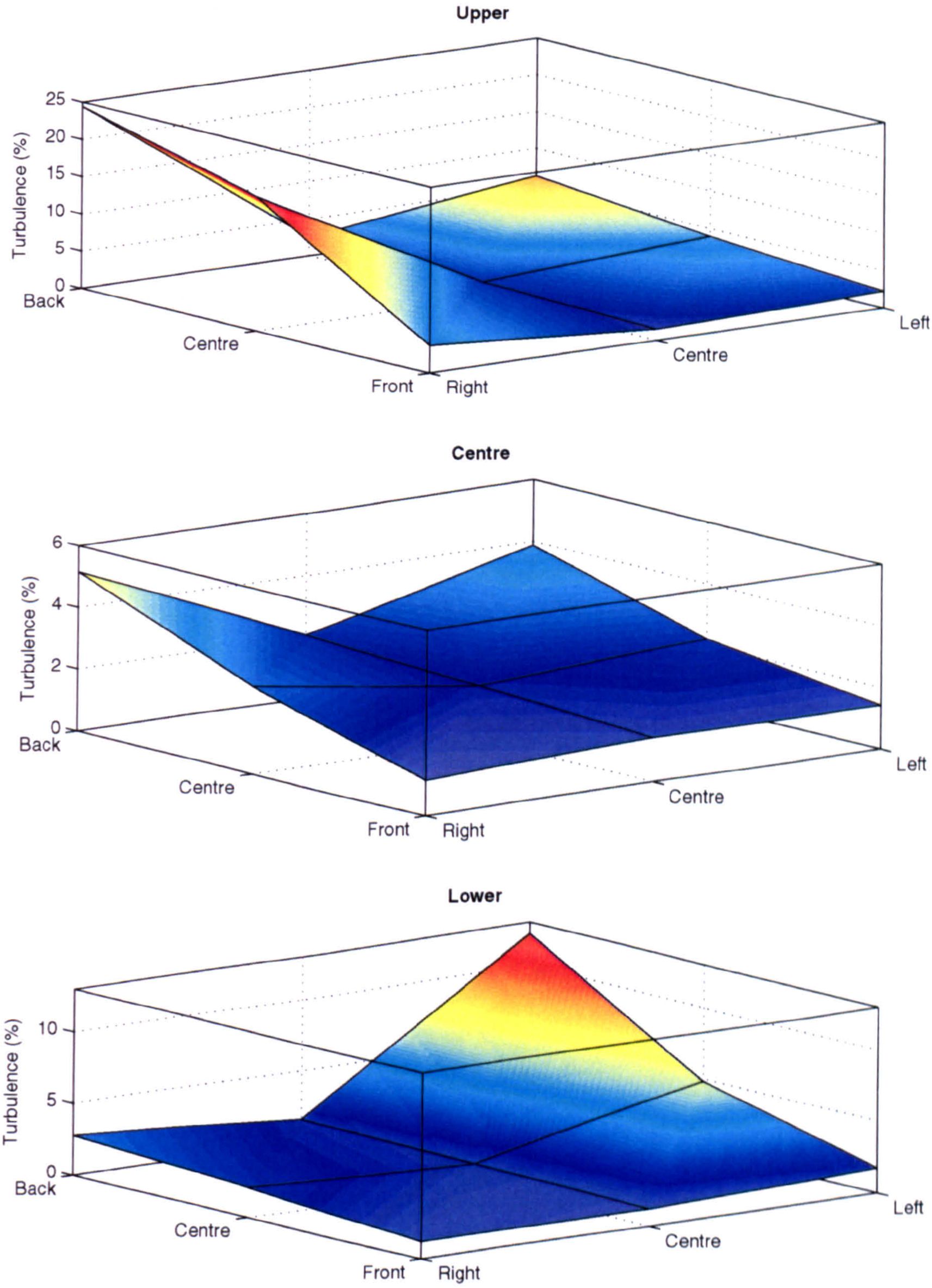


Figure B.2: Open-jet tunnel turbulence levels after the addition of the flow-smoothing tabs (20m/s).

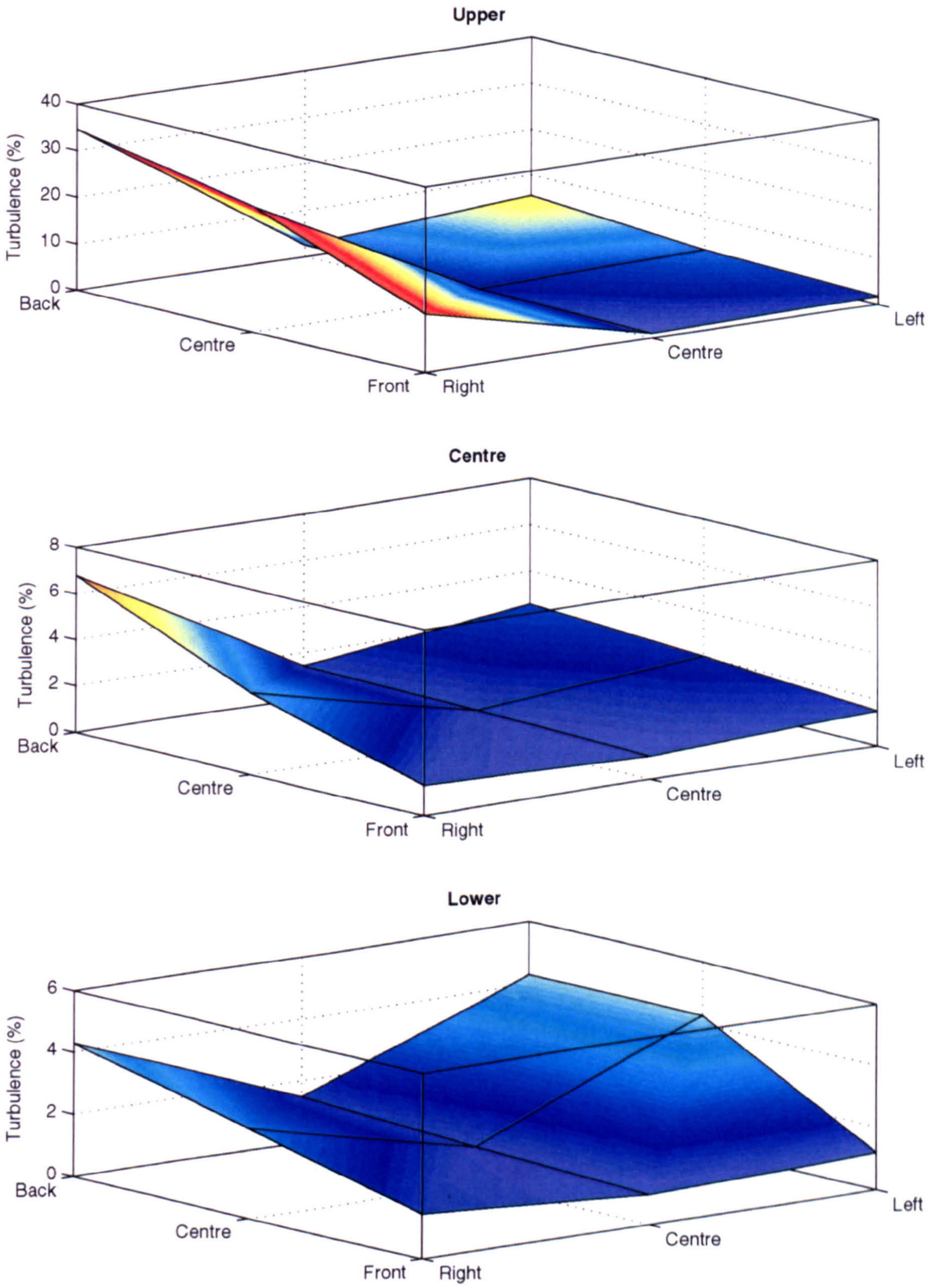


Figure B.3: Open-jet tunnel turbulence levels with flow-smoothing tabs and settling chamber wire mesh (20m/s).

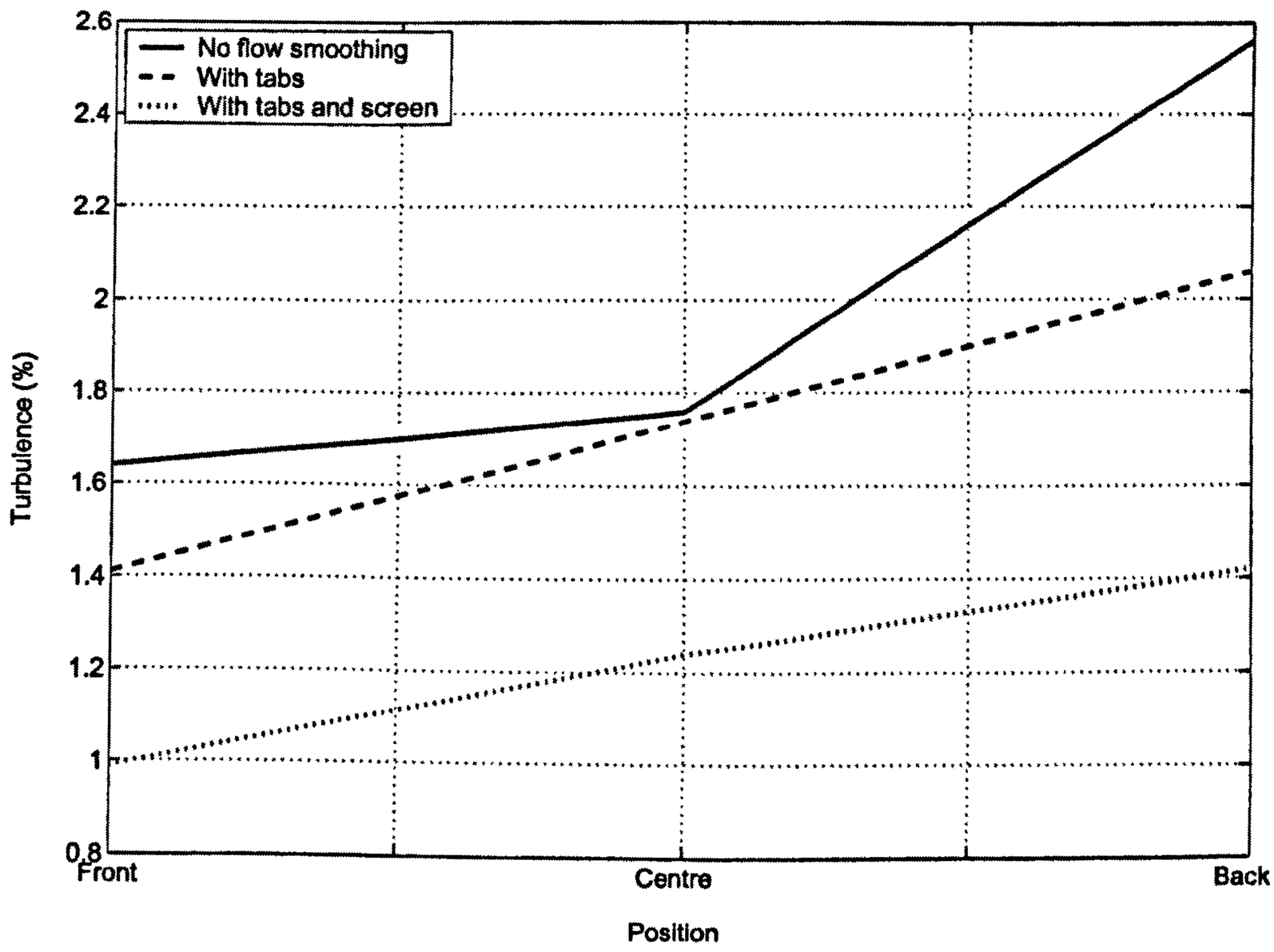


Figure B.4: Turbulence levels in the centre of the open-jet tunnel (20m/s).